Technical Report
TR-20-12
December 2020

Post-closure safety for the final repository for spent nuclear fuel at Forsmark

Climate and climate-related issues, PSAR version

SVENSK KÄRNBRÄNSLEHANTERING AB

SWEDISH NUCLEAR FUEL
AND WASTE MANAGEMENT CO

Box 3091, SE-169 03 Solna
Phone +46 8 459 84 00
skb.se

ISSN 1404-0344
SKB TR-20-12
ID 1699830

December 2020
Updated 2022-12

Post-closure safety for the final repository for spent nuclear fuel at Forsmark

Climate and climate-related issues, PSAR version

Svensk Kärnbränslehantering AB

Keywords: Climate, Glacial, Ice-sheet, Periglacial, Permafrost, Sea-level, Global warming, Safety assessment, PSAR, Spent nuclear fuel repository, KBS-3.

Update notice

The original report, dated December 2020, was found to contain both factual and editorial errors which have been corrected in this updated version. The corrected factual errors are presented below.

Updated 2022-12

Location	Original text	Corrected text
Page 401, Appendix G, second paragraph, line 10	...40–89 m ka^{-1},	...40–89 mm ka^{-1},

Updated 2021-02

Location	Original text	Corrected text
Page 46, first paragraph	...Näslund et al. 2003).	...Näslund et al. 2003, Staiger et al. 2005, Patton et al. 2016).
Page 111, last paragraph, line 9 Page 199, second paragraph, line 6 Page 200, Table 4-4 heading, line 7 Page 298, Table 5-21 heading, line 11 Page 298, first paragraph line 5 Page 300, last paragraph, line 3	...host rock has been updated −6 °C	...host rock has been updated to −6 °C
Page 143, last paragraph, line 6	...erosion at the location…	...erosion during glacial cycles at the location…
Page 150, fourth paragraph, line 1	The estimates of low future erosion at…	The estimates of low future denudation at…
Page 152, bullet list, bullet 3	The corresponding past range of…	The corresponding full past range of…
Page 181, paragraph 5, last line	...Helmens (2009).	…Helmens (2009), Helmens (2019), Scheck and Wohlfarth (2019).
Page 182, paragraph 6, line 3	...the interglacial stages…	.. the interstadial stages...
Page 202, Table 4-5, row 4	Submerged conditions	Submerged conditions (with simultaneous prevailing temperate- or periglacial climate domains)
Page 248, Table 5-10, heading, line 9	...probability, respectively).	...probability of exceedance, respectively).
Page 381, third paragraph, last line	...climate case (Section 5.2.3).	...climate case (Section 5.2.3). It should be noted, however, that the analysis in this Appendix also supports the continued use of the historical relative sea-level curve developed for the previous safety assessments SR-Site and SR-PSU.

Contents

1 Introduction

1.1 Purpose of the report

This document presents information on climate and climate-related issues relevant for post-closure safety of a KBS-3 repository for spent nuclear fuel. It supports the PSAR (Preliminary Safety Assessment Report) version of the post-closure safety assessment for the spent nuclear fuel repository at Forsmark. Parts of the report are relevant also for other purposes, such as for the construction planning of the repository.

The report documents current scientific knowledge on climate and climate-related conditions, relevant to the post-closure safety of a KBS-3 repository, to a level required for an adequate treatment in the PSAR. The report also presents several dedicated studies on climate and selected climate-related processes of relevance for the assessment of long-term repository safety. Based on this information, the report presents several possible future climate developments for Forsmark, the site selected for building a repository for spent nuclear fuel in Sweden (Figure 1-1). The presented climate developments are used as basis for the selection and analysis of PSAR post-closure scenarios in a main report (**Post-closure safety report**) in a similar way as was done in the main report of the SR-Site assessment (SKB 2011). The present report is based on research conducted and published by SKB as well as on research reported in the general scientific literature.

1.2 Strategy for managing climate-related issues in safety assessments

1.2.1 Climate and climate-related changes

Climate-related changes such as the development of permafrost and ice-sheets and variations in relative sea-level are the most important naturally occurring external factors affecting a repository for spent nuclear fuel in a time perspective up to hundreds of thousands of years. Most of the processes occurring in the biosphere and geosphere are likely to be affected by climate and climate-related changes in one way or another.

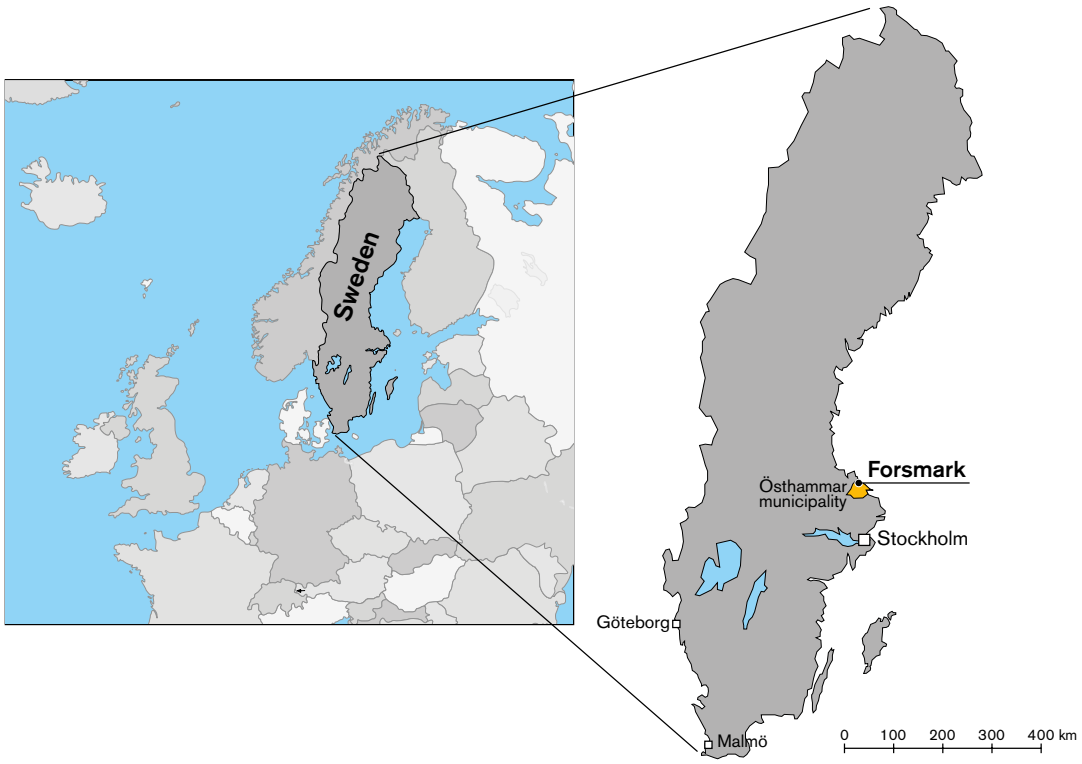

Figure 1-1. *Location map.*

Over the past 2.5 million years, Fennoscandia has experienced several cycles of glaciation (e.g. Ehlers and Gibbard 2004). Cold periods that include ice-sheets gradually growing to maximum extents are known as glacials. Intervening periods with warm climate, when the ice-sheets have extents similar to that of the present day, are called interglacials. A glacial cycle consists of a glacial and an interglacial. Within the glacial periods, warmer interstadial periods occur, as well as cool stadial periods. The alternation between glacials and interglacials, as well as between stadials and interstadials, is primarily driven by changes in the latitudinal and seasonal distribution of incoming solar radiation (insolation) due to variations in Earth's orbital configuration (Berger 1978, Berger and Loutre 1991, Laskar et al. 2004, 2011). The shifting between glacials and interglacials is depicted for instance in the variation of the content of the heavy oxygen isotope, ^{18}O, in deep-sea sediments (Lisiecki and Raymo 2005), which reflects both the deep-sea temperature and the volume of water that has been bound in land-based ice-sheets and glaciers globally, see Figure 1-2.

Figure 1-2 shows that over the last 700000 years (700 ka) (i.e. during the Middle and Late Pleistocene stages), glacial–interglacial cycles of about 100 ka duration have dominated global climate variation. The time frame of such a Late Quaternary glacial–interglacial cycle, around 100 ka, is similar to the time it takes for the radioactivity in the spent fuel to decay to levels comparable to the activity in the natural uranium that was used to manufacture the fuel, see the **Post-closure safety report**. The time-scale of a safety assessment for a final repository for spent nuclear fuel is one million years (1 Ma). The 100 ka timescale, corresponding to a first future glacial cycle, forms a basis for the analysis of repository safety. For the remainder of the assessment period, this glacial cycle is assumed to be repeated to cover the full 1 Ma period. Alternative developments over the initial 100 ka, including, for instance, periods of anthropogenic global warming, are also analysed.

In very long-time perspectives, several millions of years, geological processes like plate tectonic movements and uplift or downwarping of the Earth's crust, additional to crustal displacements due to glacial loading and unloading, will affect both the Earth climate system and the repository for spent nuclear fuel. However, the PSAR addresses timescales of up to one million years (see the **Post-closure safety report**), and therefore these geological processes are not included in the safety assessment.

1.2.2 Impact on repository performance and safety

Climate changes, permafrost development and the growth and decay of ice-sheets will alter not only surface but also subsurface conditions. Freezing of groundwater, the presence of ice-sheets, and changes in relative sea-level will change permeability, water turnover, groundwater pressure, groundwater flow and chemical composition. The ice load will alter rock stresses during different phases of a glaciation. This will, in turn, change bedrock permeability and as ice-sheets melts away, a combination of large horizontal stresses and high pore water pressures may cause glacially induced faulting. In general, the integrated effects of the continuous evolution of climate-related conditions need to be considered, but there are also several more specific phenomena of importance for repository safety that require special attention. Based on the results of earlier and the present safety assessment, these include:

- The maximum hydrostatic pressure occurring at repository depth under glacial conditions.
- The maximum permafrost and ground-freezing depth.
- The possible penetration of oxygen-rich groundwater to repository depth under glacial conditions.
- The possible penetration of dilute groundwaters to repository depth under glacial and temperate conditions, potentially causing erosion of buffer and backfill.
- The potential for glacially induced faulting.

The climate-related processes addressed in the PSAR and their possible impacts on the repository safety are summarized in Table 1-1. In addition, the climate cases describing the impact of these climate-related processes are also indicated. The handling of these cases in the PSAR post-closure scenarios is described in the **Post-closure safety report**.

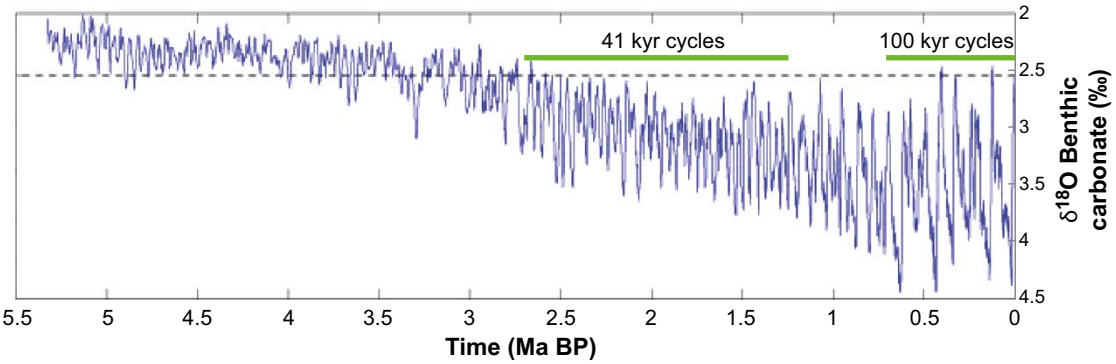

Figure 1-2. *Variations of $\delta^{18}O$ in deep-sea sediments over the last 5.5 million years (Lisiecki and Raymo 2005). High $\delta^{18}O$ values indicate large global ice volume and low sea water temperature, i.e. colder climate conditions, whereas low $\delta^{18}O$ values indicate the opposite. The last 700 ka have been dominated by 100 ka long glacial cycles. Modified from a figure by R A Rohde based on Lisiecki and Raymo (2005).*

Table 1-1. Climate-related processes addressed in the PSAR. The table gives an overview of the processes considered and associated possible impacts on repository safety. The climate cases that describe the impact of these climate-related processes are also indicated.

Climate-related process (Section of this report)	Possible impact on repository safety	Climate cases which describe climatic conditions necessary for the impact of the climate-related process
Ice-sheet dynamics (3.1)	High hydrostatic pressures affecting canister integrity. Groundwater flow.	*Weichselian glacial cycle* *Maximum ice thickness*
Glacial hydrology (3.2)	Groundwater flow and chemistry.	*Weichselian glacial cycle*
Isostatic adjustment and relative sea-level changes (3.3)	Groundwater flow. Drilling of wells in vicinity of the repository.	*Weichselian glacial cycle* *Global warming* *Extended global warming*
Permafrost (3.4)	Lowering of bedrock temperatures causing freezing of bentonite barriers and backfill.	*Weichselian glacial cycle* *Severe permafrost*
Surface denudation (3.5)	Lowering of the bedrock surface through erosion and weathering resulting in the repository being located closer to the surface and permafrost reaching closer to repository after deglaciation.	*Weichselian glacial cycle* *Extended ice-sheet duration* *Severe permafrost*

1.2.3 Strategy for managing long-term evolution of climate-related processes

Definition of climate change and climate domains

There are various definitions of *climate change*. In the present report, climate change is defined according to the definition by the Intergovernmental Panel on Climate Change (IPCC), namely as "any change in climate over time whether due to natural variability or as a result of human activity" (IPCC 2001). This differs from the definition used by United Nation's Framework Convention on Climate Change (UNFCCC) that defines climate change as "a change of climate that is attributed directly or indirectly to human activity that alters the composition of the global atmosphere, and that is in addition to natural climate variability over comparable time periods". Since climate may change due to both natural variability and to anthropogenic influences, the definition of climate change in the PSAR follows the one of IPCC.

From a safety assessment point of view, it is not possible to predict a single climate evolution in a 100 ka time perspective with enough confidence for a safety assessment. However, based on knowledge of climate variations in the past and on inferred future climate change, the extremes within

which the climate of Sweden may vary can be estimated with reasonable confidence, also within this long timeframe. Within these limits, characteristic climate-related conditions of importance for repository safety can be identified. The conceivable climate-related conditions can be represented as *climate-driven process domains* (Boulton et al. 2001a) where such a domain is defined as "a climatically determined environment in which a set of characteristic processes of importance for repository safety appear". In the following parts of the report these climate-driven process domains are referred to as *climate domains.* The identified climate domains of relevance are denominated:

- The temperate climate domain.
- The periglacial climate domain.
- The glacial climate domain.

The purpose of identifying climate domains is to create a framework for the assessment of issues of importance for repository safety associated with climatically determined environments that may occur in Sweden. If a repository for spent nuclear fuel fulfils the safety requirements for plausible climate developments, including the transitions between climate domains, then the uncertainty regarding the climate domains more precise extent in time and space is of less importance.

The *temperate climate domain* is defined as regions without permafrost or presence of ice-sheets. It is dominated by a temperate climate in a broad sense, with cold winters and either cold or warm summers. Precipitation may fall at any time of the year. The precipitation falls either as rain or snow. The temperate climate domain has the warmest climate of the three climate domains. Within the temperate climate domain, a site may also at times be submerged by the sea. Climates dominated by global warming are also included in the temperate climate domain.

The term periglacial is commonly used for a range of cold, but non-glacial, processes. In the periglacial environment, permafrost is a central, but not defining, element (French 2007). However, for the present assessment, the *periglacial climate domain* is defined strictly as regions that contain permafrost. Furthermore, the periglacial climate domain is a cold region but without the presence of an ice-sheet. In this climate domain, permafrost occurs either in sporadic (less than 50 % spatial coverage), discontinuous (between 50 and 90 % coverage), or continuous form (more than 90 % coverage). Although true for most of the time, regions belonging to the periglacial climate domain are not necessarily the same as regions with a climate that supports permafrost growth. For example, at the end of a period with periglacial climate domain the climate may be relatively warm, not building or even supporting the presence of permafrost. Instead, permafrost may be diminishing. However, as long as permafrost is present, the region is defined as belonging to the periglacial climate domain, regardless of the prevailing temperature at the ground surface. This way of defining the climate domain is used because the presence of permafrost is more important for the safety function of the repository than the actual temperature at the ground surface. In general, the periglacial climate domain has a climate colder than the temperate climate domain and warmer than the glacial climate domain. Precipitation may fall either as snow or rain. Within the periglacial climate domain, a site may also at times be submerged by the sea.

The *glacial climate domain* is defined as regions that are covered by glaciers or ice-sheets. Within the glacial climate domain, the glacier or ice-sheet may in some cases be underlain by sub-glacial permafrost. In line with the definition of the periglacial climate domain, areas belonging to the glacial climate domain may not necessarily at all times have a climate that supports the presence of ice-sheets. However, in general, the glacial climate domain has the coldest climate of the three climate domains. Precipitation normally falls as snow in this climate domain.

It is likely that all three climate domains will appear repeatedly during the one-million-year assessment period, i.e. any reasonable climate evolution will have to address them, and transitions between them.

Reference glacial cycle, climate cases and safety assessment scenarios

The climate domains are first used to describe a *reference glacial cycle* for the next 120 ka, comprising a repetition of conditions reconstructed for the last glacial cycle (Section 4.5). The *reference glacial cycle* should not be seen as a prediction of a future climate development at Forsmark, but as *one example* of a conceivable future evolution that covers climate-related conditions and sequences, with glacial conditions, that could be expected in a 100 ka time perspective. Furthermore, using a *reference*

glacial cycle based on the last glacial cycle does not mean that glacial- and permafrost processes are regarded as more probable than processes related to warm climates for e.g. the coming 100 ka. The *reference glacial cycle* is supplemented by a number of additional climate cases that describe alternative possible future developments of climate and climate-related processes at Forsmark (Figure 1-3), including warmer and colder climates. The selection and description of the additional climate cases are based on i) knowledge on past changes in climate and environmental parameters, ii) anticipated future climate change affected by anthropogenic activities, and iii) knowledge as to which processes are of importance for repository safety. A large part of the information used to select the climate cases has been obtained from previous safety assessments. In the PSAR, six future climate cases are described, including the *reference glacial cycle climate case*, see Figure 1-3 and Section 4.5 and Chapter 5. For a summary of how the climate and climate-related processes develop in the six climate cases, see Section 4.1. For a description of the rationale for using a reference glacial cycle based on a reconstruction of conditions for the last glacial cycle, see Section 4.2.

The six climate cases are in turn used as basis for the construction of safety assessment scenarios (see the **Post-closure safety report**). In the safety assessment, the *reference glacial cycle climate case* is used to construct a *main scenario*, aiming at describing a reasonable evolution of the repository system given the timing and lengths of periods with different climate domains as derived from the *reference glacial cycle climate case*. There are two variants of the main scenario, i) a *base case,* comprising the reconstruction of climate and climate-related processes as described in the *reference glacial cycle climate case*, i.e. the repetition of reconstructed last glacial cycle conditions, and ii) a *global warming variant,* defined from the *global warming climate case*, see Figure 1-3. The base case serves as one example of the evolution of climate, climate-related processes and the repository for a glacial cycle dominated by natural climate change, i.e. a development not affected by anthropogenically caused global warming. The base case is complemented by the global warming variant (Figure 1-3), where the inferred current anthropogenic influence on climate is taken into account.

Following the safety assessment analysis of the main scenario, several *additional scenarios* of importance for repository safety are selected (Figure 1-3). The scenario selection is based on the evolution in the main scenario and on an understanding of repository safety, see the **Post-closure safety report**. The latter is expressed through various safety functions and safety function indicators, used to make a structured selection of additional scenarios. Detailed information about the safety function indicators and how the scenario selections are made is found in the **Post-closure safety report**. Following the scenario selection, the additional scenarios are analysed using the information from the associated climate cases (Figure 1-3). The additional scenarios essentially address relevant situations not covered by the main scenario.

For example, for the glacial climate domain the maximum possible ice-sheet thickness is one parameter of interest for the analysis of hydrostatic pressure at repository depth. In the *base case of the main scenario*, the development of ice-sheet thickness comes from a reconstruction of the Fennoscandian ice-sheet during the last glacial cycle (Section 3.1.4), whereas in an *additional scenario* the effects of ice-sheet thicknesses greater than those during the last glacial cycle are analysed using information from the *maximum ice-sheet thickness climate case* (Section 5.4), see Figure 1-3. In this way, the main scenario describes a plausible evolution of ice-sheet thickness, and the additional scenario describes relevant variations of this evolution.

It is important to include the climate domains and sequences that have the greatest impact on repository safety, which typically includes changes related to glacial conditions. It is also important to include sequences yielding the peak risk during the assessment period. Based on results of earlier analyses, the highest risks (i.e. relating to radiogenic exposure to humans) are likely to occur during periods of temperate climate. Typical situations are i) a terrestrial system that has accumulated radionuclide releases over a long time, possibly at early stages of its evolution, in sea or lake sediments that subsequently are exposed and used for agriculture, and ii) a well intruding into the host rock and used for domestic purposes. In addition, periods of periglacial climate domain need to be considered, where permafrost conditions change transport efficiency, exposure pathways and accumulation processes, and also constrains both land-use and uses of well water.

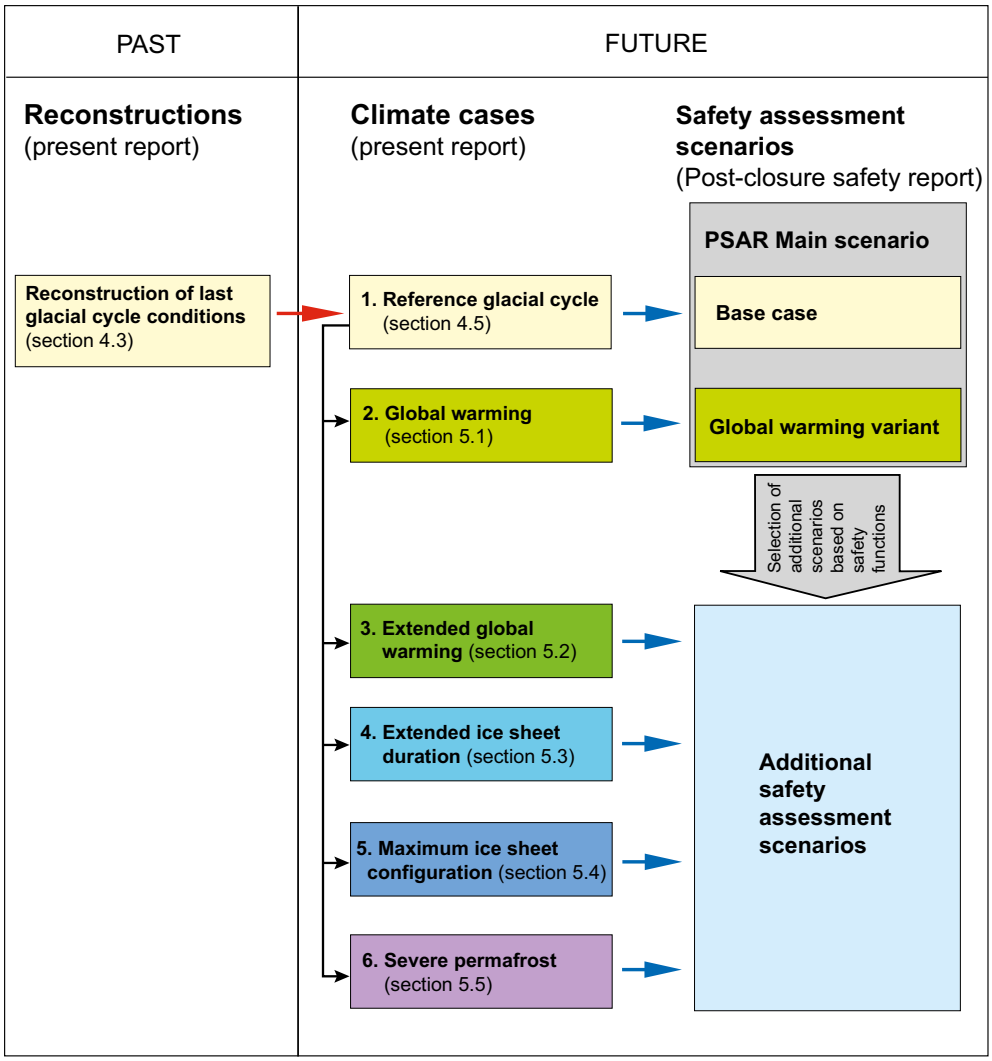

Figure 1-3. *Relationship between the reconstruction of last glacial cycle conditions, the reference glacial cycle climate case, the additional climate cases, and the corresponding PSAR post-closure scenarios. The red arrow indicates the choice of repeating the reconstructed last glacial cycle conditions for a future reference glacial cycle. The black arrows indicate modifications made to the reference glacial cycle climate case to construct additional future climate cases to obtain a comprehensive coverage of possible climate developments of relevance for post-closure safety. Blue arrows show which climate cases have been used for the analysis of which safety assessment scenario. The figure also shows in which sections the climate cases are described in the present report. For information on the PSAR post-closure scenario selection (grey arrow) see the text and the Post-closure safety report.*

Timescales

Climate studies covering long periods of time, several millennia, either use a calendar timescale (BC/AD) or a timescale related to the present (before present/after present or BP/AP). The present report covers processes acting on timescales shorter than 100 years as well as processes acting over glacial cycle timescales, i.e. 100 ka and longer. Therefore, depending on the specific processes under discussion, the present report either use the BC/AD timescale (e.g. for analysis of relative sea-level changes on shorter timescales) or the BP/AP timescale for results related to the full glacial cycle time frame. The same dual approach is used in other studies covering similar topics (e.g. the future sea-level projection study by Clark et al. 2016). Having two timescales in the same report introduces a risk for mistakes. To minimize the risk of such mistakes, the present study reports both timescales in key figure captions and in tables.

1.3 Structure of the report

1.3.1 Main references

Table 1-2 lists the main references and defines their abbreviations by which they are identified in the text. Abbreviated names are written in bold font throughout the report.

Table 1-2. Main references for the PSAR and their abbreviations used in the present report. Two of the reports will not be updated since SR-Site and hence their SR-Site references are provided.

Abbreviation used when referenced in this report	Full reference, as given in the reference list
Biosphere synthesis report	**Biosphere synthesis report, 2010.** Biosphere analyses for the safety assessment SR-Site – synthesis and summary of results. SKB TR-10-09, Svensk Kärnbränslehantering AB.
Data report	**Data report, 2022.** Post-closure safety for the final repository for spent nuclear fuel at Forsmark – Data report, PSAR version. SKB TR-21-06, Svensk Kärnbränslehantering AB.
FEP report	**FEP report, 2010.** FEP report for the safety assessment SR-Site. SKB TR-10-45, Svensk Kärnbränslehantering AB.
Geosphere process report	**Geosphere process report, 2022.** Geosphere process report for the final repository for spent nuclear fuel at Forsmark – Geosphere process report, PSAR version. SKB TR-21-04, Svensk Kärnbränslehantering AB.
Model summary report	**Model summary report, 2022.** Post-closure safety for the final repository for spent nuclear fuel at Forsmark – Model summary report, PSAR version. SKB TR-21-05, Svensk Kärnbränslehantering AB.
Post-closure safety report	**Post-closure safety report, 2022.** Post-closure safety for the final repository for spent nuclear fuel at Forsmark – PSAR version. SKB TR-21-01, Svensk Kärnbränslehantering AB.

1.3.2 Overall report structure and authors

Following this introductory chapter, the present report includes four main chapters:

- Chapter 2: an overview of the present climate in Sweden and Forsmark.
- Chapter 3: identification and discussion of climate and climate-related issues, including reconstructions of the identified variables for the last glacial cycle.
- Chapter 4: a description of climate and climate-related conditions for the safety assessment reference glacial cycle climate case.
- Chapter 5: a description of climate and climate-related conditions for the complementary climate cases.

In Chapter 3, climate-related issues relevant for the post-closure safety of a KBS-3 repository are documented to a level required for an adequate treatment in the safety assessment. Subsequently, in Chapter 4, an evolution for a 120 ka period is presented, including discussions of identified climate-related issues of importance for repository safety.

In Chapter 3 there are five sections that, in detail, describe the climate-related phenomena within the climate domains that may affect repository safety functions. These sections deal with the general characteristics of ice-sheets, glacial hydrology, changes in relative sea-level, permafrost, and surface denudation, and for most of these phenomena dedicated reconstructions of their development during e.g. the last glacial cycle are presented.

In Chapter 4 the complete reconstruction of last glacial cycle conditions is presented, together with the resulting *reference glacial cycle climate case* over a future 120 ka period. The latter thus includes the identified climate-related issues of importance for repository safety. Chapter 4 also includes a section with examples of last glacial cycle climates, since the range and variability during the last glacial cycle could be expected also for future glacial cycles.

In Chapter 5 the additional climate cases are described, complementing the *reference glacial cycle climate case* described in Chapter 4. For instance, cases of global warming are included here (including detailed information for the Forsmark site), as well as other possible future climate developments.

In this context, a short comment on timescales should be made. Since Chapter 4 (Sections 4.2 to 4.4) mainly deals with reconstructions of climate-related conditions for the last glacial cycle, the timescale runs from 120 ka BP (before present) up to present day. In Section 4.5 and onwards, on the other hand, the reconstructions from the previous parts are used to construct cases of *future* developments of climate-related conditions. Therefore, the timescale used in Section 4.5 and onwards runs from present day to 120 ka AP (after present).

In addition, the present report also includes six appendices:

- Appendix A gives a detailed account of the air- and ground-temperature data sets that are used for the PSAR, for e.g. ice-sheet (Section 3.1.4) and permafrost modelling (Hartikainen et al. 2010). The appendix presents the original data, how the data have been modified to be used in the safety assessment, and a discussion about data uncertainty.
- Appendix B describes in detail the 2D ice-sheet profiles that are used for modelling of groundwater flow under glacial conditions (Vidstrand et al. 2010) and for THM studies (Lönnqvist and Hökmark 2010). The temperature- and ice-sheet profile data sets are also presented in the **Data report**.
- Appendix C contains an account of studies on a hypothetical situation where freezing at repository depth and bentonite buffer erosion are combined, complementing the information in the buffer-freezing scenario in the **Post-closure safety report**.
- Appendix D presents an updated relative sea-level curve for Forsmark ranging from −10.8 to 0 ka AP (i.e. through the present Holocene interglacial), based on the empirical relative sea-level model by Påsse and Daniels (2015).
- Appendix E gives a short description of the Representative Concentration Pathways (RCPs) that were used in the Fifth Assessment Report (AR5) from the IPCC (IPCC 2013a) to define climate mitigation scenarios for the next hundreds of years. These scenarios have been used to broadly define the *global warming climate case* (Section 5.1) and *extended global warming climate case* (Section 5.2).
- Appendix F presents an updated construction of the surface air temperature and precipitation changes at Forsmark until 12000 AD based on the scientific literature and climate modelling. The updated surface air temperature and precipitation curves are used in the *global warming* and *extended global warming climate cases* and are therefore also shown and briefly discussed in Sections 5.1.1 and 5.2.1.
- Appendix G presents the results of total bedrock surface denudation over the coming 100 ka and 1 Ma as calculated by Hall et al. (2019a) for the higher confidence future glacial periods of Lord et al. (2019). The appendix presents individual results for the RCP 2.6, 4.5, 8.5 IPCC emission scenarios and for a 'Natural' scenario without carbon emissions.

As further described in the **Post-closure safety report** and in the **FEP report**, the content of the present report has been audited by comparison with national FEP databases from other assessment projects as compiled by Nuclear Energy Agency (NEA). The models used for the construction of the *reference glacial cycle climate case* and some of the complementary climate cases are documented in the **Model summary report**, while the data produced by the models are presented in the **Data report**. Results from the present climate report are used in the **Post-closure safety report** and in reports supporting the Post-closure safety report.

The present report follows as far as possible the PSAR template for documentation of processes regarded as internal to the repository system. However, the term 'processes' is typically not used in this report, instead the term *issue* has been used. Each issue includes a set of processes together resulting in the behaviour of a system or feature. For instance, ice-sheet dynamics is the result of several climatological, hydrological, and mechanical processes. But as the ice-sheet can be seen as one entity in its interaction with the bed, these processes are jointly accounted for under the 'Ice-sheets' heading (Section 3.1). Given the content of the report, and the aim of following the template for PSAR process reports, there is some necessary repetition of text between some of the chapters and sections.

A list of abbreviations is found in Chapter 6.

The experts involved in describing the background information about the climate system and climate-related issues are listed in Table 1-3. In addition, the sections “Handling in the PSAR” and “Handling of uncertainties in the PSAR” have been produced by Jens-Ove Näslund and Johan Liakka, SKB, in collaboration with the expert that assembled the information on the issue in question.

1.3.3 Structure for description of climate-related issues

In discussing each of the various climate-related issues, the following standardised structure has been adopted.

Overview/general description

Under this heading, a general description of the current knowledge regarding the climate-related issue is given.

Controlling conditions and factors

The external and internal conditions and factors that control each “issue” are discussed. *External* refers to systems that are not part of the described system/feature and that the described system/feature interacts with. For example, for “ice-sheets”, the atmosphere and the bed are external factors and relevant aspects of them are described. *Internal* refers to conditions and factors governing system/feature behaviour and that are generally included in models of the system/feature, e.g. for “ice-sheets” the creep process of ice. The external and internal conditions and factors are those that relate to the described behaviour of the system/feature, e.g. for “ice-sheets” air temperature, geothermal heat flow and ice properties.

Table 1-3. Contributors to individual chapters and sections in the report and present affiliations.

Chapter	Section(s)	Subsection(s)	Author(s)
1. Introduction	1.1	All	Jens-Ove Näslund, SKB
	1.2	1.2.1, 1.2.2	Jens-Ove Näslund, SKB Johan Liakka, SKB
		1.2.3	Jens-Ove Näslund, SKB
	1.3	1.3.1	Johan Liakka, SKB
		1.3.2 and 1.3.3	Jens-Ove Näslund, SKB Johan Liakka, SKB
	1.4, 1.6		Jens-Ove Näslund, SKB Johan Liakka, SKB
	1.5		Jens-Ove Näslund, SKB
2. Present and near-future climate in Sweden and Forsmark	2.1 Present-day climate in Sweden	All	Hans Alexandersson, Swedish Meteorological and Hydrological Institute (SMHI)
	2.2 Climate at Forsmark	2.2.1	Jens-Ove Näslund, SKB Johan Liakka, SKB
		2.2.2	Johan Liakka, SKB Jens-Ove Näslund, SKB

Chapter	Section(s)	Subsection(s)	Author(s)
3. Climate and climate-related issues	3.1 Ice-sheets	All	Jens-Ove Näslund, SKB
	3.2 Glacial hydrology	3.2.1	Peter Jansson, Stockholm university Joel Harper, University of Montana Toby Meierbachtol, University of Montana Jens-Ove Näslund, SKB
		3.2.2	Peter Jansson, Stockholm university Jens-Ove Näslund, SKB
		3.2.3	Peter Jansson, Stockholm university Joel Harper, University of Montana Toby Meierbachtol, University of Montana Jens-Ove Näslund, SKB
		3.2.4	Peter Jansson, Stockholm university Jens-Ove Näslund, SKB Joel Harper, University of Montana Toby Meierbachtol, University of Montana
		3.2.5	Joel Harper, University of Montana Toby Meierbachtol, University of Montana
		3.2.6	Peter Jansson, Stockholm university
		3.2.7	Jens-Ove Näslund, SKB
		3.2.8	Peter Jansson, Stockholm university Jens-Ove Näslund, SKB
	3.3 Isostatic adjustment and relative sea-level changes	3.3.1	Jens-Ove Näslund, SKB Pippa Whitehouse, University of Durham
		3.3.2	Pippa Whitehouse, University of Durham
		3.3.3	Jens-Ove Näslund, SKB
		3.3.4	Pippa Whitehouse, University of Durham Jens-Ove Näslund, SKB Johan Liakka, SKB
		3.3.5, 3.3.6	Jens-Ove Näslund, SKB Johan Liakka, SKB
		3.3.7	Jens-Ove Näslund, SKB Pippa Whitehouse, University of Durham Johan Liakka, SKB
	3.4 Permafrost	3.4.1, 3.4.5 and 3.4.7	Juha Hartikainen, Tampere university[8] Jens-Ove Näslund, SKB

Chapter	Section(s)	Subsection(s)	Author(s)
3. Climate and climate-related issues (continued)		3.4.2 and 3.4.3	Juha Hartikainen, Tampere university[8] Jens-Ove Näslund, SKB
		3.4.4	Juha Hartikainen, Tampere university[8] Jens-Ove Näslund, SKB Johan Liakka, SKB
		3.4.6 and 3.4.7	Jens-Ove Näslund, SKB
	3.5 Surface denudation	3.5.1 to 3.5.2	Jens-Ove Näslund, SKB
		3.5.3	Jens-Ove Näslund, SKB Adrian Hall, Stockholm university
		3.5.4	Jens-Ove Näslund, SKB Karin Ebert, Södertörn university[10] Bradley Goodfellow, SGU[10] Clas Hättestrand, Stockholm university[10] Adrian Hall, Stockholm university[10] Jakob Heyman, Gothenburg university[10] Maarten Krabbendam, British Geological Survey[10] Arjen Stroeven, Stockholm university[10] Mats Olvmo, Gothenburg university[9] Johan Liakka, SKB
		3.5.5 to 3.5.7	Jens-Ove Näslund, SKB
4. Climate and climate-related conditions for the PSAR	4.1 Rationale and general approach	-	Jens-Ove Näslund, SKB Johan Liakka, SKB
	4.2 Weichselian glacial history	4.2.1	Jens-Ove Näslund, SKB Johan Liakka, SKB Barbara Wohlfarth, Stockholm University[1,5] Karin Helmens, Swedish Museum of Natural History[2,3,6] Frederik Schenk, Stockholm University[5]
		4.2.2	Jens-Ove Näslund, SKB
	4.3 Examples of Weichselian climates	4.3.1	Karin Helmens, Swedish Museum of Natural History[3,6] Jens-Ove Näslund, SKB Johan Liakka, SKB
		4.3.2 Early MIS 3	Karin Helmens, Swedish Museum of Natural History[6] Jens-Ove Näslund, SKB

Chapter	Section(s)	Subsection(s)	Author(s)
4. Climate and climate-related conditions for the PSAR (continued)		4.3.2 Middle MIS 3	Jens-Ove Näslund, SKB Erik Kjellström, Rossby Centre, SMHI[7] Jenny Brandefelt, SKB[6] Gustav Strandberg, Rossby Centre, SMHI[7] Johan Liakka, SKB
		4.3.3	Jens-Ove Näslund, SKB Erik Kjellström, Rossby Centre, SMHI[7] Jenny Brandefelt, SKB[6] Gustav Strandberg, Rossby Centre, SMHI[7]
		4.3.4	Jens-Ove Näslund, SKB
		4.3.5	Jens-Ove Näslund, SKB Karin Helmens, Swedish Museum of Natural History
	4.4 Reconstructed last glacial cycle conditions at Forsmark	All	Jens-Ove Näslund, SKB
	4.5 Reference glacial cycle climate case	All, except 4.5.2 and 4.5.3	Jens-Ove Näslund, SKB
		4.5.2 and 4.5.3	Jens-Ove Näslund, SKB Johan Liakka, SKB
5. Additional climate cases for the PSAR	5.1 Global warming climate case	All, except 5.1.1, 5.1.3 Sea-level rise up to year 2100 and Sea-level-rise beyond 2100, and Section 5.1.7	Jens-Ove Näslund, SKB
		5.1.1	Jens-Ove Näslund, SKB Johan Liakka, SKB
		5.1.3 Sea-level rise up to year 2100 and Sea-level-rise beyond 2100	Jens-Ove Näslund, SKB Johan Liakka, SKB Christina Truedsson, Tintra konsult
		5.1.7	Jens-Ove Näslund, SKB Johan Liakka, SKB Erik Kjellström, Rossby Centre, SMHI[7] Jenny Brandefelt, SKB[6] Gustav Strandberg, Rossby Centre, SMHI[7]
	5.2 Extended global warming climate case	All, except 5.2.1, 5.2.3 and 5.2.7	Jens-Ove Näslund, SKB
		5.2.1	Jens-Ove Näslund Johan Liakka
		5.2.3	Jens-Ove Näslund, SKB Johan Liakka, SKB Christina Truedsson, Tintra konsult
		5.2.7	Johan Liakka, SKB Jens-Ove Näslund, SKB

Chapter	Section(s)	Subsection(s)	Author(s)
5. Additional climate cases for the PSAR (continued)	5.3 Extended ice-sheet duration climate case	All	Jens-Ove Näslund, SKB
	5.4 Maximum ice-sheet thickness climate case	All, except 5.4.2 to 5.4.5 and 5.4.7	Jens-Ove Näslund, SKB
		5.4.2 to 5.4.5	Johan Liakka, SKB Jens-Ove Näslund, SKB Florence Colleoni, National Institute of Oceanography and Applied Geophysics – OGS, Italy[12,13] Claudia Wekerle, Alfred Wegener Institute, Germany[12] Aurélien Quiquet, Laboratoire des Sciences du Climat et l'Environnement, France[13]
		5.4.7	Johan Liakka, SKB Jens-Ove Näslund, SKB
	5.5 Severe permafrost climate case	All, except 5.5.3	Jens-Ove Näslund, SKB
		5.5.3	Juha Hartikainen, Tampere university[8] Jens-Ove Näslund, SKB Johan Liakka, SKB
	5.6 Summary of climate cases for the PSAR	All	Jens-Ove Näslund, SKB Johan Liakka, SKB
	5.7 Summary of key parameters and values for the PSAR	All	Jens-Ove Näslund, SKB Johan Liakka, SKB
6. List of abbreviations	All	All	Jens-Ove Näslund, SKB Johan Liakka, SKB
7. References	All	-	Jens Ove Näslund, SKB Johan Liakka, SKB
Appendix A: Air temperature data	All	All, except A5.2	Jens Ove Näslund, SKB
		A5.2	Jens-Ove Näslund, SKB Johan Liakka, SKB
Appendix B: Ice-sheet profiles	All	All	Jens-Ove Näslund, SKB
Appendix C: Combination of buffer erosion and freezing	All	C1	Jens-Ove Näslund, SKB
		C2	Juha Hartikainen, Tampere university[8]
		C3	Martin Birgersson, ClayTech
		C4	Jens-Ove Näslund, SKB Martin Birgersson, ClayTech
Appendix D: Holocene shoreline displacement at Forsmark	All	All	Johan Liakka, SKB Jens-Ove Näslund, SKB Anders Löfgren, Ecoanalytica
Appendix E: IPCC Representative Concentration Pathways	All	All	Johan Liakka, SKB Jens-Ove Näslund, SKB

Chapter	Section(s)	Subsection(s)	Author(s)
Appendix F: Surface air temperature and precipitation until 12000 AD	All	All	Johan Liakka, SKB Jens-Ove Näslund, SKB
Appendix G: total bedrock surface denudation over the coming 100 ka and 1 Ma	All	All	Jakob Heyman, Gothenburg university Jens-Ove Näslund, SKB Karin Ebert, Södertörn university[10] Bradley Goodfellow, SGU10 Clas Hättestrand, Stockholm university[10] Adrian Hall, Stockholm university[10] Maarten Krabbendam, British Geological Survey[10] Arjen Stroeven, Stockholm university[10]

Authors with numbers have not directly contributed written parts to the report. Instead texts have been adapted by Jens-Ove Näslund or Johan Liakka from the following supporting reports:

[1] Wohlfarth (2013), [2] Helmens (2013), [3] Helmens (2019), [4] Helmens et al. (2021), [5] Schenk and Wohlfarth (2019), [6] Helmens (2009), [7] Kjellström et al. (2009), [8] Hartikainen et al. (2010), [9] Olvmo (2010), [10] Hall et al. (2019a), [11] Harper et al. (2019), [12] Colleoni et al. (2014), [13] Quiquet et al. (2016).

A table summarising the influence of the climate-related issue on the geological barrier of the repository is presented. The table includes the geosphere variables influenced by the system/feature and the variables associated with the system/feature that are required to be known to quantify the interaction between the system/feature and the repository system, e.g. for "ice-sheets" basal temperature and melt-rate. In this context, the repository system includes both the geosphere and the engineered barriers.

Natural analogues/observations in nature

Under this heading observations in nature and, when applicable, present-day natural analogues regarding the process are summarised.

Model studies

In this section, model studies of the process are summarised, with references to relevant supporting reports. This documentation focuses on process understanding and for instance includes sensitivity analyses. The handling of external and internal controlling conditions and factors are described.

Time perspective

The timescales on which the system/feature operates and changes are documented.

Handling in the PSAR

The handling of the documented interactions with the repository is discussed. From the information under this subheading, a mapping of the climate-related issues to method of treatment and, in relevant cases, applicable models are produced. The mapping is characterised on various timescales.

Handling of uncertainties in the PSAR

Given the adopted handling in the PSAR as described above, the treatment of different types of uncertainties associated with the issue, within that general framework, is summarised under the following headings.

Uncertainties in mechanistic understanding: The uncertainties in the general understanding of the issue are discussed based on the available documentation and with the aim of answering the question: Are the basic scientific mechanisms governing the issue understood to a level necessary for the suggested handling? Alternative models may sometimes be used to illustrate this type of uncertainty.

Model simplification uncertainties: In most cases, the quantitative representation of a process contain simplifications, for instance in a numerical model. These may result in a significant source of uncertainty in the description of the system evolution. Alternative models or alternative approaches to simplification for a specific conceptual model may sometimes be used to illustrate this type of uncertainty.

Input data and data uncertainties: The input data necessary to quantify the process for the suggested handling are documented. The treatment of important input and output data and associated data uncertainties are described in detail in the **Data report**, to which reference is made as appropriate.

Adequacy of references supporting the handling in the PSAR

In the SR-Site version of the present report (SKB 2010a), each process also had the sub-heading "***Adequacy of the references supporting the handling in SR-Site***". Under that heading, statements were provided concerning the adequacy of the references in a quality assurance perspective, since some references were not qualified according to the requirements in the SR-Site QA plan. Some of those references are used also in the PSAR version, without repeating the qualification statement from the SR-Site assessment. All new references in the present PSAR version are qualified according to the SKB management system, as specified in the PSAR QA plan. The mentioned sub-heading is thus obsolete and is not used in the present report.

1.4 Publications supporting the PSAR Climate report

Within the SKB climate programme, 12 supporting reports have been produced for the PSAR Climate report since SR-Site.

- Climate- and ice-sheet modelling studies on maximum ice-sheet thickness were conducted by Colleoni et al. (2014) and Quiquet et al. (2016), reconstructing climate and ice-sheet for the peak glaciation of the penultimate glacial period (at around 140 ka).
- Schenk and Wohlfarth (2019) performed a study on climate evolution and variability in Scandinavia and Europe during the transition from a glacial into an interglacial climate state, combining a multi-proxy climate study with results from high-resolution climate modelling.
- Helmens (2019) conducted an extensive multi-proxy palaeoclimate study on lacustrine and fluvial sediments spanning the last 130 years from northern Fennoscandia.
- Rath et al. (2019) reconstructed Holocene palaeotemperatures from borehole thermal data for the Forsmark and Laxemar sites by inverse modelling.
- To increase the knowledge on ice-sheet hydrological processes and their influence on both surface and subsurface environments, a comprehensive study on these subjects was made within the Greenland Analogue Project (GAP) (Claesson Liljedahl et al. 2016, Harper at al. 2016, and references therein), using the Greenland ice-sheet as a natural analogue for future possible conditions in Sweden.
- Harper et al. (2019) conducted a follow-up study (ICE) in the same region of the Greenland ice-sheet where the GAP study was performed. The aim of the ICE study was to i) interpret the physical framework of the ice-sheet bed, ii) quantify the magnitude of and spatial gradients in basal water pressure, iii) investigate the presence of short duration water pressure transients in the ice-sheet basal drainage system, and iv) advance the understanding of the distribution of water along the ice-sheet bed.

- Lord et al. (2019) used a combination of Earth system modelling techniques to simulate the possible evolution of future climate over the next one million years for a range of anthropogenic carbon dioxide (CO_2) emission scenarios. Tentative projections of future glacial periods at Forsmark were also presented for the coming 1 Ma.
- Hall et al. (2019a) conducted a study with the aim to provide estimates of past and future depths and rates of bedrock denudation (including glacial erosion) at Forsmark, using i) the Sub-Cambrian Peneplain as a reference surface against which to estimate Pleistocene glacial erosion, ii) mapping of the distribution, form and characteristics of glacial landforms and sediments on the shield surface to understand patterns and processes of glacial erosion, iii) studying fracturing related to past and future glacial erosion patterns, and iv) obtaining cosmogenic nuclide inventories for bedrock surfaces to estimate erosion rates beneath previous ice-sheets. Based on the historical denudation rates, estimates of bedrock denudation for the coming 100 ka and 1 Ma were also presented, based on the future glacial periods of Lord et al. (2019).
- Two complementary studies, investigating key conceptualisations of the basement surface, relevant for the glacial erosion study at Forsmark (Hall et al. 2019a) have also been performed (Goodfellow et al. 2019, Hall et al. 2019b).
- A theoretical analysis of glacial erosion, including the forces required for the removal of upstanding rock blocks by sliding of ice at the base of an ice-sheet under four different glacial scenarios, was performed by Krabbendam and Hall (2019).
- Pellikka et al. (2020) performed simulations of potential future sea-level rise (storm contribution and rise of mean relative sea-level) with associated statistical measures, based on recent literature and simulations dedicated for the Forsmark site. The calculations were made for different carbon emission scenarios and for different time periods (up to 2050, 2080 and 2100 AD).

Since the present report constitutes an updated version of the SR-Site Climate report (SKB 2010a), it also contains considerable information from the following SR-Site supporting reports. Studies on climate, palaeoclimate and Weichselian glacial history were conducted by Helmens (2009), Houmark-Nielsen (2009), Kjellström et al. (2009 (including erratum Feb 2010)), Wohlfarth (2009). A special issue of Boreas (Wohlfarth and Näslund 2010), with papers on conditions in Scandinavia during a long period prior to the Last Glacial Maximum of the last glacial cycle, was published as a result of a workshop on this topic arranged by SKB in 2007 (Näslund et al. 2008). Permafrost development was studied by Hartikainen et al. (2010) whereas glacial hydrology was studied by Jansson and Näslund (2009). Surface denudation (i.e. erosion and weathering) was investigated by Olvmo (2010), while borehole temperatures, geothermal heat and palaeoclimate were studied by Sundberg et al. (2009). Various aspects of glacial isostatic adjustment were studied, such as changes in sea-level and relative sea-level (Whitehouse 2009) and crustal stresses under glacial conditions (Lund et al. 2009, Lund and Näslund 2009).

The supporting reports published for the PSAR, as well as several of the supporting reports that were published for the SR-Site assessment, are also planned to be used for the SAR. The climate studies performed for the PSAR and SR-Site have resulted in more than 100 scientific publications published in *peer-reviewed* journals or as PhD theses.

In addition to the above studies, a large number of papers and reports from the general scientific literature have been used as input to the present PSAR Climate report.

1.5 Interactions between the climate programme and other parts of the PSAR programme

Data and information from the climate programme have been used within many other parts of the PSAR. Data on air temperature have been used to simulate the development of ice-sheets (Section 3.1.4) and permafrost, see Section 3.4.4, 5.5.3 (Hartikainen et al. 2010) and for evaluation of thermal gradients and geothermal heat flow (Sundberg et al. 2009). Data on changing ice-sheet configurations over time have in turn been used for studies of variations in stress in the Earth crust (Lund et al. 2009), which are used for assessing the potential for and consequences of glacially induced faulting (**Geosphere process report)**. Ice-sheet data are also needed for simulations of groundwater flow under glacial conditions

(Vidstrand et al. 2010). Data from permafrost simulations have been used to make appropriate selections of conditions when studying groundwater flow under permafrost conditions (Vidstrand et al. 2010) as well as for studies of surface hydrology under a colder climate (Bosson et al. 2010, **Biosphere synthesis report**). Data on relative sea-level change have been used for a description of the past and future evolution of the landscape as influenced by e.g. the isostatic recovery from the last glacial cycle (**Biosphere synthesis report,** Söderbäck 2008, SKB 2010b, Lindborg et al. 2018), for instance to model future lake formation. Relative Sea-level information is also used for studying groundwater flow in potential future situations when the isostatic uplift has progressed further. Data on permafrost and glacial development have also been used for investigating THM processes (Lönnqvist and Hökmark 2010) and for assessing the potential for freezing of various parts of the repository (see the **Post-closure safety report**). Data on maximum ice-sheet thickness have been used as input to the safety assessment scenario Canister failure due to isostatic load, see the **Post-closure safety report**, as well as to the canister design requirements (Posiva SKB 2017). Climate data were also included in the site selection process (SKB 2010b).

1.6 Summary of main changes made since the SR-Site Climate report

Below is a summary of changes in the PSAR Climate report compared to the SR-Site version (SKB 2010a).

Title of report

- The title of the report has been changed according to PSAR standards.

Chapter 1

- A short description of Earth's orbital variations as the primary forcing agent of glacial cycles has been added to Section 1.2.1.
- Table 1-1 has been added to Section 1.2.2, summarizing the climate-related issues covered in this report and their associated potential impact on repository safety.
- Short-references to other main references in the safety assessment have been changed to PSAR standards. A table summarizing this has been added in a new section (Table 1-2 in Section 1.3.1).
- The section describing the overall structure of the report (Section 1.3.2) has been updated with a description of the new appendices (see below).
- References to IPCC (2007) have, when applicable, been replaced with IPCC (2013a), and the referenced information has been updated when applicable.
- Author contributions in Table 1-3 have been updated with respect to the changes made in the report. Author affiliations have been updated.

Chapter 2

- Chapter 2 *The climate system* has been renamed to *Present and near-future climate in Sweden and Forsmark*. Consequently, the present report only contains a short description of the present climatology in Sweden and Forsmark as well as the projected climate change at Forsmark until 2100 AD instead of a basic description of the entire climate system. The latter information is readily found elsewhere. More detailed information on potential future climates at Forsmark are found in Chapters 4 and 5.
- In Section 2.2.1, information on the present-day near-surface air temperature and precipitation in Forsmark has been updated using the values from the SR-PSU safety assessment (SKB 2014). In addition, the present-day climatology has been extended to include all four seasons.
- Section 2.2.2 now presents the projected temperature change at Forsmark until 2100 AD based on both global (Collins et al. 2013) and regional (Sjökvist et al. 2015) climate modelling.

Chapter 3

- Section 3.1 *Ice-sheet dynamics* have been renamed to *Ice-sheets*.
- In Section 3.1.4, the description of the treatment of the climate forcing in the Weichselian ice-sheet modelling experiments have been improved.
- Section 3.2 *Ice-sheet hydrology* has been renamed to *Glacial hydrology*, and the section has been updated with new results and a new conceptual model on ice-sheet basal hydrology obtained from the GAP study (Claesson Liljedahl et al. 2016, Harper et al. 2016) and the ICE study (Harper et al. 2019).
- Section 3.3.4 on Glacial Isostatic Adjustment (GIA) modelling has been shortened. The new version only contains the essential results for the relative sea-level curves used in the safety assessment.
- In Section 3.3.4, additional explanation has been added on the use of the 80 % loading case in the *global warming climate case*.
- In Section 3.3.7, more information on the uncertainties in GIA modelling has been added. This text was previously found in Section 5.1.3.
- The background information on different denudational processes in Section 3.5.1 has been shortened. A short section on marine erosion has been added. A reference on a new theoretical study on glacial erosion (Krabbendam and Hall 2019) has been added.
- A paragraph on the long-term stable cratonic setting have been added to Section 3.5.3.
- Section 3.5.4 to 3.5.7 have been updated with respect to new detailed studies on past denudation, including glacial erosion, for the Forsmark site, adjacent areas in the Uppland province, and other areas of relevance in southern Sweden (Hall et al. 2019a, b, 2020, Goodfellow et al. 2019). Other relevant newer references have also been added, e.g. on tectonic block faulting (Grigull et al. 2019). The update also includes new estimates on possible future surface denudation for the Forsmark site over the coming 1 Ma (Hall et al. 2019a), given different scenarios for greenhouse-gas emissions and for the duration of future ice-sheet coverage at Forsmark provided by Lord et al. (2019).
- Section 3.4.4 has been updated with respect to the new temperature (−6 °C) used in the PSAR for which a frozen buffer clay and backfill material may start having detrimental effects on the canister and surrounding host rock respectively.

Chapter 4

- Sections 4.2.1 and 4.3.1 have been updated based on results from the recent SKB-funded palaeoclimate studies of Wohlfarth (2013), Helmens (2013, 2019) and Schenk and Wohlfarth (2019).
- The text on the climate modelling simulations by Kjellström et al. (2009) in Section 4.3.2 has been shortened based on the version in SR-PSU (SKB 2014).
- A new Section 4.3.5, describing the relevance and implications of the palaeoclimate studies made at the Sokli site (Helmens 2009, 2013, 2019, Helmens et al. 2021), northern Finland, has been added.
- Section 4.5.2 has been updated with a more detailed description on how the relative sea-level curve was constructed for the *reference glacial cycle climate case*.
- Section 4.5.3 has been updated with respect to the new temperature (−6 °C) used in the PSAR for which a frozen buffer clay and backfill material may start having detrimental effects on the canister and surrounding host rock respectively.
- In Sections 4.5.4 and 5.6, the total duration of each climate domain in the *reference glacial cycle climate case* has been corrected in Figure 4-34 and Table 4-5 and Table 5-23, as well as in the text. The previous values in the figures and tables were not in agreement with the data.
- In Section 4.5.5, the text on ice-sheet hydrology has been updated with respect to the results from the GAP study (Claesson Liljedahl et al. 2016, Harper et al. 2016) and the ICE study (Harper et al. 2019).
- Section 4.5.7 on surface denudation for the *reference glacial cycle climate case* has been updated with respect to new results on past and future surface denudation at the Forsmark site (Hall et al. 2019a).

Chapter 5

- A figure from Liakka et al. (2021), showing projected times of the next future glacial inception from different studies, has been added to Section 5.1.1.
- In Section 5.1.3, the sub-section *Ice-sheets and sea-level* has been removed. The information that was included under this heading is now included in other updated sections of the report.
- In Section 5.1.3, a sub-section on the present-day relative sea-level changes at Forsmark has been added.
- In Section 5.1.3, the projections of future sea-level rise for the *global warming climate case*, and the associated assessment of relative sea-level change at the Forsmark site, have been updated, based on (i) an extensive review of sea-level literature published between 2012 and 2018, and (ii) a study dedicated to estimate the relative sea-level at Forsmark up until 2100 AD (Pellikka et al. 2020).
- In Section 5.2.3, the projections of future sea-level rise for the *extended global warming climate case*, and the associated assessment of relative sea-level change at the Forsmark site, has been updated, based on (i) an extensive review of sea-level literature published between 2012 and 2018, and (ii) a study dedicated to estimate the relative sea-level at Forsmark up until 2100 AD (Pellikka et al. 2020).
- In Section 5.2.3, a relative sea-level curve for the period −10.8 to 120 ka AP has been added in the *extended global warming climate case* where it is also discussed.
- In Section 5.2 *extended global warming climate case,* a subsection describing results from a study of the climate over the coming 1 Ma (Lord et al. 2019) has been added (Section 5.2.7).
- Section 5.3.3 on surface denudation for the *extended ice-sheet duration climate case* has been updated with respect to new results on past and future surface denudation at the Forsmark site (Hall et al. 2019a).
- In Section 5.4 *maximum ice-sheet thickness climate case,* the estimate of the maximum possible ice thickness over Forsmark (and associated maximum isostatic load) has been updated, based on results from two dedicated SKB-funded studies. In addition, the name of the climate case was changed from *maximum ice-sheet configuration climate case,* used in SR-Site, to *maximum ice-sheet thickness climate case.*
- A section (5.4.7) has been added describing new results on subglacial water pressures higher than overburden pressure.
- Section 5.5.3 has been updated with respect to the new temperature (−6 °C) used in the PSAR for which a frozen buffer clay and backfill material may start having detrimental effects on the canister and surrounding host rock respectively.
- In section 5.5.4, the consequences on freezing depths are investigated for a hypothetical case with a total denudation of 20 m per glacial cycle. The realism of this case is also evaluated.
- The surface air temperature and precipitation changes at Forsmark until 12000 AD for the *global warming* and *extended global warming climate cases* have been updated based on data in the scientific literature and climate modelling. Figures and tables of the surface air temperature and precipitation based on the updated curves are also shown and briefly discussed in Sections 5.1.1 and 5.2.1.
- A Section 5.7 has been added, presenting a summary of key parameters and values obtained from the various climate cases considered in the PSAR.

Chapter 6

- The list of abbreviations has been updated.

Reference list

- The reference list has been updated to the present SKB formatting standard.

Appendices

- Results from Helmens (2019) has been added to the discussion of early Weichselian temperatures in Fennoscandia in Appendix A.
- The value of maximum hydrostatic pressure has been updated in Appendix C with respect to the new maximum possible ice-sheet thickness estimate in Section 5.4.
- The relative sea-level curve at Forsmark for the Holocene has been updated, including present-day relative sea-level, using a more recent empirical model (Påsse and Daniels 2015 instead of Påsse 2001). The old relative sea-level curve has been replaced with the new one in Figure 4-20, Figure 4-23, Figure 4-27, Figure 4-35 and Figure 5-7. A detailed description of the construction of the updated relative sea-level curve is provided in a new appendix (D).
- In Appendix E, a description of the emission scenarios in the fifth IPCC assessment report (IPCC 2013a) has been added, i.e. the Representative Concentration Pathways (RCPs), upon which the *global warming* and *extended global warming climate cases* are based.
- A detailed description of the construction of the updated surface air temperature and precipitation curves for the *global warming* and *extended global warming climate cases* presented in Chapter 5 is provided in a new appendix (F).
- New results of total bedrock surface denudation over the coming 100 ka and 1 Ma, as calculated by Hall et al. (2019a) for the higher confidence future glacial periods of Lord et al. (2019), are presented in a new Appendix (G). The appendix presents individual results for the RCP 2.6, 4.5, 8.5 IPCC emission scenarios and for a 'Natural' scenario without carbon emissions.

2 Present and near-future climate in Sweden and Forsmark

In this section, the present-day climate in Sweden and Forsmark is described (Sections 2.1 and 2.2.1). In addition, a description of the projected climate change in the Forsmark region until 2100 AD is given in Section 2.2.2. Changes in climate on such short timescales are of importance for the planning and construction of the spent nuclear fuel repository when it comes to associated changes in sea-level, see also Sections 5.1.3 ans 5.2.3.

2.1 Present-day climate in Sweden

The following description of the present climate in Sweden is taken from Ministry of the Environment (2001). Sweden is located in the northerly west wind belt, an area where the prevailing winds come from the south and west. The North Atlantic Drift and the numerous areas of low pressure produce a climate with winters that are 20–30 °C warmer than at corresponding latitudes in Siberia and Canada. The precipitation brought by the frequent low pressures gives regular rain and snow falls, although there is some rain shadow effect east of the Norwegian mountains.

According to the Köppen climate classification system, Sweden has a temperate, moist climate with year-round precipitation. Along the coasts of southern Sweden, the climate is warm-temperate, with a natural cover of deciduous forest. The climate in the rest of the country is cool temperate, with the predominant vegetation being coniferous forest. Tundra conditions prevail in the mountains.

Summer temperatures are largely governed by altitude and to a lesser extent by latitude. Thus, the mean temperature in July is 15–16 °C along the entire coast. The mean temperature in summer drops by 0.6 °C with every 100 m of altitude. Even though there is little difference in temperature between southern and northern Sweden in high summer, summer itself (defined as the time of the year when the mean diurnal temperature is above 10 °C) is much longer in the south than in the north. For example, in southernmost Sweden, summer lasts for five months, compared with three in the northernmost region. The turn of the seasons in spring and autumn, when the mean daily temperature is between 0 and 10 °C, is also much shorter in the north. Thus, in Lapland in northernmost Sweden, winter lasts for just over half the year, whereas the coast of Skåne, in the far south, only has winter for a few weeks. The vegetation growing season, defined as the part of the year when the mean diurnal temperature is over 5 °C, varies considerably over the country. It lasts for between 210 and 220 days in southernmost Sweden (western and southern Skåne and the coast of Halland) but is only half as long in the far north.

Local conditions such as topography and proximity to the sea or large lakes influence the climate locally. The mean temperature in January can be extremely low in valleys with open terrain in inland areas of northern Sweden (−15 to −17 °C). Elsewhere in northern Sweden the January mean temperature is generally between −9 and −14 °C, except along the coast in the south of the region where, as in much of the central inland region, the mean January temperature is −5 to −8 °C. In the southern and eastern part of central Sweden, the mean temperature is −3 to −5 °C in January, whereas it is −1 to −2 °C in southern coastal areas owing to the ameliorating effect of the nearby open sea. The temperature can vary a great deal, from approximately −50 to almost +40 °C. The lowest recorded temperature is −53 °C, recorded at two locations in northern Sweden. Elsewhere in Sweden the coldest recorded temperatures are −30 to −40 °C, except along some parts of the southern coast, where it has never fallen below −25 to −30 °C. The highest recorded temperatures display much less geographical variation than the lowest; in southern and central Sweden and along the northern coast, the records are between 34 and 36 °C. Very occasionally, temperatures also rise above 30 °C in other parts of the country.

Over much of Sweden, annual precipitation is between 600 and 800 mm. Annual precipitation in the mountains, most exposed to westerly winds in northern Sweden (western Lapland and Jämtland), is between 1500 and 2000 mm. On the western slopes of the southern uplands, maximum annual precipitation is 1300 mm. The Abisko area in northernmost Sweden has least precipitation, approximately 450 mm per year. This area lies in the rain shadow of the mountains to the west. Precipitation is heaviest

during July–November in most of the country. Most precipitation falls along fronts as areas of low pressure move across the country. Several weeks may pass in spring and early summer without any rain. Most of Sweden typically has a snow cover in winter. In the mountains of Lapland, the ground has a snow cover for an average of 225–250 days a year. Most of the rest of northern Sweden is covered in snow for more than 150 days a year. In central Sweden and upland areas of the south, there is snow cover on average between 100 and 150 days each winter. In the rest of southern Sweden, there is snow cover for between 50 and 100 days, except along the west coast and the far south, where snow lies for less than 50 days each winter. The maximum snow depth averages more than 60 cm throughout almost all of northern Sweden; the mountains generally have more than a metre of snow.

An overview of climate proxy data and what they can tell us about climate in Sweden during the last millennium, or in some cases even longer back in time is presented in Moberg et al. (2006). That study also provides more detailed climate information from Swedish instrumental data for the last 260 years. A tentative evolution of climate in Sweden for the last millennium, as simulated by a climate model, is also provided. Taken together, these three basic types of information are used to illustrate possible Swedish climate variations during the last millennium. Moberg et al. (2006) provides a benchmark for the likely range within which our regional climate has varied naturally during the last millennium.

2.2 Climate at Forsmark

2.2.1 Present climate

The present climate in the Forsmark region has typical values for a climate on the Swedish east coast (Table 2-1), with a mean annual air temperature of c +5.5 °C for the period 1961–1990 (Larsson-McCann et al. 2002). This can be compared with a mean annual air temperature of c +7 °C (Werner et al. 2014) for the period 2004–2010. The difference between these values may partially be explained by the observed recent warming in the region. However, due to the short averaging period of seven years in Werner et al. (2014), their value is sensitive to natural variability, which may also explain part of the difference.

Precipitation in the Forsmark area for the period 1961–1990 is represented here by the nearby station Högmasten (Table 2-1). Mean annual precipitation at this station was 568 mm for this period (Johansson 2008). This can be compared with a mean annual precipitation of c 589 mm (Werner et al. 2014) for the period 2004–2010.

The climate in Sweden and the Forsmark region is characterised by a large variability within the 100 ka glacial cycle timescale associated with the growth and decay of ice-sheets (e.g. Figure 1-2). Possible future and past climate conditions within this time perspective have been analysed in a set of regional climate model simulations of typical periglacial, ice-covered and CO_2-induced warm conditions in Sweden (Kjellström et al. 2009). The main results for Sweden and the Forsmark area from those simulations are outlined in Sections 4.3.2, 4.3.3 and 5.1.7. In addition to the modelling studies, the historical climate of Fennoscandia has also been studied by analyses of geological climate archives and climate modelling (e.g. Helmens 2009, 2019, Schenk and Wohlfarth 2019, Rath et al. 2019). A summary of those studies is provided in Section 4.2.1.

Table 2-1. Present-day climate data for the Forsmark region (mean values for the period 1961–1990 AD). The precipitation was measured at Högmasten and the surface air temperature was measured at Örskär (Larsson-McCann et al. 2002). Abbreviations in the table header are DJF = December-January-February, MAM = March-April-May, JJA = June-July-August and SON = September-October-November.

Variable	Winter (DJF)	Spring (MAM)	Summer (JJA)	Autumn (SON)	Year
Surface air temperature (°C)	−2.6	+2.8	+14.6	+7.1	+5.5
Precipitation (mm)	127	91	176	175	568

2.2.2 Climate until 2100 AD

To produce climate projections for the next few centuries, coordinated experiments, in which many climate models run a set of scenarios, have become the standard (Knutti and Sedláček 2013). A number of emission scenarios or scenarios for atmospheric concentrations are used in these multi-model ensembles, which sample uncertainties in emission scenarios, model uncertainty and initial condition uncertainty, and provide a basis to estimate projection uncertainties. The Coupled Model Intercomparison Project Phase 6 (CMIP6; Eyring et al. 2016), coordinated by the World Climate Research Programme in support of the Intergovernmental Panel on Climate Change Sixth Assessment Report (IPCC AR6, expected to be finalized in 2021 AD) is the most recent of these activities. As of February 2019, climate modelling experiments are being submitted to CMIP6, but key results from these experiments have not yet been published. The fifth IPCC assessment report, which was based on CMIP5 (Taylor et al. 2012), was published in 2013 (IPCC 2013a).

The CMIP5 projections of climate change are driven by concentration or emission scenarios consistent with the representative concentration pathways (RCPs; Appendix E, Meinshausen et al. 2011). The numbers associated with the RCPs provide rough estimates of the anthropogenic radiative forcing in the year 2100 AD (relative to preindustrial conditions). A higher number thus generally means a larger concentration of atmospheric greenhouse gases and a warmer climate (see Appendix E for details). The RCPs also constitute the bases for the *global warming climate case* and *extended global warming climate case* in this report (Figure 1-3, Sections 5.1 and 5.2).

Multi-model CMIP5 ensemble mean changes for 2081–2100 AD in surface air temperature relative to the 1986–2005 AD reference period are displayed in Figure 12.11 of Collins et al. (2013). The surface air temperature anomaly for the Forsmark region ranges from 1.0–1.5 °C for the low emission RCP2.6 scenario, 2.0–3.0 °C for the intermediate emission RCP4.5 scenario, and 4–5 °C for the high emission RCP8.5 scenario (Table 2-2). Most of the temperature increase is projected to occur in the winter season. Note that the surface air temperature ranges given here represent the shaded interval in Figure 12.11 of Collins et al. (2013) and hence give no indication of the uncertainty in the projected change.

Multi-model CMIP5 ensemble mean changes for 2081–2100 AD in annual precipitation relative to the 1986–2005 AD reference period are displayed in Figure 12.22 of Collins et al. (2013) for the high emission scenario RCP8.5. For the other RCPs, the median change (corresponding to the 50 % percentile) from the CMIP ensemble is used for the 2081–2100 AD projection of annual precipitation (IPCC 2013b). The annual precipitation is projected to increase by 10–20 % for RCP8.5 (Table 2-2), of which most of the increase is expected to occur in the winter season (Collins et al. 2013). For the other scenarios the precipitation increase by 2100 AD is projected to be more modest as they all fall within the 0–10 % range (Table 2-2).

In summary, for the lowest emission scenario (RCP2.6) there would only be a modest increase of the temperature and precipitation at Forsmark until 2100 AD, whereas for the moderate emission scenario (RCP4.5) there would be a clear increase of the temperature, with an annual mean temperature that could reach around +8 °C and a modest increase in precipitation by 2100 AD. For the highest emission scenario (RCP8.5), on the other hand, the annual-mean temperature could well exceed +10 °C and the annual precipitation could potentially increase by more than 100 mm by 2100 AD (Table 2-1 and Table 2-2).

In addition to the CMIP5 simulations (Collins et al. 2013), regional climate projections for Sweden until 2100 AD have been carried out by the Swedish Meteorological and Hydrological Institute (SMHI). They used results from different CMIP5 models in Collins et al. (2013) as boundary conditions in 21st century regional climate model projections under the RCP2.6, 4.5 and 8.5 emission scenarios. The resulting projected 21st century changes in climate for Uppsala County, where Forsmark is located, is presented in Sjökvist et al. (2015). The projected changes in annual mean temperature and precipitation for 2070–2099 AD relative to 1961–1990 AD from Sjökvist et al. (2015) are summarized in Table 2-2.

In general, the regional climate model projections of the end of 21st century surface air temperature and precipitation changes in the Forsmark region by Sjökvist et al. (2015) agree well with the global climate model projections reported in Collins et al. (2013) and IPCC (2013b) (Table 2-2). A notable result from

Sjökvist et al. (2015) is the large ensemble spread in the projected annual precipitation change under the RCP4.5 and 8.5 emission scenarios. This illustrates that future projections of precipitation changes are typically associated with a lower confidence than the corresponding projections of the surface air temperature.

The projected increases of the global mean surface air temperature by 2100 AD and 2300 AD are provided in Appendix E. The constructed temperature and precipitation changes at Forsmark until 12000 AD are presented and discussed in Sections 5.1 and 5.2, and in Appendix F.

Table 2-2. Projected end of 21st century changes in annual mean surface air temperature and precipitation in the Forsmark region under different scenarios of future greenhouse gas emissions (RCPs, see Appendix E) from global (Collins et al. 2013, IPCC 2013b) and regional (Sjökvist et al. 2015) climate modelling. The projected changes are for the period 2081–2100 AD relative to the 1986–2005 AD reference period in Collins et al. (2013) and IPCC (2013b), and for 2071–2099 AD relative to 1961–1990 AD in Sjökvist et al. (2015).

Study	Surface air temperature change by 2100 AD (°C)				Precipitation change by 2100 AD (%)			
	RCP2.6	RCP4.5	RCP6.0	RCP8.5	RCP2.6	RCP4.5	RCP6.0	RCP8.5
Collins et al. (2013), IPCC (2013b)[1]	1.0–1.5	2.0–3.0	3.0–4.0	4.0–5.0	0–10[2]	0–10[2]	0–10[2]	10–20
Sjökvist et al. (2015)	1.8[3] [1.6–2.1]	2.9[4] [2.1–3.7]	-	4.6[4] [3.8–5.4]	6[3] [5–6]	15[4] [4–25]	-	23[4] [11–31]

[1] Data are from multi-model CMIP5 ensembles, and the ranges given in the table represent intervals from map figures in Collins et al. (2013) and IPCC (2013b), and therefore give no indication of the uncertainty in the projected change.

[2] Values represent the median change (50 % percentile) from the CMIP5 ensemble (instead of the mean change).

[3] Value represents the ensemble-mean regional climate model projection based on boundary condition data from three different global CMIP5 models. The values within the square brackets represent the ensemble minimum and maximum of those three simulations.

[4] Value represents the ensemble-mean regional climate model projection based on boundary condition data from nine different global CMIP5 models. The values within the square brackets represent the ensemble minimum and maximum of those nine simulations.

3 Climate and climate-related issues

In this chapter there are five sections that, in turn and in detail, describe the climate-related phenomena within each of the climate domains (Section 1.2.3) that may affect repository safety. These sections deal with the general characteristics of ice-sheets, glacial hydrology, changes in relative sea-level, permafrost, and surface denudation, and for most of these features dedicated reconstructions of the development during the last glacial cycle are presented. The last glacial cycle reconstruction is subsequently used for the construction of a future reference glacial cycle (Section 4.5).

3.1 Ice-sheets

3.1.1 Overview/general description

Glaciers and ice-sheets may form in climate regions where, in places, the winter snow precipitation is not completely melted away during summer. A glacier is an ice mass that has been formed by successive local accumulation of snow, with ice movement due to ice deforming under its own weight. An *ice-sheet* is defined as a glacier that spreads out in all directions from a central dome, i.e. a large glacier (> 50000 km^2 in area) that is not confined by the underlying topography. In reality, the flow pattern of ice-sheets is not radial from a single dome. Instead, ice often flows out from a number of elongated *ice divides*, with the ice divides constituting the highest parts of the ice-sheet.

Generally, ice flow velocities are moderate to slow within an ice-sheet, with ice moving a few tens of metres per year. However, certain well-defined parts of ice-sheets, so called *ice streams*, exhibit significantly faster ice flow. Ice streams are typically some tens of kilometres wide and several hundreds of kilometres long. Ice velocities within present-day ice streams are several hundred metres per year, in some cases exceeding 1000 m a^{-1} (cf. Joughin et al. 2004). Since surrounding ice typically moves considerably slower, high velocity gradients across the ice stream margins produce distinct *shear zones* with heavy crevassing. Because of the high ice flux in ice streams, these features may drain large portions of ice-sheets. Ice streams are often characterised by specific basal thermal and hydrological conditions, differing from those of the surrounding ice-sheet.

The margin of an ice-sheet may be either on land or in water. If the ice margin is positioned in the sea or in a lake, it is common that the outer part of the ice-sheet is floating on the water, constituting an *ice shelf*. The boundary between the floating and grounded ice is the ice-sheet *grounding-line*.

If the basal thermal and topographical conditions are favourable, sub-glacial melt water may accumulate in topographic lows beneath the ice, forming *sub-glacial lakes*. These are common features under the present Antarctic ice-sheet, whereas none have so far been found beneath the Greenland ice-sheet.

Mass balance

The growth and decay of ice-sheets are determined by the *mass balance*, which is the result of the mass gain, or *accumulation*, and the mass loss, or *ablation*, typically averaged over one year. The mass gain of an ice-sheet is completely dominated by the process of snow accumulation. Most of the snow falls and accumulates during winter seasons, but snow may also accumulate during summer. For ice-sheet ablation on the other hand, several processes may be involved, the two most significant being surface melting of snow and ice (if the summer climate is warm enough) and calving of ice bergs from ice shelves (when the margin is at the sea). In addition, mass may also be lost from the ice-sheet by melting of basal ice, and locally on the surface by sublimation of ice and snow. When a certain part of an ice-sheet exhibits more accumulation than ablation over one year, that part is said to belong to the *accumulation area* of the ice-sheet. This is in contrast to the *ablation area*, where there is a net loss of mass over one year. Central parts of ice-sheets typically constitute accumulation areas, whereas in the case of surface melting, lower parts of ice-sheets constitute ablation areas (Figure 3-1). The line between the accumulation- and ablation areas is called the *equilibrium line*.

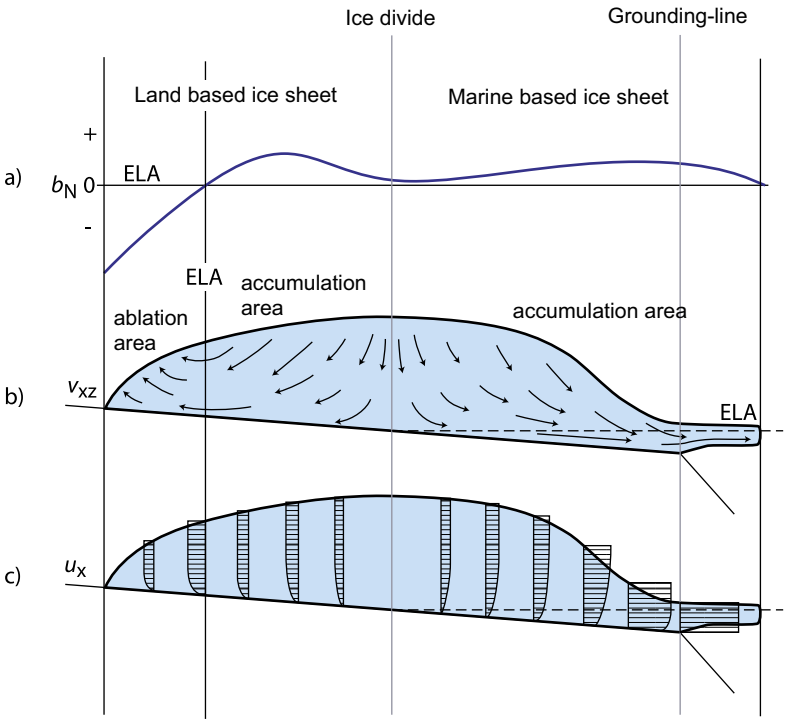

Figure 3-1. *Schematic ice-sheet cross section. Panel a) shows the surface net balance distribution (b_N), panel b) shows ice velocity trajectories (v_{xz}) as well as distribution of accumulation- and ablation areas, and panel c) shows the horizontal velocity component (u_x). ELA denotes equilibrium line altitude. Modified from Holmlund and Jansson (2003), after Denton and Hughes (1981).*

If the total ice-sheet accumulation is greater than the total ablation over one year, the mass balance is defined to be positive, whereas the opposite case produces a negative mass balance. If accumulation and ablation are equal, the mass balance is zero.

A positive mass balance over several successive years makes an ice-sheet grow, whereas a negative mass balance reduces its size. However, changes in the size of ice-sheets are very slow, acting over hundreds and thousands of years. The *response time* of an ice-sheet is the time it takes for a steady-state ice-sheet to come to a new steady-state condition after a climate change. Since climate is constantly changing, ice-sheets are never in true steady-state, but are constantly adjusting their size and shape to the prevailing climate.

Ice temperature

The temperature of the ice is of fundamental importance for the behaviour and characteristics of glaciers and ice-sheets. Among other things, it has a strong effect on the movement, dynamics and hydrology of the ice. Two types of glacier ice can be defined based on temperature; 1) *Temperate ice* (or *warm ice*) with the ice temperature at the pressure melting point, and 2) *Polar ice* (or *cold ice*) with the ice temperature below the pressure melting point. Cold ice is harder than temperate ice and also impermeable to water unless crevasses are present.

Glaciers and ice-sheets are often classified according to their thermal characteristics. In the simple case, a glacier where all ice has a temperature at the pressure melting point throughout the year is called a *temperate glacier* or *temperate ice-sheet,* whereas a glacier in which all the ice is below the pressure melting point throughout the year is called a *polar glacier* or *polar ice-sheet*. However, an ice-sheet or glacier need not consist exclusively of temperate or polar ice. In many cases, it can contain both ice types, and in such a case it is called *polythermal*.

Of specific interest is the temperature of the ice at the ice-sheet bed, i.e. the basal thermal condition. An ice-sheet can be *cold-based* or *warm-based*. A cold-based ice-sheet has cold basal ice, and it is frozen to its bed. There is no free water at the bed, and no sliding of basal ice over the substrate is taking place. A warm-based ice-sheet is at the pressure melting point at the bed. Free water is, in this case, present at

the ice/bed interface, and the ice may slide over the substrate. This has important consequences both for ice kinematics and landform development. A polar ice-sheet may be either cold-based or warm-based. In the case of a warm-based polar ice-sheet, it is typically only the lowermost part of the ice that is at the pressure melting point, whereas most of the ice-sheet consists of polar ice. One part of a polar ice-sheet may thus be cold-based at the same time as other parts are warm-based. This is the present case for the Greenland and Antarctic ice-sheets. Warm-based and cold-based ice-sheets are also called *wet-bed ice-sheets* and *dry-bed ice-sheets*.

Glaciers and ice-sheets experience melting of basal ice where the basal ice temperature is at the pressure melting point. Heat for this melting can be added from geothermal heat flux and from frictional heating by internal deformation of basal ice. The thermodynamic situation at the base of an ice-sheet is determined by the thermal properties of ice. Energy can be transferred by diffusion along a temperature gradient in ice as in all materials. Also, the solidus of the ice-water vapour phase space has a negative slope, which means that the melting or freezing temperature is depressed with increasing pressure by 0.09 K Pa^{-1}. As a general statement, freezing of liquid water occurs when temperature and pressure satisfy the generalised Clapeyron equation (e.g. O'Neill and Miller 1985):

$$\frac{p_w}{\rho_w} - \frac{p_i}{\rho_i} = \frac{L}{273.15} T + \frac{P_0}{\rho_w} \qquad \text{Equation 3-1}$$

where p_w = water pressure, ρ_w = water density, p_i = ice pressure, ρ_i = ice density, L = ice density coefficient of latent heat of fusion, T = temperature in degrees centigrade, and P_0 = osmotic pressure. Equation 3-1 couples the effect of temperature and pressure. It is a general thermodynamic relationship that is not specific for the case of ice-sheets and glaciers. However, the phase change of the ice-water system is not only controlled by temperature and pressure. Two other factors may also be of importance; 1) the presence of solutes in water, and 2) surface tension arising from interface curvature. Just as in the case with an increasing pressure, an increase in solutes in liquid water also depresses the melting/freezing point. This effect is referred to as the osmotic pressure (e.g. Padilla and Villeneuve 1992), and it is included in Equation 3-1. If liquid water is present at the base of an ice-sheet, and it contains solutes, this will together with the pressure modify the ice melting point. The second factor constitutes an ice/water interfacial effect. The finer grains that a sediment has, the higher the curvature of the ice-water interface becomes, which in turn lowers the melting point (Hohmann 1997). For example, in clays, liquid water has been observed at temperatures down to −10 °C (O'Neill and Miller 1985).

If the effect of phase curvature is taken into consideration the Clapeyron equation may be modified to Raymond and Harrison (1975):

$$T = -\frac{273.15}{L}\left(\frac{1}{\rho_i} - \frac{1}{\rho_w}\right) p_w - \frac{273.15\sigma_{iw}}{L\rho_i r_p} - \frac{273.15}{\rho_w L} P_o \qquad \text{Equation 3-2}$$

where σ_{iw} = ice-water surface energy, and r_p = characteristic particle radius. Equation 3-2 is the fundamental equation for the ice-water phase transition given by Hooke (2004). In this equation, the first of the three terms describes the effect of pressure on the ice-water phase transition, the second term describes the effect of interfacial pressure, and the third term the effect of osmotic pressure. Equation 3-2 thus gives the complete treatment of the ice-water phase transition. Commonly only the first term is used for calculations of the pressure melting point beneath glaciers and ice-sheets, often rewritten in glaciological literature to give a simplified expression for calculating the pressure melting point (cf. Remy and Minster 1993):

$$T = -\frac{h}{1503} \qquad \text{Equation 3-3}$$

where T = pressure melting point temperature (°C), and h = ice thickness (m). The effect of the lowering of the pressure melting point described above is, in the case of an ice-sheet, that the melting point is lowered by c 2 K beneath 3 km of ice. This is very important, since the basal conditions change drastically if the bed of an ice-sheet becomes melted or frozen. This affects ice-sheet flow by turning on and off basal sliding, governs if glacial erosion can take place or not, and of course has a profound impact on basal hydrology.

To demonstrate the effect of ice-sheet surface conditions on the temperature distribution within polar ice-sheets, we start with a simplified case of a steady-state ice-sheet with no ice flow, corresponding to an artificial situation at an ice divide (no horizontal flow) without any precipitation (no vertical flow). Figure 3-2A shows the vertical temperature profile through such an ice mass given a surface temperature of −20 °C and a specified geothermal heat flux at the base. The resulting temperature profile is a straight line from the surface temperature down towards the bed. In this case, the vertical temperature profile reaches the pressure melting point temperature near the bed, resulting in a warm-based polar ice-sheet.

Next, we consider the same case but with snow accumulation at the ice-sheet surface, which means we are introducing an ice movement directed vertically downward. Generally, this lowers the temperatures within the ice-sheet as seen in Figure 3-2B. Due to the vertical velocity and cold surface climate, cold ice is advected downward, while the geothermal heat warms this descending ice. The upper part of the ice-sheet develops an almost isothermal zone, whereas the ice warms quickly near the bed. In this example the ice-sheet below this accumulation area has become cold-based. Higher precipitation rates at the surface, i.e. higher vertical velocities, result in an increased thickness of the isothermal zone and decrease the basal temperature. Furthermore, lower air temperatures at the ice-sheet surface also decrease the ice column temperatures, and vice versa.

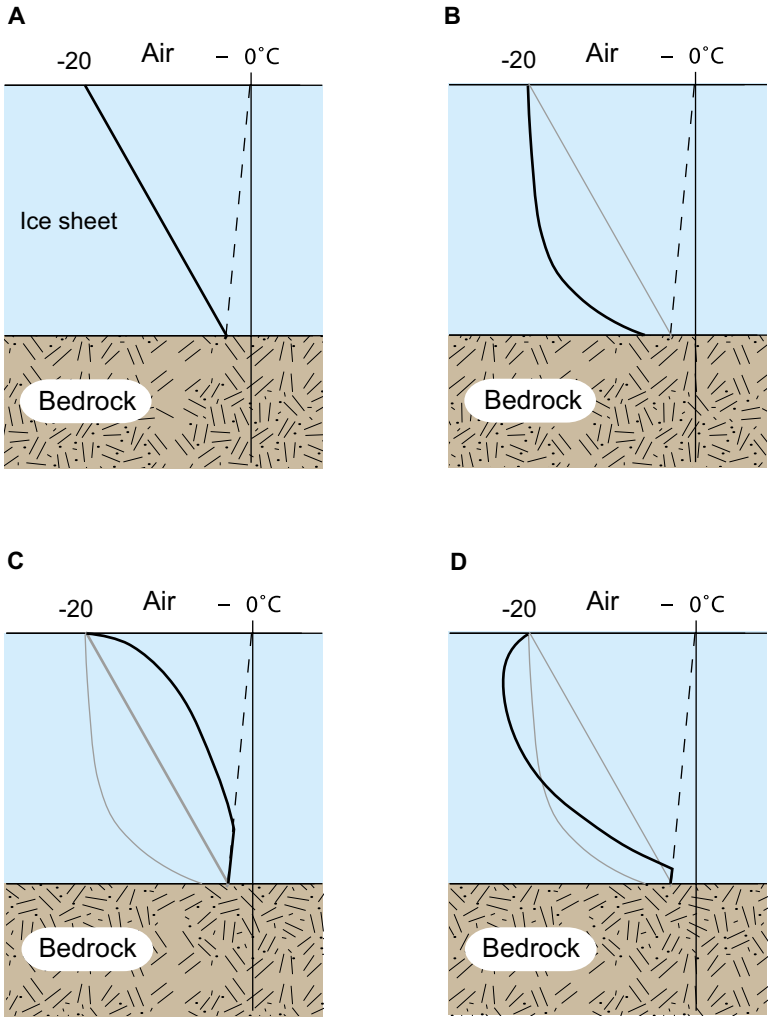

Figure 3-2. *Vertical temperature profiles through a 2000 m thick theoretical polar ice-sheet. The dashed line denotes the pressure melting point temperature. A) No ice flow (dead-ice body), B) Vertical ice flow only – accumulation area (reflecting only a surface accumulation rate), and C) Vertical ice flow only – ablation area, D) Horizontal and vertical ice flow – accumulation area. Grey lines show the cases from the previous plates. Modified from Holmlund and Jansson (2003), after Sharp (1960).*

If we instead consider an ablation area, with net mass loss at the surface, the vertical ice movement will be directed upwards. In this case, the upward vertical velocity produces a generally warmer ice column, in this example resulting in temperate conditions at the bed (Figure 3-2C).

The last case to consider is a more realistic situation, when we also have horizontal ice movement. Figure 3-2D shows a typical situation within the accumulation area of an ice-sheet, but not located directly on an ice divide. The horizontal velocity component is advecting cold ice into the site, ice that was formed in higher, colder parts of the ice-sheet. Compared with the situation in Figure 3-2B, the minimum temperature is now found at some depth below the surface, since the ice at the surface, formed locally at the site, is warmer (Figure 3-2D). This positive temperature gradient near the surface has been observed in several deep drill holes, see for example the Mirny, Century 13, and Byrd 9 drill hole temperatures in Figure 3-3. Furthermore, due to the horizontal ice movement, ice in the lower part of the ice-sheet is warmed by internal friction, as this is where most of the internal deformation of the ice is taking place. In this example, the ice-sheet has again become warm-based.

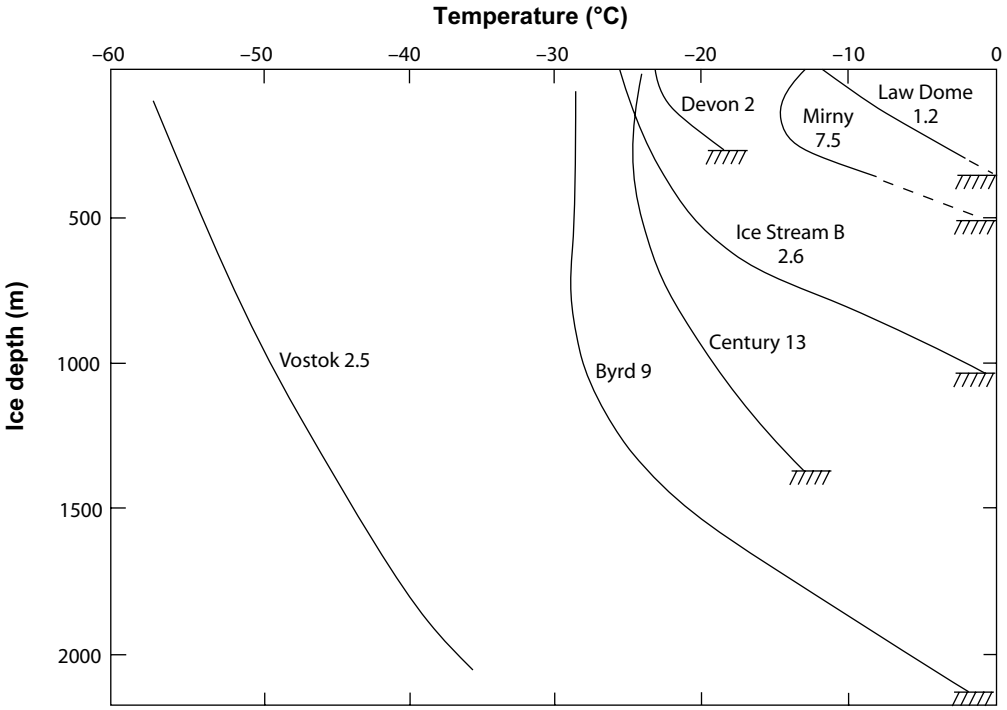

Figure 3-3. *Borehole temperature data from the Greenland and Antarctic ice-sheet. Modified from Holmlund and Jansson (2003), after Paterson (1994).*

Including these processes, the resulting englacial and subglacial temperatures along a flow line are as shown in Figure 3-4. Typical polar ice-sheet accumulation rates and air temperatures are assumed. The lowest englacial temperatures are found in the highest central parts of the ice-sheet, and the highest ice temperatures are found near the front. Basal melting is taking place in the interior part of the ice-sheet and close to the margin, with a zone of basal frozen conditions in between. A narrow zone of basal frozen conditions at the margin may also occur due to decreasing vertical velocity.

In nature, the topography of the landscape beneath the ice-sheet is also of great importance for the basal temperature distribution. Topographic lows are more prone to experience basal melting conditions that topographic heights. This is both because the pressure melting point is lowered more in depressions (due to the greater ice thickness and higher basal pressures) than over surrounding higher terrain, and due to the lower insulating capacity of thinner ice over topographic highs. The result is, for example, that a floor of a large valley in general is more likely to have experienced longer periods of basal melting than surrounding elevated areas (e.g. Näslund 1997).

An additional important process affecting ice temperature takes place if the air temperate allows surface melting during spring periods, for example at low elevations of an ice-sheet in a warming deglaciation climate, or during times of early ice-sheet formation. After the winter period with cold temperatures, the temperature in the upper snow/firn pack of the ice-sheet is well below the freezing point. As surface melting starts, meltwater percolates down in to the snow pack and re-freezes at some depth. During the re-freezing process, latent heat is released (334 kJ kg^{-1}, corresponding to the latent heat of fusion for ice) which warms the surrounding snow. As the process continues the entire snow pack can be transformed to temperate conditions during a few weeks. This is a very efficient process, and the result is that temperate ice instead of cold ice is formed at the location. This may have been an important process during build-up phases of Fennoscandian ice-sheets, having an important effect on the thermal characteristics of early ice-sheets (Näslund 1998).

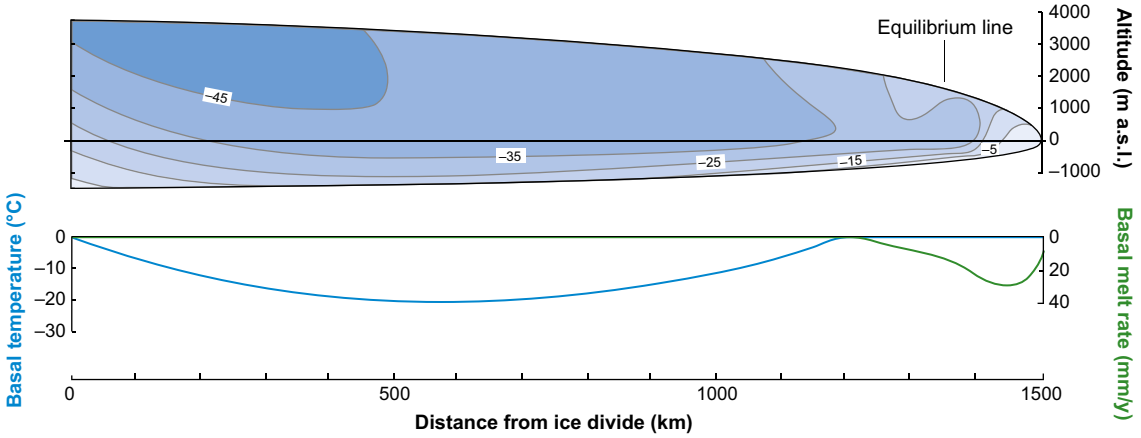

Figure 3-4. *Example of modelled ice-sheet temperature distribution along a flow line. Ice temperatures are in °C. Basal melt rates are high near the terminus because of the strain heating effect from rapid ice flow in the region around the equilibrium line. Modified from Hooke (1977).*

Ice movement and thermodynamic feedback

The stresses induced by the mass of overlaying ice induce deformation or strain in the ice. The resulting ice movement, often referred to as *internal deformation*, is present in all glaciers (being one of the main criteria for the term *glacier*). The shear stress at the base of an ice-sheet is calculated from:

$$\sigma = \rho g h \sin\alpha \qquad \text{Equation 3-4}$$

where σ is the shear stress, g is the acceleration of gravity, h is the ice thickness, and α is the ice-sheet surface slope. The most common flow law of ice describing the strain rate of ice under pressure is Glen's flow law (Glen 1955):

$$\dot{\varepsilon} = \left(\frac{\sigma}{B}\right)^n \qquad \text{Equation 3-5}$$

where $\dot{\varepsilon}$ is the strain rate, σ is the shear stress, B is a viscosity parameter that increases as the ice gets more difficult to deform, a parameter depending on among other things ice temperature and crystal fabric, and n is an empirically determined constant (~ 3) that depends on the specific creep process that is operating. The main effect of Glen's flow law is that moderate increases in stress (ice thickness) result in a substantial increase in strain rate. For example, a doubling of the amount of stress results in 2^3, that is 8, times higher deformation rate (Figure 3-5).

In ice-sheets the horizontal ice velocity increases from the ice divides, where it is zero toward the margin. The steeper surface slope at the margin induces larger driving stresses which makes the ice deformation rate high. For an ice-sheet with an ablation area, i.e. an ice-sheet ending on land (Figure 3-1) the maximum horizontal velocity is at the equilibrium line, whereas in the case of a marine ice-sheet margin, the maximum velocity is at the ice-sheet grounding-line (Figure 3-1).

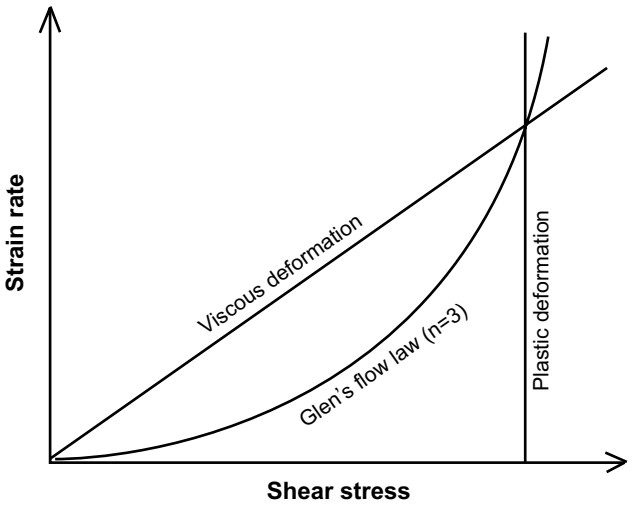

Figure 3-5. *Deformation rate versus shear stress for various flow laws, including Glen's flow law for ice. Modified from Holmlund and Jansson (2003).*

The stress that acts on the uppermost layer of a glacier does not produce a creep or plastic deformation. Instead the uppermost part of the ice, about 30–100 m thick depending on ice temperature, is brittle, often resulting in typical fractures, or *crevasses*. Most of the internal deformation takes place near the bed where stresses are highest. The overlying ice moves along more or less as a uniform block on top of the deforming ice. This is indicated as the internal deformation portion of the ice velocity in Figure 3-6.

There is also another process that may contribute to glacier movement. If the ice-sheet is wet-based, the ice may slide over the substrate, and the substrate itself may deform, especially if the water pressure at the bed is high. The surface ice velocity is, in this case, the sum of the component from internal deformation and the component from basal sliding and deformation (Figure 3-6). For all practical purposes, one can assume that *basal sliding* does not occur if the bed is frozen. Therefore, not all glaciers, or all parts of an ice-sheet, have the sliding ice flow component. However, where it is present, it may be of great importance, for example in ice streams, which are typically warm-based. Here, the observed surface flow may be completely dominated by basal sliding (Engelhardt and Kamb 1998). High basal water pressures are favourable for intense basal sliding (Engelhardt et al. 1990), as well as smooth bed topographies and deformable, water-saturated tills (e.g. Kamb 2001, Iverson et al. 1995).

Within glaciers and ice-sheets there are important thermodynamic feedback mechanisms, in the following exemplified by a discussion on ice streams. As seen above, the viscosity of the ice is affected by the ice temperature, with higher ice temperatures giving more easily deformable ice. At the same time, the internal deformation itself produces frictional heat, with higher velocities producing more heat. This gives a positive feedback mechanism; high internal deformation rates increase the temperature of the ice, which in turn makes the ice even easier to deform.

On the other hand, looking at the basal thermal conditions of ice streams, there may be additional thermodynamic processes acting. A fast-flowing warm-based ice stream may drain a lot of ice from the ice-sheet. Over time this will reduce the thickness of the ice, also over the ice stream itself. The thinner ice insulates less well from cold surface temperatures, which leads to less melting at the bed, and eventually also to a shift from warm-based to cold-based conditions. This reduces the velocity of the ice stream considerably and the ice flux deformational heating reduces accordingly. The ice stream now drains much less ice than before, which in time results in increased ice thicknesses (Payne 1995). The larger ice thickness warms the bed, which again may become wet-based and basal sliding may start again. This process suggests that ice streams may have an inherited built-in unstable behaviour. It has been suggested as one explanation for the cyclic Dansgaard-Oeschger events recorded in glacial marine sediment (cf. Andrews and Barber 2002).

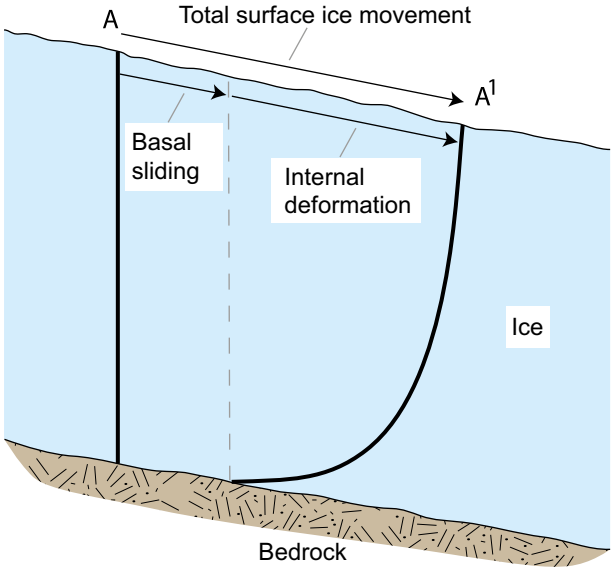

Figure 3-6. *Internal deformation and basal sliding demonstrated by the deforming of a steel rod from time A to A[1]. Modified from Holmlund and Jansson (2003), after Sharp (1960).*

In addition, the dynamics of an ice-sheet, and specifically its ice streams, and the ice-sheet response to changes in climate, are to a large degree governed by the prevailing subglacial hydrology. This field of knowledge is in rapid advance, see further Section 3.2. One process that traditionally has not been incorporated in large-scale ice-sheet models is the coupling of longitudinal stresses within the ice (e.g. Pattyn 2003), that is downstream and upstream push- and pull effects, a process of importance for proper modelling of ice streams and grounding-line features. Several recent studies and ice-sheet models have implemented this, see e.g. Pattyn et al. (2008) and references therein.

3.1.2 Controlling conditions and factors

The upper boundary of the ice-sheet system is the ice-sheet surface, whereas the lower boundary is the ice-sheet bed, i.e. the interface between basal ice and substrate. In accordance with ice-sheet fluctuations, the lateral extent of these boundaries as well as the vertical location of the upper boundary changes over time.

Upper boundary condition – Climate

The boundary condition at the ice-sheet surface is the prevailing climate, i.e. air temperature and precipitation, including its variation over time. The air temperature at the ice-sheet surface is determined mainly by the latitude, altitude and climate changes. The latitude at a site is fixed, but the altitude varies with the local thickness variations of the ice-sheet and associated isostatic responses. The typical air temperature pattern over an ice-sheet is with the lowest temperatures in the ice-sheet interior, and higher surface temperatures closer to the margin. If temperatures are greater than 0 °C during summer, surface melting takes place on the lower parts of the ice-sheet surface. This melting typically amounts to several meters of ice per year, with large variations according to the prevailing temperature regime. Surface melt rates are lower closer to the equilibrium line. In general, during cold stages of ice-sheet growth, the amount of surface melt water production is small compared with the amounts of water produced during ice-sheet deglaciation under warmer climate conditions.

Most precipitation that falls on ice-sheets falls as snow. During relatively warm climates at low ice-sheet elevations, precipitation may occur as rain. Snow accumulation and surface ablation are not distributed evenly over the ice-sheet surface. The precipitation pattern reflects ice-surface elevation and degree of continentality, often giving a pattern of high accumulation rates close to the ice-sheet margin with diminishing values towards the interior. On mid-latitude ice-sheets, like the former Fennoscandian ice-sheet, the precipitation pattern is strongly affected by the prevailing west-wind belt and associated low-pressure tracks. This results in an orographic effect which gives most precipitation on the western side of large Fennoscandian ice-sheets. Typical coastal accumulation rates of the Antarctic ice-sheet are 0.3–0.6 m a^{-1} (water equivalents), whereas the interior parts get less than 0.1 m a^{-1} in precipitation (Giovinetto and Zwally 2000), i.e. here polar desert conditions prevail. On an ice-sheet surface, regional and local variations of great magnitude in the amount of snow accumulation often occur, mainly due to wind re-distribution of snow in regions close to the ice-sheet margin (Figure 3-7).

To initiate ice-sheet growth in a non-glaciated region, local climate needs to change. That can either occur due to global climate change, towards lower local summer temperatures or higher winter precipitation rates, or, over long timescales, by tectonic uplift, or a combination of climate and tectonics. Generally, ice-sheet formation in Fennoscandia involves small alpine glaciers in the Scandinavian mountain range that grow into a mountain-centred ice-sheet, and then grow to a full-scale ice-sheet (Andersen and Mangerud 1989, Lundqvist 1992, Kleman et al. 1997). Increasing evidence suggests very dynamic ice-sheet and climate behaviour during the last glacial cycle, with ice-sheet growth phases interspersed by extended periods with restricted ice coverage, see also Section 4.3.

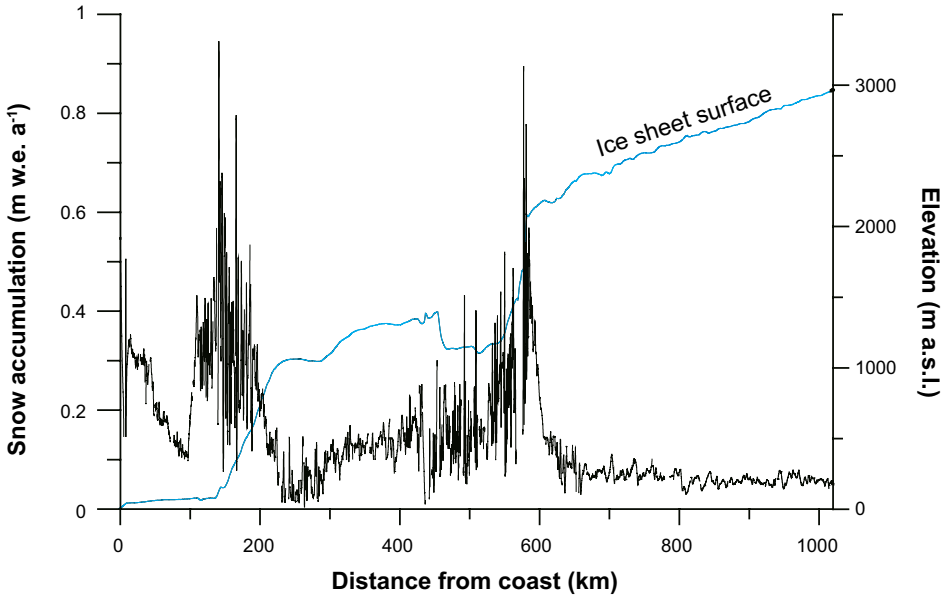

Figure 3-7. *Accumulation rates (in metres water equivalents per year) and ice-surface elevations (in metres above sea-level) along a profile in over the East Antarctic ice-sheet. The accumulation is high in the coastal area and low in the interior. Exceptionally high values of snow accumulation are found in areas of nunataqs and steep surface slope as a result of wind-redistribution of snow and increased topographically-induced precipitation. Modified from Richardson (2004).*

Lower boundary condition – Ice-sheet bed

The lower boundary condition of the ice-sheet system is the ice-sheet bed. The substrate typically either consist of bedrock, in Fennoscandia normally crystalline rocks, or bedrock covered by till. There are two important parameters to consider here; 1) the topography of the landscape, and 2) the amount of geothermal heat flow.

The topography of the bed is of importance for the basal boundary conditions of ice-sheets, as discussed above. Above all, an ice-sheet bed with strong relief produces basal thermal conditions with stronger lateral temperature gradients than an ice-sheet bed with smooth topography. The first case also implies larger spatial variations in basal melt water production.

The geothermal heat flux is also of great importance for the basal condition of ice-sheets (e.g. Waddington 1987), affecting basal ice temperatures, hydrology, ice dynamics, and the erosional capacity of the ice. Typically, for a 3 km thick ice-sheet at steady-state, a 20 % error in geothermal heat flux generates a 6 K error in calculations of basal ice temperatures. This has direct implications on, for example, numerical ice-sheet modelling. If the geothermal heat flow is not realistic in the model setup, ice-sheet models will not produce useful data on basal melting and other characteristics. Numerical ice-sheet modelling studies have also shown that basal ice temperatures are sensitive to relatively small changes in geothermal heat flow (e.g. Greve and Hutter 1995, Siegert and Dowdeswell 1996).

For the modelling study presented in Section 3.1.4, (Näslund et al. 2005) calculated a distributed, high-resolution geothermal heat flow data set for an approximate core area of the Fennoscandian ice-sheet, and embedded this within lower-resolution data published for surrounding regions. In the following, a brief overview of the geothermal heat flux calculation is given.

The geothermal heat flow, or surface heat flow density (HFD), in cratonic areas consists of two components: (1) heat produced within the mantle and core of the Earth and (2) heat produced within the crust. The contribution from the Earth's interior (so-called Moho- or reduced heat flow) arises from the cooling of the Earth and formation of a solid core, and from radiogenic heat production (e.g. Pollack et al. 1993). The crustal component consists of radiogenic heat production where heat is produced by the natural radioactive decay of primarily ^{238}U, ^{232}Th, and ^{40}K (Furlong and Chapman 1987). The Moho heat flow has a smooth spatial variation, possibly depending on mantle convection cell distribution

(Beardsmore and Cull 2001), whereas the spatial variation in concentration of radioactively decaying nuclides in the lithosphere generates a heat flow with large spatial variations. The surface HFD can be estimated by a heat flow-heat production (Q-A) relationship of the form

$$Q = q_0 + DA_0 \qquad \text{Equation 3-6}$$

(Birch et al. 1968, Lachenbruch 1968, Beardsmore and Cull 2001) where Q is the surface heat flow density (or geothermal heat flow), q_0 is the Moho heat flow, D represents the vertical distribution of heat-producing radionuclides in the lithosphere and A_0 is the radiogenic heat production from near-surface rocks.

The regional HFD pattern does not correlate with gravity variations (Balling 1984), magnetic anomalies (Riddihough 1972), or crustal thickness (Čermák et al. 1993). However, within the Baltic shield, as well as in other areas with similar geological settings, there is close correlation between HFD and regional geological units, with higher heat flow from acid (commonly granitic) areas and lower heat flow values from basic areas (e.g. Landström et al. 1979, Malmqvist et al. 1983).

The calculation of HFD values for Sweden and Finland were based on detailed data sets from numerous γ-emission measurements from bedrock and till. In Sweden, airborne surveys of γ-emissions have been carried out by the Geological Survey of Sweden (SGU), sampling data at 70 m intervals along flight lines with 17 km separation. To avoid shielding effects from vegetation and lakes, only data from exposed bedrock and till surfaces were used in the calculations. The Finnish data set is based on radiometric γ-emission measurements of 1054 till samples providing full spatial coverage of the country (Kukkonen 1989).

The calculation of HFD is performed in several steps. First, the concentrations of ^{238}U, ^{232}Th, and ^{40}K are calculated from the γ-emission measurements, using information from detailed reference measurements over calibration plates with well-known isotopic concentrations. Near-surface heat production was then calculated from the concentrations of radionuclides. In addition, the Moho heat flow contribution needs to be considered. The distributed Moho heat flow by Artemieva and Mooney (2001) was added to the near-surface heat production data set. Finally, the HFD data set was re-sampled to a grid with 5 km resolution. To provide HFD coverage for the entire model domain, data for surrounding areas were added from the much coarser observed global HFD data set provided by Pollack et al. (1991). The resulting geothermal heat flow distribution is shown in Figure 3-8.

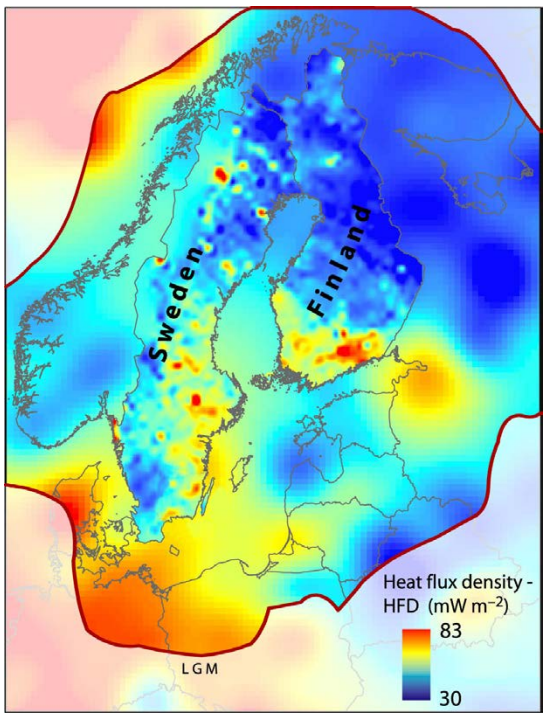

Figure 3-8. *Geothermal heat flow distribution over Fennoscandia. Modified from Näslund et al. (2005).*

Within the LGM ice margin, the new data set shows that the geothermal heat flow varies by a factor of as much as 2.8 (geothermal heat flow values ranging between 30 and 83 mW m^{-2}), with an average of 49 mW m^{-2}. This average value is 17 % higher than 42 mW m^{-2}, the typical uniform value used in ice-sheet modelling studies of Fennoscandia. Using this new distributed data set on geothermal heat flow, instead of a traditional uniform value of 42 mW m^{-2}, yields a factor of 1.4 larger total basal melt water production for the last glacial cycle (Näslund et al. 2005). Furthermore, using the new data set in high-resolution modelling, results in increased spatial thermal gradients at the bed. This enhances and introduces new local and regional effects on basal ice temperatures and melt rates. The results show that regional to local variations in geothermal heat flow need to be considered for proper identification and treatment of thermal and hydraulic bed conditions under the Fennoscandian and other similar ice-sheets (Näslund et al. 2005).

Ice properties

The exponent n in Glen's flow law (Equation 3-5) is dependent on the active creep process. Numerous field experiments and laboratory tests of glacier ice suggest that n should be ~~3. The typical creep process that is considered is a simple power-law creep, where the creep rate is proportional to the stress raised to some power greater than 1, for example:

$$\dot{\varepsilon} \propto \sigma^3 \qquad \text{Equation 3-7}$$

On the other hand, with certain temperature, stress, and grain-size combinations, diffusional creep instead of power-law creep could take place in ice-sheets (Duval et al. 1983), which would lower the value of n to less than 3. Other recent studies suggest that n should be between 1 and 2 for deformation at low stresses, low temperatures, and low cumulative strains (Alley 1992, Montagnat and Duval 2000). However, some of these conditions are likely to be important only down to depths of a few hundred metres in the coldest parts of ice-sheets.

The viscosity constant B in Glen's flow law is dependent on a large number of parameters. Therefore, various modifications of Glen's flow law have been developed taking into account temperature, hydrostatic pressure, and crystal orientation. The last case is the most difficult, and it is done by introducing an anisotropy enhancement factor. The *c*-axes of the ice crystals are, to a large degree, uniformly distributed in the upper part of the ice-sheet, i.e. the ice is basically isotropic. When the ice over time is affected by the weight of the accumulating overlying ice mass, it is vertically compressed and longitudinally stretched, which results in a conical distribution of c-axes orientations. Subsequently, when the ice is affected by the simple shear close to the ice-sheet bed, the *c*-axes are typically re-oriented to a preferred single orientation. Development of *c*-axis fabrics has been obtained by re-crystallisation and ice-grain rotation. Since it is known from ice-core studies that the crystal orientation in ice-sheets is not isotropic at depth, a non-isotropic flow law of ice improves, for example, the results of ice-sheet modelling (e.g. Placidi et al. 2010).

The ice-sheet dynamics described above may affect a number of geosphere variables of importance for a deep geological repository (Table 1-1, Table 3-1).

3.1.3 Natural analogues/observations in nature

Palaeo-ice-sheets

The mid-latitudes of the Northern Hemisphere have experienced repeated continental-scale glaciations during the Quaternary period. As previously mentioned, these periods are referred to as *glaciations* and the warm periods between the glacials are called *interglacials*. The present interglacial is called the Holocene, and in north–western Europe, the last glaciation is named the Weichselian.

Palaeo-ice-sheets have left geological traces in previously glaciated terrain in Fennoscandia, North America and Siberia, as well as abundant glacio-marine traces in adjacent ocean basins. Studies of North Atlantic marine sediments have shown that the first traces of eroding glaciers in Greenland and Fennoscandia date back to between 12 and 6.6 Ma BP (Jansen and Sjøholm 1991, Fronval and Jansen 1996), with larger ice-sheets present in Fennoscandia from around 2.75 Ma BP. During the last ~ 700 ka, glaciation cycles have been about 100 ka long (cf. EPICA community members 2004, Lisiecki and Raymo 2005), preceded by a period of shorter (41 ka) glacial cycles (e.g. Raymo et al. 1998, McIntyre et al. 2001).

Geological information on till stratigraphy, interstadial deposits, glacial landforms in loose sediments and in bedrock have for a long time been used for making reconstructions of the Weichselian glacial history. A summary of that work is provided in Lokrantz and Sohlenius (2006). Section 4.3 describes several studies that have been used for the reconstruction of the Weichselian glacial history for the PSAR and of climate conditions during this glacial cycle.

Table 3-1. A summary of how geosphere variables are influenced by ice-sheets.

Geosphere variable	Climate issue variable	Summary of influence
Ground temperature	Basal ice temperature	During periods of cold-based ice coverage, low basal ice temperatures contribute to the formation of permafrost. During periods of warm-based ice coverage, basal ice temperatures at the pressure melting point contribute to permafrost degradation.
Groundwater flow	Basal thermal condition Basal melt rate Supply of surface melt water	If the ice-sheet is cold-based, no free water is available and there will be no groundwater recharge from basal melt water. If the ice-sheet is warm-based, basal melting occurs at the ice/bed interface and groundwater recharge takes place. In addition, meltwater from the ice-sheet surface will, in both cases, be transported to the bed in frontal-near areas of the ice-sheet (see further Section 3.2). Groundwater recharge and flow will be determined by the presence of the ice-sheet.
Groundwater pressure	Basal thermal condition Ice-sheet thickness Basal melt rate Supply of surface melt water	If the ice-sheet is warm-based, the water pressure at the ice/bed interface may reach as much as the ice-sheet overburden pressure, and in certain cases more. The groundwater pressure also depends on the melt water supply and the flow properties of the en- and sub-glacial hydrological systems (see further Section 3.2). The groundwater pressure is also affected by the ice-load compression of the bedrock pores and fractures.
Rock stresses	Basal condition Englacial ice temperatures Ice-sheet thickness	Rock stresses will be influenced by the ice load and the hydrostatic pressure. Independently of basal conditions there will be an increase in vertical stresses corresponding to the ice thickness. The horizontal stresses will also increase. If the ice-sheet is warm-based, the prevailing water pressures at the ice/bed interface will also alter rock stresses. The alteration of rock stresses also depends on the duration of the ice load and the slope of the ice-sheet surface. The slope of the ice-sheet surface near the front is in turn highly dependent on englacial ice temperatures and basal thermal conditions.
Groundwater composition	Glacial melt water composition	The glacial melt water is oxygen rich. The combination of abundant melt water supply and high water pressures may cause injection of glacial melt water to larger depths than for non-glacial conditions. Also, the consumption of oxygen close to the surface may be limited due to the lack of organic matter and microbiological activity.

Various types of glacial landforms may also be used to infer information on basal thermal conditions of palaeo-ice-sheets (e.g. Lagerbäck 1988a, Kleman et al. 1997, Kleman and Hättestrand 1999, Kleman and Glasser 2007).

Present ice-sheets

At present there are two ice-sheets on Earth, the Antarctic (14 Mkm^2) and Greenland (1.7 Mkm^2) ice-sheets. Large portions of these quasi-stable ice-sheets are more than 3 km thick. In both cases, the ice-sheet load has depressed the bed so that large portions are situated below sea-level. Offshore marine sediments have shown traces of waxing and waning Antarctic ice-sheets of continental proportions back to 40–36 Ma (Haq et al. 1987, Hambrey et al. 1992), and Antarctic alpine glaciers may trace back to the Oligocene (Näslund 2001). The present configuration of the Antarctic ice-sheet is thought to have been relatively stable for the last 15–11 Ma (cf. Shackleton and Kennett 1975, Marchant et al. 1993).

The spatial patterns of basal thermal characteristics of the Antarctic and Greenland ice-sheets are complex due to ice-sheet dynamics, bed topography, and geothermal heat flux variability. For both ice-sheets, parts of the bed are cold-based whereas other parts are warm-based, as seen from modelling

studies (Figure 3-9), radar soundings and drill hole data. Ice-sheet modelling has also, together with geological field observations and remote sensing studies, showed that ice streams are prominent features of the Antarctic ice-sheet, penetrating far into the ice-sheet interior (Figure 3-10). This has also been shown by remote sensing Interferometric Synthetic Aperture Radar (InSAR) studies (Joughin and Tulaczyk 2002). The outer coastal-near parts of these ice streams are typically wet-based, whereas their upstream parts, high in the catchment areas, often are cold-based.

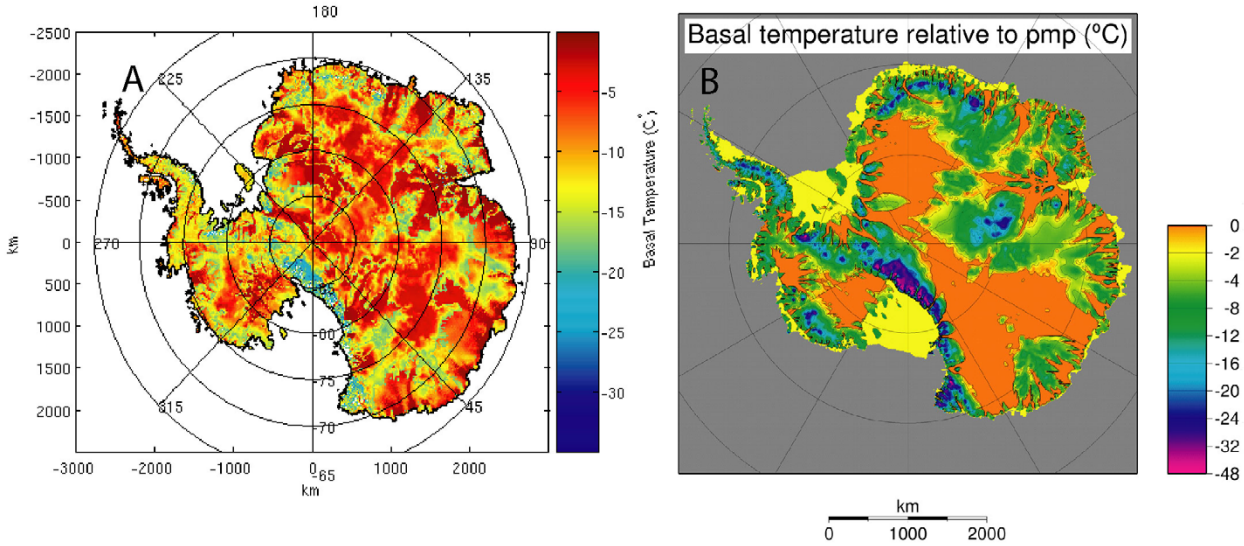

Figure 3-9. *Two examples of modelled present-day Antarctic ice-sheet basal temperatures. Temperatures are expressed relative to the pressure melting point (pmp). Figures modified from a) Johnson (2004) and b) Huybrechts (2006).*

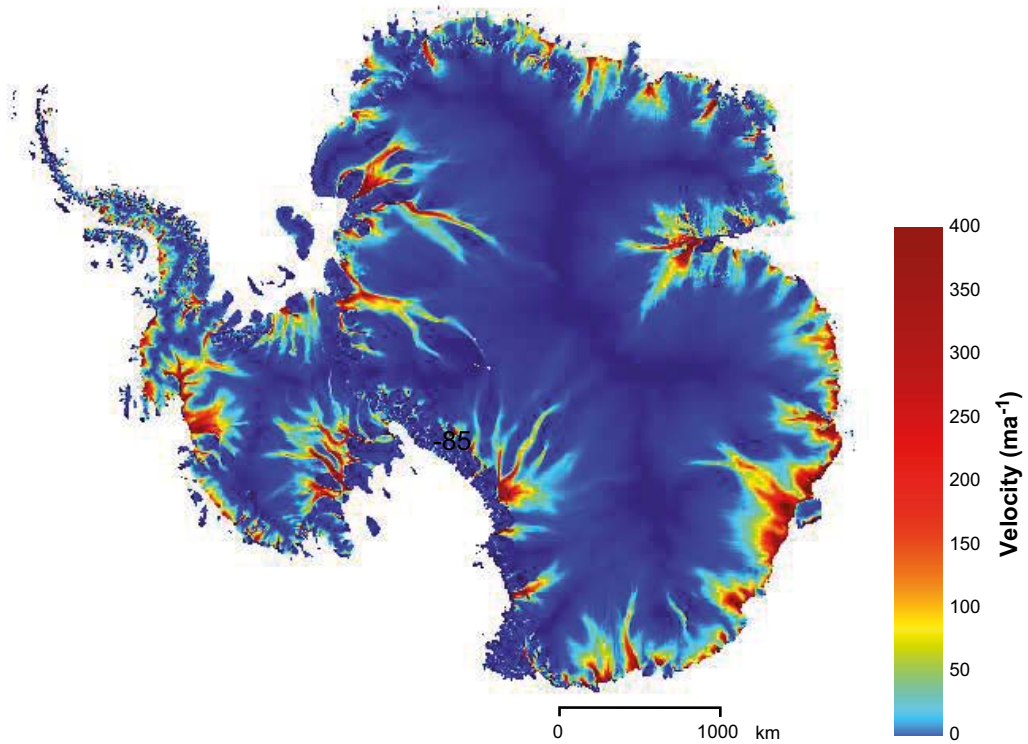

Figure 3-10. *Modelled Antarctic ice surface velocities. Fast-flowing ice streams (red/yellow/green colour) reach far into the ice-sheet interior. Modified from Johnson (2004) with numerical methods described in Staiger et al. (2005).*

During the Middle and Late Pleistocene glacial periods (last ~800 ka), the Greenland and Antarctic ice-sheets had a larger extent than at present. The major limiting factor on their maximum lateral extent is the bed topography; the Antarctic and Greenland ice-sheet margins are both today located close to the coast line. The continental crust does not extend out very far from the present-day coast lines, and at the continental margin the water depth quickly becomes deeper. When the ice-sheets grow larger the grounding-line migrates outward, resulting in a larger area for the grounded part of the ice-sheet. The grounding line cannot advance past the continental margin due to the larger water depths outside. The continental margin thus constitutes a definite constraint on the maximum spatial size of Antarctic and Greenland ice-sheets during Quaternary ice-sheet fluctuations. The situation was similar for part of the Fennoscandian ice-sheet. From a bed topography point of view there were no constraints on ice-sheet growth from the Scandinavian mountain range towards east (the Baltic depression is not deep enough in this context), but, towards the west, Fennoscandian ice-sheets, including the last Weichselian ice-sheet, could not and did not extend farther west than the offshore continental margin (Svendsen and Mangerud 1987, Zweck and Huybrechts 2003).

Although the sizes of the Antarctic and Greenland ice-sheets were greater during the Middle and Late Pleistocene glacials, the maximum thicknesses need not have been larger. On the contrary, because of atmospheric moisture starvation during the colder climates, the interior parts of the ice-sheets probably were thinner during the coldest parts of the glacial cycles (e.g. Huybrechts 1990). In contrast, at the ice-sheet margins the ice-sheet thickness varies considerably during a glacial cycle. Areas where the ice thickness is zero during a warm interglacial period (i.e. at the exact margin) may experience an increase in ice thickness of several hundred metres, up to one kilometre, during a glacial maximum ice configuration (Näslund et al. 2000). In turn, this means that the temporal changes in basal conditions of the ice-sheets, for example changes in basal ice temperatures from the present interglacial pattern, were highly complex. For example, due to the changed ice configuration affecting ice-sheet dynamics, some parts of the Antarctic ice-sheet were warmer at the LGM ice configuration than at present, whereas at the same time, other parts were colder (Figure 3-11) (cf. Näslund et al. 2000).

Recently, the coupling between the dynamic behaviour of the Greenland ice-sheet and ice-sheet hydrological processes have been inferred from several studies, see Section 3.2.

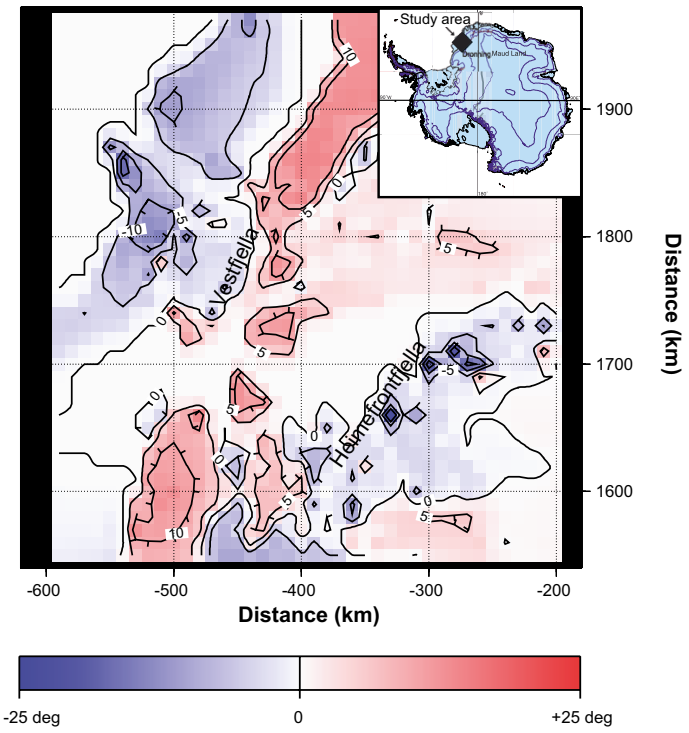

Figure 3-11. *Modelled difference in basal temperature between the present-day ice configuration and a maximum Pleistocene ice-sheet configuration for part of the Antarctic ice-sheet. For this single change in ice configuration, ice-sheet thermodynamics induces complex changes in basal thermal pattern; some parts of the ice-sheet become warmer at the bed the same time as other parts become colder. From Näslund et al. (2000).*

3.1.4 Model studies

Thermo-mechanical ice-sheet modelling is a well-established and useful tool for studying a large array of ice-sheet-specific and ice-sheet-related issues. Although ice-sheet models have limitations, see e.g. SCAR (2007), they can be used to study characteristics and behaviour of present ice-sheets, palaeo-ice-sheets, and in some cases also inferred future ice-sheets. As computer capacity has increased, more sophisticated models have been able to be run at higher spatial resolutions, which in turn has made it meaningful to compare detailed model output with various types of geological information, both for model verification and testing of glacial-geological hypotheses (e.g. Pattyn et al. 1989, van Tatenhove and Huybrechts 1996, Näslund et al. 2003, Staiger et al. 2005, Patton et al. 2016).

Reconstructions of palaeo-ice-sheet configurations, including ice thicknesses, may be done by two main groups of models. One group is thermo-mechanical ice-sheet models that are based on ice physics and thermo-mechanical interactions (e.g. Huybrechts 1986, Boulton and Clarke 1990, Fastook 1994, Ritz et al. 1996, Payne and Dongelmans 1997, Marshall and Clarke 1997). The second group of models are isostatic rebound models that are used to invert observations of crustal rebound and shoreline locations to estimate palaeo-ice thicknesses (e.g. Lambeck et al. 1998, Peltier 2004).

For the present study, UMISM (University of Maine Ice-sheet Model) (Fastook and Chapman 1989, Fastook 1990, 1994, Fastook and Prentice 1994, Johnson 1994) was selected for the simulation of last glacial cycle ice-sheet configurations. The UMISM code was selected because a large number of simulations of the last glacial cycle Fennoscandian ice-sheet have been done with this model over the years (e.g. Fastook and Holmlund 1994, Holmlund and Fastook 1995, Näslund et al. 2003). The UMISM was part of the European Ice-sheet Modelling Initiative (EISMINT) model intercomparison experiment and yielded output in agreement with many other physically-based ice-sheet models (Huybrechts et al. 1996, Payne et al. 2000), which further motivated the choice of model.

The resulting reconstruction of last glacial cycle ice-sheet configurations for the Forsmark site (e.g. Figure 4-19) shows large similarities with corresponding data for a North American last glacial cycle scenario modelled using the Peltier model (Garisto et al. 2010). This indicates that the selection of type of model is not critical for the general appearance of the ice-sheets reconstructed for the last glacial cycle. In detail, however, the development of ice configurations over time in e.g. these two studies are expected to differ for several reasons, including that the studies deal with two different geographical areas and indeed two different ice-sheets (the Weichselian ice-sheet over Eurasia and the Laurentide ice-sheet over North America). For instance, the last glacial cycle Laurentide ice-sheet is known to have been considerably larger and thicker than the Fennoscandian ice-sheet.

The ice-sheet system constitutes three main sub-systems: mass-balance, ice movement, and ice temperature. For these sub-systems the selected ice-sheet model solves differential equations describing conservation of mass, momentum, and energy, respectively. In addition, the ice-sheet model needs to be forced by the climate, described by the air temperature and precipitation. The spatial distribution of the precipitation is calculated from the air temperature field, based on an empirical relationship developed from the Antarctic ice-sheet (Fastook and Prentice 1994). The model hence calculates the precipitation based on air temperature, as well as on several other parameters such as distance from the pole, saturation vapour pressure (function of altitude and lapse-rate), and surface slope. Over a certain model domain, with a topography described by a Digital Elevation Model (DEM), this climate description gives a spatial pattern of precipitation and air temperatures at ground level.

The UMISM also includes a simplified isostatic description for the behaviour of deforming bedrock due to the weight of the modelled ice-sheet configuration. This is not a full self-gravitational spherical Earth model as used in the Glacial Isostatic Adjustment (GIA) modelling in Section 3.3. Instead, it is a hydrostatically supported elastic plate model, considered adequate for placing the ice-sheet surface at an appropriate altitude, and hence at an appropriate air temperature, for the mass balance calculations. Furthermore, the UMISM also includes a subglacial hydrology model (Johnson 1994) that can transport basal meltwater under the ice-sheet according to prevailing pressure potentials governed by ice-sheet thickness and basal topography.

A palaeo-temperature record was employed to run the ice-sheet model (Figure 3-12). For the reconstruction of the Weichselian ice-sheet, see below, the temperature proxy record for the last 120 ka from the Greenland GRIP ice core was used (Dansgaard et al. 1993). The temperature file that was used contains 50-year averages of the original time series. For a detailed description of this temperature data set, including its use in the ice-sheet modelling and its estimated uncertainties, see Appendix A and the **Data report**.

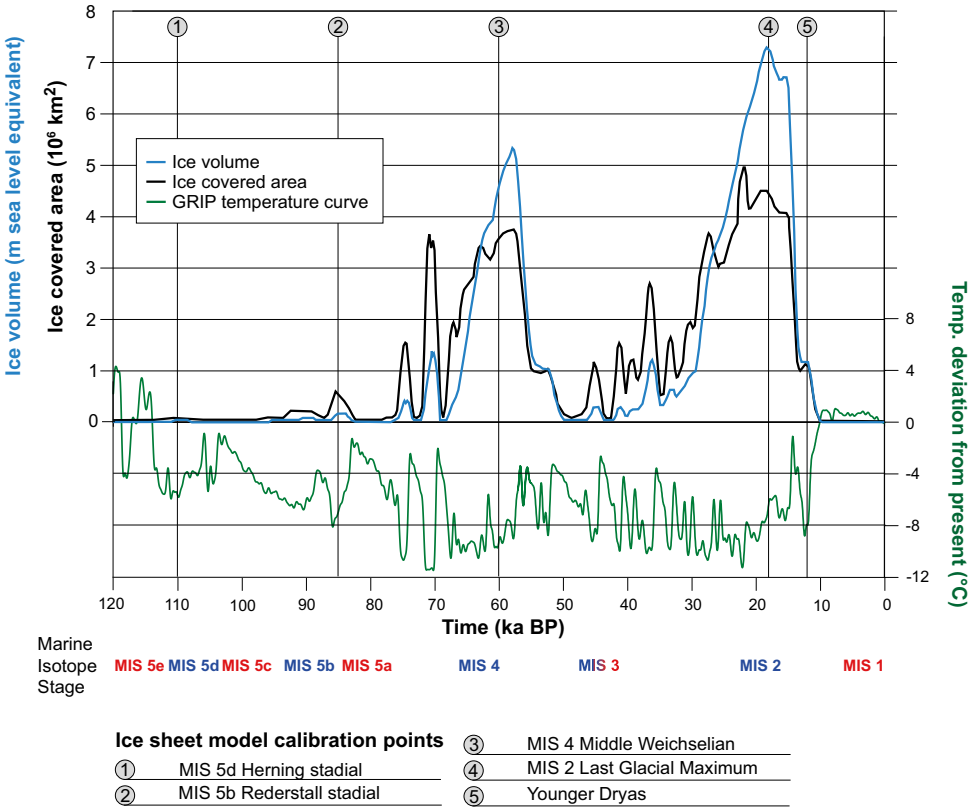

Figure 3-12. *GRIP proxy temperature curve, and reconstructed ice-covered area and ice volume for the reconstruction of the Weichselian ice-sheet. Times of model calibration are shown, as well as Marine Isotope Stages (MIS) (warm stages in red and cold stages in blue).*

In the modelling process, the variations in the temperature proxy curve are used to change the climate pattern (temperature and precipitation) over the model domain, initiating ice-sheet growth in Fenno-scandia. Once glaciers/ice-sheets are formed, the modelled thermo-dynamic ice-sheet system starts to evolve over time. In this way, the ice-sheet model simulates the behaviour of the ice-sheet as it responds to the external forcing such as changing climate or sea-level, as well as internal dynamics, such as ice-stream variations caused by internal temperature oscillations at the bed.

The following are input parameters to the ice-sheet model in the simulations of the Weichselian ice-sheet:

1. The thermodynamic properties of the ice, including flow laws, sliding laws, feedback mecha-nisms etc.
2. Upper boundary conditions: Climate description (annual air temperature, and precipitation rates) from the mass balance parameterisation.
3. Lower boundary conditions:
   A. A DEM over Fennoscandia with a moderately high spatial resolution. For the reconstruction of the Weichselian ice-sheet a grid size of 50 km was used. This resolution is sufficient to capture the general large-scale dynamics of the ice-sheet but would be too coarse in regions with large and highly variable topography. However, this is not the case for south-central Sweden which is in general characterized by a relatively flat to very flat topography. DEM data were taken from the ETOPO2 data base[1], depicting both continental topography and bathymetry;
   B. Geothermal heat flux at the bed.
4. Sea-level changes during the last 120 ka.
5. Proxy curve of palaeo-air temperatures during the past 120 ka (GRIP data).

[1] ETOPO2, 2001. Global Digital Elevation Model (ETOPO2) representing gridded (2 minute by 2 minute) elevation and bathymetry for the world. Data were derived from the National Geophysical Data Center (NGDC) ETOPO2 Global 2' Elevations data set from September 2001.

The modelling started 120 ka BP, and the model was run at a five-year time step forward in time up to time zero (present). For each time step, the output data that were calculated for each grid cell and grid node included:

1. Ice thickness.
2. Englacial and basal ice temperatures.
3. Ice velocity.
4. Direction of ice movement.
5. Isostatic depression of crust.
6. Amount of basal melting or freeze-on of water.

Model setup

A model domain was selected to cover the maximum extent of the Weichselian ice-sheet over Fennoscandia, with a spatial DEM resolution of 50 km. The thermomechanical coupling between ice movement and ice temperature was enabled, as well as a function by which the amount of basal sliding is coupled to the amount of basal meltwater present at the ice-sheet bed. The n parameter in Glen's flow law (Section 3.1.2) was set to 3, whereas the values for the viscosity parameter B differed depending on ice temperature. Exemplified calculated values of B are seen in Figure 3-13. In the final model run, the model was run with a five-year time step and data was saved from the model simulation at a 100-year interval.

The traditional way of specifying the basal thermal boundary condition in ice-sheet modelling is to apply a single, uniform value of geothermal heat flow for the entire model domain. The magnitude of this geothermal heat flow value has often been set according to the general geological setting for the area to be studied. Thermodynamic modelling of Fennoscandian ice-sheets has, for instance, used a single geothermal heat flow value typical for the Pre-Cambrian shield, the most common reported value being 42 mW m^{-2} (e.g. Boulton and Payne 1992, Huybrechts and T'siobbel 1995, Payne and Baldwin 1999). Others have used higher values, around 50–55 mW m^{-2} (e.g. Hindmarsh et al. 1989, Forsström et al. 2003).

For the model reconstruction of the Weichselian ice-sheet, the geothermal data set of Näslund et al. (2005) was used as basal boundary condition. A so-called higher-order model, taking into account longitudinal push-and-pull effects within the ice-sheet was used for specific studies of ice flow behaviour in relation to geothermal heat-flow anomalies in Sweden, see Näslund et al. (2005).

Model calibration

In studies in which ice-sheet modelling aims at simulating palaeo-ice-sheets, one needs to calibrate the behaviour of the model against known information on ice-sheet extents. The reason for this is that we do not have full knowledge on several the processes and boundary conditions involved, for example climatic conditions in the past, or ice-sheet basal processes. In the present reconstruction of the Weichselian ice-sheet, the UMISM model was calibrated by adjusting the proxy air temperature curve (Figure 3-12). Over the years, a large number of such simulations of the Fennoscandian ice-sheet have been done with the UMISM model using this climate curve, which has given extensive experience of how to perform the model calibration. As mentioned above, the forcing in temperature for the ice-sheet model is based on the GRIP ice core (Dansgaard et al. 1993), see also Appendix A. In the ice-sheet calibration process, the entire temperature curve was shifted and amplified (Figure 3-14) to obtain calibrated ice-sheet configurations that fitted as well as possible with geological observations on dated marginal positions. Model calibration was made for ice margins as described in Lokrantz and Sohlenius (2006) for MIS 5d (~110 ka BP), MIS 5b (~85 ka BP), MIS 4 (~60 ka BP), MIS 2 (~18 ka BP), and for the Younger Dryas (~12 ka BP) (Figure 3-12). Keeping all other input data constant in the calibration process, the modified temperature curve after model calibration resulted in Late and Middle Weichselian ice-sheet configurations in good agreement with dated ice-marginal positions and Early Weichselian configurations in reasonably good agreement with geological interpretations. The characteristics and applicability of the GRIP temperature curve for the present study is further described and discussed in Appendix A.

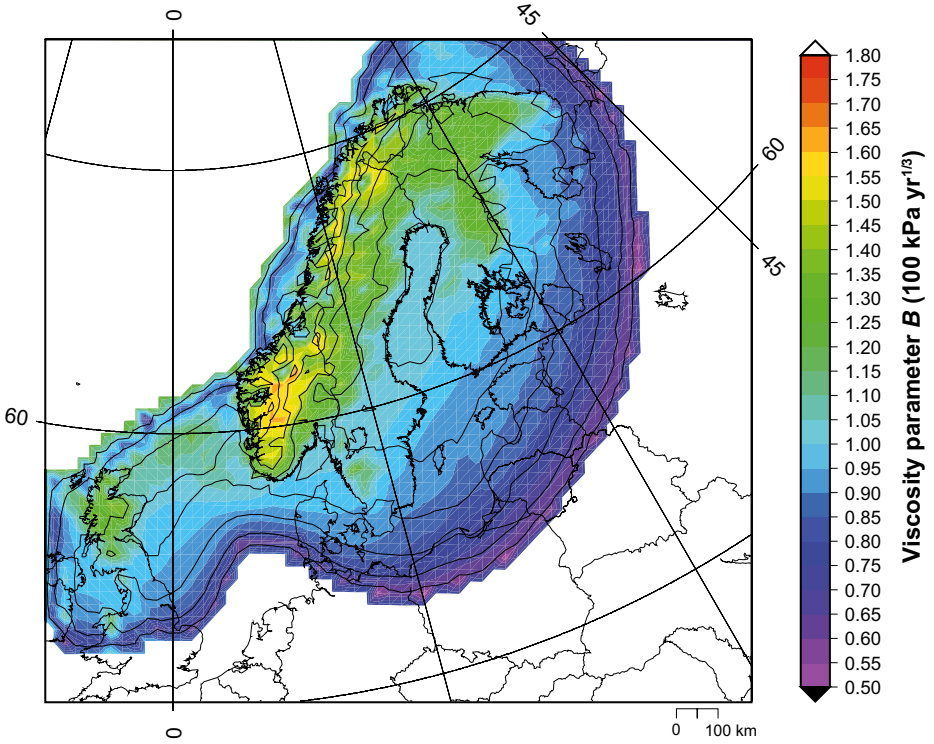

Figure 3-13. *Calculated flow-law viscosity parameter B at 18.5 ka BP (at around Last Glacial Maximum), shown as vertically integrated values along the ice column. Colder and harder ice is seen in the central parts of the ice-sheet and over the Scandinavian mountain range (larger B values), whereas warmer and softer ice is seen closer to the ice margin (smaller B values). The black lines show ice thickness contours with a 500 m interval.*

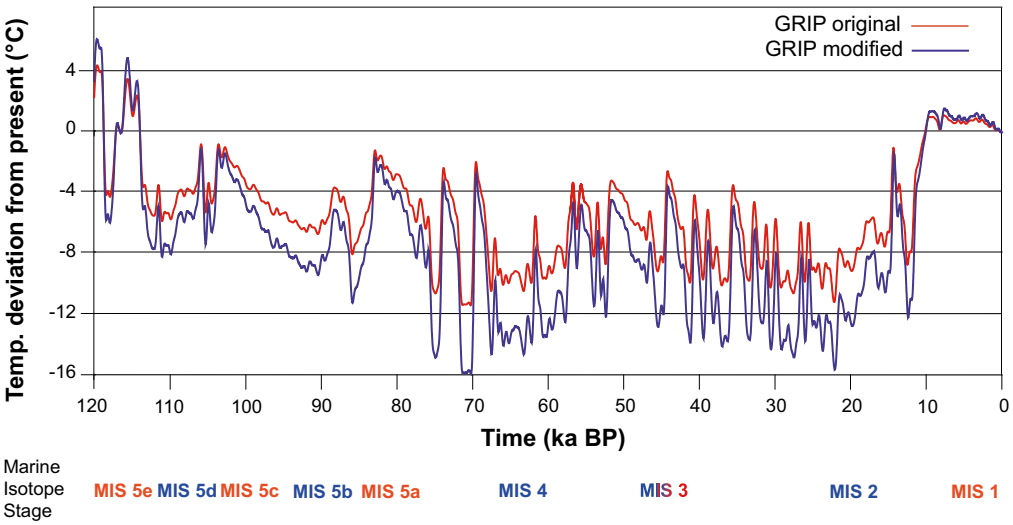

Figure 3-14. *Proxy palaeo-air temperature curves from the calibration process of the UMISM ice-sheet model. The final calibrated curve that was used (blue) has larger amplitude that the original data (red), i.e. cold periods were even colder in the calibrated curve. In the calibration process, it was chosen to always change the entire curve in the same way. The temperature curve is discussed in detail in Appendix A.*

Model results

The resulting calibrated reconstruction of the Weichselian ice-sheet is seen in Figure 3-12 and Figure 3-15. Ice extends over the model domain during the cold stadials during Marine Isotope Stages (MIS) 5d, 5b, 4, and 2. During warmer interstadials, such as MIS 3, the ice cover is more restricted. As expected, there is a clear trend of more and more pronounced ice coverage during the stadials through the glacial cycle, with the LGM peak occurring at around 18 ka BP.

Different types of output data have been extracted and post-processed from the reconstruction of the Weichselian ice-sheet, for example 1) basal and surface melt rates for groundwater modelling (Jaquet and Siegel 2006), 2) Basal and subaerial temperatures for permafrost modelling (Section 3.4 and Appendix A), 3) ice-thickness variations for modelling of global isostatic adjustment (Section 3.3) and crustal stresses (Lund et al. 2009), and 4) 2D ice-sheet profiles for modelling of groundwater flow under glacial conditions (Vidstrand et al. 2010), see also Appendix B.

For more information on the ice-sheet model, see the **Model summary report** and for further descriptions of model simplifications and uncertainties, see Section 3.1.7.

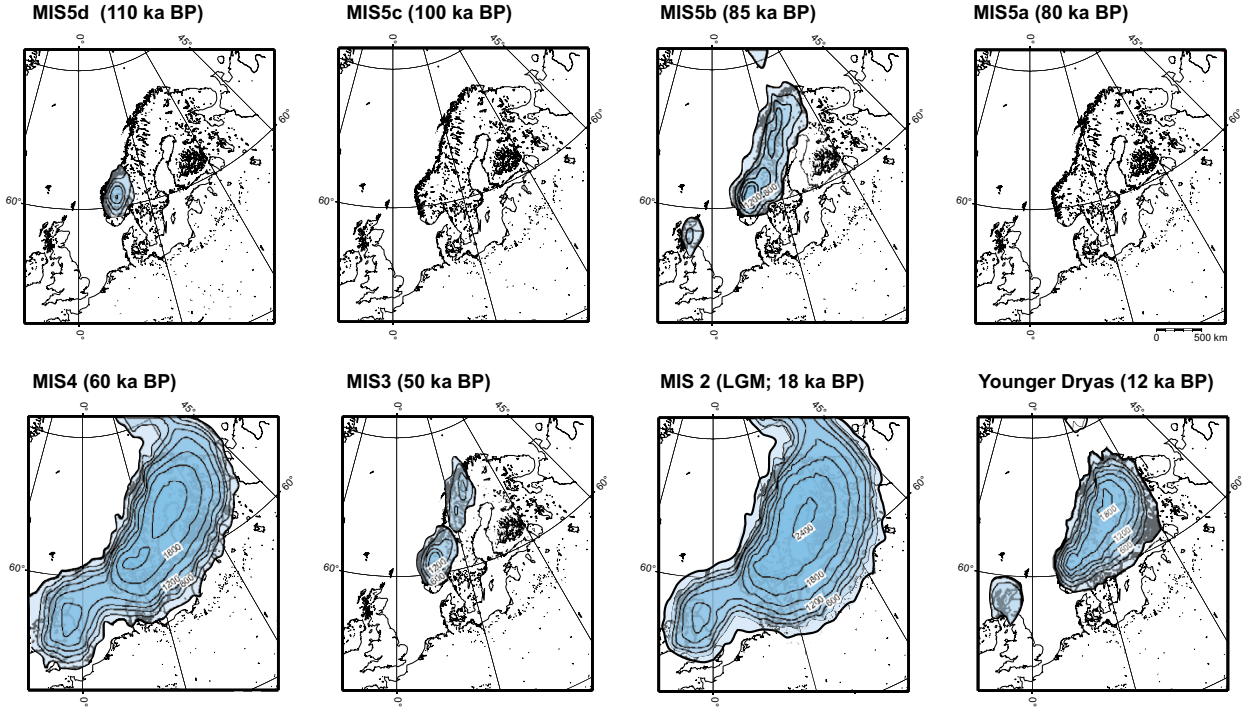

Figure 3-15. *Selected maps of ice-sheet surface topography for the reconstructed Weichselian ice-sheet. The ice-sheet grows to its full LGM configuration in progressive phases of increasing maximum extent, with intervening periods of more restricted ice coverage. Contour lines show ice-surface elevation with a 300 m contour interval. All maps show present day shoreline position.*

3.1.5 Time perspective

It is generally agreed that ice-sheets take longer to grow than to decay. However, our knowledge of the final deglaciation phase is much better than of inception phases, reflecting the fact that there are more geological traces from the last deglaciation than from early stages. Since ablation by surface melting is a more efficient process than snow accumulation, this suggests that the time for ice-sheet decay should be faster than the growth time (Paterson 1994). This is also accentuated due to efficient ice-shelf calving processes for marine parts of ice-sheets, for example calving of the Fennoscandian ice-sheet in the Gulf of Bothnia. In line with the present modelling results relating to the Weichselian ice-sheet (Figure 3-12 and Figure 3-15) it is generally concluded that ice-sheets may build up in a series of glacial build-up periods, peaking in a glacial maximum close to the end of the glacial. The Fennoscandian ice-sheet seems to have exhibited such dynamic behaviour during the last glacial cycle, Section 4.3. This has also been inferred from studies of so called Heinrich events (cf. Heinrich 1988) recorded in North Atlantic marine sediments, suggesting that even large ice-sheet systems are dynamic features, responding relatively quickly to rapid changes in climatic forcing.

During the last 700 ka, glacial cycles have typically had a duration of about 100 ka, with interglacials lasting around 10 to 20 ka (e.g. McIntyre et al. 2001, Tzedakis et al. 2009). As noted above and discussed in Section 4.3, the last glacial cycle was also characterised by a number of cold growth phases and intervening warmer periods with less ice, although from the geological record we still do not know how to date or correlate all observed interstadial localities (Lokrantz and Sohlenius 2006). A typical cold Weichselian stadial had a duration of some thousands of years, see e.g. Figure 3-12 and Section 4.4.4. The deglaciation of the Weichselian ice-sheet from the LGM ice margin to the last ice remnants in the Scandinavian mountain range took about 8 ka, including several temporal halts in the retreat, the most pronounced one occurring during the Younger Dryas (about 13–11.5 ka BP).

3.1.6 Handling in the PSAR

The evolution of ice-sheets is investigated by means of numerical modelling. The base case of the main scenario in the PSAR is constructed from a *reference glacial cycle climate case* based on an ice-sheet model reconstruction of the Weichselian glaciation. The thermodynamic ice-sheet model used is capable of simulating realistic ice-sheets which are typically not in balance with the climate. Derived ice temperatures, together with density variations with depth, control ice viscosity and ice flow. The thermodynamic calculation accounts for vertical diffusion, vertical advection and heating caused by internal shear. The climate input, forcing ice-sheet evolution, is the mean annual air temperature at sea-level, and its variation over time. The mass balance is determined from an empirical relationship based on a simple parameterisation of the ice-sheet's effect on local climate (Fastook and Prentice 1994). Distributed temperatures over the model domain are determined from height above sea-level and distance from the pole.

The model simulation of the Weichselian ice-sheet over Fennoscandia was controlled by the proxy temperature curve from the GRIP ice core, obtained from central Greenland (e.g. Dansgaard et al. 1993), see also Appendix A, a typical method used in ice-sheet modelling of the Weichselian glacial cycle. The geothermal heat flow and its spatial variation has been shown to be of importance for obtaining realistic modelled basal ice temperatures and basal melt rates (Waddington 1987, Näslund et al. 2005). Basal temperatures and basal water conditions are in turn important for the overall ice flow and ice dynamics. A detailed dataset of geothermal heat flux values, based on national measurements of gamma emissions in Sweden and Finland has been compiled (Näslund et al. 2005), and has for the first time been used as input to an ice-sheet model. This eliminates previous large uncertainties in geothermal heat flow, and associated uncertainties in modelled basal conditions of the ice-sheet.

The ice-sheet model was calibrated so that modelled ice-sheet configurations agreed with dated geological information on ice-marginal positions (Section 3.1.4). For this purpose, geological information on the Weichselian glaciation history of Scandinavia was compiled by Lokrantz and Sohlenius (2006). For further information on the ice-sheet modelling, see the preceding parts of Section 3.1.

3.1.7 Handling of uncertainties in the PSAR

Uncertainties in mechanistic understanding

Model simplification uncertainty. The most important simplifications made in the ice-sheet modelling in the model reconstruction of the Weichselian ice-sheet are the following.

The temperature proxy climate curve driving the model is the GRIP Greenland temperature curve. First, this curve describes the climatic conditions at Greenland, but in the absence of similar palaeoclimate data from Fennoscandia, or other closer areas, these are the best data available. With the applied modelling approach, the Greenland proxy data generates Fennoscandian ice-sheets that are in fair agreement with geological information on LGM and Younger Dryas ice margin positions, even *without* model calibration, which is a justification that this approach is valid. There are also uncertainties introduced by the conversion from oxygen isotope values in the ice core to Greenland palaeo-air temperatures (Johnsen et al. 1995), see also Appendix A. The temperature proxy climate curve is probably the biggest assumption made in the modelling experiments, and therefore this parameter was selected for adjustment in model calibration.

In the model, the amount of basal sliding is coupled to the thickness of the basal water layer of the ice-sheet. This is a simplification, but still a reasonable way of handling the difficult topic of basal sliding and the coupling between glacier hydrology and ice-sheet dynamics. One thing that is excluded in the model is the possible presence of subglacial deformable sediments, for example in the Baltic depression, which may enhance ice velocities, especially in ice streams. The exclusion of the effects of such sediments could, in some cases, lead to some overestimation of ice thickness.

In the UMISM model, as in many other ice-sheet models, the so-called shallow-ice approximation is used. This means that the horizontal velocity is only dependant on the local driving stress. Horizontal and longitudinal englacial stresses are neglected, i.e. there are no push-and-pull effects within the ice-sheet, as in nature. This is an appropriate assumption for the major part of the ice-sheet, except for near-frontal parts and ice divides. However, the model has not been used in such a way as to make this a significant weakness.

In the UMISM model, horizontal advection of heat was not included in the thermodynamic treatment of the ice. The result is that the model may overestimate basal ice temperatures to some extent. This is likely to be of importance only in fast-flowing situations like ice streams.

The hydrostatically supported elastic-plate routine included in the UMISM model is a simplification, but is adequate for adjusting bed- and ice-sheet surface elevations to obtain a reasonably good surface mass balance.

The UMISM model does not include an ice-shelf model. Instead, ice shelves are simulated by adjusting a marine calving rate directly at the dynamic grounding line.

The spatial resolution of model domain is approximately 50 km. This resolution may be too coarse to correctly depict smaller features in, for example, the geothermal heat flow pattern and topography.

Input data and data uncertainty

The temperature proxy climate curve. See Section 3.1.4 on Model simplification and uncertainty above, and Appendix A.

Digital elevation data. The accuracy of the ETOPO2 DEM is good enough for the 50 km and 10 km resolution ice-sheet model simulations made.

Geothermal heat flux. The high-resolution data set on spatially varying geothermal heat flux is of high quality in the context of ice-sheet modelling. In the new data set, high resolution geothermal data are available only for Sweden and Finland, not for the entire area covered by the Weichselian ice-sheet. However, this does not affect modelled basal conditions in Sweden, since basically all parts of Sweden are located down-stream from areas with high-resolution data. There are assumptions made in the calculation of the data set that could be refined to improve the data set in the future, for example using a varying lithospheric thickness in the calculation of surface heat flow. Also, denser data on γ-emission

measurements from bedrock are available for parts of Sweden, which may be used for future versions of the data set. All in all, this new type of ice-sheet model input has improved ice-sheet modelling significantly from all previous reconstructions of palaeo-ice-sheets by numerical modelling.

Sea-level. The sea-level curve used as input is derived from numerical ice-sheet modelling of all Northern Hemisphere ice-sheets. The present volume of the Antarctic ice-sheet was held constant. The maximum lowering of sea-level in this data set is 100 m, somewhat less than the ~120–135 m of global sea-level lowering at the LGM deduced from coral-reef data (Yokoyama et al. 2000). However, this is of minor importance since the position of the grounding-line in the western Atlantic part of the ice-sheet is determined by the bed topography (i.e. continental shelf location), and the eastern part is advancing and retreating over the Baltic Sea which does not have contact with the Atlantic during such low global sea-levels.

3.2 Glacial hydrology

This part of the report summarises the knowledge on water flow in and beneath glaciers and ice-sheets. Many concepts in hydrology and hydraulics are applicable to water flow in glaciers. However, the unique situation of having the liquid phase of water flowing in conduits of the solid phase of ice is not encountered elsewhere. This situation means that the heat exchange between the phases and the resulting phase changes must be accounted for in the analysis. The fact that the solidus in the pressure-temperature dependent phase diagram of water has a negative slope provides further complications. It means that ice can melt or freeze from both temperature and pressure variations.

3.2.1 Overview/general description

The hydrology of glaciers has been reviewed by several authors (Weertman 1972, Lang 1987, Röthlisberger and Lang 1987, Hooke 1989, Hubbard and Nienow 1997, Fountain and Walder 1998, Schneider 2000, Boulton et al. 2001b, Jansson et al. 2003, Hock and Jansson 2005, Hock et al. 2005). However, most reviews concern specific topics and do not provide an overview. Therefore, Jansson et al. (2007) provided an overview of the theoretical knowledge on water flow in and beneath glaciers and ice-sheets, and how these theories are applied in models to simulate the hydrology of ice-sheets. The study provides both a broad overview and an in-depth understanding of glacier hydrology to be applied to ice-sheets. In order to describe in detail the current understanding of water flow in conjunction with deforming ice and to provide understanding for the development of ideas and models, emphasis has in Jansson et al. (2007) been put on the mathematical treatments, which are reproduced in detail. Qualitative results corroborating theory or, perhaps more often, questioning the simplifications made in theory, are also given. The overarching problem with our knowledge of glacier hydrology is the gap between the local theories of processes and the general flow of water in glaciers and ice-sheets. Water is often channelized in non-stationary conduits through the ice, features which due to their minute size relative to the size of glaciers and ice-sheets are difficult to incorporate in spatially larger models. New work is emerging that attempts to bridge the gap between the ice-sheet spatial-scale modelling and the details of our process understanding, see Jansson et al. (2007). Current state-of-the-art models for subglacial hydrology at the scale of an ice-sheet simulate mean conditions over elements of model domains, rather than discrete and specific features of the drainage system (e.g. Schoof 2010).

The general hydrological processes, summarized by e.g. Jansson et al. (2007) are similar under both glaciers and ice-sheets since the driving forces are the same, differing only in magnitude and spatial scale. Bell (2008) has reviewed the role of water beneath the ice-sheets on their stability and hence their mass balance, since the dynamics influences fluxes of ice into the oceans. Indications also emerge that temperate basal conditions favouring sliding in the presence of water may be important for the observed waxing and waning of past ice-sheets (Bintanja and van de Wal 2008). Bamber et al. (2007) have summarized the developments in our view of ice-sheets going from slow behemoths responding on time perspectives of millennia or longer to dynamically active features, capable of reactions on the order of years to decades.

The traditional view of the glacier hydrological system is similar to a combination of a groundwater system and a limestone karst system of shafts and tunnels, and consists of supra-, en- and sub-glacial system components. Figure 3-16 shows the situation on a typical glacier in summer.

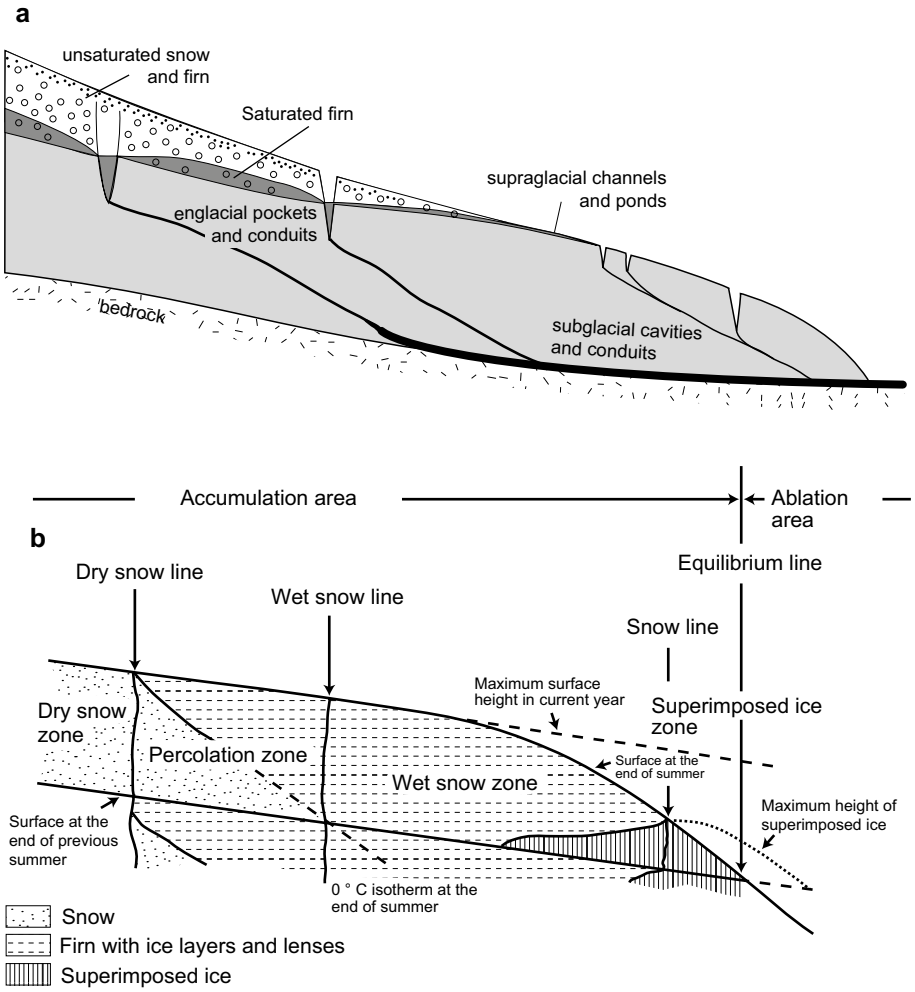

Figure 3-16. *a) The hydrological system of a glacier consists of supra-, en- and subglacial subsystems and interacts with the substrate hydrological systems. Modified from Holmlund and Jansson (2003), after Röthlisberger and Lang (1987). b) The glacier surface can be divided into different facies starting with the dry snow zone through the percolation zone to the wet snow zone. Modified from Benson (1961), Müller (1962), Paterson (1994).*

The surface can be divided into two parts, a lower part where the surface consists of solid ice, referred to as the ablation area since a net loss of mass occurs in this area, and where water will run off by mostly channelized surface flow and an upper part, referred to as the accumulation area because a net mass gain occurs, where the surface consists of permeable snow or firn, snow that has survived at least one year of melting. The snow and firn pack is porous and allows water to percolate into the glacier and accumulate at depth as firn water bodies, equivalent to groundwater bodies whereas ice effectively is impermeable. Recent drilling and radar studies in Greenland have revealed large areas with liquid water at depths of 10s of meters within the firn, which have been termed 'Perennial Firn Aquifers' (Forster et al. 2013). These newly discovered aquifers do not exist everywhere, and the conditions controlling their formation and discrete spatial distribution are not yet fully understood.

On an ice-sheet, the snow-covered area can be further subdivided into zones depending on their thermal conditions, see Figure 3-16. At the centre of ice-sheets, an example of which is modern Greenland, the snowpack is cold and only limited surface melting may occur during the summer season. This is the *dry snow zone*. At some point at lower elevation, surface melting can occur because of warmer conditions caused by the atmospheric temperature lapse rate. Hence there is a zone where percolation occurs, increasingly wetting the upper part of the snow pack at lower altitude since the potential for melt increases at lower altitude. This zone is called the *percolation zone*. At some elevation the melting is strong enough, together with the latent heat release from refreezing the melt water, to completely warm the snow pack. The zone of completely temperate snow is called the *wet snow zone*. These zones

describe the conditions met during parts of the season. During winter most of the ice-sheet will be covered by dry snow and development of the different zones initiate as air temperature rises during spring and summer. This also means that the different zones start to develop at lower altitude and move upglacier as the season progresses to reach their uppermost position at the end of the melt season or when the annual temperature cycle has reached maximum temperature. This also indicates that the surface flow system will develop throughout the entire melt season with accompanying effects on runoff and water input to an en- and subglacial drainage system.

Water is also generated at the base of ice-sheets where the basal temperature is at the pressure melting point. The amount of energy available for melting is given by the geothermal heat flux, heat generated from friction as the ice slides over its bed, and the deformational energy, so called *strain-heating*, in the ice produced by ice flow. The geothermal heat flux varies spatially according to the geologic structure of the Earth's crust (Näslund et al. 2005) but does not vary significantly in time over the time periods under consideration for a geologic repository for spent nuclear fuel. The energy available from strain and frictional heating varies both spatially and temporally with the waxing and waning of the ice-sheet as well as with the induction and demise of faster flow features in the ice-sheet. There is, therefore, a strong feedback between ice flow, heat production, and water production available for enhanced sliding beneath temperate-based parts of an ice-sheet. The cold-temperate boundary is also affected by the strain heating, which may enlarge the areas subjected to basal melting. Typical basal melt rates may vary from a few to up to 10 mm a^{-1}, although even higher melt rates can probably occur under special circumstances where ice flow is very rapid or geothermal heat fluxes are abnormally high (e.g. Hooke 2004, p 34). Such circumstances do not, however, occur on an ice-sheet-wide scale.

Water generated at the surface from melt and liquid precipitation can enter the en- and subglacial system through crevasses and vertical shafts, *moulins*. If the ice is temperate, it may also be slightly permeable. Water that enters the glacier will flow through an englacial system for some time. Commonly water reaches the bed within a couple of ice thicknesses in distance but englacial drainage can occur over longer distances. Most often this is associated with over-deepened basins.

The area over which surface water can penetrate the ice-sheet and reach the bed is not well known. Remote sensing of e.g. the Greenland ice-sheet indicates that surface melting occurs up to very high altitudes but also that the melting zone varies substantially from year to year. Such conditions were surely present on the Weichselian ice-sheet, especially during its retreat phase. Hence, water is in ample supply. Mechanisms whereby connections from the surface to the bed may be established through ice below the pressure melting point have been debated.

However, Alley et al. (2005) have shown theoretically that water-filled crevasses may penetrate even cold ice and thus constitute a mechanism for establishing hydraulic connection between surface and bed, even on a thick largely cold ice-sheet. Although observations in Greenland have shown that the drainage of a supra-glacial lake can provide the water necessary to drive a crevasses to the bed (Das et al. 2008), there are no observations of crevasses in the ablation zone forming bed connections otherwise – either from water provided by a stream source or without water. Indirect evidence suggests that in select areas of the accumulation zone having a liquid firn aquifer, occasional crevasses can hydrofracture to the bed (Poinar et al. 2017).

Nevertheless, observations on the Greenland ice-sheet show that surface streams all eventually terminate in moulins (Smith et al. 2015, Thomsen et al. 1989). The ice surface across the ablation zone is partitioned into numerous drainage catchments feeding moulins which have an average spacing on the order of one every 5 km^2 (Poinar et al. 2015, Yang and Smith 2016). Above the equilibrium line, surface melt water likely reaches the bed in only a few select locations, apparently limited by the necessary coincidence of a firn aquifer with a location where ice-flow dynamics permit crevassing. It is likely that the zones on the waning Weichselian ice-sheet were at least similar in extent. Since the waning ice-sheet probably exhibited surface profiles lower in elevation than, say, the modern quasi-steady state Greenland ice-sheet, ablation zones were likely larger simply because larger areas of the Weichselian ice-sheet were at lower elevation.

Once water enters the bed it is transported toward the margin either through a sediment matrix or along the ice/bedrock interface, depending upon the basal framework. Water flow in a drainage system can range from fast to slow. The fastest systems can be thought of as tunnel systems with larger water flux. The slowest systems transmit smaller quantities of water, while maintaining higher pressure and

holding larger volumes of water. One example of such a system is the so-called linked cavity system (Kamb 1987). Figure 3-17 shows an example of how a slow system may be configured. The fast systems are self-organising and tend to occur at a spacing that is determined by flow volumes, although the mechanisms are not completely understood. The slow systems are dependent on smaller-scale roughness features. Detailed descriptions of the subglacial hydrological systems are given in Jansson et al. (2007).

Because of the seasonal variations in water input from the surface (basal contributions do not vary on a seasonal basis), the en- and subglacial drainage pathways transmitting such water also experience seasonal variations (see also Jansson and Näslund 2009). Conduits in ice adapt to transient hydraulic conditions by creep closure if water pressure is lower than hydrostatic ice pressure in the ice surrounding the conduit. If water fluxes increase, pressure builds to force more water through the conduits. This causes an increase in the viscous dissipation of heat and results in melting of the conduit walls and hence an increase in flow capacity of the system. The enlargement by melting may be faster than the creep closure depending on the transient hydraulic conditions. Hence, glacier conduit systems respond quickly to increases in water fluxes by enlarging the conduits. When water fluxes decrease, pressures in the system may drop drastically until creep closure has equilibrated to the water flux to maintain a balance between closure and conduit wall melting.

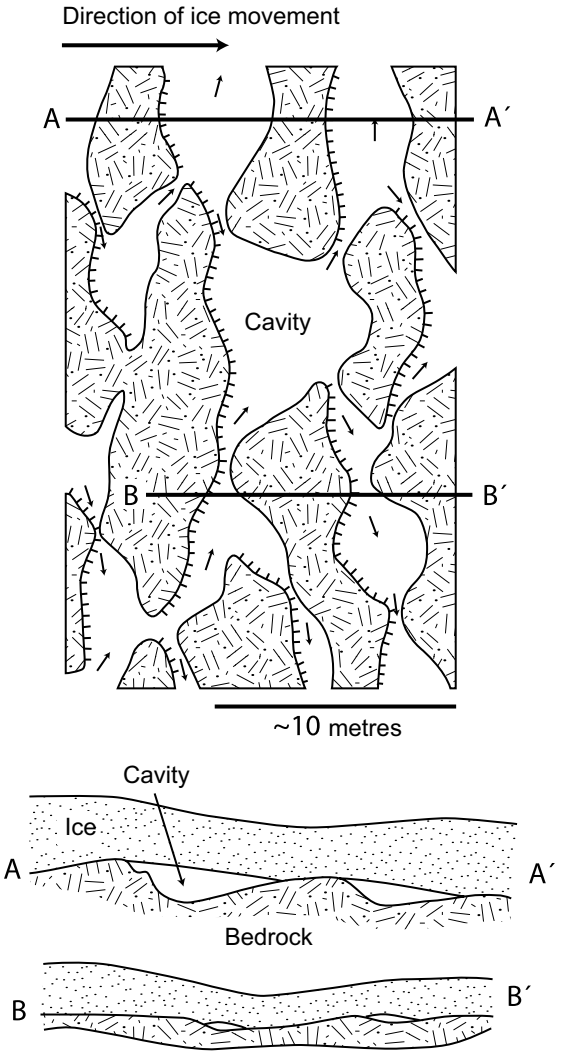

Figure 3-17. *Linked cavity system, an example of a subglacial slow flow system. Modified from Holmlund and Jansson (2003), after Kamb (1987).*

Seasonal, as well as shorter term, variations in water influx will affect the basal water pressures (e.g. Jansson and Näslund 2009), although it is unlikely that diurnal variations in water pressure will significantly affect the pressure variations in an underlying groundwater aquifer in the case where these high frequency variations must diffuse through a porous medium.

A detailed account of the supra-, en-, and subglacial hydrological system is given in Jansson et al. (2007).

Groundwater composition is indirectly influenced by ice-sheet hydrology, since it is the hydrological conditions at the ice/bed interface that control the recharge of glacial melt water into the bed which in turn will affect the composition of the groundwater.

3.2.2 Controlling conditions and factors

Climate – melt water supply

The coupling between the climate system and the hydrological system of glaciers and ice-sheets is through the energy exchange between the atmosphere and the glacier surface. Energy arriving at the ice surface will be expended by first warming the surface to the melting point (if below melting to start with) and second to melt snow and ice at the surface. The energy balance at the glacier surface is given by (e.g. Paterson 1994; all terms are in units W m^{-2})

$$M+\Delta G = R+H - L_v E+L_f P' \qquad \text{Equation 3-8}$$

where M is the heat used to melt snow and ice; this term represents a gain in heat and is negative if melt water refreezes in the snow pack; ΔG is the rate of gain of heat in a vertical column from the surface to the depth at which vertical heat transfer is negligible; H is the rate of heat transfer from the air to the surface by turbulence (H is negative if the air is cooler than the surface); L_v is the specific latent heat of vaporisation (2.8×10^6 J kg^{-1}); E is the rate of evaporation from the surface (E is negative if condensation occurs); L_f is the specific latent heat of fusion for ice (3.34×10^5 J kg^{-1}); and P' is the precipitation rate of rain (negligible if the surface is melting but significant for warming up the snow pack from refreezing under cold conditions). R is the net radiation, defined as $R = Q(1-\alpha)+I_i-I_o$, where Q is the rate of incoming solar direct and scattered radiation at the surface; α is the ratio between reflected and incident solar radiation, *albedo*; I_i is the rate of incoming long-wave radiation at the surface; and I_o is the rate of emission of long-wave radiation by the surface.

The surface melting can be calculated by applying Equation 3-8 to measured data from meteorological stations on glaciers and ice-sheets. However, for estimating conditions on palaeo-ice-sheets simpler solutions must be applied since all parameters in Equation 3-8 cannot be easily estimated. This has led to the development of statistical approaches to melt estimation. The most successful and most widely used is the *degree-day method* approach (e.g. Hock 2005).

The degree-day method is based on the notion that melting is a function of the time the air is at a positive temperature. Hence degree-day methods use the integrated time of positive temperature as a proxy for the heat exchange and hence melting through empirical correlation between measured melting and integrated time of positive temperature. In its simplest form the sum is of positive degree-days, hence the name of the method, defined by $S = \Sigma_i \alpha_i T_i$ where T_i is the mean daily temperature and $\alpha_i = 1$ if $T_i \geq 0$ °C and $\alpha_i = 0$ if $T_i < 0$ °C. The melting is associated to the degree-day sum by a degree-day factor, λ, as $M = \lambda T$. Hock (2005) has summarised degree-day factors which show significant variation depending on local conditions. The degree-day approach has also been refined by Hock (1998) to yield a temporally varying sub-daily variation by introducing the potential direct solar radiation as a modulating factor γ_t to the empirical relationship, $M_t = \gamma_t \lambda T$, where subscript t denoted conditions at a specific time t.

Melt water is also generated englacially, and at the base of glaciers and ice-sheets. The deformation that occurs as ice is flowing generates heat that can melt minute amounts of water. Water production through strain heating requires the ice to be temperate and varies proportionally to the deformation rate. There is a positive feedback between strain heating and melting in that strain heating also warms colder ice to the pressure melting point and thereby allows the ice to melt; water increases velocity which in turn increases the strains. The amounts produced by strain heating are relatively small. Estimates are difficult to make since they depend on the deformation rates which vary spatially. Based on the typical flow regime of an ice-sheet, strain heating is negligible near the ice divide and is likely to increase towards the margins of the ice-sheet.

Water is also generated subglacially through energy supplied by geothermal heat. The resulting melt rates will be directly proportional to the geothermal heat gradient in the bed rock. As with internal heating, geothermal heat may also first warm basal ice to its melting point resulting in subsequent melting. Näslund et al. (2005) have shown the importance of geothermal heat on the basal temperature and water production beneath the past Weichselian ice-sheet.

The ice-sheet hydrology described above may affect several geosphere variables of importance for a deep geological repository (Table 3-2).

Table 3-2. Summary of how geosphere variables are influenced by glacial hydrology.

Geosphere variable	Climate issue variable	Summary of influence
Groundwater flow	Sub-glacial hydrological system	Groundwater recharge and flow will be determined by the temperature regime, melt-water production and thickness of the ice-sheet (see Section 3.1). It is the configuration of the basal hydrological system that ultimately determines the distribution of melt water and thus groundwater recharge and the distribution of water pressures at the ice/bed interface determining the gradients for groundwater flow.
Groundwater pressure	Sub-glacial hydrological system Melt-water supply	The groundwater pressure depends on the pressure of the water at the ice/bed interface, the ice-sheet thickness and the ice load compressing the subsurface (see Section 3.1). The pressure of the water at the ice-bed interface is determined by the supply of melt water and the conductivity and distribution of conductive features in the sub-glacial system.

3.2.3 Natural analogues/observations in nature

Our knowledge on the hydrology of glaciers and ice-sheets is largely based on observations from valley glaciers. However, there is no reason to believe that other processes would be present in association with an ice-sheet, although the magnitude of the processes will be scaled proportionally to the differences between valley glacier scale (1–100 km^2) and ice-sheet scale (1000–10000 km^2 and larger) (Jansson et al. 2007, Jansson and Näslund 2009). The far greater ice thickness and generally lower surface slope of ice-sheets may also impact the rates of physical processes relative to valley glaciers. Given today's climatological situation in Greenland, allowing for both ice-sheet surface melting and, in general, cold, high polar surface conditions in the ice-sheet interior, the best present analogue situation for a future Fennoscandian ice-sheet is the Greenland ice-sheet. Most of the descriptions of ice-sheet observations in nature below therefore are from the Greenland ice-sheet.

Indirect observations of the ice-sheet hydrological system

There are some studies that implicitly involve a subglacial drainage system and processes therein. Observations of large, and from a glaciological perspective, abrupt changes in ice dynamics without corresponding changes in for example driving stress imply changes in the basal boundary condition. Ongoing thinning of sectors of ice-sheets (e.g. Wingham et al. 2009) may occur from changes in mass balance or from changes in ice dynamics. Joughin et al. (1996) observed a three-fold increase in velocity over a seven-week period, for the Ryder Glacier, north Greenland, after which the velocities decreased to the original values. Drainage of supraglacial lakes into the ice-sheet could have been responsible for this event.

Zwally et al. (2002) used GPS measurements at the equilibrium line near Jakobshavn to show that the ice-sheet undergoes large annual variations in surface speed. They attributed these variations to the seasonal variations in water influx to a basal water system through moulins and crevasses, since velocity variations were clearly correlated to seasonal melt rates variations. Price et al. (2008) used modelling to show that variations in ice velocity, such as observed by Zwally et al. (2002), need not be forced locally but can also be the result of longitudinal coupling effects from movement further downstream.

Moon and Joughin (2007) used satellite interferometry to investigate the spatial variability in ice front position of 203 Greenland outlet glaciers. Their results indicate that the behaviour is closely linked to climate variability, thus implying that dynamic responses are forced by climate and are not sustainable unforced processes. van de Wal et al. (2008) recorded large velocity variation along a transect of the Russell Glacier, a land-terminating outlet glacier in east Greenland. They show annual velocity variations varying by up to a factor of four. The increase in velocity occurs within days of measured melt rate increase. Shepherd et al. (2009) used a combination of satellite imagery and continuous dGPS measurements to show how the Russell Glacier catchment of the West Greenland ice-sheet undergoes both temporal and spatial seasonal velocity variations as well as diurnal speedup and uplift events. More recently, numerous studies have used observations of ice-sheet surface velocity varying over timescales ranging from diurnal (Bartholomew et al. 2012) to seasonal (Bartholomew et al. 2010, Sole et al. 2013, Sundal et al. 2011) and even extending to decadal (Tedstone et al. 2015), to infer evolution of the basal drainage system beneath Greenland's ablation zone.

Joughin et al. (2004) observed changes in the flow speed of the Jakobshavns Isbrae where velocity was seen to decrease in the period 1985–1992 and then accelerate between 1992 and 2000 with additional acceleration up to 2003. Their study clearly indicates that the ice stream response can be complex and include both periods of deceleration and acceleration. Holland et al. (2008) proposed a different cause for the speed-up of Jakobshavns Isbrae. A sudden increase in subsurface ocean temperature occurred in 1997 along the entire west coast of Greenland. Such warm water could have accelerated the basal melting of the ice stream at the grounding line and hence caused it to become unstable. Whereas this process will be able to affect outlets reaching the sea, it does not help to explain the general increase in velocity observed around the perimeter of the Greenland ice-sheet (Rignot and Kanagaratnam 2006, Joughin et al. 2008). Joughin et al. (2008) showed that the land-terminating parts of the Greenland ice-sheet underwent seasonal velocity changes. Howat et al. (2007) showed that two of Greenland's major outlets, the Helheim and Kangerdlugssuaq, underwent a rapid increase in flow in 2004 with a subsequent decrease in 2006 to near the pre-2004 levels. They argue that this response is due to re-equilibrium of the terminus after a calving event.

There is thus ample evidence that ice-sheet dynamics change on time periods from diurnal and up to perhaps millennia. The variations observed on diurnal to annual scales are in perfect harmony with theory and observations on valley glaciers where the coupling to variability in the hydraulic system is evident. Ice-sheets seem to have larger time-scale variability than typically observed on valley glaciers. This longer period variability is due to processes that occur on scales that cannot be found on valley glaciers and thus cannot produce similar features on the smaller glaciers.

Observations of ice-sheet surface melt

The surface hydrology of the Greenland ice-sheet has been studied by Thomsen et al. (1989) in relation to a proglacial river near Illulissat/Jakobshavn for hydroelectric power production planning. The study showed that the surface of the ice-sheet was punctured by numerous moulins, each draining a well-defined area of the ice surface (Figure 3-18). Satellite-based imagery indicates that the surface of the eastern flank of the ice-sheet is covered by perennial supraglacial lakes interconnected by streams (Figure 3-19). These lakes may experience episodic catastrophic drainage (e.g. Das et al. 2008, Shepherd et al. 2009). More recent and extensive work has shown similar conditions exist in the Kangerlussuaq sector of the ice-sheet, where the ice surface has numerous streams (Smith et al. 2015) terminating in moulins (Poinar et al. 2015) and lakes, some of which occasionally drain (Fitzpatrick et al. 2014).

Satellite-based radar imagery also provides a good overview of the facies distribution on the Greenland Ice-sheet. Figure 3-20 shows the conditions from the centre of the ice-sheet to the margin. The ablation area at this section of the ice-sheet is approximately 100–150 km wide and the percolation and wet snow zones combined are 300–400 km wide. Unfortunately, it is impossible to conclude how much of the combined percolation and wet snow zone contributes to runoff around all areas of the ice-sheet, and how this contribution changes from year-to-year. One detailed study of a transect in west-central Greenland, however, found that a fraction of the surface melt is partitioned into horizontal runoff, beginning at about one quarter of the distance up the percolation zone (Humphrey et al. 2012). A reasonable assumption is that this is representative of much of the ice-sheet. Furthermore, in ACIA (2005) it was shown that the different zones vary substantially in location from year to year. The lack of long-time series of data makes it impossible to draw any conclusions as to the typical situation.

Water generated at the glacier surface, and thus available for input to the glacier hydrological system, comes from a combination of melting of ice and snow and from rain. Direct measurements of melt have occurred within the framework of local projects. van de Wal (1996) and Six et al. (2001) have summarized some of the data originating from transects. Their data shows a potential four-year cycle in melt with no clear trend.

The Gravity Recovery and Climate Experiment (GRACE) has provided means for establishing mass change signals for regions such as the Greenland ice-sheet where mass change due to climate change occurs. Chen et al. (2006), Luthcke et al. (2006), Ramillien et al. (2006), Velicogna and Wahr (2006) used GRACE data to evaluate mass losses from the Greenland ice-sheet. Their results provide a strong independent indication that mass loss from the southern part of the Greenland ice-sheet has increased substantially, thus verifying more local studies from Rignot et al. (1997), Howat et al. (2005), Rignot and Kanagaratnam (2006), Luckman et al. (2006). Much of the mass losses observed are from dynamic responses at outlet glaciers. It is unclear if this acceleration is due to increased surface melt, and associated basal lubrication, or if there are other critical triggering factors. It seems unlikely, however, that simultaneous response over larger lengths of the Greenland ice-sheet margin should be caused by local triggering factors. Wouters et al. (2008) expand on the previous GRACE investigators' results and provide a refined and extended data record showing continued mass loss from the ice-sheet including large losses from the upper parts of the ice-sheet, which was not observed in earlier studies. Hanna et al. (2008) verified the results from Velicogna and Wahr (2006) and found that the increase in melt on the ice-sheet is coupled an increase in regional Northern Hemisphere air temperatures. Clearly the partitioning of total mass change into surface mass balance and dynamic components is prone to substantial spatial complexity. At the ice-sheet scale, early estimates that Greenland mass loss was composed of approximately equal parts surface runoff and ice discharge (van den Broeke et al. 2009), have more recently been updated to reveal that surface mass balance accounted for approximately 70 % of total mass loss between 2009 and 2012 (Enderlin et al. 2014). Hence, recent studies suggest that surface-melt processes comprise a large and, in case of a warming climate, increasing fraction of total Greenland mass loss.

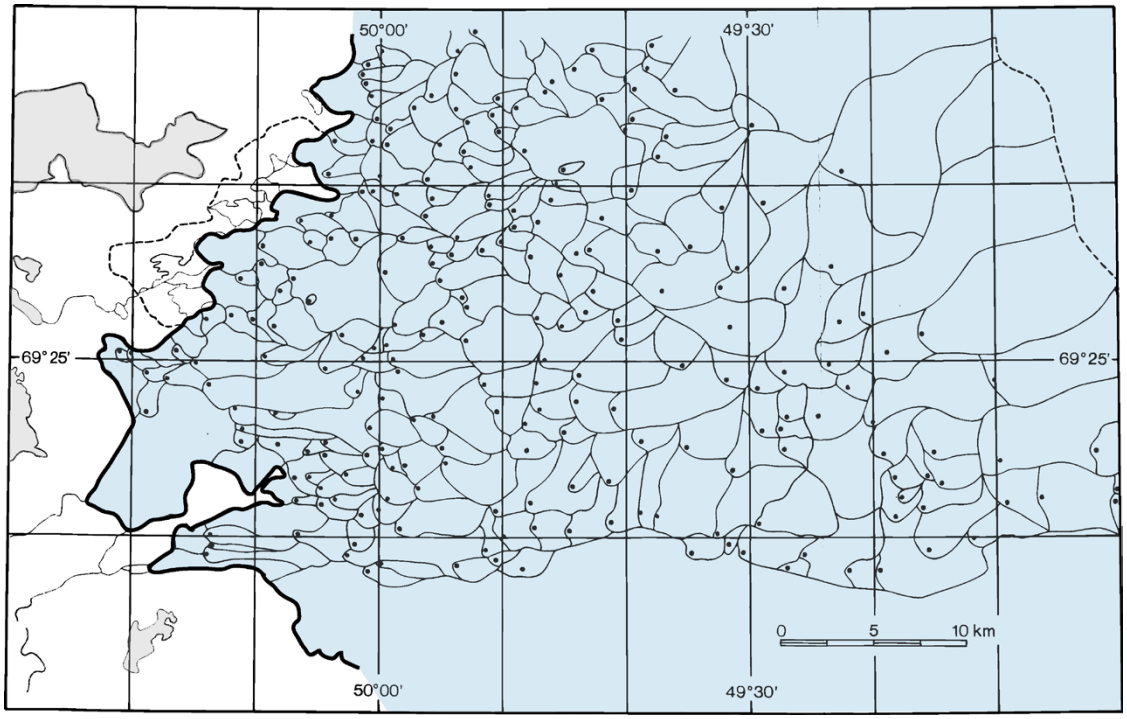

Figure 3-18. *Surface drainage basins on the ablation area of the Greenland Ice-sheet near the Ilulissat/ Jakobshavn area. Filled circles mark the location of moulins in each surface drainage basin. Modified from Thomsen et al. (1989).*

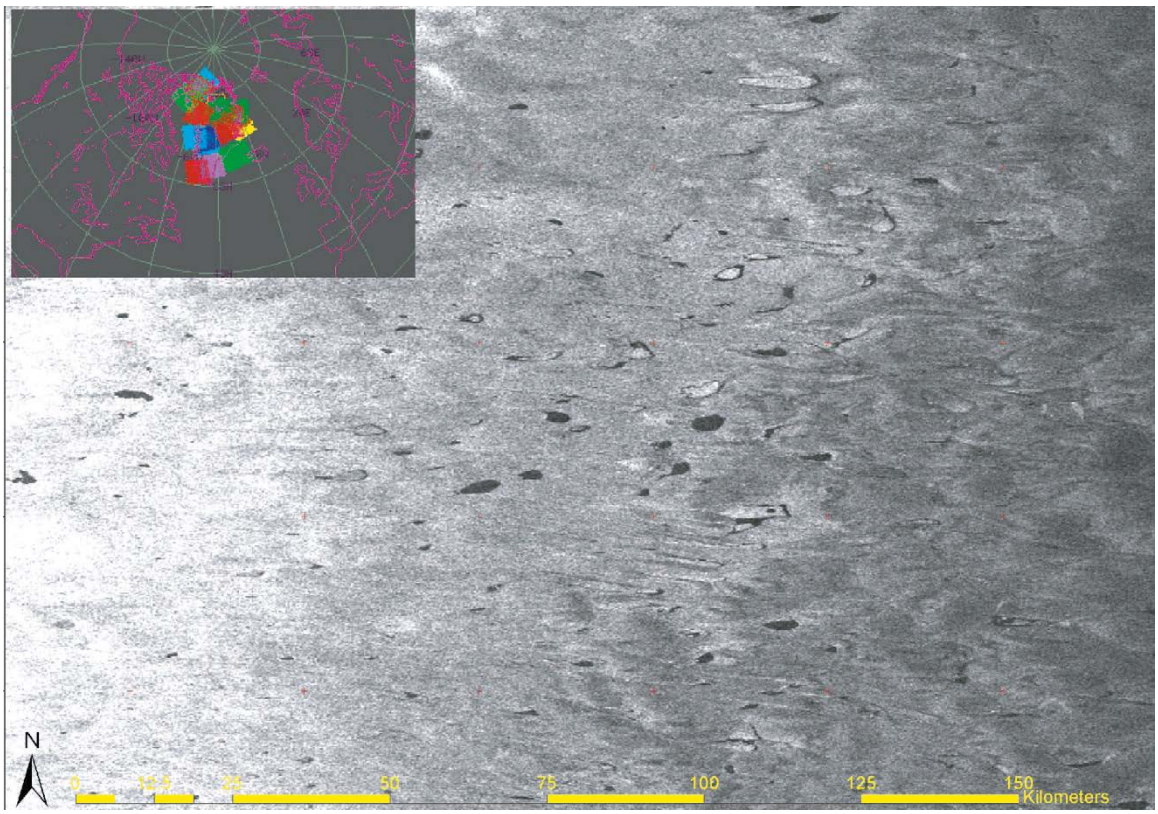

Figure 3-19. *Radarsat-1 ScanSAR image of the ablation zone of the Greenland Ice-sheet near Kangerlussuaq, East Greenland. The background grey scale indicates surface conditions from bare ice (white) through superimposed ice (medium grey) to wet snow (dark grey). The black areas are lakes that absorb the radar waves completely. Some lakes near the right centre have complete or partial lake ice cover, in some cases indicated by a central floe surrounded by a black rim of open water.*

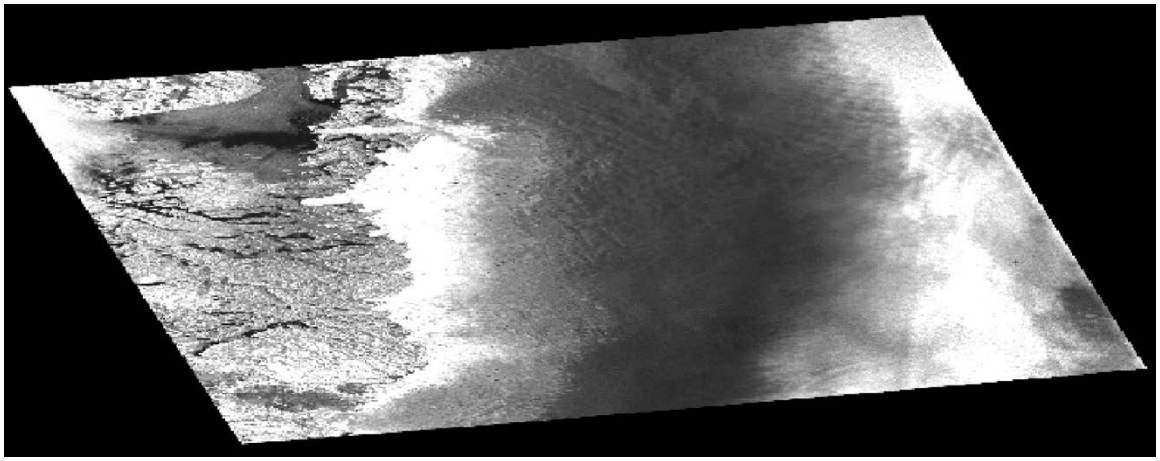

Figure 3-20. *Radarsat-1 ScanSAR image over east Greenland. The dark area at the centre of the image (between approximately −48° W and −44° W) comprises the percolation and wet snow zones that are bounded by the white dry snow zone to the right and the bare ice of the ablation zone to the left. The speckled grey zone to the extreme left in the image is bare ground outside of the ice-sheet. A part of Disco Island is visible in the upper left corner of the image.*

Through measurements of passive microwave emissions, Steffen et al. (2004), Figure 6.18, p 205 in ACIA (2005) show how the Greenland ice-sheet experiences large spatially variable melt conditions. Bougamont et al. (2005) have reproduced Steffen et al.'s observations by applying a surface mass balance model to the Greenland ice-sheet and forcing the model with ERA-40 re-analysis data (data from an analysis of meteorological observations from 1957 to 2002 produced by the European Centre for Medium-Range Weather Forecasts together with other institutions). Their work indicates surface melt can readily be obtained from large-scale re-analysis data given model tuning through surface meteorology data from the ice-sheet. Several different re-analysis models, for example RACMO (Ettema et al. 2009), MAR (Fettweis et al. 2017), and HIRHAM5 (Lucas-Picher et al. 2012), have since become highly evolved and applied Greenland to investigate surface mass balance over various time intervals and length scales. New statistical downscaling methods enable modelling of the surface mass balance to be highly resolved, such as daily values at 1 km resolution (Noël et al. 2016). Bhattacharya et al. (2009) use the melt-area time series covering the period 1979–2008 to show that the melt-area abruptly increased in 1995. This change can be related to a sign-reversal in the North Atlantic Oscillation. The change is also manifested in higher measured temperatures around the ice-sheet. One issue in discussing ice-sheet hydrology is estimating the potential melt rates under a retreat scenario for both past and future ice-sheets. Ridley et al. (2005) performed numerical modelling experiments with the Greenland ice-sheet under warming scenarios. When subjecting the ice-sheet to a $4 \cdot CO_2$ scenario for 3000 years the ice-sheet almost completely disappeared. One lesson from this experiment is that when more ground is exposed around the perimeter of the ice-sheet, feedbacks from local summer circulation produced from warm ground around the ice-sheet can augment the melting.

The Greenland ice-sheet surface mass balance is obviously variable and directly coupled to the forcing climate variability. The water produced by melting also seems to affect the dynamics, not only on diurnal and annual timescales but also by affecting longer-term trends in mass loss of peripheral parts, probably by influencing the dynamics of the Greenland ice-sheet.

Observations of shorter-term variations of subglacial water pressure have been carried out on many glaciers, among them Storglaciären. Figure 3-21 shows a typical water pressure record from Storglaciären, northern Sweden. The hydrological system in this part of the glacier has been inferred to be a distributed tunnel (fast) system. The data shows how water pressures vary very rapidly in response to environmental factors influencing water input, air temperature governing glacier melt, and liquid precipitation causing rapid runoff events on the glacier surface. Such fast systems are characterised by rapid flow and pressures that fluctuate rapidly due to the inability of the system to maintain high pressures. For more details on these types of observation and their interpretation, see Jansson and Näslund (2009).

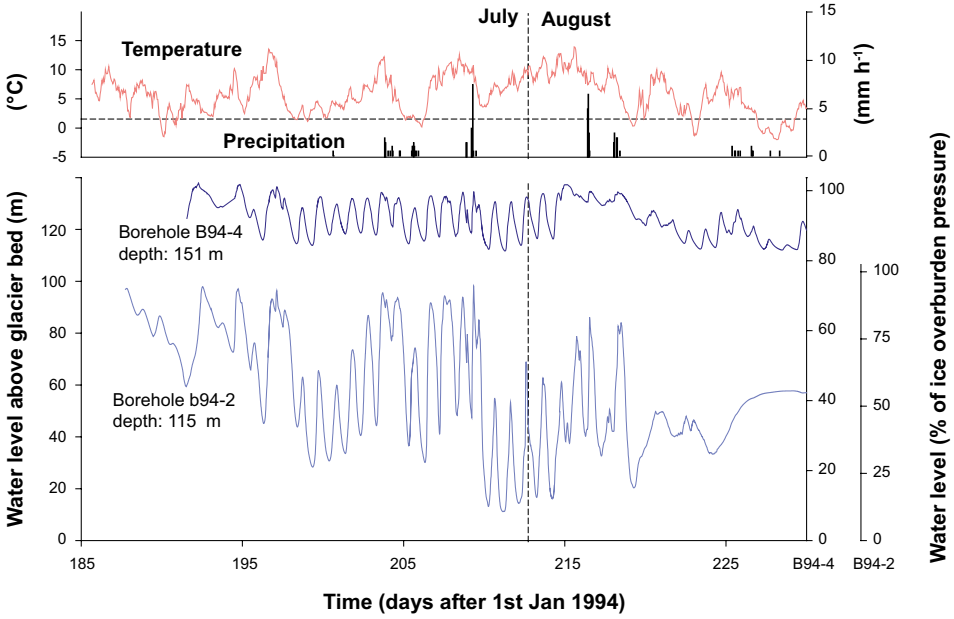

Figure 3-21. *Water pressure record from Storglaciären showing large diurnal variations in water pressure from near zero to near overburden pressure. Longer-term changes in the pattern of the water pressure fluctuations can also be seen. From Jansson and Näslund (2009).*

Observations of transfer of water from the ice-sheet surface to the bed

Theories of how water can create pathways from the surface of a glacier or ice-sheet, through cold ice, to the bed have been presented by e.g. Weertman (1973), van der Veen (1998a, b, 2007) and Alley et al. (2005). The idea is that water-filled crevasses may propagate downwards through the ice. The crucial point for both Weertman's and Alley et al.'s work is the continuous recharge of water to the crevasse to keep it over-pressurized. Having crevasses form across supra-glacial streams or in surface melt ponds is thus an excellent environment for the process to be active. In the ablation area of glaciers, water is generally abounding and it is not hard to meet these criteria anywhere. Fountain et al. (2005a, b) also observed englacial water filled crevasses at varying depths in Storglaciären, where they appear to be an intrinsic part of the drainage system. This study changed the notion that englacial crevasses could not exist under typical conditions found in glaciers.

Observations of surface lake drainage events on Greenland revitalized the theories by Weertman (1973), Alley et al. (2005), van der Veen (2007). Das et al. (2008) observed the complete drainage of a 5.6 km^2 supra-glacial lake in ~ 1.5 hours into an opening crevasse on the Greenland ice-sheet. They also observed significant changes in the velocity of the ice-sheet as well as local uplift during the event. From this Das et al. (2008) inferred that water reached the bed through 980 m of ice. Although the actual drainage pathways were not investigated or mapped, water seems at least to have gained access to the bed near the input point. This work shows compelling indications that the process described by Weertman (1973) and Alley et al. (2005) is realistic. Krawczynski et al. (2009) used a model to calculate the volume of water required to propagate crevasses through the Greenland ice-sheet. They found that small lakes of 250–800 m in diameter are sufficient to drive crevasses through 1–1.5 km of ice. In addition to volumetric constraints, tensile stresses in the ice must be sufficient to facilitate fracture initiation. (Poinar et al. 2015) used principal strain rates, computed from radar-derived surface velocity, as a proxy for conditions supportive of fracture initiation. They found that fracture initiation in western Greenland is generally limited to < 1600 m elevation. Hence, while the conditions for propagating crevasses through the Greenland ice-sheet are commonly met, fracturing is not likely pervasive across the entire ice-sheet and at all elevations.

Catania et al. (2008) used common offset radar images to detect drainage pathways between the surface and the bed of the Greenland ice-sheet in the vicinity of Jakobshavn. They found that detected connections are more abundant in the ablation zone than near or above the equilibrium line. Furthermore, the drainage features coincided with inferred regions of longitudinal extension, indicating that crevasse formation may play a decisive role for the location of moulins also on the ice-sheet. In a subsequent, ground penetrating radar-based study, Catania and Neumann (2009) identified that the drainage connections between surface and bed seemed to be associated with areas of significant basal melting. Their conclusion was thus that the drainage features were persistent. This also implies that the general characteristics of the drainage system to some extent are persistent in space. The transfer of water from the surface of an ice-sheet such as in Greenland, through its cold interior mass of ice, is thus possible. The mechanisms outlined by Weertman (1973), Alley et al. (2005), van der Veen (2007) allows for propagation of water-filled surface crevasses to the bed for as long as the steady sufficient supply of water is maintained. Since melt water occurs in abundance in the ablation area and wet snow zone during the melt season, conditions are favourable over large areas of the Greenland Ice-sheet marginal zone.

Recent work has documented the internal temperature of ice in Western Greenland through borehole temperature measurements (Harrington et al. 2015, Hills et al. 2017). Observations reveal a complex thermal structure within the ice, with ice warming as it moves across the ablation zone Figure 3-22. The upper ~ 15 m of ice undergoes seasonal temperature swings in response to atmospheric forcing, and then ice temperatures become colder with depth until about half way through the ice thickness. In the lower half of the ice thickness, temperature increases with depth until reaching the pressure melting point above the bed. A layer of ice at the pressure melting point existed in all locations where the temperature was measured. The thickness of this layer increased along the ice flow direction from a couple of tens of meters at 45 km distance from the ice margin, to more than 150 m at 30 km distance from the ice margin. Within a few km of the ice margin, the entire ice column is at the pressure melting point.

The basal layer of temperate ice is maintained by local heat sources, including geothermal heating, frictional heating from ice sliding motion, and/or latent heat supplied by freezing basal water in the drainage system. Strain heating from enhanced deformation in the warm layer may also provide heat to progressively warm the ice. Internal melting from ice deformational heat is not expected in the Greenland ice-sheet. Deformational heat will, however, affect the temperature gradient near the base and affect the amount of basal melting possible beneath the ice-sheet.

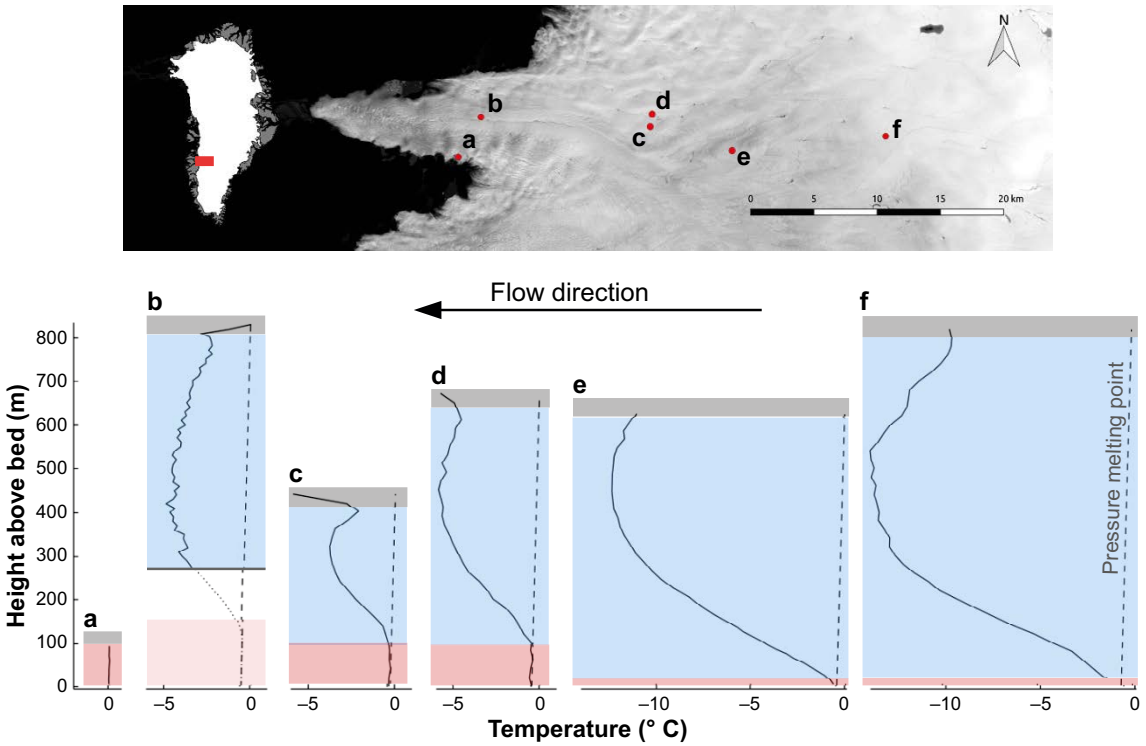

Figure 3-22. *Ice-temperature profiles measured in boreholes spaced along the ablation zone of western Greenland, modified after Harrington et al. (2015) and Hills et al. (2017). Letters indicate location of profiles shown in top panel. Bottom 275 meters of profile B are calculated based on estimated depth of ice. Gray bars indicate ice with seasonal temperature variability due to the winter cold wave; red bars indicate ice at the pressure melting point. Dashed line indicates calculated pressure melting point.*

Observations of water generation at the ice-sheet bed

Some observations of basal melt regimes beneath ice-sheets have been presented. Dahl-Jensen et al. (2003) used NorthGRIP data and an ice flow model to calculate geothermal heat flow along a flow line obtaining variations between 50 and 200 mW m^{-2}. This yields basal melt rates of between 7.5 mm a^{-1} at the drill site and 11 mm a^{-1} further upstream from the NorthGRIP site. Fahnestock et al. (2001) used age-depth relationships from internal layering obtained from airborne radar surveys to calculate basal melt rates in northern Greenland. In one region, melt rates reach and exceed 100 mm a^{-1}, indicating geothermal heat fluxes of up to 970 mW m^{-2}. Such high geothermal heat fluxes indicate the presence of an unusual geological setting not found in the marginal areas of the Greenland ice mass. Oswald and Gogineni (2008) used radar echo intensity to map the occurrence of subglacial water beneath the northern part of the Greenland ice-sheet. They concluded that significant portions of the bed may be melting. Basal conditions at ice-core drilling sites verify their results (e.g. Fahnestock et al. 2001, Dahl-Jensen et al. 2003). Oswald and Gogineni's data show that approximately 17 % of the total flight line lengths indicated melting conditions. A comparison of eight different thermo-mechanically coupled ice-flow models, each using slightly different boundary conditions and modelling assumptions, revealed complete consensus among models in simulating unfrozen bed conditions across that the outer flanks of western Greenland (MacGregor et al. 2016). Detailed modelling studies along transects in this region suggest that heat generated from sliding fraction generally increases toward the margin, with basal melt from all sources of up to 10 mm a^{-1} in some areas (Brinkerhoff et al. 2011, Meierbachtol et al. 2015).

Basal melt contributes significant volumes of water to the basal drainage system. In areas of surface influx of water to the bed during summer, the basally generated volumes are over-printed by the surface influxes. During winter, the entire basal drainage system experiences the basal melt derived fluxes. Basal melt is thus important in that it maintains subglacial flow throughout the year and in all areas where the ice-sheet base is at the pressure melting point.

Subglacial lakes beneath ice-sheets have been known to exist since the discovery of Lake Vostok, East Antarctica (Kapitsa et al. 1996). Such lakes may be of substantial size; the largest lake, Lake Vostok, is 280 km long, 50–60 km wide and more than 1000 m deep. Numerous large lakes have since been identified to exist beneath the Antarctic ice-sheet (Siegert et al. 1996, 2005, Siegert 2005) by e.g. satellite-based remote sensing methods. Because the ice-sheet is locally floating in the water of the lakes, the basal shear stress is locally zero which produces a near-horizontal ice surface over the lake.

The presence of subglacial lakes on Greenland has been confirmed through observations of rapid elevation change (Palmer et al. 2015, Willis et al. 2015) indicating lake drainage and refilling. Subglacial lakes in Greenland however appear to be far rarer than in Antarctica. It is not known if subglacial lakes may have existed beneath the former Fennoscandian ice-sheets.

Subglacial drainage

It is possible that unstable hydraulic situations can be caused by periodic build-up and release of subglacial lakes. Alley et al. (2006) suggested a mechanism for producing periodic outburst floods and accompanying dynamic events. The mechanism involves growth of ice shelves onto proglacial sills where they freeze on producing a seal. Water is thus trapped in deeper parts upstream of the sill, which with a growing ice-sheet can become over-pressurized. If the basal temperature increases on the sill, the over-pressurized water may escape causing an outburst flood. They suggest this process may have been involved with the so-called *Heinrich events* (e.g. Hemming 2004) seen in marine sediment cores in the north Atlantic and for creation of subglacial lakes such as Lake Vostok. Evatt et al. (2006) developed a numerical model to investigate the potential for subglacial lakes. They find that lakes should fill and drain periodically, basically as a function of the filling rate. The calculations allowed Evatt et al. to predict possible locations for subglacial lakes beneath the former Laurentide ice-sheet in North America. Their locations agree with the positions of the palaeo-subglacial lakes proposed by Munro-Stasiuk (2003) and Christoffersen et al. (2008), however, the larger predicted lakes have not yet been identified.

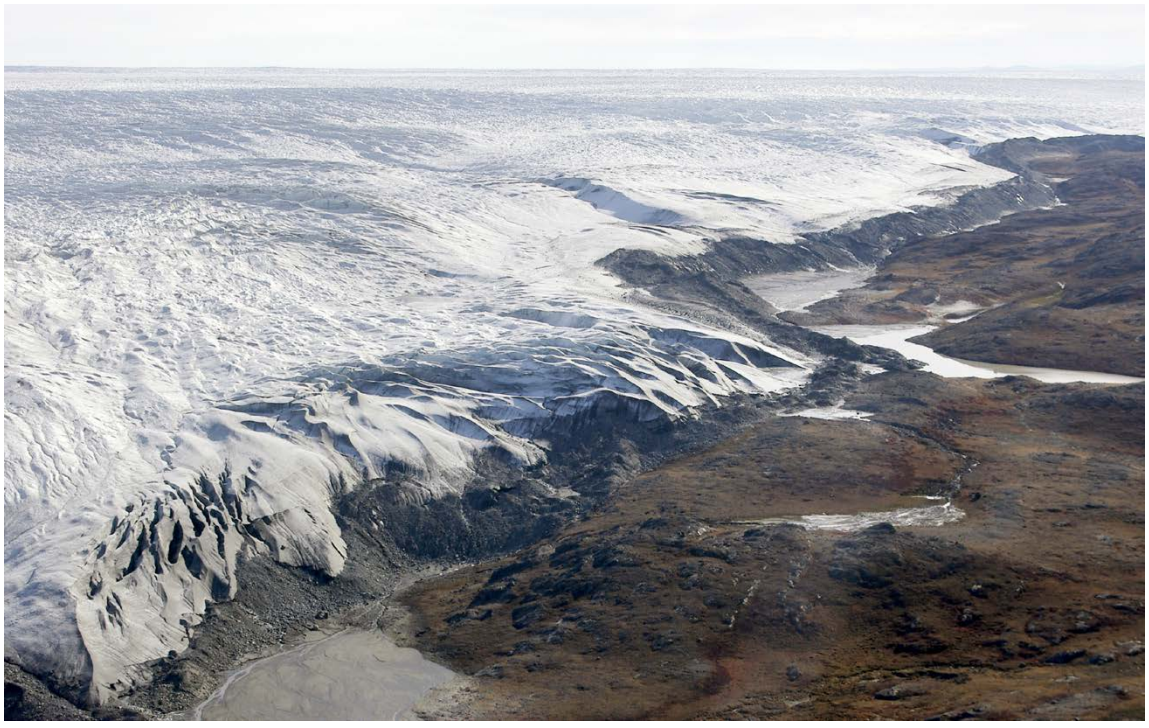

Figure 3-23. *Part of the Greenland ice-sheet in the Kangerlussuaq region, western Greenland. Within this region, SKB, Posiva and NWMO carried out the international Greenland Analogue Project (GAP) in order to study glacial hydrology, hydrogeology, and hydrochemistry (Claesson Liljedahl et al. 2016, Harper et al. 2016). In the same area, SKB also carried out the Greenland Analogue Surface Project (GRASP), studying surface hydrology and transport of chemical compounds in a periglacial environment (Johansson 2016, Lindborg 2017). Photo: Jens-Ove Näslund.*

In Antarctica, e.g. Denton and Sugden (2005), Lewis et al. (2006) discuss observable melt water generated geomorphological features originating from larger extents of the ice-sheet. Sawagaki and Hirakawa (1997) observed traces of meltwater in coastal areas of Antarctica. There are indications that large quantities of water drained through the Laurentide ice-sheet during its waning phase (e.g. Barber et al. 1999, Clarke et al. 2003). Some of the observations from Antarctica have been heavily discussed, but the evidence is mounting that major drainage events may occur. Hence, large-scale, low-frequency drainage phenomena are possible in ice-sheets.

In Greenland, vast amounts of surface meltwater are routed seasonally through an evolving subglacial drainage system, the physics of which depend critically on the substrate of the bed. Field studies in western Greenland have in places interpreted measurements to reflect a till bed (Booth et al. 2012, Dow et al. 2013, Walter et al. 2014). Alternatively, a suite of field measurements in boreholes drilled at six sites during the Greenland Analogue Project (GAP), Claesson Liljedahl et al. (2016) indicated the ice-bed contact to be bedrock, with perhaps a thin mantle of coarse sediment (Harper et al. 2016). The collective studies identify spatially variable basal conditions beneath Greenland, but interpretation of measurements within the context of the basal drainage system must bear this physical framework in mind.

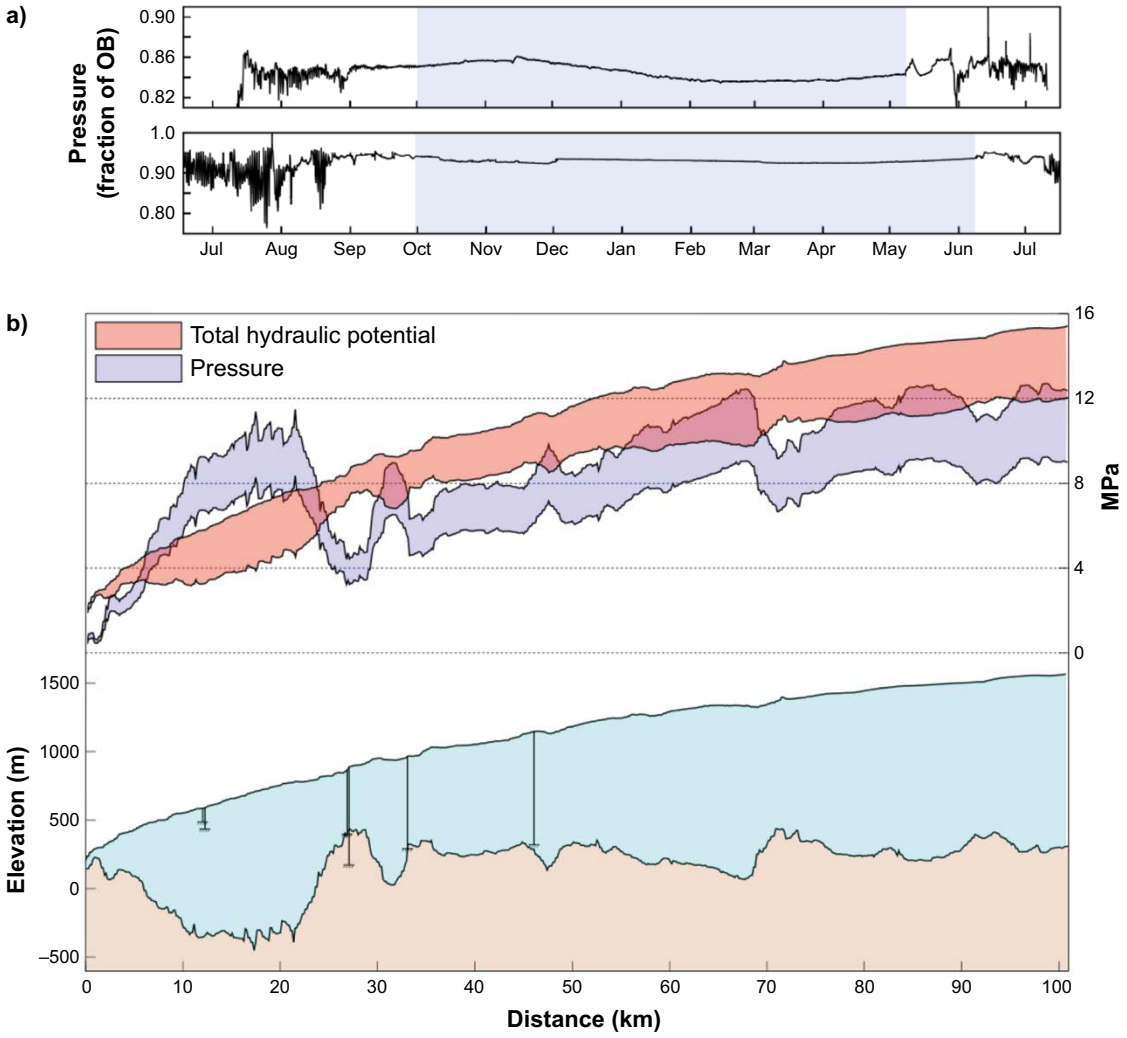

Figure 3-24. *(A) Typical annual water pressure records from two sites in western Greenland measured during the GAP project (Claesson Liljedahl et al. 2016). Pressure records illustrate diurnal variability during the melt season about a high baseline pressure. Winter pressure is characterized by the absence of high frequency variability and consistent high pressure. Blue shaded region reflects the winter period (different for different years and sites). (B) Basal water pressure (blue shaded region) and total hydraulic potential (red shaded region) along the transect of field sites where water pressures were drilled during the GAP project, as illustrated in the lower panel. Vertical lines in the lower panel reflect borehole drilling sites. Total hydraulic potential shaded region illustrates long length scale gradients associated ice-sheet thickness and basal topography. Thickness of the shaded region illustrates the range of plausible hydraulic potential, informed by the suite of GAP borehole pressure measurements. Modified from Wright et al. (2016).*

Measurements made in a network of 32 boreholes drilled to the ice-sheet bed as part of the GAP (Claesson Liljedahl et al. 2016, Harper et al. 2016) and ICE (Harper et al. 2019) projects have identified key characteristics of Greenland's subglacial drainage system. The basal drainage network is composed of discrete water-routing elements of varying transmissivity (Meierbachtol et al. 2016). Borehole measurements revealed basal water pressures that vary over diurnal and seasonal scales (Wright et al. 2016) in response to basal drainage system processes responding to varying surface melt. Despite this variability, the basal drainage system has been found to maintain high pressure during both winter and melt seasons; measured pressures in all but one borehole at sites ranging from < 1 km to 46 km from the ice margin ranged from 0.8 to 1.1 as a fraction of local overburden pressure (Figure 3-24). Taken together, the hydraulic measurements and analyses from the ice boreholes made within the GAP study (Claesson Liljedahl et al. 2016) imply that ice overburden hydraulic pressure (i.e. a hydraulic head corresponding to 92 % of ice thickness) provides an appropriate description of the basal hydraulic pressure as an average value for the entire ice-sheet over the year.

Spatially, the hydraulic potential gradient beneath Greenland's ablation zone is controlled by ice thickness and basal topography gradients at long length scales (e.g. many ice thicknesses). At shorter length scales (e.g. an ice thickness and less), pressure gradients arising from drainage system processes are superimposed on topography-controlled gradients (Wright et al. 2016) (Figure 3-24). Time changes in drainage system processes result in a dynamic hydraulic potential field that is underpinned by a pressure potential from overlying ice thickness and an elevation potential from basal topography. This results in a characteristic hydraulic potential gradient field beneath Greenland's ablation zone with short length scale drainage system gradients superimposed on long length scale gradients controlled by ice-sheet and basal topography (Wright et al. 2016).

3.2.4 Model studies

In a study made for SKB, Boulton et al. (2001b) developed a theory of sub-glacial drainage beneath ice-sheets based on flow in sub-glacial tunnels (R-channels), which are supposed to be the main agents of large-scale longitudinal melt water discharge. The widespread glacial melt water is supplied to the tunnels as groundwater flow. The drawdown of the piezometric pressure by the tunnels provides the mechanism for predominantly transverse groundwater flow towards the tunnels. The tunnels are developed from water-filled cavities formed at the ice/bed surface. The groundwater head elevation rises as a result of increased water supply to the bed or if the ice-sheet advances over a low-conductive bed. Hence, in the theory of Boulton et al. (2001b), tunnel spacing is a function of the relation between bed transmissivity and melt water input.

In the summer season the high discharge by surface melting is expected to create short-lived water-filled voids between the large tunnels. Many of these voids will form locally beneath the bases of water-conducting moulins and crevasses. In the winter seasons such drainage routes will be closed by internal ice flow. Boulton et al. (2001b) argued that the relatively long winters and short summers representative of the climate around large ice-sheets will inhibit the development of well-integrated summer drainage patterns, except very close to the ice-sheet margin.

Ice-sheet hydrology can be modelled in one of two main ways. Commonly the flow is represented by simple routing routines that follow the basic ideas laid down by Shreve (1972) where the discrete flow routing of water is not described, but where the water pressure potential is used to predict the direction of flow. This type of modelling probably correctly handles the flow paths of water but not the quantities of water involved. Only three models exist in which the entire hydrological system or parts of it are modelled using a physically based model. In these models, the paths and quantities of water flowing in the system are handled. The choice of model depends on the purpose of the analysis in question, what geometric scale is to be studied, and available data. Two models describe the complete hydrology of a glacier (Arnold and Sharp 2002, Flowers and Clarke 2002a, b).

Modelling the physics of glacier hydrology is complex, since it involves the liquid phase, namely water, moving through the solid phase, namely ice, at the melting temperature. Furthermore, ice is deformable under relatively low stresses, which allows channels and conduits in glaciers to change size and shape much more rapidly than channels eroded in rock or sediment. The glacier system is thus transient on all timescales and over all spatial scales.

The first physically based models in glaciology were made to reproduce simple observable phenomena in glacier hydrology. Röthlisberger (1972) and Shreve (1972) presented simple numerical models (Röthlisberger: conduit flow; Shreve: water pressure potential flow) for water flow in glaciers. The

assumptions made were that the rate of melt enlargement is balanced by creep closure (Röthlisberger) and that water pressure is in balance with ice pressure (Shreve 1972). Nye (1976) and Spring and Hutter (1981) presented a physically based theory of unsteady flow through interglacial channels. Hooke (1984) investigated the effects of non-steady conditions, in particular open channel flow, on the Röthlisberger system. This was elaborated by Kohler (1995) who investigated the ratio of open-to-filled channel flow in a subglacial system. Most models have assumed circular cross-section pipe flow and semi-circular tunnels. However, discrepancies between measurements and model calculations led Hooke et al. (1990) to propose low broad tunnels in place of semi-circular ones to be able to apply Glen's flow law of ice deformation with reasonable viscosity parameter values. Conduit flow was found not to reproduce water pressure and fluxes observed during the surge of Variegated Glacier, Alaska. This prompted Kamb (1987) to propose the linked cavity system which combined large cross-section with small flow velocities. Walder and Fowler (1994) extended Röthlisberger's model to include 'canals' cut into deformable till.

A first approach to producing a complete physically based model for a glacier was reported in Arnold et al. (1998), henceforth referred to as the Arnold model. This model has three components. A surface-energy sub-model calculates distributed glacier surface melt water production. A routing sub-model takes rain- and melt-water and either delivers the total water flux to *a priori* prescribed moulins, where it enters the glacier interior or supraglacially to the ice margin. The third and final component is a subglacial sub-model that involves a conduit system. The englacial drainage is treated as part of the subglacial conduit system and simulated analogous to a sewage pipe system. Subglacial conduits are fed by a network of "drains", which represent moulins where water can enter or overflow from the system. Subglacial conduits can enlarge and contract in response to changes in the rates of wall melting and creep closure associated with changes in water inputs. In addition, the configuration of the system can change between a distributed system and a channelized system represented by different predefined numbers and geometries of conduits. "Distributed" links were changed to "channelized" flow paths as the modelled snowline passed in the up-glacier direction over each moulin. From this perspective the subglacial model is rigid, since switching between systems does not permit smooth transitions with the bed being partially drained by each system. The model was applied to Haut Glacier d'Arolla, Switzerland, and performed well in comparison with proglacial stream discharge, but limitations are indicated by discrepancies between model outputs and field observations of subglacial water pressure and water velocities, although the substantial features of these records could be reproduced.

Flowers and Clarke (2002a, b), henceforth referred to as the Flowers model, developed a different approach to a complete physically based model. The model comprises coupled surface runoff, englacial, subglacial, and groundwater systems. Each of the four components is represented as a two-dimensional, vertically integrated layer that communicates with its neighbours through water exchange. Melt is computed by a distributed temperature index model. Englacial hydrology is represented by describing a variety of bulk storage elements and allowing water transport between them in a system of cracks. Hence, the englacial system is treated as fracture-connected crevasses and pipes. The Flowers model was built to represent conditions at Trapridge Glacier, Canada, which is underlain by thick porous sediments. Their subglacial model, therefore, comprises flow through macroporous glacier sediments at the ice-bed interface and subsurface aquifers of buried sediment layers not directly exposed to the base of the glacier. Hence there are no explicit tunnels as in the Arnold model. The model reproduced well diurnal cycles of subglacial water pressure as measured in boreholes.

A crevasse-like englacial network, as adopted in the Flowers model, has been observed on Storglaciären, Sweden (Fountain et al. 2005a, b), countering previous notions of englacial water flow through a few melt-enlarged conduits. If permeable subglacial sediments are present, groundwater flow may be a significant part of the system, as in the Flowers model, or flow may occur in channels eroded into the subglacial sediments. On harder beds or beds of less permeable sediments such as tills, water flow may occur in conduit systems melted into the ice or in linked cavity systems. Hence, a general physically-based model would have to accommodate all these possibilities and even couple different types of systems beneath different parts of a glacier. Such a model would be inherently complex.

Another issue that is not satisfactorily addressed in existing models is the time-transgressive development of subglacial systems. In the Flowers model, this is not necessary since flow through porous sediments does not involve significant time-dependent changes, except possible changes such as development of piping or siltation of the porous media from fines produced through sediment deformation. In the case of the Arnold model, it is widely reported (e.g. Nienow et al. 1998) that the subglacial drainage system changes both in sizes of conduits and in complexity of the network of channels through the course of

a season. The subglacial system is very dynamic, and it seems as if a complete and accurate model description of this system may be distant. However, most changes in such a system occur in response to rapid changes, both increases and decreases in water inputs, so a first-order approximation may be to switch between a series of systems prompted by key events in the forcing.

During the past decade substantial effort has targeted advancements in subglacial hydrology modelling, with particular focus on inclusion of physics for both 'efficient' channelized systems and 'inefficient' linked cavity networks in a single model framework (Hewitt 2011, 2013, Hoffman et al. 2016, Hoffman and Price 2014, Schoof 2010, Werder et al. 2013). Specifically, water flow in a linked cavity network is accommodated through a continuum approach (Hewitt 2011, Werder et al. 2013). Averaged over large areas of the bed, discrete water flow is generalized as an equivalent porous sheet. The transmissive capacity of the network is described by a prescribed hydraulic conductivity and the sheet thickness, the latter of which is set by the average cavity size and prone to transience in response to water flow and ice sliding influencing cavity opening/closing rates. Physics for conduit flow is applied along the edges of the two-dimensional model grid. Most recently a third, low permeability drainage component has been introduced to the above formulation, which exchanges water flow with the sheet component and is conceptually meant to reflect the presence of a weakly connected component of the subglacial drainage system.

Results from these recent model developments have generated basal drainage system behaviour that is qualitatively similar to conceptualized drainage evolution in alpine glaciers (Werder et al. 2013). Low discharge rates favour slow flow through the sheet network. At higher discharge, such as occurs during the onset of the melt season, meltback of the conduit walls results in conduit growth along the model edges, with an associated pressure reduction which draws water from the adjacent sheet network.

Despite the significant advances in subglacial hydrology models, key issues persist that limit their prognostic capacity. Critically, model efforts have revealed a limited capacity to generate basal water pressures that are consistent with physical reason over an annual cycle in the ice-sheet setting. Common practice is to tune hydraulic conductivity in order match melt season observations. This practice, however, results in modelled winter pressures that are far lower than observed (e.g. de Fleurian et al. 2016). Alternatively, if hydraulic conductivity is set too low, modelled pressures are prone to widespread overpressure that is physically implausible. Because model physics struggles to sufficiently reproduce existing conditions, the prognostic capacity of these coupled efficient–inefficient models is limited. Nevertheless, the advances have proven valuable in elucidating driving processes over ice-sheet domains.

3.2.5 Spatial Perspective

Basal thermal conditions define the maximum spatial extent of active drainage system processes and meltwater recharge to the groundwater system. The inland extent of melted basal conditions depends on the magnitude of processes acting to warm (geothermal heat flux, strain heating) or cool (vertical advection of cold ice from the surface). These depend on ice-flow processes that are subject to change in time. Current consensus is that in Greenland the boundary between frozen and melted conditions generally extends well beyond the ELA. Temperate basal conditions persist from this inland boundary to the ice-sheet margin (Figure 3-25). Beneath the ablation zone, substantial water is seasonally input to the bed from the surface, leading to drainage system/sliding speed interactions. As the surface can generate as much meltwater in one day as is generated in one year at the bed by basal melt, the surface conditions have a substantial impact on bed conditions across this reach.

Collectively, model results and in situ pressure observations in Greenland support a view of the basal drainage system beneath the ablation zone in which basal melt conduits grow in response to seasonal surface melt routed to the ice-sheet bed, but the extent of conduit growth is limited to within 20–25 km of the margin (Figure 3-25). Further inland, a conductive linked cavity system likely remains stable, transporting basal and surface-derived melt towards the margin. Nevertheless, the water flux across a large portion of this region has been observed to be relatively large and fast flowing (Chandler et al. 2013). Rare conduits may extend deeper beneath the ablation zone if, for instance substantial englacial storage provides a water source preventing complete conduit shutdown during the winter, or if the closure of conduits is impeded by pinching off of the conduit closer to the margin in response to some unconstrained process. Alternatively, a linked cavity system could maintain stability if its conductivity (and therefore transmissivity) increased during the melt season, as may occur from increasing connectivity along the bed in response to substantial basal melt fluxes. Such processes enhancing conduit or linked cavity stability are without modelled or observed evidence, however, and therefore remain speculative.

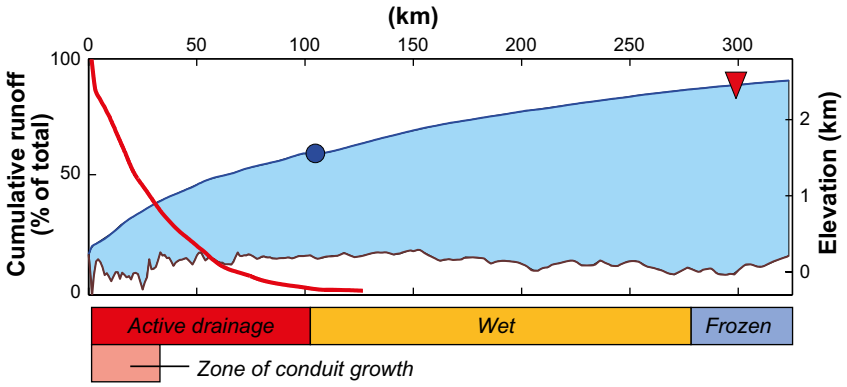

Figure 3-25. *Conceptual view of the thermal and hydrological framework at a snapshot in time. Melted basal conditions extend beyond the ELA (represented by the blue circle). Below the ELA surface melt increases such that cumulative runoff increases exponentially towards the ice-sheet margin (red curve). An active drainage system develops in response to surface melt routing to the bed. Basal melt conduit development in the drainage network is limited to a region near the ice-sheet margin where sufficient melt energy promotes conduit growth during the melt season. Left y-axis refers to the red runoff curve. Red triangle refers to the inland limit of surface melting. Conceptual schematic is developed based on the GAP project transect in western Greenland.*

3.2.6 Temporal perspective

The time perspective of glacier hydrology can be divided in two main categories, timescales under which the ice-sheet undergoes significant changes in volume and extent and where the associated hydrological conditions change with the ice-sheet; and timescales under which the ice-sheet can be considered constant in volume and extent and where the variability of the acting processes dominates.

Seen under the perspective of an entire glaciation, the hydrological system varies spatially with the size of the ice-sheet. This means that different parts of the bed are either temperate or cold and can be associated with hydrological systems of different overall structure and parameterisation. The distribution of cold and temperate basal conditions changes in time and also in location with the waxing and waning ice-sheet. From this perspective, a possible repository site will experience changing conditions of active hydrology under thawed bed conditions or cold frozen bed conditions. With changing ice-sheet configuration, the basal hydraulic conditions also vary so that shifts in location of drainage pathways occur. How much time a specific location is subjected to either kind of condition is determined by the large-scale fluctuations of the ice volume and extent.

The processes in the hydrological system of an ice-sheet exhibit variations ranging from diurnal (in the case of temperature-dependent melt variations) or possibly shorter duration (in the case of rainfall-induced variations) to seasonal variations that depend on temperature variations on an annual basis. Since all variations in temperature-induced melting and liquid precipitation yield variations in input to the hydrological system, they also yield variations in subglacial water pressure with oscillations on similar timescales. This means that the base of an ice-sheet will exhibit variations on a diurnal and subdaily scale superimposed on longer-term variations coupled to weekly variations due to changing air masses of different temperature and lastly variations due to seasonal temperature fluctuations.

3.2.7 Handling in the PSAR

Information from natural analogues and model studies, Section 3.2.3 and 3.2.4 has been used for giving a description of the evolution of hydrological conditions and groundwater for glacial periods in the *reference glacial cycle climate case* (Section 4.5.5), and also for setting up boundary conditions and discussing results of groundwater flow modelling for glacial conditions.

3.2.8 Handling of uncertainties in the PSAR

Uncertainties in mechanistic understanding

Although the theories and empirical studies of glacier hydrology are of appropriate quality to reproduce observed phenomena at individual glaciers or sites on glaciers, there are no generally applicable theories for the spatial and temporal variations in hydrology and hydraulic conditions. Perhaps more importantly, the coupling between discrete drainage pathways and the continuum mechanics of ice-sheet models is not, thereby preventing integrated modelling. The main obstacle to enhancing our understanding of the dynamics of glacier hydrology is the transient nature of the system and difficulties in observing its structure and behaviour. The division between subglacially derived and surface-derived water emanating from, say, the Greenland ice-sheet is also unknown. Almost exclusively, process studies have been made on valley glaciers. However, there is no reason to believe that other processes would be present in association with an ice-sheet, although the magnitude of the processes will be scaled proportionally to the differences between valley glacier scale and ice-sheet scale (Jansson et al. 2007, Jansson and Näslund 2009).

3.3 Isostatic adjustment and relative sea-level changes

In addition to the descriptions in the present section, a detailed in-depth description of the physics of glacial isostatic adjustment (GIA), how it affects sea-level, and the methods that are employed to study and understand these processes are presented in Whitehouse (2009, 2018) and SKB (2010a).

The major part of Section 3.3.1 is adapted from SKB (2006a, Section 3.3 written by P. Whitehouse), whereas some parts are adapted from Lund and Näslund (2009). Section 3.3.2 is adapted from SKB (2006a). Section 3.3.3 is from Lund and Näslund (2009), and Section 3.3.4 is adapted from SKB (2006a) and Whitehouse (2009).

3.3.1 Overview/general description

The redistribution of mass associated with the growth and decay of continental ice-sheets gives rise to major glacial loading and unloading effects over timescales of several tens of thousands of years. The response of Earth's crust, mantle and gravitational field is referred to as Glacial Isostatic Adjustment (GIA). For instance, during the decay of a major ice-sheet, the unloading of mass results in a post-glacial rebound of the crust that continues well after the disappearance of the ice. This process is well known from previously glaciated regions such as Canada and the United States, Fennoscandia, the British Isles and Siberia (e.g. Ekman 1991); areas where this process is still active today, some 10–15 ka after the last deglaciation. In previously glaciated terrain without strong tectonism, glacial isostatic adjustment is the most significant geodynamic process governing vertical deformation of the crust (e.g. Peltier 1994).

During the Last Glacial Maximum (LGM), around 20 ka BP, the Laurentide ice-sheet of Canada and the United States, and the Fennoscandian ice-sheet had maximum thicknesses of around 2.5–3 km. When these large ice masses slowly formed, their weight resulted in a slow downwarping of Earth's crust. One important factor that governed both this process and the following glacial unloading is the physical properties of Earth's crust and mantle. In the downwarping process, mantle material is displaced and flows laterally in order to make room for the flexing crust. At times of ice-sheet decay, mantle flow is reversed and the crust rebounds. Since the mantle viscosity is high, the downwarping and subsequent rebound are slow processes. Furthermore, it has been shown that a deglaciation of large Northern Hemisphere ice-sheets results in deformation of the Earth's entire surface, producing a series of upwarps and downwarps away from the areas of the former ice-sheets (Figure 3-26). However, the deformation is largest in the regions that were glaciated.

The glacial isostatic adjustment process manifests itself not only in the slow rebound regions of past ice-sheets. Current melting of glaciers produces additional GIA effects. As an example, Iceland is currently undergoing rapid glacial rebound due to a mass loss of Vatnajökull and other smaller ice caps (e.g. Árnadóttir et al. 2009). Since the viscosity of the mantle is inferred to be three orders of magnitude lower beneath Iceland (Árnadóttir et al. 2009) than below for example Fennoscandia, uplift rates on Iceland are on the order of 20 mm a^{-1}, in spite of the much smaller volume of ice loss.

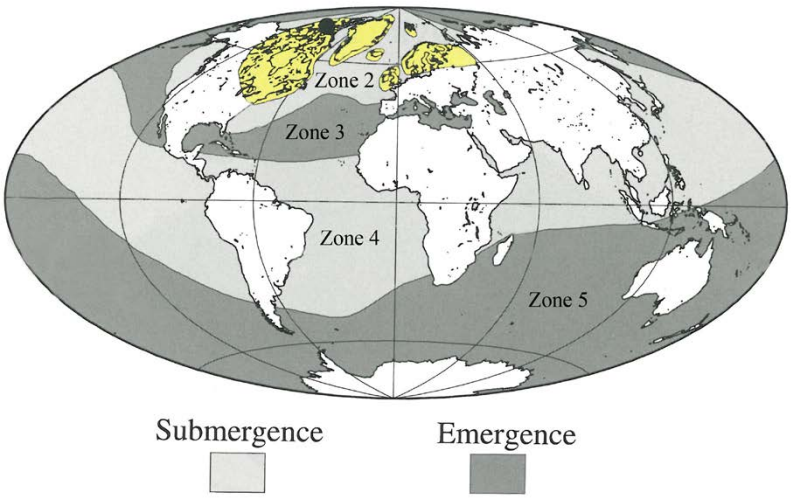

Figure 3-26. *Calculated deformation resulting from an instantaneous unloading of Northern Hemisphere last glacial cycle ice-sheets at 16 ka BP. The results show five sea-level zones with similar sea-level histories within each zone. Sea-level zone 1 is marked in yellow. The entire Earth is affected by the unloading through a series of elevated and subsided regions away from the areas of the former ice-sheets. Modified from Clark et al. (1978).*

Outside the ice-sheet margin, an uplifted forebulge, or peripheral bulge, is formed (e.g. Mörner 1977, Fjeldskaar 1994, Lambeck 1995). The forebulge is caused by flexure and a lateral displacement of mantle material extending outside the ice margin, and it may stretch for several hundreds of kilometres beyond a major ice-sheet. The uplift of the forebulge is considerably smaller than the downwarping of the crust beneath the central parts of the ice-sheet; on the order of tens of metres. During and after deglaciation, the area of the forebulge experiences land subsidence, exemplified by the ongoing lowering of the Netherlands, southern England and the east coast of the United States. It is worth noting that land subsidence in these regions is also a result of ongoing marine sediment loading. The location of maximum forebulge uplift migrates toward the formerly glaciated region as the ice-sheet withdraws. In addition to the formation of the forebulge, the elasticity of the lithosphere may result in a downwarping of the crust, not only under the ice-sheet, but also to some extent outside the ice margin. This produces a flexural depression between the ice margin and the forebulge, a depression where lakes may form from glacial meltwater.

At present, the crust beneath the Antarctic and Greenland ice-sheets is depressed in a similar way as previously occurred under the Laurentide, Fennoscandian and Siberian ice-sheets. In Greenland and Antarctica, the crust would also be subject to significant glacial rebound if these areas were to be deglaciated in the future.

The geoid is the equipotential surface of the Earth's gravitational field which best fits the undisturbed surface of the oceans. Shoreline migration is the result of changes in the height of the geoid relative to the solid surface of the Earth. Sea-level is defined to be zero on land and positive in the oceans, where it corresponds to the depth of the ocean. The surface of the ocean corresponds to the geoid surface (see Figure 3-27). Relative sea-level is the vertical height difference between the geoid at an arbitrary time and the present height of the geoid, where the height of the geoid is measured relative to the height of the solid surface (see Figure 3-27). Relative sea-level is defined to be zero at the present day. It is positive during *transgression*, when the intersection of the geoid with the solid surface is higher than present, and negative during *regression*, when the intersection of the geoid with the solid surface is lower than present. The shape of the geoid is governed by the gravitational field of the Earth and varies over time. Over timescales of 100 years to 100 ka, changes in relative sea-level throughout Fennoscandia are dominated by the process of glacial isostatic adjustment.

Relative sea-level changes associated with GIA are a result of the coupled phenomena *isostasy* and *eustasy.* Isostasy is the response of the solid Earth to loading or unloading by ice or water, and/or unloading and loading due to denudation and sedimentation, whereas eustasy refers to changes in global sea-level arising from a change in ocean water volume following a mass exchange between continental ice masses and the oceans.

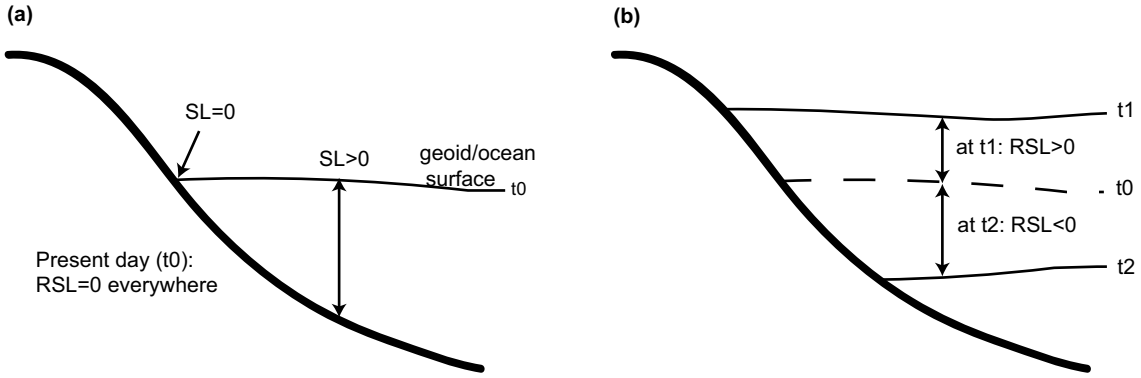

Figure 3-27. *(a) At time t0 sea-level (SL) is zero where the depth of the sea is zero, and positive where the depth of the sea is positive. Sea-level is defined to be zero on land. (b) At time t1 and t2 relative sea-level (RSL) is higher and lower respectively, as a result of the processes described in the text. Note that the change in relative sea-level is not uniform over the oceans, due to changes in the shape of the geoid.*

Global relative sea-level changes exhibit complex spatial and temporal patterns and are strongly dependent upon the location relative to major ice-sheets. Relative sea-level change at locations far from ice-sheets (hereafter referred to as far-field locations) is dominated by the eustatic signal; during deglaciation monotonic sea-level rise causes land inundation and the shift of shorelines inland. At locations close to ice-sheets (hereafter referred to as near-field locations) the isostatic signal dominates; rebound of the solid surface from the time of deglaciation onwards causes land emergence and the migration of shorelines oceanwards. These are two end-member cases, and, in general, sea-level change, and hence shoreline migration, is governed by a complex interplay of isostatic and eustatic processes, operating on different timescales.

GIA-induced sea-level changes depend on the following factors (see Figure 3-28):

- The location and thickness of ice-sheets.
- The depth and extent of the oceans.
- The structure and properties of the solid Earth and its response to surface loading.

Changes in surface loading arise due to the exchange of mass between ice-sheets and ocean basins throughout a glacial cycle. The presence of ice-dammed lakes and the redistribution of sediments also contribute to changes in surface loading, although, in Fennoscandia, the short-lived nature of ice-dammed lakes, and their shallow depth, means that this perturbation to the pattern of surface loading probably has a negligible effect when considering the solid Earth response. The denudation of bedrock and redistribution of associated sediments persists over a much longer timescale, on the order of millions of years. On a regional scale, over a single glacial cycle, the effect of sediment redistribution upon solid Earth deformation is negligible in relation to the ice load, but over several glacial cycles, or locally, it may be of significance.

The Earth consists of the crust, the upper and lower mantle, and the outer and inner core. The lithosphere comprises the crust and part of the upper mantle. The average thickness of the lithosphere is c 100 km, although this value varies between less than 30 km for oceanic lithosphere and up to more than 200 km for continental lithosphere (Watts 2001). Lithospheric thicknesses in Fennoscandia range between ~60 km in the north–west and ~200 km in the south–east (Watts 2001). The lithosphere is less dense than the mantle below and responds approximately elastically to forces applied at the surface. The deformation of this layer is short-lived once the load is removed. The mantle responds viscoelastically to forces applied over a timescale of ~100 ka. The recovery of this layer to a state of isostatic equilibrium following loading takes several orders of magnitude longer than the recovery of the lithosphere. The rheological properties of the lithosphere and upper and lower mantle determine the precise magnitude and duration of solid Earth deformation during a glacial cycle, and are discussed further in Sections 3.3.2 and 3.3.4. The outer and inner cores are not affected by GIA processes.

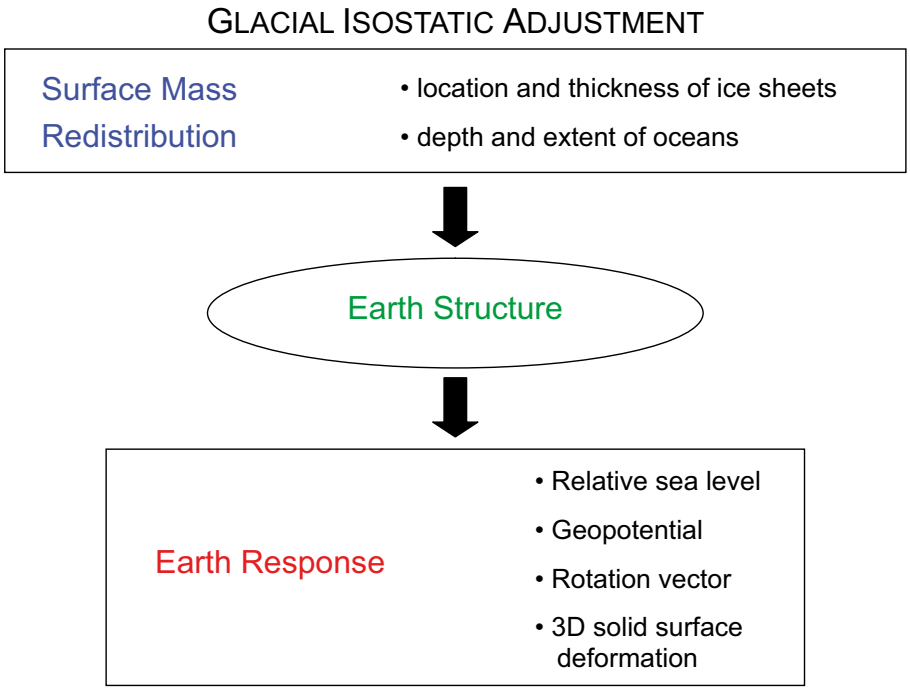

Figure 3-28. *The theory of Glacial Isostatic Adjustment (GIA): inputs and outputs of the system.*

GIA-induced sea-level changes arise because of the gravitationally-consistent redistribution of water between ice-sheets and ocean basins, and thus the evolution of surface loading. Any redistribution of surface mass alters the shape of the geoid, which in turn defines the position of the surface of the oceans.

The height of the geoid, or mean ocean surface, is dependent upon *direct* and *indirect* geoid perturbations (Milne et al. 2002), as well as changes in ocean water volume and the capacity of the ocean basins. *Direct* effects refer to the deflection of the geoid due to the direct attraction of surface mass loads, such as ice-sheets. *Indirect* effects refer to geoid perturbations arising due to the surface load-induced deformation. The volume of the oceans varies as water is transferred to and from the ice-sheets. Also changes in ocean capacity and bathymetry arise because of crustal and geoidal perturbations in response to ice and ocean loading. The ice-loading solid surface response includes the depression and rebound of the solid surface in the location of ice-sheets, and the raising and lowering of glacial forebulges in areas surrounding the ice-sheets. The ocean-loading response is like the ice-loading response. However, at continental margins ocean loading induces a levering of the continental lithosphere and a subsidence of offshore regions, this is referred to as *continental levering* (Clark et al. 1978) (see Figure 3-29). The combination of ice and ocean loading leads to a decrease in the volumetric capacity of the ocean basins during glaciation, and an increase during deglaciation due to the growth and decay of offshore peripheral bulges, resulting in a globally uniform rise or fall in sea-level, respectively. The ongoing fall in sea-level following the last deglaciation due to the migration of water from equatorial regions to subsiding peripheral bulge regions has been termed *equatorial ocean syphoning* (Mitrovica and Peltier 1991, Mitrovica and Milne 2002).

Changes in relative sea-level result in shoreline migration. A rise in relative sea-level and the consequent inland migration of the shore may be due to solid Earth subsidence, an increase in the height of the geoid/ocean surface because of ice-sheet melting, or a combination of these processes. Similarly, a fall in relative sea-level and the consequent migration of the shore towards the ocean may be due to isostatic rebound, a fall in the height of the geoid/ocean surface due to ice-sheet build up, or a combination of these processes. In the vicinity of the Fennoscandian ice-sheet, the effects of isostatic deformation and changes to the height of the geoid/ocean surface occur simultaneously and may have opposite effects on the position of the shoreline. Further, the surface of the Baltic Sea does not solely depend on the height of the geoid/ocean surface, but also on the elevation of its sills relative to the Atlantic sea-level, and ice thicknesses at locations with potential connections to the sea; these may cause it to become isolated from the global ocean.

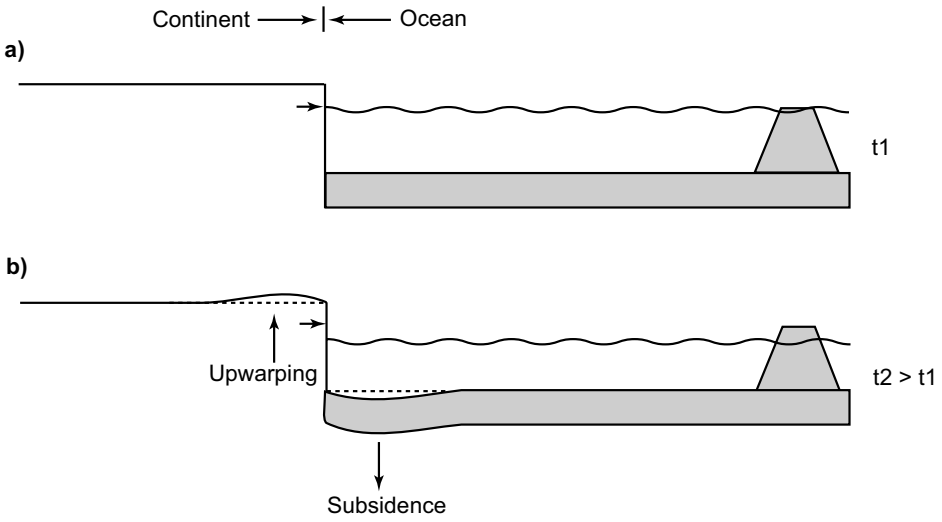

Figure 3-29. *Continental levering: the migration of water into offshore regions following deglaciation results in offshore subsidence and onshore upwarping. Ocean floor subsidence results in sea-level fall at far-field sites.*

Indirectly, groundwater flow and composition are influenced by shoreline migration. If the site is not subject to permafrost, and it is not covered by an ice-sheet, the sea, or a lake, then the groundwater surface follows a subdued version of the topography. Groundwater flow will be driven by topography, assuming precipitation exceeds evaporation. If the site is submerged the situation will be almost stagnant and groundwater flow will be driven by density only, see the **Geosphere process report**. Groundwater composition is affected, since relative sea-level affects the salinity of the Baltic Sea. Relative sea-level and the extent of the ice-sheet determine whether there is a connection between the Baltic Sea and the ocean. This together with the runoff to the Baltic basin, determines the salinity in the sea/lake water.

3.3.2 Controlling conditions and factors

Loading

The main factors governing the evolution of relative sea-level, and hence shoreline migration, throughout Fennoscandia are the loading history – both by ice and ocean water – and the rheological parameters governing the response of the solid Earth to such a load.

Near-field relative sea-levels are very sensitive to variations in the evolution of the near-field ice-sheet (Lambeck et al. 1998, Davis et al. 1999, Tamisiea et al. 2001, 2003, Milne et al. 2002, Kaufman and Lambeck 2002). There remain uncertainties in the details of ice loading during the last glacial cycle, especially in estimates of ice thickness within Fennoscandia.

The details of far-field ice-sheets are irrelevant for the prediction of relative sea-level change in Fennoscandia (Peltier 1998, Mitrovica et al. 2001, Tamisiea et al. 2003, Bassett et al. 2005); mass changes in the far field mainly provide an influence on global eustatic sea-level change. However, the overall characteristics of far-field ice-sheets may also generate a long wavelength isostatic response in Fennoscandia. This response is likely to be dominated by the signal from a massive North American (Laurentide) ice complex. Due to the position of Fennoscandia on the Laurentide forebulge during the LGM (Mitrovica et al. 1994), the presence of the Laurentide ice-sheet is predicted to have generated 25–30 m of solid Earth uplift in central Fennoscandia at this time (Section 3.3.4 in SKB 2010a). The magnitude of this signal does not vary greatly across Fennoscandia (unlike the relative sea-level signal due to local ice loading) and is not dependent upon the local geometry of the Laurentide ice-sheet; only its volume.

During the last deglaciation an ice-dammed lake prevailed within the Baltic depression when non ice-covered sills were above sea-level and all other potential connections between the Baltic Sea and the North Sea were dammed by the ice-sheet ice (e.g. Björck 1995, Lambeck 1999). The surface of the ice-dammed lake was constrained by the height of the ice-sheet above sea-level and the surrounding topography, i.e. the sill levels, and there is evidence to suggest that immediately prior to the draining

of the so-called Baltic Ice Lake its surface was 25 m above the contemporary relative sea-level (Björck 1995). Due to the relatively small volume of water released to the oceans as the ice lake drained the resulting perturbation of global sea-levels was insignificant (Lambeck 1999). The shallow depth and the short duration of the ice lake mean that its impact on isostasy was negligible in comparison with the ice load.

Another process that may impact the loading is erosion and sediment transfer. Erosion and transport of sediment took place beneath warm-based parts of the ice-sheet during previous glacial cycles, and this mass redistribution affects isostatic loading and topography. However, the average total depth of glacial erosion of basement rock over all Quaternary glacial cycles in lowland parts of Fennoscandia is on the order of a few tens of metres, see Section 3.5. Therefore, on the timescale of one glacial cycle, the average unloading/loading effect of this process may be neglected. However, any local reshaping of the land will affect the evolution of the shoreline, and this needs to be taken into account.

Rheological parameters and topography

To determine the Earth's response to surface loading its internal rheological and density structure must be specified. The characteristic timescale for loading during a glacial cycle will excite both elastic and viscous responses, therefore a viscoelastic (Maxwell) rheology is adopted. Such a system behaves elastically on a short timescale and viscously on a long timescale when placed under stress.

Parameters describing the rheological properties of the Earth's lithosphere and upper and lower mantle define its response to loading during a glacial cycle. The average density and elastic structure of the Earth are taken from Dziewonski and Anderson (1981). The lithosphere is generally regarded as elastic for the purposes of GIA studies; this has been shown to be a good approximation throughout the development of the subject (McConnell 1968).

The upper mantle lies below the lithosphere, extending to a depth of 660 km, and then the lower mantle extends to 2900 km below the Earth's surface. The viscosities of the upper and lower mantle have been constrained to lie in the ranges $1 \times 10^{20} - 2.6 \times 10^{21}$ Pa s and $2 \times 10^{21} - 1 \times 10^{23}$ Pa s, respectively, as determined from previous GIA studies (Davis and Mitrovica 1996, Mitrovica and Forte 1997, 2004, Simons and Hager 1997, Lambeck et al. 1998, Davis et al. 1999, Milne et al. 2001, 2002, 2004). Lateral variations in radial viscosity structure may be derived from seismic shear-velocity models by converting velocities to temperatures, and then using temperature to estimate viscosity.

Present-day topography is used to constrain palaeotopography. When calculating palaeotopography, see Section 3.5, we assume that all changes to the shape of the land arise from the differential GIA response across the region; however, topography is also affected by tectonic, erosional and depositional processes.

The isostatic adjustment and shoreline migration described above may affect several geosphere variables of importance for a deep geological repository (Table 3-3).

3.3.3 Natural analogues/observations in nature

The GIA process may be observed by studying relative sea-level markers, both from the geological record and from tide gauge data, GPS observations of the 3D deformation of the solid surface, the time-variation of the gravity field as observed by satellites and land-based gravity surveys, and changes in the orientation of the Earth's rotation vector and length of day.

Geological and tide gauge data complement each other. Tide gauge data consist of monthly or annual observations of mean sea-level relative to a local solid Earth marker at coastal sites throughout the world. The data may be accessed through e.g. the "Permanent Service for Mean Sea-level" at www.pol.ac.uk/psmsl. In the Baltic region, such sea-level observations have been conducted systematically for more than a century. When measuring isostatic uplift rates with this method, it is necessary to correct the result to exclude the effect from eustatic variations. In non-coastal areas, present post-glacial rebound rates have been estimated by repeated geodetic levelling, tied to locations of sea-level observation. The results from these measurements show that the present uplift rate displays a concentric uplift pattern over Fennoscandia, with a maximum rate of slightly more than 9 mm a^{-1} in the northernmost part of the Baltic Sea, see Figure 3-30.

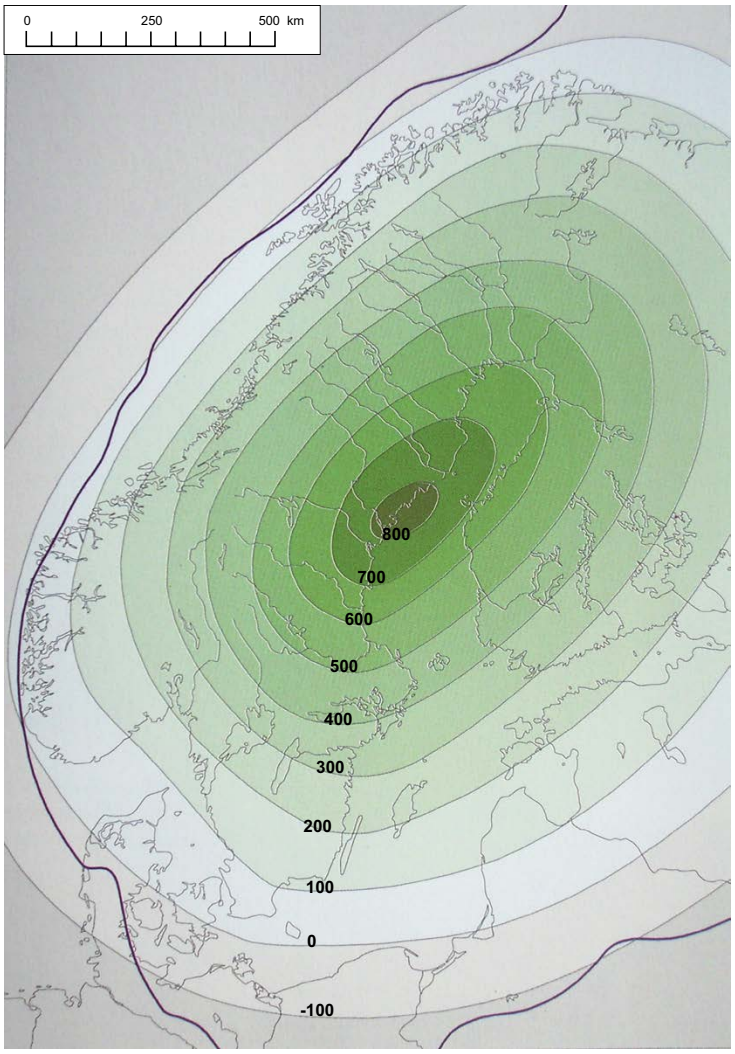

Figure 3-30. *Total amount of glacial rebound (metres) that has taken place due to the decay of the Fennoscandian ice-sheet. The bold line shows the approximate maximum extent of the last Fennoscandian ice-sheet. Note that the total amount of rebound is more than twice as large as the amount of rebound that may be inferred from raised beaches formed at the highest post-glacial sea-level (see the text). Modified from Fredén (2002).*

The geological data, including palaeoshoreline positions, lake isolation and tilting information, cover a longer period than the tide gauge data, but the tide gauge data are more accurate, both in terms of their vertical resolution and the dating of the information. In this context, shorelines or other geomorphological features that formed at the highest post-glacial sea-level, in front of the retreating ice-sheet margin, provide the oldest estimate of former relative sea-level positions. However, the total amount of post-glacial uplift at a site is typically larger than can be inferred from, for example, raised beaches. A significant portion of the uplift takes place as the ice-sheet starts to decay, *prior to the actual deglaciation* of a typical site situated at some distance from the maximum ice margin. The total maximum amount of glacial rebound that has occurred due to the decay of the Fennoscandian ice-sheet is around 800 m (e.g. Mörner 1979) (Figure 3-30). This may be compared with the largest value on rebound as inferred from the highest marine limit, which is situated at ~280 m a.s.l. in the Swedish coastal region of the Gulf of Bothnia. Another related method to study glacial rebound is to analyse the amount and direction of tilt of palaeoshorelines of glacial lakes that formed behind the retreating ice margin. A selection of geological relative sea-level data for Fennoscandia can be found in e.g. Lambeck et al. (1998), Påsse (2001), Eronen et al. (2001), Kaufmann and Lambeck (2002), Whitehouse (2007[2]), Påsse and Daniels (2015), and references therein, but at present a complete compilation of such data does not exist.

[2] Whitehouse P, 2007. A relative sea-level data base for Fennoscandia. Durham university, February 2007. Excel data base stored at SKB, SKBdoc 1265613.

Table 3-3. A summary of how geosphere variables are influenced by isostatic adjustment and shoreline migration.

Geosphere variable	Climate issue variable	Summary of influence
Rock stresses	Isostatic depression/rebound	The deformation of the Earth's crust will lead to altered rock stresses.
Groundwater pressure	Relative sea-level	If the site is not covered by the sea or a lake the groundwater pressures will be determined by topography and groundwater recharge. If the site is submerged the groundwater pressure will be determined by depth of the sea/lake.

Care must be exercised when interpreting palaeoshoreline data from the Baltic Sea; it is important to determine whether the data relate to sea-level or a lake level. An overriding problem with geological data in Fennoscandia is the lack of relative sea-level data prior to the LGM. Most of the evidence of shorelines prior to this time has been destroyed by the ice-sheet. This makes it difficult to test relative sea-level predictions from before 20 ka BP. Furthermore, the fact that shorelines can only form in ice-free locations provides an important temporal constraint on shorelines that would otherwise be undated.

As previously mentioned, observations of relative sea-level are required in both the near and far field. Far-field data provide constraints on eustatic sea-level change and hence the volume of ice contained in far-field ice-sheets. Near-field data exhibit a more complex dependence upon the local distribution of ice and the Earth model.

One way of making direct observations of ongoing post-glacial crustal deformation is to use high quality data from networks of continuously operating permanent GPS receivers. GPS data provide satellite-measured observations of changes in baseline distances which yield present-day rates of vertical and horizontal motion at a series of discrete positions. GPS data from the BIFROST project (Johansson et al. 2002) provide excellent spatial coverage of present-day solid Earth deformation throughout Fennoscandia to a high degree of accuracy. Typically, the GPS stations used in the BIFROST project were established within national land survey programmes with an initial aim of providing reference coordinates for other GPS measurements. The detailed analyses of data from such permanent GPS stations have provided new insight into the processes of post-glacial rebound or GIA in Fennoscandia and Canada (cf. Scherneck et al. 2001, Henton et al. 2006). The results provide information on both the rate of the vertical uplift component, as well as on the associated smaller horizontal component of crustal motion (e.g. Johansson et al. 2002) (Figure 3-31). The vertical component of GIA for the Forsmark site amounts to 6.7 ± 0.2[3] mm a^{-1} (Vestøl et al. 2019). Uplift determined by these GPS observations show the same concentric uplift patterns as those derived from sea-level and levelling measurements. The fastest rebound occurs approximately in the areas where the Laurentide and Fennoscandian ice-sheets had their greatest thicknesses. The maximum vertical uplift rate measured in this way in the area of the former Laurentide ice-sheet is ~13 mm a^{-1} (Henton et al. 2006), while the corresponding value for Fennoscandia is ~10 mm a^{-1} (Figure 3-31). The largest horizontal displacements are generally found in the area of the ice margins of the maximum extent of the ice-sheet. The difference between the maximum vertical uplift rates as observed from sea-level/levelling measurements and from the analysis of GPS data is to a large extent covered by the uncertainty errors of the measurements, mainly in the sea-level measurements.

Since the GPS network yields an estimate for the full 3D deformation field, and the horizontal and vertical components of this field have different sensitivities to the ice history and Earth model, this opens up the possibility of constraining model parameters more accurately when these data are combined with sea-level observations. Combining the GPS data with sea-level data is particularly important when one considers that the GPS data are limited by their relatively short time span and can only yield information about present-day deformation rates. In contrast, sea-level data are limited by their poor spatial coverage; a factor that is addressed by the distribution of GPS observations throughout the interior of Fennoscandia.

[3] The uncertainty interval (1σ) constitute a preliminary estimate by the Swedish National Land Survey.

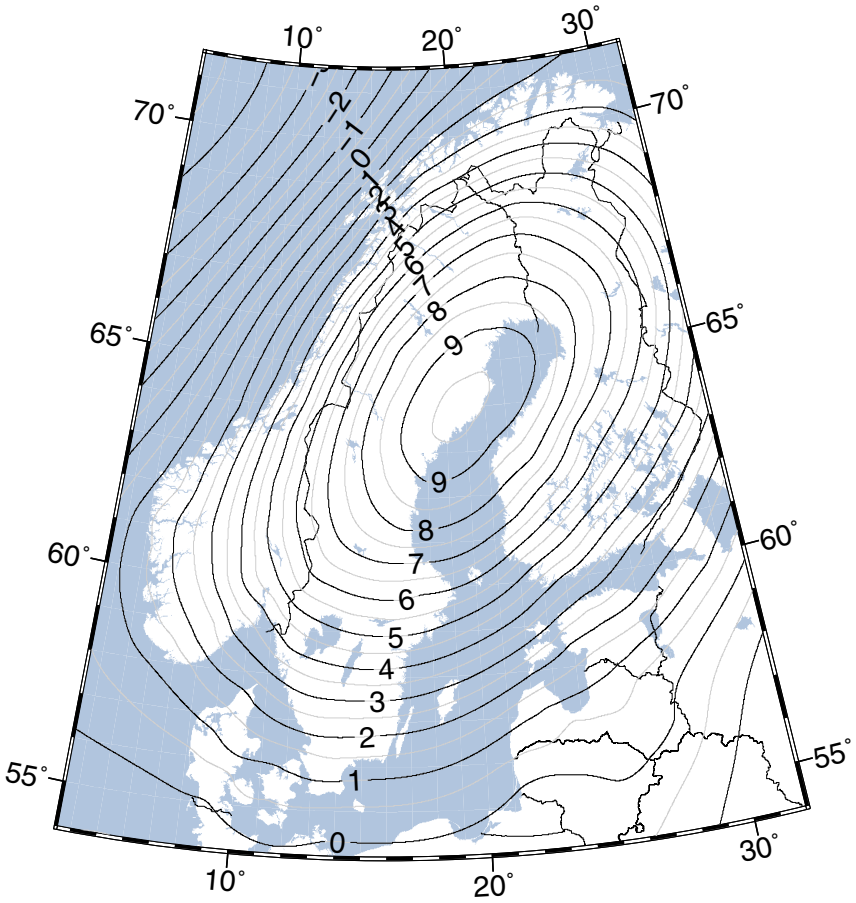

Figure 3-31. *Present-day crustal deformation over Fennoscandia (in mm a^{-1}) as observed by continuous GPS measurements. The crustal rebound displays a concentric pattern with a maximum rebound rate of ~10 mm a^{-1} located approximately in the area of the former maximum ice-sheet thickness. The present-day land uplift for the Forsmark site amounts to 6.7 ± 0.2 mm a^{-1}. Modified from Vestøl et al. 2019).*

Another, indirect, way of studying ongoing post-glacial rebound is by absolute gravity measurements (e.g. Lambert et al. 2001, Mäkinen et al. 2005), a method that may be used to estimate also the remaining uplift in areas where the process is not complete.

3.3.4 Model studies

For a comprehensive and detailed review of GIA models, see Whitehouse (2009, Chapter 4). That chapter includes descriptions of different GIA approaches used by various research groups and the relative accuracy of these methods. Recent improvements of GIA theory are described, as well as current shortcomings of the models. The various data sets used to calibrate and verify the accuracy of the modelling are also briefly discussed. A shorter description of GIA models is given here, followed by the GIA simulations performed for the safety assessment.

The majority of GIA models solve the sea-level equation that was originally developed by Farrell and Clark (1976) and describes the gravitationally-consistent redistribution of water from ice-sheets to ocean basins, and thus the evolution of the distribution of water between oceans and land-based ice-sheets. Any redistribution of surface mass alters the shape of the geoid, which in turn defines the redistribution of water in the ocean basins; therefore, an iterative procedure is required to solve the sea-level equation.

The GIA model

The GIA model used in this study was developed by Milne (1998), Milne and Mitrovica (1998), Milne et al. (1999). Three refinements to the original sea-level equation presented by Farrell and Clark (1976) have been developed by Mitrovica and Milne (2003). Firstly, time-dependent shoreline positions are taken into account when calculating the ocean-loading function. Shorelines can change position by several hundreds of kilometres in flat terrains, and this must be accounted for in applying the ocean load. Secondly, the water influx into regions vacated by retreating, marine-based ice is carefully accounted for in the distribution of the load (Milne et al. 1999). And thirdly, changes to the rotational state of the Earth because of both surface and internal mass redistributions are considered. The model used to generate predictions of relative sea-level change in this study is based on a new general theoretical foundation that includes all these advances. In this study, an Earth model with a laterally homogenous (1D) structure was used, since using a 3D model was out of scope at the time of the study. Subsequently, a comparison between the results obtained from the 1D model was made with results from a 3D model (with a laterally variable Earth structure) was made, also described below.

The sea-level equation

The sea-level equation takes account of changes to the height of the geoid and the Earth's solid surface. Local factors, such as changes to the tidal regime, the consolidation of sediments, and tectonic processes, are neglected in this study.

$$\Delta\xi_{rsl}(\tau,\varphi) = \Delta\xi_{eus}(\tau)+\Delta\xi_{isos}(\tau,\varphi)+\Delta\xi_{local}(\tau,\varphi) \qquad \text{Equation 3-9}$$

In the above expression the left-hand side refers to changes in relative sea-level at time τ and location φ. The first term on the right-hand side is the time-dependent eustatic signal, the second term varies in space and time, and relates to the isostatic effects of glacial rebound, including both ice and water load contributions, and the third term refers to local factors, as described above. To solve Equation 3-9 in a gravitationally self-consistent manner, a pseudospectral algorithm (Mitrovica and Peltier 1991, Milne and Mitrovica 1998) is employed. Green's functions are constructed to determine the GIA-induced perturbations to the geopotential and solid surfaces due to loading. The resulting temporal convolutions are evaluated by describing the GIA loading history as a series of discrete Heaviside increments. The spatial convolutions are performed by transforming the problem to the spectral domain and employing the pseudospectral algorithm (Mitrovica and Peltier 1991, Milne and Mitrovica 1998).

The method by which relative sea-level is calculated at a certain position, at a certain time, is displayed in Figure 3-32. At the start of the model run, loading is applied to an Earth model that is assumed to be in isostatic equilibrium. Once an ice load is applied at each time step the resulting deformation of the solid Earth and the perturbation to the geoid are calculated. The new shape of the geoid determines the redistribution of water in the oceans and the new extent of the oceans. However, this redistribution of water in turn affects the shape of the geoid and the deformation of the solid Earth in oceanic regions, therefore an iterative procedure is used to ensure the correct treatment of perturbations to the solid and geoid surfaces; recalculations of the perturbation to the geoid and the redistribution of water are carried out until there are no further changes, at which point loading for the next time step is applied. Loading is applied via forward time stepping.

The final output of the GIA model consists of a series of global relative sea-level predictions for all time steps used in the model. In the method used here, relative sea-level is defined to be zero at the present day, and heights are given relative to this 'zero level' for all times in the past and future. Corrections are applied using present-day topography to determine the height of any point above or below sea-level at any given time. Assuming that the underlying topography is unaltered by erosion and sedimentation the evolution of palaeotopography is calculated via the following equation:

$$T(\varphi,\tau_p) = T(\varphi,\tau_0) - \xi_{rsl}(\varphi,\tau_p) \qquad \text{Equation 3-10}$$

where T is topography, defined to be the height of the solid surface above sea-level at time τ, and ξ_{rsl} is relative sea-level at time τ. τ_p refers to a time in the past, τ_0 refers to the present day, and φ is the location on the surface of the Earth. Shoreline positions at time τ_p are determined by the zero palaeotopography contour at that time.

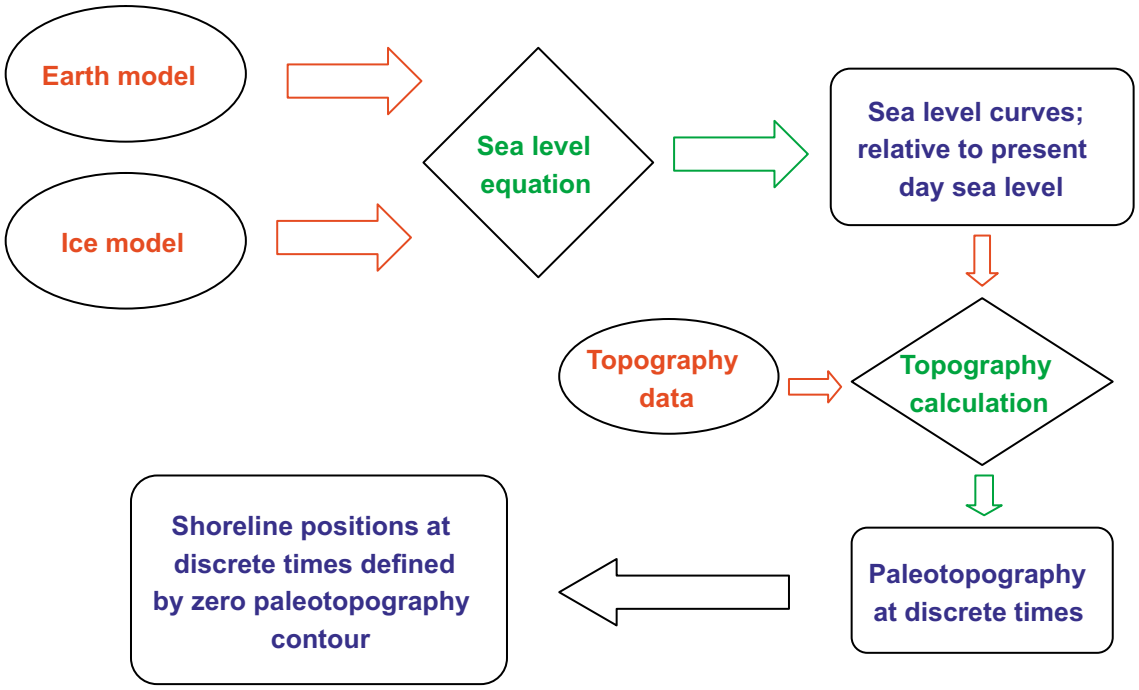

Figure 3-32. *Flow chart outlining the inputs (in red), calculations (in green) and outputs (in blue) required to calculate palaeoshoreline positions due to GIA processes.*

Ice loading

The global ice loading model used in this study is modified from the ICE3G deglaciation history (Tushingham and Peltier 1991) and has been calibrated using far-field relative sea-level data (Radtke et al. 1988, Fairbanks 1989, Bard et al. 1990, 1996, Chappell and Polach 1991, Chappell et al. 1996, Hanebuth et al. 2000, Yokoyama et al. 2000). A eustatic curve has been used to tune the mass of ice contained within far-field ice-sheets. The near-field ice loading for Fennoscandia is the one described in Section 3.1.4 and has been derived using a thermodynamic ice-sheet model employing a proxy data palaeotemperatures curve. From this model, the extent and thickness of the Fennoscandian ice-sheet at a series of discrete times from 116 ka BP to the present day has been derived and used.

Main results

In this section, only the experiments with different ice loading histories in Fennoscandia are presented, as these constitute the most important GIA modelling results for constructing the resulting relative sea-level curves used in the safety assessment (see Section 3.3.5). All other GIA modelling results from this study, e.g. sensitivity experiments with respect to Earth's rheology, isostatic memory and far-field ice-sheets, are described in detail in SKB (2010a, Section 3.3.4).

Ice loading history within Fennoscandia is the principal factor governing relative sea-level change in Fennoscandia. The loading history presented in Section 3.1.4 was perturbed to investigate the sensitivity of sea-level change to differences in ice thickness, the timing of deglaciation, the pattern of ice build-up, and the timescale over which loading is considered (Table 3-4). The extent of ice at each time step since the LGM was not perturbed because the geometry of the ice-sheets during this period is relatively well constrained by geological data. Details of the ice build-up prior to the LGM are less well constrained because geological evidence subsequently has been destroyed. However, for consistency, the ice extents for this period were also not altered. An Earth model consisting of a 96 km-thick elastic lithosphere, an upper mantle of viscosity 0.5×10^{21} Pa s, and a lower mantle of viscosity 1×10^{22} Pa s was used to investigate the response to the different loading models.

Table 3-4. Summary of ice loading models used in this study. In all cases the ICE3G global ice model is used to constrain the distribution and thickness of ice outside Fennoscandia.

Model	Description of loading model	Model run time
1	Weichselian glacial cycle as described in Section 3.1.4	116 ka
2	Two Weichselian glacial cycles run after each other to give a double glacial cycle	232 ka
3	Weichselian glacial cycle, loading only applied from 40 ka BP	40 ka
4	Weichselian glacial cycle with 90 % ice thickness in Fennoscandia	116 ka
5	Weichselian glacial cycle with 80 % ice thickness in Fennoscandia	116 ka
6	Weichselian glacial cycle with the timing of deglaciation advanced by 500 years	116 ka
7	Weichselian glacial cycle modified with ice thickness allowed to increase linearly between 60 and 20 ka BP	116 ka

In Figure 3-33a, results using the same Fennoscandian surface loading are shown, but the model run was initiated at different times. Due to the assumption that the Earth is initially in isostatic equilibrium there will be some discrepancy between relative sea-level predictions at early times in a model started at 116 ka BP and one that has already been running for 100 ka because the Earth's response is dependent upon loading history as well as the instantaneous load. Because the Earth has undergone a series of glacial cycles, a loading model that accounts for loading and unloading of the Earth during the previous cycle will give more realistic predictions for relative sea-level during the cycle of interest. However, the negligible difference between relative sea-level predictions from the single cycle, double cycle and 40 ka models (models 1, 2, and 3 in Table 3-4), for times between 25 ka BP and the present day, imply that no long-term error is introduced when a model with a later start time is used. It is important that the shortest possible time steps are used to ensure that the full loading history is captured; failure to do so will miss short timescale fluctuations in ice distribution, leading to a decrease in the accuracy of the relative sea-level predictions.

The effect of altering the thickness of ice in the loading model is illustrated in Figure 3-33b. There is little difference in the shape and magnitude of predicted relative sea-level curves for the 80 %, 90 % and 100 % loading models during the minor glaciation between ~65 and ~50 ka BP (models 5, 4 and 1 in Table 3-4), but comparing results from the 80 % and 100 % models at the LGM yields differences of ~100 m at Forsmark. The larger the range of ice thicknesses used, the greater the range of relative sea-level predictions, as illustrated by the range of curves for Forsmark.

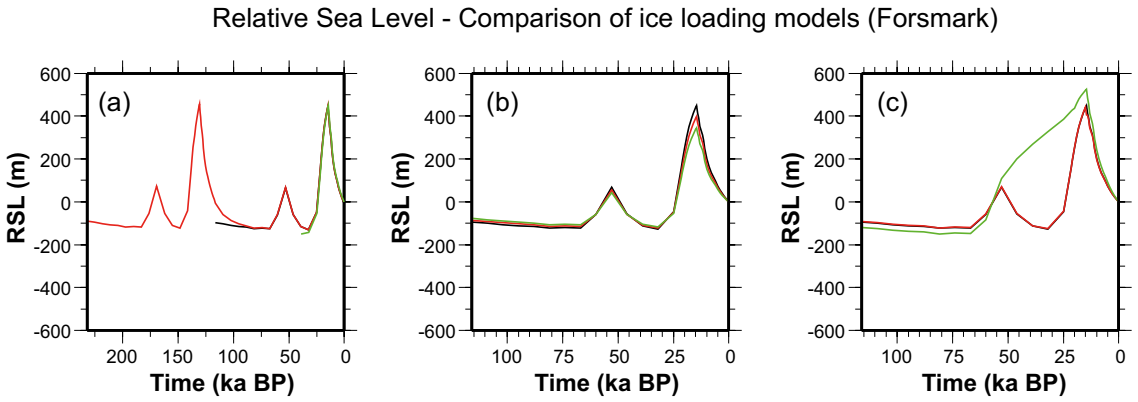

Figure 3-33. *Predicted relative sea-level (RSL) curves for Forsmark. See Table 3-4 for details of the ice-loading models. An Earth model with a thin lithosphere and low upper mantle viscosity has been used in all cases. a) black: model 1, red: model 2, green: model 3. b) black: model 1, red: model 4, green: model 5. c) black: model 1, red: model 6, green: model 7.*

The timing of maximum relative sea-level is the same for all loading models except where the timing of deglaciation is brought forwards by 500 years (model 6 in Table 3-4). In this case, maximum relative sea-level also occurs 500 years earlier. Apart from this time shift, which decays to zero by the present day, there is otherwise no difference between predictions for this model, and the Weichselian glacial cycle. The magnitude of the maximum relative sea-level is identical to that predicted by the single cycle, double cycle and 40 ka loading models (models 1, 2 and 3 in Table 3-4).

In model 7 (Table 3-4), ice thickness is allowed to increase linearly between 60 and 20 ka BP. This model has been developed to test the postulation that there was a continuous ice-sheet presence in Fennoscandia during this period (Lundqvist 1992), see also Section 4.3 and 4.5 The pattern of continuous, linear ice-sheet growth is purely an assumption of this model sensitivity test; the maximum ice thickness of the Weichselian glacial cycle is never exceeded, but the cumulative effect of loading the Earth for a longer period result in a greater amount of isostatic depression throughout Fennoscandia, and a greater relative sea-level maximum (Figure 3-33c). Therefore, the GIA signal is not only a function of the thickness and timing of ice loading at a given time, but also the evolution of the loading.

The rate of change of relative sea-level throughout the glacial cycle is similar for all the loading models except the model where the pattern of ice-sheet growth has been markedly altered prior to the LGM (model 7 in Table 3-4, Figure 3-33c). However, predictions of present-day uplift rates for the various models do highlight small differences between the models (see Figure 3-34). Uplift rates for the single cycle, double cycle, 40 ka loading model and the model where the timing of deglaciation is shifted by a small amount are virtually identical. The best fit between the predictions from the GIA model and the present-day uplift rates is obtained when reducing the Weichselian ice-sheet thickness to 80 % (cf. Figure 3-31 and Figure 3-34e). The GIA experiment with loading model 5 is therefore used as a representative for the isostatic rebound for the coming 100 ka in the *global warming climate case*. To construct the resulting relative sea-level curve at Forsmark over these timescales, a possible eustatic development is also taken into account (see Section 5.1.3). Note that one of the main assumptions in the *global warming climate case* is that glacial conditions, represented by the Weichselian glacial cycle, are shifted 50 ka into the future as a result moderate anthropogenic greenhouse gas emission (Section 5.1). Therefore, only the first, relatively modest, peak of the relative sea-level resulting from the GIA experiments (Figure 3-33) is assumed to influence Forsmark over the coming 100 ka. For this peak, the difference between the 100 % , 90 % and 80 % ice loading in predicting the relative sea-level is minor (Figure 3-33b).

The final model, where the pattern of ice-sheet growth has been altered, yields much greater present-day uplift rates, reflecting the fact that the solid Earth has to rebound from a position of greater isostatic depression at the LGM. In this final case, the area over which rebound is still taking place is greater than that predicted by the other loading models.

Comparisons between predictions from the GIA model, using the ice loading from the Weichselian glacial cycle as outlined in Section 3.1.4 (model 1 in Table 3-4), and observations of relative sea-level and present-day uplift rates in Fennoscandia show that the modelling overpredicts the GIA response (see Figure 3-35 and Figure 3-36). There may be several reasons for this; either the ice load has been too large in the ice-load history, as tested above with load models 4 and 5 reducing the Weichselian glacial cycle ice-sheet thickness to 90 % and 80 % respectively, or the misfit could be a result of assuming a laterally homogeneous (1D) Earth structure, discussed in the section *A GIA case study with a Fennoscandian 3D Earth structure* below, or a combination of the two. Unlike the geological evidence relating to the spatial extent of the Weichselian ice-sheet, very few constraints upon the ice-sheet thickness exist, and one explanation for the misfit could be that ice thicknesses in the loading model are too large. As pointed out by Denton and Hughes (1981), early ice-sheet modelling studies of steady-state ice-sheets, including their own, produced ice thicknesses that were greater than one would expect from ice-sheets during a natural glacial cycle. This has since been confirmed by GIA modelling, showing that those thick ice-sheet profiles result in a poor fit to relative sea-level observations. Subsequent dynamical approaches to ice modelling outlined in Section 3.1, including the model used in the present study, produce considerably thinner ice-sheets, for example at the LGM. These models yield a closer fit to relative sea-level observations when used as an input to GIA models, but in the present study there is still a misfit to explain. Some of this difference may be explained by the fact that there are still gaps in our knowledge of basal processes related to, for example, sliding and sediment deformation under ice-sheets. Another explanation could be that the assumption of a uniform Earth structure results in a too large GIA response, see below.

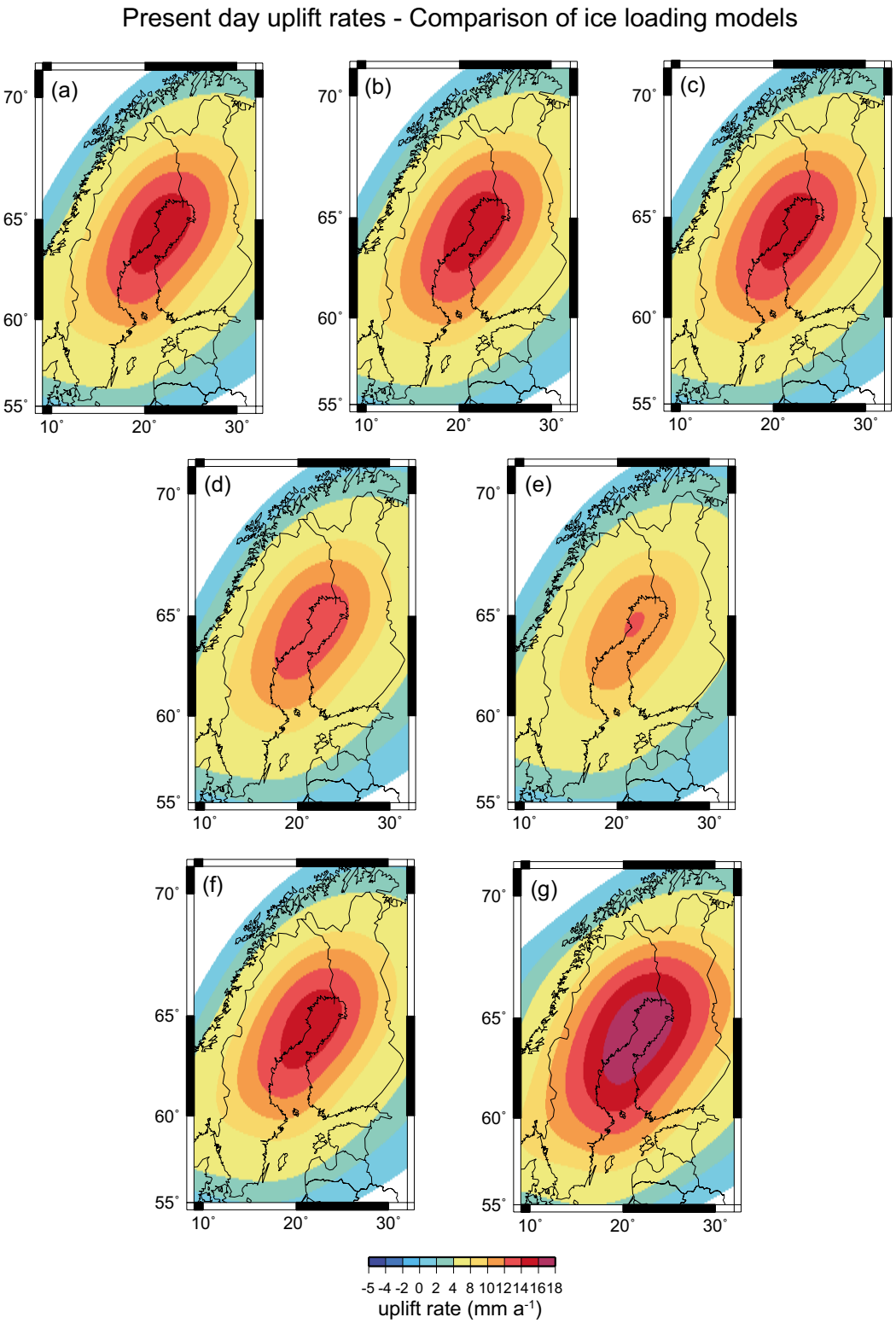

Figure 3-34. *Predicted present-day uplift rates throughout Fennoscandia for the various ice-loading models. See Table 3-4 for details of the loading models. An Earth model with a thin lithosphere and a low upper mantle viscosity has been used in all cases. a) Loading model 1. b) Loading model 2. c) Loading model 3. d) Loading model 4. e) Loading model 5. f) Loading model 6. g) Loading model 7.*

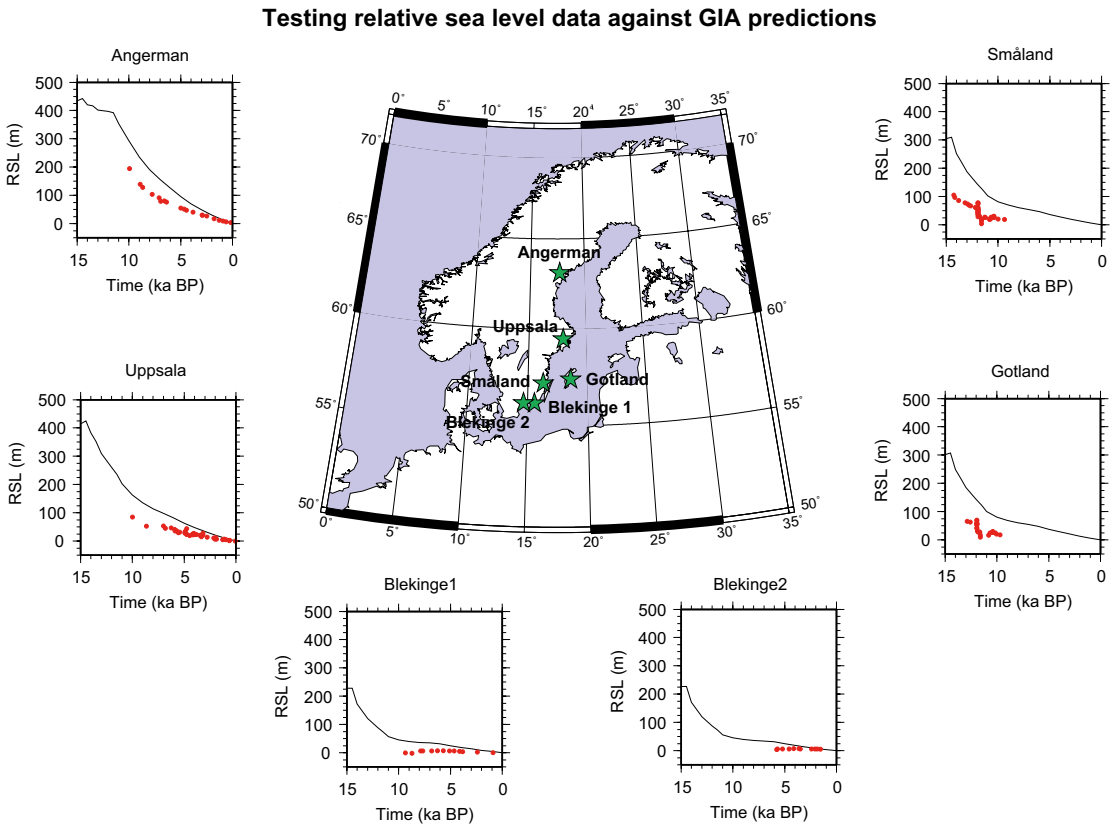

Figure 3-35. *Comparison between predicted relative sea-level (black line) and observations from relative sea-level markers (red points) at six sites in Fennoscandia (green stars) for the last 15 ka. Data compiled from Lambeck et al. (1998).*

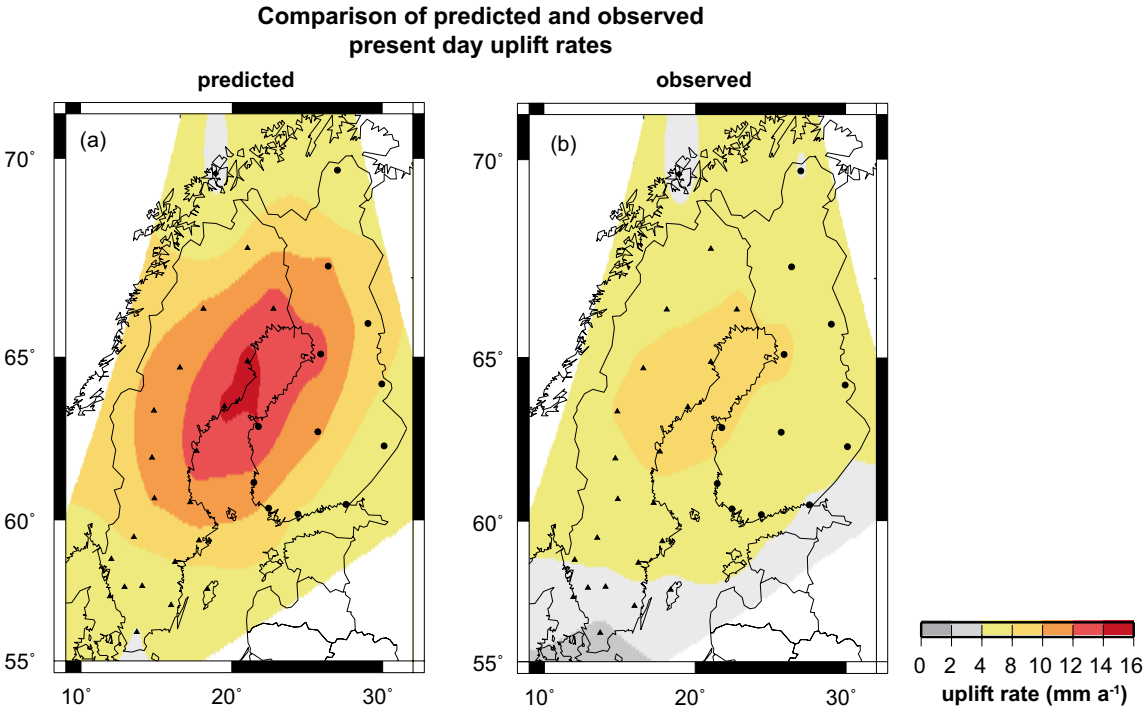

Figure 3-36. *Comparison of predicted and observed present-day uplift rates. a) Predicted present-day uplift rates interpolated at GPS sites (black dots and triangles). Data generated using the Weichselian glacial cycle loading model (model 1 in Table 3-4) and an Earth model consisting of a 96 km-thick elastic lithosphere, an upper mantle of viscosity 0.5×10^{21} Pa s, and a lower mantle of viscosity 1×10^{22} Pa s. b) Observed present-day uplift rates interpolated at GPS sites. Data from the BIFROST project (Johansson et al. 2002).*

A GIA case study with a Fennoscandian 3D Earth structure

In this 3D Earth structure case study, adapted from Whitehouse (2009), the overall aim was to investigate the sensitivity of GIA predictions to lateral Earth structure. To this end, a comparison was made between dedicated 1D and 3D GIA simulation where the Earth structure has been specifically adjusted to give a relevant comparison between the two models. In turn, this means that the Earth structures have not been selected to give a best fit of e.g. uplift rates and relative sea-level changes against observed data. Also note that the 1D–3D comparison study described here uses a different ice-sheet load history from the Weichselian glacial cycle used in the 1D simulations described in previous parts of Section 3.3.4. The 3D model was adapted from Latychev et al. (2005). In the following, a brief overview of the most important results from this case study is provided. The study is adapted from Whitehouse (2009), but is also thoroughly described in SKB (2010a, Section 3.3.4).

The main result from Whitehouse (2009) is that the 3D Earth structure likely helps to improve the present-day uplift rates in the model. This is evident when comparing the predictability between the 1D and 3D models of the relative sea-level history for most of the Holocene (the last ~ 11 ka) (Figure 3-37). Whereas the introduction of a 3D Earth structure appears to only have a limited influence on the Holocene sea-level along the Norwegian west coast (upper left panel of Figure 3-37), it significantly helps to improve the simulation of relative sea-level along the Swedish east coast (represented by Ångermanälven) with respect to observations (upper right panel of Figure 3-37). The improvement obtained with the 3D model is explained by a reduction of the predicted uplift rates in most areas covered by the Fennoscandian ice-sheet (bottom panel of Figure 3-37).

The difference in relative sea-level predictions for the 1D and 3D models is also plotted for Oskarshamn and Forsmark in Figure 3-38. To exemplify the magnitude of the error introduced by using a 1D Earth model instead of a 3D Earth model to predict relative sea-level, as was done in the GIA studies, the difference at 10 ka BP is ~ 60 m at Forsmark (Figure 3-38).The difference between 1D and 3D GIA simulations presented in this case study means that ignoring lateral Earth structure and using a 1D Earth model in Fennoscandia leads to an overestimation of present-day uplift rates during deglaciation. This, in turn, conclusively shows that a significant part of the misfit between the 1D GIA model results and GPS observations (Figure 3-36) arises from the 1D Earth structure.

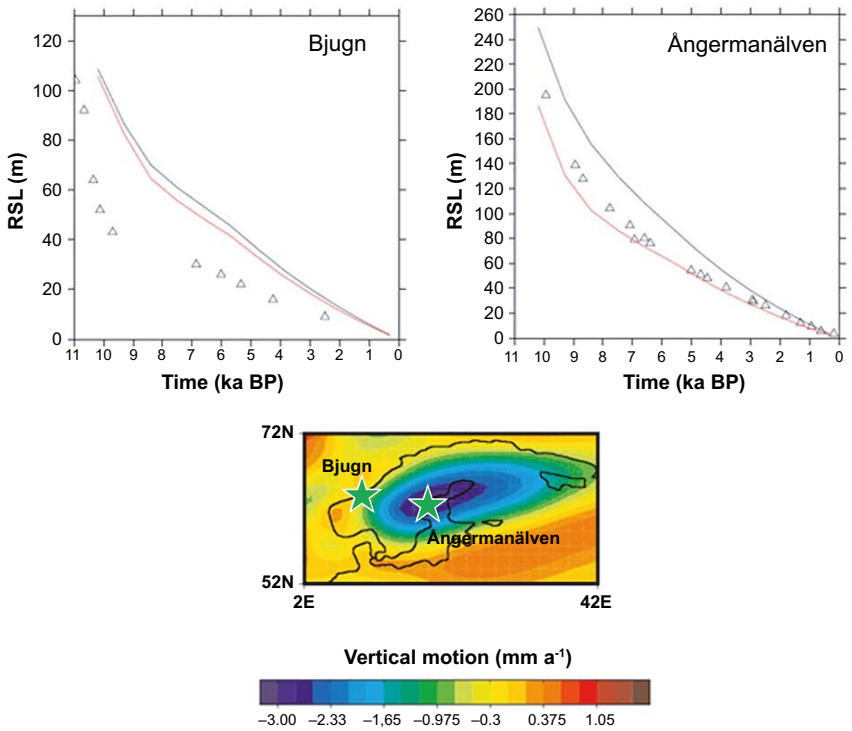

Figure 3-37. *Predicted relative sea-level (RSL) history at Bjugn (top left) and Ångermanälven (top right) for the last 10 ka. Black line: 1D model. Red line: 3D model. Relative sea-level proxy data are shown as triangles; see Lambeck et al. (1998) for references. Bottom plot: Location map for Bjugn and Ångermanälven overlaid upon the difference in predicted present-day uplift rates between the 3D and 1D models.*

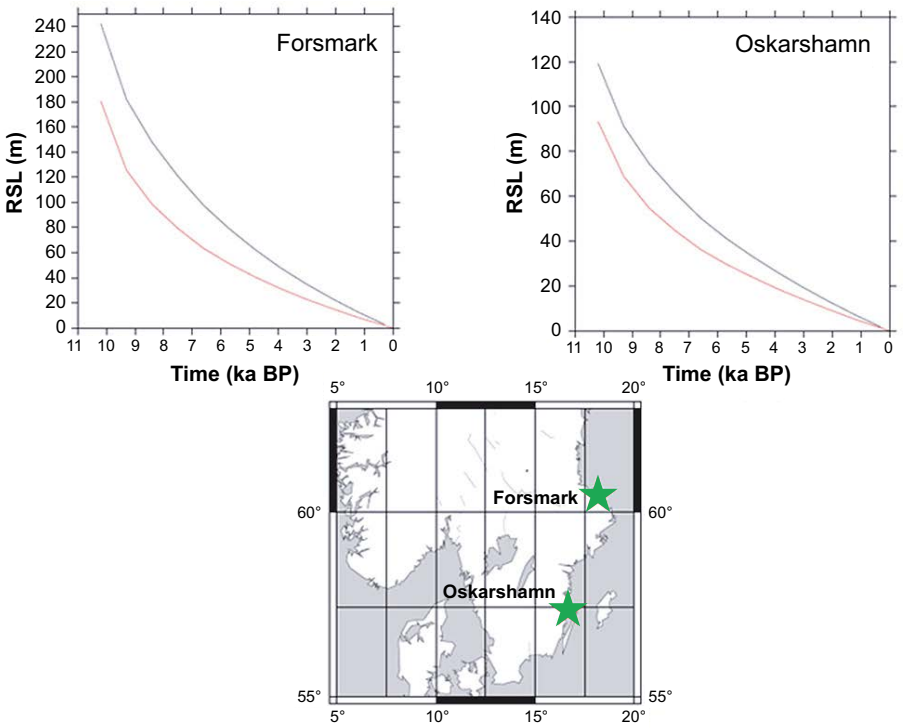

Figure 3-38. *Predicted relative sea-level (RSL) curves for Forsmark and Oskarshamn calculated using 1D (black line) and 3D (red line) Earth models. Note that both the 1D and 3D GIA simulations used for this plot use a different ice-load history from that used in the 1D GIA simulations in the previous parts of Section 3.3.4. The results should only be used to exemplify the error introduced by using 1D instead of 3D GIA modelling. At Forsmark, the difference at 10 ka BP is ~60 m.*

3.3.5 Time perspective

Shoreline migration is an ongoing process. It is strongly coupled to the global distribution of water between the oceans and land-based ice-sheets, and the isostatic response of the Earth to loading during a glacial cycle. This isostatic deformation is a slow process in relation to the rate at which ice-sheets grow and decay during such a cycle.

As ice-sheets grow, water is removed from the oceans and global eustatic sea-level falls. During the build-up to the last glaciation, eustatic sea-level fell at a mean rate of ~1.3 mm a^{-1} between 120 and 20 ka BP (Fleming et al. 1998, Yokoyama et al. 2000, Clark and Mix 2002, Milne et al. 2002, Peltier 2002, Mitrovica 2003), although there were many departures from this rate during the build-up period, due to higher frequency climatic oscillations (Imbrie et al. 1984, Lambeck et al. 2002, Waelbroeck et al. 2002, Siddall et al. 2003). During deglaciation, the initial rate of eustatic sea-level rise between ~21 and 17 ka BP was only ~6 mm a^{-1}, followed by an average rate of ~10 mm a^{-1} for the next 10 ka (Fleming et al. 1998). Perturbations from this rate occurred during meltwater pulses at ~14.5 and ~11 ka BP. These are attributed to rapid melting events, during which rates of eustatic sea-level rise reached ~15 mm a^{-1} (Fairbanks 1989, Bard et al. 1990, 1996, Clark et al. 1996, Fleming et al. 1998, Lambeck and Chappell 2001, Lambeck et al. 2002, Peltier 2005, Bassett et al. 2005). Rates of eustatic sea-level change fell to negligible values following the end of deglaciation around 5 ka BP. However, meltwater is not distributed uniformly throughout the oceans due to the alteration to the shape of the geoid following the redistribution of surface masses. Sea-level can fall at sites within ~20° of a melting ice-sheet (Farrell and Clark 1976), therefore the rate of eustatic sea-level change is a poor indicator of local rates of sea-level change, especially for a local melt source.

The local rate of relative sea-level change incorporates both local changes in sea-level and the isostatic deformation of the solid Earth. The balance between rates of isostatic deformation and local sea-level change determine whether a site has advancing or retreating shorelines.

During the final build-up of the Fennoscandian ice-sheet from ~32 ka BP, isostatic rates of solid Earth subsidence due to surface loading by ice are estimated to have reached values of 40 mm a^{-1} (see Section 3.3.4). During future glacial cycles, modelling predictions imply that maximum rates will be attained immediately prior to the time of greatest ice thickness. In general, the time of maximum ice thickness is predicted to precede the time of maximum solid Earth deformation, with the latter being delayed by up to ~3 ka. During the period between maximum ice thickness and maximum deformation, the rate of solid Earth subsidence will decrease to zero.

There is usually a delay between the time of maximum deformation and the time at which a location becomes ice-free. Again, modelling predictions imply that as an ice-sheet thins, rates of isostatic rebound will be low; < 20 mm a^{-1} for this reconstruction of the Weichselian. Maximum rebound rates occur immediately following the final removal of an ice-sheet, with uplift rates reaching ~75 mm a^{-1} in this model at sites which had the greatest ice cover. The rate of rebound then decays exponentially with time; maximum rates at the centre of present-day uplift in Fennoscandia are ~10 mm a^{-1}, and these are expected to decay to negligible values within the next 30 ka (see Section 3.3.4).

During a glacial cycle, immediately following the removal of ice, local uplift rates are far greater than the rate of local sea-level changes, consequently a situation of regression dominates, and shorelines migrate oceanwards. The rate of shoreline migration depends upon the local gradient of topography. A typical Swedish Baltic Sea shoreline with a gradient of 2 m of elevation per 1 km would experience 35 m a^{-1} of oceanward shoreline migration for an uplift rate of 70 mm a^{-1}, or 5 m a^{-1} of oceanward shoreline migration for an uplift rate of 10 mm a^{-1} (the present maximum in the Baltic region), assuming negligible changes in local sea-level.

A combination of decreasing rates of isostatic rebound and sea-level rise due to far-field melting slows the rate of regression with time, with a switch to transgression taking place if rates of local sea-level rise exceed the rate of local isostatic rebound. This situation is likely to arise during a global meltwater pulse at sites with low rebound rates, but will not be maintained, because melting takes place on a shorter timescale than isostatic rebound. Rebound will once again become the dominant factor governing shoreline migration as sea-level changes become negligible. During the current interglacial period decaying uplift rates will persist into the future. These, along with processes related to ocean syphoning (see Section 3.3.1), act to maintain a situation of gradual oceanward shoreline migration throughout the majority of the Baltic region for the first few 10 ka of an interglacial so long as the higher interglacial temperatures do not give rise to a longer-term melting event, such as the destabilization, and subsequent melting, of the Greenland Ice-sheet.

3.3.6 Handling in the PSAR

Isostatic evolution and shoreline displacement have been investigated by means of numerical modelling. In this context, the main question for the safety assessment is whether the Forsmark site is submerged or not. The salinity in the lake/sea covering the site is also of interest. A 1D GIA model (Mitrovica and Milne 2003) has been used to simulate the shoreline migration, using a loading function based on the Weichselian ice-sheet simulation described in Section 3.1.4. The *global* ice-loading function used in the study is modified from the ICE3G deglaciation history (Tushingham and Peltier 1991) and has been calibrated using far-field relative sea-level data. A eustatic curve has been used to tune the mass of ice contained within far-field ice-sheets. The Earth model is based on Maxwell rheology with a 1D radial three-layer structure. The lithosphere is represented by a 96 km thick layer with a very high viscosity and thus behaves as an elastic medium over GIA timescales, the density and elastic structure are from the preliminary reference Earth model (PREM) which has been determined to a high degree of accuracy by seismic methods (Dziewonski and Anderson 1981).

At the start of a GIA model run, the Earth is assumed to be in isostatic equilibrium. In reality, the Earth is unlikely to reach such a state if glaciations occur with similar periodicity as in the past. To correct for this, the GIA modelling has been initiated by a glacial loading history yielding shorelines comparable to those reported by Funder et al. (2002) at the peak of marine inundation in the Early Eemian about 130 ka BP.

Ultimately, two GIA experiments are used in the safety assessment. The latter of the two consecutive Weichselian glacial cycles (Model 2 in Table 3-4) is used in the *reference glacial cycle climate case* (Section 4.5), and the Weichselian glacial cycle with 80 % ice thickness in Fennoscandia is used in

the *global warming climate case* (Section 5.1). The GIA curve for the *global warming climate case* has been further modified by assuming no ice loading for the first 50 ka and a complete melting of the Greenland ice-sheet.

For the analysis of the biosphere and hydrological evolution, the shoreline displacement during the first thousands of years after present is extrapolated from empirical shoreline data in the *reference glacial cycle climate case* (Påsse and Daniels 2015), see Sections 4.5.2 and 5.1.3.

3.3.7 Handling of uncertainties in the PSAR

Uncertainties in mechanistic understanding

The processes involved in GIA, and their effect upon shoreline migration, are very well understood. There are no major uncertainties in our understanding of the mechanistic processes that cause shoreline migration.

Model simplification uncertainty

- Discussions of the uncertainty in the calculated shoreline are based on the sensitivity analysis and case study presented above. The assumption of a 1D Earth model is a simplification of the situation in Fennoscandia. A comparison between 1D and 3D GIA simulations Whitehouse (2009) shows that the assumption of a laterally homogeneous (1D) Earth structure over Fennoscandia probably results in an over-prediction of the isostatic response to ice-sheet load and present-day uplift rates. As an example, the 1D–3D GIA model comparison shows that the 1D simulation potentially over-estimates the relative sea-level change over the last 10 ka by up to 60 m at Forsmark.
- The time discretisation of the basic loading model is fairly coarse (every 7 ka) between 116 and 21 ka BP, reflecting the lack of constraints upon ice history and sea-level prior to the LGM. If long time steps are used the loading function may be under- or over-estimated, leading to inaccuracies in relative sea-level, and hence shoreline migration, predictions for this period. A higher time resolution has been investigated, and discrepancies in relative sea-level predictions may be up to 50 m between a model that uses a time step of 7 ka and one that uses a time step of 1 ka, during periods of rapid change in ice-sheet geometry. However, using a coarse timescale during the early stages of a model run has a negligible effect upon predictions of relative sea-level change during the latter stages of a model run. A high-resolution timescale has been used for ice loading since the LGM, i.e. for the period when ice history is known reasonably accurately.
- At the beginning of a model run, the Earth is assumed to be in a state of isostatic equilibrium, with no deformation remaining from a previous glacial cycle or any other process that upsets the isostatic balance of the system. In reality, when the Earth enters each glacial cycle it will be pre-stressed, with deformation ongoing as a result of the previous loading event. GIA-induced deformation decays over a few tens of thousands of years, and after this period there will be a negligible difference between predictions from a model that started from equilibrium and one that was pre-stressed. However, to reproduce the relative sea-level evolution for the Weichselian as closely as possible the model was run twice in succession, with the second run taken to represent the Weichselian development. Nevertheless, a degree of inaccuracy remains at early times in the model since deformation will depend upon the details of the previous Saalian deglaciation, about which very little is known.

Input data and data uncertainty

Uncertainties in the lithospheric thickness and mantle viscosity parameters are currently significant. However, in SR-Site (SKB 2010a) a great similarity of the shoreline prediction for a range of rheological parameters was demonstrated. The values of such parameters will be more tightly constrained following detailed analysis of the results of the GIA modelling in comparison with relative sea-level and GPS data.

Another source of uncertainty is associated with the ice load. Sensitivity tests using the 1D GIA model revealed that a reduction in ice thickness to 80 % of the value in the *reference glacial cycle* yielded GIA results on present uplift rates that were in accordance with the observed present-day uplift. It is important to note, as discussed above, that this result is only valid for the 1D GIA model as the 3D model results in a better agreement with present-day uplift rates using full (100 %) ice thickness (Figure 3-37 and Figure 3-38).

3.4 Permafrost

3.4.1 Overview/general description

Permafrost is defined as ground that remains at or below 0 °C isotherm for at least two consecutive years (French 2007). This definition is based exclusively on temperature, and disregards the texture, degree of compactation, water content, and lithologic character of the material. As a result, the term *permafrost* does not always equate to *perennially frozen ground*, since, depending on pressure and composition of groundwater and on adsorptive and capillary properties of ground matter, water in the ground may freeze at temperatures below 0 °C. Therefore, permafrost encompasses the perennially frozen ground and a surrounding so-called *cryopeg*, i.e. a ground layer in which water remains unfrozen at sub-zero temperatures.

Permafrost and perennially frozen ground originate from the ground surface depending on a complex heat exchange process across the atmosphere/ground boundary layers and on an almost time-invariant geothermal heat flow from the Earth's interior. The heat exchange between the atmosphere and the Earth's surface is governed by solar radiation, longwave terrestrial and atmospheric radiations, sensible and terrestrial heat fluxes, and evaporation and condensation (Lockwood 1979, Washburn 1979, Lunardini 1981, Williams and Smith 1989, Smith and Riseborough 1996, Yershov 1998).

Freezing of water within permafrost is based on the thermodynamics of interdependent thermal, hydraulic, mechanical, and chemical processes in the ground. In addition, freezing of water influences the thermal, hydraulic, mechanical, and chemical behaviour of the ground. Thermal properties change from those of unfrozen ground to those of frozen ground, affecting the heat transfer process. Ice formation in pores of the ground confines groundwater flow through the presence of almost impermeable frozen ground, therefore altering the overall groundwater circulation. Ice formation can also cause deformation of the ground and changes in the mechanical stress state. Frost weathering and degradation of the ground surface and patterned ground are additional consequences of cyclic freezing and thawing processes. Moreover, exclusion of salts in the freezing of saline groundwater can lead to increased salinity concentrations in the unfrozen cryopeg.

Issues associated with permafrost development in the geosphere are comprehensively explained in Washburn (1979), Williams and Smith (1989), Yershov (1998), French (2007) and reviewed in e.g. Gascoyne (2000), Ahonen (2001) and Vidstrand (2003). Experimental investigations of thermal-, hydrochemical- and mechanical impacts of freezing on bedrock properties have been reported by e.g. Mackay (1997), Ruskeeniemi et al. (2002, 2004), whereas model studies dealing with permafrost development in ground under climate change can be found in e.g. Lunardini (1995), Kukkonen and Šafanda (2001). Some model studies on thermo-hydro-mechanical impacts of freezing processes on bedrock properties with implications for interactions between glaciers and permafrost in a time frame of a glaciation cycle (~100 ka) have been conducted, e.g. Bauder et al. (2003), Hartikainen (2004), SKB (2006a), Person et al. (2007) and Lemieux et al. (2008a, b, c). The effects of freezing of the geosphere on groundwater flow have been studied by e.g. Vidstrand et al. (2010).

3.4.2 Controlling conditions and factors

Climate and surface conditions

The principal factors controlling the heat exchange between the atmosphere and the Earth's surface are climate, topography, vegetation and snow cover, soil characteristics and water bodies. These factors are mutually dependent and can vary considerably in time and location. The main climatic parameters are insolation, air temperature, wind, and precipitation. Insolation is a driving force governing the heat exchange between the atmosphere and the Earth's surface and affecting the other climatic parameters. Air temperature, which is commonly applied to map permafrost distribution, controls the longwave atmospheric radiation, turbulent heat exchange, and evaporation and condensation. Wind, in turn, mainly influences the sensible heat exchange, but also latent heat production and loss. Precipitation together with evaporation and condensation determine groundwater recharge, affecting the groundwater content and flow and hence the terrestrial heat flux.

Topography has a significant impact on climate conditions. Generally, air temperature decreases as altitude increases being affected by radiation, convection and condensation. The average air temperature decrease is approximately 0.65 °C for every 100 metres increase in height (Danielson et al. 2003). In addition, inversions are common in hilly terrain causing low-slope low-lying areas to experience

significantly lower temperatures than higher lying and steeper-slope areas. Furthermore, the slope angle and azimuth affect the flux of shortwave radiation, and where topographical differences are large a patchier distribution of permafrost is expected.

Vegetation and snow cover are sensitive to climatic conditions and topography. The characteristic parameters of the surface cover are surface albedo, emissivity, and roughness controlling the incoming shortwave radiation, the longwave terrestrial radiation and turbulent heat exchange, respectively, as well as the thermal properties and the thickness of the surface cover affecting terrestrial heat transfer. In general, the vegetation and snow cover moderate the ground temperature and thus the aggradation of permafrost. Vegetation is an insulating cover limiting cooling in winter and warming in summer, hence reducing the annual fluctuation of ground temperature. Vegetation is also important for the creation of snow cover, which protects the ground from heat loss in winter. However, the high albedo of snow can lead to a snow surface temperature almost 2 °C lower than the mean winter air temperature (Yershov 1998). As a rule, for most surface covers, permafrost can build downward from the ground surface if the annual mean air temperature is lower than a value ranging between −9 and −1 °C (Washburn 1979, Williams and Smith 1989, Yershov 1998, French 2007). An exception occurs with peat layers, which can insulate the ground from warming in summer more effectively than from cooling in winter, with the resulting effect that permafrost can exist where the mean annual air temperature is above 0 °C (Williams and Smith 1989).

Properties and thickness of the soil cover affect the terrestrial heat flow. Of importance are the porosity and water content of the soil, influencing the annual fluctuation of ground temperature and the thickness of the active layer, i.e. the seasonally thawing ground layer. The soil cover also acts as an insulating cover, since the thermal conductivity of the soil cover is lower than that of the underlying bedrock.

Water bodies, i.e. sea, lakes, and watercourses, influence permafrost creation and distribution considerably since they have high specific heat content. A talik, i.e. an unfrozen layer, can exist beneath water bodies that do not freeze to their bottom in winter. Depending on the characteristics of the climatic zone, the critical depth of a water body to remain unfrozen in winter is approximately 0.2 to 1.6 metres (Yershov 1998).

Sea water extensively reduces the development of costal permafrost. On the other hand, when the relative sea-level of a highly saline sea is rising, submerged permafrost and perennially frozen deposits can survive for a long time beneath a cold seabed (Washburn 1979, Yershov 1998).

The hydrological conditions on the ground surface affect the freezing of groundwater. Especially under glaciated conditions, a warm-based overlying ice-sheet increases the subglacial groundwater pressure, in which case the freezing point may decrease to such a degree that the subglacial ground is kept unfrozen. A similar, but minor, effect may occur when cold ground becomes submerged and submarine freezing is reduced by the pressure of the sea water. Furthermore, groundwater flow, whether carrying fresh glacial meltwater or saline seawater, can influence the freezing process by altering the chemical groundwater composition.

Table 3-5 summarises how geosphere variables are influenced by permafrost development.

Subsurface and repository

The ground temperature that defines the presence of permafrost and primarily governs the freezing of water in ground is principally controlled by the ground thermal energy balance in terms of heat transfer, geothermal heat production, the specific heat content and the amount heat generated by phase change processes of water. Heat transfer within the ground can occur through conduction, convection and radiation (Sundberg 1988). In general, only conduction is regarded as important to permafrost evolution, since radiation is of importance only in unsaturated high-porosity ground at high temperatures, and convection is of importance only when groundwater and gas fluxes are large.

Heat conduction depends on the ground temperature gradient, ambient temperature conditions, and the thermal properties of the ground matter. Thermal conductivity, describing the ability of material to transport thermal energy, and heat capacity characterising the capability of material to store heat, depend on several variables such as mineralogy, porosity and groundwater content. Having typically three to four times higher conductivity than other common rock-forming minerals, quartz is the most important mineral for determining thermal characteristics in native rock materials.

Table 3-5. Influence of permafrost development on geosphere variables.

Geosphere variable	Climate issue variable	Summary of influence
Temperature	Permafrost depth	Permafrost is by definition a thermal condition hence having no influence on temperature.
Groundwater flow	Frozen/unfrozen fraction of groundwater	Freezing occurs at temperatures below the freezing point, see the **Geosphere process report**. Groundwater transformed from liquid to solid phase can be regarded as immobile. Filling fractures and pores, ice also affects the groundwater flow through permeability, which decreases with a reduction in the unfrozen fraction of groundwater.
Groundwater pressure	Frozen/unfrozen fraction of groundwater	The volume increase in the phase change of water from liquid to solid state causes an increase in the pressure of water which remains liquid. Moreover, freezing of water in porous ground matter can lead to cryosuction and depression of groundwater pressure in the unfrozen ground.
Groundwater composition	Frozen/unfrozen fraction of groundwater	When saline water is transformed from the liquid to solid phase, the solutes are typically not incorporated in the crystal lattice of ice but transferred to the liquid phase. Therefore, the salinity in the unfrozen fraction increases.
Rock stresses	Frozen fraction of groundwater	Deformations due to ice formation will lead to changes in rock stresses. The effect of the changes is strongest nearest to the surface where in situ stresses are lowest.
Fracture geometry	Frozen fraction of groundwater	Freezing can have some influence on the fracture geometry at shallow depths due to frost cracking. Close to the ground surface frost wedges can form to the depth of some metres. Also, there can be widening of fractures due to freezing but the effect may be reversible as thawing takes place.

When the porosity is less than 1 %, freezing of water has a minor effect on heat transfer in water-saturated ground. The degree of saturation has relevance to the thermal properties of ground due to the very low thermal conductivity and heat capacity of air, e.g. the thermal conductivity of 1 %-porosity granite can decrease by over 10 % with decreasing saturation (Clauser and Huenges 1995). In rock, heat capacity is not very dependent on ambient temperature and pressure conditions, whereas thermal conductivity is a rather variable function of both temperature and pressure. The thermal conductivity of granite decreases with increasing temperature by approximately 5 to 20 % per 100 °C and increases with increasing pressure by about 1 to 2.5 % per 100 MPa (Seipold 1995). The pressure dependence of thermal conductivity is increased when rocks are unsaturated (Sundberg 1988, Clauser and Huenges 1995). Moreover, Allen et al. (1988) reported a strong correlation between lithology and permafrost depth, which could be directly explained by differences in thermal conductivity.

In addition to the thermal properties above, the hydrogeochemical and mechanical properties of the ground important for freezing of groundwater are permeability, porosity, adsorptive capacity of ground matter, chemical composition of groundwater and deformation properties of the ground.

Also, in the context of assessing the post-closure safety of repositories for spent nuclear fuel, the spent nuclear fuel will generate heat with an exponentially decreasing rate for a considerable amount of time. This heat will warm up the surrounding bedrock (see the **Geosphere process report**) and may thus act to reduce the thickness of permafrost above and near the repository (Section 3.4.4).

3.4.3 Natural analogues/observations in nature

At present, approximately 25 % of the total continental land area of the Earth is occupied by permafrost. Permafrost distribution may be characterised into: i) continuous (more than 90 % spatial coverage), ii) discontinuous (between 90 and 50 % coverage), iii) sporadic (less than 50 % coverage), and iv) subglacial forms. About one fifth of this permafrost is estimated to be subglacial in Antarctica and Greenland. Permafrost is abundant in Alaska, the northern parts of Canada and Russia, and in parts of China (French 2007). Along the coast of southern and south–western Greenland both continuous and discontinuous permafrost can be found (Mai and Thomsen 1993). The Northern Hemisphere distribution of permafrost is illustrated in Figure 3-39.

The deepest known permafrost occurs in the central part of Siberia in Russia, where thicknesses of up to 1500 m have been reported (Fotiev 1997). The extensive region of continuous permafrost in central Siberia corresponds to areas that are believed not to have been covered by Quaternary ice-sheets and that experienced cold subaerial climate conditions during the last glacial cycle and earlier. In coastal areas, submarine permafrost may also exist, such as in northern Siberia where the permafrost formed during ice-free periods of the last glacial cycle in regions subsequently covered by the Arctic Ocean. Furthermore, permafrost is frequently observed in mountainous terrain. For example, in the area of Tarfala in the Kebnekaise massif in northern Sweden, discontinuous permafrost has been reported to be 100 to 350 m thick at an altitude above 1500 m a.s.l. (King 1984, Isaksen et al. 2001).

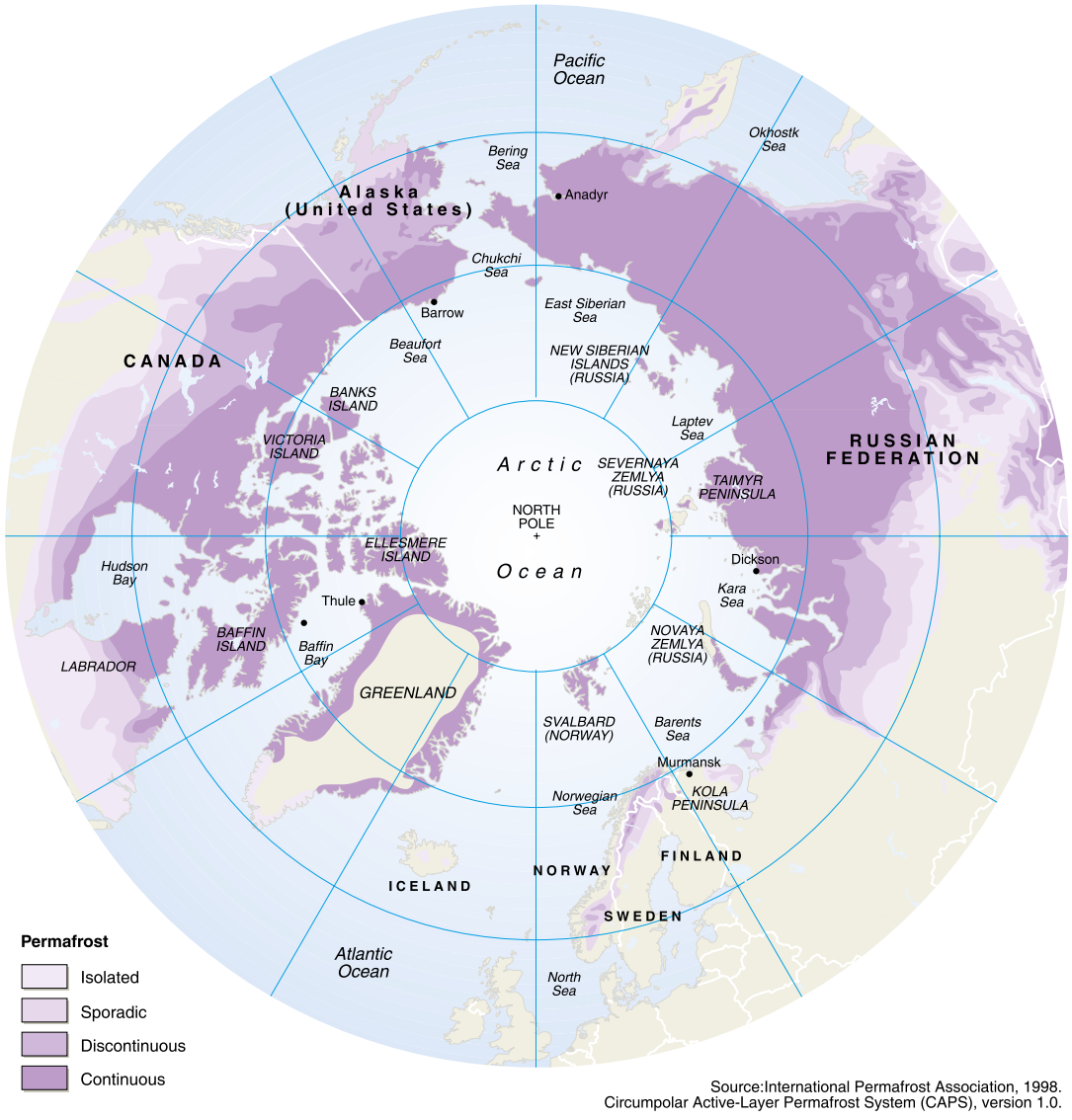

Figure 3-39. *Permafrost distribution in the Northern Hemisphere. From UNEP/GRID-Arendal (2005).*

SKB, together with co-funding parties from Finland (Geological Survey of Finland and Posiva), Great Britain (UK Nirex Ltd) and Canada (Ontario Power Generation and University of Waterloo), carried out a research project on permafrost at the Lupin gold mine in northern Canada (Ruskeeniemi et al. 2002, 2004). In this area, the depth of the permafrost extends to ~500−600 m. The main objective of the project was to provide data describing the subsurface conditions in a permafrost area with crystalline bedrock. Permafrost depth, temperatures, groundwater composition and hydraulic properties were measured. The mean annual air temperature at this site is −11 °C and the annual mean precipitation is low; ~270 mm (Ruskeeniemi et al. 2002). Based on a seismic refraction survey, the depth of the active layer has been interpreted to be ~1.5 m, varying between 1.2 and 1.8 m. The present permafrost depth is believed to have been developed over the last 5000 years. In the Lupin area, all shallow lakes freeze down to the bottom during winter. Lakes deeper than 2–3 m are expected to have unfrozen bottoms all year. The latter lakes may have the potential to support closed taliks. The large Lake Contwoyto, located about 1300 m from the mine at surface, provides the most significant talik structure that may extend through the deep permafrost. However, direct observations beneath this lake are lacking.

To investigate the distribution of permafrost and locate salinity differences in the deep groundwaters, a number of electromagnetic soundings were conducted in the Lupin mine area. Furthermore, drillings were made from the deeper parts of the mine through the base of the permafrost to sample groundwaters and to study the distribution of open fractures and hydraulic conditions. The main result of the electromagnetic sounding surveys was the identification of anomalies forming a sub-horizontal layer at depths between 400 and 700 m. (Paananen and Ruskeeniemi 2003) made the interpretation that this conducting layer represents saline or brackish water at the base of the permafrost. According to the temperature measurements made in the mine, the base of the permafrost occurs at a depth of 540 m. The drillings revealed the existence of a ~100 m thick unsaturated or dewatered zone below the permafrost. An alternative interpretation of the sub-horizontal conductor at ~650 m depth could be that it represents the groundwater table (Ruskeeniemi et al. 2004). The dry zone below the permafrost could either be a natural result of very limited recharge through the permafrost or an effect of mine drainage. No pressurised water or gas flow was observed in the boreholes. The available data from water sampling do not provide any evidence of highly saline water below the permafrost (Ruskeeniemi et al. 2004).

3.4.4 Model studies

Two climate cases have been studied by permafrost modelling; i) the *Reconstructed last glacial cycle* and ii) the *severe permafrost climate case*, see Figure 1-3. In addition, a broad range of sensitivity tests have been made, covering the range of uncertainties associated with various parameters of importance for permafrost development. The simulations of the *Reconstructed last glacial cycle* are described in this section, whereas the simulations of the *severe permafrost climate case* are described in Section 5.5.

The simulations of permafrost for the reconstruction of the last glacial cycle have been done with two types of models, a 1D permafrost model and a 2D permafrost model improved from the 1D model. The 1D modelling was performed for the SR-Can safety assessment SKB (2006a, Section 3.4), but some of the results are used also for the PSAR. The 1D simulations were conducted specifically for the repository location. The 2D modelling (Hartikainen et al. 2010, Hartikainen 2018) was conducted for SR-Site and the PSAR and covers a 15 km long and 10 km deep vertical cross-section crossing most of the Forsmark site. Both simulations use site-specific input data from the Forsmark site investigation programme. Details on the input data used for the 1D permafrost simulations are found in Section 3.4 in SKB (2006a), and for the 2D simulations in Hartikainen et al. (2010) and Hartikainen (2018).

The purpose of the modelling studies was to analyse the main factors of importance for the development of permafrost and perennially frozen ground at Forsmark. The permafrost models include mathematical expressions for freezing and thawing of saline groundwater-saturated bedrock. The bedrock is considered as an elastic porous medium and the groundwater as an ideal solution of water and ionic solvents. The models are based on the principles of continuum mechanics, macroscopic thermodynamics and the theory of mixtures being capable of describing heat transfer, freezing of saline water, groundwater flow and deformations of bedrock. In the 2D version of the model, the freeze-out and transport of solutes is included (Hartikainen et al. 2010). The models are described further in Hartikainen (2004), SKB (2006a), Hartikainen et al. (2010).

To capture the most important factors and parameters affecting the development of permafrost, sensitivity analyses were performed considering the following issues:

- Surface conditions.
- Subsurface conditions.
- Presence of the repository.

Surface temperatures, together with the influence of surface covers such as snow, vegetation and water bodies, were included as factors of importance in the surface conditions. The investigated bedrock conditions were variations in thermal properties of the bedrock and the geothermal heat flow. The sensitivity simulations carried out with the 2D permafrost model (Hartikainen et al. 2010) are presented in this report. Similar sensitivity experiments were carried out also with the 1D model (SKB 2006a, Section 3.4). However, since the sensitivity experiments conducted with the 2D model (Hartikainen et al. 2010) cover a broader range of cases than the sensitivity cases studied with the 1D model (SKB 2006a), only some selected sensitivity tests from the 1D experiments are described in the present report. The heat generated by the spent fuel has been included in most simulations and is also analysed in a dedicated 2D sensitivity simulation. In this context, it should be noted that the repository depth was changed between SR-Can (for which the 1D simulations were made) where it was 400 m and SR-Site and the PSAR (for which the 2D simulations were made) where it is 450 m. Despite this, the resulting permafrost and freezing depths are very similar between the two studies, as demonstrated below.

In the following, the 1D permafrost simulations for the location of the repository are described first, followed by the 2D simulations across the Forsmark site.

1D reconstruction of last glacial cycle permafrost conditions at the repository location

The 1D modelling experiments described below, conducted for the repository location, are from SKB (2006a, Section 3.4).

The 1D calculations were carried out in two steps; i) by using constant surface temperatures, and ii) using surface temperatures from the reconstruction of last glacial cycle conditions. The first task was to investigate the ground surface temperatures required to reach different permafrost depths. A set of constant mean annual ground surface temperatures were assumed and applied to a 1D subsurface model based on present-day reference data for Forsmark (Table 3-6, Figure 3-40). Note that since the 1D permafrost experiments were conducted, these input data have been updated for the Forsmark site. Updated input data on bedrock and groundwater properties were used for the 2D modelling studies (Hartikainen et al. 2010), described in the second half of the present section.

Table 3-6. Site-specific reference physical properties and conditions of rock mass and groundwater at Forsmark used for the 1D permafrost modelling (SKB 2006a), mainly from site description model Forsmark 1.2 (SKB 2005). Note that since the 1D permafrost experiments were conducted, these data have been updated. Updated input data on bedrock and groundwater properties were used for the 2D modelling studies (Hartikainen et al. 2010), described in the second half of the present section.

Rock mass

Thermal properties

Parameter	Unit	Reference	Min	Max	Temperature dependency
Thermal conductivity	W $(m \cdot K)^{-1}$	3.6	3.2	4.0	11.0 % decrease per 100 °C increase
Heat capacity	MJ $(m^3 \cdot K)^{-1}$	2.3	2.1	2.5	27.5 % increase per 100 °C increase
Thermal diffusivity	$mm^2\ s^{-1}$	1.57	1.28	1.9	38.6 % decrease per 100 °C increase

Interior Earth conditions by depth

		0 m			10000 m		
Parameter	**Unit**	**Reference**	**Min**	**Max**	**Reference**	**Min**	**Max**
Geothermal heat flow	mW m^{-2}	59.0	48.0	65.0	43.2	41.7	46.0
Radiogenic heat prod.	µW m^{-3}	2.5	1.0	3.0	0.92	0.37	1.1

Table 3-6 continued.

Reference temperature conditions by depth

Parameter	Unit	400 m	500 m	600 m
Temperature	°C	10.6	11.7	12.8
Temperature gradient	°C km^{-1}		11.0	

Reference hydro-mechanical properties by depth

Parameter	Unit	100 m	200 m	300 m	≥ 400 m
Bulk density	kg m^{-3}	2700	2700	2700	2700
Young's modulus	GPa	74	74	74	74
Poisson's ratio	-	0.26	0.26	0.26	0.26
Kinematic porosity	-	0.00001	0.00001	0.00001	0.00001
Total porosity	-	0.0001	0.0001	0.0001	0.0001
Permeability	m^2	1.0×10^{-13}	1.0×10^{-15}	1.0×10^{-17}	1.0×10^{-18}

Groundwater

Reference salinity concentrations by depth

Ionic solvent	Unit	10 m	100 m	300 m	500 m	≥ 1000 m
Na^+	g m^{-3}	65	500	2000	2000	2000
Ca^{2+}	g m^{-3}	60	250	1200	1000	3500
Cl^-	g m^{-3}	15	1300	5500	5500	10000
SO_4^{2-}	g m^{-3}	20	170	500	400	50

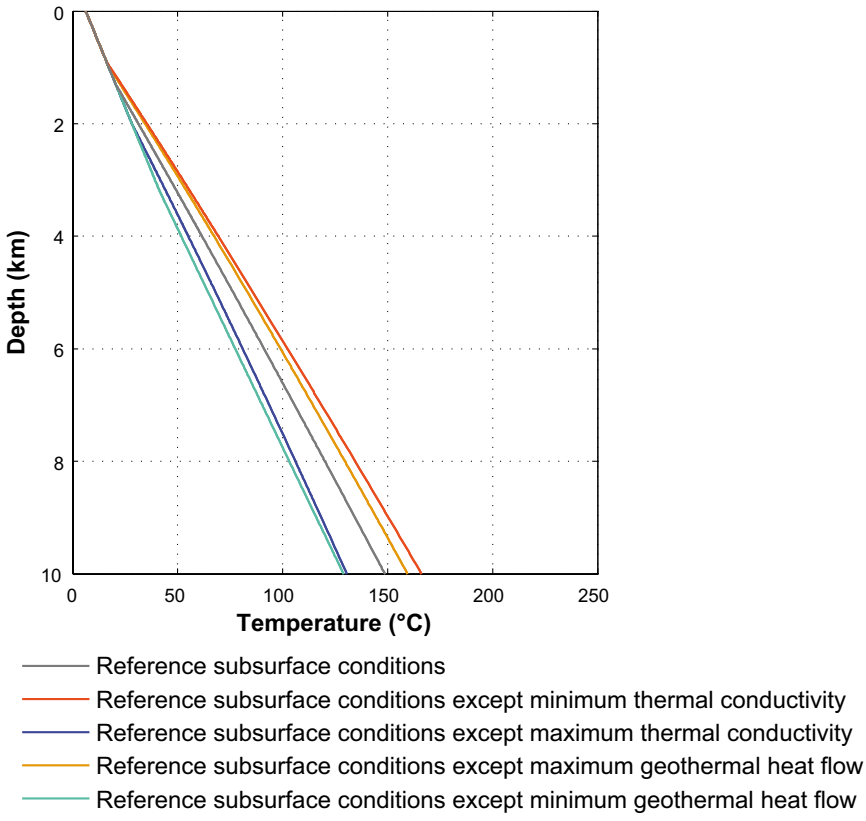

Figure 3-40. *Modelled present-day bedrock temperatures at the Forsmark repository location using the site-specific reference subsurface conditions in Table 3-6.*

The intention with the constant surface temperature simulations was to find steady state permafrost depths. The modelling, however, showed that no steady state could be reached in a timeframe of two glaciation cycles. The results from this modelling effort for a period of 120 ka are shown in Figure 3-41. The modelling indicates that reaching a permafrost depth of 450 m at Forsmark, without a heat contribution from spent fuel, requires a mean annual surface temperature of −8 °C for around 120 ka. With the heat contribution from the fuel, surface temperatures need to be lower than −8 °C. The thickness of the cryopeg varies from some metres to over 70 m (Figure 3-41). The results for permafrost development rates (aggradation rates) are shown in Figure 3-42.

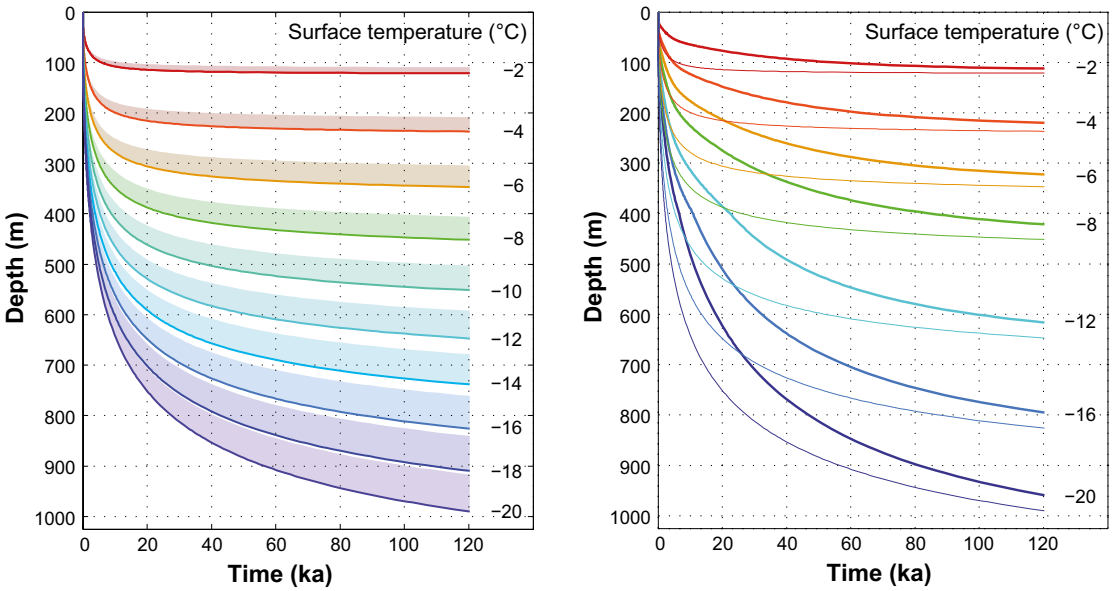

Figure 3-41. *Left: Evolution of permafrost depth (thick lines) and related cryopegs (shadowed areas) for constant ground surface temperatures of −2, −4, …, −20 °C at the Forsmark repository location when reference subsurface properties are assigned. Right: Evolution of permafrost depth for different constant ground surface temperatures with and without the heat contribution from the repository (6000 canisters). Bold lines show calculations with heat from the repository, whereas thin lines show calculations with no repository heat contribution.*

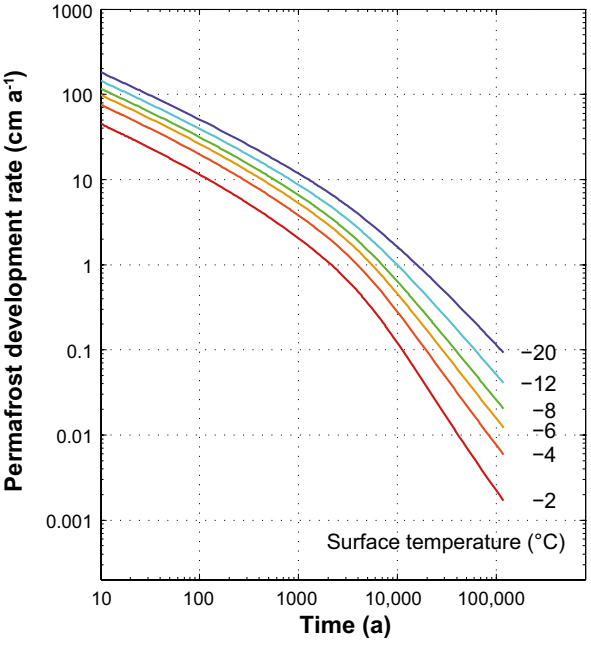

Figure 3-42. *Evolution of permafrost development rate for constant ground surface temperatures of −2, −4, −6, −8, −12 and −20 °C at Forsmark when site-specific subsurface properties are assigned.*

In the 1D modelling of surface conditions, the objective was to define a correlation between air and surface temperatures in consideration of the insulating effects of surface covers. The so-called *n*-factor concept (Lunardini 1978) yields an empirical relationship between the mean annual surface temperature $\overline{T}_s$ and the mean annual air temperature $\overline{T}_a$ as

$$\overline{T}_s = f(\overline{T}_a, A_a; n_{fr}, n_{th}) \qquad \text{Equation 3-11}$$

where A_a is the amplitude of annual air temperature variations, which can be defined as the half of the temperature difference between the monthly mean summer maximum and monthly mean winter minimum. n_{fr} and n_{th} are so-called freezing and thawing n-factors. These factors are ratios between the surface and air freezing indexes, i.e. annual time integrals of associated temperatures below the freezing point, and the surface and air thawing indexes, i.e. annual time integrals of associated temperatures above the freezing point, respectively. Depending on the type of surface cover, freezing n-factors can vary between 0.1 and 1 whereas thawing n-factors can have values in the range from 0.3 to 1.5 (Lunardini 1978, Shur and Slavin-Borovskiy 1993, Taylor 1995, 2001, Klene et al. 2001, Karunaratne and Burn 2004). Figure 3-43 shows the relation of the mean annual air temperature to the mean annual ground surface temperature at Forsmark obtained for a reference surface cover when vegetation and snow are considered and for a bare surface when no vegetation and snow exist. The relationship is based on the assumption that ground surface and air temperature is constant over the whole glacial cycle, when the surface is not covered by ice-sheet or submerged.

Since the factors of major importance to the subsurface conditions are the bedrock thermal properties and the conditions affecting the geothermal heat flow, the development of permafrost was in SKB (2006a) investigated for extreme thermal diffusivities and geothermal heat flows as shown in Table 3-6. These results are not repeated here, since similar sets of sensitivity tests were made with updated information on the geothermal properties at Forsmark with the 2D permafrost model (Hartikainen et al. 2010), see below in this section.

After the sensitivity analysis using constant surface temperatures, permafrost development was modelled for time-varying site-specific surface conditions. For this purpose, the ice-sheet model in Section 3.1.4 was used to extract estimates of site-specific time series of ground-level annual air temperatures and basal ice-sheet temperatures, as well as information on site-specific ice thickness variations. A description of these reconstructed temperatures for the last glacial cycle, including a discussion and estimates of their uncertainties, is found in Appendix A. The GIA modelling described in Section 3.3.4 was used to produce input data on relative sea-level changes.

The 1D permafrost model was used to reconstruct the permafrost conditions at the repository location for the reconstruction of the last glacial cycle. It was also used for studying a case with extreme surface conditions favouring permafrost growth (SKB 2006a). The latter case is equivalent to the *severe permafrost climate case* analysed with the 2D model (reported in Hartikainen et al. (2010) and later in Section 5.5.3) and is, therefore, not included here. For the reconstruction of permafrost for the last glacial cycle, the air temperature curve shown in Figure 3-44 was applied. When the site is covered by the reconstructed the Weichselian ice-sheet, surface temperatures equal the basal temperatures from the ice-sheet model. When the site is submerged, as seen in the reconstruction of Weichselian relative sea-level variations, the surface temperature is set to +4 °C.

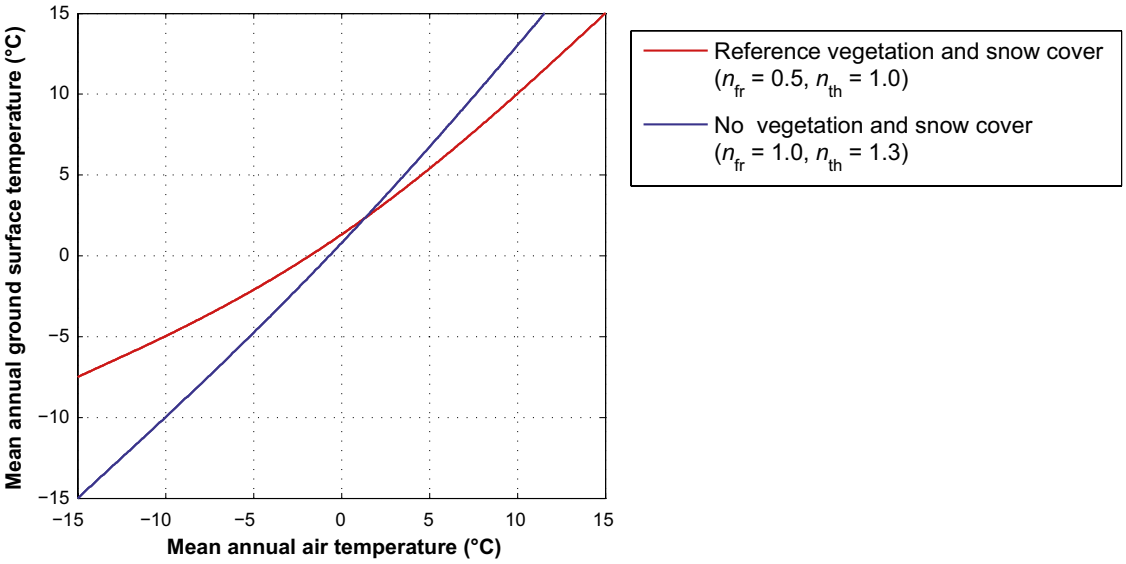

Figure 3-43. *Relationship between the mean annual air temperature and the mean annual ground surface temperature at Forsmark considering reference vegetation and snow cover, and no vegetation and snow cover.*

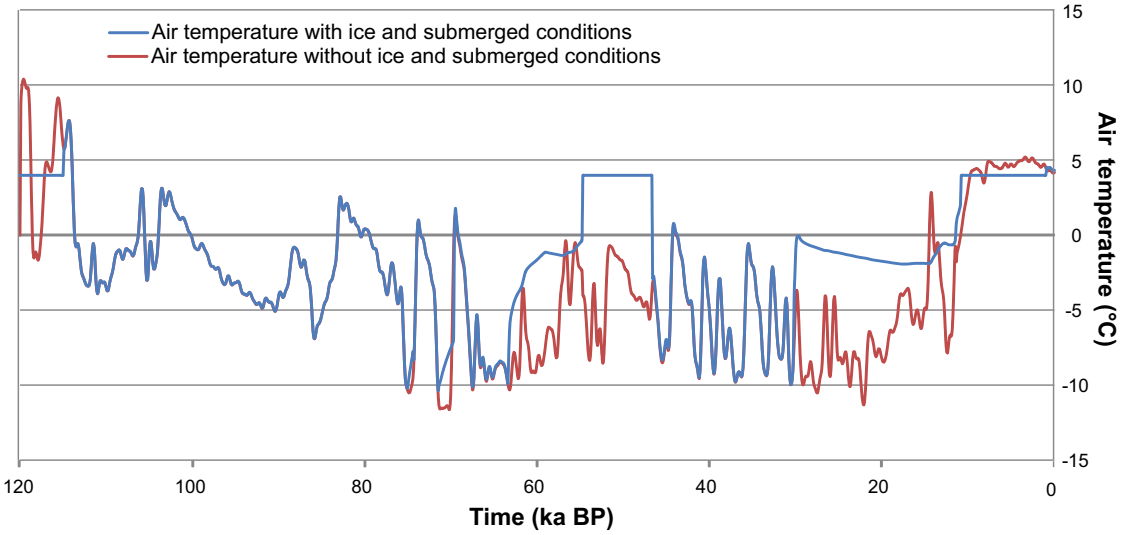

Figure 3-44. *Reconstructed air temperature curve for the Forsmark region for the past 120 ka, including estimated submerged periods of the Eemian, Mid-Weichselian and Holocene interglacials (blue line), see Appendix A. The red line shows reconstructed last glacial cycle air temperatures without a presence of an ice-sheet and submerged periods. The blue line includes periods of ice-sheet coverage, i.e. it shows simulated basal ice temperatures for glaciated periods, air temperatures for ice-free periods, and a temperature of +4 °C for submerged periods. The curves have been used as input to the PSAR 1D and 2D permafrost simulations (SKB 2006a, Hartikainen et al. 2010). A submerged period during the Eemian was not included in the 1D permafrost simulations. The uncertainties of the temperature curves are discussed in Appendix A, and the implications for modelled permafrost depths in the part of Section 3.4.4 describing the sensitivity studies made with the 2D permafrost model.*

The results of the development of permafrost, perennially frozen subsurface and cryopeg for reference surface conditions (Table 3-6) with vegetation and snow cover, and considering heat from the spent fuel are shown in Figure 3-45. The uncertainty in the modelled permafrost and freezing depths are analysed and discussed in the 2D permafrost modelling section below. The associated rates of permafrost aggradation and degradation are shown in Figure 3-46. The rather thick cryopeg layers during glaciations are due to large water pressures created by warm-based ice-sheets keeping the subglacial bed unfrozen down to a temperature about −2 °C.

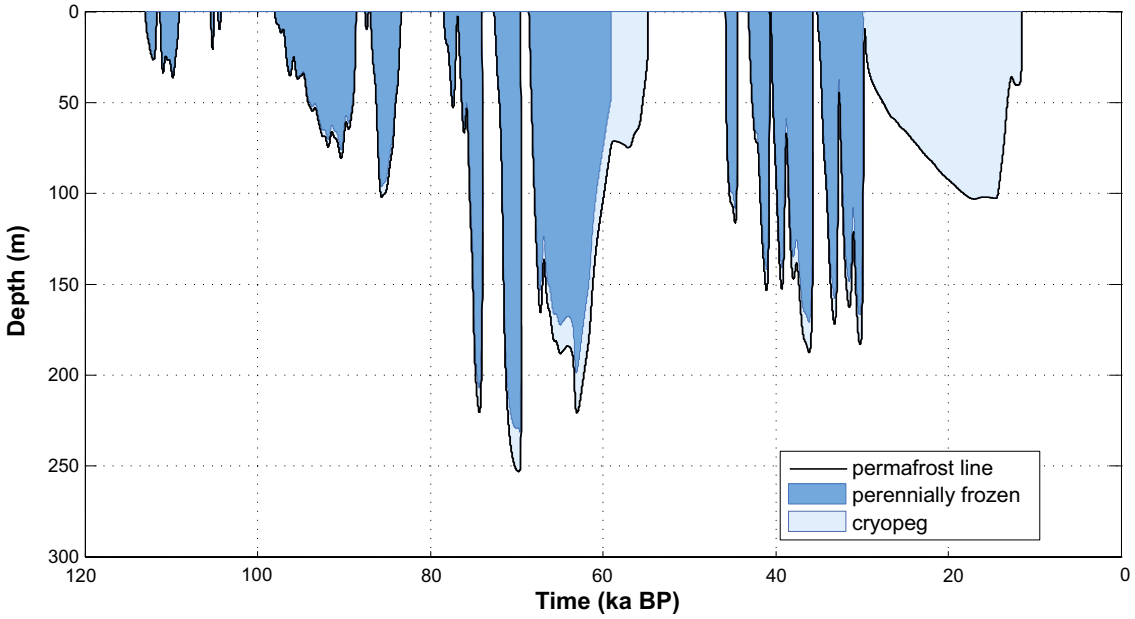

Figure 3-45. *Evolution of permafrost, perennially frozen subsurface and cryopeg at the repository location in Forsmark considering reference surface conditions, reference subsurface properties and heat from the spent fuel, see also SKB (2006a). The uncertainty in the modelled permafrost and freezing depths are analysed and discussed in the 2D permafrost modelling section below.*

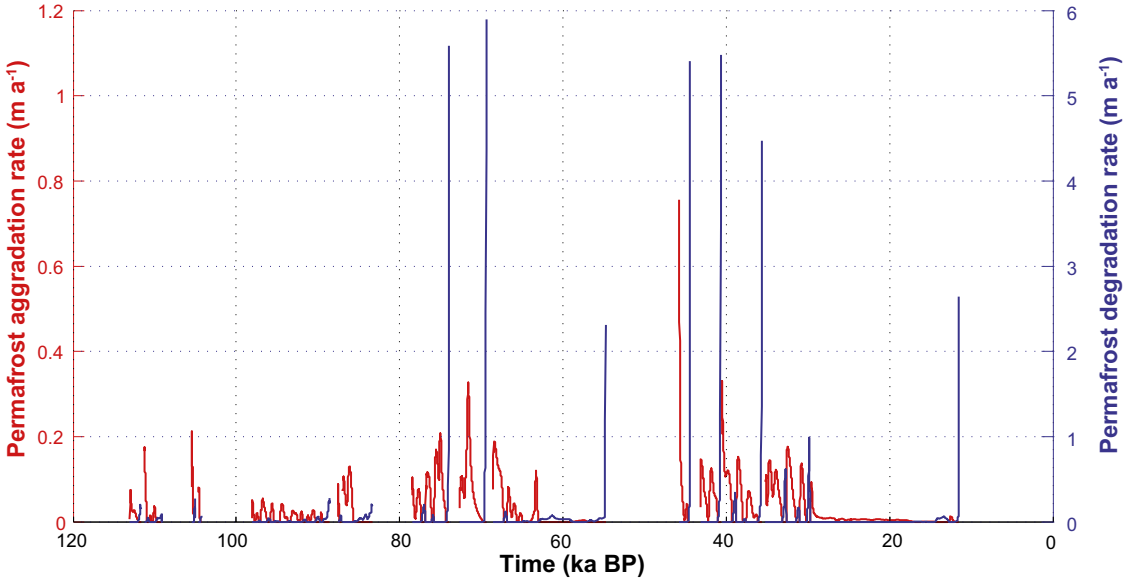

Figure 3-46. *Evolution of permafrost aggradation and degradation rates at the repository location in Forsmark considering reference surface conditions with vegetation and snow cover, reference subsurface properties and heat from the spent fuel, see SKB (2006a).*

The results show that surface conditions are the driving force for the development of permafrost, with the subsurface conditions and the heat from the spent fuel acting as either reducing or enhancing factors. The results indicate that permafrost (0 °C isotherm) can develop to near repository depth under the reference surface conditions when the insulating effects of vegetation and snow cover are excluded.

Large water bodies will affect permafrost depth and will be associated with the presence of taliks. A talik can exist beneath a water body when the water bottom temperature remains above the freezing point. Based on field tests on temperature measurements in lakes (e.g. Yershov 1998, Burn 2002), it was determined that a two metre deep water body maintains its bottom temperature above 0 °C and that a water body deeper than 8 m has a bottom temperature around +4 °C. The size of the water body required to retain a talik was investigated by permafrost modelling. To this end, permafrost development was simulated in the vicinity of circular lakes with constant positive lake bottom temperatures and constant negative lake bottom level bedrock temperatures. The results shown in Figure 3-47 (left panel) indicate that an open talik, completely penetrating the permafrost, can survive beneath a circular shallow lake, if its radius is greater than the thickness of surrounding undisturbed permafrost thickness. Furthermore, the results in Figure 3-47 (right panel) demonstrate that a radius greater than 0.6 times the thickness of surrounding undisturbed permafrost is big enough for a deep circular lake to maintain an open talik. The results apply for different lake bottom level bedrock temperatures.

For further sensitivity experiments conducted with the 1D permafrost model, see SKB (2006a).

In summary, the 1D permafrost study shows that the surface conditions are the driving force for the development of permafrost at Forsmark, while the subsurface conditions and the heat from the spent fuel acted as either reducing or enhancing factors. Permafrost can aggregate from some cm to some dm in a year whereas its degradation can take place several times faster, especially when the surface temperature rises above 0 °C and permafrost degrades simultaneously from the bottom upwards and from the top downwards. The results further show that the maximum permafrost depth in the reconstruction of last glacial cycle conditions occurs at 70 ka BP, prior to the first main ice-sheet advance over the site. The permafrost depth is ~250 m at the repository location at that time. However, the uncertainty of surface and subsurface conditions also needs to be taken into account, something that was done in SKB (2006a). In the present report, this is done in the 2D permafrost study described below.

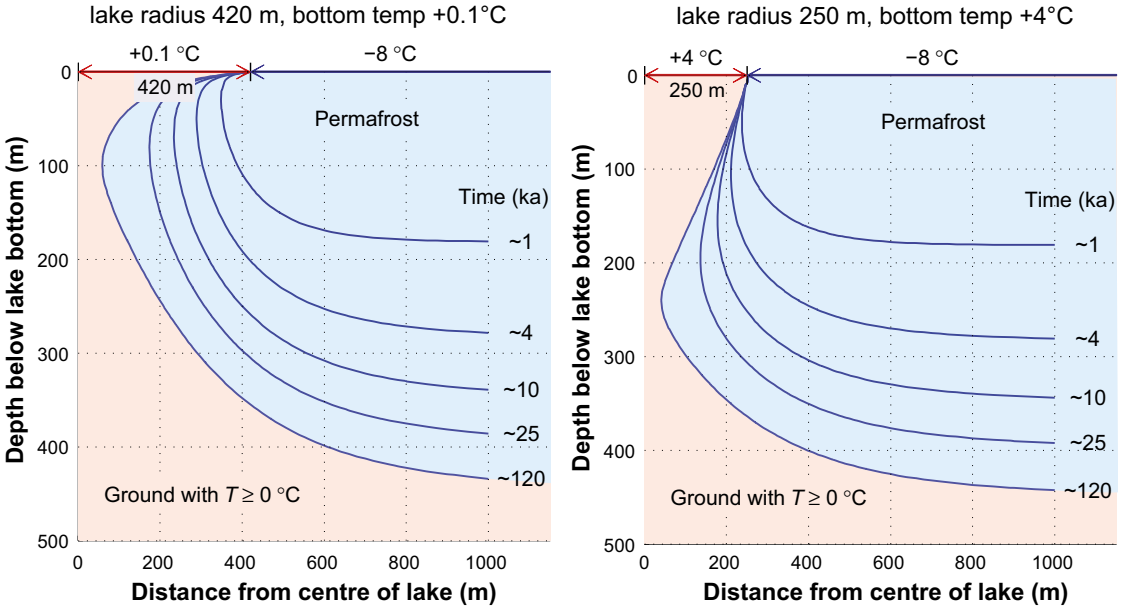

Figure 3-47. *Evolution of permafrost in the vicinity of a circular lake (red) at Forsmark. Left panel: the lake radius is 420 m and the constant lake bottom temperature +0.1 °C. Right panel: the lake radius is 250 m and the constant lake bottom temperature +4 °C. In both cases, a constant bedrock temperature of −8 °C prevails at the lake bottom level.*

2D reconstruction of last glacial cycle permafrost conditions at the Forsmark site

The 2D permafrost study was a continuation and complement to the 1D study performed for SR-Can SKB (2006a, Sections 3.4 and 4.4.1). The overall aim was to exemplify how permafrost and frozen ground develops over the Forsmark site (and not only at the repository location) during cold but ice-free periglacial phases of glacial cycles, and to further demonstrate the effects of uncertainties associated with processes and phenomena of importance for permafrost development. To this end, the 2D study provides a numerical estimation of the development of permafrost and perennially frozen ground along a profile covering a major portion of the Forsmark site and crossing the repository location (Figure 3-48), using site-specific surface and subsurface conditions. The objective was to investigate effects of multidimensional features of surface and subsurface conditions on the occurrence, development and distribution of permafrost and perennially frozen ground. Special emphasis was put on the modelling of surface conditions, including climate (temperature and humidity), soil, vegetation, water bodies and topography, lateral variations in bedrock and surface physical properties and heat generation from the spent fuel. In addition, groundwater flow and salt transport processes were considered (in 2D); processes that were neglected in the 1D SR-Can study.

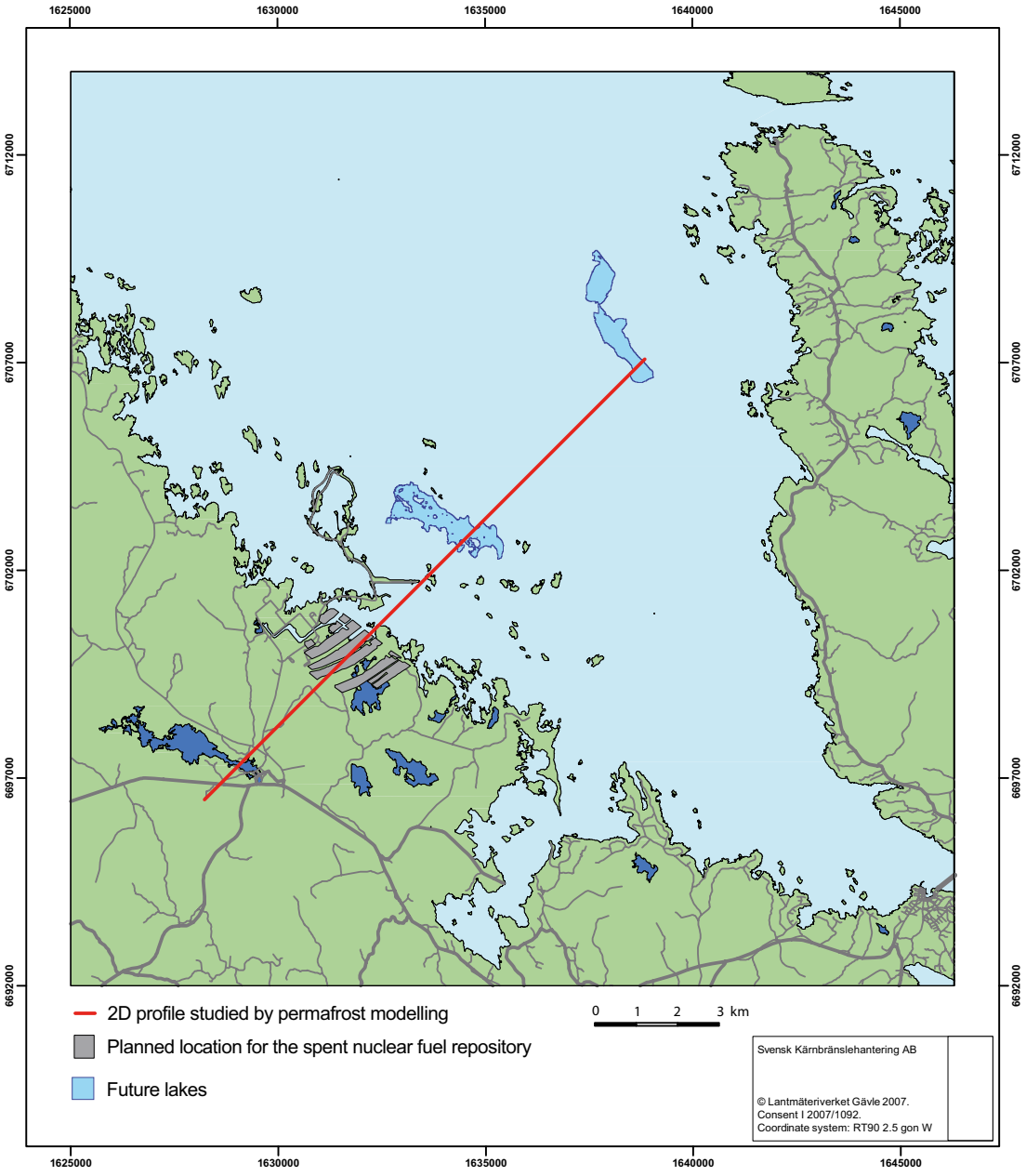

Figure 3-48. *The ~15 km long profile analysed in the 2D permafrost modelling study (red line), the planned repository location (grey), and future lakes.*

The mathematical model for freezing and thawing of the subsurface, based on the approach described in Hartikainen and Mikkola (2006), has been used in SKB (2006a). The model is capable of describing heat and mass transfer in a porous medium with freezing of groundwater depending on groundwater pressure and salt concentration and freezing-induced groundwater flow. In the present 2D study, by using the theory of mixtures and basic principles of continuum mechanics and thermodynamics, the mathematical model was reformulated in terms of Gibbs free energy functions by taking into account the effects of temperature, pressure and salinity concentration on the properties of groundwater and ice in a more accurate way. The reformulated thermo-hydro-chemically coupled model consists of balance laws of mass, momentum and energy, and the constitutive laws of state and diffusion. A new feature of the model is the capability of describing the exclusion of salt during freezing and the density dependent groundwater flow in unfrozen and partially frozen ground. In addition, the effects of pressure and salinity concentration on the freezing temperature of groundwater are considered more accurately. A more detailed description of the 2D permafrost model used for the reconstruction of last glacial cycle permafrost conditions is found in Hartikainen et al. (2010).

The same climate development as used for the 1D permafrost simulations was used, complemented with more comprehensive sensitivity studies on e.g. air temperature uncertainties. However, the 2D reconstruction of last glacial cycle permafrost conditions did not consider the entire last glacial cycle, but instead only the ice-free period from 115 to 70 ka BP, i.e. the period prior to the first phase of ice-sheet coverage in the reconstruction of the Weichselian ice-sheet (see Section 3.1.4). This was motivated by the fact that this period ends with the deepest permafrost reconstructed at the site for the entire last glacial cycle, see SKB (2006a) and the description of this 1D permafrost study above. However, for the *severe permafrost climate case* (Section 5.5), 2D permafrost simulations were carried out for the full glacial cycle, from 115 ka BP to present. Initial conditions were assumed to correspond to the present-day conditions (i.e. bedrock temperature, groundwater, salinity and pressure). Heat generated by the spent fuel in the repository was included in the simulations at 112 ka BP (see also Section 3.4.7).

Based on the results of the permafrost simulations in SKB (2006a, Section 3.4 and 4.4.1), the present analysis focuses on the following issues:

Subsurface conditions:

- Spatial variation of bedrock and soil thermal and hydraulic properties.
- Site-specific geothermal heat flow.
- Convectional heat transfer due to 2D groundwater flow.
- Heat generation from the repository for spent fuel.
- Salinity exclusion due to freezing and salt transport.

Surface conditions:

- Air temperature and its variation over time.
- Topographical features including slope and relief.
- Water bodies (sea and lakes), including the effect of isostatic uplift.
- Vegetation and snow cover as related to climate and topographical conditions.

The profile is located along the, very low, regional topographic gradient. In the direction of the profile, it covers a major part of the Forsmark site as defined by the biosphere model domain (Figure 3-48). For further description of the selection of the profile location, see Hartikainen et al. (2010, Appendix A).

Subsurface properties and conditions

The model domain encompasses an approximately 15 km long and 10 km deep vertical section consisting of six soil layers, 23 rock domains and 31 deformation zones as shown in Figure 3-49 and Figure 3-50. Figure 3-50 illustrates the thermally different rock mass domains, the deformation zones of the upper 2.1 km of the model domain, as well as the present-day Baltic sea-level. The soil layers are shown in Figure 3-51. The thermal and hydraulic properties of soil domains are given in Hartikainen et al. (2010, Table 2-1), whereas Table 2-2 and Table 2-3 in the same publication give the thermal and hydraulic properties of the rock mass domains. Hydraulic properties of the deformation zones are

presented in Hartikainen et al. (2010, Appendix D). The thermal properties of deformation zones are assumed identical to those of the corresponding rock mass domain. The bedrock below the depth of 2.1 km is assumed to have the same thermal and hydraulic properties as the rock domain in which the repository is located. The material properties of the bedrock are described in detail in Hartikainen et al. (2010, Appendices D and E). For the treatment of e.g. unfrozen groundwater content, also see Hartikainen et al. (2010). The numerical simulations were carried out using an unstructured finite element mesh of linear triangle elements. The mean grid spacing varied from less than 10 m close to the ground surface to about 300 m at the bottom of the model domain. The maximum time step for the adaptive time-integration scheme was limited to 100 years.

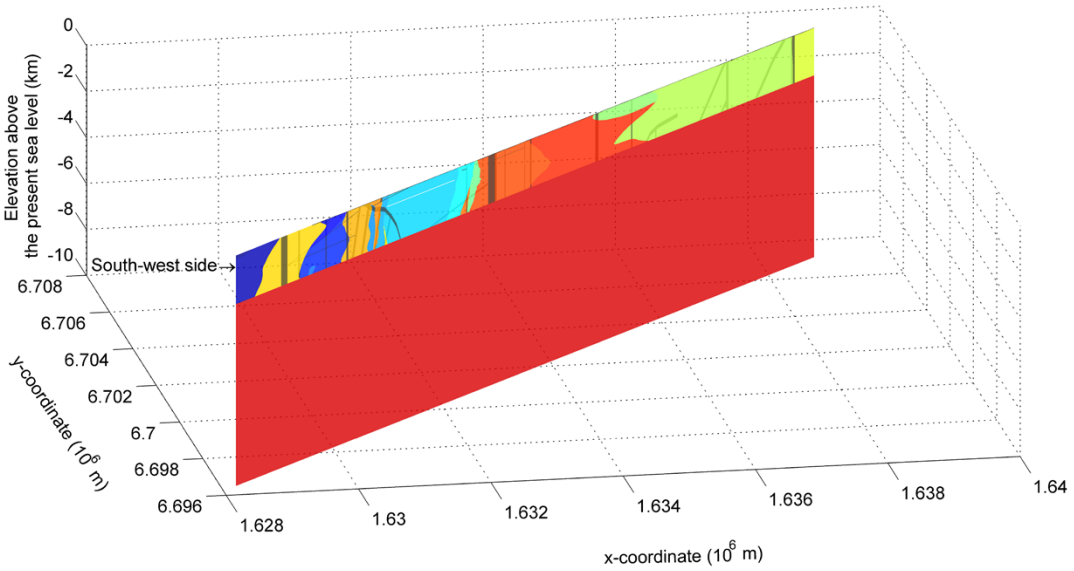

Figure 3-49. *The model domain used in the 2D permafrost simulations. Colours from blue to red signify the 23 rock domains considered and grey the 31 deformation zones. Physical and thermal characteristics for the rock domains and deformations zones were obtained from the site investigation programme at Forsmark, see Hartikainen et al. (2010). The six soil layers described in Hartikainen (2010, Appendix B) and Figure 3-51, are too thin to be seen in this figure. The x-axis is directed eastward and y-axis northward. The RT-90 coordinates of the south–west corner are x = 1628228 m, y = 6696472 m.*

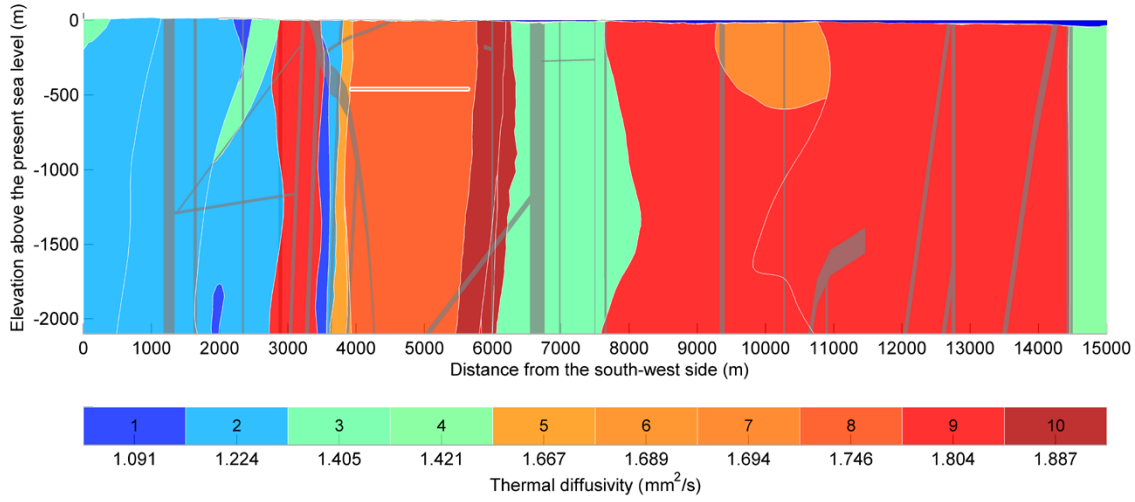

Figure 3-50. *The upper 2.1 km of the 2D model domain. Colours from blue to red signify rock domains with different thermal diffusivity. Numbers from 1 to 10 indicate the rock domains of Table 2-2 in Hartikainen et al. (2010). The location of deformation zones is illustrated in grey and the repository in white, at a depth of 450 m starting at about 4000 m along the profile. The thin blue layer on the top surface represents the present-day Baltic sea-level. Further description and references for these data are given in Hartikainen (2010, Appendix C).*

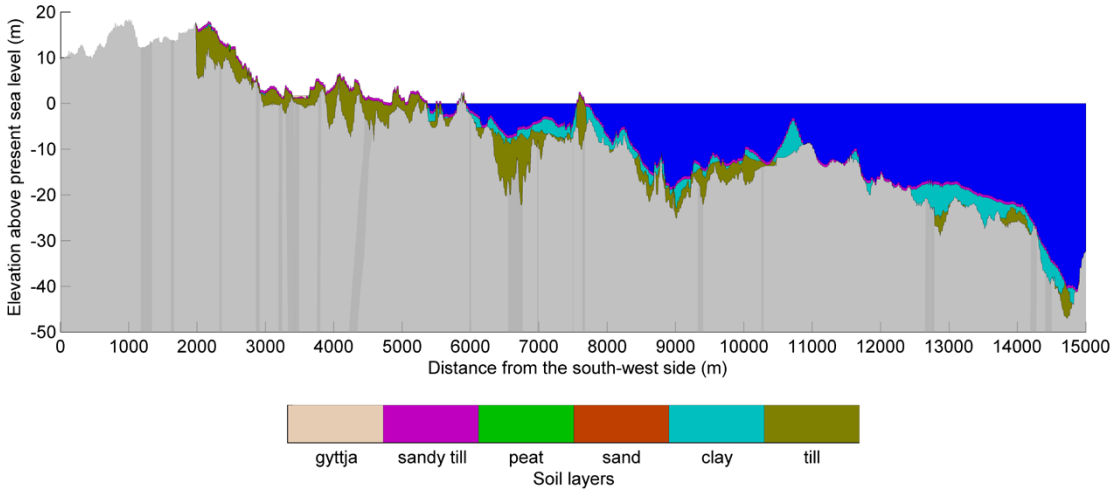

Figure 3-51. *The soil layers of the 2D model domain. Grey colour represents bedrock and blue the present-day Baltic Sea. The gyttja, peat and sand layers are too thin to be seen in this figure. In addition, because the first 2000 m of the model domain is outside the area of detailed site investigations, no information about the soil cover is used there. Further description and references for these data are given in Hartikainen et al. (2010, Appendix B). Note that the vertical axis has a scale that gives a strong vertical exaggeration of topography.*

The geothermal heat flow is an important subsurface parameter for permafrost modelling. The geothermal heat flow, crustal radiogenic heat production and ground temperature depth to ~1 km were based on Sundberg et al. (2009), see also Hartikainen et al. (2010, Appendices B–F). For a description of how these parameters were modelled for depths from ~1 km to 10 km, see Hartikainen et al. (2010). Figure 3-52 shows the initial ground temperature calculated for mean thermal properties.

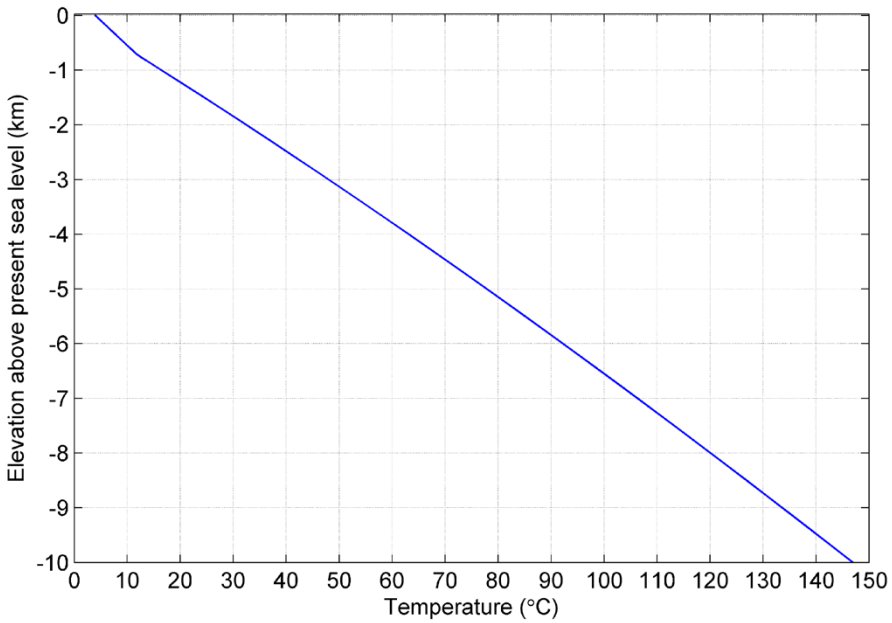

Figure 3-52. *Distribution of initial ground temperature for mean thermal properties used in the 2D permafrost modelling. For a description of these properties, see Hartikainen et al. (2010, Table 2-2).*

The initial salinity concentration of groundwater for depths to ~1.5 km is described in Hartikainen et al. (2010, Appendix F), and for depths from ~1.5 km to 10 km it was obtained as a stationary solution using present concentration values on the surface and at the depth of 1.5 km. Figure 3-53 shows the initial salinity distribution in the model domain.

The present-day groundwater pressure was determined as hydrostatic pressure based on the initial conditions of ground temperature and groundwater salinity concentration as well as the hydrostatic pressure at the bed of the Baltic Sea. The results for initial groundwater pressure are shown in Figure 3-54.

For a description of the localisation of the repository along the profile and the treatment of heat produced by the spent nuclear fuel, see Hartikainen et al. (2010).

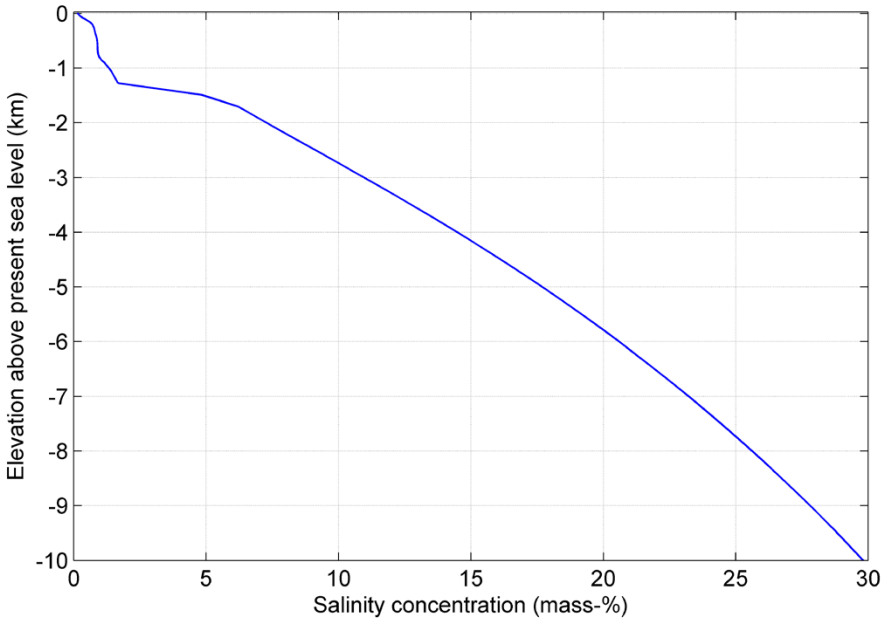

Figure 3-53. *Distribution of initial salinity concentration of groundwater Hartikainen et al. (2010).*

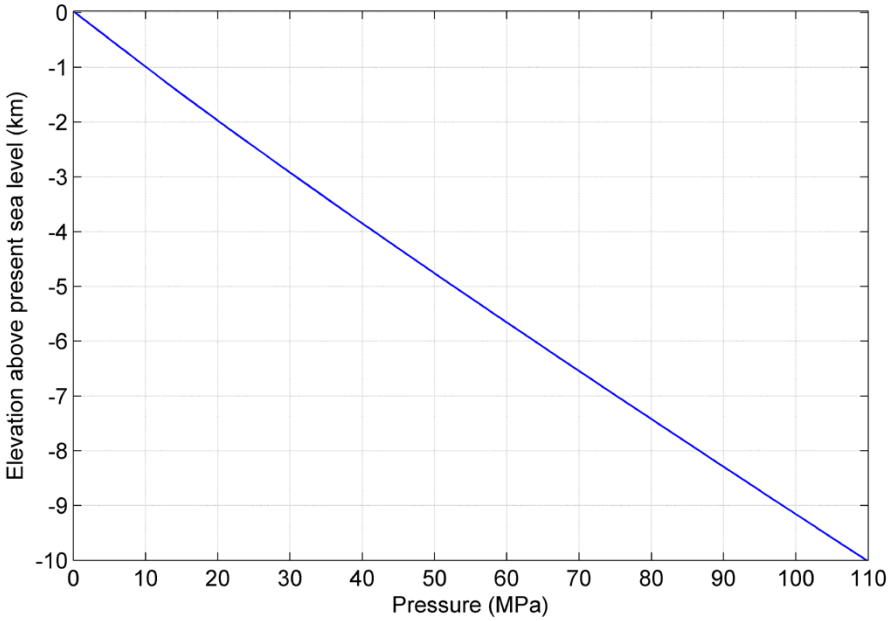

Figure 3-54. *Distribution of initial groundwater pressure associated with the temperatures and salinity concentrations shown in Figure 3-52 and Figure 3-53.*

Surface properties and conditions

Due to significant uncertainties associated with descriptions of the surface conditions, two variants, one humid and one dry, were analysed. This was expected to yield a lower and upper limit for the permafrost and perennially frozen ground development, see further below.

As mentioned above, the 2D reconstruction of last glacial cycle permafrost conditions analyse the period from 115 to 70 ka BP, that is a ~85 ka long period from the Eemian interglacial up to the first phase of glacial conditions as reconstructed for the Forsmark site (SKB 2006a). Based on the Köppen climate classification (Lohmann et al. 1993) and long-term observations (Eugster et al. 2000) both climate variants may be divided into three climate zones: *Boreal*, *Subarctic* and *Arctic*, which may be characterized by the annual mean air temperature, the monthly mean maximum summer air temperature and the monthly mean minimum winter air temperature, together with the monthly mean maximum summer and winter precipitations (Table 3-9). The large ranges in the monthly mean air temperatures and precipitations are explained by the fact that the description and modelling of surface conditions involves significant uncertainties, see Appendix A and later in Section 3.4.

The relative sea-level development (Section 4.5.2) and evolution of lakes along the profile, as described in the PSAR biosphere studies, were included in the modelling, see Hartikainen et al. (2010 Appendix I). As a result of isostatic uplift, two lakes are formed along the profile, in the area today covered by the Baltic Sea (Figure 3-48).

The vegetation and snow cover are closely related to the prevailing climate conditions as well as to other landscape parameters. The presence of different vegetation types within different biomes has been described in numerous publications (e.g. Breckle 2002, Archibold 1994) and the regional response of vegetation types to e.g. periglacial climate conditions has been studied by Kjellström et al. (2009, 2010a). In the present study, a detailed picture of the distribution of prevailing major vegetation types for *Boreal*, *Subarctic* and *Arctic* climate zones for the reconstruction of last glacial cycle conditions was described by using local variations in TWI (Table 3-7). The spatial resolution of the TWI information was 20 × 20 m. For a more detailed description of the adopted TWI approach, see Hartikainen et al. (2010).

Table 3-7. Main vegetation cover types at Forsmark for three different climate zones and corresponding Topographic Wetness Index (TWI) values. For a more detailed description of the use of e.g. the TWI index in this study, see Hartikainen et al. (2010 Appendix J).

Climate zone	Vegetation cover type and TWI values				
	Forest	Shrubs	Grassland	Barren	Peatland
Boreal	Mixed TWI > 0	-	-	-	Peat TWI > 13.2
Subarctic	Tree line/tundra forest TWI > 13.2	Moderate/short 10.9 ≤ TWI ≤ 13.2	Short TWI < 10.9	-	Peat TWI > 13.2
Arctic	-	Short TWI > 13.2	Tussocks 10.9 ≤ TWI ≤ 13.2	Bare TWI < 10.9	Peat TWI > 13.2

Table 3-8. Freezing (winter) and thawing (summer) n-factors for the reconstruction of last glacial cycle conditions. See also Hartikainen et al. (2010). The numbers within brackets in the last four columns are Topographic Wetness Index (TWI) intervals.

Climatic zone	Season	Monthly mean max./min.	Monthly mean max.	n-factors for specified surface conditions and associated TWI intervals			
		Air temperature (°C)	Precipitation (mm month^{-1})	Dry (< 10.9)	Fresh-moist (10.9–13.2)	Wet (> 13.2)	Peatland (> 13.2)
Boreal	summer	+10 – +20	10–60	1.2–1.4	1.2–1.4	1.2–1.4	1.0
	winter	–15 – +5	1–50	0.2–0.3	0.2–0.3	0.2–0.3	0.1
Subarctic	summer	+5 – +15	5–60	0.8–1.0	0.7–0.9	0.6–0.8	0.8–1.0
	winter	–25 – −10	1–40	0.5–0.9	0.4–0.8	0.2–0.6	0.1–0.4
Arctic	summer	< +5 – +10	5–60	1.0–1.2	0.5–0.8	0.4–0.7	0.6–0.9
	winter	–35 – −20	1–40	0.7–1.0	0.4–0.8	0.3–0.6	0.2–0.5

Table 3-9. Climate information for the reconstruction of last glacial cycle conditions.

Climate zone	Annual mean air temperature (°C)	Monthly mean max. summer air temperature (°C)	Monthly mean min. winter air temperature (°C)	Monthly mean max. summer precipitation (mm month^{-1})	Monthly mean max. winter precipitation (mm month^{-1})
Boreal	> 0	+10 – +20	−15 – +5	10–60	1–50
Subarctic	0 – −6	+5 – +15	−25 – −10	5–60	1–40
Arctic	< −6	< +5 – +10	−35 – −20	5–60	1–40

The impact of vegetation, snow cover and other climate factors on the ground surface temperature and permafrost development is well investigated (Washburn 1979, Williams and Smith 1989, Yershov 1998, French 2007). In general, an annual mean air temperature ranging between −9 and −1 °C is required to build up permafrost for most surface covers, depending on other climatic conditions and topography. The surface conditions can be modelled by thermodynamic and hydrodynamic models using surface energy and water balance equations and information on climate conditions and topography such as radiation, precipitation, cloudiness and wind, and their annual and diurnal variations (Riseborough et al. 2008). However, these models are unsuitable for the long timespans associated with glacial cycles, since no climate data besides the air temperature can be adequately constructed. Therefore, an empirical approach based on *n*-factors (Lunardini 1978), i.e. statistical correlations between air and ground surface temperature, has been used to construct the ground surface temperature from the reconstructed air temperature (Table 3-8). For a detailed motivation for and description of the *n*-factors approach as an approach to treatment of surface conditions, see Hartikainen et al. (2010).

When the site is submerged by the Baltic Sea or the two lakes, the ground surface temperature was set to +4 °C for water depths greater than 6 m. For shallower depths the temperature was interpolated between the value of 4 °C and the prevailing ground surface temperature.

Figure 3-55 exemplifies the evolution of modelled ground surface temperatures for the reconstruction of last glacial cycle conditions at one location along the profile with fresh-moist surface conditions (at ~4800 m from the south–west end). Examples of modelled ground surface temperatures for other surface condition types (wet, dry and peatland) are found in Hartikainen et al. (2010). Figure 3-56 illustrates the modelled ground surface temperatures along the profile at four different times during the last glacial cycle, considering different climate conditions: 111.5 ka BP – subarctic and partially submerged, 103.5 ka BP – boreal, 95 ka BP – subarctic, 70 ka BP – arctic. The results concerning the humid climate variant are obtained using the lowest *n*-factors of Tables 2-7 and 2-8 in Hartikainen et al. (2010), whereas the highest *n*-factors from the same tables yield the results for the dry climate variant.

The ground surface temperature of +4 °C indicates the times when the profile is submerged by the Baltic Sea or the two lakes. The dry surface condition type generates the lowest ground surface temperatures, and the peatland condition the highest ground surface temperatures in the subarctic and arctic climate zones. Furthermore, due to thin vegetation and snow cover, the dry variant of the reconstruction of last glacial cycle conditions results in the lowest ground surface temperatures in the subarctic and arctic climate zones but highest in the boreal climate zone.

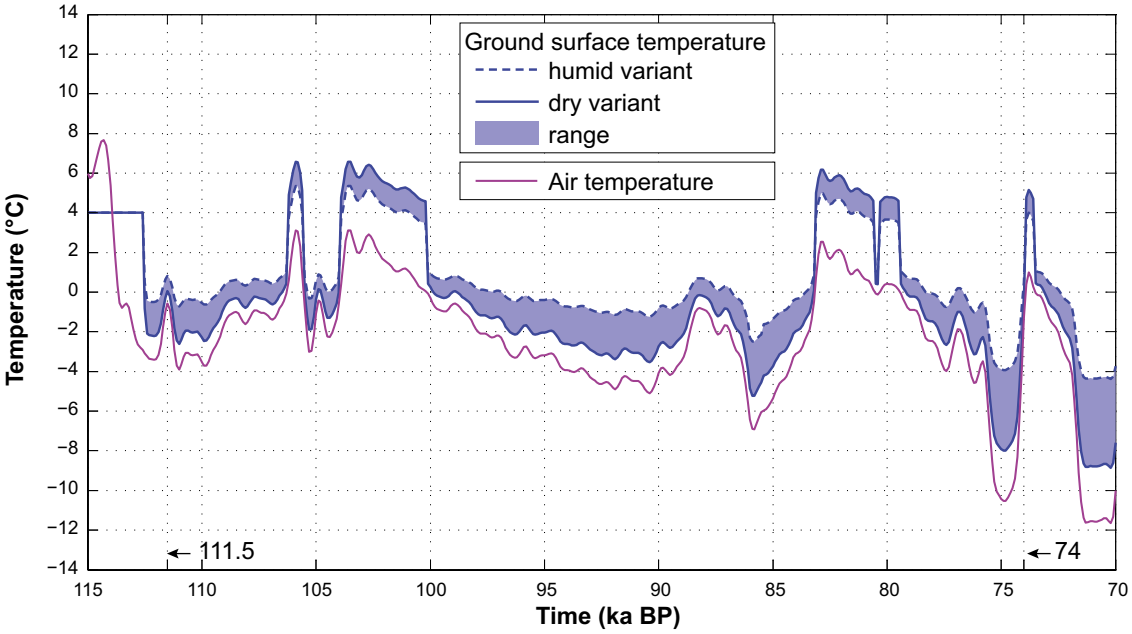

Figure 3-55. *Example of evolution of air temperature and modelled ground surface temperatures for a part of the profile with fresh-moist surface conditions (~4800 m from the south–west end of the profile, above the repository, see Figure 3-48) for the reconstruction of last glacial cycle conditions.*

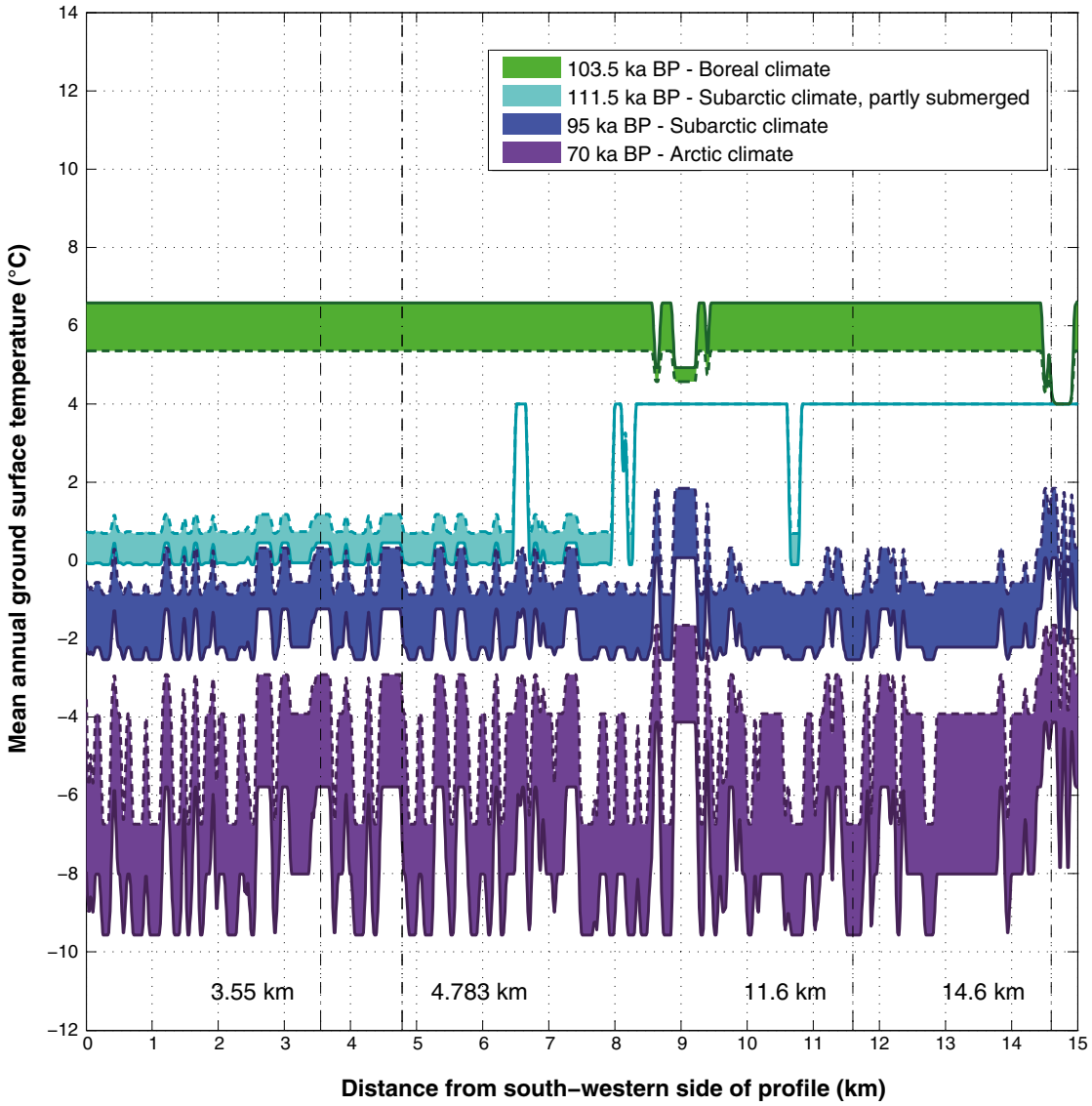

Figure 3-56. *Modelled ground surface temperatures along the profile at four different times for the last glacial cycle case considering different climate conditions: Boreal climate at 103.5 ka BP, Subarctic climate and partially submerged conditions at 111.5 ka BP, Subarctic climate at 95 ka BP, Arctic climate at 70 ka BP. The solid border lines of the shadowed areas indicate the dry variant of the climate case and dashed ones the humid variant of the reconstruction of last glacial cycle conditions. The dashed vertical line at 4.8 km denotes the location used as example for the fresh-moist surface condition types (Figure 3-55).*

Descriptions of cases simulated with the 2D permafrost model

For the reconstruction of permafrost conditions for the last glacial cycle, two main simulations were made constituting one dry and one humid climate variant. The minimum values of *n*-factors shown in Table 3-8 describe the humid variant whereas their maximum values yield the dry variant. Mean subsurface properties and conditions were used for both variants (e.g. mean thermal and mechanical properties of soil and bedrock, and chemical properties of groundwater, see Hartikainen et al. (2010).

Main simulations:

1. Dry climate variant of last glacial cycle.
2. Humid climate variant of last glacial cycle.

The uncertainties related to surface conditions including moisture conditions, vegetation and snow cover as well as ground surface temperature were considered in the main simulations by means of the humid and dry variant of the climate cases studied. Variations in hydraulic properties and ionic composition of groundwater were considered to be of negligible significance in regard to permafrost development, and hence were not included in the sensitivity analyses. Following this approach, and taking results from previous studies into account (SKB 2006a), the following sensitivity studies were done:

1. uncertainty in air temperature, uncertainty in geothermal heat flow,
2. uncertainty in bedrock thermal conductivity,
3. uncertainty in bedrock thermal diffusivity,
4. combination of uncertainties in bedrock thermal properties,
5. combination of uncertainties in surface and bedrock thermal properties,
6. combination of uncertainties in air temperature, surface conditions and bedrock thermal properties,
7. influence of heat from the repository,
8. convective heat transfer by groundwater flow.

Description and results of main simulations

Resulting ground temperatures and extent of perennially frozen ground at times of 111.5, 95, 74, 70 ka BP are illustrated in Figure 3-57 and Figure 3-58 for the humid and dry variant of the reconstruction of last glacial cycle conditions. The selected times in the figures represent the four different situations regarding climate zone, relative sea-level development and permafrost conditions:

- 111.5 ka BP: subarctic climate prevails, the profile is partially submerged by the Baltic and the exposed ground surface is partially underlain by permafrost. The temperature is at a maximum within the repository,
- 95 ka BP: subarctic climate prevails and discontinuous permafrost is developing,
- 74 ka BP: subarctic climate is turning into a warmer boreal climate and permafrost is degrading, changing from continuous or sporadic permafrost,
- 70 ka BP: arctic climate prevails and continuous permafrost reaches its maximum depth.

The evolution of maximum permafrost depth, maximum depth of perennially frozen ground and the maximum depths of the −2 and −4 °C isotherms over the repository for the reconstruction of last glacial cycle conditions (both dry and humid climate variants) is shown in Figure 3-59. Figure 3-60 shows the same results for the whole profile and for the repository location, as well as the spatial extent of permafrost summarised along the investigated profile. In SR-Site, the −4 and −2 °C temperatures corresponded to the temperature criterion used for freezing of the buffer clay and backfill material (SKB 2011, Section 12.3). In the PSAR, the temperature for which a frozen buffer clay and backfill material may start having detrimental effects on the canister and surrounding host rock has been updated to −6 °C for both materials, see the **Post-closure safety report** Section 8.3.2 and 8.4.4. The maximum permafrost depths, maximum depths of perennially frozen ground, and the extent of permafrost distribution are summarised in Table 3-10.

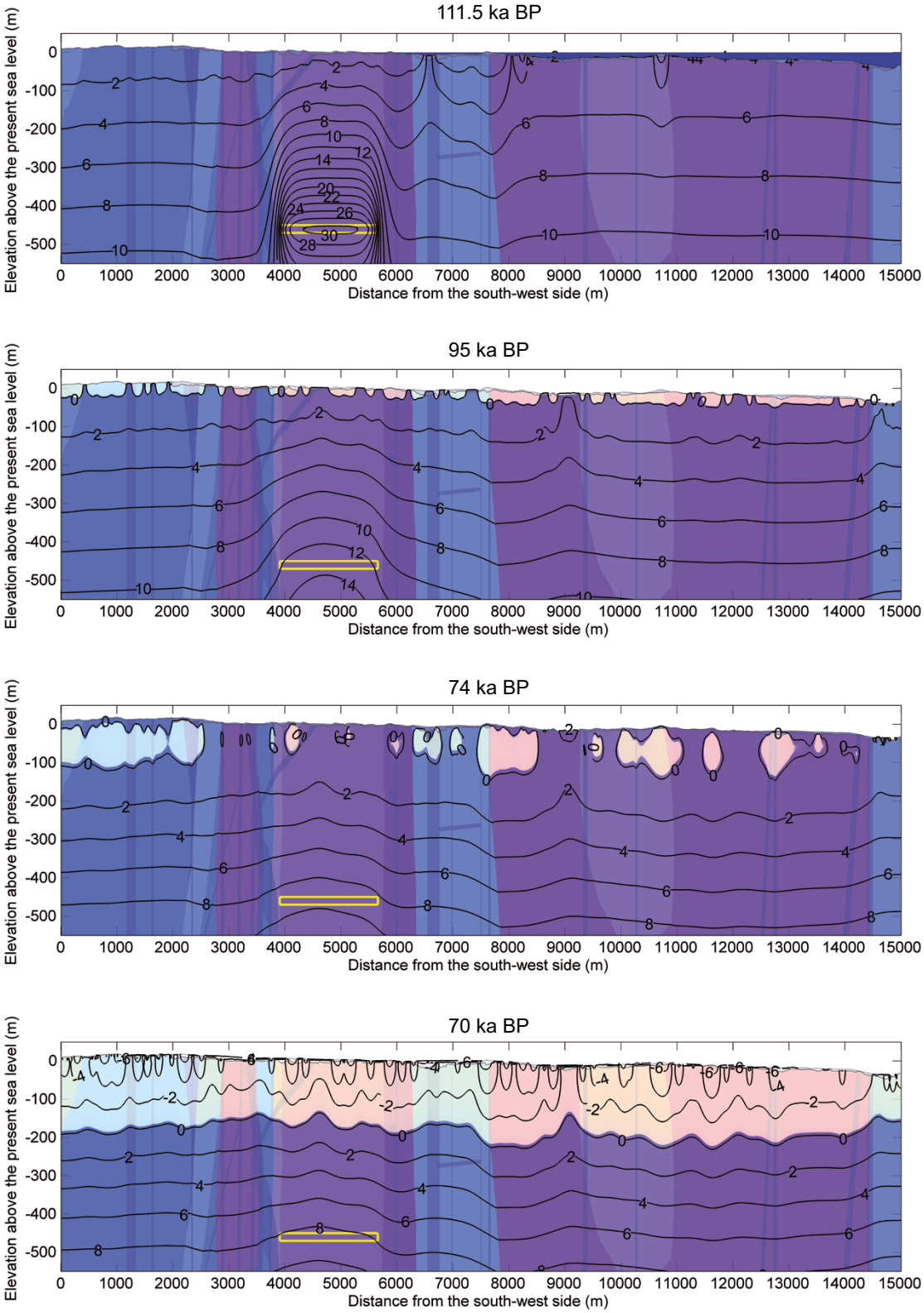

***Figure 3-57**. Temperature contours in (°C) and the extent of perennially frozen ground (light colour) and permafrost (0 °C isotherm) at times 111.5, 95, 74, 70 ka BP for the humid variant of the reconstruction of last glacial cycle conditions. Blue colour on the top of the profile at 111.5 ka BP shows the Baltic Sea. The yellow rectangle indicates the location of the repository.*

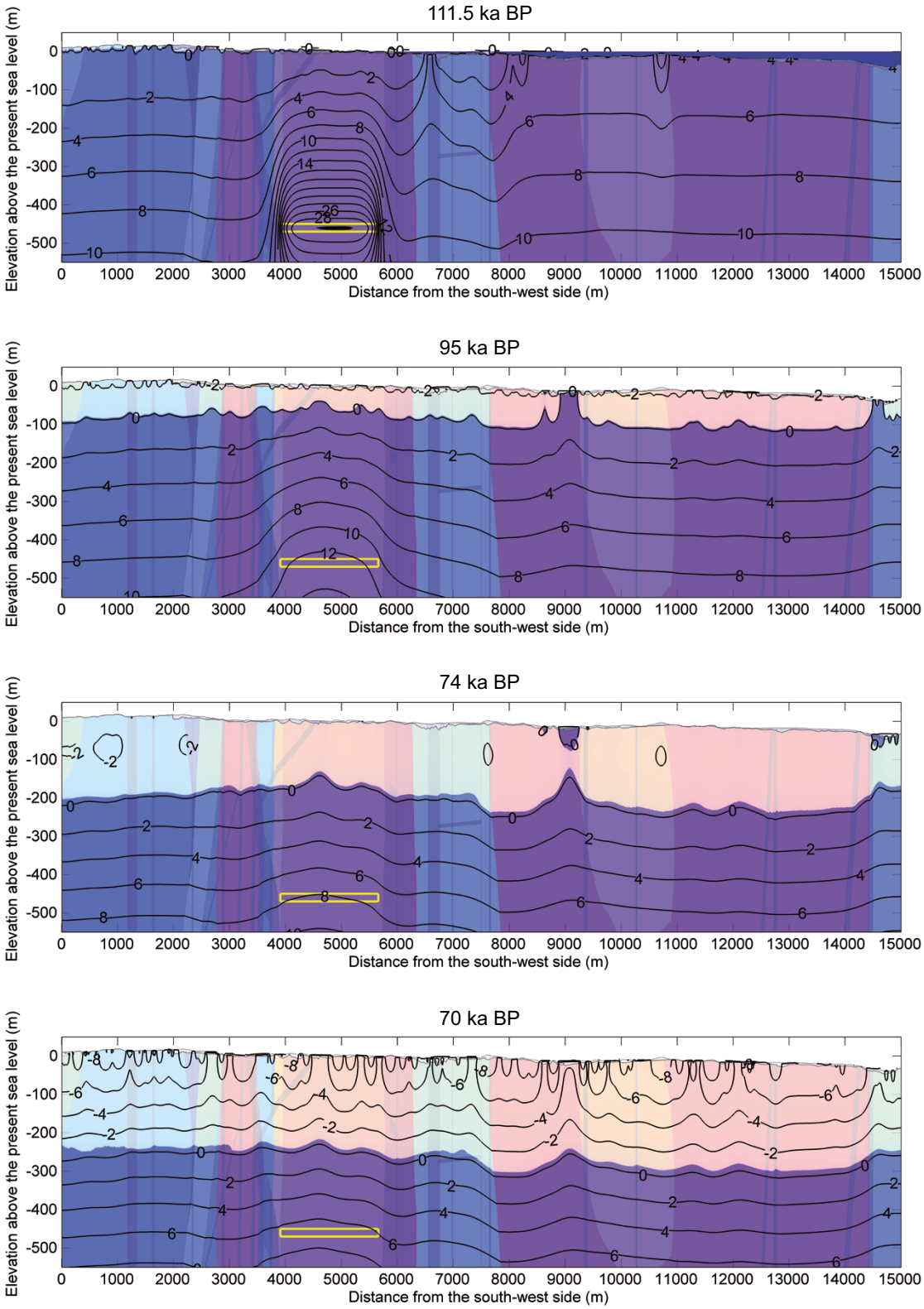

Figure 3-58. *Temperature contours in (°C) and the extent of perennially frozen ground (light colour) and permafrost (0 °C isotherm) at times 111.5, 95, 74, 70 ka BP for the dry variant of the reconstruction of last glacial cycle conditions. Blue colour on the top of the profile at 111.5 ka BP shows the Baltic Sea. The yellow rectangle indicates the location of the repository.*

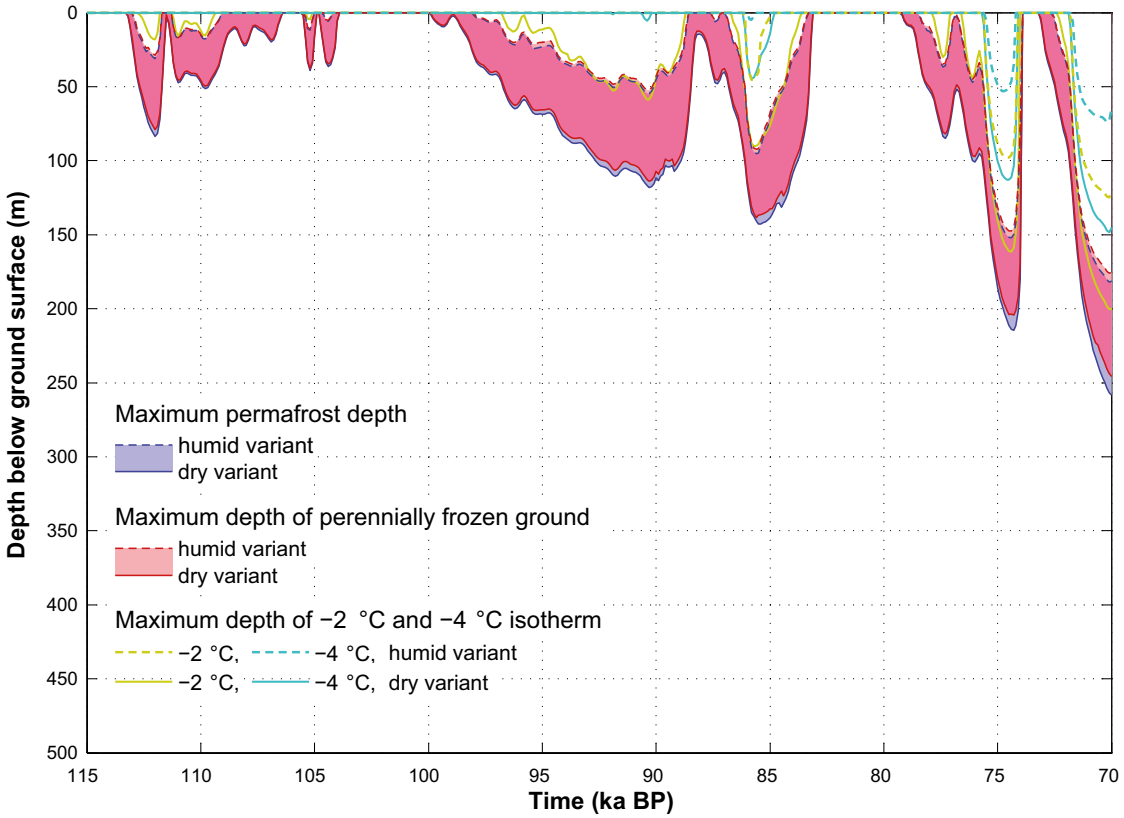

Figure 3-59. *Evolution of maximum permafrost depth, maximum depth of perennially frozen ground and maximum depths of the −2 and −4 °C isotherms over the repository for the reconstruction of last glacial cycle conditions. The upper permafrost surface, for periods of degradation from above, is not shown. The shaded area in blue and red represents the range when considering the dry and humid climate variants. The lilac colour indicates that the results for permafrost and perennially frozen ground overlap.*

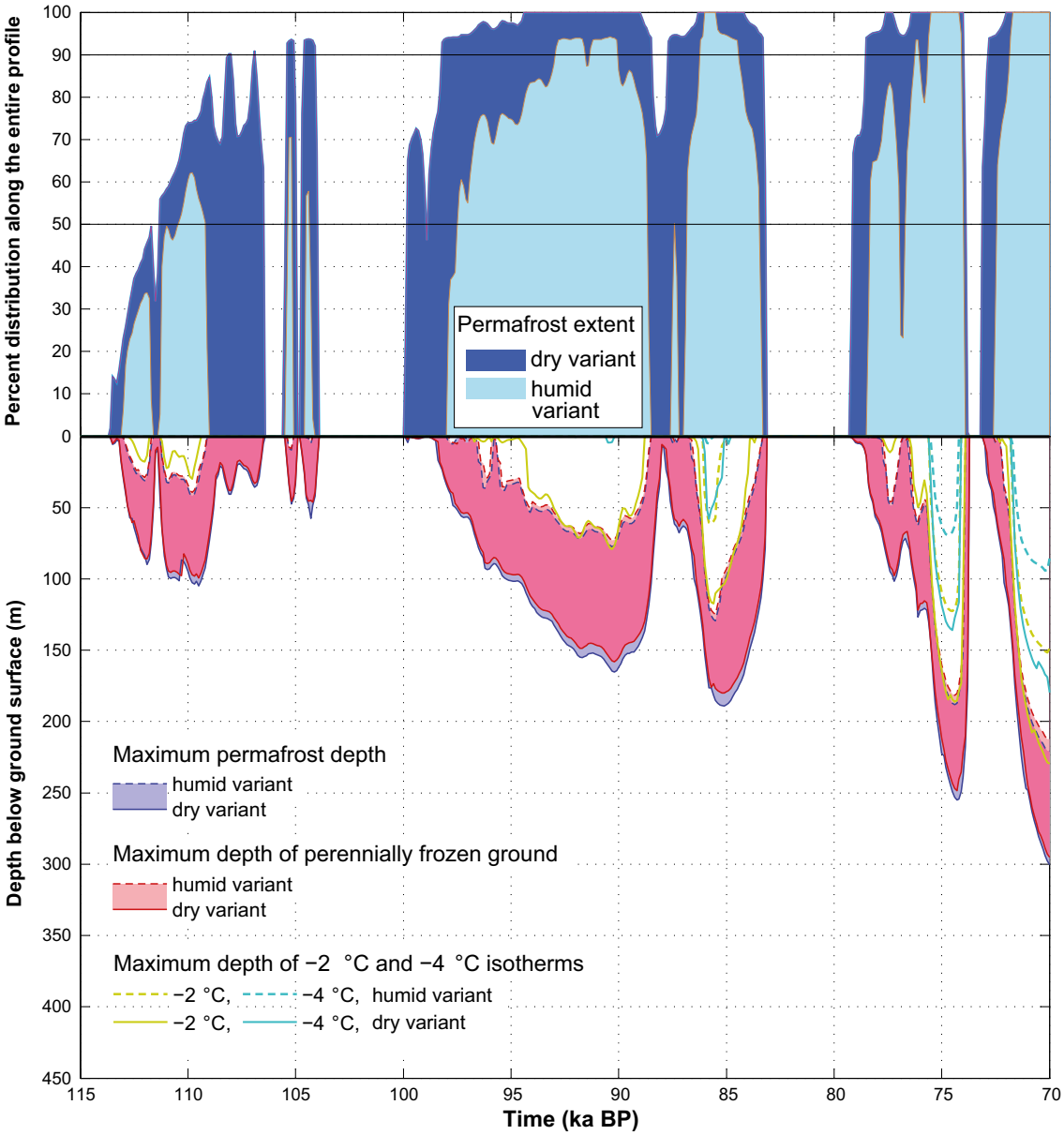

Figure 3-60. *Evolution of maximum permafrost depth, maximum depth of perennially frozen ground and maximum depth of −2 and −4 °C isotherms over the whole profile for the reconstruction of last glacial cycle conditions. The figure also shows the percent permafrost distribution along the profile. The transition from sporadic to discontinuous permafrost occurs at 50 % permafrost coverage and from discontinuous to continuous permafrost at 90 % coverage. The upper permafrost surface, for periods of permafrost degradation from above, is not shown. The shaded area in blue and red represents the range when considering the dry and humid climate variants. The lilac colour indicates that the results for permafrost and perennially frozen ground overlap.*

Table 3-10 and Table 3-11. In addition, Table 3-12 and Table 3-13 show the evolution of permafrost depth and depth of perennially frozen ground over the repository and whole profile, respectively.

Table 3-10. Times of permafrost occurrence and associated maximum permafrost depth and maximum depth of perennially frozen ground over the whole profile and over the repository for the humid variant reconstruction of last glacial cycle conditions. The table also gives the time and horizontal location of maximum permafrost depth and the percent extent of permafrost distribution.

Time periods of permafrost occurrence (ka BP)	Over the whole profile					Over the repository			
	Maximum permafrost depth (m)	Time of occurrence of maximum permafrost depth (ka BP)	Distance from the south–west side (m)	Maximum depth of perennially frozen ground (m)	Percent extent of permafrost distribution (%)	Maximum permafrost depth (m)	Time of occurrence of maximum permafrost depth (ka BP)	Distance from the south–west side (m)	Maximum depth of perennially frozen ground (m)
113–111.7	31	112	4960	29	34	31	112	4960	29
111.3–109.1	42	109.8	7960	39	62	18	111	5540	17
105.4–105.1	10	105.2	14290	9	71	12	105.2	5540	11
104.6–104.2	2	104.4	14320	1	58	6	104.4	5540	5
98–88.6	77	90.3	12750	73	94	55	90.3	4970	52
87.5–87.2	1	87.4	14320	4	50	6	87.4	5540	5
86.9–83.4	129	85.5	11620	125	100	95	85.6	5160	92
78.4–74	188	74.4	11630	182	100	152	74.4	5120	148
72.6–70	221	70	11630	212	100	182	70.1	5110	176

Table 3-11. Times of permafrost occurrence and associated maximum permafrost depth and maximum depth of perennially frozen ground over the whole profile and over the repository for the dry variant reconstruction of last glacial cycle conditions. The table also gives the time and horizontal location of maximum permafrost depth and the percent extent of permafrost distribution.

Time periods of permafrost occurrence (ka BP)	Over the whole profile					Over the repository			
	Maximum permafrost depth (m)	Time of occurrence of maximum permafrost depth (ka BP)	Distance from the south–west side (m)	Maximum depth of perennially frozen ground (m)	Percent extent of permafrost distribution (%)	Maximum permafrost depth (m)	Time of occurrence of maximum permafrost depth (ka BP)	Distance from the south–west side (m)	Maximum depth of perennially frozen ground (m)
113.6–106.4	104	109.7	7950	98	74	84	112	4100	79
105.5–104	48	104.4	13970	46	94	39	105.2	5540	38
99.9–83.2	189	85.1	12770	180	100	143	85.5	5652	137
79.2–73.8	255	74.3	12810	249	100	215	74.3	5650	204
73.1–70	301	70	12820	295	100	259	70	5650	246

Table 3-12. Evolution of maximum permafrost depth and maximum depth of perennially frozen ground specifically over the repository, modelled for the reconstruction of last glacial cycle conditions. The table also shows the prevailing mean annual air temperatures.

Time (ka BP)	Mean annual air temperature (°C)	Maximum permafrost depth (m)		Maximum depth of perennially frozen ground (m)	
		Humid variant of the reconstruction of last glacial cycle	Dry variant of the reconstruction of last glacial cycle	Humid variant of the reconstruction of last glacial cycle	Dry variant of the reconstruction of last glacial cycle
112	−3.4	31	84	29	79
111.5	−0.6	0	3	0	1
110	−3.5	15	47	15	46
108	−1.5	0	22	0	21
106	2.5	0	0	0	0
104	−0.6	0	6	0	5
102	1.6	0	0	0	0
100	−0.3	0	0	0	0
98	−1.9	2	30	0	28
96	−2.9	18	62	16	60
95	−3.2	23	69	20	66
94	−3.9	35	84	33	81
92	−4.8	49	108	47	103
90	−4.1	45	112	43	107
88	−0.9	0	15	0	13
86	−6.4	73	116	71	113
84	−3.1	31	108	29	104
82	2.1	0	0	0	0
80	0.4	0	0	0	0
78	−2.5	12	52	10	50
76	−4.2	45	101	43	97
75	−10.4	135	186	131	179
74	−1.3	85	180	77	168
72	−3.6	33	86	31	82
70	−10	181	259	175	246

Table 3-13. Evolution of maximum permafrost depth and maximum depth of perennially frozen ground over the entire 15 km profile, modelled for the reconstruction of last glacial cycle conditions. The table also shows the prevailing mean annual air temperatures.

Time (ka BP)	Mean annual air temperature (°C)	Maximum permafrost depth (m)		Maximum depth of perennially frozen ground (m)	
		Humid variant of the reconstruction of last glacial cycle	Dry variant of the reconstruction of last glacial cycle	Humid variant of the reconstruction of last glacial cycle	Dry variant of the reconstruction of last glacial cycle
112	−3.4	31	84	29	86
111.5	−0.6	0	12	0	10
110	−3.5	37	95	34	89
108	−1.5	0	41	0	38
106	2.5	0	0	0	0
104	−0.6	0	23	0	20
102	1.6	0	0	0	0
100	−0.3	0	0	0	0
98	−1.9	0	34	0	32
96	−2.9	29	93	26	89
95	−3.2	34	101	31	97
94	−3.9	49	119	46	114
92	−4.8	70	151	66	145
90	−4.1	70	162	65	155
88	−0.9	0	7	0	6
86	−6.4	96	153	93	147
84	−3.1	50	155	46	147
82	2.1	0	0	0	0
80	0.4	0	0	0	0
78	−2.5	1	59	1	56
76	−4.2	55	122	52	117
75	−10.4	165	222	160	212
74	−1.3	150	239	140	222
72	−3.6	44	110	41	105
70	−10	221	301	212	295

Figure 3-61 and Figure 3-62 show vertical bedrock temperature profiles in the middle of the repository location (with fresh-moist surface cover) for the humid and dry variants of the reconstruction of last glacial cycle conditions. Similar examples of vertical bedrock temperature profiles, including other surface cover types (wet, dry, peatland) are provided in Hartikainen et al. (2010).

The modelling results for the reconstruction of last glacial cycle conditions show that annual mean ground surface temperature at the Forsmark site can vary considerably in time and location depending on the prevailing climate zone and surface moisture condition type, see Figure 3-55 and Figure 3-56, and Hartikainen et al. (2010). For the first ~50 ka of the reconstructed last glacial cycle, the dry surface condition resulted in arctic climate zone ground surface temperatures below −11 °C and boreal climate ground surface temperatures over +6 °C. The wet surface condition yielded milder ground surface temperatures in both the arctic and boreal climate zones ranging from below −3 °C to over +5 °C over the same period. Furthermore, the peatland surface condition, having the moistest surface conditions, resulted in even milder ground surface temperatures ranging approximately between −2 °C and +4 °C. In addition, the difference in ground surface temperature could be several degrees from place to place along the investigated profile, see Figure 3-56. The same figure shows that the spatial fluctuation in ground surface temperature is largest in the arctic climate zone when the air temperature is lowest, and lowest in the boreal climate zone when the air temperature is close to 0 °C.

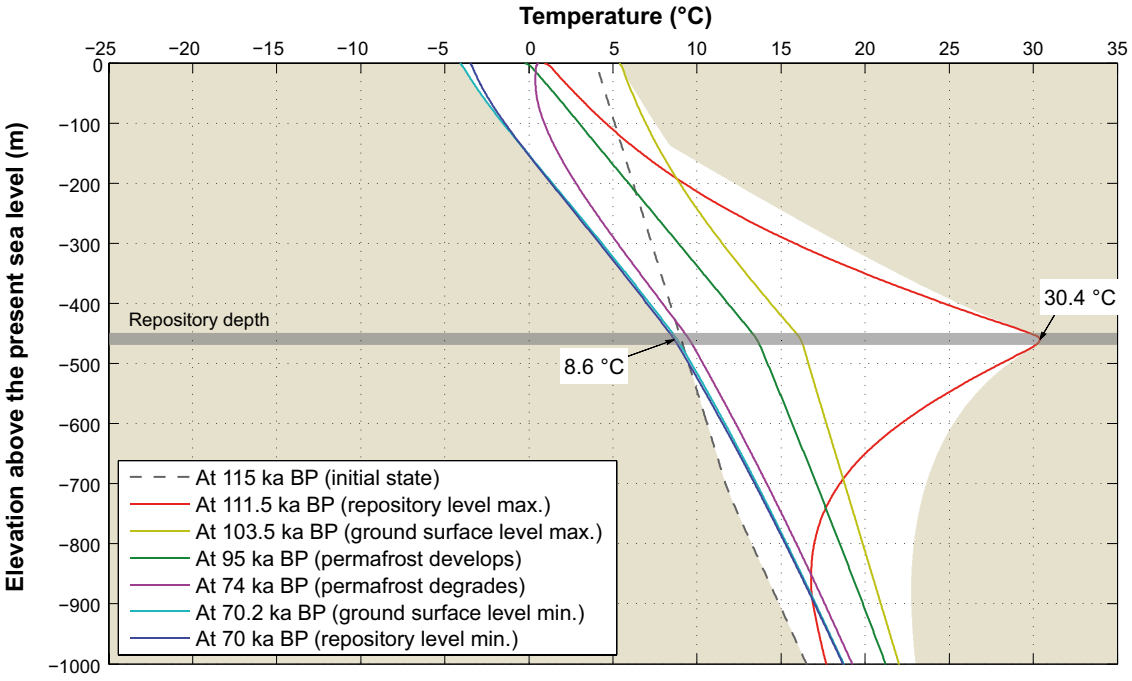

Figure 3-61. *Bedrock temperature along a vertical profile located in the middle of the repository at 4783 m from the south–western end of the profile the for the humid variant of the reconstruction of last glacial cycle conditions. The surface cover type reflects fresh-moist conditions. The white colour envelope represents the range of bedrock temperature fluctuation, simulated over the period of 115–70 ka BP. For more examples of modelled bedrock temperatures, see Hartikainen et al. (2010).*

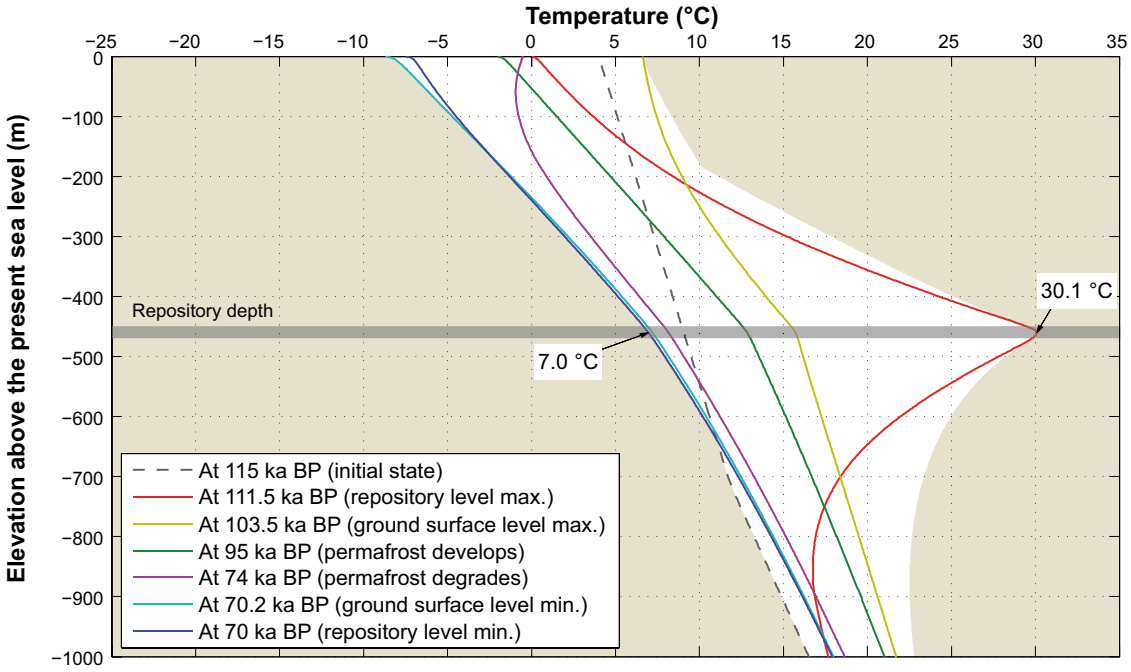

Figure 3-62. *Ground temperature along a vertical profile located in the middle of the repository at 4783 m from the south–western side of the profile for the dry variant of the reconstruction of last glacial cycle conditions. The surface cover type reflects fresh-moist conditions. The white colour envelope represents the range of bedrock temperature fluctuation, simulated over the period of 115–70 ka BP. For more examples of modelled bedrock temperatures, see Hartikainen et al. (2010).*

The simulation results (Figure 3-59) demonstrate that development of discontinuous permafrost is characteristic for the humid climate variant of the reconstruction of last glacial cycle conditions whereas continuous permafrost development prevails for long periods of the dry climate variant. In all cases permafrost became a continuous spatial distribution when the annual mean air temperature decreased below −6 °C and the maximum permafrost depth exceeded a depth of ~50 m.

During some periods, short distinct changes in climate results in phases of fast decay and growth of permafrost, such as at around 74 ka BP (Figure 3-60). Similar rates of permafrost growth and decay have been reported in Delisle (1998) and Kukkonen and Šafanda (2001).

The variation in ground surface temperature has the strongest effect on bedrock temperature fluctuations within the upper part of the vertical profile, see Figure 3-60 and Figure 3-61 and Hartikainen et al. (2010). The fluctuation is largest at the surface and reduces considerably with depth except where the heat from the repository has a large influence.

Regarding the evolution of permafrost depth and depth of perennially frozen ground, the results for the reconstruction of the last glacial cycle that considered variations in surface moisture conditions and mean bedrock thermal properties indicated that permafrost (defined by the 0 °C isotherm) can reach a depth between ~180 m and ~260 m over the repository (Figure 3-59) and a depth between ~220 m and ~300 m outside the repository (Figure 3-60) in a time frame of 45 ka. The maximum depth of perennially frozen ground can range between ~180 m and ~250 m over the repository and between ~210 m and ~300 m over the whole site at the same time. As seen from the 1D permafrost simulations of the full last glacial cycle (Figure 3-45), these numbers represent the largest depths during the entire glacial cycle.

A comparison between results from the present 2D modelling for the reconstruction of last glacial cycle conditions and the corresponding 1D modelling simulation performed for SR-Can, see previous part of Section 3.4.4 and SKB (2006a, Section 3.4) shows a good agreement regarding the maximum permafrost depth at 70 ka BP (Figure 3-63). The differences observed in Figure 3-63 reflect the higher thermal conductivity and lower geothermal heat flow values used in SKB (2006a) as well as differences in prescribed surface conditions.

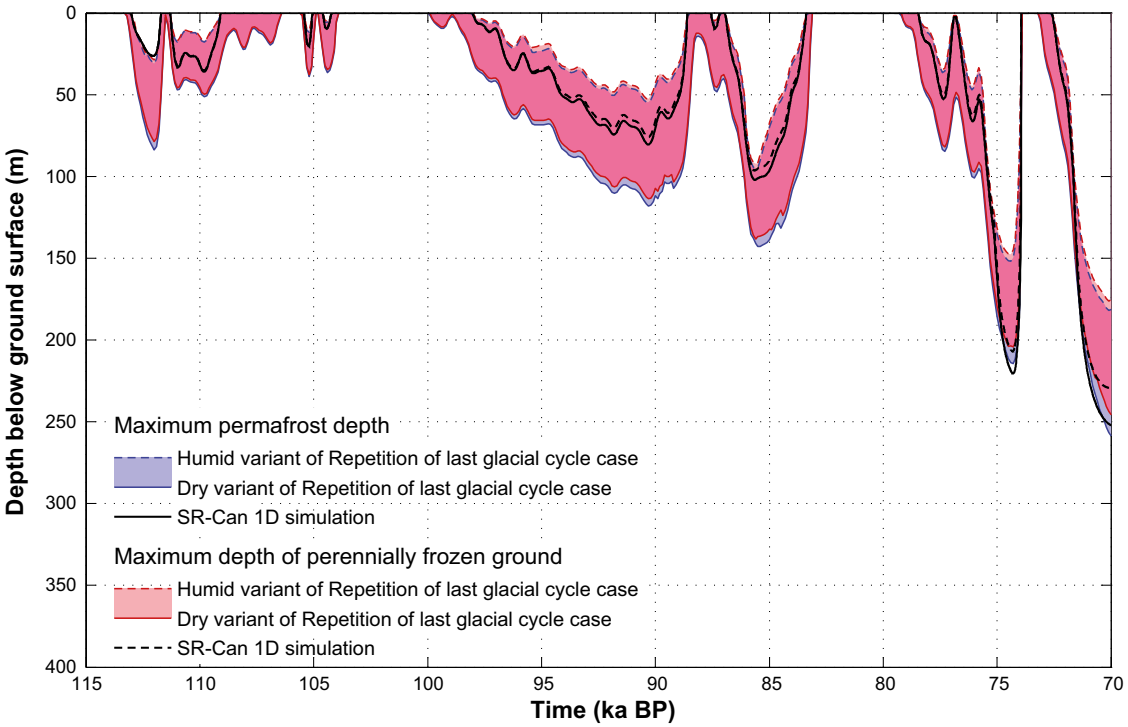

Figure 3-63. *Evolution of permafrost and frozen ground depth over the repository location from the 2D reconstruction of last glacial cycle conditions and from the 1D simulation of "the reference surface conditions of the base variant" from SKB (2006a). The results of the 1D and 2D permafrost models are in good agreement. The shaded area in blue and red represents the range when considering the dry and humid climate variants of the present study. The lilac colour indicates that the results for permafrost and perennially frozen ground overlap.*

Unfrozen water content and talik formation in reconstruction of last glacial cycle conditions

Figure 3-64 and Figure 3-65 show the unfrozen water content within the frozen bedrock as well as the 2D groundwater flow (Darcy velocity) directions at a time of 90.4 ka BP for the humid and dry variants of the reconstruction of last glacial cycle conditions. The figures show the whole profile, and close-ups of the highly conductive deformation zone ZFMA2 at a distance of 4000 m from the south–west end of the profile, and the near-by area of the two lakes at distances of 9000 m and 14600 m. The results show that during phases of the simulated period, taliks form at these lake locations (Figure 3-58 and Figure 3-65). The corresponding results for other time periods are found in Hartikainen et al. (2010).

The results show a maximum groundwater flow velocity of ~50 m a^{-1} when no permafrost occurred and some metres per year beneath the perennially frozen ground. The results show that under continuous permafrost conditions both the local and regional groundwater flow are reduced considerably in the perennially frozen ground but also in the unfrozen ground beneath permafrost, see Figure 3-64 and Figure 3-65 and Hartikainen et al. (2010). On the other hand, the results demonstrate that when the unfrozen groundwater content is greater than 10 %, groundwater flow may occur through a continuous partially frozen permafrost zone, although the flow velocity is very low, only some millimetres per year (Figure 3-65). This indicate, that under continuous permafrost conditions taliks can form under lakes through perennially frozen ground down to ~50 m depth, if favourable groundwater flow conditions with open flow paths prevail. When the freezing of ground is advanced to a degree with unfrozen water content less than 10 %, groundwater flow is reduced considerably, and thus a talik is not able to form or survive. A 2D model approach is in this context is sufficient to justify the likelihood of talik occurrence, but not to determine their groundwater flow and precise geometrical characteristics.

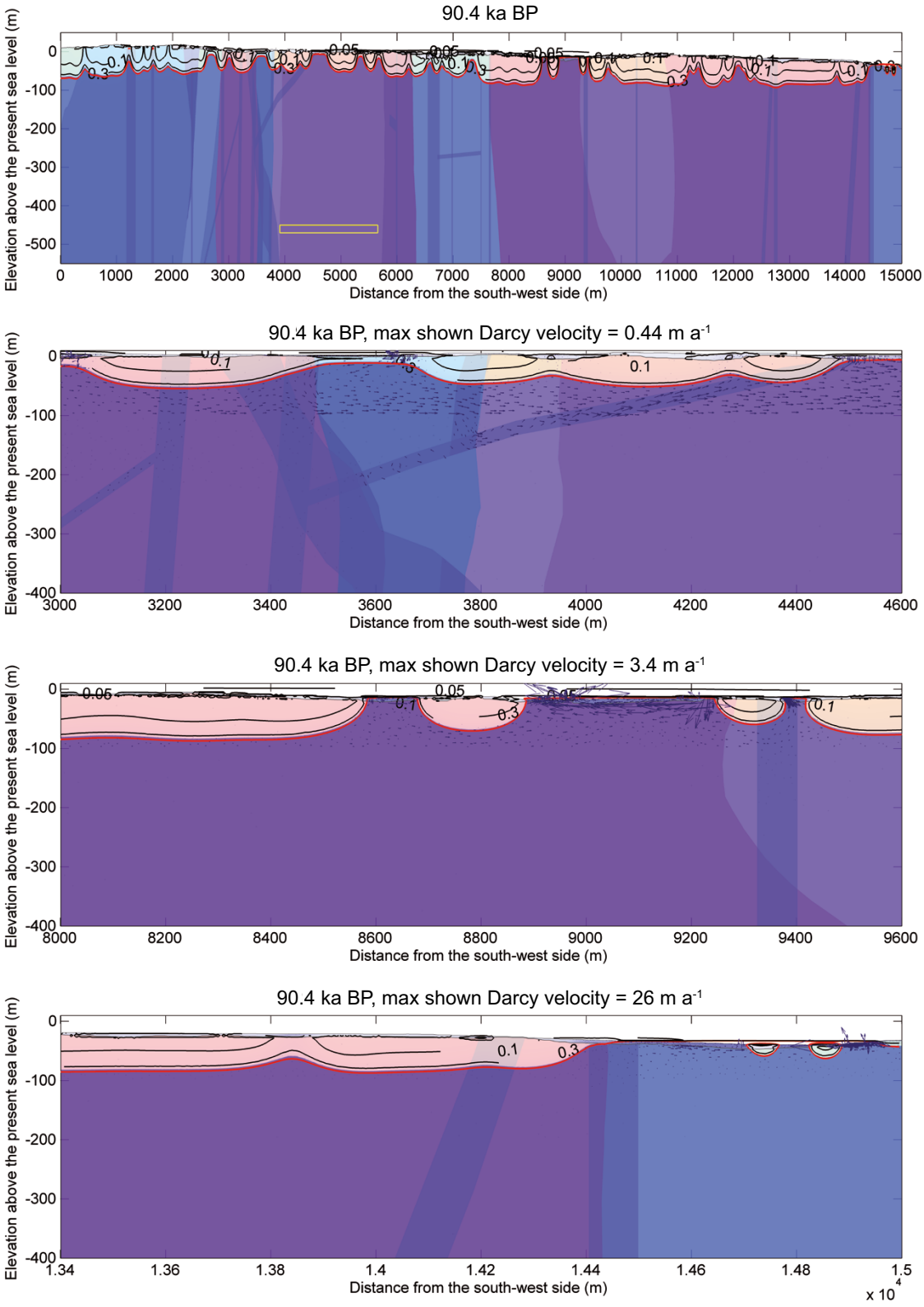

Figure 3-64. *Unfrozen volumetric (m^3 m^{-3}) groundwater content contours and Darcy flow directions at 90.4 ka BP for the humid variant of the reconstruction of last glacial cycle conditions. The upper panel shows the whole profile, followed by close-ups of the deformation zone ZFMA2 at ~4000 m, and the near-by area of the lakes at the distances 9000 m and 14600 m from the south–west side of the profile. Light colour shows the extent of perennially frozen ground, the red line shows the 0 °C isotherm (i.e. permafrost depth), and the yellow box in the upper panel shows the repository. For further examples of these results, see Hartikainen et al. (2010).*

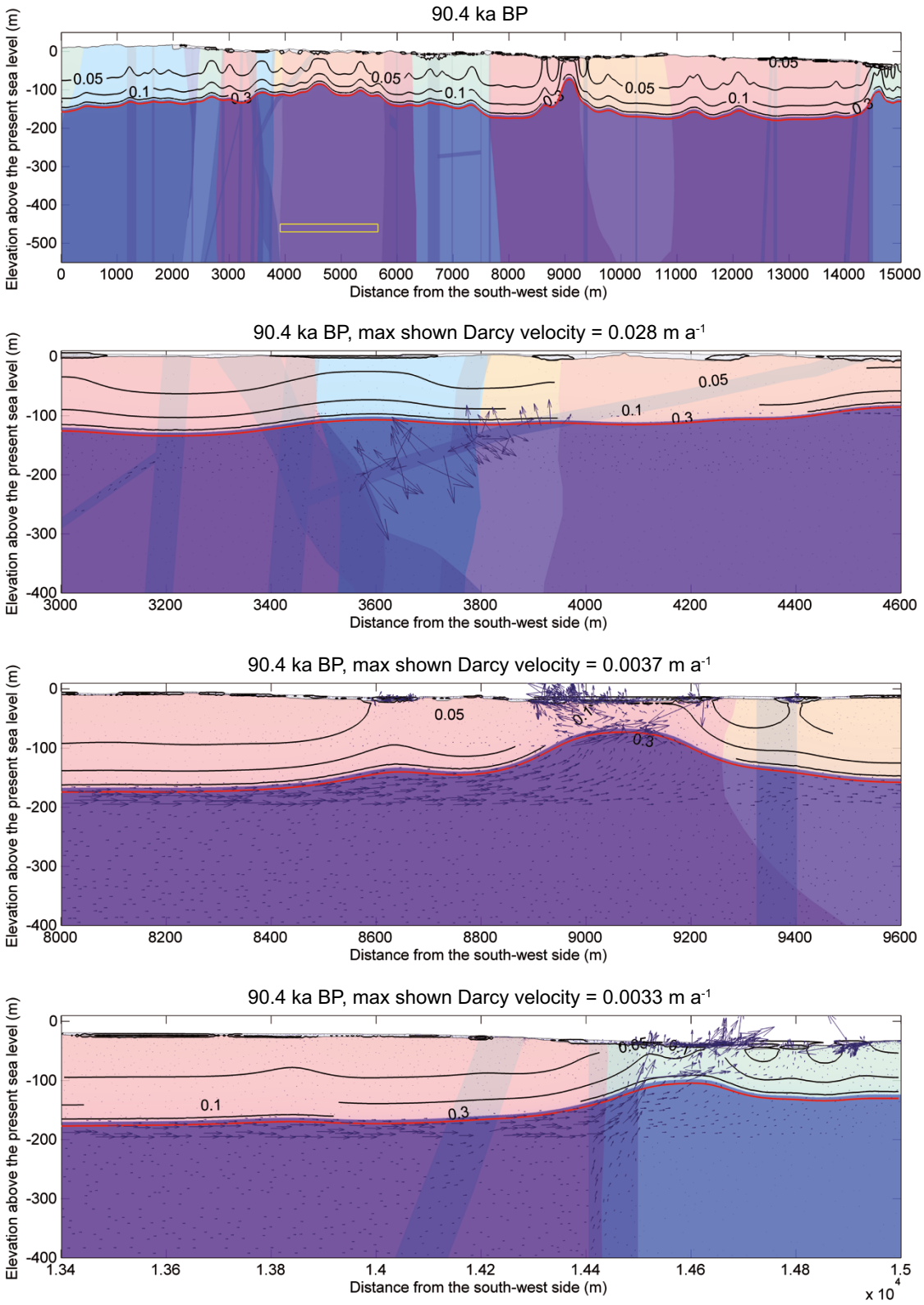

Figure 3-65. *Unfrozen volumetric (m^3 m^{-3}) groundwater content contours and Darcy flow directions at 90.4 ka BP for the dry variant of the reconstruction of last glacial cycle conditions. The upper panel shows the whole profile, followed by close-ups of the deformation zone ZFMA2 at ~4000 m, and the near-by area of the lakes at the distances 9000 m and 14600 m from the south–west side of the profile. Light colour shows the extent of perennially frozen ground, the red line shows the 0 °C isotherm (i.e. permafrost depth), and the yellow box in the upper panel shows the repository. For further examples of these results, see Hartikainen et al. (2010).*

Salinity concentration in reconstruction of last glacial cycle conditions

Given the permafrost and freezing results presented above, the associated results on salinity concentrations at times of 111.5, 95, 74, 70 ka BP are illustrated in Figure 3-66 and Figure 3-67. Due to low salinity concentrations at shallow depths, the impacts of freezing on salinity exclusion and redistribution are difficult to see from the results. However, under more severe conditions when the air temperature is decreased exceptionally, i.e. by 8 °C, the freezing occurs more intensively and an increase in salinity concentration due to the exclusion can be seen (Hartikainen et al. 2010).

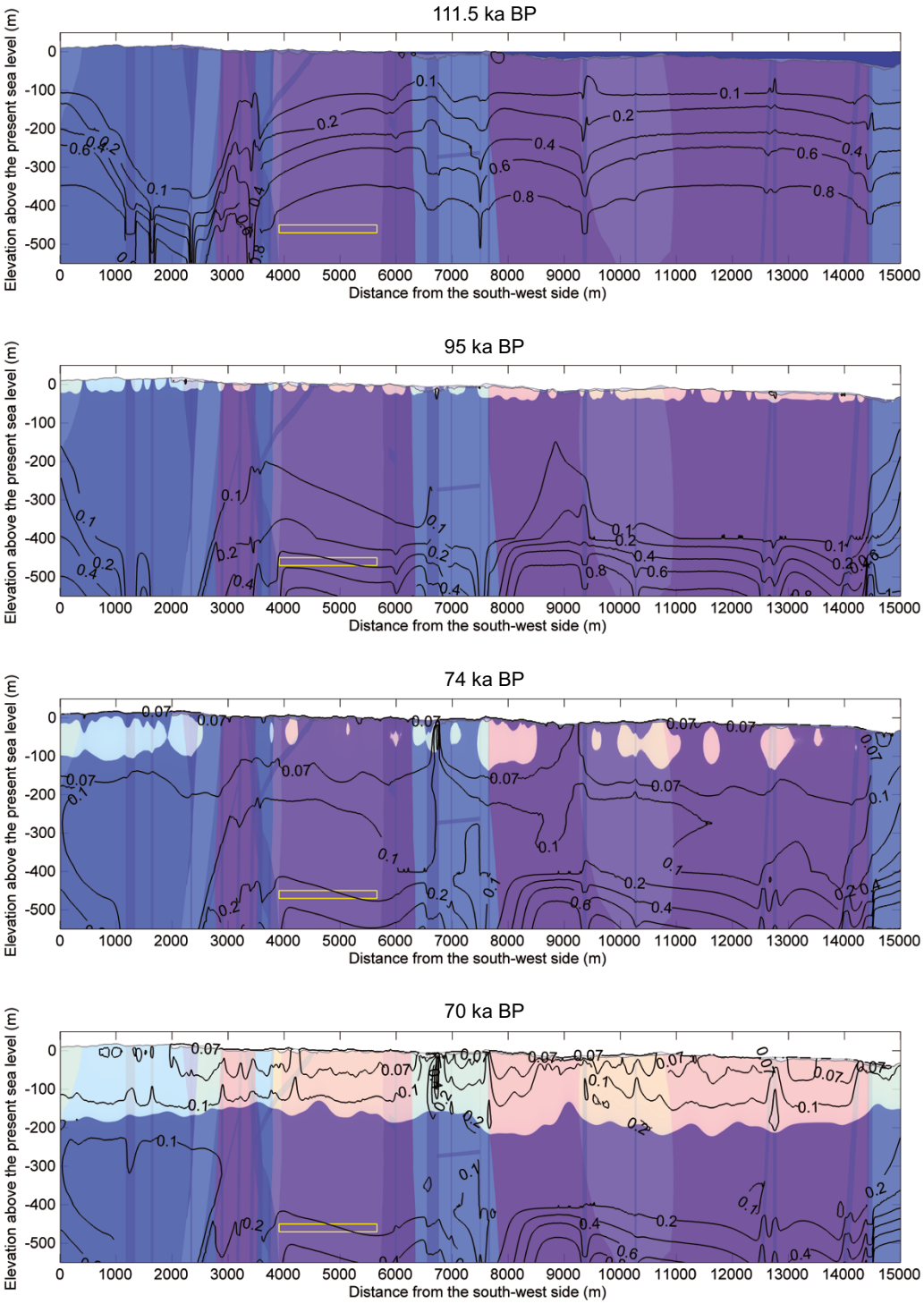

Figure 3-66. *Salinity concentration isolines in (mass-%) at times 111.5, 95, 74, 70 ka BP for the humid variant of the reconstruction of last glacial cycle conditions. The isolines show 0.07, 0.1, 0.2, 0.4, 0.6 and 0.8 mass-% salinity. Blue colour on the top of the profile at 111.5 ka BP shows the Baltic Sea and the light colour the extent of perennially frozen ground. For further examples of similar results, see Hartikainen et al. (2010).*

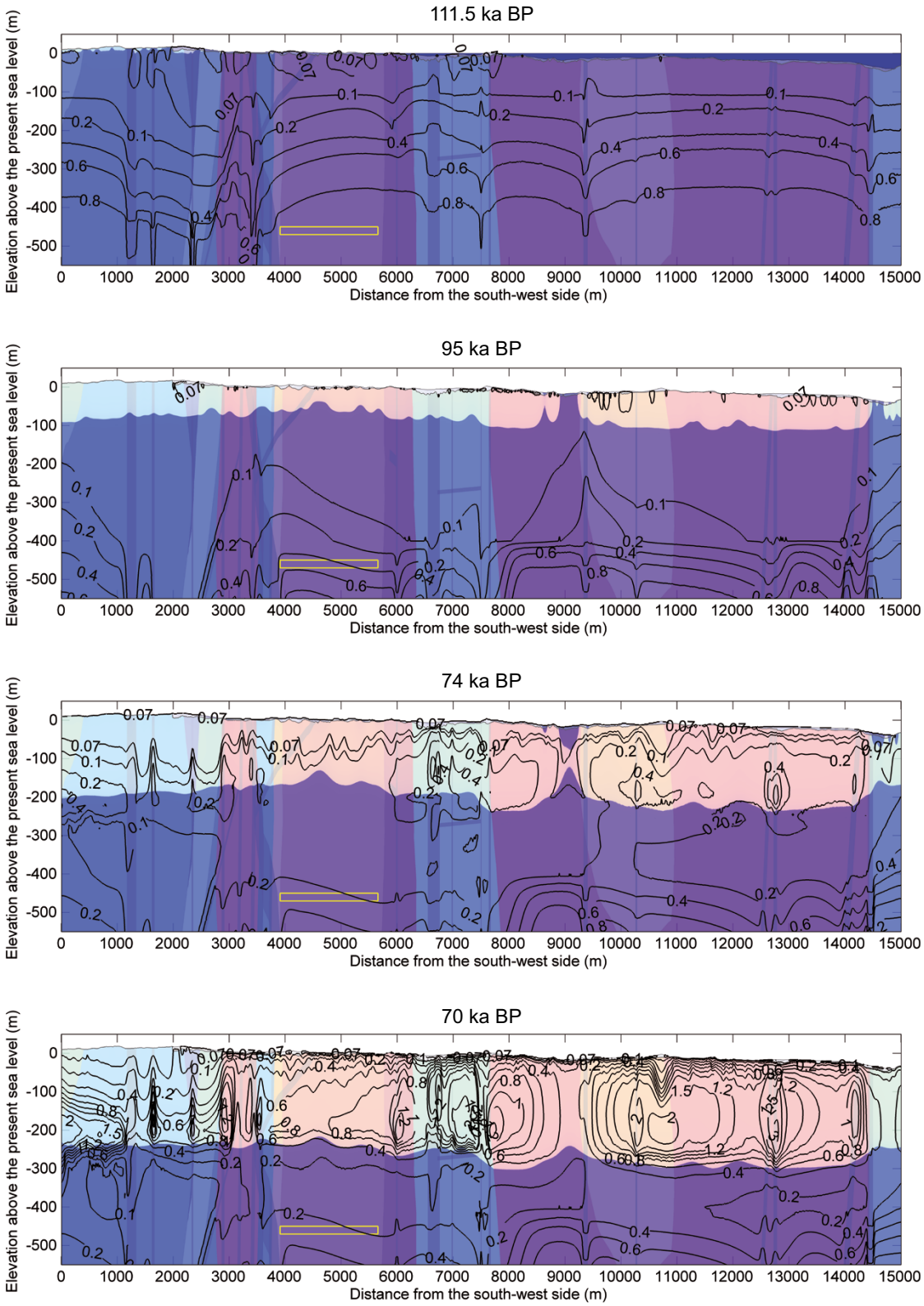

Figure 3-67. *Salinity concentration isolines in (mass-%) at times 111.5, 95, 74, 70 ka BP for the dry variant of the reconstruction of last glacial cycle conditions. The isolines show 0.07, 0.1, 0.2, 0.4, 0.6, 0.8, 1, 1.2, 1.5, 2 and 3 mass-% salinity. Blue colour on the top of the profile at 111.5 ka BP shows the Baltic Sea and the light colour the extent of perennially frozen ground. For further examples of similar results, see Hartikainen et al. (2010).*

Groundwater flow is an integral part of the salinity transport modelling, which hence suffers from the same restrictions as the 2D groundwater flow modelling. However, the results for salinity concentration (Figure 3-67) and Hartikainen et al. (2010, Figures 5-32 to 5-35) show that freezing can induce salt exclusion and transport when perennially frozen ground development exceeds 200 m depth. This can be seen as increased salinity concentrations extending downwards in front of the partially frozen bedrock. At shallow depths, the impacts of freezing cannot be seen since the salinity concentration of the groundwater has been diluted prior to the development of perennially frozen ground. The increased salinity concentration within the perennially frozen ground is mainly because salt transport occurs more slowly than the freezing zone advances.

Description and results of sensitivity experiments

Sensitivity experiment 1 – uncertainty in air temperature

In sensitivity experiment 1, the objective was to investigate the impact of the estimated uncertainty in the air temperature curve. The description of the temperature curve and its estimated uncertainty is found in Appendix A. From this description, it is estimated that an uncertainty range of ± 6 °C is relevant for the temperature curve used as input. In addition, it was investigated how much the air temperature curve is required to be lowered to get the 0 °C, −2 °C and −4 °C isotherms to reach the 450 m repository depth. Based on the SR-Can results (SKB 2006a), temperature shifts of 4, 6, 8, 10, 12, 14 and 16 °C were chosen (Figure 3-68). As a pessimistic case, the dry variant of the reconstruction of last glacial cycle conditions was simulated, since it results in deeper permafrost than the humid variant. The mean thermal properties of the subsurface were used.

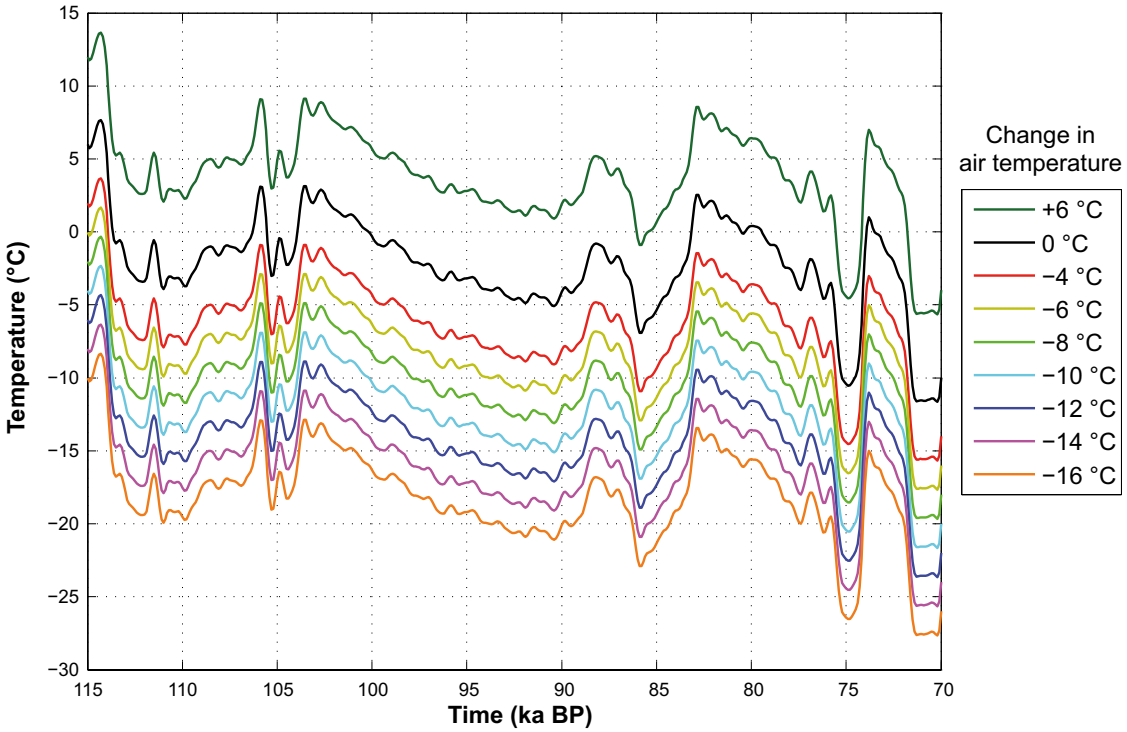

Figure 3-68. *Investigated temperature evolutions after shifting the entire reconstructed last glacial cycle temperature curve by −16, −14, −12, −10, −8, −6, −4, 0 and +6 °C compared to the reconstruction of the last glacial cycle. The 0 °C curve constitutes the temperature curve reconstructed for the last glacial cycle.*

The evolution of maximum permafrost depth and maximum depth of perennially frozen ground at the repository location considering mean thermal properties and the air temperature changed by −6, 0 and +6 °C are shown in Figure 3-69. The evolution of maximum 0 °C isotherm depth, i.e. maximum permafrost depth, and maximum depth of perennially frozen ground over the repository and the whole profile for the dry variant of the reconstruction of last glacial cycle conditions considering mean thermal properties and the air temperature changed by −4, −6, −8, −10, −12, −14 and −16 °C are shown in Figure 3-70 and Figure 3-71. The evolution of maximum −2 °C and −4 °C isotherm depth over the repository are shown in Figure 3-72 and Figure 3-73, respectively. It can be seen that temperature shifts of ~8, ~10 and ~14 °C are needed to get the 0 °C, −2 °C and −4 °C isotherms to reach the repository at the time with deepest permafrost at 70 ka BP. For details on the setup and results of this experiment, see Hartikainen et al. (2010).

The results from the investigation of uncertainties in air temperature show that a 6 °C lowering of the entire temperature curve reconstructed for the last glacial cycle (corresponding to the estimated maximum uncertainty in the temperature curve, Appendix A) increased permafrost depth by almost 60 %, from the range of ~180–260 m to ~290–410 m, while a corresponding change of the entire curve of +6 °C reduce permafrost depth by 60 to 75 %, to a range of ~40–100 m (Figure 3-69). A similar effect can be seen in the depth of perennially frozen ground, i.e. the temperature curve shift of −6 °C results in a change from the range ~190–260 m to ~280–380 m, while a +6 °C temperature shift reduces the range to ~40–100 m. In addition, the results in Figure 3-70 show that, for the dry variant of the last glacial cycle, the temperature curve reconstructed for the last glacial cycle needs to be lowered by almost 8 °C to make permafrost reach the repository depth. Furthermore, the results show that a shift of the reconstructed temperature curve of ~10 °C and ~14 °C are needed to get the −2 °C and −4 °C isotherms to reach the repository depth (Figure 3-72 and Figure 3-73). The major part of the difference (of up to more than 100 m) between results for the repository location and results from the entire profile (Figure 3-70 and Figure 3-71) is due to the heat from the repository. The effect of topography is minor and further reduced with depth. A less important factor is that some rock domains (RFM026, RFM033, RFM034, RFM040) outside the repository have higher thermal conductivity (2.8 %) than the one (RFM029) where the repository is located.

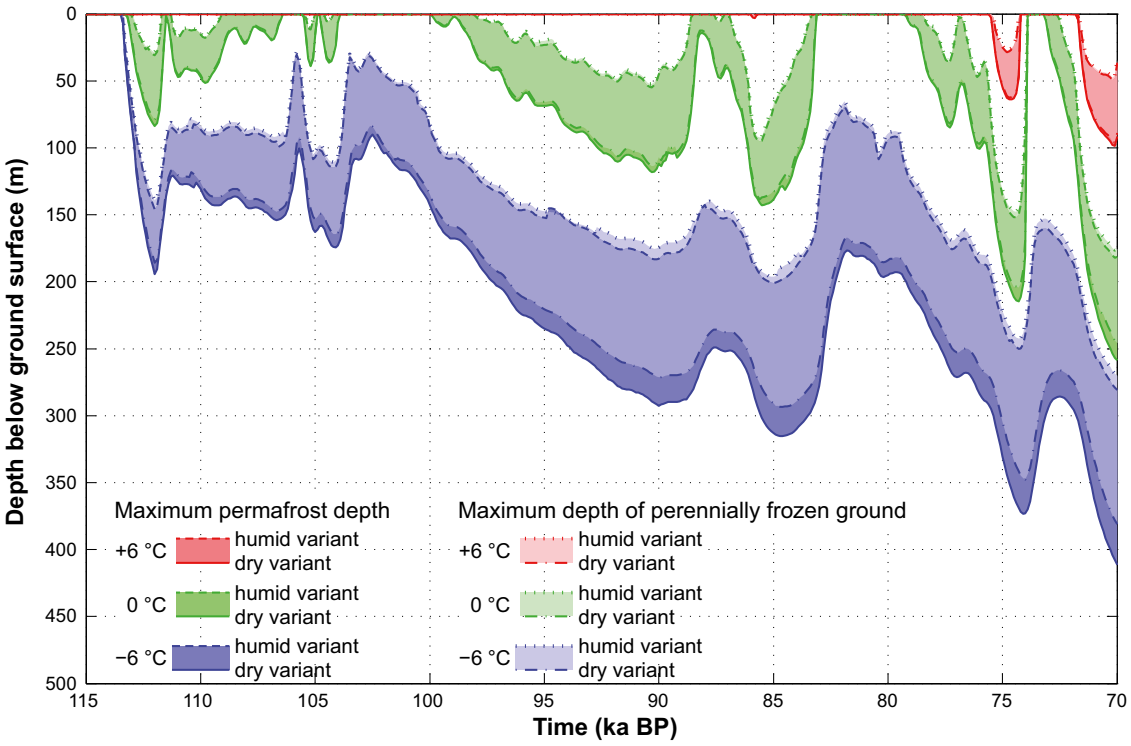

Figure 3-69. *Result of sensitivity experiment on uncertainty in air temperature. Evolution of maximum permafrost depth (solid lines) and maximum depth of perennially frozen ground (dashed lines) over the repository location considering mean thermal properties and the air temperature curve changed by −6, 0 and +6 °C. The shaded areas in blue, green and red represents the range when considering the dry and humid climate variants. Note that the results for permafrost and perennially frozen ground overlap to a large degree.*

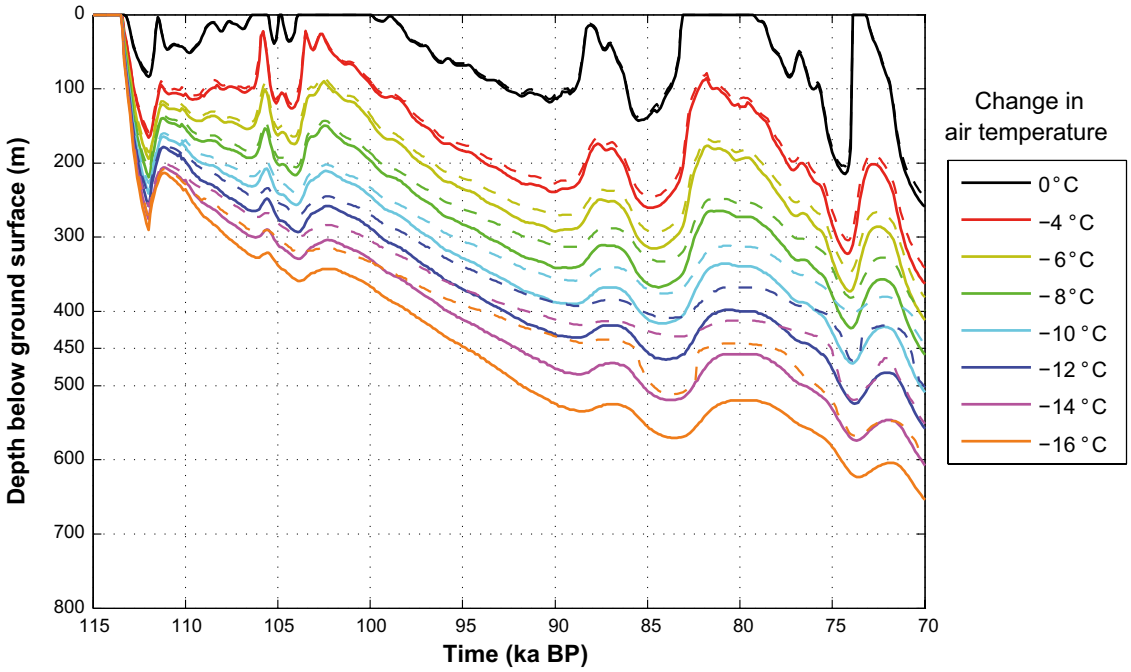

Figure 3-70. *Evolution of maximum permafrost depth (black solid line) and maximum depth of perennially frozen ground (black dashed line) at the repository location for the dry variant of the reconstruction of last glacial cycle conditions. The figure also shows corresponding results with the air temperature curve lowered by −4, −6, −8, −10, −12, −14 and −16 °C compared with the reconstruction of the last glacial cycle (coloured lines).*

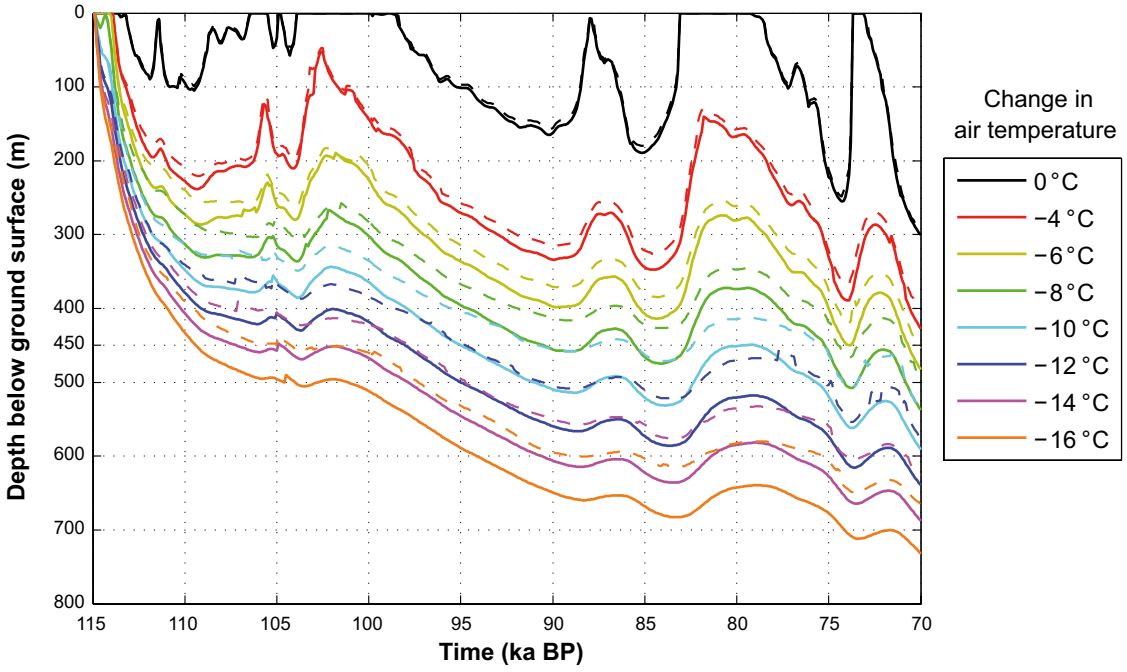

Figure 3-71. *Evolution of maximum permafrost depth (black solid lines) and maximum depth of perennially frozen ground (black dashed lines) over the whole profile for the dry variant of the reconstruction of last glacial cycle conditions. The figure also shows corresponding results with the air temperature curve lowered by −4, −6, −8, −10, −12, −14 and −16 °C (coloured lines).*

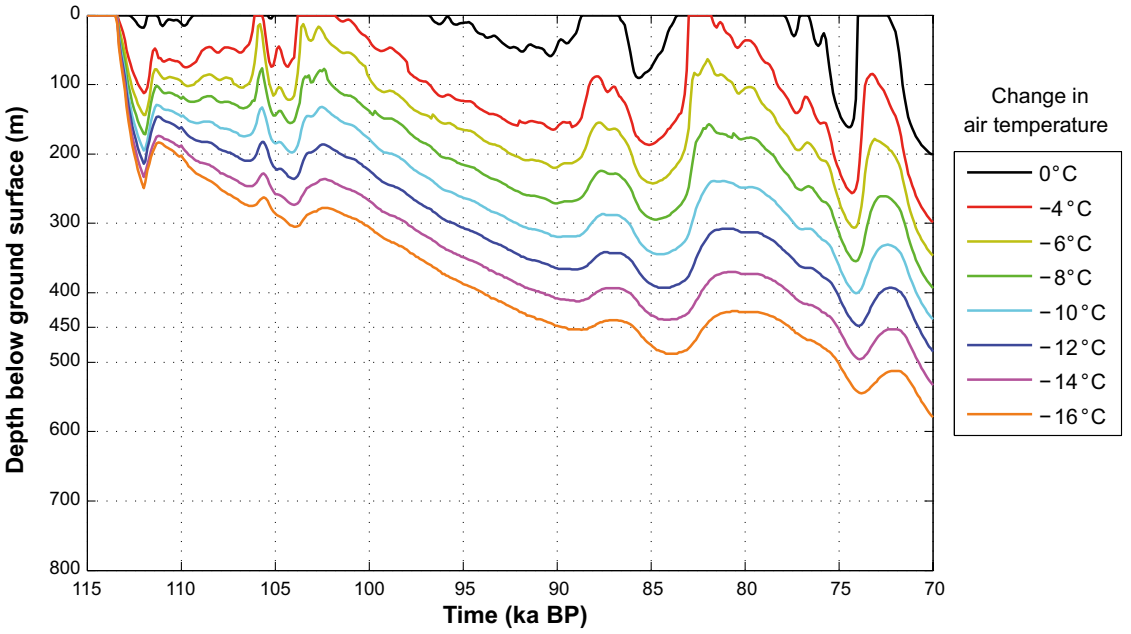

Figure 3-72. *Evolution of maximum −2 °C-isotherm depth at the repository location for the dry variant of the reconstruction of last glacial cycle conditions (black line). The figure also shows corresponding results with the air temperature curve lowered by −4, −6, −8, −10, −12, −14 and −16 °C compared with the reconstruction of the last glacial cycle (coloured lines).*

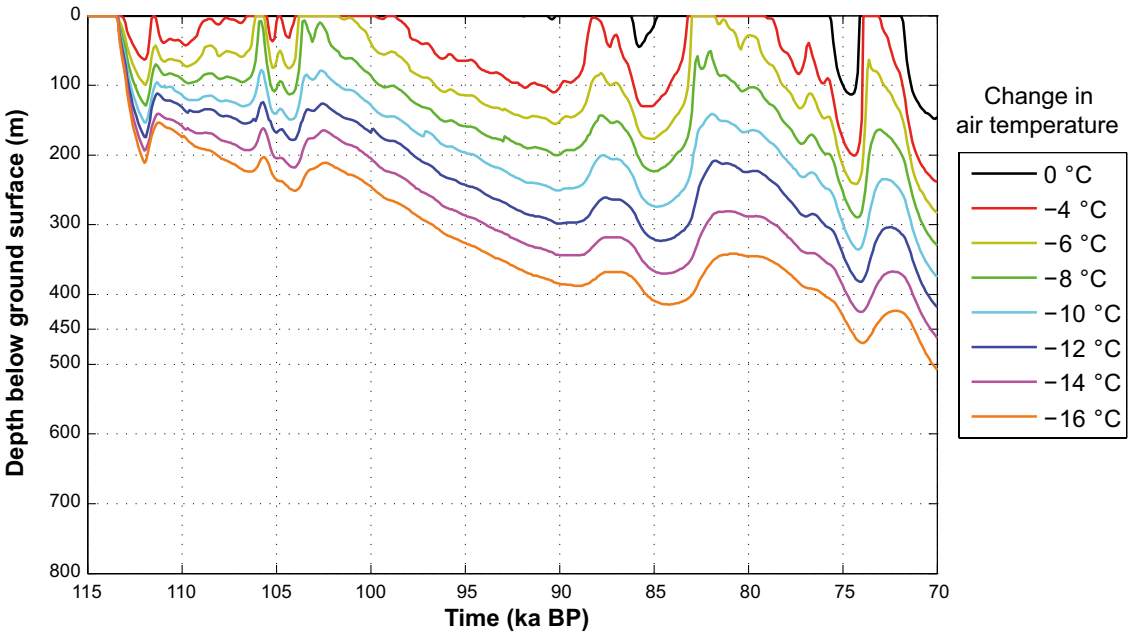

Figure 3-73. *Evolution of maximum −4 °C-isotherm depth at the repository location for the dry variant of the reconstruction of last glacial cycle conditions (black line). The figure also shows corresponding results with the air temperature curve lowered by −4, −6, −8, −10, −12, −14 and −16 °C compared with the reconstruction of the last glacial cycle (coloured lines).*

Sensitivity experiment 2 – uncertainty in geothermal heat flow

Sensitivity experiment 2 investigated the effects of uncertainties in geothermal heat flow. The mean surface level value of 61 mW m^{-2} and the range from −14 % (minimum) to +12 % (maximum) (Sundberg et al. 2009) were used for the dry climate variant of the reconstruction of last glacial cycle conditions. For details on the setup of this experiment, see Hartikainen et al. (2010). The results show that a variation of −14 % to +12 % in geothermal heat flow can cause an approximate fluctuation of +8.0 % to −6.3 % (~280 m to ~240 m) in permafrost depth, and correspondingly an approximate fluctuation of +7.7 % to −5.7 % (~260 m to ~230 m) in the depth of perennially frozen ground.

Sensitivity experiments 3 and 4 – uncertainty in bedrock thermal conductivity and thermal diffusivity

Sensitivity experiment 3 was made to study the consequences of uncertainty in thermal conductivity (mean, minimum and maximum). In sensitivity experiment 4, the uncertainty was investigated in relation to the mean, minimum and maximum thermal diffusivities. In addition, the effect of heterogeneity of thermal properties on the development of permafrost and frozen ground was studied by using mixed thermal diffusivities, which were obtained by using values of highest difference for adjacent rock domains, see Hartikainen et al. (2010). For details on the setup of this experiment, see Hartikainen et al. (2010).

The results for thermal conductivity indicated that the mean variation of −6.1 % to +8.6 % in thermal conductivity can cause an approximate fluctuation of −4.6 % to +2.7 % (~250 m to ~270 m) in permafrost depth, and correspondingly an approximate fluctuation of −4.1 % to +2.7 % (~240 m to ~250 m) in perennially frozen ground depth. The uncertainty in thermal diffusivity causes a slightly larger variation in permafrost depth than solely the uncertainty in thermal conductivity. The results demonstrate that the mean variation of −11.5 % to +14.6 % in thermal diffusivity can cause an approximate fluctuation of −6.0 % to +3.4 % (~240 m to ~270 m) in permafrost depth, and correspondingly an approximate fluctuation of −5.5 % to +3.4 % (~230 m to ~250 m) in perennially frozen ground depth. In addition, the variation in thermal properties between adjacent rock domains has a minor effect on the development of permafrost and perennially frozen ground. The reason for this is probably the flat topography of the site, in consequence of which heat transfer mainly takes place vertically. This is also supported by the results for the ground temperature and perennially frozen ground (Figure 3-57 and Figure 3-58) which show rather uniform permafrost development with depth when it occurs in continuous form.

Sensitivity experiment 5 – combination of uncertainties in bedrock thermal properties

In sensitivity experiment 5, the objective was to investigate the combination of uncertainties in dominant thermal properties of the bedrock. The limits for the uncertainty interval were obtained by combining the thermal properties that are anticipated, based on results from SKB (2006a), to enhance permafrost development, i.e. maximum thermal conductivity, minimum heat capacity and minimum geothermal heat flow, as well as the thermal properties that are expected to diminish permafrost development, i.e. minimum thermal conductivity, maximum heat capacity and maximum geothermal heat flow. The dry variant of the reconstruction of last glacial cycle conditions was simulated. For details on the setup of this experiment, see Hartikainen et al. (2010). The resulting evolution of maximum permafrost depth and maximum depth of perennially frozen ground over the repository are shown in Figure 3-74. The results show that the combined uncertainties can cause a variation of −8.9 % to +12.2 % (~240 m to ~290 m) in the permafrost depth and a variation of −6.2 % to +14.4 % (~230 m to ~280 m) in the depth of perennially frozen ground.

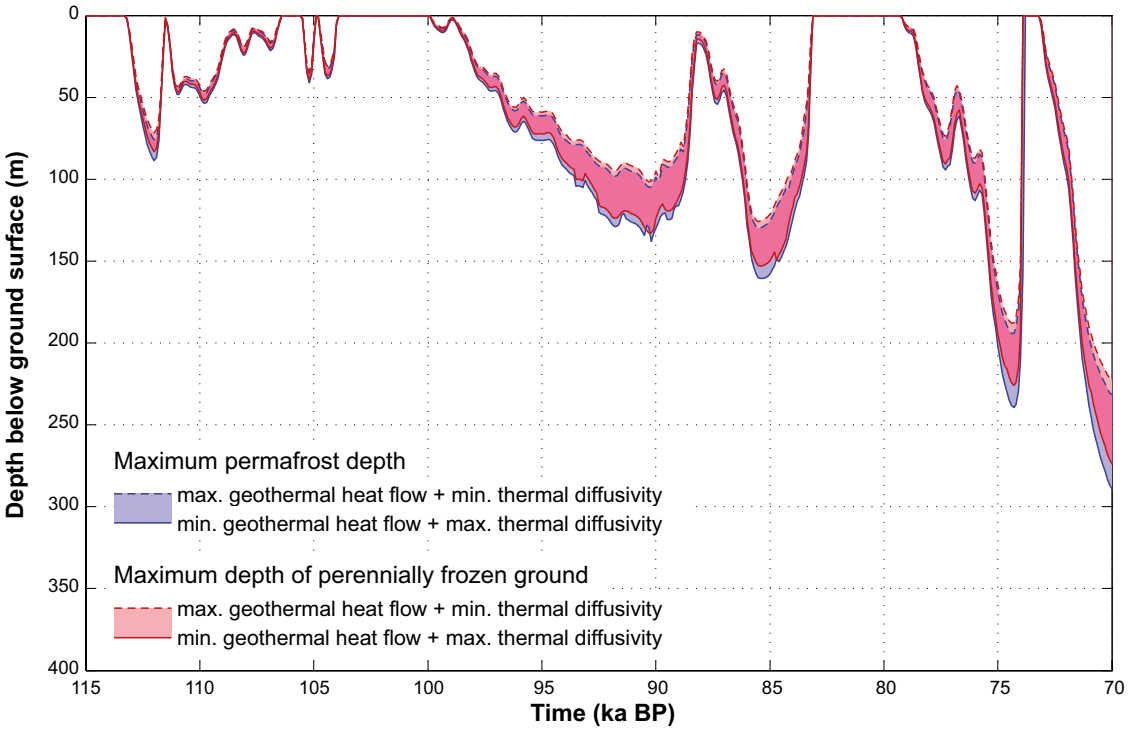

Figure 3-74. *Evolution of maximum permafrost depth and maximum depth of perennially frozen ground over the repository for the dry variant of the reconstruction of last glacial cycle conditions considering combined uncertainty in bedrock thermal conditions and geothermal heat flow. The shaded area in blue and red represents the range when considering the dry and humid climate variants. The lilac colour indicates that the results for permafrost and perennially frozen ground overlap.*

Sensitivity experiment 6 – combination of uncertainties in surface and bedrock thermal properties

In sensitivity experiment 6 the uncertainties in subsurface thermal properties from experiment 5 were combined with the uncertainties in surface conditions (excluding air temperature). For the reconstruction of last glacial cycle conditions, the uncertainty interval was obtained by combining the dry variant with the thermal properties enhancing permafrost development, and the humid variant of the same case with thermal properties diminishing permafrost development.

Figure 3-75 shows the evolution of maximum permafrost depth and maximum depth of perennially frozen ground over the repository for the reconstruction of last glacial cycle conditions considering combined uncertainties in surface conditions and thermal properties as described in Hartikainen et al. (2010, Sections 2.2 and 2.4, and Appendices E, H, I and J). The calculated uncertainty range for the maximum permafrost depth at 70 ka BP is 170–290 m and for the maximum depth of perennially frozen ground 170–280 m. For details on the setup and results of this experiment, see Hartikainen et al. (2010).

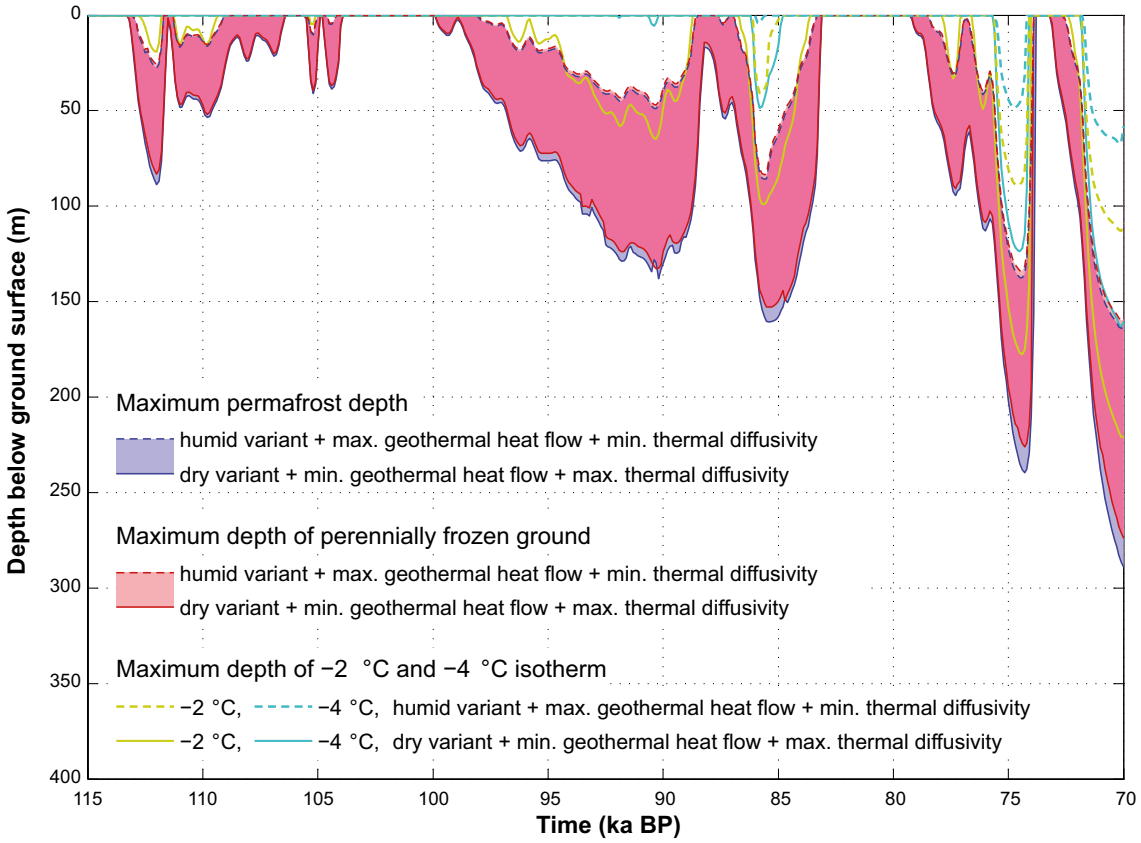

Figure 3-75. *Evolution of maximum permafrost depth, maximum depth of perennially frozen ground and maximum depth of −2 and −4 °C isotherms over the repository for the reconstruction of last glacial cycle conditions considering combined uncertainties in surface conditions and bedrock thermal properties (including geothermal heat flow). The shaded area in blue and red represents the range when considering the dry and humid climate variants. The lilac colour indicates that the results for permafrost and perennially frozen ground overlap.*

Sensitivity experiment 7 – combination of uncertainties in air temperature, surface conditions and bedrock thermal properties

This case was studied to illustrate the effect of setting *all* known uncertainties to their extreme end (air temperature, surface conditions, geothermal heat flow and all thermal properties) so that they either promote or reduce permafrost growth. Note that the case was constructed for illustrational purposes, and that having this combination of parameter settings describes a virtually unrealisable case. For this purpose, both the dry and humid variants of the reconstruction of last glacial cycle conditions were used together with an air temperature change of ± 6 °C and all thermal properties and geothermal heat flow either enhancing or diminishing permafrost development, see Hartikainen et al. (2010, Sections 2.2 and 2.4, and Appendices E, H, I and J). Based on the estimates of uncertainty in the air temperature curve (Appendix A) and on the nature of the conceptual- and data uncertainty associated with the temperature curve, see the **Data report**, it is considered adequate to lower the temperature curve reconstructed for the last glacial cycle (Figure 3-44) by 6 °C as a most pessimistic case in the sensitivity analysis for examining the effect of the temperature curve uncertainty for the reconstruction of last glacial cycle conditions.

Figure 3-76 shows the resulting evolution of maximum permafrost depth and maximum depth of perennially frozen ground over the repository. The results show, as expected, a very large fluctuation in both permafrost depth (~40 m to ~460 m) and perennially frozen ground depth (~40 m to ~420 m). These two cases indicate that if all uncertainties have their most pessimistic settings, which is considered to be an unrealistic case, permafrost is able to reach the repository depth of 450 m in the reconstruction of last glacial cycle conditions.

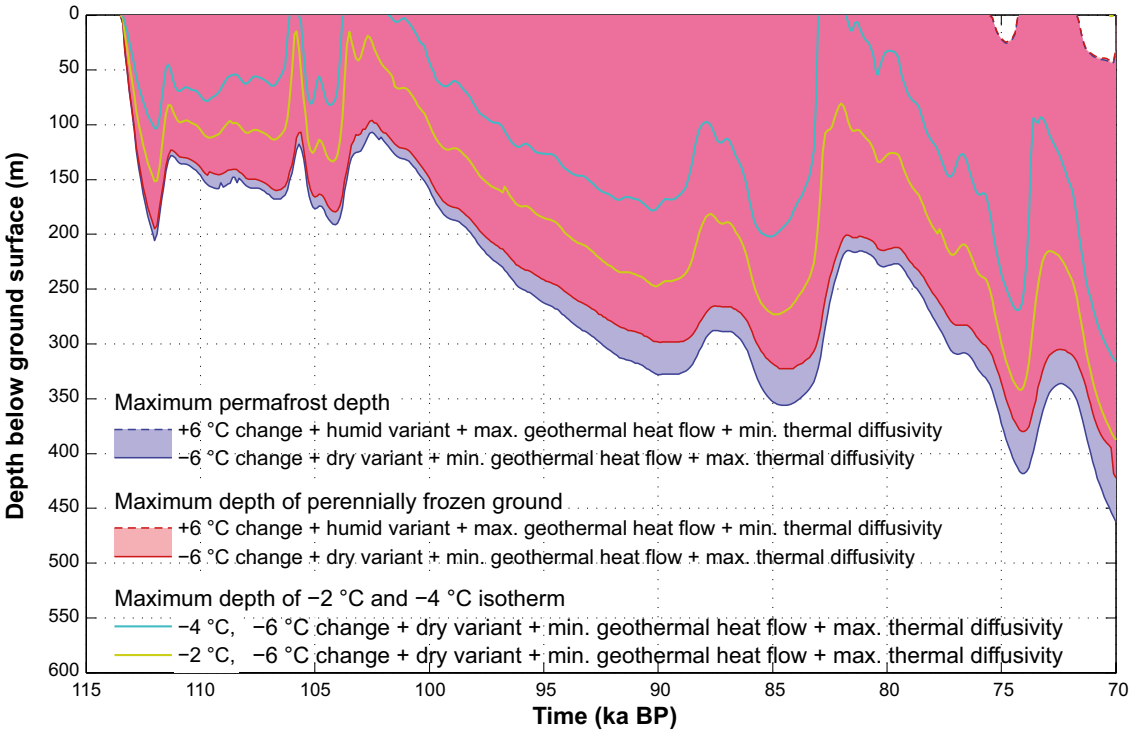

Figure 3-76. *Evolution of maximum permafrost depth, maximum depth of perennially frozen ground and maximum depth of the −2 °C and −4 °C isotherms over the repository for the reconstruction of last glacial cycle conditions considering the unrealistic combination of uncertainties in air temperature, surface conditions, geothermal heat flow and thermal properties all set in their most extreme position favouring permafrost growth.*

Sensitivity experiment 8 – repository heat

For illustrative purposes, sensitivity experiment 8 studied the effect of including or excluding the heat generated by the spent fuel. However, the heat from the repository should not be regarded an uncertainty. Cases with heat and without heat from the repository together with the dry variant of the reconstruction of last glacial cycle conditions were simulated. The resulting evolution of maximum permafrost depth and maximum depth of perennially frozen ground is illustrated in Figure 3-77. The results show, as expected, that the heat from the repository reduces the permafrost and perennially frozen ground depths, e.g. permafrost depth is reduced by ~38 % at 109700 years BP and by ~14 % at 70 ka BP (Figure 3-77). The calculated range for the maximum permafrost depth at 70 ka BP is 259–295 m and for the maximum depth of perennially frozen ground 246–280 m.

Sensitivity experiment 9 – convective heat transfer by groundwater flow

Sensitivity experiment 9 investigated the impact of convective heat transfer due to groundwater flow and salt transport on the evolution of permafrost and perennially frozen ground. Cases with and without 2D groundwater flow and salinity transport in the dry variant of the reconstruction of last glacial cycle conditions were simulated. The resulting evolution of maximum permafrost depth and maximum depth of perennially frozen ground over the repository with and without groundwater flow and salinity transport are shown in Figure 3-78.

The results show that the effect of convective heat transfer due to groundwater flow and salinity transport on the development of permafrost and perennially frozen ground is very weak. The permafrost depths with groundwater flow and salinity transport are less than a metre greater than those without it (for a permafrost depth of ~260 m). A somewhat larger difference in frozen depth (~5 metres) is possibly a consequence of reduced salinity concentration due to salt transport. It should again be emphasised that the results for groundwater flow and salinity are limited in validity by the 2D modelling approach. However, the topography of the site is rather flat and does not generate significant hydraulic gradients, suggesting that the inclusion of 3D flow would only have a minor impact on the results for non-glacial conditions.

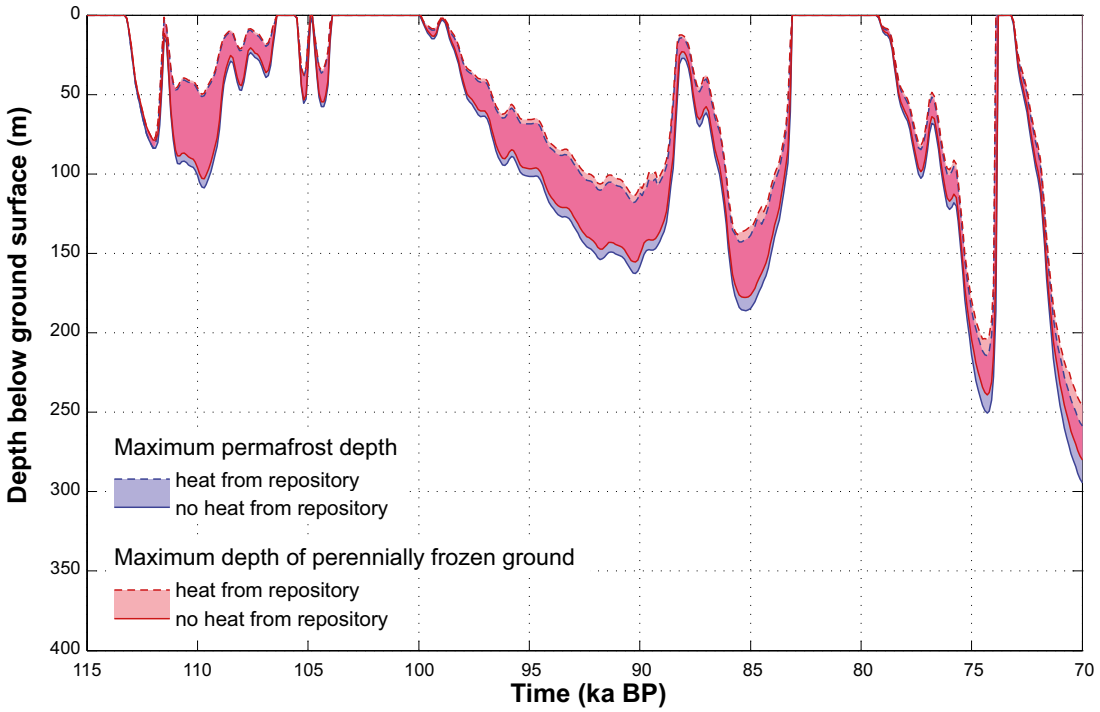

Figure 3-77 . *Evolution of maximum permafrost depth and maximum depth of perennially frozen ground over the repository for the dry variant of the reconstruction of last glacial cycle conditions considering mean thermal properties and variable heat production from the repository from zero to the reference value, see Hartikainen et al. (2010). The shaded area in blue and red represents the range when considering the dry and humid climate variants. The lilac colour indicates that the results for permafrost and perennially frozen ground overlap.*

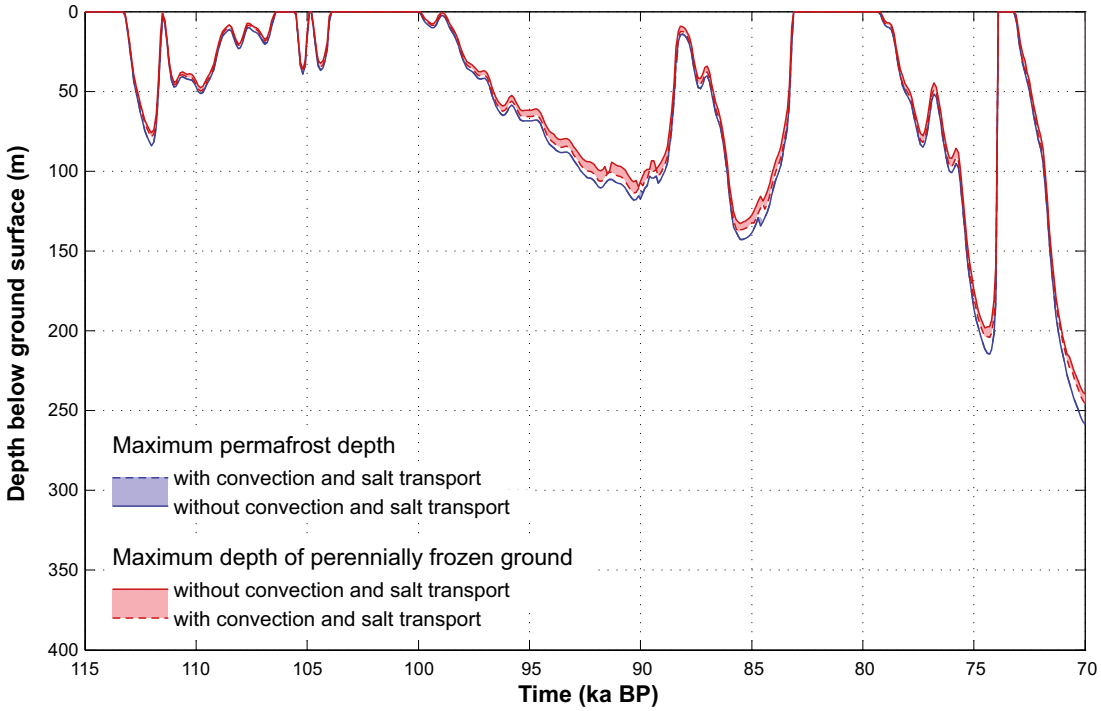

Figure 3-78. *Evolution of maximum permafrost depth and maximum depth of perennially frozen ground over the repository for the dry variant of the reconstruction of last glacial cycle conditions considering mean subsurface thermal conditions, and with and without 2D groundwater flow and salinity transport. The shaded area in blue and red represents the range within which a result is expected to lie when considering groundwater flow and salt transport between the reference case and case without groundwater flow and salt transport. The lilac colour indicates that the results for permafrost and perennially frozen ground overlap.*

A study dedicated at looking at 3D groundwater flow under permafrost conditions at Forsmark, using a simplified approach to model permafrost, is found in Vidstrand et al. (2010). The same study also includes a comparison between the results from the simplified permafrost solution (as used in DarcyTools), and the 2D permafrost study reported here and in Hartikainen et al. (2010).

Main conclusion from the 2D permafrost modelling study

The conclusion drawn from the 1D permafrost investigations (SKB 2006a) that the surface conditions are the driving force for the development of permafrost has been strengthened by the 2D study. In addition, the conclusion that the subsurface conditions and the heat from the spent fuel act as either reducing or enhancing factors for permafrost and perennially frozen ground development is also supported. The following main conclusions can be drawn from the 2D permafrost study:

- Given the temperature climate development reconstructed for the last glacial cycle, the study demonstrates how the site-specific spatial- and temporal development of permafrost and perennially frozen ground takes place at the Forsmark site, developing from sporadic-, to discontinuous- to continuous coverage in various combinations and extents.
- The study provides a full range of sensitivity analyses of uncertainties in sub-surface, and surface conditions, including the reconstructed input air temperature curve for the last glacial cycle.
- For the reconstruction of last glacial cycle conditions, the simulated maximum permafrost (the 0 °C isotherm) depth over the repository is between 180 and 260 m depending on the surface conditions. The corresponding range for the entire investigated profile is from 220 to 300 m.
- For the reconstruction of last glacial cycle conditions, the simulated maximum depth of perennially frozen ground over the repository is between 180 and 250 m depending on the surface conditions. The corresponding range for the entire investigated profile is from 210 to 300 m.
- The prevailing surface conditions, such as temperatures and surface moisture conditions, are the main factors governing the spatial and temporal development of permafrost and perennially frozen ground at the Forsmark site.
- Subsurface conditions, such as bedrock thermal properties, geothermal heat flow and groundwater salinity, modify the spatial and temporal development of permafrost and perennially frozen ground, but are of secondary importance for modelled permafrost depths compared with surface conditions.
- The variation in thermal properties along the profile as well as 2D groundwater flow only has a slight influence on permafrost (the 0 °C isotherm) development. Therefore, the uncertainties introduced by excluding lateral variations in thermal properties, boundary conditions and convective heat transfer in the 1D model study (SKB 2006a) are considered insignificant.
- If making the very pessimistic combination of setting all known uncertainties (in air temperature, surface conditions, bedrock thermal conductivity and heat capacity, and geothermal heat flow) in the condition most favourable for permafrost growth, permafrost may extend to 450 m depth in 45 ka in the reconstruction of last glacial cycle conditions. However, it should be noted that this combination of assumptions is very unrealistic.
- Under continuous permafrost conditions, the unfrozen groundwater content in the perennially frozen ground under lakes can exceed 10 % down to a ~50 m depth. This may indicate that taliks are able to form under lakes through perennially frozen ground if favourable groundwater flow conditions with open flow paths prevail. When the unfrozen groundwater content decreases below 10 %, groundwater flow is reduced considerably, and taliks are no longer able to form or survive.
- Freezing can induce salt exclusion and salt transport when perennially frozen ground develops deeper than ~200 m. At shallower depths the impacts of freezing are difficult to see since the salinity of groundwater has been diluted prior to the development of perennially frozen ground. When salt transport occurs more slowly than the freezing zone advances, the salinity concentration is increased within the perennially frozen ground.
- The uncertainty in dealing with groundwater flow with this permafrost model remains, since the 3D flow network is omitted in the 2D model. However, the topography of the site is rather flat to generate significant hydraulic gradients, suggesting that extension to 3D would only have a minor impact on the results for non-glacial conditions.

- The model uncertainty regarding the neglect of salinity transport in the 1D model (SKB 2006a) seems to be insignificant, mainly due to the low rock porosity, although the present 2D model is not able to describe the groundwater flow realistically.
- Based on the results and the investigations on ground temperature modelling by Sundberg et al. (2009) the uncertainty associated with determination of the ground surface temperature from the air temperature as well as with estimation of the in situ temperature and geothermal heat flow for the 1000–10000 m-depth for the thermal boundary and initial conditions of the model is reduced considerably.
- Further results from the 2D modelling are found in the *severe permafrost climate case* (Section 5.5).

3.4.5 Time perspective

Changes in annual ground surface temperature due to climate change can lead to development of permafrost and freezing of the ground. If the mean annual ground surface temperature decreases continuously from the present-day value to approximately −8 °C, permafrost can develop to the depth of 400 m in a period of 26 ka at Forsmark (Figure 3-41). Under periglacial conditions, permafrost can aggregate from some centimetres to some decimetres in a year whereas its degradation can take place several times faster than that (Figure 3-46), especially when the surface temperature rises above 0 °C and permafrost decays simultaneously from the bottom upwards and from the top downwards. Large degradation rates can occur also at the onset of glaciation when the surface temperature rises sharply to the freezing point beneath an advancing ice-sheet.

3.4.6 Handling in the PSAR

The last-glacial-cycle evolution of permafrost has been investigated by means of numerical modelling. The results were used to construct parts of the PSAR *reference glacial cycle climate case*. A broad range of sensitivity experiments was conducted to describe the effects of uncertainties in bedrock, surface or climate conditions. Two numerical permafrost models were used, a 1D model that was used for simulations of permafrost at the repository location, and a 2D model that investigated spatial development of permafrost along a profile that crossed the repository site. The permafrost models include a mathematical expression for freezing and thawing of saline-groundwater-saturated bedrock. The bedrock is considered as an elastic porous medium and the groundwater as an ideal solution of water and ionic solvents. The models are based on the principles of continuum mechanics, macroscopic thermodynamics and the theory of mixtures, and are capable of describing heat transfer, freezing of saline water, groundwater flow and deformations of bedrock. To capture the most important factors and parameters affecting the development of permafrost, sensitivity analyses have been performed considering the following issues:

- Surface conditions and climate.
- Subsurface conditions.
- Presence of the repository.

Surface temperatures, together with the influence of surface covers such as snow, vegetation and water bodies, have been included as factors of importance in the surface conditions. The investigated subsurface conditions are thermal properties of the bedrock and geothermal heat flow. The heat generated by the spent fuel has been included in most simulations. The calculations were carried out in two steps; 1) by using constant surface temperatures, and subsequently 2) using surface temperatures based on site-specific climate cases. For further, detailed information on the permafrost modelling, see the preceding parts of Section 3.4.4.

3.4.7 Handling of uncertainties in the PSAR

Uncertainties in mechanistic understanding

There are no major uncertainties in understanding of mechanistic processes regarding permafrost development. Minor uncertainties in the 1D modelling experiments are associated with the fact that the exclusion of salts in freezing of groundwater is not included. The process of freeze-out of salts is included in the 2D modelling performed.

Model simplification uncertainty

The major model simplification in the 1D permafrost modelling study is the exclusion of lateral variations in physical properties, boundary conditions and geometry. For example, full consideration of the anisotropy of thermal conductivity and heat capacity and the features of water bodies and topography, as well as the heat generation from the spent fuel, requires 3D modelling. However, this is to a large extent taken care of by the 2D modelling study reported here.

The 1D modelling approach could, in certain situations, result in somewhat higher temperatures than would be calculated using a 2D or full 3D approach. In the context of permafrost development, the effect of groundwater flow, cooling down the bedrock, is the most important factor here. However, compared with heat conduction, groundwater flow has only a minor role in permafrost development, as indicated by the 2D modelling results that included groundwater flow. Furthermore, the anisotropy of thermal properties is not a problem in 1D or 2D, since one can choose a combination of thermal properties that would give lowest temperatures, or at least very close to the lowest temperatures. Therefore, it is unlikely that 3D simulations would yield notably lower temperatures than the range obtained by the full series of 1D and 2D sensitivity modelling that have been performed.

The 2D modelling approach used for studying talik formation has limitations since the important 3D groundwater flow network is missing.

Input data and data uncertainty

Bedrock data

Some data uncertainty exists when it comes to thermal conductivity and heat capacity of rock at the Forsmark site. In the calculation of ground temperature and the rate of freezing, thermal conductivity is the most important input parameter in terms of thermal properties of the ground. Some uncertainty also exists in determination of hydraulic and mechanical properties of bedrock and salinity concentrations of groundwater versus depth, see appendices in Hartikainen et al. (2010) and references therein.

The *in situ* ground temperature has been measured in boreholes to a depth between 500 and 1400 m. Between different boreholes the temperature varies in a range of 2 °C (SKB 2005, 2006a, b). A considerable uncertainty in the 1D permafrost study is associated with determination of the *in situ* temperature and geothermal heat flow in the depth range of 1000–10000 m for the thermal boundary and initial conditions of the model. Based on the results and the investigations on ground temperature modelling by Sundberg et al. (2009), the uncertainty associated with determination of the ground surface temperature from the air temperature as well as with estimation of the *in situ* temperature and geothermal heat flow for the 1000–10000 m-depth for the thermal boundary and initial conditions of the model have been reduced considerably in the 2D permafrost modelling study.

The uncertainty in geothermal heat flow was investigated and described in Sundberg et al. (2009).

In general, the uncertainty in thermal characteristics of the bedrock and geothermal heat flow has a significantly smaller impact on modelled permafrost and freezing depths than uncertainties related to ground conditions and climate.

Surface conditions

As a complement to the 1D permafrost studies made for Forsmark (SKB 2006a, Sections 3.4 and 4.5.1), the main objective of the 2D modelling study was to investigate impacts of surface conditions on the spatial (along the profile) development of permafrost and perennially frozen ground using site-specific information on climate and landscape features including water bodies and topography. An approach based on TWI was introduced to describe the vegetation and snow cover in relation to the prevailing evolving climate and surface moisture conditions. TWI was used to identify and locate four relevant surface condition types, dry, moist-humid, wet and peatland, that could be expected to occur on the profile in Boreal-, Subarctic- and Arctic climate zones. Thereafter, ground surface temperatures were calculated from an air temperature curve by making use of *n*-factors that yield a statistical relation between the air and ground surface temperatures in consideration of climate and surface moisture

conditions (Hartikainen et al. 2010). Due to considerable uncertainties related in description of surface conditions by TWI and modelling of ground surface temperatures by means of *n*-factors, two variants, one humid and one dry for the reconstruction of last glacial cycle conditions and a *severe permafrost climate case* were analysed.

Temperature curve

Major uncertainties exist in the temperature curve used for the permafrost modelling, including uncertainties as to its representativity for the last glacial cycle climate as well as for its application to describe possible future climate cases. A detailed discussion and description of these uncertainties can be found in Appendix A and the **Data report**. To cover the estimated uncertainties in the air temperature curve reconstructed for the last glacial cycle, a large range of sensitivity cases and alternative temperature climate variations of the temperature curve have been analysed. This was also motivated by the fact that the variation in surface conditions and climate has a larger impact on modelled permafrost and freezing depth than bedrock thermal conditions and geothermal heat flow.

Input data for the permafrost modelling are described in Hartikainen et al. (2010 Appendix H) and in the **Data report**.

In addition, to cover the uncertainty in future climate development, a case with cold non-glaciated conditions, occurring during a significantly longer period than analysed here, is presented in Section 5.5.

Repository heat

In the 1D permafrost study made for SR-Can, repository heat was initiated at 120 ka BP, whereas in the 2D study made for SR-Site and the PSAR it was initiated at 112 ka BP. However, this temporal difference has a negligible effect on the timing of the first permafrost over the repository (see Figure 3-77) since it is the surface conditions that are the main factor for the initiation and development of permafrost. Furthermore, the difference in timing also has a negligible effect on the maximum permafrost and freezing depths, since, at the time when permafrost depths are largest (at ~ 70 ka BP), repository heat has declined very much (to ~ 0.3 % of the initial value). If heating had been initiated at 120 ka BP in the 2D study, it is estimated that the maximum permafrost and freezing depths would have been no more than a few metres deeper.

3.5 Surface denudation

3.5.1 Overview/general description

The downwearing of the Earth's surface by exogenic processes is accomplished by weathering, erosion, and transportation of material. The combined effect of all weathering and erosion processes is referred to as denudation, i.e. denudation is the sum of the processes that results in the wearing away or the progressive lowering of continental relief. The energy needed for the denudation processes is gained from endogenic and exogenic sources. Glacial erosion is usually regarded as the dominant erosion process in Fennoscandia during the Quaternary. However, as large parts of Fennoscandia were not covered by ice during significant periods of the Quaternary (Porter 1989) including the last glacial cycle (Section 4.2), other denudation processes must also be considered in quantifications of erosional budgets (e.g. Lidmar-Bergström 1997).

Weathering

Weathering can be defined as mechanical and/or mineralogical break down of rock to form regolith through the cumulative effects of physical, chemical and biological processes operating at or near the surface (e.g. Reiche 1950, Selby 1993). The definition indicates that weathering occurs when minerals/rocks are exposed to temperatures, pressures and moisture conditions characteristic of the atmosphere and hydrosphere, i.e. in a near-surface environment that differs significantly from the conditions at depth in which most igneous and metamorphic rocks, as well as lithified sedimentary rocks, were formed. In this way, the alteration of rocks by weathering forms new materials (minerals) that are in near-equilibrium with conditions at or near the Earth's surface.

By definition, weathering occurs *in situ* and does not directly involve erosion. This means that it leads to the formation of a residual material that differs from the parent, unweathered rock with respect to its physical and chemical properties. Weathering normally lowers the strength of rock and increases the permeability of the surface material and thus makes it more prone to mass wasting and easy to erode by running water, glaciers, wind etc. In addition, it is also an important prerequisite for the widespread development of flora and fauna on land by releasing nutrients to soils that are taken up by plants and other organisms.

Weathering is generally divided into physical-, chemical- and biological components. Physical or mechanical weathering occurs when volumetric expansion or other stresses lead to failure and disintegration of the rock. For example, volume changes due to decreased overburden load can result in the creation of new fractures at various scales. Crystallisation and volumetric alteration of salt crystals, freezing of water and freeze-thaw effects, as well as thermal fatigue due to repeated (diurnal) heating and cooling, may also cause physical weathering.

Chemical weathering comprises reactions between water and rock minerals. Examples are solution of minerals, carbonation, hydrolysis, hydration, and oxidation and reduction. Common to chemical weathering processes is that they depend on water composition, for example pH, salinity, CO_2 and redox potential. The prevailing temperature is another important parameter determining the type and efficiency of chemical weathering.

Under present temperate climate conditions in Sweden, weathering occurs slowly where bedrock is exposed. Swantesson (1992) has estimated the postglacial weathering of bare bedrock surfaces in southern Sweden during the Holocene to be less than 0.02 m. Weathering rates beneath soils in tropical climates range between 2 and 48 m Ma^{-1} (Thomas 1994). Although the tropical weathering rates have a large span, due to differences in rock type, temperature and humidity conditions, they show that weathering is a slow process even under the most favourable tropical climatic conditions.

For a description of climatological-, hydrological- and geological factors affecting weathering, see e.g. Olvmo (2010, Section 3.3.3). Estimated denudation rates for the Forsmark region are presented and discussed below.

Erosion

Erosion can be defined as the removal and transport of bedrock and earth materials by a moving natural agent, such as air, water or ice. Erosion is often preceded by weathering and followed by transport and sedimentation. Air or water flowing over a bed of loose particles generates a shear stress that tends to initiate particle movement (Collinson 2005a). There is a critical boundary shear stress related to wind velocity and turbulence and water flow velocity above which particle movement occurs. With the exception of small grain sizes, the critical shear stress will increase as the grain size increases. For small grain sizes (less than 0.1 mm, silt and clay) increased cohesive strength and lower surface roughness means that higher velocities are required to initiate movement. In this section, a brief description is given of the main mechanisms of aeolian-, marine-, fluvial- and glacial erosion. erosion

Aeolian erosion

Erosion of sediments by the wind, i.e. aeolian erosion, occurs in environments with sparse or non-existent vegetation, a supply of fine-grained sediments and strong winds, for example periglacial regions, semi-arid and or arid. Aeolian processes depend on weathering or other natural agents, e.g. rivers and waves, to supply sediments for transport. Particle movement is achieved due to wind shear stress and atmospheric turbulence. Particles begin to move when wind forces exceed the effect of weight and cohesion; the first particles to move dislodge or impact other grains and the number of particles in movement increase exponentially. However, the particles reduce the near-bed velocity of the wind and the transport reaches a dynamic equilibrium state in a few seconds. The mass flux of particles is related to the wind shear velocity, abrasion and the impact of particles moved by saltation and creep. The latter mobilise fine-grained material affected by cohesion but easily carried by the wind. Thus, the transport rate is limited both by wind shear velocity and the supply of particles.

Marine erosion

Marine erosion is largely limited to the reworking of sediment in the shore zone. In regions of rapid post-glacial emergence, such as in the Forsmark region, it is very low in solid rock because a shoreline at a given elevation is exposed to marine erosion for only a short period of time. Furthermore, the smooth, glaciated surfaces generally lack loose, fractured rock that can be exploited by wave action. Also, the wave energy in the Baltic Sea is relatively low, reducing the efficiency of marine erosion further.

Fluvial erosion

Less than 0.005 % of the global water is stored in rivers. Nevertheless, they are one of the most, if not the most, potent erosional forces operating on the Earth's surface. Rivers cut valleys, transport sediments and deposit their loads in a variety of depositional environments, such as flood plains and deltas. Vertical erosion by rivers is a striking feature of the world's mountainous areas where deep valleys dissect the landscape and form steep slopes, thereby creating the conditions for mass movement processes that are closely linked to fluvial vertical erosion.

Erosion and deposition of particles by water, i.e. fluvial erosion and deposition, is related to flow velocity. To generate water flow, a water supply and a flow gradient are required. Therefore, erosion by water generally requires a slope. Fluvial erosion occurs on slopes, in ditches, and in brooks and rivers. As with wind erosion, erosion by water depends on shear stress and turbulence, and particles begin to move when water fluid forces exceed the effects of weight and cohesion. The relation between grain size, flow velocity and different modes of erosion and deposition are illustrated in a Hjulström-Sundborg diagram, see Figure 3-79.

The material is transported in two distinct ways, it is either carried along with the fluid or it is in intermittent contact with the bed, described in e.g. Collinson (2005b). In the first case, fine-grained particles are supported by the upwards component of turbulence and carried away with the fluid in suspension. In the second case, generally referred to as bedload transport, coarser-grained material rolls (creep or erosion reptation) or bounces (saltation) on the bed. Particles carried in suspension will enhance the erosive capability of the fluid by abrasion and particles moved by saltation, creep or reptation will set other grains in motion.

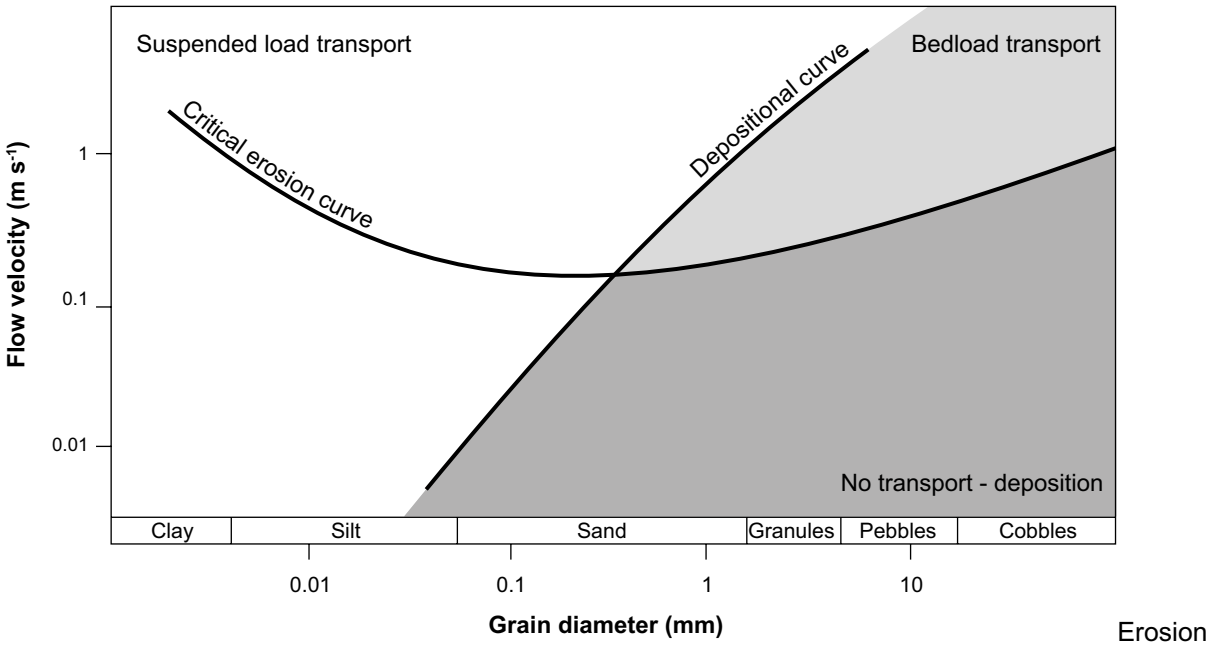

Figure 3-79. *A Hjulström-Sundborg diagram showing the relation between flow velocity, grain size and fluvial erosion.*

Fluvial erosion at the base of slopes releases material that is transported to brooks and rivers, and into lakes and the sea. Erosion by water on a slope increases with increased intensity of rain or snowmelt, increased inclination and length of the slope and decreased resistance to erosion of the soil. As for wind erosion, the presence of vegetation may strongly reduce the erosion rate. For more information on fluvial erosion, see e.g. Olvmo (2010, Section 4.1) and references therein. When rivers reach the sea, the flow velocity falls, erosion ceases and the sediment load is deposited.

Glacial erosion

Glacial erosion has been the dominant process of erosion in and around the Baltic Sea Basin over at least the last 1 Ma (e.g. Hall and van Boeckel 2020). Glacial erosion is complex and depends on material properties of ice and rocks, ice thermodynamics, friction and lubrication, chemical effects and subglacial hydrology. In addition, glacial erosion in bedrock is enhanced by pre-glacial sub-aerial weathering processes.

In recent years, interpretations of geomorphological features (e.g. Kleman et al. 1997, 2008), measurements of cosmogenic radionuclides (e.g. Stroeven et al. 2002a, Hall et al. 2019a) and ice-sheet modelling (e.g. Näslund et al. 2003) have identified the high variability of glacial erosion over Fennoscandia. In some areas, over time dominated by basal frozen conditions, glacial erosion has been limited, whereas in other areas, where basal melting and sliding (see Section 3.1) have occurred, erosion was more considerable.

Glacial erosion is traditionally divided into two components; plucking and abrasion. Plucking is the process by which rock fragments of different size are loosened, entrained and transported away from the glacier bed. Plucking is responsible for the characteristic irregular and fractured surfaces of lee sides of bedrock bumps and small hills in formerly glaciated areas. Abrasion is the grinding of the substrate by rock fragments held in moving basal ice (cf. Sugden and John 1976, Benn and Evans 1998). Abrasion scours the bedrock by debris carried in the basal layers of the glacier (cf. Sugden and John 1976, Drewry 1986). The process leads to striation and polishing of bedrock surfaces (cf. Benn and Evans 1998) and is typical of the stoss side of rock bumps in formerly glaciated terrain. Yet another process of glacial erosion, called glacial ripping, have recently been suggested by Hall et al. (2020). This process invokes disruption of surficial bedrock by dilation of bedrock fractures under high hydrostatic pressures. Resistance to movement is reduced so that traction from the overriding ice-sheet causes disintegration of rock surfaces and ripping apart into blocks. A theoretical analysis of glacial erosion, including the forces required for the removal of upstanding rock blocks by sliding of ice at the base of an ice-sheet under four different glacial scenarios, was performed by Krabbendam and Hall (2019).

Most glacial erosion exploits existing rock fractures, but subglacial processes can form new fractures at different scales. Pre-existing weakness, such as joints, cracks and foliation, and also pre-glacial weathering, exert strong control over rock mass strength (cf. Olvmo and Johansson 2002). Glacially induced cyclic water pressure variations may be important for new bedrock crack propagation (e.g. Hooke 1991, Iverson 1991), a process by which rock fragments may be formed and eroded from the bedrock. Many minor fracture features, such as chattermarks and crescentic gouges, observed on glacially affected rock surfaces, indicate that normal stress at the glacier bed, exerted by clasts travelling over the bed, may be sufficient to cause failure in some rocks. Loosening of rock fragments along fractures is caused by stresses set up by differential ice loads and high water pressures at the ice-bedrock interface (cf. Sugden and John 1976, Drewry 1986, Benn and Evans 1998). Melting of ice on the stoss side and refreezing of meltwater on the lee side of obstacles at the ice-sheet bed may occur under certain thermal and pressure conditions. This so-called regelation process may also contribute to glacial erosion and transportation of subglacial till (e.g. Iverson 1993, 2000).

The magnitude of glacial erosion by ice-sheets differs widely both in time and space. At a continental scale, the large-scale pattern of glacial erosion is controlled by ice-sheet thermal regime and topography of the subglacial landscape. Based on a simple glaciological model Sugden (1977, 1978) made a reconstruction of the thermal regime of the Laurentide ice-sheet. The reconstructed thermal pattern shows an inner wet-based area and an outer cold-bed area, which broadly corresponds to the pattern of glacial erosion indicated by the distribution of erosional landforms. The most intense erosion as indicated by areas with high lake density coincide with the transition zone between wet-based and cold-based ice in the model, which probably favours plucking and debris entrainment.

Näslund et al. (2003) used a numerical ice-sheet model to study regional ice flow directions and glacial erosion of the Weichselian ice-sheet in Fennoscandia. A new quantity, basal sliding distance, was introduced, describing the accumulated length of ice that has passed over the landscape by basal sliding. It was suggested that this entity could be used as a proxy for glacial erosion. The results indicate high basal sliding distance values in SW Sweden/SE Norway, in the Skagerrak, and along the Gulf of Bothnia, implying relatively large amounts of glacial erosion in these regions. On elevated parts of the Scandinavian mountain range and on adjacent plains in the east the basal sliding distance values are low, implying weaker glacial erosion, which is fairly in agreement with geological and geomorphological evidence (cf. Lagerbäck and Robertsson 1988, Riis 1996, Stroeven et al. 2002b, Olvmo et al. 2005). The method of estimating glacial erosion by simulated basal sliding distance (Näslund et al. 2003) was further developed by Staiger et al. (2005) who introduced a normalization of the sliding values by the duration of ice cover over a site. Staiger et al. (2005) also set up a relationship between normalized sliding distance and rate of glacial erosion. A basal sliding parameter is integral to recent ice-sheet erosion models (Patton et al. 2016).

Another approach to the issue of glacial erosion is presented by Hallet et al. (1996) who made a comprehensive review of glacial erosion rates based on sediment yields. They found that rates of glacial erosion vary by many orders of magnitude from 0.01 mm yr^{-1} for polar glaciers and thin temperate plateau glaciers on crystalline bedrock, to 0.1 mm yr^{-1} for temperate valley glaciers also on resistant crystalline bedrock in Norway, to 1.0 mm yr^{-1} for small temperate glaciers on diverse bedrock in the Swiss Alps, and to 10–100 mm yr^{-1} for large and fast-moving temperate valley glaciers in the tectonically active ranges of southeast Alaska. These major differences highlight the importance of the glacial basal thermal regime, glacial dynamics and topographic relief on the rates of glacial erosion.

Yet another approach was presented by Påsse (2004). To estimate the average glacial erosion in the bedrock in non-mountainous regions he used seismic data and well-depth data on the thickness of the minerogenic Quaternary sediments in Sweden and Denmark. The average thickness of Quaternary sediments was estimated to be 16 m in the investigated area, which corresponds to 12 m of bedrock assuming that the whole volume is the result of glacial erosion of fresh bedrock. Since a part of the sediments likely consists of glacially redistributed Tertiary regolith, this number may be an overestimation of the glacial erosion depth in the bedrock. Considering this, Påsse concluded that the average glacial erosion during a full glacial period may be estimated to between 0.2 m and 4 m. This agrees with estimates of glacial erosion in the Precambrian basement based on geomorphological observations (Lidmar-Bergström 1997, Ebert 2009). Lidmar-Bergström distinguishes the estimates of glacial erosion of Tertiary saprolites (decomposed rock formed by weathering) from glacial erosion of fresh bedrock. The glacial erosion of saprolites is estimated between 10 and 50 m and glacial erosion of fresh bedrock is estimated at some tens of metres (Lidmar-Bergström 1997), although with great variations. Comparison of Pleistocene sediment volumes with geomorphological evidence for glacial erosion around the Baltic Sea Basin support depths of glacial erosion on basement in Sweden of 20 m over the last 1 Ma (Hall and van Boeckel 2020).

However, in Fennoscandia as a whole, large spatial differences in thicknesses of Quaternary deposits occur and distinct patterns of glacial scouring and deep linear erosion are observed in places. Kleman et al. (2008) point to the relative roles of mountain ice-sheets and full-sized Fennoscandian ice-sheets for this zonation and use spatio-temporal qualitative modelling of ice-sheet extent and migration of erosion and deposition zones through the entire Quaternary to suggest an explanatory model for the current spatial pattern of Quaternary deposits and erosion zones.

Also on a more regional to local scale, the amount of glacial erosion of basement rock may vary considerably, as demonstrated for the Forsmark region by Hall et al. (2019a), see Section 3.5.4.

Glacial meltwater erosion may be an effective agent of erosion along meltwater routeways both in subglacial and proglacial environments. The sediment concentrations of glacial meltwater streams are often high, and the flow is often very rapid and turbulent, which mean that flows transitional between debris flows and normal stream flow are common (Benn and Evans 1998). The erosivity of glacial streams is therefore often high both on bedrock and sediments. Apart from the high erosivity and the potential for high hydrostatic pressure in meltwater tunnels, the mechanisms of glacial meltwater erosion are the same as normal fluvial erosion including abrasion, cavitation, fluid stressing and particle entrainment from cohesionless beds as well as chemical erosion.

The relative efficacy of fluvial and glacial erosion, on a global basis, is presented in Koppes and Montgomery (2009). For a more detailed description of erosional and weathering processes relevant for Fennoscandian conditions and the Forsmark area in a 0.1 to 1 Ma time perspective, see Olvmo (2010). Estimated denudation rates for the Forsmark region are presented and discussed below.

3.5.2 Controlling conditions and factors

As mentioned above, weathering and erosion are complex processes affected by the prevailing environmental conditions. Given the characteristics of the rock, the degree of weathering depends on the availability of weathering agents such as salt, moisture, biota (e.g. microorganisms and lichens), and on the microclimatic conditions to which the rock is exposed. Weathering occurs in all climates, but high temperatures and humid conditions increase weathering rates. In areas where frost and/or permafrost occur, freezing and freeze-thaw effects are important geomorphic processes. However, weathering in periglacial environments is also affected by salt (in combination with freezing), wetting and drying, thermal fatigue and biological agents (French 2007).

During temperate climate conditions, the dominant erosion process is fluvial erosion. During periglacial climate conditions, when the climate can be expected to be drier and vegetation sparse, aeolian erosion may also be important. During spring when the snow melts, there may be significant erosion of sediments in the active layer in periglacial permafrost areas. Under glaciated conditions, ice-sheet erosion is paramount. It is mainly affected by the prevailing thermal and physical conditions at the ice-sheet/substrate interface. In areas where the ice is frozen to the bed, the ice acts to preserve its subsurface and practically no erosion occurs, whereas in areas of basal melting, erosion of bedrock and pre-existing sediment is likely to occur, with more erosion generally associated with faster ice flow. In sub-glacial tunnels, where melt water flows towards the ice-sheet margin, erosion of loose sediments and bedrock can be significant.

The topographic relief in Fennoscandia is generally low outside the Scandinavian mountains (e.g. Lidmar-Bergström and Näslund 2005). The resistance to denudation of the Precambrian rocks that dominate in Fennoscandia is rather uniform, as compared with, for example, the variation between the Caledonian bedrock types in the Scandinavian mountains. Although the relief locally may be steep at many places, the relatively homogeneous denudation resistance has contributed to the moderate to low relief of the Precambrian rock basement. Available relief is generally controlled by fracture patterns at different scales. The relative relief is exceptionally low (up to a few tens of metres) along significant portions of the Baltic Sea coastline of southern and south–central Sweden, due to the presence of the *sub-Cambrian peneplain*. This peneplain is interpreted as a denudation surface formed in crystalline rock down to sea-level prior to the Cambrian period (cf. Rudberg 1954, Lidmar-Bergström 1995), with a typical relief of less than 20 m. A more recent study in southern Sweden by Hall et al. (2019b) follow the same overall interpretation of the sub-Cambrian peneplain but uses the term sub-Cambrian unconformity, emphasising the importance in the Uppland province of relief inheritance from this basement unconformity. An alternative explanation for the formation of specific parts of this flat denudation surface in southern Sweden, involving glacial erosion processes, have been presented by Goodfellow et al. (2019).

The low relief of this crystalline bedrock surface favours low subaerial erosion rates, for example, the most important subaerial erosion process, fluvial erosion, increases with steeper topographical gradients.

A deep dissection of the landscape cannot occur by fluvial erosion in Forsmark under present conditions because of the location just a few m above the Baltic Sea. The sea-level acts as the base-level for fluvial erosion, i.e. fluvial erosion cannot cut deeper than sea-level. The expected maximum lowering of the Baltic sea-level during glacial cycles (18 m, see Section 4.5.2) sets, together with the present altitude of the ground surface above the repository (a few metres), a maximum limit of ~20 m to the amount of future fluvial erosion during glacial cycles at the location of the planned repository for spent nuclear fuel. Table 3-14 summarises how geosphere variables are influenced by surface denudation.

3.5.3 Natural analogues/observations in nature

The current landforms in Fennoscandia are a result of the interaction between tectonic processes, weathering, erosion and sedimentation and consequently the traces of these processes can be observed and interpreted in nature. In Fennoscandia, large-scale bedrock landforms outside the Scandinavian mountain range, such as denudation surfaces and landscapes of weathering and stripping of saprolites, are common, and reflect the varying phases of weathering, erosion, and sedimentation that have occurred in association with tectonic events and climate change (e.g. Lidmar-Bergström 1997, Lidmar-Bergström and Näslund 2002).

Forsmark is situated inside the Svecokarelian orogen, active at 1.9–1.8 Ga, in the south–western part of the Fennoscandian Shield, a basement terrain which forms one of the ancient continental crustal fragments on Earth (Stephens 2010). Far-field tectonic events after 1.8 Ga included orogenic activity related to crustal build-up and crustal reworking at 1.7−1.6 Ga, at 1.6−1.5 Ga (Gothian), at 1.5−1.4 Ga (Hallandian) and at 1.1−0.9 Ga (Sveconorwegian), rifting during the Meso- and Neoproterozoic, and rifting and the development of a passive continental margin in the northern part of Europe during the latest part of the Neoproterozoic and the Cambrian (e.g. Stephens 2010). Deep denudation was largely complete by ~1.5 Ga when Jotnian sandstones were deposited on hilly to low relief basement surfaces on what is now the floor of the Bothnian Sea off Uppland (Hall et al. 2019a). These cover rocks, plus any additional sedimentary cover that once accumulated in the Sveconorwegian foreland basin, were removed from Uppland by the time of formation of the sub-Cambrian peneplain at ~541 Ma. The juxtaposition of the sub-Jotnian and sub-Cambrian unconformities at approximately the same erosional level indicates the exceptional stability of the craton over the last 1.5 Ga (Hall et al. 2019a). Although the craton has been buried repeatedly by thick foreland basin sediments (Larson et al. 1999), since eroded away, the ancient basement surface has experienced limited erosion.

During the Quaternary glacial cycles, ice-sheets have repeatedly covered parts or the whole of Fennoscandia, producing glacial erosional landforms in bedrock (e.g. Rudberg 1954) and moulding surficial deposits to form landforms such as drumlins (e.g. Kleman et al. 1997, 2008). Traditionally, it has been thought that a considerable part of the bedrock relief is a result of glacial erosion. However, as mentioned above, it has been shown that the amount of glacial erosion of Precambrian basement rock in low-land areas of Sweden in general is on the order of a few tens of metres (Lidmar-Bergström 1997, Hall et al. 2019a), with more erosion along valleys and depressions. Within the Scandinavian mountain range, valleys may have experienced several hundred metres of glacial erosion (Kleman and Stroeven 1997). Furthermore, during the last decades, our understanding of ice-sheet thermodynamics has developed a lot, showing that different parts of the ice-sheet may have very different potential for glacial erosion, and that this changes in time and space during the course of a glacial cycle. Large portions of ice-sheets may be cold-based and thus have a negligible erosive effect. Over the same period, numerous glacial geological studies have shown that the occurrence of pre-glacial saprolite remnants is solid evidence that ice-sheets under certain circumstances cause very restricted glacial erosion, or even have a preserving effect on pre-glacial landforms (Lagerbäck 1988a, b, Kleman 1994), whereas under other conditions they may be highly erosive.

Table 3-14. Influence of surface denudation on geosphere variables.

Geosphere variable	Influence present (Y/N)	Summary of influence
Groundwater flow	No	The process refers to weathering and erosion at the surface. Even if there is no absolute boundary between surface- and groundwater this process only includes the action of surface water.
Groundwater composition	Yes	Surface weathering may to some degree change groundwater composition. The effect is judged as negligible for the safety assessment.
Rock stresses	Yes	The removal of bedrock by denudation changes the stress field.
Fracture geometry	Yes	Weathering may change fracture aperture in the upper metres of bedrock, for instance by widening of fractures due to freezing.

3.5.4 Model studies

Quantification of denudation can be made by i) numerical models that *per se* describe the processes involved in the denudation, for instance the processes resulting in glacial erosion, ii) by estimates based on interpretation of landform development over time, or iii) cosmogenic nuclide exposure dating. A review of numerical modelling of glacial erosion can be found in Fisher (2009), whereas the second approach may be exemplified by Olvmo (2010). Hall et al. (2019a) used both geomorphological analysis and cosmogenic nuclide analysis in studies of glacial erosion and long-term denudation history of southern Sweden and Forsmark.

The long-term denudation history of southern Sweden is interesting for two reasons. Firstly, it may help to understand the denudation rate through time in the Forsmark area. Secondly, it is important because the different landforms and surfaces that have been recognised, such as the sub-Cambrian peneplain mentioned above, may be used as reference surfaces to understand the magnitude and patterns of denudation and glacial erosion, at least on a regional scale (cf. Hall et al. 2019a). This is an important issue with respect to the time perspective of the safety assessment.

Some examples from Sweden of calculated long-term denudation rates are available, most of them using ancient smooth bedrock denudation surfaces (unconformities) as reference surface. In eastern Småland and southern Östergötland, the maximum denudation of the tectonically uplifted sub-Cambrian peneplain is approximately 100 m. Once overlying sedimentary cover rocks had been removed, denudation and removal of the denudation products would have required a period of between 2 and 50 Ma (Lidmar-Bergström et al. 1997). On the Swedish west coast, a so-called *Sub-Cretaceous etch surface* has been incised into the sub-Cambrian peneplain by weathering. In some places, it has resulted in a maximum bedrock lowering of 135 m. The time required for this amount of denudation has been suggested to be between 3 and 68 Ma (Lidmar-Bergström et al. 1997), with the denudation occurring during the Jurassic-Early Cretaceous (around 200–100 Ma). Finally, saprolite thicknesses of 50 m in Skåne were interpreted to have been produced by weathering over a time interval of 1–25 Ma (Lidmar-Bergström et al. 1997).

Given the specific tectonic and climatic evolution, including phases of denudation, sedimentation, and stripping of saprolites, the above examples clearly show that the evolution of the sub-Cambrian peneplain in southern Sweden into a younger incised landscape has been a slow process, and that the total amount of material removed from the crystalline bedrock has not been large considering the very long time periods involved. The total maximum denudation of bedrock in areas of Precambrian crystalline basement in southern Sweden during the last 540 Ma is on the order of a few hundred metres. A significant part of this denudation took place during Mesozoic (250–65 Ma) tropical climate conditions, considerably more favourable for chemical deep weathering than for instance a temperate climate. More detailed accounts of the long-term landform development and associated denudation in southern Sweden are given in Olvmo (2010) and Hall et al. (2019b).

From a bedrock geomorphological point of view, the Forsmark region (Figure 3-80) can be divided into distinctive areas with different relief: i) a central area, hosting the Forsmark site, characterized by less than 20 m topographic relief of basement rock, ii) a coastal region SE of Forsmark with coast-parallel lineaments, iii) a southern part with more pronounced relief characterised by east–west trending fault scarps, and iv) an area with hilly relief in the northwest (Olvmo 2010). The low relief in the central area, including the Forsmark site, is characteristic of areas where the present bedrock surface has not been significantly lowered from that of the sub-Cambrian peneplain, in line with the interpretation by e.g. Lidmar-Bergström (1997). This central area of low relief has been dislocated by block faulting and tilting (Grigull et al. 2019). South of this low relief central area, an area with the peneplain broken into smaller blocks as compared to the area around Forsmark is found. Some of the blocks are elevated and partly dissected by weathering and erosion. South of the Forsmark area, the elevated rims of the uplifted blocks give rise to eas–west trending horst ridges (Grigull et al. 2019), whereas in the Stockholm region the peneplain is highly dissected and gives rise to a so-called *joint valley landscape*, consisting of plateaux bounded by shallow straight, structurally controlled valleys (Figure 3-80). In the coastal low-lying areas between Forsmark and Uppsala, the relief is quite considerable along coast parallel tectonic lineaments. Here, the relative relief locally rises to 50 m along these fracture zones, often where Jotnian and Ordovician sedimentary rocks have been eroded from small half-grabens (Hall et al. 2019a). In this area, ~25 km southeast of Forsmark, the coastal landscape is more dissected. The

area coincides with areas with a high frequency of rock outcrops which suggests that glacial erosion has been more effective in this region than at Forsmark, probably due to the closeness to the Baltic Sea depression (Olvmo 2010, Hall et al. 2019a). The Baltic depression may both have been formed by, and been influencing, Fennoscandian ice-sheet flow (e.g. Holmlund and Fastook 1993, Clason et al. 2014, Hall and van Boeckel 2020).

Even if the Forsmark site is situated within the area of the sub-Cambrian Peneplain, the present extension of overlying Lower Palaeozoic sedimentary cover rocks is not far away (10–20 km, see Figure 3-80). For a description of the erosion and burial history of basement rock in this region, see Chapter 2 in Hall et al. (2019a). In the Forsmark area, the most elevated parts of the bedrock surface are probably close to the original peneplain surface (Olvmo 2010, Hall et al. 2019a). The bedrock relief (Figure 3-80) is up to a few tens of metres only, see Figures 2-11 and 2-19 in Hall et al. (2019a). Glacial lineations in the Quaternary drift cover and other glacial landforms are, in general, also common features in the landscape (e.g. Figures 4-13, 4-19, and 4-27 in Hall et al. 2019a). As previously mentioned, the low-relief bedrock surface around Forsmark is dissected by block faulting (e.g. Grigull et al. 2019) probably of post-Ordovician age (after ~450 Ma) (Hall et al. 2019a). Over the past 1.8 Ma, this area has been subject to relatively stable large-scale tectonic conditions (Lidmar-Bergström and Näslund 2002, Olvmo 2010, Hall et al. 2019a).

A comprehensive study on past and future denudation has been performed in the Forsmark area and elsewhere in lowland southern/south–central Sweden (Hall et al. 2019a, b, Goodfellow et al. 2019). The aim of the study was to quantify the total historical denudation at the Forsmark site, including glacial erosion, as well as related questions such as bedrock surface stability, by employing a range of methodologies. To this end, Hall et al. (2019a) used a combination of cosmogenic nuclide analysis, geomorphological analysis of bedrock landforms and landforms in Quaternary deposits, bedrock fracture analysis, and shallow bedrock stress modelling, with the overall purpose to quantify the amount of denudation over the past 100 ka and 1 Ma. Another purpose was to assess the potential amount of glacial erosion over the coming 1 Ma. In the following, the main results of the Hall et al. (2019a) study are presented.

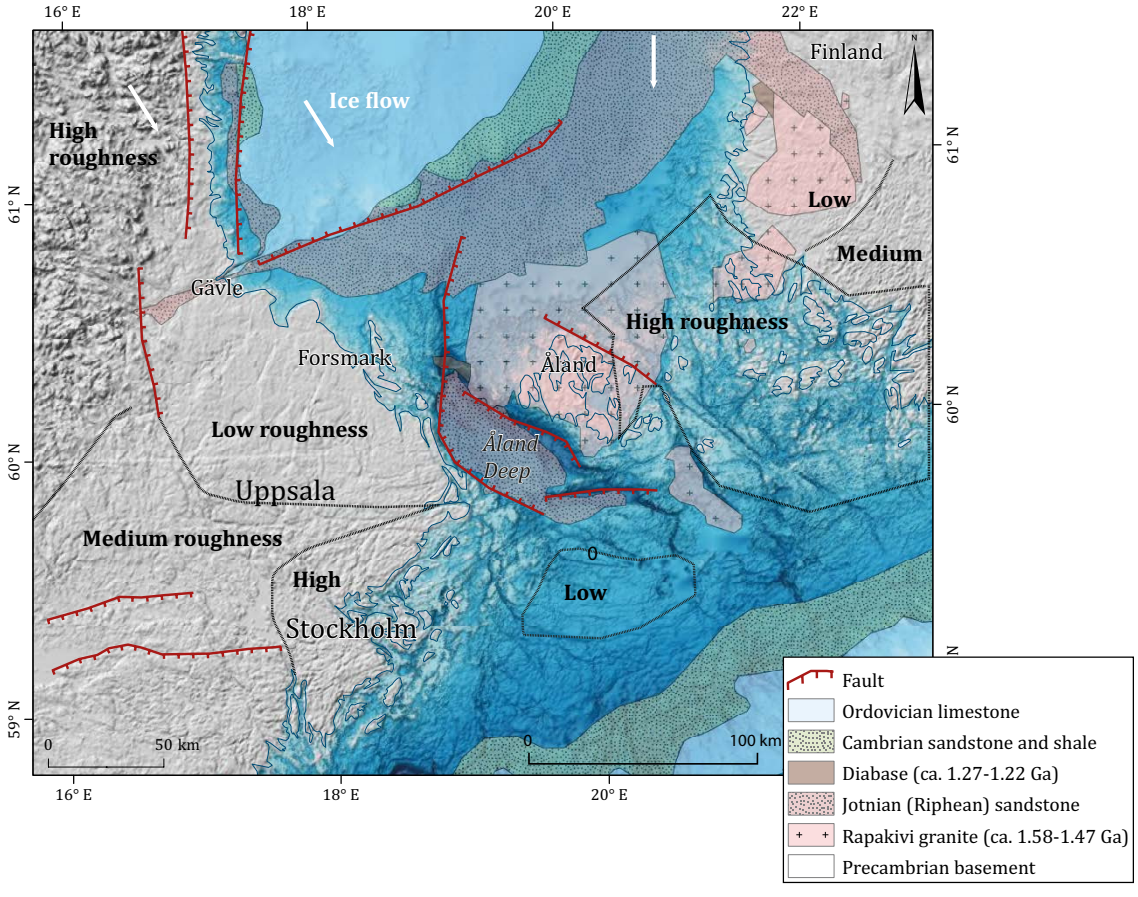

Figure 3-80. *Bedrock roughness (relief) at the landscape scale at Forsmark and surrounding areas. The map also shows the present distribution of remaining sedimentary cover rocks. From Hall et al. (2019a).*

Quantification of past denudation – cosmogenic nuclide analysis

Quartz in 32 surface bedrock samples and three boulder samples collected at the Forsmark site and in neighbouring areas of the Uppland province (Figure 3-81) was analysed for paired cosmogenic ^{10}Be and ^{26}Al nuclide concentrations. For a description of the cosmogenic nuclide exposure dating technique, see Hall et al. (2019a), where bedrock sampling procedures are described in Section 5.2.1, exposure age calculations in Section 5.2.2, and glacial erosion simulation methodology in Section 5.2.3.

Under the assumption that all glaciations that previously covered the Forsmark area and the Uppland province eroded the crystalline basement rock with similar mode and intensity, and using minimum and maximum values on non-glacial denudation of 0 and 5 mm ka^{-1} for ice free periods, the mid-range (25 % and 75 % percentiles) of the total denudation (i.e. including glacial erosion and all other non-glacial denudation processes) over the last 100 ka was estimated by Hall et al. (2019a) to 1.6–3.5 m (Table 3-15). The full range (0 % and 100 % percentiles) of the total denudation for the last 100 ka varies between 0 and 8.6 m. The corresponding mid-range of the total denudation for the last 1 Ma is 13–27 m with the full range varying between 2 and 61 m (Table 3-15). Since the calculated denudation values do not show a correlation against elevation above sea-level, bedrock relief, bedrock hardness (Schmidt hammer R-values), bedrock fracture spacing, latitude or (glacial) terrain type, see Hall et al. (2019a), the mid-range values probably are representative of the mean denudation rates in the area. However, in this context it is also worth noting that updated simulations have been performed on the Forsmark cosmogenic samples since the publication of Hall et al. (2019a). In the new simulations, a central best-fit value is calculated together with an asymmetric positive and negative uncertainty (J. Heyman, personal communication October 2020), whereas for the values in Hall et al. (2019a) shown in Table 3-15, a simple min–max span was been calculated. The newer improved simulations provide similar results, but also show that the lower denudation values are more realistic than the higher ones (cf. Table 3-15).

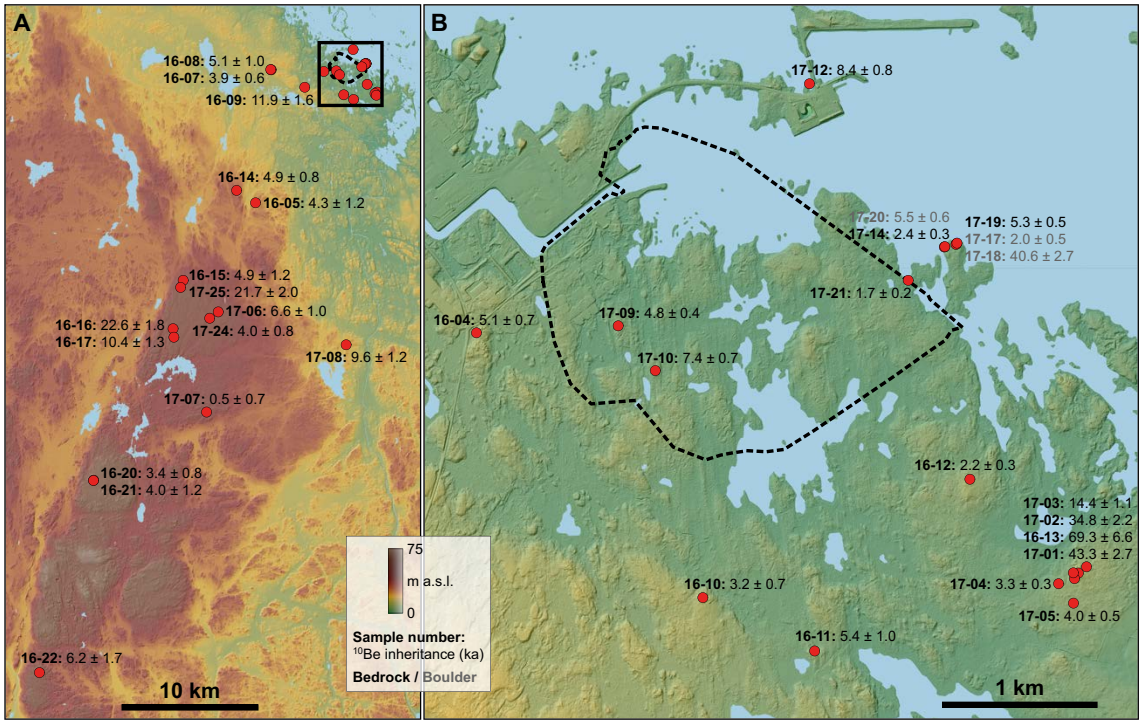

Figure 3-81. *Topographic maps showing locations of outcrops sampled for paired cosmogenic ^{10}Be and ^{26}Al nuclide concentrations at Forsmark and adjacent areas of the Uppland province (red dots). At the sample sites, sample numbers (bold characters) and calculated ^{10}Be inheritance ages (regular characters) are given. A) Distribution of cosmogenic nuclide sample locations across the wider study area of Hall et al. (2019a), from the location of the planned spent nuclear fuel repository at Forsmark (black box; left panel) and along an NNE–SSW directed topographic ridge. B) Footprint area of the planned repository (dashed line) and cosmogenic nuclide sample locations within and immediately beyond this area. In addition, two depth profile samples were taken from a quartz vein exposed in a road cut adjacent to sample 16-04 (NRD-001 and NRD-003, not shown). The topographic maps are derived from a 2 m resolution LiDAR DEM, see Hall et al. (2019a). From Hall et al. (2019a).*

The 19 samples that were collected closest to the planned repository (within a ~5 km radius of the repository) is of higher relevance for the safety assessment than values collected further away (Figure 3-81). For these 19 samples, the mid-range of the total denudation over the last 100 ka is 1.6–3.5 m, whereas the corresponding denudation over the last 1 Ma is 12–29 m (Table 3-15). If analysing only the two samples that were collected directly above the planned repository, the mid-range of the total denudation over the last 100 ka was estimated to 1.7–2.9 m, with a corresponding range of 13–22 m over the last 1 Ma (Table 3-15).

The above ranges in denudation of basement rock represent variations of simulated denudation from point samples and illustrate that, as expected, glacial erosion (the most efficient denudation process in this region) has a strong spatial variation over the investigated areas. To a smaller extent, the ranges also reflect uncertainties in assumptions adopted regarding different modes of glacial erosion in the calculations of erosion depths (see Hall et al. 2019a, Section 5.2.3, and Appendix G). Nevertheless, given the large number of samples and their wide spatial distribution, the ranges of denudation are well-clustered and they indicate limited denudation, and hence also limited glacial erosion, in this low relief landscape (Hall et al. 2019a). For a summary of values on total denudation of basement rock from the cosmogenic nuclide analysis, see Table 3-15.

Quantification of past denudation – geomorphological analysis

In order to further estimate the total past denudation of crystalline basement rock at Forsmark and the Uppland province, an analysis of the difference between a reconstructed summit envelope surface (with the idea of closely representing the sub-Cambrian peneplain or unconformity) and the present land surface was made (Hall et al. 2019a). Since the values obtained by this GIS method are calculated from the reconstructed reference envelope surface, which is constructed by connecting present-day summit heights and assuming zero denudation of these summits (see Hall et al. 2019a, Section 4.3.5), any lowering of the summits needs to be added to the numbers calculated in the GIS. In Hall et al. (2019a), the summit lowering was preliminarily estimated to be 10 m.

If adopting the 10 m surface lowering value (Hall et al. 2019a, Figure 4-46), the results indicates that a mean of ~24 m of basement rock has been lost, in total, to denudation across the north–eastern Uppland region up until present-day, with increasing depths of erosion towards the south (Hall et al. 2019a). At the Forsmark site (Hall et al. 2019a, Figure 4-47), the equivalent mean denudation depth in basement rock is ~22 m (Table 3-16). The smallest total denudation is around 10 m, whereas the larger denudation depths, often around 30 m, come from rock trenches and basins. The overall highest denudation depth at the Forsmark site from this analysis (50 m) is found in the trench along the West Gräsö Fault that lies 10 km east of Forsmark (Table 3-16 and Hall et al. 2019a, Figure 4-47). At this specific location, the erosion has exploited a pre-existing fault/fracture zone along the western base of the Gräsö fault block. Note that at this site, the additional 10 m of surface lowering has not been added to the GIS denudation value since this site is located at close proximity to the margin of overlying Ordovician strata to the west, see Hall et al. (2019a, Figure 2-21). This proximity indicates recent re-exposure of basement rock for this site and hence negligible basement summit lowering. Typical denudation depths at the Forsmark site, as well as the denudation depths at the repository location, are considerably shallower than the 50 m value along the West Gräsö Fault (Hall et al. 2019a). Performing the geomorphological analysis over the footprint area of the planned repository results in a total mean denudation of basement rock, up to the present-day, of ~18 m with a range of ~10–33 m (Figure 3-82B). For a summary of values on total denudation of basement rock from the geomorphological GIS analysis, see Table 3-16.

In this context, it is worth noting that the denudation depths obtained by the cosmogenic nuclide analysis over the past 1 Ma were larger than the 10 m surface height correction value used for the Forsmark site (see above). This could either mean that the summit lowering has been greater than 10 m, and/or that the larger 1 Ma denudation depths derived from cosmogenic nuclides also include removal of formerly overlying sedimentary cover rocks, see Hall et al. (2019a). In any case, if assuming a re-exposure of basement rock from below Early Palaeozoic cover rocks by glacial erosion within the last 1.1 Ma (Hall et al. 2019a, Hall and van Boeckel 2020), the results of the geomorphological analysis suggest that the total denudation of basement rock at the Forsmark site, and within the repository footprint area, has been low. For more details on the geomorphological analysis, see Hall et al. (2019a).

The relief map in Figure 3-80 shows the present ground surface relief, i.e. it includes the relief of both bedrock and overlying Quaternary deposits. Within the Forsmark area, Quaternary deposits are thin, typically less than 5 m (Hall et al. 2019a Figure 2-27B), with an even lower mean thickness. Nevertheless, the geomorphological analysis of historical denudation of basement rock described above has been performed using the bedrock topography with surficial sediment cover removed (Figure 3-82B).

Summary on past denudation

The results on total denudation of basement over the last 100 ka and 1 Ma from the cosmogenic nuclide analysis and geomorphological GIS analysis show similar results (Table 3-15 and Table 3-16). Both the cosmogenic nuclide analysis and the geomorphological analysis suggest that typical total denudation of the crystalline rock at the Forsmark site over the past 1 Ma, including all Late Quaternary ice-sheet erosion, have been restricted, from a few metres up to around 30 m (Table 3-15 and Table 3-16), depending on the exact location within the site. A few locations may have experienced a denudation up to 50–60 metres. The typical denudation depths (25 % and 75 % percentiles) over the last 100 ka is 1.6–3.5 m for the Forsmark site (Table 3-15), whereas the full range (0 % and 100 % percentiles) is 0–8.6 m. Most of this denudation constitute glacial erosion.

The range in total denudation shows, as expected, that the amount of erosion has varied over the site, seemingly reflecting stochastic spatial variations in erosion depths and processes on topographic highs and fracture control on topographic lows. In an area further away from the Forsmark site, around 25 km towards southeast, glacial erosion have been more efficient and has produced a more pronounced relief along structurally aligned valleys.

The overall result of limited denudation and glacial erosion at Forsmark and adjacent areas of the Uppland province in the past (Hall et al. 2019a) is in line with the overall result obtained in the more restricted study by Olvmo (2010) used in the SR-Site safety assessment. The results are also in line with conclusions in Lidmar-Bergström (1997), whom estimated a total amount of glacial erosion by all Late Cenozoic ice-sheets in lowland terrain in Sweden to be ~10 m, as well as with the wider erosion budget for the Baltic Sea Basin and its surroundings (Hall and van Boeckel 2020).

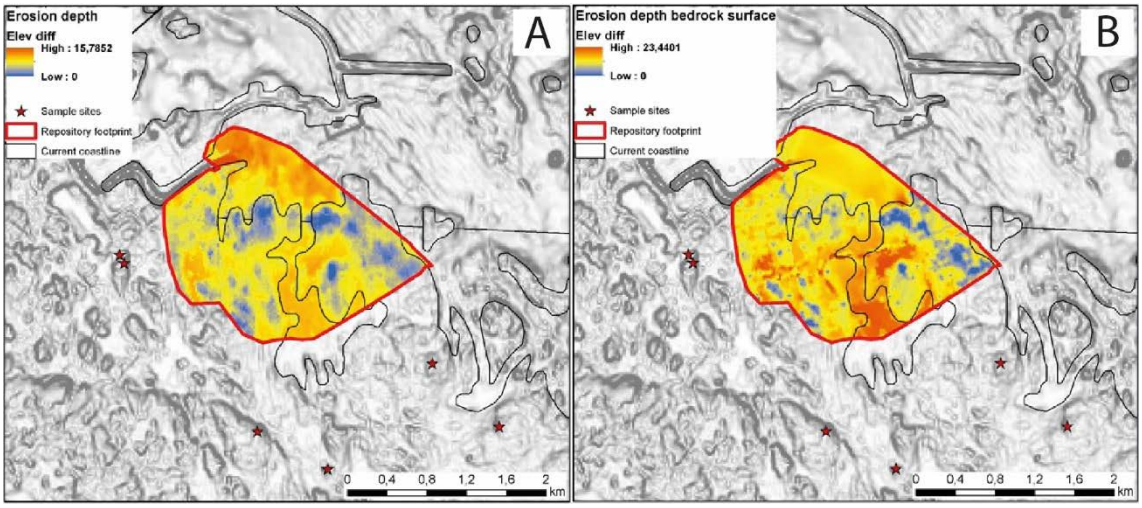

Figure 3-82. *Denudation of basement rock for the Forsmark repository footprint area based on geomorphological analysis. A) Denudation depths (m) reconstructed using the DEM of the current land surface (i.e. including Quaternary deposits) and assuming zero denudation of high points. The mean denudation across the footprint in plate A is 6 m, with a maximum value of 16 m. B) Denudation depths using the bedrock surface model (i.e. with Quaternary deposits removed) and assuming zero erosion of high points. The mean denudation across the footprint in plate B is 8 m with a maximum value of 23 m. However, for an estimation of the total denudation of the basement bedrock surface, the lowering of surface heights (estimated to be up to 10 m) need to be added to these values, see the text and Table 3-16. From Hall et al. (2019a).*

It is worth noting that the low denudation and glacial erosion rates at Forsmark in the past do not contradict the fact that there are glacially eroded bedrock landforms such as roche moutonnées in the area, since these landforms are relatively small. Similar results of low denudation have been found in other parts of Sweden, for example on the Swedish west coast, where cosmogenic exposure ages from around Hunnebostrand, an area with abundant roche moutonnées and large dislocated rock slabs, have shown that the Weichselian ice-sheet only eroded up to a few metres of bedrock (Stroeven et al. 2016, J. Heyman personal communication). The results from the studies at Forsmark and Hunnebostrand show that estimates of past glacial erosion require methods such as cosmogenic nuclide analysis, and/or the use of a reference surface against which glacial erosion can be measured, in order to make quantitative statements on the total amount of past glacial erosion.

Quantification of future erosion at Forsmark

Lord et al. (2019) provided a first-order estimate of the timing and durations of ice-sheet coverage over Forsmark for the coming 1 Ma, based on e.g. IPCC greenhouse-gas emission scenarios (Appendix E). Hall et al. (2019a) concluded that if typical erosion depths for Forsmark over the past 1 Ma are assumed to be representative for erosion depths during the future high confidence ice covered periods modelled by Lord et al. (2019), then erosion rates over the coming 1 Ma will be restricted, just as concluded for the past. Adopting the higher-confidence future glacial periods of Lord et al. (2019) in the cosmogenic nuclide analysis, and using minimum and maximum values on non-glacial denudation of 0 and 5 mm ka^{-1} for the ice free periods, Hall et al. (2019a) estimated the total denudation depth of basement rock, including glacial erosion, over the coming 100 ka to be less than 1 m (95 % percentile) at the Forsmark site (Table 3-15) for the full range of RCP emission scenarios investigated in Lord et al. (2019).

Over the coming 1 Ma, the mid-range (25 % and 75 % percentiles) of total denudation depths was estimated to 5–28 m, whereas the full range (5 % and 95 % percentiles) was estimated to 2–43 m (Table 3-15). These projected total denudation depths are valid under the assumption that glacial erosion depths in the past are representative of glacial erosion depths in the future. Just as for the ranges obtained for past denudation described above, the ranges of the projected future denudation depths mostly reflect spatial variations in erosion across the investigated area, i.e. differences in erosion between the 32 sites examined by cosmogenic nuclide analysis (Figure 3-81). All in all, the results in Hall et al. (2019a) indicate that the total maximum denudation of basement rock at Forsmark over the coming 1 Ma will be low, less than 50 m (Table 3-15). Within this range, the higher values are expected in topographic lows and/or along major fracture zones, especially if such features are located along the general ice flow direction. Denudation rates for individual RCP emission scenarios and the 'Natural' scenario of Lord et al. (2019), as calculated by Hall et al. (2019a) for the coming 100 ka and 1 Ma, are presented in Appendix G.

The estimates of low future denudation at Forsmark is consistent with i) the long-term denudation of basement rock being low up until present, ii) the bedrock topography in the area having a very low relief that acts in favour of low glacial erosion (as compared to more commonly found higher relief settings), iii) the bedrock consisting of crystalline rock, which typically has a relatively high resistance to erosion, and iv) the level of the Baltic sea constituting a base-level under which fluvial erosion cannot act. The present sea-level would result in a maximum possible fluvial incision of a few m at the location of the planned repository, whereas lower sea-levels stands during future glacial periods would resulting in ~20 m of fluvial erosion as a maximum, see Section 3.5.2.

The result of restricted erosion in the Forsmark area over the coming 1 Ma is in line with the results by Olvmo (2010) whom estimated that future glacial erosion could amount to 2–5 m per glacial cycle, under the assumption that the future glacial cycles are comparable with the last one. The same study also showed that for a large region at and around the Forsmark site, the potential future, non-glacial component of future denudation is between 0 and 5 m for the coming 1 Ma (Olvmo 2010, Figure 9-3).

In the context of the low past and future glacial erosion rates for Forsmark obtained by e.g. Hall et al. (2019a), it is important to note that higher glacial erosion rates of smaller glaciers in e.g. steeper mountainous environments (see under the heading *Glacial erosion* in Section 3.5.1) are not applicable for an ice-sheet setting with a dramatically lower bedrock relief, such as in Forsmark. For instance, the sliding rates of basal ice, and hence the effectiveness of glacial erosion, may be very different between these two topographic settings. For examples of various glacial erosion rates from different climatological and topographic environments, see e.g. Olvmo (2010) and references therein.

The dissected coastal area ~25 km south–east of Forsmark, with a higher bedrock relief, may experience stronger glacial erosion during future glaciations than expected for the Forsmark site (see above). In this area, glacial erosion of more than 10 m in one glacial cycle may be expected locally in low topographic positions (Olvmo 2010). If considering a case where this area of higher glacial erosion south–east of Forsmark in the future would migrate towards the repository site through e.g. headward erosion, the distance over which this increased glacial erosion needs to occur is considerable. It is likely that this would require several glacial cycles, if it were to happen at all. Furthermore, given the result of a theoretical case with 20 m of erosion per glacial cycle at Forsmark, combined with the low temperature required for a frozen buffer clay and backfill material to start having detrimental effects on the canister and surrounding host rock (−6 °C), see Section 5.5.4, it is considered unrealistic that such low temperatures could reach repository depth in the coming 1 Ma even in this pessimistic headward erosion case.

Summary and conclusions on future denudation at Forsmark

The quantification of the total amount of past and future denudation of crystalline bedrock from the cosmogenic nuclide analysis and geomorphological analysis of Hall et al. (2019a) are summarised in Table 3-15 and Table 3-16.

Table 3-15. Estimates of total denudation (i.e. including glacial erosion, non-glacial erosion, and weathering) from the cosmogenic nuclide analysis of basement rock at the Forsmark site by Hall et al. (2019a). Denudation has been calculated for past and future 100 ka and 1 Ma based on paired cosmogenic 10Be and 26Al nuclide concentrations measured for 32 surface bedrock samples at the Forsmark site and adjacent parts of the Uppland province (see Figure 3-81). The estimates of future denudation are calculated by combining the information on past glacial erosion with future periods of ice-sheet coverage at Forsmark as estimated by Lord et al. (2019), see the text. The values on total denudation are given for a mid- and a wide range scenario, see the text. The value marked by * has been corrected since Hall et al. (2019a), where it was erroneously given as 5.6 m. The values marked by ** include a very short period of ice-sheet coverage at the end of the 100 ka period emanating from the 'Natural' climate scenario adopted by Lord et al. (2019). If excluding the 'Natural' scenario and only using the results of the RCP scenarios from Lord et al. (2019), which do not have any ice-sheet coverage over the coming 100 ka, the maximum denudation value is 0.5 m. This can be readily seen in Appendix G, presenting denudation results for the individual RCP emission scenarios and for the 'Natural' scenario of Lord et al. (2019), as calculated by Hall et al. (2019a) for the coming 100 ka and 1 Ma.

	Range	Total denudation last 100 ka (Weichselian glacial cycle) (m)	Total denudation Last 1 Ma (m)	Total denudation coming 100 ka (m) (using all emission scenarios of Lord et al. 2019)	Total denudation coming 1 Ma (m) (using all emission scenarios of Lord et al. 2019)
All samples	Mid-range	1.6–3.5 (25 % and 75 % percentiles)	13–27 (25 % and 75 % percentiles)	< 1 (0–0.79** m, 25 % and 75 % percentiles)	5–28 (25 % and 75 % percentiles)
	Full range	0–8.6 (0 % and 100 % percentiles	2–61 (0 % and 100 % percentiles	< 1 (0–0.99** m, 5 % and 95 % percentiles)	2–43 (5 % and 95 % percentiles)
19 samples closest to and within repository footprint (5 km radius)	Mid-range (25 % and 75 % percentiles)	1.6–3.5	12–29	< 1	-
	Full range (0 % and 100 % percentiles)	0–8.6	2–61	< 1	-
Two samples within the repository footprint	Mid-range (25 % and 75 % percentiles)	1.7–2.9	13–22	< 1	-
	Full range (0 % and 100 % percentiles)	1.0–6.1*	6–42	< 1	-

Table 3-16. Estimates of past and future total denudation (i.e. including glacial erosion, non-glacial erosion, and weathering) of basement rock in the Uppland province, the Forsmark site, and for the footprint area of the planned repository at the Forsmark, from the geomorphological bedrock analysis in Hall et al. (2019a). In order to obtain the total denudation of basement rock, a summit lowering value (preliminary estimated to 10 m) have been added to the values from the GIS analysis (column four), see the text under the heading Quantification of past denudation – geomorphological analysis in the present section. *The additional 10 m of surface lowering has not been added to the GIS denudation value for the site with the largest denudation (50 m) since this site is located at close proximity to the margin of overlying sedimentary strata, see the text.

Analysed area	Value	Total denudation of basement rock up to present-day from GIS analysis (m)	Total denudation of basement rock up to present-day from GIS analysis with added summit lowering, see the text (m)	Estimated future denudation of basement rock
NE Uppland province excluding offshore area (see also Figure 4-46 in Hall et al. 2019a, showing results without summit lowering)	Mean	14	~24	-
Forsmark site, including offshore area (see also Figure 4-47 in Hall et al. 2019a, showing results without summit lowering)	Mean	12	~22	~2 m per glacial cycle. In basins and trenches, erosion rates may exceed 3 m per glacial cycle.
	Full range	0–50	10–50*	
Repository footprint area (see also Figure 3-82B, showing results without summit lowering)	Mean	8	~18	~2 m per glacial cycle. In basins and trenches, erosion rates may exceed 3 m per glacial cycle.
	Full range	0–23	~10–33	

The main results of the analyses above are as follows:

- The Forsmark area has a very low topographic bedrock relief and the rock type is crystalline bedrock. Also, the planned repository location is not situated in a major fracture zone or topographic depression. This results in a setting not prone to effective glacial erosion and denudation.
- The geomorphological analysis shows that the average past denudation of basement rock over the Forsmark site, since (an estimated) re-exposure of basement 1.1 Ma ago, has been ~22 m, with a corresponding average denudation over the repository footprint area of ~18 m.
- The corresponding full past range of denudation from the geomorphological analysis is 10–50 m for the Forsmark site and ~10–33 m for the repository footprint area.
- The typical denudation depths (25 % and 75 % percentiles) over the last 100 ka is 1.6–3.5 m for the Forsmark site (Table 3-15), whereas the full range (0 % and 100 % percentiles) is 0–8.6 m. Most of this denudation constitute glacial erosion.
- The total range of denudation of basement rock over the past 1 Ma based the cosmogenic nuclide analysis is between 2 and 61 m.
- The expected average (25 % and 75 % percentiles) denudation of basement rock over the Forsmark site over the coming 1 Ma from the cosmogenic nuclide analysis is 5–28 m, whereas the full range (5 % and 95 % percentiles) is 2–43 m.

Based on the above information, and the discussion of the results above, a conservative estimate of the maximum total denudation of bedrock (i.e. by glacial erosion, non-glacial erosion, and weathering) at the Forsmark site over the coming 1 Ma is here set to 50 m. Most locations within the Forsmark site are expected to have considerably lower bedrock denudation, ranging from a few metres up to around 30 m (Table 3-15). Over the coming 100 ka, the corresponding amount of total bedrock denudation is expected to be less than 1 m (Table 3-15, Appendix G). Note that the denudation over the coming 100 ka hence is estimated to be lower than the values for the last 100 ka. The reason for this is a shorter total period of ice-sheet coverage, and therefore less glacial erosion, over the coming 100 ka (Lord et al.

2019 Figure 4-10) as compared to that of the Weichselian glacial cycle (Section 4.4.1). For subsequent future glacial cycles, typical amounts of total denudation are estimated to be around 2 m per (~100 ka) glacial cycle (Table 3-16). In basins and trenches, erosion rates may exceed 3 m per glacial cycle.

3.5.5 Time perspective

Weathering, erosion and sedimentation are active processes over most of the Earth's surface. In Sweden, rates of denudation can be expected to be limited in tectonically stable, lowland areas of low topographic relief. In the Uppland province, the Precambrian basement remained largely buried and protected from erosion for much of the last 540 Ma until it was re-exposed by glacial erosion in the Pleistocene (2.5 Ma to ~11 ka). For the region around Forsmark, the maximum glacial erosion rate over the last 1 Ma is estimated to be 50 m (Section 3.5.4). The rates of weathering and erosion however have varied in time and space over this period.

3.5.6 Handling in the PSAR

Present-day knowledge on denudation processes suggests that denudation of crystalline bedrock generally will be limited in lowland parts of Fennoscandia during the assessment period, just as it has been in the past (Hall et al. 2019a). In areas where the bedrock is highly fractured, denudation can be expected to be significantly more rapid than the numbers reported here. However, such circumstances do not apply for the repository location at Forsmark. The impact of weathering and erosion on groundwater flow is considered to be insignificant over the 1 Ma time period covered by the safety assessment. In a very long time perspective, several million years, weathering and erosion may alter topography by redistribution of sediments and rock mass. In an even longer time perspective, many tens or hundreds of millions of years or longer, the repository may be brought to the ground surface due to tectonic uplift in conjunction with a combination of denudation processes, such as glacial- and fluvial erosion and weathering processes.

Current knowledge on past and future denudation at Forsmark and in adjacent regions (e.g. Hall et al. 2019a and Olvmo 2010) supports a conclusion that the amount of future surface denudation will not affect repository safety in the time perspectives of 100 ka to 1 Ma. The amount of denudation of basement rock over the coming 100 ka is estimated to be less than 1 m, whereas the maximum total bedrock denudation at the Forsmark site over the coming 1 Ma is pessimistically to be 50 metres, with average values from a few metres to around 30 metres (Table 3-15).

3.5.7 Handling of uncertainties in the PSAR

Denudation rates vary as climate and environmental conditions change. Since the rate of weathering and erosion also depends on rock and sediment characteristics, as well as on topography, denudation rates at a given point in time may also vary considerably within a certain area, such as the Forsmark site. In spite of the uncertainties in future environmental conditions, there is no reason to believe that future denudation rates in the Forsmark region would diverge significantly from the values estimated above. The area consists of crystalline bedrock with a low surface relief and low topographic gradients, working in favour of limited fluvial and glacial erosion at the site.

Uncertainties in mechanistic understanding

There are uncertainties in the understanding of the detailed mechanisms of erosion and weathering. However, for the safety assessment, the approach of estimating the amount of erosion and weathering over long time-scales by cosmogenic nuclide analysis and associated modelling of glacial erosion rates, as well as by analysing the long-term development of large-scale bedrock landforms, the total knowledge is sufficient for estimating the amount of denudation of bedrock during the assessment period.

Model simplification uncertainties in the PSAR

Not relevant for this process.

Input data and data uncertainties in the PSAR

Not relevant for this process.

4 Climate and climate-related conditions for the PSAR

4.1 Rationale and general approach

As mentioned in Section 1.2, the main scenario of the safety assessment includes a *base case* and a *global warming variant* of climate evolution. The base case is based on a *reference glacial cycle climate case* which in turn constitutes a repetition of conditions reconstructed for the last glacial cycle, the Weichselian and the Holocene, see Figure 1-3. By modifications of the *reference glacial cycle climate case*, this evolution is used also for constructing additional climate cases with a potentially larger impact on repository performance. For example, by defining a longer period of glacial conditions, the *reference glacial cycle climate case* has been used to construct an *extended ice-sheet duration climate case* (Figure 1-3), used for analysis in the additional safety assessment scenarios of the PSAR.

In order to make relevant and well-motivated definitions of the climate cases, it is essential to first have good knowledge on the climate and glacial history of the Weichselian glacial cycle, i.e. the glacial cycle upon which the *reference glacial cycle climate case* is based and the additional climate cases are constructed (Figure 1-3). To this end, Sections 4.2 describes the present knowledge on Weichselian climate and glacial history to a level required to give adequate input to the definition and description of the *reference glacial cycle climate case* and the additional climate cases. The description in Section 4.2 is based both on geological information and climate modelling.

Section 4.3 gives an overview and detailed examples of climates that occurred during the last glacial cycle, from geological information and from climate modelling.

Section 4.4 presents the reconstruction of last glacial cycle conditions that subsequently are used for the *reference glacial cycle climate case* (the base case of the PSAR main safety assessment scenario Figure 1-3) presented in Section 4.5. The global warming climate case is described in Section 5.1. Since it is not possible to describe an expected evolution of climate conditions for the time perspective of the safety assessment, the base case and global warming variant should not be seen as forecasts or attempts to predict future climate evolutions. Instead, they are *examples* of future evolutions that in a realistic way cover all relevant climate-related changes that can be expected in a 100 ka time perspective. They are complemented with additional climate cases with a potentially larger impact on long-term repository safety, described in Chapter 5.

For the reconstruction of the last glacial cycle conditions in Section 4.4, an ice-sheet model reconstruction of the Weichselian glacial is used (Section 3.1.4). Despite remaining uncertainties regarding the Weichselian glacial history, especially during the earlier phases of the glacial, see Section 4.2, the Weichselian is the best-known glacial cycle. This gives possibilities to use geological information for testing and constraining the adopted models. In line with the discussion above, the purpose is not to produce a “true picture” of the Weichselian evolution, a task that obviously is not possible to achieve, but rather to construct a scientifically reasonable starting point for the analysis of potential climate impacts on repository safety.

The reconstruction of last glacial cycle conditions in Section 4.4 extends over 120 ka. Three numerical models are used to yield boundary conditions for the reconstruction:

1. A dynamic ice-sheet model.
2. A Glacial Isostatic Adjustment (GIA) model.
3. A permafrost model.

The ice-sheet model is the University of Maine Ice-sheet Model (UMISM) (see Section 3.1.4), the GIA model was developed at the University of Durham (see Section 3.3.4) and the permafrost model at Helsinki University of Technology (see Section 3.4.4), see also the **Model summary report**. The basis for the *reference glacial cycle climate case* is a reconstruction of the Fennoscandian ice-sheet during the Weichselian employing the ice-sheet model. The generated ice-sheet evolution has been used as input to the global isostatic adjustment (GIA) model. The third main component in the reconstruction

of Weichselian conditions is the permafrost model, yielding permafrost depths given the evolution of ice-sheet, relative sea-level development, and other surface conditions. The main data flows between the ice-sheet, GIA and permafrost models are shown in Figure 4-1.

The *reference glacial cycle climate case*, described in Section 4.5 and used for the base case of the PSAR main scenario (Figure 1-3) is one example of a conceivable evolution of climate and climate-related processes and covers conditions and sequences that could be expected in a 100 ka time perspective. The *global warming climate case*, described in Section 5.1 and used for the Global warming variant of the main scenario, depicts an evolution with a warming climate due to an anthropogenically increased greenhouse effect. Other possible future climate evolutions are described in additional climate cases, described in other parts of Chapter 5. A summary of the climate cases is found in Table 4-1.

In Chapter 4, the sections on Weichselian climate and glacial history (Section 4.2) and reconstruction of last glacial cycle conditions (Section 4.4) describe *past* events, and therefore the timescale in the text and figures is time before present (BP). The sections on the PSAR *reference glacial cycle climate case* (Section 4.5), and the section on additional climate cases (Chapter 5) all describe possible *future* climate developments and therefore the timescale in these sections reflects this.

All in all, six climate cases depicting possible future climate development at the Forsmark site are presented (Table 4-1) and used for the analysis of long-term repository safety (see the **Post-closure safety report**).

Table 4-1. Climate cases in the PSAR.

Case number (section in present report)	Climate case	Short description
1 (Section 4.5)	*Reference glacial cycle*	Repetition of reconstructed last glacial cycle conditions
2 (Section 5.1)	*Global warming*	Longer period of initial temperate conditions than in case 1
3 (Section 5.2)	*Extended global warming*	Longer period of initial temperate conditions than in case 2
4 (Section 5.3)	*Extended ice-sheet duration*	Longer duration of ice-sheet coverage than in case 1
5 (Section 5.4)	*Maximum ice-sheet thickness*	Largest ice configuration in the past two million years
6 (Section 5.5)	*Severe permafrost*	Favourable for early and deep permafrost growth

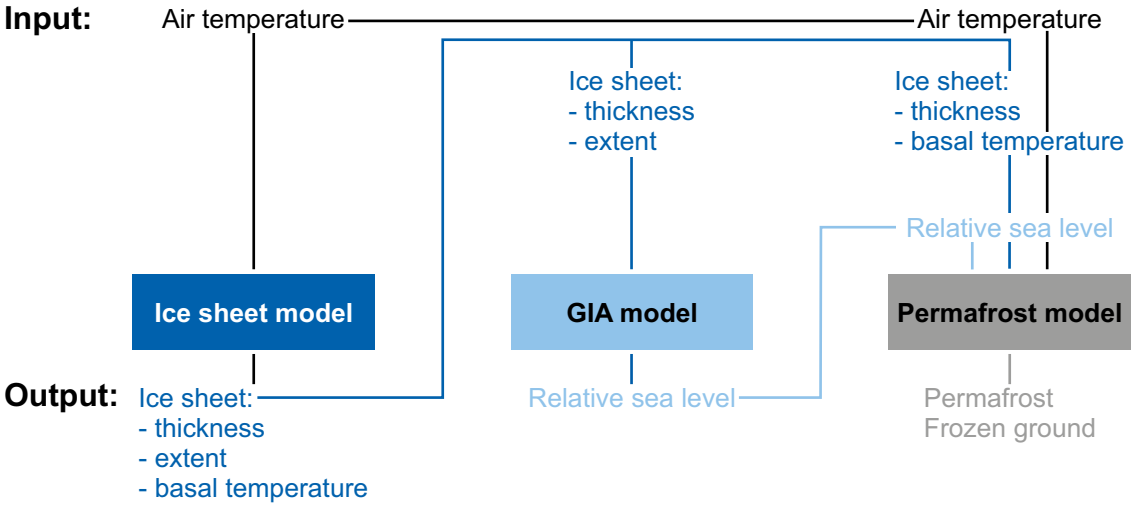

Figure 4-1. *Models used to provide boundary conditions for analysis of the impact of climate-related changes on the repository. Only input and output data shared between the models used to generate the boundary conditions are shown.*

4.2 Weichselian glacial history

In the previous sections, the importance of Weichselian conditions for the assessment of long-term repository safety has been described. Since the Weichselian constitutes the basis for the construction of the future *reference glacial cycle climate case* in the PSAR, a brief description of the Weichselian glacial history is presented here. Much of the following discussion is based on the main findings from the SKB-funded studies of Helmens (2013, 2019), Wohlfarth (2013) and Schenk and Wohlfarth (2019). Broadly, these studies cover the following topics:

- The review by Wohlfarth (2013) addresses the transition from the last interglacial (the Eemian, MIS 5e) into the Weichselian glaciation in Europe, based on state-of-the-art palaeoclimatic and palaeoenvironmental information from selected terrestrial, marine and ice-core records.
- The review by Helmens (2013) compared five Late Pleistocene terrestrial climate proxy records from central, temperate and northern, boreal Europe, using pollen, lithology and macrofossil- and insect-based temperature inferences.
- Helmens (2019) presented the results of a detailed study on sediments of MIS 5e age (i.e. the Eemian interglacial between c 130 and 115 ka BP), MIS 5d–c age (stadials and interstadials during the Early Weichselian c 115 to 90 ka BP) and the present Holocene interglacial (last ~ 11 ka) recovered from the small Sokli sedimentary basin in boreal north–eastern Finland. By applying multiple proxies and various quantitative climate reconstruction methods, a comprehensive reconstruction of environmental and climate conditions at Sokli during these time-intervals is made.
- Schenk and Wohlfarth (2019) performed a study on climate evolution and variability in Scandinavia and Europe during the transition from a glacial into an interglacial climate state, combining multi-proxy climate records with results from high-resolution climate modelling for the Bølling-Allerød (14.7–12.9 ka BP) and Younger Dryas periods (12.9–11.7 ka BP) of the last deglaciation.

In addition, special attention is given to describing ice-marginal fluctuations during the Weichselian deglaciation (Lokrantz and Sohlenius 2006), since such periods are of interest e.g. when assessing changes in groundwater flow around a KBS-3 repository, see Vidstrand et al. (2010) and the **Post-closure safety report**.

4.2.1 Overview of Weichselian glacial history and climate

The different warm interstadial and cold stadial phases of the last glacial cycle are divided into numbered so-called Marine Isotope Stages (MIS). For a better understanding of the temporal aspect in the description of the last glacial cycle below, these stages are summarised and described for the Eemian, Weichselian and the Holocene in Table 4-2.

Table 4-2. Summary and description of Marine Isotope Stages, ages, stadials and interstadials of the Eemian, Weichselian and Holocene. Regional variations from the denoted warm/cold state occur and there is a wide range of regional names used for each of the stadials/interstadials, see e.g. Lokrantz and Sohlenius (2006), Helmens (2013, 2019) and Wohlfarth (2013).

Marine Isotope Stage	Age (ka BP)	Stadial/ Interstadial	Warm/ Cold	Name (several other names are also used in the literature)	Weichselian phase
MIS 5e	c 130–115(110)	Interglacial	Warm	Eemian	-
MIS 5d	115(110)–105	Stadial	Cold	Herning (Melisey I)	Early Weichselian
MIS 5c	105–93	Interstadial	Warm	Brørup (St Germain 1c)	Early Weichselian
MIS 5b	93–85	Stadial	Cold	Rederstall (Melisey II)	Early Weichselian
MIS 5a	85–74	Interstadial	Warm	Odderade (St Germain II)	Early Weichselian
MIS 4	74–59	Stadial	Cold	Middle Weichselian stadial	Middle Weichselian
MIS 3	59–24	Interstadials/ Stadials	Warm/ cold	Middle Weichselian interstadials	Middle Weichselian
MIS 2	24–~ 11	Stadial	Cold	Stadial including Last Glacial Maximum	Late Weichselian
MIS 1	~ 11–0	Interglacial	Warm	Holocene	-

MIS 5, including the transition from the Eemian interglacial

The transition from the last interglacial (the Eemian, MIS 5e, see Table 4-2) to the first phase of the Weichselian glacial (MIS 5d), as seen in NGRIP ice core records, is depicted in Figure 4-2 together with changes in the incoming solar radiation (insolation).

The end of the Eemian interglacial period and the transition into the subsequent glacial was initially triggered by a decrease in summer insolation at high northern latitudes (Wohlfarth 2013, Figure 4-2). The change in orbital configuration led to a series of time-transgressive changes (e.g. gradual vegetation replacement; changes in sea-surface temperature, salinity, strength of the North Atlantic Current). As Northern Hemisphere ice-sheets started to grow and expand these changes became progressively more pronounced (Wohlfarth 2013).

The sequence of events leading from the Eemian into the last glacial has been described using climate models of different complexity and using various boundary conditions, palaeodata series, and comparisons between model outputs and palaeodata (see Wohlfarth 2013 for review). One possible scenario for the mechanisms involved relates to the development of summer sea ice in the northern North Atlantic already during the latter part of the Eemian interglacial, as a response to decreasing summer insolation. This would have accelerated a vegetation shift, which in turn would have led to a decrease in albedo. More extensive sea ice could, through brine formation, have increased the Atlantic meridional overturning circulation, which would have supplied more moisture to the cold high northern latitudes. This in turn would have favoured the growth of ice-sheets.

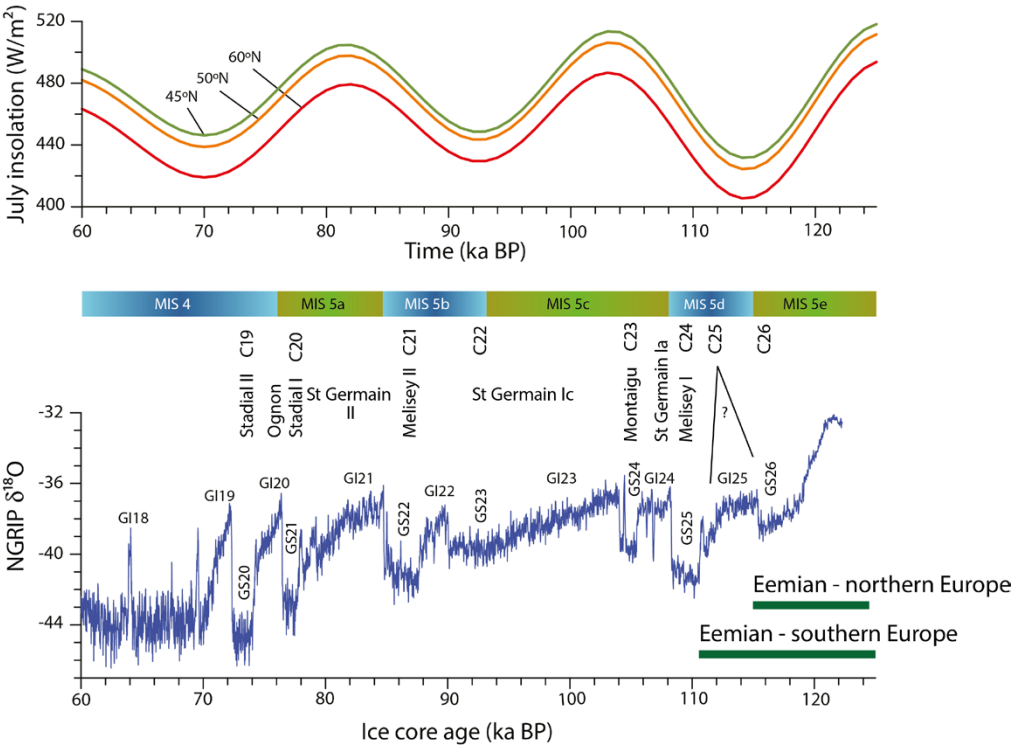

Figure 4-2. *Summer insolation at 60°, 50° and 45° N (Berger 1978) compared with the NGRIP $\delta^{18}O$ record (NorthGRIP community members 2004). The North Atlantic sea-surface cooling episodes (C26 to C19) and the terrestrial vegetation zones are according to Sánchez Goñi (2007). The correlation between marine and terrestrial events and the NGRIP record was inferred from Figure 13.1 in Sánchez Goñi (2007). The correlation between marine isotope stages (MIS 5e–4) and the NGRIP isotope record is tentative and partly follows Sánchez Goñi (2007) and partly Chapman and Shackleton (1999). The end of the terrestrial Eemian is according to Müller and Kukla (2004) and Sánchez Goñi (2007). GS = Greenland stadials; GI = Greenland interstadials. Note that the correlation of C25 and C26 to Greenland stadials is not entirely clear. C26 likely corresponds to GS26. From Wohlfarth (2013).*

The response of the vegetation in northern Europe to the decrease in summer insolation and to increased summer sea ice may be seen as early as 122–120 ka BP, but became most distinct around 115 ka BP, when North Atlantic sea-surface temperatures show signs of a first minor cooling (Wohlfarth 2013). This cold event (labelled sea surface cooling event C26, see Figure 4-2) defines the MIS 5e/5d transition in marine sediment cores and seems to correlate with Greenland stadial GS26. This first distinct, but minor cooling event on Greenland is paralleled by cold temperatures in Antarctica, which implies synchronous cooling in both hemispheres. However, while Antarctica remained cold, Greenland started to warm just before 110 ka, suggesting the start of the so-called bipolar see-saw mechanism. The first marked cooling over Greenland at 110–108 ka BP (GS25, Figure 4-2) was accompanied by a distinct drop in North Atlantic sea-surface temperatures (C24 event), by an increase in ice-rafted debris and by marked vegetation changes in southern Europe. This shift in vegetation defines the end of the terrestrial Eemian in southern Europe, which in comparison to marine records, occurred during MIS 5d. Palaeorecords thus suggest that the response of the vegetation to North Atlantic cooling events was delayed in southern Europe by at least 5 ka as compared with northern Europe (Wohlfarth 2013).

The decrease in summer insolation at high northern latitudes thus led to a series of feedback mechanisms, which gradually became stronger as ice-sheets grew larger. The initiation of the bipolar see-saw mechanism at around 110–112 ka BP seems to have triggered the series of abrupt and recurrent shifts between warmer interstadials and colder stadials that characterised the last glacial. While tundra and steppe-tundra vegetation seem to have developed in response to severe stadial conditions, the vegetation response to warmer interstadial temperatures was regionally different (Figure 4-3).

The overall conclusion from Wohlfarth (2013) is thus that the transition from the warm Eemian interglacial state (MIS 5e) to full glacial conditions during e.g. MIS 4 was complex, involving climate variability on different temporal and spatial scales. One aspect of this variability was manifested as the shifts between cold stadials and warm interstadials of multi-millennial duration during the Early Weichselian (MIS 5d–a) (Figure 4-2). Another aspect is associated with the millennial-scale climate variability superimposed on the longer-lasting climate fluctuations (Figure 4-2).

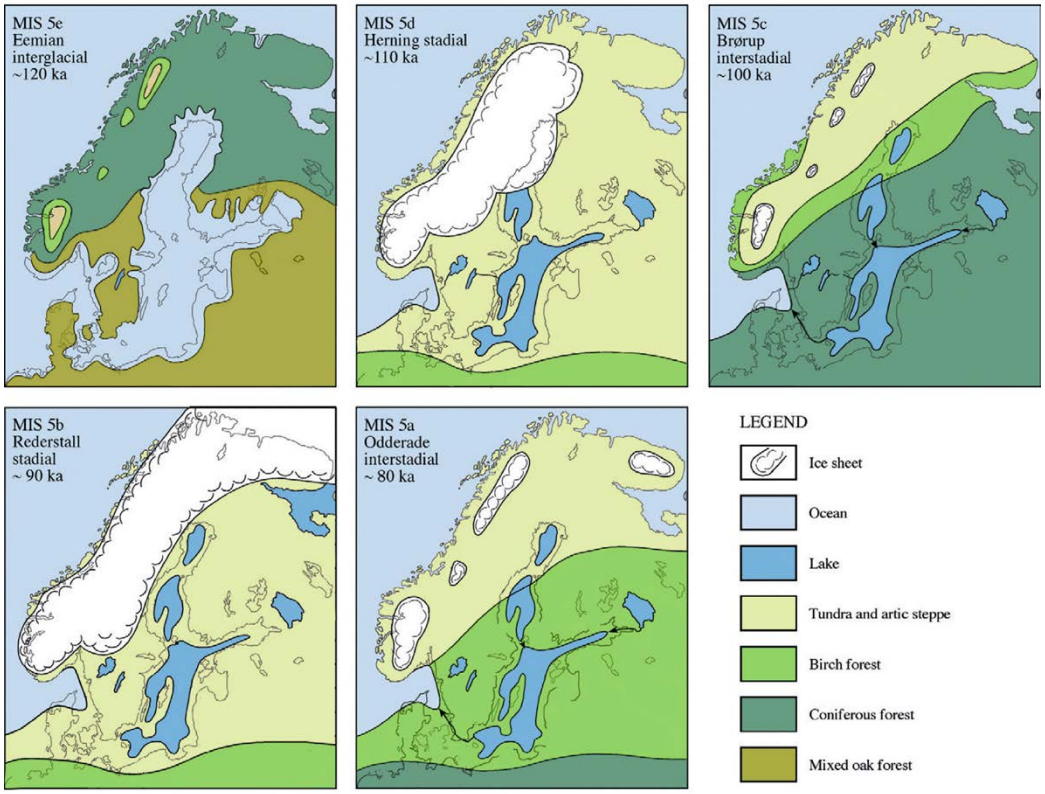

Figure 4-3. *Conceptual maps illustrating the development of the Weichselian ice-sheet during the Eemian and Early Weichselian (MIS 5e–a). According to this reconstruction, the Weichselian ice-sheet did not reach south–central Sweden and Forsmark during these periods of ice-sheet growth. Modified after Lundqvist (1992) and Mangerud et al. (2011). From Wohlfarth (2013).*

The high variability of the MIS 5 climate is also supported by the findings in Helmens (2013). More specifically, Helmens (2013) reported that the MIS 5 was characterised by three long mild forested interstadials (MIS 5e, 5c and 5a), both in temperate- and northern boreal Europe. These periods were interrupted by two cold and dry stadials (MIS 5d and 5b) with mountain-centred glaciation over Fennoscandia, shown in Figure 4-3. Also suggested in Figure 4-3 is that the Weichselian ice-sheet did not reach south–central Sweden and the Forsmark region during the Early Weichselian stadial periods.

Helmens (2019) presents a detailed study on sediments of MIS 5e–c age (130–90 ka BP) recovered from the small Sokli sedimentary basin in boreal north–eastern Finland. The study exploits the unique *in situ* preservation of Late Quaternary sediments in the Sokli basin as well as the unusual large thickness and fossil-richness of the geological beds. The results from Sokli revise earlier palaeo-environmental and palaeo-climate reconstructions for the Early Weichselian in Fennoscandia. The earlier palaeo-climate reconstructions were based on the long-distance correlation of poorly-dated stratigraphic fragments with the marine oxygen-isotope record which was used as a proxy for global ice volumes. One of the main results from Helmens (2019) is that the summer temperature during the MIS 5d stadial remained relatively high in northern Fennoscandia, comparable to present-day values (Figure 4-4). This is contrast to earlier studies that have suggested that the temperature in the region was several degrees lower during MIS 5d than at present (e.g. Engels et al. 2010).

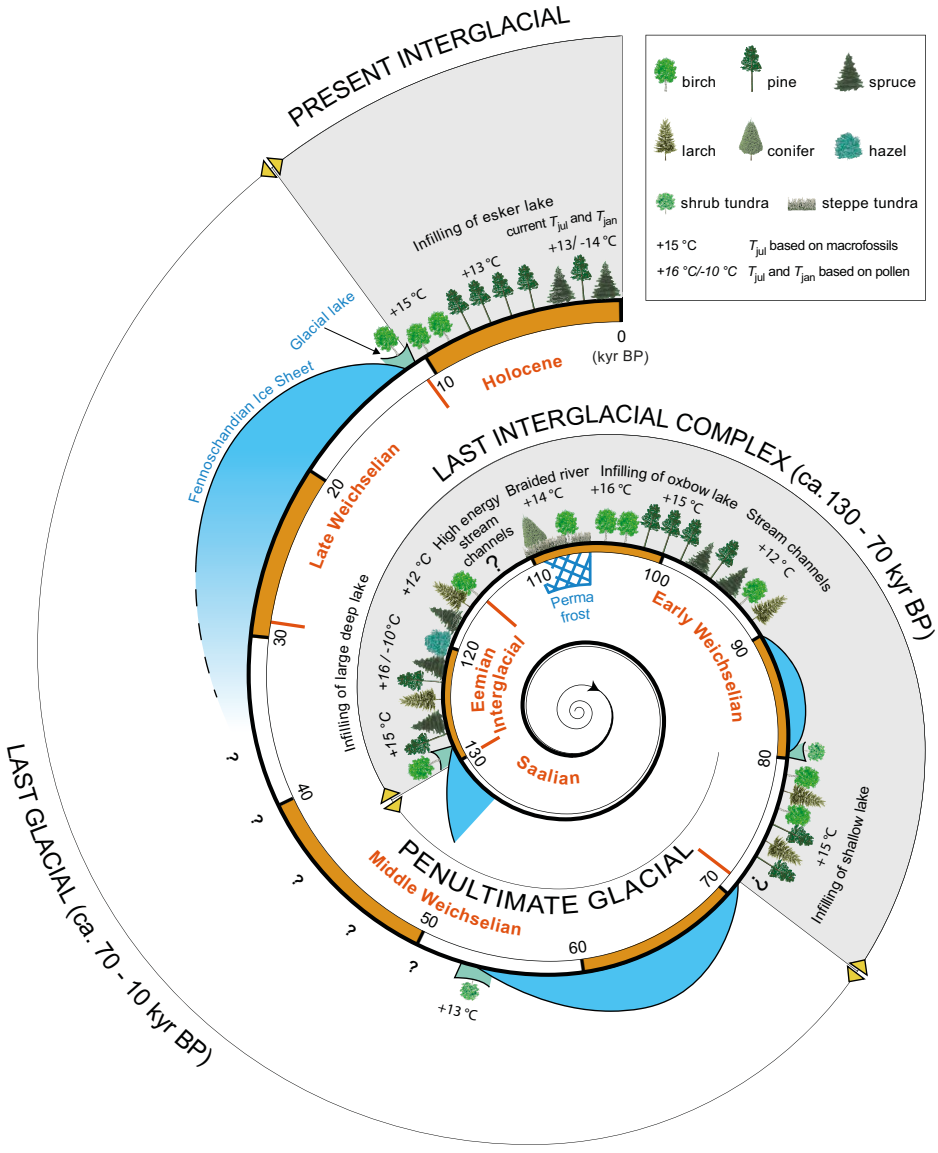

Figure 4-4. *Environmental and climate conditions at Sokli during the last interglacial–glacial cycle (ca 130 ka) based on the study of Helmens (2019).*

Helmens (2019) also provides a detailed description of the MIS 5 vegetation evolution in the Sokli area. During MIS 5d the presence of steppe-tundra vegetation and a braided river system demonstrate ice-free conditions with a severe continental climate. In contrast to MIS 5d, MIS 5c shows a more complex vegetation development of pioneer birch vegetation being replaced by pine-dominated forest and then mixed boreal forest. The exceptionally rich plant macrofossil assemblages associated with an overall fluvial depositional environment suggest that the summer temperature in the area was several degrees higher than today.

MIS 4 to MIS 2

Helmens (2013) compared five Late Pleistocene terrestrial climate proxy records from central, temperate and northern, boreal Europe. The records comprise the classic proxy records of La Grande Pile (NE France) and Oerel (N Germany) and more recently obtained records from Horoszki Duże (E Poland), Sokli (N Finland) and Lake Yamozero (NW Russia). The Sokli sedimentary sequence from the central area of Fennoscandian glaciation has escaped major glacial erosion in part due to non-typical bedrock conditions. Multi-proxy studies on the long Sokli sequence drastically change classic ideas of glaciation, vegetation and climate in northern Europe during the Late Pleistocene.

The comparison allows a re-examination of the environmental history and climate evolution of the last interglacial–glacial (MIS 5–2), and it shows that environmental and climate conditions during MIS 5 (c 130–70 ka BP) were different from those during MIS 4–2 (c 70–15 ka BP). As mentioned above, MIS 5 was characterised by three long warm intervals interrupted by two shorter cold and dry intervals. Subsequently, MIS 4–2 shows open vegetation both in central and northern Europe (Helmens 2013). It includes two glacial maxima (MIS 4 and 2) with sub-continental scale glaciation over northern Europe and dry conditions in strongly continental eastern European settings. During the cold MIS 4 and 2, south–central Sweden and the Forsmark region were ice covered (Figure 4-5). This is in contrast to the MIS 3 period, during which climate oscillations of millennial scale (so-called Dansgaard–Oeschger events) dominated. Summer temperatures approaching present-day values are recorded for various warming events during MIS 3 (Helmens 2013), i.e. during the Middle Weichselian (Table 4-2). Mild climate conditions in early MIS 3 at around c 50 ka BP were accompanied by large-scale deglaciation of the Weichselian ice-sheet. Ice-free conditions with Betula-dominated vegetation (including tree birch) persisted over large parts of Fennoscandia, possibly interrupted by glaciation, into the middle part of MIS 3 to c 35 ka BP.

Overall, MIS 5 was mostly mild with warmest or peak interglacial conditions at the very start during MIS 5e. MIS 4–2 was mostly cold with most extreme or peak glacial conditions in the closing phase during MIS 2. Additionally, the reviewed data (Helmens 2013) reveals restricted ice cover during MIS 3 and indicates that climate variability during parts of the last interglacial–glacial cycle was expressed mostly in terms of changes in degree of continentality possibly due to changes in sea-ice cover.

The MIS 3 period is also characterized by the presence of millennial scale climate oscillations (so-called Dansgaard–Oeschger events; Section 4.3.4), yielding summer temperatures similar to present-day values for some of the warming events (Helmens 2013). There are still unsolved questions related to an ice-free interstadial period during parts of MIS 3, many of them concerning the datings of various interstadial and ice-advance phases. Nevertheless, it seems clear that the Weichselian ice-sheet was considerably more dynamic during the MIS 3 period of the Middle Weichselian than previously thought, in line with the variable climate (Section 4.3.4). One implication of such a revised MIS 3 glacial history is that the Forsmark site was free of ice for a considerable amount of time during the Middle Weichselian, prior to the LGM. If so, the climate at the end of MIS 3 at Forsmark was probably of a periglacial character, allowing permafrost conditions to develop and be maintained, see Section 4.3.2.

After the MIS 3 period, during MIS 2, the Weichselian ice-sheet advanced to its Last Glacial Maximum (LGM) configuration. During the LGM, the entire area of Fennoscandia was covered by the ice-sheet, including south–central Sweden and the Forsmark region (lower panel of Figure 4-5). The ice volume was at its largest at ~20–21 ka BP, with the southern ice margin located in Germany and Poland. The ice reached its maximum LGM position at different times in different regions.

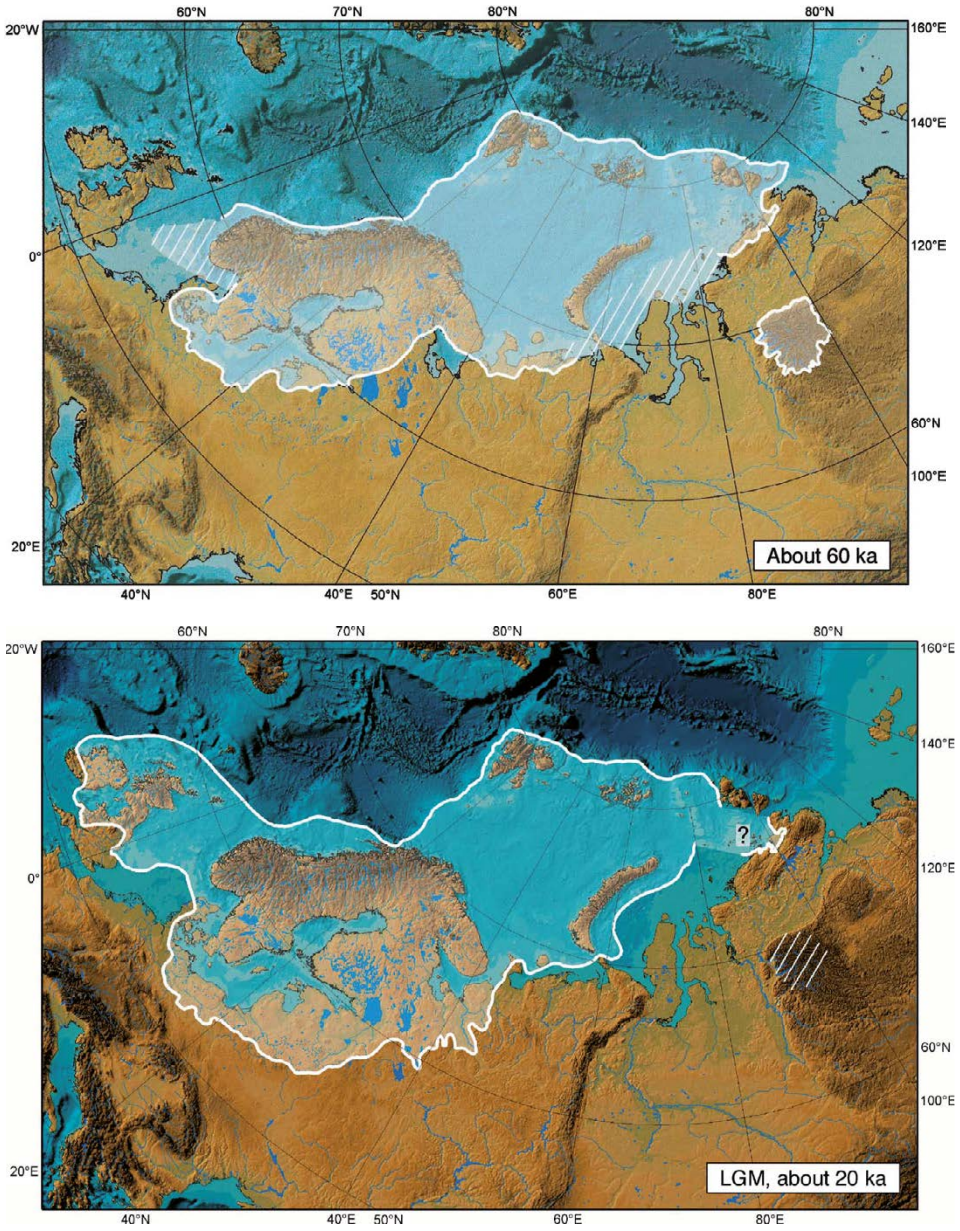

Figure 4-5. *Extent of the Eurasian ice-sheet during the glacial maximum stages of, the Middle Weichselian (60–50 ka BP, MIS 4) and the Late Weichselian (LGM, around 20 ka BP, MIS 2) as reconstructed from Quaternary geology. Between these stages of maximum ice-sheet extent, the ice-sheet had a more restricted configuration. From Svendsen et al. (2004).*

Deglaciation from LGM to the Holocene (MIS 2 to MIS 1)

Following the LGM, the ice-sheet started to retreat across e.g. northern Germany and Poland and subsequently over Fennoscandia, a sequence of events that is well-dated (e.g. Stroeven et al. 2016). Several re-advances took place during the deglaciation of the Danish and Norwegian coast. Furthermore, from Quaternary geological information it is known that temporary halts in the ice-sheet retreat took place several times in southern and south–central Sweden during the last deglaciation (e.g. Lundqvist and Wohlfarth 2000, Fredén 2002). For instance, the deglaciation was interrupted during the Younger Dryas stadial (12.9–11.7 ka BP), following the relatively warm Bølling-Allerød interstadial (14.7–12.9 ka BP). The ice-marginal deposits formed during the Younger Dryas can be identified all around Fennoscandia. A description of the characteristics of these stillstands during the last deglaciation in Fennoscandia is found in Section 4.2.2.

In the combined proxy data-climate modelling study by Schenk and Wohlfarth (2019) and Schenk et al. (2018) it was found that the rapid climate shift between the Bølling-Allerød interstadial and the Younger Dryas stadial was primarily a result of changes in seasonality, rather than a reduction of the summer temperature.

Based on several lake records from southern Sweden, they found clear evidence from plant macrofossils that remarkably high summer temperatures of at least c +16 °C prevailed throughout the deglaciation. Based on the oldest Swedish records, the high summer temperatures existed already directly after the ice-sheet retreated over southern Sweden during the pre-Bølling (15.5 ka BP) and remained high until the lakes became peatlands during the early Holocene (~ 10 ka BP).

In contrast to the warm summer air temperatures captured by plant macrofossils, lake water temperatures reconstructed from chironomids indicate distinct shifts between cold stadials and warm interstadials. These shifts co-vary with proxy-evidence from lipid biomarkes for dry conditions and a fresh moisture source during stadials and wetter conditions and a saltier moisture source. The compilation and quantification of minimum mean July temperatures based on climate indicator plant species from over 120 European sites suggests that the warm summers seen in southern Swedish lake records were present also on a broader regional scale during the Bølling-Allerød and Younger Dryas.

In the high-resolution climate model simulations, Schenk and Wohlfarth (2019) and Schenk et al. (2018) found that summer temperatures during the Younger Dryas stadial remained at least as high as during the preceding Allerød, consistent with the proxy evidence from southern Sweden and 120 European records. The persistence of high summer temperatures seen in both, proxy records and our climate simulation, results from atmospheric blocking of westerly winds over the Fennoscandian Ice-sheet during summer. The atmospheric blocking linked to the presence of the ice-sheet is intensified by the cold North Atlantic sea-surface temperatures during the Younger Dryas stadial. The blocking is however only stable during a short summer period and severe cooling dominates during the Younger Dryas in spring, autumn and winter. The simulation hence supports previous studies which suggest that the abrupt climate shifts are dominated by a shift in seasonality with increased continentality during stadials.

In addition, the climate model simulation in Schenk and Wohlfarth (2019) and Schenk et al. (2018) supports the proxy evidence of drier stadial conditions which, according to the model, might have been extreme owing to much lower humidity in response to a very cold ocean state and southern sea-ice front. During summer, the intensified blocking further reduces the advection of precipitation from the North Atlantic. Based on the comprehensive multi-proxy study and climate modelling results, they found a high agreement between proxy data and climate simulations that the shifts between cold stadials and warm interstadials during the deglaciation are dominated by shifts in seasonality/continentality where cold ocean states during a weak AMOC leads to severe winter–spring cooling and aridity and warm ocean states during a strong AMOC leads to milder winters and increased precipitation.

After the Younger Dryas, the ice retreated towards the Fennoscandian mountain range more or less continuously. The retreat of the ice-sheet, and associated increase of the summer temperature in northern Fennoscandia, is also seen in the Holocene lake sequence from the Loitsana Lake in the Sokli basin (Helmens 2019). Whereas the quantitative temperature reconstruction for the Holocene based on pollen of terrestrial plant taxa in the Loitsana sediments follows the classical trend of gradually increasing early Holocene mean July air temperatures in Fennoscandia, with a mid-Holocene maximum July warming between c 8 and 4 ka BP, plant macrofossils of telmatic vegetation, and chironomids, indicate an early onset of the maximum in July air temperatures in the early-Holocene prior to c 10 ka BP (Helmens 2019). The Holocene summer temperature evolution, recently reconstructed by aquatic/wetland taxa at several sites in northern Fennoscandia, follows the gradually decreasing orbitally-forced June insolation at 60 °N since 11 ka BP. The chironomid-inferred continentality-index suggests a more continental climate regime, with warm summers and cold winters, during the early Holocene than at present (Helmens 2019).

Hence, several independent studies, using different methodologies, suggest surprisingly warm summer conditions, up to present-day temperatures and above, and rich biotic communities during the last deglaciation (Schenk et al. 2018, Schenk and Wohlfarth 2019, Helmens 2018, 2019), and also during previous last glacial cycle deglaciations (Helmens et al. 2018, Helmens 2019).

Note that the typical Quaternary ice-sheet configuration over Fennoscandia was considerably smaller than that of a full ice-sheet configuration, and also considerably smaller than during the Younger Dryas. For average Quaternary ice-sheet conditions, the ice-sheet is centred over the Scandinavian mountain range (e.g. Porter 1989, Kleman et al. 2008), resulting in ice-free conditions in south–central Sweden including Forsmark.

For more detailed descriptions of the Weichselian glacial history, see Lokrantz and Sohlenius (2006), Lundqvist (2007), Wohlfarth (2010, 2013), Helmens and Engels (2010), Lambeck et al. (2010), Mangerud et al. (2011), Lundqvist et al. (2011, Figure III.3), Helmens (2013, 2019), and Schenk and Wohlfarth (2019).

4.2.2 Ice-marginal stillstands during the last deglaciation

From Quaternary geological information it is known that temporary halts in the ice-sheet retreat took place several times in southern and south–central Sweden during the Weichselian deglaciation (e.g. Lundqvist and Wohlfarth 2000, Fredén 2002). Similar, and in cases corresponding, halts are also documented from e.g. Finland, Denmark, Norway, Russia, Poland and Germany (e.g. Lagerlund et al. 1995, Marks 2002, Houmark-Nielsen and Kjær 2003, Lunkka et al. 2004). At these locations, dated marginal moraines, once formed along the former ice-sheet margin, indicate areas and periods when the ice margin was more or less stable at a certain location. No traces of such moraines, indicative of temporary halts, have been found from the growth phases of the Weichselian ice-sheet. It is possible that stillstands did occur also during growth phases, but that the resulting moraines have been obliterated by the subsequent ice coverage. However, during the Early Weichselian stadials, i.e. during MIS 5d and MIS 5b (Table 4-2), maximum ice configurations, with ice margins that may have been quasi stable for some period of time, have been envisaged for central Sweden (Lundqvist 1992), see also Lokrantz and Sohlenius (2006).

The longest and most prominent halt during the last deglaciation took place during the cold Younger Dryas stadial. On the basis of data from the GRIP ice core from Greenland, the Younger Dryas stadial began around 12.8 ka BP and ended around 11500 BP, resulting in a ~1300 year long Younger Dryas period. Quaternary geological information suggests that the associated Younger Dryas ice-sheet margin stillstands in Sweden occurred during a period of around 900 years (Fredén 2002). On glaciological grounds, Fastook and Holmlund (1994) concluded that the climatic event responsible for the Younger Dryas stillstand could have been short, even less than 500 years.

It should be noted however that during the Younger Dryas period, as well as for several other less prominent stillstands south of the Younger Dryas moraine complex, the position of the ice margin was not completely stable. Instead, as a response to climate variability and ice-sheet dynamics, the ice front typically oscillated back and forward, in cases up to several tens of km (e.g. Lundqvist and Wohlfarth 2000, Lunkka et al. 2004). For the Younger Dryas, the resulting zone of ice-marginal deposits is typically around 20–25 km wide in central and eastern Sweden (Fredén 2002). During shorter halts in the deglaciation, this zone may be considerably narrower or absent. During phases of maximum ice-sheet configuration, such as during the LGM, the ice margin typically also oscillates back and forward as a response to ice-sheet dynamics and climate variability.

South of the Younger Dryas zone, at least six older stillstands in the Weichselian deglaciation of southern Sweden have been documented (Lundqvist and Wohlfarth 2000). At several of these sites, ice-marginal moraines have been suggested to have formed during periods of up to 100–200 years, such as the large Göteborg Moraine which formed sometime between 15.4 and 14.5 ka BP (Lundqvist and Wohlfarth 2000). The suggested, often maximum, formation times of these moraines indicate that the ice margin was relatively stable for these periods or shorter. In southern Finland, it has been estimated that the largest Younger Dryas end moraine complexes, i.e. the First and Second Salpausselkä end moraines, as well as the younger Central Finland end-moraine, also were formed during periods up to a few hundred years long (Lunkka et al. 2004). These estimates thus give an indication of the duration of periods with stable ice-margin position during the last deglaciation.

In summary, it may be concluded that during the deglaciation of the Weichselian ice-sheet, the general ice-sheet retreat temporarily halted several times. This is seen from dated ice-marginal moraines, including the deposits from the Younger Dryas stadial. During such halts, the ice margin either oscillated back and forth or moved slowly within a zone that could be many km wide, in the case of the

Younger Dryas, several tens of km. During the formation of individual moraine ridges, the ice margin is estimated to have been at stable positions for up to a few hundred years. It must be assumed that similar types of stillstands may occur also during phases of ice-sheet advance, see Section 4.5.1.

4.3 Examples of Weichselian climates

During the Weichselian, climate shifted many times between warmer and colder periods, as reflected in the growth and decay phases of the Weichselian ice-sheet, see Section 4.2.1. The variability and range within which the climate shifted during the last glacial cycle could be expected also during future glacial cycles. Therefore, quantitative descriptions of prevailing climate conditions for periods with fundamentally different climates during the Weichselian are given below for Sweden and the Forsmark region.

The aim of the following descriptions of Weichselian climates is not to give a full review of all that is known on climate and climate variability during the last glaciation. Instead, the intention is to provide examples of Weichselian climates by selecting climate reconstructions for both stadial and interstadial phases and to cover a broad time span of the glacial cycle.

4.3.1 Early Weichselian (MIS 5d–5a; 115–74 ka BP)

The Fennoscandian climate during the Early Weichselian (MIS 5d–5a, 115–74 ka BP, Table 4-2) varied significantly, as described in Section 4.2.1. Past environmental and climate conditions have been reconstructed for MIS 5d (the Herning stadial 115–105 ka BP, Table 4-2) by analyses of pollen from the Sokli sediment sequence (Helmens et al. 2012, Helmens 2019). The results show that, for the ice-free stadial conditions at the investigated site, the summer July air temperature was at least +12–14 °C (present summer mean temperature is 13 °C) accompanied by steppe-tundra vegetation with a local presence of birch trees and conifers for this period.

During MIS 5c (the Brørup interstadial, 105–93 ka BP), summer temperatures inferred from plant macrofossil remnants indicate surprisingly warm conditions for northern Fennoscandia (Väliranta et al. 2009, Engels et al. 2010). Minimum July temperatures were as high as 16 °C, which is 3 °C warmer than at present (Väliranta et al. 2009, Helmens 2019), probably driven by higher summer insolation. At that time, open birch woodland existed at the site within a subarctic climate. This result contrasts with other (lower-resolution) reconstructions from northern Fennoscandia which indicate MIS 5c temperatures 6–7 °C lower than present, see Engels et al. (2010). However, several central European sites indicate that there was a phase during the MIS 5d interstadial that was characterised by high summer temperatures, and a comparison between the high-resolution reconstructions from western Europe and the results presented in Engels et al. (2010) suggests that the north–south July air temperature gradient between the mid- and high-latitudes was much weaker during MIS 5c than at present.

Results from the multi-proxy data obtained for MIS 5a (Helmens 2019, Helmens et al. 2021) suggest, following deglaciation of a MIS 5b ice-sheet cover of the site, the development of shrub tundra vegetation to sub-arctic birch forest and then pine-dominated forest with larch. The minimum July temperatures for this time are comparable to the present day (in the order of +12 to +15 °C, Figure 4-4). One suggested reason for the warm climate conditions during this interstadial is that the contemporary astronomical forcing resulted in a weaker north–south temperature gradient and a longer growing period, creating more favourable climate conditions than at present (Väliranta et al. 2009).

4.3.2 Middle Weichselian (MIS 4 – MIS 3; 74–24 ka BP)

Examples of Fennoscandian climates during the MIS 3 interstadial (59–24 ka BP) have been studied by use of geological information (Helmens 2009, Wohlfarth 2009) and by climate modelling (Kjellström et al. 2009, including erratum Feb 2010). MIS 3 covers a long period that includes both rapid millennial-scale climate shifts and longer trends in changing climate, see Wohlfarth (2009), Helmens (2013) and Section 4.3.4. A few examples of climates occurring during MIS 3 are given below.

Early MIS 3 (at ~ 50 ka BP)

A comprehensive environmental reconstruction of early MIS 3 conditions, at around 50 ka BP, was made based on multi-proxy analysis on a two-metre thick laminated, lacustrine clay-silt sequence obtained at the Sokli site in northern Finland (Helmens 2009). The analyses included lithological characteristics; organic content (loss-on-ignition, LOI); plant microfossils (pollen, spores, algal and fungal remains); macrofossils of plants (e.g. seeds, moss remains) and of aquatic animals (e.g. statoblasts of Bryozoa); head-capsules of chironomids (i.e. aquatic insects); and diatoms and other siliceous microfossils (e.g. phytolits, chrysophyte stomatocysts). Additionally, geomorphic evidence and analysis of DEM data are employed in the environmental reconstruction. Mean July temperatures were reconstructed by applying transfer functions to the pollen, chironomid and diatom records.

The results have been surprising in various aspects, seriously challenging previous concepts on environmental conditions during early MIS 3 in the near-central area of the Weichselian glaciation. Traditionally, the area is thought to have been ice covered throughout MIS 4–2, i.e. from around 60 ka BP to the final deglaciation, see above. Helmens (2009) showed not only ice-free interstadial conditions but also climate warming to present-day temperatures. The laminated sediments seem to have been deposited in a sheltered embayment of a glacial lake impounded along the ice front of the Weichselian ice-sheet. Throughout the deposition of the lacustrine sediments, the reconstructed terrestrial ecosystem on the deglaciated land is low-arctic shrub tundra very similar in composition to modern tundra in the continental sector of northern Fennoscandia. The distributional ranges of pine and tree birch were probably only a few hundred kilometres south or south–east of the Sokli site. This is concordant with the sparse evidence for the presence of boreal tree taxa during MIS 3 in the Baltic countries and further east in Europe, but contradicts with the commonly inferred treeless tundra or grass-dominated steppe conditions in central Europe.

Mean July air temperatures in the magnitude of present-day values are reconstructed by the chironomid and diatom records as well as by fossils from aquatic plants and Bryzoa. Temperature inferences based on the terrestrial pollen are consistently lower than the temperatures reconstructed from the fossil aquatic assemblages. It is possible that the regional terrestrial and the local aquatic systems responded differently to the climatic and landscape features at around 50 ka BP. Warmest and moistest conditions are recorded in the lower part of the laminated lacustrine sequence. The chironomid-inferred mean July air temperatures are around 13 °C (i.e. the current temperature) ± 1.15 °C in the lower part of the lake sequence and to around 12 ± 1.15 °C in the upper part. The mean July air temperatures inferred from the terrestrial pollen data lie within the range of around 12 ± 1.5 °C (lower part of sequence) and around 11 ± 1.5 °C (higher part of sequence). Hence, the records suggest, albeit with some uncertainty, that there is a gradual cooling during this time. This is consistent with the pattern of the Greenland millennium-scale Dansgaard–Oeschger interstadials in which abrupt warming is followed by a gradual cooling (Dansgaard et al. 1993). High summer temperatures are ascribed in part to enhanced July insolation compared with present at the high latitude site of the site.

Comparison with recently published, well-dated sediment sequences in eastern and western Finland suggests ice-free and warm conditions in major part of eastern Fennoscandia at ~ 50 ka BP. Open birch forest seems to be registered in eastern Finland during part of the warming event. Direct evidence is lacking to reconstruct the total time span with ice-free conditions at the studied sites. It is argued that the Sokli site was glaciated during the overall colder late MIS 3. The absence of well-dated geological data in northern Sweden hampers a reconstruction of the total ice-marginal retreat in the continental sector of the Fennoscandian Ice-sheet during the early MIS 3 climate warming event. For more details on this study, see Helmens et al. (2007, 2009), Engels et al. (2008), Bos et al. (2009), Helmens (2009), Helmens and Engels (2010), Engels et al. (2010).

A warm climate during early MIS 3, such as reconstructed for northern Fennoscandia by e.g. Helmens (2009), is in line with, and probably necessary for, a deglaciation of the large ice-sheet that existed during MIS 4.

Middle MIS 3 (at 44 ka BP)

A comprehensive climate modelling study was performed to investigate climate extremes within which the climate in Fennoscandia may vary on a 100 ka timescale (Kjellström et al. 2009, including erratum dated Feb 2010). Three different periods were simulated, a cold glacial climate (at LGM, ~21 ka BP), a periglacial climate (at MIS 3, 44 ka BP) and a warm future climate dominated by global warming (a few thousands of years after present). In the present section, results from the periglacial climate simulation are presented. Results from the LGM climate simulation are presented below in the present section, under the heading "Late Weichselian including LGM (24–12 ka BP)", whereas results from the global warming simulation are described in Section 5.1.7.

The choice of period to simulate for MIS 3 followed from a workshop on MIS 3 organised by SKB in September 2007 (Näslund et al. 2008) with the specific purpose of supporting this selection. Only limited and in some cases controversial, palaeo-information is available to reconstruct the extent of the Fennoscandian ice-sheet during the different warm and cold intervals of MIS 3. We here assumed, in line with several recent studies, see above, that the southern part of Fennoscandia was ice free during some of the MIS 3 stadials.

The modelling activities included the use of; i) a fully coupled Atmosphere-Ocean General Circulation Model (AOGCM; Community Climate System Model version 3, CCSM3), ii) a Regional Climate Model (RCM; Rossby Centre Regional Climate Model, RCA3), and iii) a dynamic vegetation model (DGVM; the LPJ-GUESS model). The AOGCM was used to simulate the global climate in steady-state simulation for the selected period. Even though AOGCMs are powerful models they are relatively coarse in their resolution due to computational limitations. Therefore, the output from the AOGCM was used as input to a RCM that provides output at a relatively high horizontal resolution for Europe. Both global and regional climate models hold descriptions of the land surface, including vegetation. In the regional model, it is important to describe the vegetation cover with a high degree of regional detail. Such details are missing in available global fields and details of the vegetation cover must be estimated, based on the global fields and consideration of, among other things, land/sea distribution. To improve the representation of the regional vegetation, a dynamic vegetation model was used to simulate the European vegetation resulting from the RCM-simulated climate. In a subsequent step, the new vegetation was used in a new RCM simulation that provided the final climate output. For the studied MIS 3 period, data on relevant climate parameters was extracted from the regional model for the Forsmark area.

The global model simulation of the periglacial MIS 3 climate used a CO_2 concentration in the atmosphere of 200 ppmv (parts per million volume) (Kjellström et al. 2009). An ice-sheet with a restricted configuration was assumed, and, in line with this, a simulated MIS 3 ice-sheet configuration obtained from the Weichselian ice-sheet reconstruction described in Section 3.1.4 was used (Kjellström et al. 2009). For a detailed description of the assumptions made in the modelling process, model forcing and initial conditions (such as astronomical and solar forcing, concentration of greenhouse gases and aerosols in the atmosphere, extents of ice-sheets, distribution of land and sea, topography and vegetation), also see Kjellström et al. (2009).

In addition to the modelling activities, an effort was made to collect palaeoclimatic information by compiling various MIS 3 and LGM proxy data from different sources (Kjellström et al. 2009, Wohlfarth 2009). Part of this palaeoclimatic information was used to constrain the forcing conditions used in the climate models. Other proxy data were used for model evaluation purposes. Results from the global climate model were compared with proxy records of sea-surface temperatures and with terrestrial climate records. The regional climate model results have been compared with existing terrestrial palaeoclimate records from Europe.

Global climate

Figure 4-6 shows the simulated global climate from the middle MIS 3 simulation. Seasonal mean changes in temperature as compared with a simulation of the pre-industrial climate (with forcing conditions set at levels consistent with those preceding the 18th century) are also shown.

The annual mean surface cooling in the MIS 3 simulation as compared with pre-industrial conditions is most pronounced over the Laurentide and the Fennoscandian ice-sheets and over the Greenland-Iceland-Norwegian Sea, with a maximum cooling of 25 °C (Figure 4-6). A large portion of the cooling over the Fennoscandian and Laurentide ice-sheets is due to the increased elevation over the ice-sheet. The cooling amounts to 5–10 °C north of 40 °N in the Atlantic Ocean, the Arctic Ocean and over Antarctica and the Southern Ocean. The sea-ice extent is increased in the MIS 3 simulation in the North Atlantic and north Pacific as compared with the pre-industrial simulation (Figure 4-6).

Even though proxy data for the period around 44 ka BP are sparse, comparison with available sea surface temperature data shows that the globally modelled temperatures and proxy data are in reasonable agreement. For further results and discussion of the MIS 3 simulation from the global climate model, and for details about the comparison with MIS 3 climate proxy data, see Kjellström et al. (2009).

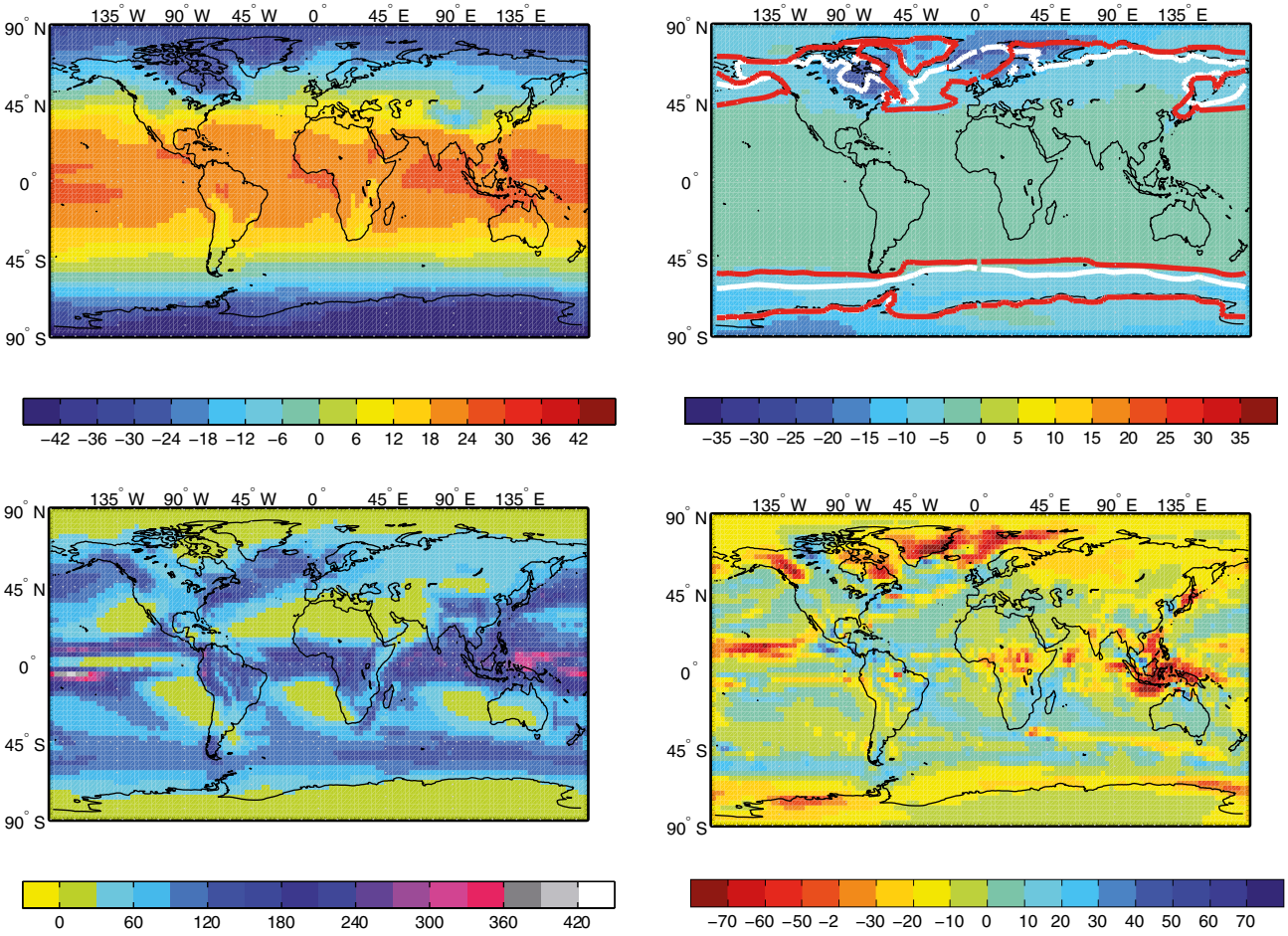

Figure 4-6. *Annual mean near-surface air temperature in the MIS 3 simulation (upper left) and the difference compared with a simulated pre-industrial climate (upper right). Units are °C. Also shown is the annual mean sea ice edge (defined at 10 % areal sea ice cover) for the pre-industrial simulation (white; upper right)) and the MIS 3 simulation (red; upper right). The lower panels show the simulated precipitation (lower left) and the difference compared with the simulated pre-industrial climate (lower right). Units are mm month^{-1}. From Kjellström et al. (2009).*

Climate in Europe and Sweden

The regional climate model was then used to downscale the model results of the global climate model to obtain a higher resolution data over Europe and Sweden. The resulting climate over Europe was used to produce a new vegetation distribution with the vegetation model. This vegetation was in turn, used as input to the regional climate model, to produce a climate in line with the new vegetation. An evaluation of the results from this iterative process is given in Kjellström et al. (2009). Figure 4-7 to Figure 4-10 present selected results on temperature and precipitation from the regional modelling.

During this part of the middle Weichselian, the temperature climate is dominated by a very strong seasonal cycle (Figure 4-8) and a pronounced north–south gradient in the winter (Figure 4-7, upper row, middle panel). In the north, the effect of the Weichselian ice-sheet is clearly seen in the isolines of temperature showing low temperatures in parts of Fennoscandia. The isotherm showing 0 °C annual mean temperature goes south of Ireland, through England and the southern parts of Denmark, just south of Sweden and then eastwards (Figure 4-7, upper row, right panel). Compared with the present climate (1961–2000), the annual mean temperature in the MIS 3 simulation is ~5 °C colder around the Mediterranean, 5–10 °C colder in central Europe and more than 8 °C colder in the ice-free parts of Fennoscandia (Figure 4-7, lower row, right panel). The same values as for difference in annual temperature apply for winter temperature in southern and central Europe. The winter temperature of the British Isles is 10–15 °C colder and the southern tip of Fennoscandia around 15 °C colder in comparison with the present climate (Figure 4-7, lower row, middle panel). Over the ice-sheet in northern Fennoscandia, temperatures are at least 30 °C colder than in the present climate (1961–2000) simulation. On Iceland and over the Norwegian Sea, the difference from the late 20th century is even larger. In summer, most of continental Europe is 0–5 °C colder than in the late 20th century, western Europe and the British Isles are 5–10 °C colder and northern Fennoscandia is 10–15 °C colder than in the simulated present climate (Figure 4-7, lower row, left panel).

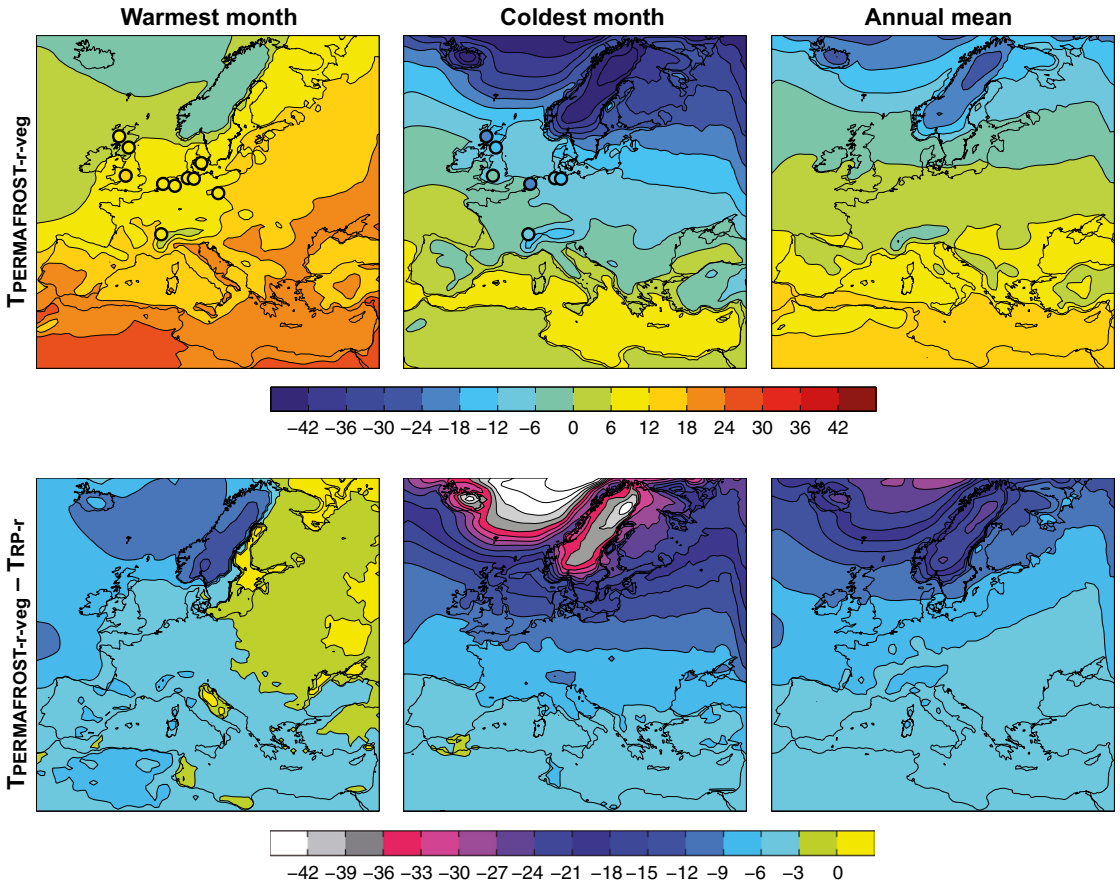

Figure 4-7. *Mean air temperatures of the warmest month, coldest month and annual mean in the MIS 3 simulation (top). Shown also are temperature estimates based on proxy data as described in Kjellström et al. (2009) (coloured circles). The lower row shows the differences between the simulated MIS 3 climate and a recent-past climate simulated for the period 1961–2000. From Kjellström et al. (2009).*

The annual mean precipitation in the MIS 3 simulation is characterized by considerably drier conditions than in the simulated present climate (1961–2000), by more than 360 mm a^{-1} in large parts of Fennoscandia and over the North Atlantic, and by an increase in precipitation of up to 360 mm a^{-1} in parts of the southwest (Figure 4-9, upper row right panel). In the rest of the model domain, differences are, with few exceptions, smaller.

The drier climate in northern Europe is reflected in the seasonal cycle of precipitation. For Sweden there is a reduction of more than a factor of two in winter and substantial reduction also during summer (Figure 4-10). Further south, the reduction is most evident in the winter half of the year whereas in southernmost Europe the changes relative to the present climate are small for all months.

For further results, on the European scale, from the MIS 3 climate simulations, including results and discussion of the simulations of MIS 3 vegetation, comparisons with climate proxy data, and comparisons with other model simulations of MIS 3 climates, see Kjellström et al. (2009).

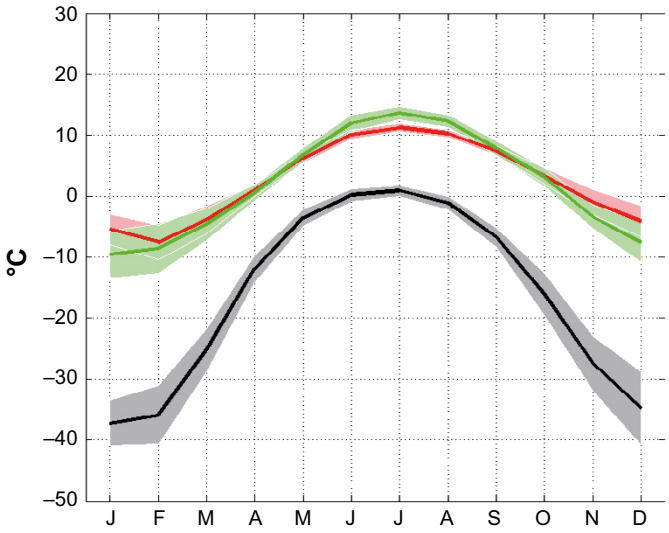

Figure 4-8. *Annual temperature range in Sweden for MIS 3 (black), simulated present climate (red) and according to the CRU (Climate Research Unit, East Anglia) observational data for the period 1961–1990 (green). Shaded areas in corresponding colours indicate the ±1 standard deviation range of individual monthly averages in the three data sets. From Kjellström et al. (2009).*

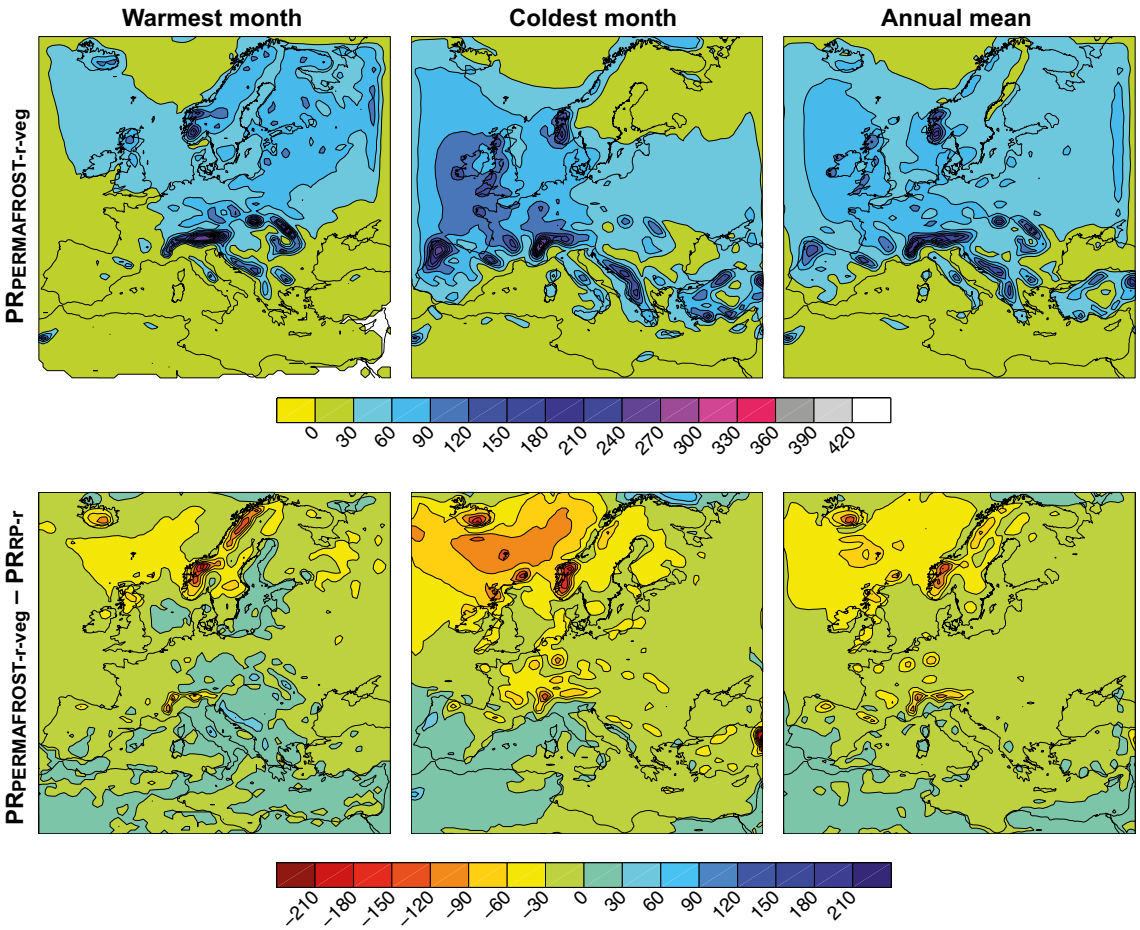

Figure 4-9. *Mean precipitation of the warmest month, coldest month and annual mean in the MIS 3 climate simulation (upper row). Also shown are differences between MIS 3 simulation and the simulation of the present (1961–2000) climate. Units are mm month^{-1}. From Kjellström et al. (2009).*

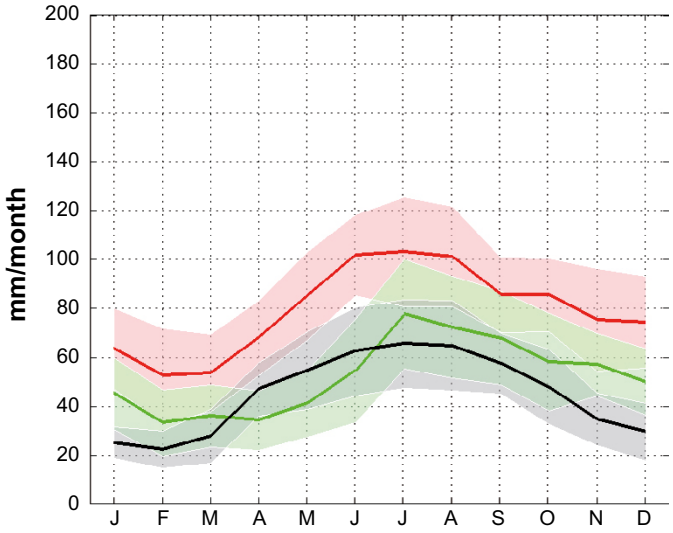

Figure 4-10. *Annual precipitation range in Sweden in the MIS 3 simulation (black), present climate simulation (1961–2000) (red) and according to the CRU observational data (green). Shaded areas in corresponding colours indicate the ±1 standard deviation range of individual monthly averages in the three data sets. From Kjellström et al. (2009).*

Do the results support a cold and dry climate favourable for permafrost growth? Heginbottom et al. (1995) examined the relation between ground temperature and permafrost continuity. An annual ground temperature of between −5 and −2 °C is defined as the boundary for discontinuous permafrost (50–90 % of landscape covered by permafrost) and −5 °C and colder as the boundary for continuous permafrost (90–100 %). However, it is also stated that a large part of areas with continuous permafrost has a ground temperature warmer than −5 °C. Since the ground temperature differs from the near-surface air temperature by a few degrees, see Section 3.4, the simulated annual mean ground temperatures over Europe for MIS 3 are presented in Figure 4-11.

In central and northern Fennoscandia, outside of the prescribed ice-sheet, the modelled MIS 3 annual average ground temperature is colder than −5 °C (Figure 4-11), which suggest that the climate conditions are favourable for development of continuous permafrost. South of this, the modelled annual average ground temperature increases, reaching 0 °C in the southernmost parts of Fennoscandia. The higher ground temperatures in the southern areas including northernmost Denmark, southern Sweden, Estonia and part of what today is the Baltic Sea and Gulf of Finland do not fulfil the thermal requirements for extensive permafrost. However, it is cold enough for sporadic permafrost (less than 50 % of landscape covered), which may exist when the annual mean ground temperature is between 0 and −2 °C. Based on these results of Kjellström et al. (2009) it is concluded that conditions are favourable for permafrost growth in the inferred ice-free parts of Fennoscandia.

Do the results support a restricted MIS 3 Fennoscandian ice-sheet? The global and regional climate models do not include dynamical modelling of ice-sheets and thus an ice-sheet cannot form in the models, even if the climate conditions are favourable for ice-sheet growth. The snowpack is, however, allowed to build up in the model. If the snow depth increases in time in a specific region, we can take this as an indication that an ice-sheet would grow in this region if such processes were included in the model. However, the opposite situation, a lack of snow accumulation in front of, or at the margins of, a prescribed ice-sheet, does not necessarily mean that the ice-sheet would not grow (simply the lowermost part of the ice-sheet would have a net mass loss, which is typical for ice-sheets ending on land). Growth of the ice-sheet could still be possible if the precipitation over the ice-sheet were large enough compared with its mass loss by melting, i.e. if conditions for the common pattern of ice-sheet growth were satisfied.

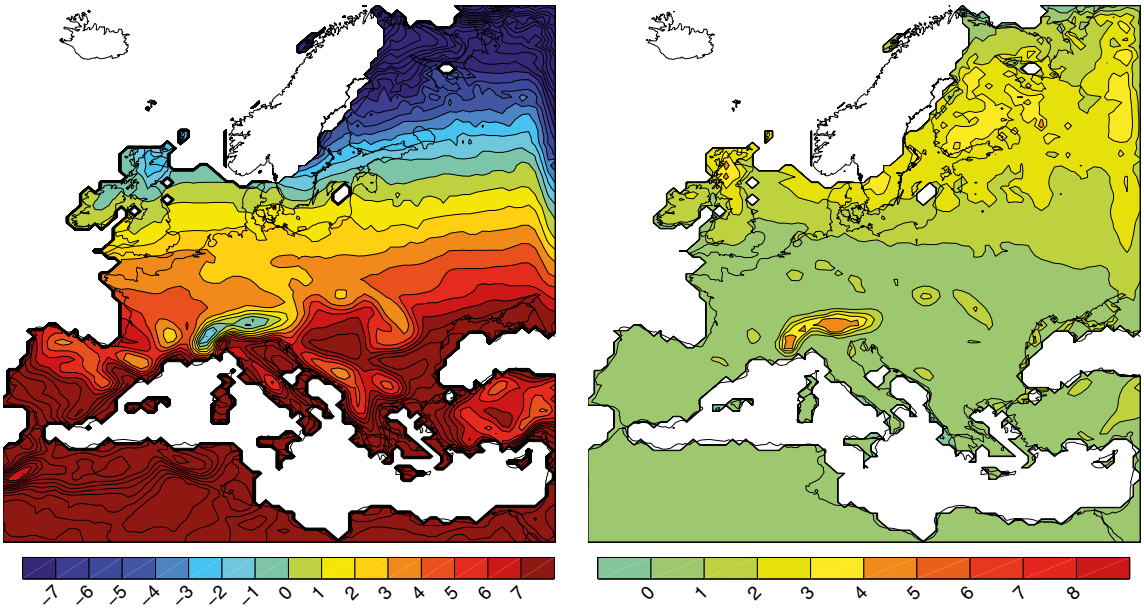

Figure 4-11. *Annual mean ground temperature (left) and difference between near-surface air temperature and the ground temperature (right) in the MIS 3 simulation. Units are °C. White areas in Fennoscandia are covered by the prescribed restricted MIS 3 ice-sheet. From Kjellström et al. (2009).*

In the middle MIS 3 simulation, the snow depth in eastern Sweden, including the Forsmark region, does not increase in time. The annual minimum snow depth (occurring in September) is close to zero (varying from 0–0.02 m equivalent water depth). For the issue of whether the simulated climate is in line with the prescribed restricted middle MIS 3 ice-sheet configuration, with ice-free conditions in e.g. the Forsmark region (Figure 4-11), one can therefore conclude that 1) an ice-sheet would not grow locally from the local precipitation in front of the ice margin, 2) the modelled temperature and precipitation climate in front of the ice-sheet is consistent with the assumed ice-free conditions and restricted ice-sheet coverage, but it does not exclude the possibility of a larger ice-sheet.

Climate in the Forsmark region

Figure 4-12 and Figure 4-13 show average air temperature and precipitation for a 50-year period of the simulated MIS 3 climate, and a comparison with the climate simulated for present conditions. The results show that the climate is significantly colder and drier than at present, with arctic climate conditions prevailing in the Forsmark region.

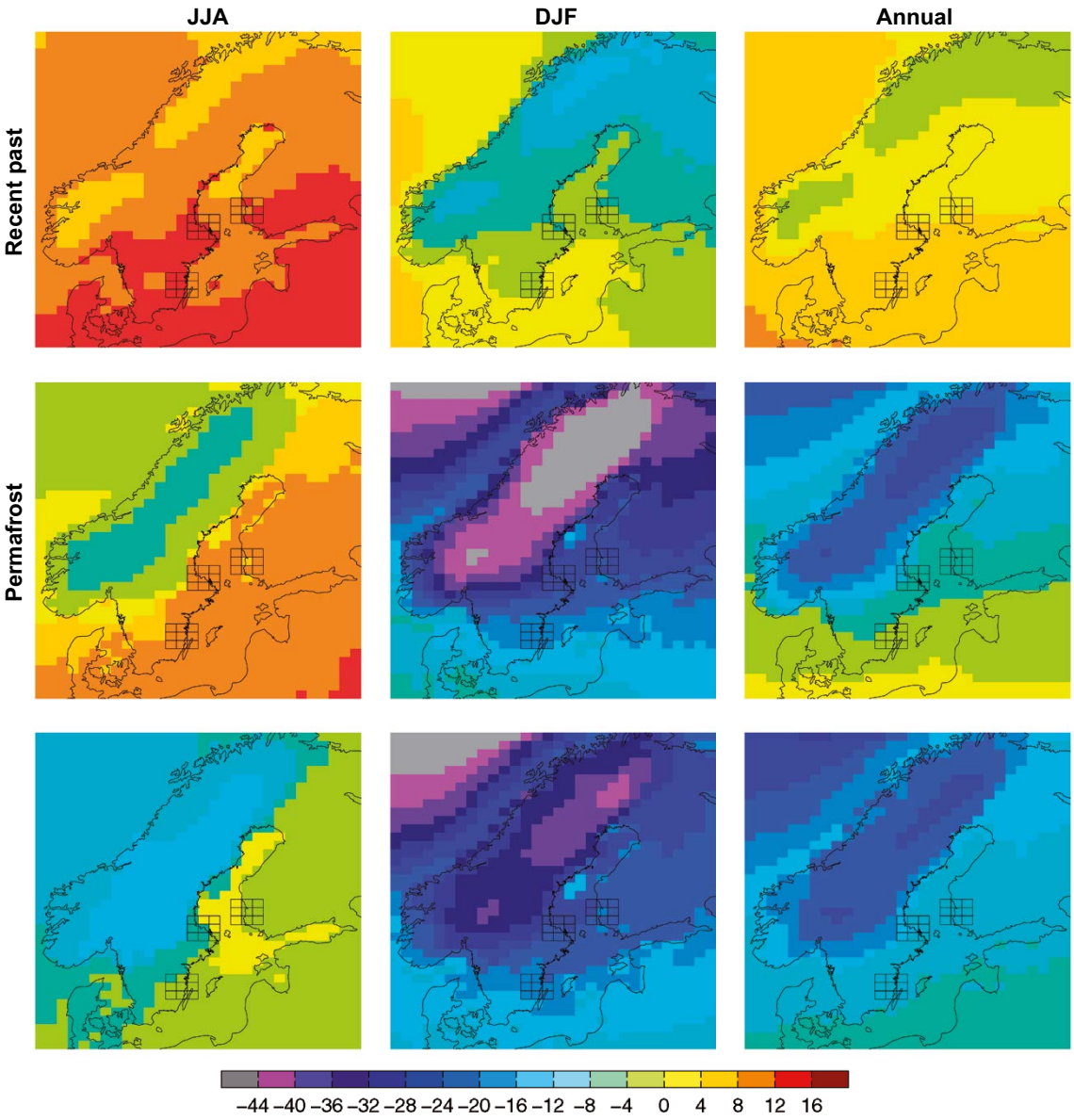

Figure 4-12. *Seasonal and annual mean temperature for the present (1961–2000) (upper row) and MIS 3 (middle row) climate simulations. The lower row shows the difference between the two. Units are °C. From Kjellström et al. (2009).*

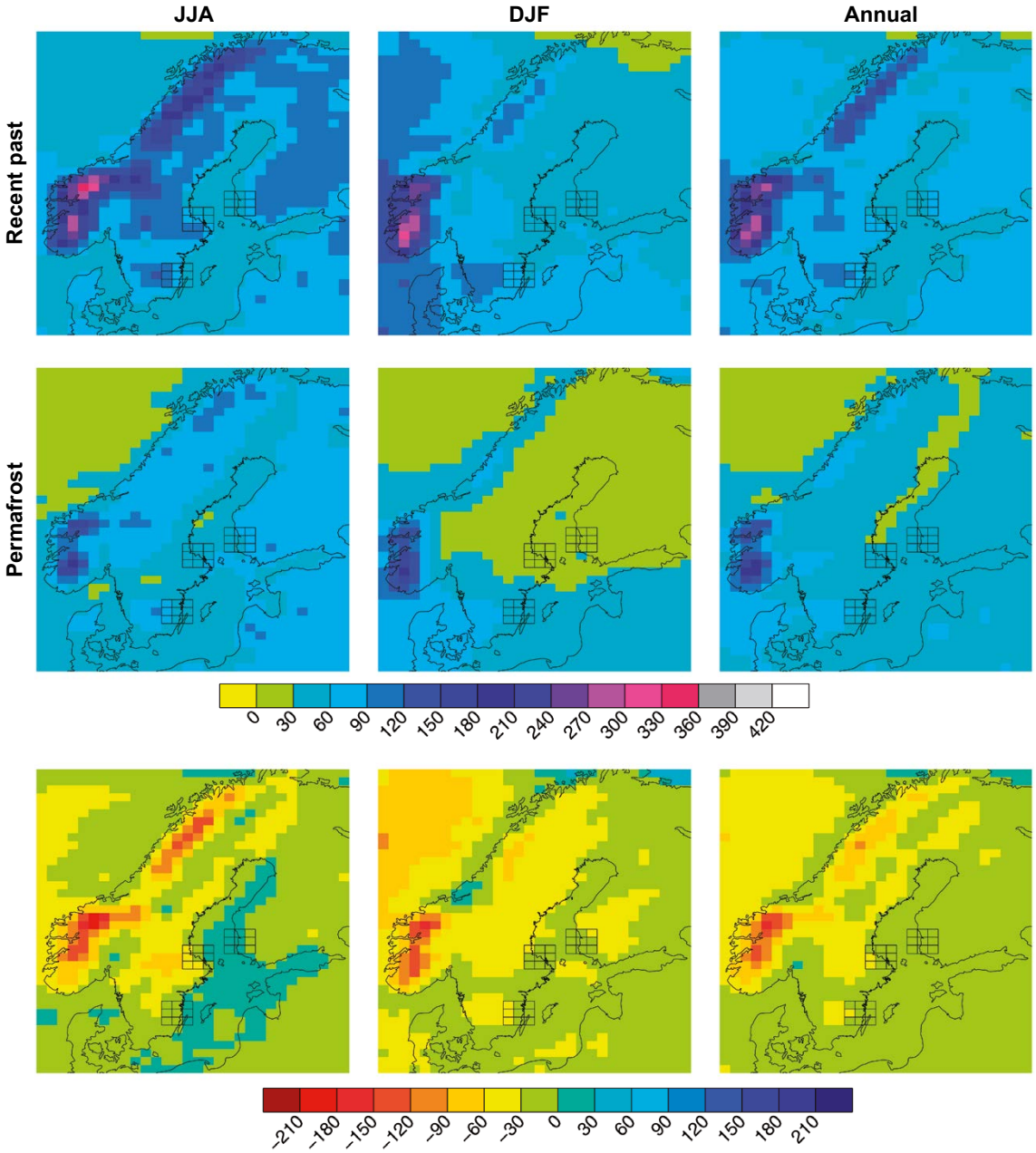

Figure 4-13. *Seasonal and annual mean precipitation in the present (1961–2000) (upper row) and MIS 3 (middle row) climate simulation. The lower row shows the difference between the two. Units are mm month^{-1}. From Kjellström et al. (2009).*

The last step in the MIS 3 climate modelling study was to extract climatological data for the Forsmark region from these regional modelling results. Figure 4-14 shows the grid boxes used for extraction of data. Information was extracted from the model grid point located closest to the Forsmark site.

50-year averages values from the regional MIS 3 climate simulation show that the annual mean air temperature in the Forsmark region is −7.6 °C during the inferred ice free stadial 44 ka ago. This is 12 degrees lower than in the simulated present climate (1961–2000). The largest difference compared with the simulated present climate in the seasonal cycle of temperature is seen in winter (Figure 4-15, upper row, second column).

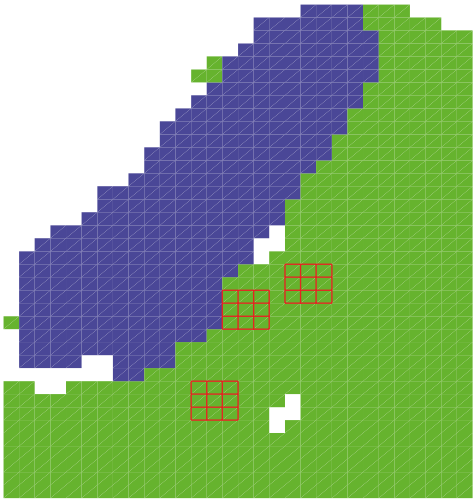

Figure 4-14. *Land (green), ice-sheet (blue) and sea extent (white) in the Fennoscandian region used for the MIS 3 climate simulation. The 3 × 3-grids represent grid boxes covering the Forsmark, Oskarshamn and Olkiluoto sites (centre box) and the eight surrounding boxes. Grid boxes with a land fraction lower than 20 % are not filled. Results from Oskarshamn and Olkiluoto are presented in Kjellström et al. (2009). From Kjellström et al. (2009).*

The mean annual precipitation in the Forsmark region is 441 mm, which is 225 mm (or 30 %) less compared with the simulated present climate. In this periglacial climate, the precipitation is lower than in the present climate for most parts of the year, and there is a very strong seasonal cycle in snow cover as the temperatures during summer get well above 0 °C allowing complete snow melting (Figure 4-15, upper and lower row, second column). The length of the completely snow-free season is three months and there is a more or less constant snow cover over at least 3 months.

The annual surface runoff is 139 mm in this exemplified periglacial climate, which is somewhat less (36 mm a^{-1}) than in the simulated present climate. In the MIS 3 climate, there is a clear spring peak in runoff connected with the snow melt which is more extensive than in the simulated present climate, since more snow is accumulated on the ground during the winter. During the remaining part of the year, the runoff is fairly small, due to the cold conditions during winter and the relatively small amounts of precipitation during summer. Given the uncertainties and assumptions used in the climate modelling, the model results thus show that the MIS 3 climate in the Forsmark region may be characterized by a significantly colder and drier climate than at present and also that the surface runoff is reduced.

The annual mean ground temperature is about −4 °C in the Forsmark region (Figure 4-11). According to Heginbottom et al. (1995) these temperatures indicate that climate conditions are favourable for discontinuous permafrost (covering 50–90 % of the landscape). The cold and dry climate with partially snow-free conditions implies that the climate is very favourable for permafrost growth.

In summary, the results from Kjellström et al. (2009, including erratum Feb 2010) show that i) the climate models produce a cold and dry arctic climate in the Forsmark region for a stadial during MIS 3, ii) the resulting climate is in agreement with ice-free conditions in south–central Fennoscandia and iii) that this climate is suitable for permafrost growth in the Forsmark region.

The major uncertainties in the climate simulation are related to uncertainties in forcing, model formulation and natural variability. These uncertainty aspects are discussed in detail in Kjellström et al. (2009). For further details on the setup, results, and discussion of the MIS 3 climate modelling results, see Kjellström et al. (2009, including erratum Feb 2010), Kjellström et al. (2010a), Brandefelt et al. (2011).

Following the very warm temperatures reconstructed for *early* MIS 3, described above, which are suggested to have resulted in ice-free conditions over large parts of Fennoscandia during MIS 3 (e.g. Helmens et al. 2009, Wohlfarth 2009, Wohlfarth and Näslund 2010), the low air temperatures simulated for Fennoscandia for the middle MIS 3 stadial (44 ka BP) are in line with the view that the Weichselian ice-sheet needs to re-grow to attain the known large MIS 2 (LGM) ice configuration in a relatively short time.

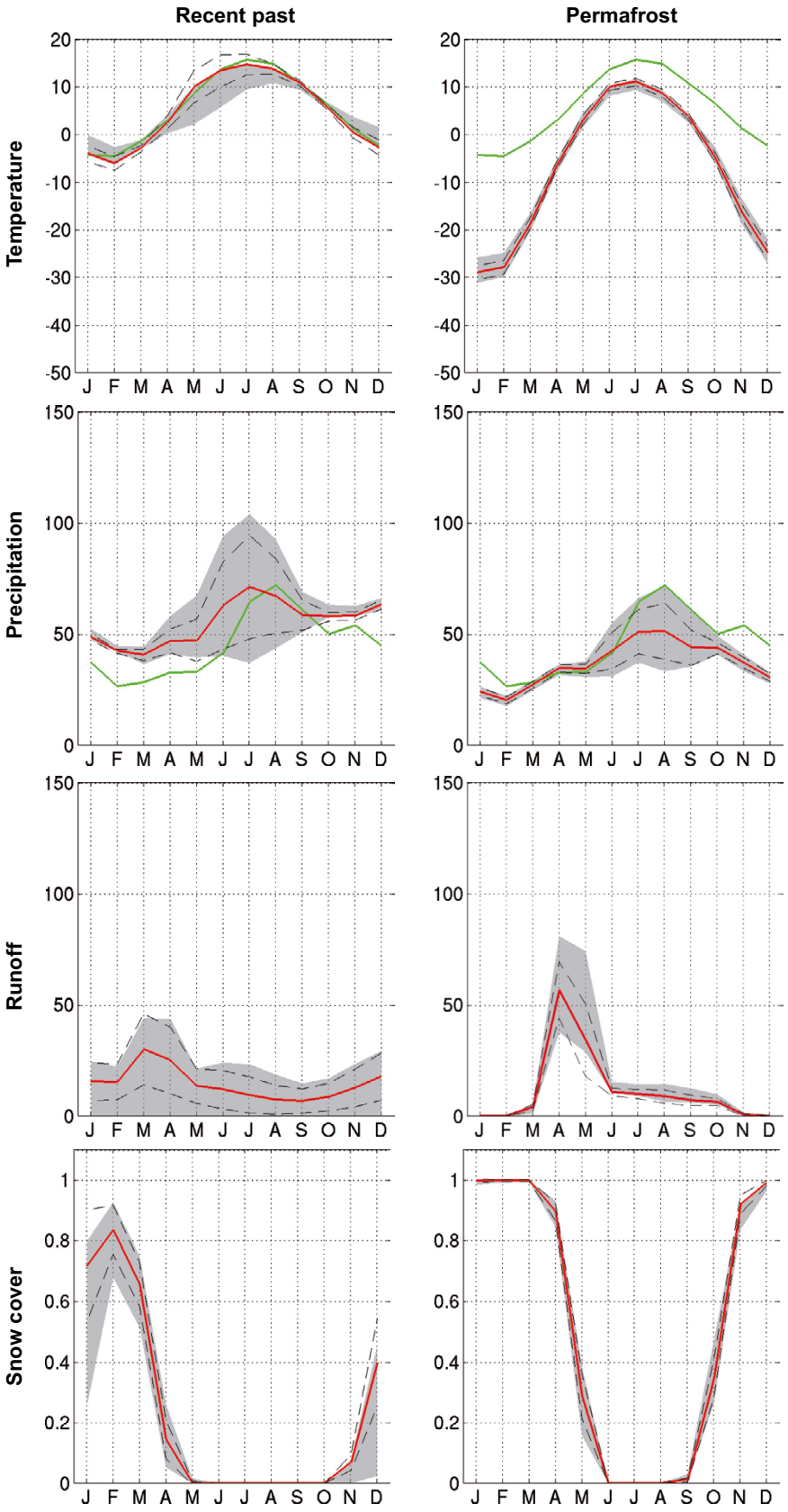

Figure 4-15. *Simulated seasonal cycles of temperature (°C), precipitation (mm/month), runoff (mm month^{-1}) and snow fraction (dimensionless ranging from 0 to 1) at the grid box closest to the Forsmark site (red line). The spatial variability in the 3 × 3-grids (Figure 4-14) is displayed with the dashed lines representing ±1 standard deviation calculated from the 9 grid boxes, and the grey area representing the absolute maximum and minimum, of the 9 grid boxes. The green line for temperature and precipitation is the observed seasonal cycle from the CRU data set in the period 1961–1990, see Kjellström et al. (2009). From Kjellström et al. (2009).*

4.3.3 Late Weichselian including LGM (24–12 ka BP)

As previously mentioned, all of Fennoscandia was covered by the Weichselian ice-sheet during the Last Glacial Maximum (LGM), which occurred during the Late Weichselian (Figure 4-5, lower panel). At that time, air temperatures were among the lowest of the last glacial cycle (Jouzel et al. 2007). In order to study the climate during the LGM in a consistent way with the simulation of a periglacial climate, the same models and modelling approach as for the periglacial climate modelling described in Section 4.3.2 was used for LGM simulations. The LGM climate model simulations were set up to resemble conditions at the time of LGM in a way as similar as possible to what was done in the Palaeoclimate Modelling Intercomparison Project (Joussaume and Taylor 2000, Harrison et al. 2002). This choice facilitates comparisons with other GCM results. It also allows the use of pre-existing long simulations with the general circulation model CCSM3 performed at the National Centre for Atmospheric Research (NCAR) in the USA (Otto-Bliesner et al. 2006), reducing the model spin-up time needed for this study. Further, as the LGM is part of the most recent Weichselian glacial period, there is a higher possibility of finding climate proxy data than for earlier cold stadials during the Weichselian. The orbital year 21 ka BP and a CO_2 level of 185 ppmv were used in the LGM simulation. Ice-sheet configurations were the same as in the PMIP-2 project (Harrison et al. 2002), which were based on the ICE-5G data (Peltier 2004). For a description of the set-up of all other forcing conditions, see Kjellström et al. (2009).

Global climate

The global LGM simulation is a continuation of a LGM simulation performed at NCAR (Otto-Bliesner et al. 2006). The simulation was originally initiated from a simulation of pre-industrial climate, except for the ocean which was initiated by adding three-dimensional anomalies of ocean temperature and salinity derived from a LGM simulation with the Climate System Model version 1.4 (CSM1.4) (Shin et al. 2003) to the CCSM3 pre-industrial simulation. The simulation was first run for 400 years at NCAR and was then continued for another 856 years within the present study. The annual global mean surface temperature reaches quasi-equilibrium after 100–150 years, then it continues to cool and reaches a new quasi-equilibrium after a total of 750–800 years. This second quasi-equilibrium extends until the simulation is ended at model year 1538 (Kjellström et al. 2009 erratum Feb 2010). The annual global mean surface temperature is 9.0 °C in the first quasi-equilibrium and 7.9 °C in the second LGM equilibrium, i.e. 4.5 °C and 5.6 °C colder than the corresponding simulated pre-industrial temperature (Kjellström et al. 2009, Brandefelt and Otto-Bliesner 2009). The second equilibrium also results in a 30 % reduction in the strength of the Atlantic Meridional Overturning Circulation (AMOC) compared with the first quasi steady-state (Brandefelt and Otto-Bliesner 2009).

The global climate model LGM simulation thus shows that the global mean air temperature during the LGM could have been more than one degree colder than previously thought, and also that the variability in global mean temperature was larger. The variability is attributed to coupled ocean-atmosphere-sea ice variations in the North Atlantic region. The difference between globally warm and cold years is focussed over oceans in the Northern Hemisphere outside the tropics. The largest difference between cold and warm years is found over Greenland and Northern Europe, with a maximum of 6.8 °C. The total amount of precipitation is up to 32 % higher over the North Atlantic and North Pacific region in warm years than in cold years at the LGM. Furthermore, the sinking branch of the AMOC is shifted further north in globally warm years as compared with cold years. Further results, and discussions of their significance, are found in Kjellström et al. (2009, including erratum dated Feb 2010).

Significant effort was made to compile LGM climate proxy data for model validation. For the comparison between global LGM model results and marine and terrestrial LGM climate proxy data, see Kjellström et al. (2009, Section 3.2.1).

Climate over Europe and Sweden

A very cold LGM climate, with annual mean temperatures below 0 °C in all of Europe north of about 50 °N and also in high-altitude regions in southern Europe is clearly seen in the regional climate model results (Figure 4-16., upper row right). In winter the situation is even more striking with the 0 °C line encompassing basically all continental Europe and monthly mean temperatures below −40 °C over the northern parts of the ice-sheet (Figure 4-16., upper row middle). During summer, the area with the lowest temperatures is more confined to the ice-sheet, the extent of which is readily visible in Figure 4-16. (upper left). In winter when most parts of Europe are snow covered, the gradient is less pronounced as there is no abrupt shift from snow-covered to snow-free conditions. The annual mean temperature in the LGM simulation is 25–30 °C lower than the simulated present climate. Over the southern parts of the ice-sheet (British Isles, southern Fennoscandia) the annual mean temperature is around 15 °C lower than today. At the edge of the ice-sheet, there is a strong gradient towards smaller temperature differences. Central Europe is around 8 °C colder than today and southern Europe around 6 °C colder. In winter, the temperature over the Fennoscandian ice-sheet is around 40 °C colder than present Fennoscandian temperatures.

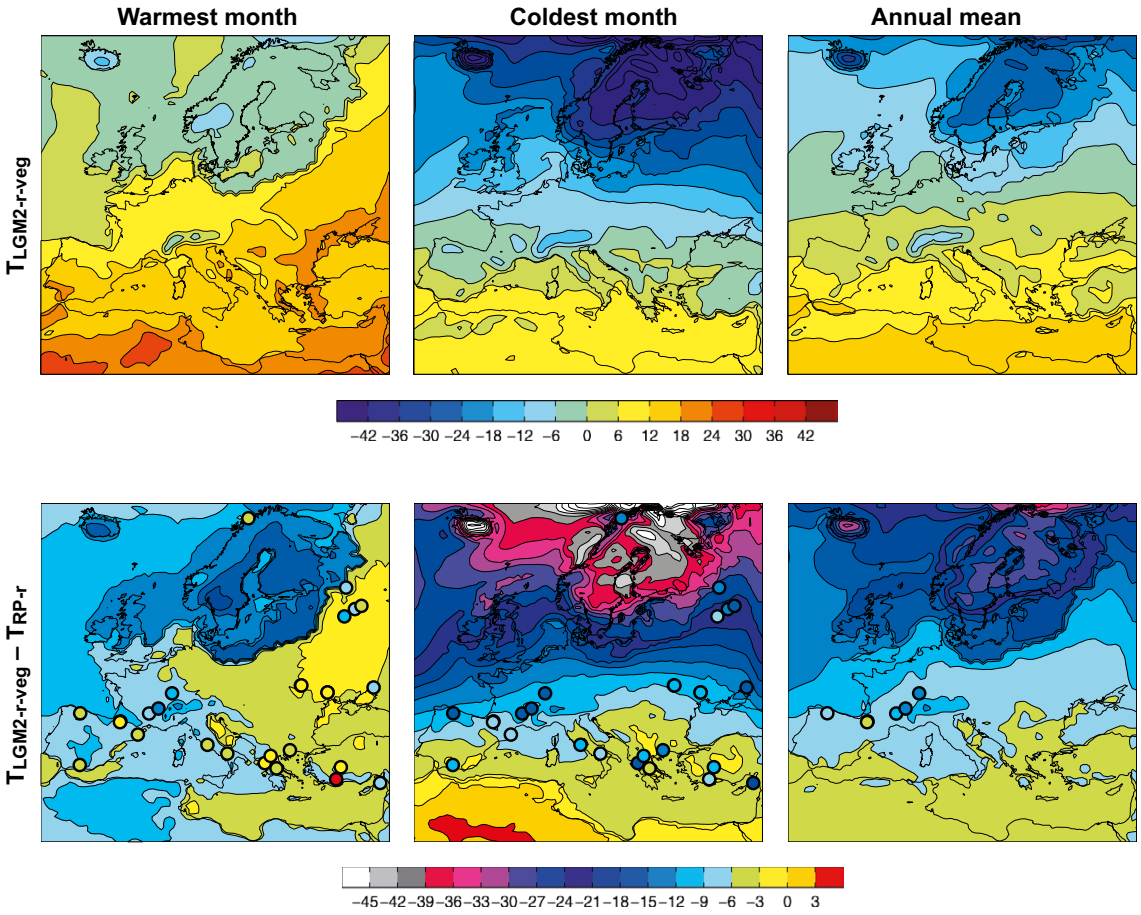

Figure 4-16. *Mean temperatures of the warmest and coldest month and annual mean for the LGM simulation (denoted LGM2-r-veg) (upper row). Also shown are differences between the LGM simulation and the simulation of the present climate (years 1961–2000) (denoted RP-r) (lower row). Climate proxy-based temperature reconstructions are denoted in the filled circles. Units are °C. From Kjellström et al. (2009).*

Annual mean precipitation has its maximum over the North Atlantic and over parts of western Europe (Figure 4-17., upper right). Relatively small amounts of precipitation are simulated in the northern parts of Fennoscandia and over the Mediterranean Sea and North Africa. Compared with the simulated present climate (1961–2000), Fennoscandia, the British Isles and Iceland are drier (Figure 4-17, lower right). More precipitation than at present is seen in southernmost Europe (the Iberian Peninsula, Italy) and northwest Africa. Fennoscandia and western Europe receive less precipitation than in the present climate. The steep coastlines of western Fennoscandia and Scotland which today are facing the ocean and therefore get a lot of precipitation were, during the LGM, parts of the ice-sheet that extended further westward. Without the strong orographic effect, precipitation is considerably smaller in this region during the LGM. In summer, as in winter, precipitation is less than in the present climate in most parts of northern Europe. However, more precipitation in the LGM simulation is seen on the edge of the Weichselian ice-sheet northwest of Fennoscandia and the British Isles (Figure 4-17, upper and lower left panels). Another area with more precipitation than in the present climate is the area of what is today the Baltic Sea. During the LGM this area partly coincided with the most elevated parts of the ice-sheet in which the regional climate model produces large amounts of precipitation during summer.

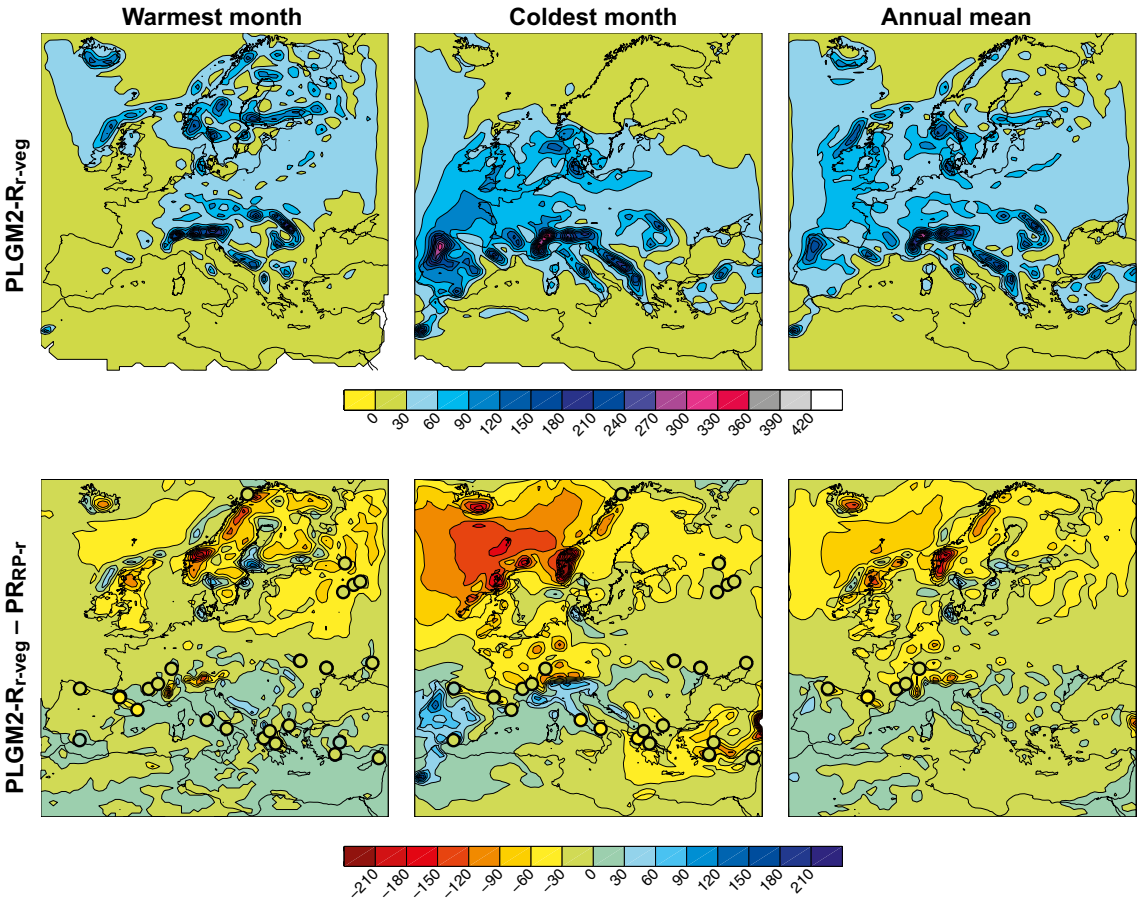

Figure 4-17. *Mean precipitation of the warmest month, coldest month and annual mean in the LGM simulation (denoted PLGM2-r-veg) (upper row). Also shown are differences between the LGM simulation and the simulation of the present (year 1961–2000) (denoted RP-r) (lower row). Units are mm month^{-1}. From Kjellström et al. (2009).*

Comparison with other model simulations

The simulated annual global mean temperature in the LGM simulation (i.e. the second quasi-equilibrium described at the beginning of this section) is 6.9 °C lower than in the present climate. This is a stronger response than in most of the PMIP1 (full range is 1.85–9.17 °C colder than in the present climate) and PMIP2 simulations (3.4–5.46 °C colder than the pre-industrial climate) presented by Kageyama et al. (2006). The results indicate that much of the strong cooling is associated with low Sea Surface temperatures (SSTs) (up to 6 °C colder than some proxy data indicates) and extensive sea-ice cover in the North Atlantic and North Pacific.

These changes in sea-ice extent are a result of the changes in the temperature climate, but they also act to amplify the changes, as increased sea-ice extent leads to a colder climate through the feedback mechanisms involving increased surface albedo and reduced heat fluxes from the ocean to the atmosphere. This connection between low SSTs at high northern latitudes and the global mean temperature for the LGM simulation is in contrast with the PMIP simulations discussed by Kageyama et al. (2006). They find that winter and summer temperature changes over the North Atlantic, Europe and western Siberia do not relate closely to global temperature changes. Another uncertainty relates to the response of the Atlantic Meridional Overturning Circulation (AMOC). This has previously been shown to differ among different PMIP2 models for the LGM; one model gives an unchanged AMOC, whereas two models give an increased AMOC strength (Otto-Bliesner et al. 2007). The simulations presented in Kjellström et al. (2009) indicate a relatively severe weakening of the AMOC; the strength is reduced by more than 50 % in the LGM simulation compared with the pre-industrial climate.

Regardless of possible biases in SSTs, the simulated changes in annual mean temperatures over Europe in the global model are similar to those obtained in the high-resolution atmosphere-only CCM3-simulations by Kim et al. (2008). In both our global and regional models, the coldest month of the year is warmer than proxy data indicate. This is a result also shown for the PMIP1 and PMIP2 simulations (Ramstein et al. 2007, Kageyama et al. 2006). However, even though the models are warmer than the proxy data indicates, (Ramstein et al. 2007) conclude that they are within the confidence interval of the proxy-based reconstructions. Wu et al. (2007) suggest that LGM winter temperatures were ~10–17 °C lower than today outside the ice-sheet margin in Eurasia, with a more significant decrease in northern regions. This is in line with the results by Kjellström et al. (2009).

For a description of the results obtained using an improved European vegetation for the regional LGM climate simulations, as well as for a detailed description of the comparison with climate proxy data, see Kjellström et al. (2009).

Just as for the simulation of a periglacial climate (Section 4.3.2), results from the regional climate modelling were extracted for the Forsmark region also for the LGM simulation. However, for this situation, the results naturally show the climate conditions prevailing at the ice-sheet surface, high above the overridden Forsmark landscape. They are thus of less importance for the present report and are therefore not included here. The interested reader is referred to Kjellström et al. (2009).

4.3.4 Climate variability during the last glacial cycle

The difference between the present warm interglacial temperatures and the *coldest* temperatures during the last glacial cycle as recorded in the GRIP ice core is on the order of 12 °C (Figure 3-14). Using an alternative way of interpreting $\delta^{18}O$ values from the ice core in terms of air temperature, Lang et al. (1999) suggested that this cold event reflects a temperature change of 16 °C, which is several degrees more than proposed in Dansgaard et al. (1993). From the LGM climate modelling study described in Section 4.3.3, annual air temperatures in front of the southern sector of the ice-sheet are around 9–12 °C colder than at present (Figure 4-16, lower right) while further towards northeast, annual air temperatures are around 12–15 °C lower than at present. The largest difference compared to present occurs during the winter season (Figure 4-16, middle).

In a similar way, the air temperature simulated for the Forsmark region for an prescribed ice-free MIS 3 stadial at 44 ka BP (see Section 4.3.2) are low, 12.5 degrees lower than at present (Figure 4-12, lower right). Also for this situation, the largest change compared to present occurs during the winter season.

As exemplified by the climate development around the modelled cold stadial at 44 ka BP, such cold events were relatively short lived, around a few thousands of years long, and alternated with warmer interstadials. A striking climate variability was found also in the simulated LGM climate (Section 4.3.3). These results, from geological archives and from climate modelling, illustrate a typical feature of the last glacial cycle, namely that the climate was highly variable on both long and short timescales. This is also described in for instance the section on abrupt climate change in the description on palaeoclimate characteristics in IPCC (2013a). The last glacial cycle climate variability is also seen for example by looking at the full GRIP temperature proxy record (Figure 3-14). When severe cold conditions occur, these conditions do not persist for long periods of time. Such climate variability is observed also in frequency analyses of climate records (Moberg et al. 2005, Witt and Schumann 2005).

How low could temperatures have been in the Forsmark region during the last glacial cycle? The simulated temperatures for the MIS 3 stadial suggest that the annual mean air temperature in the Forsmark region was −7.6 °C, which is 12.5 °C lower than at present. If looking at the air temperature curve produced for the region (Figure 3-14), transferred from Greenland conditions to regional conditions in Sweden in a rather simplistic way (Appendix A), the curve suggests that annual mean air temperatures during the ice-free stadials of the last glacial cycle may have been around −10 to −11 °C in the Forsmark region (Figure 3-14), that is c 2–3 degrees colder than the temperature modelled for MIS 3 (Greenland Stadial 12) at 44 ka BP. However, considering the uncertainties in e.g. the transfer functions between $\delta^{18}O$ and temperature when constructing the temperature proxy curve (Appendix A), temperatures could even have been lower.

The climate variability seen during the last glacial cycle, e.g. (Figure 3-14 and Figure 4-18) was caused by the combined effect of variations in Earth's orbital configuration and internal feed-back mechanisms within and between the atmosphere, ocean, cryosphere and vegetation systems. These mechanisms will continue to operate also in the future. Therefore, it is reasonable to assume that a similar climate variability that was characteristic for the last glacial cycle would be characteristic also for future glacial cycles.

For further descriptions of last glacial cycle temperatures, see Appendix A. Descriptions of geological climate archives from various parts of the last glacial cycle found in Fennoscandia and Europe are presented in e.g. Hohl (2005), Kjellström et al. (2009), Wohlfarth (2009), Helmens (2009), Helmens (2019), Scheck and Wohlfarth (2019).

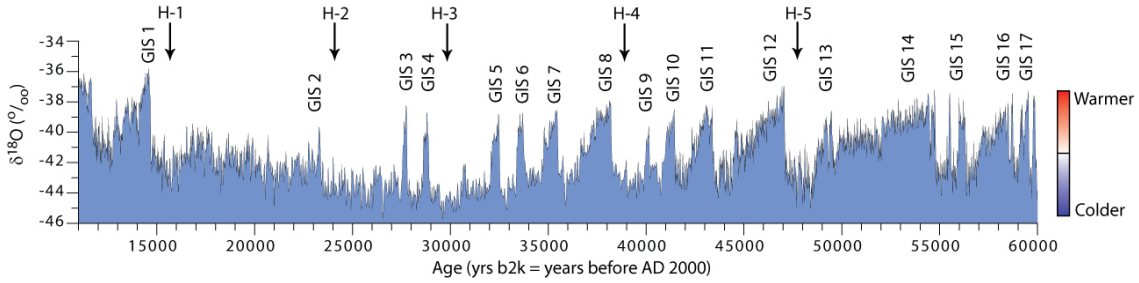

Figure 4-18. *The NorthGRIP oxygen isotope ($\delta^{18}O$) stratigraphy for MIS 2 and 3. Warmer Greenland interstadials were succeeded by colder stadial intervals. Heinrich (H) events 1–5, which have been described from North Atlantic marine sequences, occurred after a series of progressively colder interstadials and in the coldest phase of a stadial. From Wohlfarth (2009), modified after Krogh Andersen et al. (2006).*

4.3.5 Relevance and implications of the palaeoclimate studies made at the Sokli site, northern Finland

Prior to the palaeoclimate studies conducted at the Sokli site (e.g. Helmens 2009, 2013, 2019, Helmens et al. 2021), there were no terrestrial palaeoclimate record for Fennoscandia that covered the full last interglacial–glacial cycle (MIS 5–2; c 130–10 ka BP) including the Holocene (last 12–11 ka) and the Eemian (ca 130–115 ka BP) interglacials, and it was generally assumed that a steep latitudinal temperature gradient existed from northern to central Europe. The Sokli studies have provided such a palaeoclimate record, which gives important insight into the last interglacial–glacial cycle climate and environmental conditions. This is of relevance not only for northern Fennoscandia, but also for e.g. south–central Sweden including Forsmark, as described in the following. To date, no such palaeoclimate record is available for southern or central Sweden.

Given that the results from Sokli conclusively show non-glaciated conditions and summer temperatures reaching present-day levels for part of the Middle Weichselian MIS 3 period (ca 50 ka BP) (Helmens 2009), the more southerly located Forsmark site also must have been deglaciated during part of MIS 3. This result is in line with the restricted MIS 3 ice-sheet configuration obtained by ice-sheet modelling for the reconstruction of Weichselian glacial conditions (that in turn form the basis for the safety assessment reference glacial cycle), see Section 4.4.1.

The climate proxy studies conducted at Sokli have also revealed interglacial conditions with summers significantly warmer than today for the interstadials of the Early-Weichselian (MIS 5c and 5a at around c 95 and 80 ka BP, respectively). Together with results from central Europe obtained in other studies, the results from the Sokli studies have demonstrated, in contrast to what was previously assumed, that there was only a weak temperature gradient from northernmost to central Europe during MIS 5c and 5a. Helmens (2013, 2019) and Helmens et al. (2021), suggest that these Early Weichselian climate reconstructions shorten the last glacial period by c 50 ka, to MIS 4–2, as compared to the traditional view of the Weichselian glacial period being ca 100 ka long. In the PSAR, this new suggested re-definition of the Early Weichselian has not been employed, whereas the associated reconstructed palaeoclimates of the Early Weichselian stages are included.

Since summer air temperatures as high, and even higher, than at present existed in the Sokli region north of Forsmark during the interstadial stages of MIS 5 and during the early part(s) of MIS 3 (Helmens 2009, 2019), similar to those in central Europe (e.g. Helmens 2013, Helmens et al. 2021), it is likely that south–central Sweden, including the Forsmark region, experienced similar warm summer climates during these interstadial periods. For these periods, the weak north–south temperature gradient can be used to estimate summer air temperatures for the Forsmark site, based on e.g. the temperatures at Sokli.

During the cold MIS 5d stadial of the Early Weichselian (at around 110 ka BP), the Sokli region, as well as central European sites, experienced a climate supporting a steppe-tundra type of vegetation (Helmens 2013), i.e. a cold climate characterized by a high degree of continentality. Given the similarity of these climates north and south of south–central Sweden, it is likely that the Forsmark region also experienced a cold climate supporting a steppe-tundra vegetation during MIS 5d. For this period, the temperature gradient from northernmost to central Europe was also weak.

In summary, the overall results obtained from the Sokli studies is of high relevance also for the Forsmark site. These include i) summer climates as warm, and warmer, than at present during the interstadial stages of the Early Weichselian, ii) ice free conditions and warm summers during part of the Middle Weichselian, and iii) a considerably more dynamic behaviour of the climate and ice-sheet during the last interglacial–glacial cycle than traditionally assumed. These features have been considered in the definition of the reference glacial cycle (Section 4.5).

In general, the biota palaeoclimate proxies used in the Sokli studies have strong links to summer conditions but only weak links to winter conditions. Therefore, the Sokli palaeotemperature reconstructions have focused on reconstructing summer air temperatures, since this is what available palaeoclimate proxy methods at the latitude of Sokli are adequate for. Winter temperatures are important for e.g. reconstructions the degree of continentality for a site. Winter temperatures have been possible to quantitatively reconstruct for the warmest interval at Sokli, i.e. the Eemian interglacial (MIS 5e). In addition, relatively low winter temperatures can be inferred for MIS 5d at Sokli based on the occurrence of steppe-tundra vegetation.

The Sokli investigations also include climate proxy studies of the Holocene sequence. This is important since i) the Holocene is a period for which relatively abundant climate and environmental proxy information are available from other sites. It is very useful to compare the results from Sokli with other studies in order to verify that the results from the Sokli site does not contradict other results from this period, and ii) a lot of environmental information from the Holocene are preserved in the landscape today, and hence comparing this information with the one interpreted from the Holocene sediment sequence helps in interpreting the biota climate proxies in the sediment. The interpretations made from the older deposits that pre-date the Holocene hence also are improved. Therefore, a long palaeo-record of climate and environment conditions, such as the one obtained from the Sokli site, needs also the most recent period to be studied in order to improve the interpretations of the proxies used and to demonstrate the applicability of the methodologies employed.

4.4 Reconstructed last glacial cycle conditions at Forsmark

In this section, results from Sections 3.1.4, 3.3.4 and 3.4.4 are summarized to present key parameters (development of ice-sheet, relative sea-level, and permafrost) for the reconstruction of last glacial cycle conditions at Forsmark. Additional results from these simulations are presented in Section 4.5, where the results have been used for the construction of the future *reference glacial cycle climate case*. Section 4.5 also presents the resulting evolution of climate domains, as defined in Section 1.2.3.

4.4.1 Ice-sheet evolution

In Section 3.1.4, an ice-sheet model simulation of the Weichselian ice-sheet was made, based on e.g. the temperature reconstruction of the last glacial cycle (Appendix A). The modelled ice-sheet configurations during Weichselian stadials were calibrated against the known maximum ice margin positions for these periods. In the Weichselian ice-sheet reconstruction, the overall behaviour of the ice-sheet can be characterised as being distinctly dynamic throughout the glacial cycle (Figure 3-15). For instance, during the MIS 3 period (which was *not* used for model calibration), large parts of Fennoscandia were modelled to be ice free (Figure 3-15), in agreement with several recent independent Quaternary geological studies (Section 4.2.1).

From the ice-sheet simulation, data on ice-sheet thickness was extracted for the Forsmark region (Figure 4-19). The Forsmark region was subject to two phases of ice-sheet coverage, during the cold stadials of MIS 4 and 2. During the last glacial maximum, the ice-sheet thickness reached ~2900 m. Further description and discussion of this ice-sheet evolution is given when these data are used to construct the PSAR *reference glacial cycle climate case* (Section 4.5).

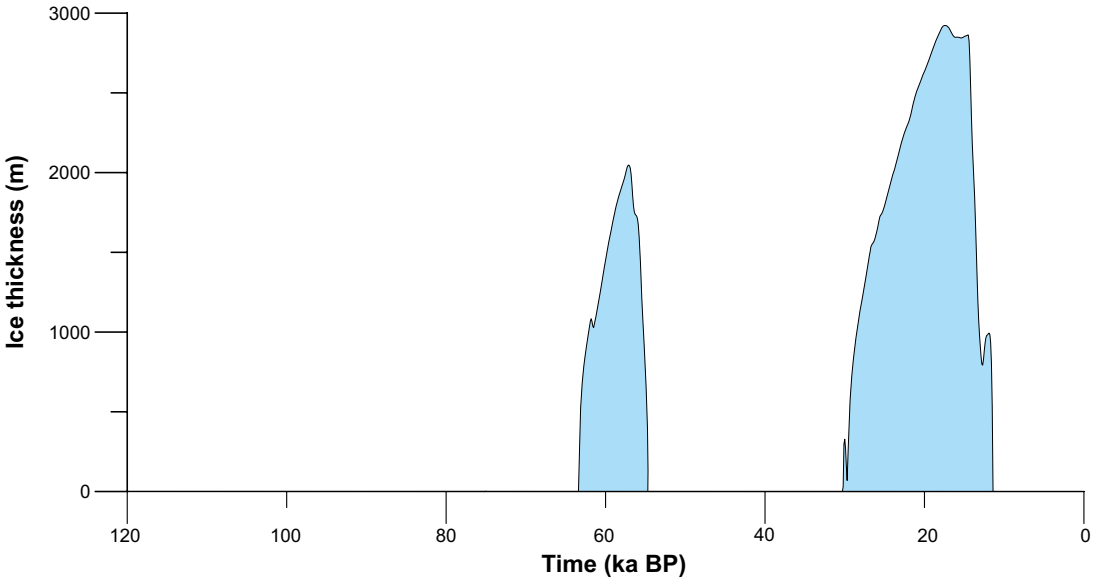

Figure 4-19. *Reconstructed ice-sheet thickness over Forsmark for the last glacial cycle (Section 3.1.4).*

In this ice-sheet reconstruction, the two short phases of ice-sheet coverage at Forsmark at around 70 ka BP (with 40 and 750 m of ice thickness occurring over 500 and 1900 years) are considered highly uncertain. They are the result of two short and severe cold phases existing in the palaeotemperature curve used to run the ice-sheet model. However, the ice-sheet model response to these very rapid and strong temperature events is considered uncertain. Therefore, these short phases of ice coverage are not included here, nor in the construction of the PSAR *reference glacial cycle climate case* (Section 4.5). However, a case with longer periods of ice-sheet coverage than in the *reference glacial cycle climate case* is described in the *extended ice-sheet duration climate case* (Section 5.3). Further uncertainties related to the ice-sheet model simulation are discussed in Sections 3.1.4, 3.1.7 and Appendix A.

4.4.2 Relative sea-level evolution

In Section 3.3.4, a GIA model was used to reconstruct changes in relative sea-level during the last glacial cycle, given input from various Earth models as well as an ice-load history from Section 3.1.4. Relative sea-level data were extracted for the Forsmark region (Figure 4-20) showing that the area was submerged after both reconstructed phases of ice-sheet coverage (Figure 4-19). At times of maximum isostatic depression, the Forsmark region was covered by the Weichselian ice-sheet. The uncertainties in reconstructed levels are rather large (Section 3.3.4). This implies that, at the time of deglaciation (10800 BP), the inferred water depth at Forsmark in Figure 4-20 probably is too large (Söderbäck 2008). Therefore, the results from the GIA modelling have been combined with empirical reconstructions of the Holocene relative sea-level (Appendix D) in order to decrease the uncertainty (Section 4.5.2).

Further description and discussion of this relative sea-level change, and the associated development of the Baltic Sea, is given when these data are used to construct the future PSAR *reference glacial cycle climate case* (Section 4.5). Uncertainties related to the GIA model simulation are discussed in Section 3.3.4.

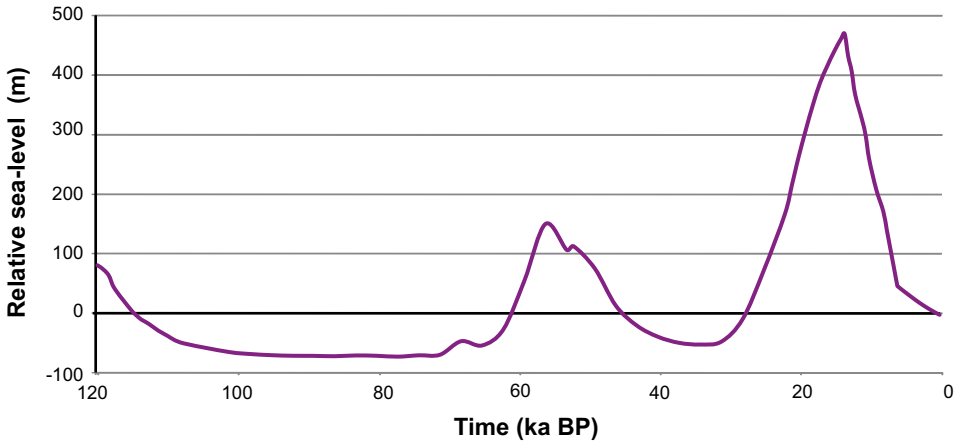

Figure 4-20. *Reconstructed relative sea-level at Forsmark for the last glacial cycle using GIA modelling (Section 3.3.4) and Holocene data (Appendix D). The reconstructed sea-level change for the Holocene was only applied to the deglaciation phase of the Weichselian glacial cycle (Appendix D). If the Holocene data were omitted, the resulting relative sea-level from the GIA modelling at 0 ka BP would be identical to the value at 120 ka BP (~80 m). Uncertainties related to the GIA modelling are discussed in Section 3.3.4). Positive values mean that the area is submerged under the contemporary level of the Baltic Sea. Note that during periods of maximum isostatic depression, the area is situated under the ice-sheet.*

4.4.3 Permafrost evolution

In Section 3.4.4, reconstructions of permafrost and freezing depths for the last glacial cycle at Forsmark were made using two permafrost models (Figure 4-21 and Figure 4-22). The simulations were made by employing the air temperature curve reconstruction for the last glacial cycle (Appendix A and Section 3.1.4) together with site-specific data on e.g. bedrock, soil, groundwater, lakes and relative sea-level development, see Section 3.4.4 and Hartikainen et al. (2010).

The maximum Weichselian permafrost depth at the Forsmark repository location is ~250 m and it occurs around 70 ka BP, prior to the MIS 4 ice-sheet advance over the region (Figure 4-21 and Figure 3-59). The maximum permafrost in the surrounding region, here represented by a 15 km long profile, is ~300 m and it occurs at the same time (Figure 4-22 lower part). At that time, the area is subject to continuous permafrost coverage (more than 90 % spatial coverage), see Figure 4-22, upper part. During periods of ice-sheet coverage, permafrost declines, especially during periods when the ice-sheet is warm-based (Figure 4-23). At the time of the deglaciations, there is no permafrost or frozen ground present.

The values estimated for last glacial cycle air temperatures at ground level (Section 3.4.4 and Appendix A) are typically 2–4 °C lower than mean annual temperature in the uppermost part of the ground for the same climate, see Section 3.4.4 and Figure 4-11. As discussed above, really low air temperatures during the last glacial cycle only prevailed during stadials which had a restricted duration. During cold ice-free periods, permafrost developed at the Forsmark site, but climate variability with alternating cold and warm periods, e.g. Figure 3-44 and Figure 3-55, as well as the presence of the ice-sheet (e.g. Figure 4-19), prevented permafrost from developing to great depths (Figure 4-21 and Figure 4-22) and Section 3.4.4. Further description and discussion of this permafrost evolution is given when these data are used to construct the future PSAR *reference glacial cycle climate case* (Section 4.5).

It should be noted that in the reconstruction of last glacial cycle permafrost development, heat from the repository has been included to make the results useful for the subsequent construction of a future *reference glacial cycle climate case* with a repository present. The difference between including and excluding heat from the repository has also been evaluated, see Figure 3-41, Figure 3-77, as well as SKB (2006a, Figure 3-59). All uncertainties related to the permafrost simulations are examined in detail in Section 3.4.4 and in Hartikainen et al. (2010).

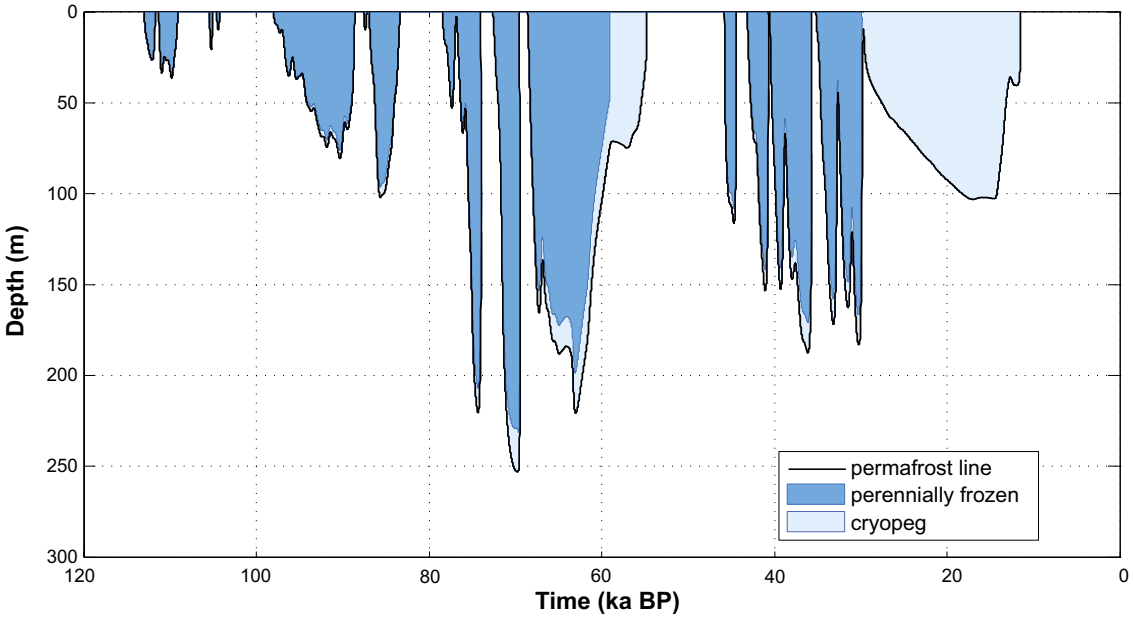

Figure 4-21. *Evolution of permafrost and perennially frozen ground depth for the reconstruction of last glacial cycle conditions for the repository location in Forsmark. The results were obtained using a 1D permafrost model (Section 3.4.4). Due to the high sub-glacial pressure, a thick unfrozen cryopeg exists within the permafrost (defined by the 0 °C isotherm) after 60 ka and after 30 ka BP (including the LGM). For the corresponding 2D modelling results see Figure 3-59.*

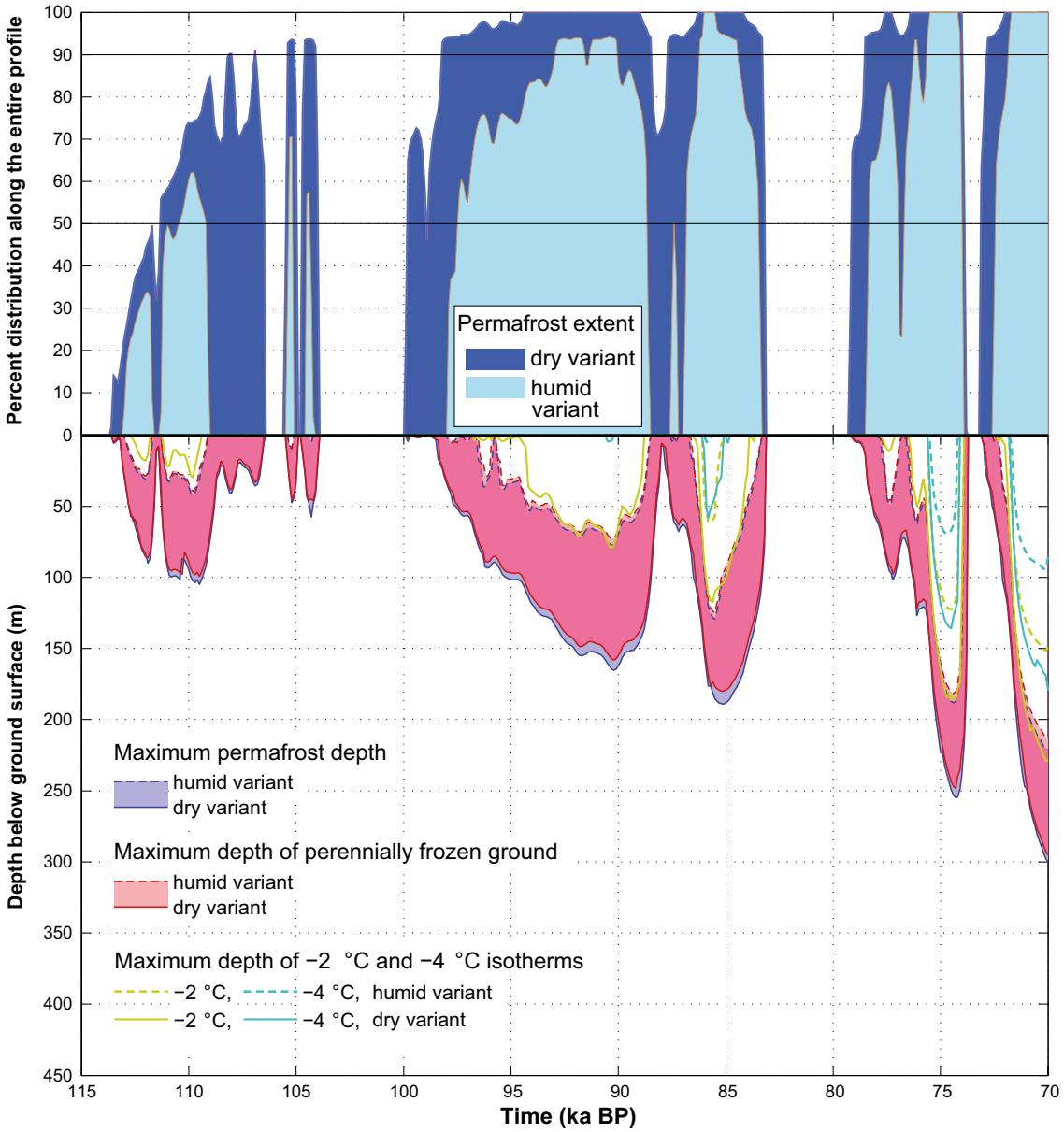

Figure 4-22. *Reconstructed evolution of maximum permafrost depth, maximum freezing depth and percent permafrost distribution over a 15 km long transect over the Forsmark area for the first 50 ka of the last glacial cycle, see Section 3.4.4 . Upper panel: the transition from sporadic to discontinuous permafrost occurs at 50 % spatial coverage and from discontinuous to continuous permafrost at 90 % coverage. Lower panel: the shaded area in blue and red represents the range obtained when considering one dry and one humid climate variant. The lilac colour indicates that the results for permafrost and perennially frozen ground overlap.*

4.4.4 Combined reconstructed last glacial cycle parameters

Figure 4-23 shows the combined evolution of ice-sheet thickness, relative sea-level changes, permafrost- and frozen ground depth at Forsmark as reconstructed in Sections 3.1.4, 3.3.4, 3.4.4 and above. This reconstruction was used to construct the PSAR *reference glacial cycle climate case* for the coming 120 ka (Section 4.5).

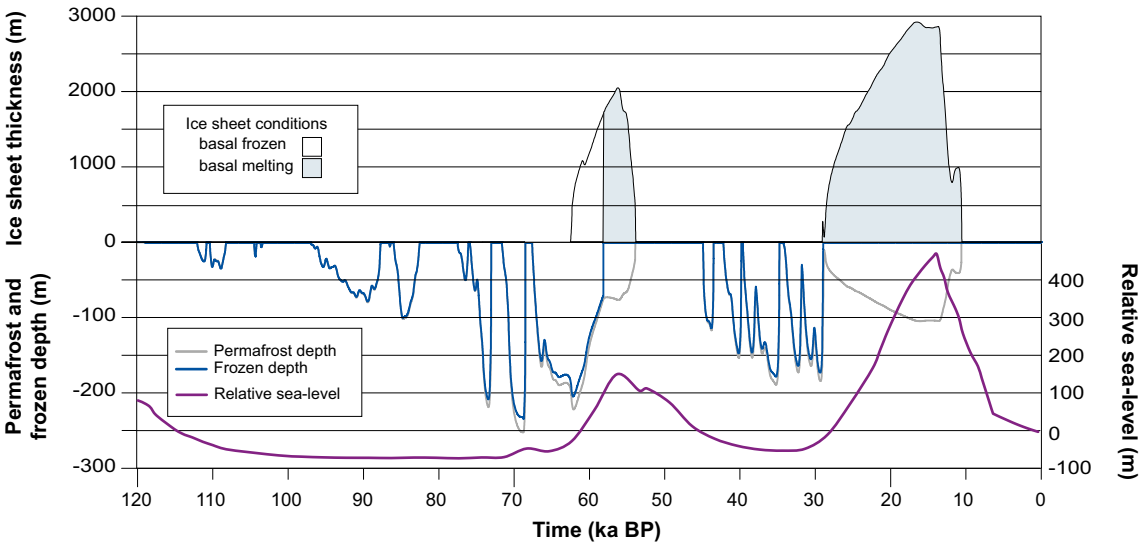

Figure 4-23. *Reconstructed Weichselian evolution of ice-sheet, relative sea-level, permafrost and frozen ground at Forsmark. This evolution was used to construct the PSAR reference glacial cycle climate case.*

4.5 Reference glacial cycle climate case

The PSAR *reference glacial cycle climate case* describes a conceivable future evolution of climate and climate-related conditions and sequences that could be expected in a 100 ka time perspective. It is constructed by repeating the reconstructed conditions for the last glacial cycle described in Section 4.4. The *reference glacial cycle climate case* constitutes a climate evolution fully dominated by natural climate change, i.e. without anthropogenic influence on climate. Therefore, the length of the present temperate interglacial period is assumed to be within the range of interglacial durations as observed within the past 800 ka (Tzedakis et al. 2009), see further Section 4.5.4. The case of having a climate evolution affected by increased amounts of greenhouse gases in the atmosphere due to human activity, resulting in a longer duration of the present interglacial period, is dealt with in Section 5.1 and 5.2.

In the PSAR, the *reference glacial cycle climate case* is used for constructing the base case of the Main scenario, see Figure 1-3.

The climate evolution of the *reference glacial cycle climate case* starts in the present warm interglacial climate, characterized as a temperate, humid cold climate with year-round precipitation. For a description of the present climate at Forsmark, see Section 2.2.1.

4.5.1 Ice-sheet evolution

In the *reference glacial cycle climate case*, the lowering of air temperature during the onset of the glacial results in ice-sheet inception. Following the ice-sheet evolution in the model reconstruction of the Weichselian glacial, see Section 3.1 and 4.4, the evolution of ice-covered area and ice volume for the *reference glacial cycle climate case* are shown in Figure 4-24. The corresponding ice configurations for selected time slices, depicting future stadial and interstadial configurations in the *reference glacial cycle climate case*, are shown in Figure 4-25. During the glacial cycle, the ice-sheet grows progressively larger in several distinct growth phases, with intervening phases of more restricted ice coverage. The Glacial Maximum (corresponding to the LGM of the Weichselian glaciation), is reached at around 100 ka into the future. As described in the previous section, the overall behaviour of the ice-sheet can be characterised as being distinctly dynamic throughout the glacial cycle.

The dynamic behaviour of the ice-sheet during the glacial cycle is seen also at the Forsmark site. The site is covered by ice during the cold stadials at around 60 and 100 ka AP (Figure 4-26). Between these stadials, the site experiences ice-free warmer interstadial conditions (corresponding to Marine Isotope Stage 3 in the reconstructed Weichselian glacial cycle). Advances of the Fennoscandian ice-sheet during stadials around 14 and 38 ka AP do not reach the Forsmark site (Figure 4-25), although the ice-sheet margin is close to Forsmark during the latter stage. Note that even though an ice-sheet is present in Fennoscandia during most of the glacial cycle (Figure 4-24), the Forsmark site, located in south–central Sweden, is not covered by the ice-sheet for the majority of the time (Figure 4-26).

In the *reference glacial cycle climate case*, the Forsmark region is covered by the ice-sheet for a total time of ~30 ka. For most of the ice-covered time, the numerical ice-sheet modelling suggests that the site is covered by warm-based ice with free water present at the ice-bed interface. Forsmark is covered by wet-based ice for ~23 ka, corresponding to about 75 % of the ice-covered time. This means that during most of the time when the ice-sheet covers the site in the *reference glacial cycle climate case*, meltwater is present at the ice-sheet bed, typically produced at rates of a few mm/year, up to ~10 mm a^{-1}, and hence groundwater recharge by glacial meltwater takes place.

The short periods of cold-based conditions, with no basal water production, always follow immediately after each time the site become ice-covered. During these periods, as well as during deglaciation periods when the site is close to becoming ice free, water from *surface* melting may still reach the bed. However, in cases when the ice-sheet margin is located over permafrost, this melt water would not contribute significantly to groundwater recharge. This situation can occur under cold climate conditions, and is therefore more likely to be present during phases of ice-sheet advance than during phases of retreat. The prerequisites for groundwater flow under glacial- and permafrost conditions are further discussed below. A study of groundwater flow under glacial- and permafrost conditions is found in Vidstrand et al. (2010).

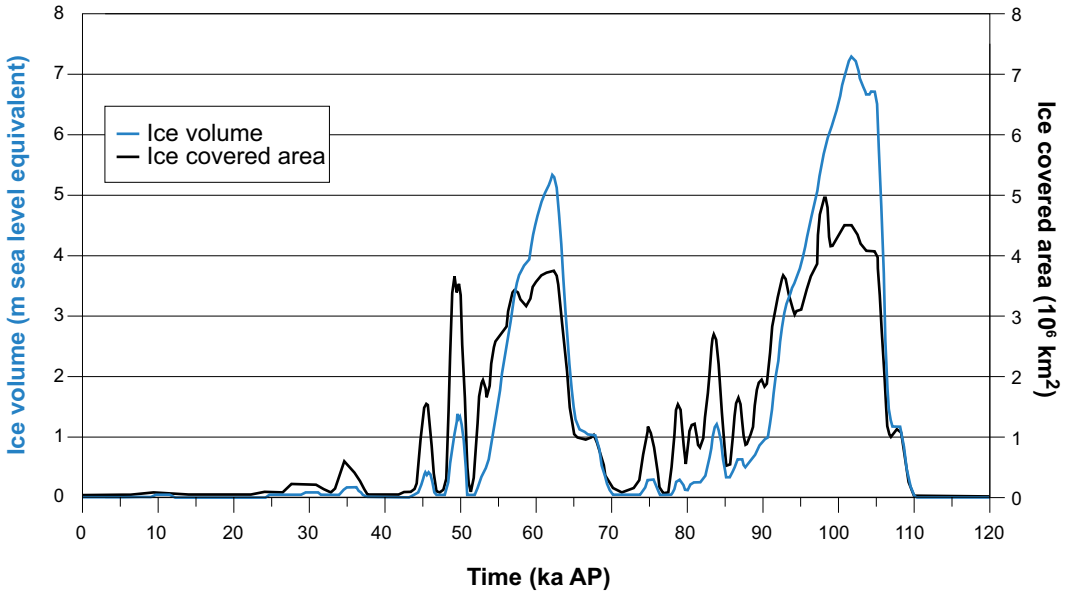

Figure 4-24. *Ice-sheet volume and ice-covered area for the reference glacial cycle climate case.*

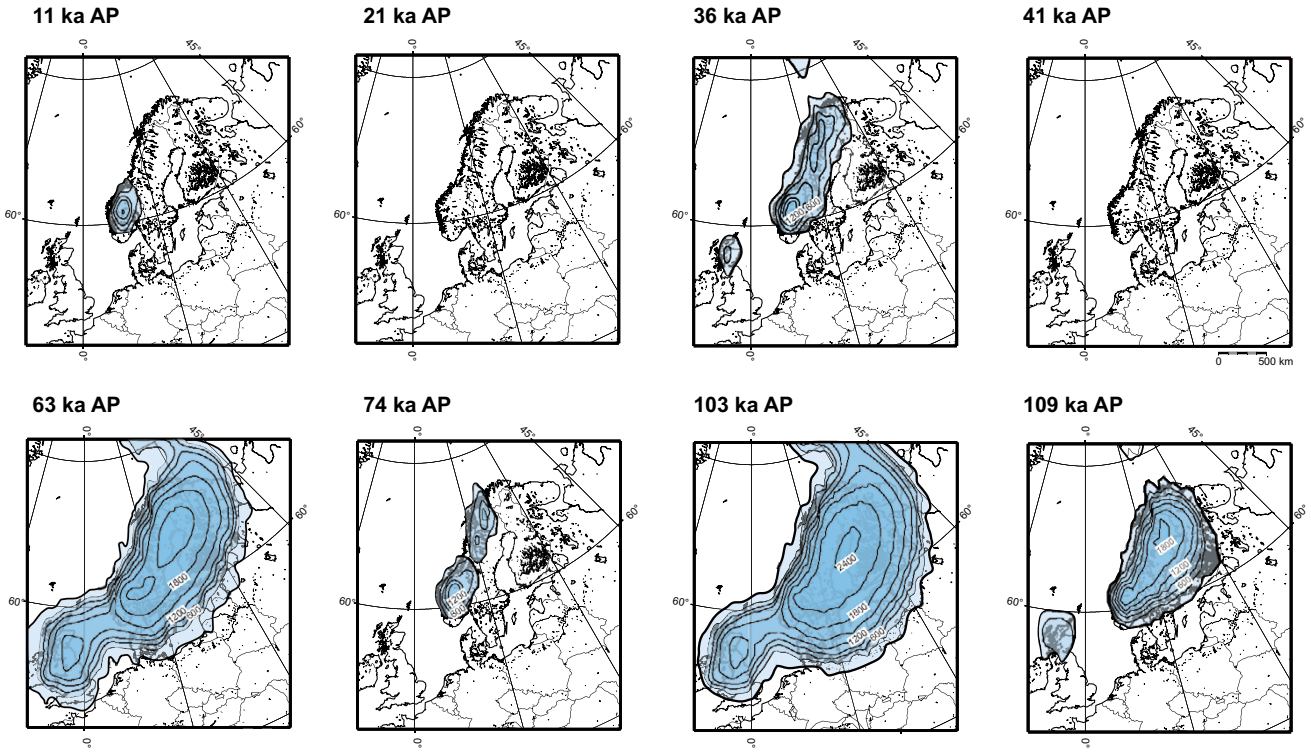

Figure 4-25. *Ice-sheet configurations at stadials and interstadials for the reference glacial cycle climate case. Contour lines show ice-surface elevation with a 300 m interval. All maps show the present-day shoreline position.*

During the glacial maximum of the *reference glacial cycle climate case*, at around 100 ka AP, the maximum ice-sheet thickness over Forsmark is ~2900 m (Figure 4-26). It is worth noting that the modelled ice-sheet reaches significant thickness over the site not only during the glacial maximum, but also during the cold stadial at around 60 ka AP. At that time, the modelled maximum ice thickness is ~2000 m.

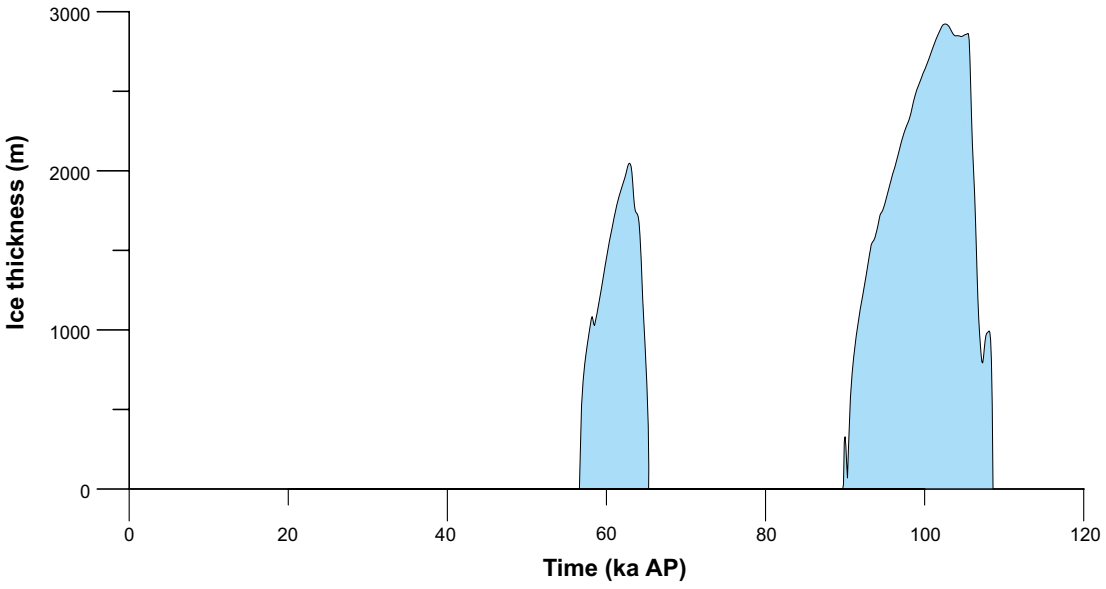

Figure 4-26. *Development of ice-sheet thickness at the Forsmark site in the PSAR reference glacial cycle climate case. Note that even though an ice-sheet is present in Fennoscandia during most of the glacial cycle (Figure 4-24) the Forsmark site is not covered by the ice-sheet for most of the time.*

The groundwater pressure at repository depth is, for non-glacial conditions, determined by the depth of the repository, and for glacial conditions by the repository depth as well as an additional pressure induced by the ice load. The ice-sheet thickness sets a limit to the maximum hydrostatic pressure that may occur at the ice-sheet/bed interface. The additional hydrostatic pressure related to the maximum thickness in the *reference glacial cycle climate case* (Figure 4-26) is 26 MPa for Forsmark. This value is listed in Table 5-16 together with an estimate of the *maximum* possible ice load and associated *maximum* hydrostatic pressures.

Ice-marginal stillstands

Although not the case during the deglaciation of the Weichselian ice-sheet, or in the PSAR *reference glacial cycle climate case*, future periods of ice-sheet-frontal stillstands cannot be excluded for the Forsmark site during ice advance, maximum or retreat phases, given suitable climate conditions. An extreme case in terms of hydraulic gradients and associated increased groundwater flow would occur if the ice front came to a temporary halt with the frontal part of the ice-sheet situated above the repository. According to Vidstrand et al. (2010) there is an approximately one km wide zone of high groundwater fluxes in front of the ice-sheet margin and a similarly wide zone of increased flux behind the ice-sheet margin, i.e. a two km wide influence area with significantly increased groundwater flux. This situation is valid when there is no permafrost at the Forsmark site. If continuous permafrost is present, which is the case in the PSAR *reference glacial cycle climate case* and is also very likely during a future glaciation of the Forsmark site, a zone of increased groundwater flow is significantly less pronounced (Vidstrand et al. 2010). Using a two km wide near-frontal zone with significantly increased groundwater flux is therefore a pessimistic choice for an analysis of the probability of occurrence and consequences of a future situation with an ice margin stillstand over the repository.

Assuming that future periods of ice-margin stillstands would have the same characteristics as the stillstands associated with the last deglaciation described above, one could make an estimate of the probability of having such a situation occurring at the Forsmark site. By generalizing the development of the last deglaciation, one could postulate ten temporary halts of shorter duration and one major halt of longer duration, corresponding to the Younger Dryas event, for a deglaciation of a full-sized ice-sheet equivalent to the one of the LGM. For halts of short duration, completely stable ice margin conditions are set to persist for 200 years, while during the major stillstand a completely stable position of the ice margin is pessimistically set to 1000 years. This is somewhat longer than the period that the ice margin was located somewhere within the 20–25 km wide Younger Dryas zone in Sweden, which lasted around 900 years. In reality, it is likely that, during such long phases, the ice margin would move slowly and/or oscillate within an ice-marginal zone. Nevertheless, to cover uncertainties in future ice-sheet behaviour, a completely stable margin position for 1000 years is assumed for the major stillstand. In this way, the major stillstand constitutes a pessimistically chosen case in terms of the duration of a high hydraulic gradient and associated high groundwater fluxes.

The deglaciation of the Weichselian ice-sheet, from its LGM position in Poland and Germany to the Scandinavian mountain range, occurred over a distance of ~2500 km (Fredén 2002). For each of the postulated stillstands, there is a ~2 km wide frontal zone with significantly increased groundwater fluxes (Vidstrand et al. 2010). For each advance- or deglaciation phase, the probability of having a 200 year long stillstand at Forsmark is therefore 0.008 (10 × 2 km/2500 km), while the probability of having the postulated 1000 year long stillstand at Forsmark is 0.0008 (2 km/2500 km). For a complete glacial cycle with two phases of ice advance and two phases of deglaciation over Forsmark, i.e. a glacial cycle similar to the PSAR *reference glacial cycle climate case*, the probabilities for the 200 year and 1000 year ice-margin stillstands at Forsmark are 0.03 (0.008× 4) and 0.003 (0.0008 × 4), respectively. For the full assessment period of 1 million years, comprising eight repeated identical glacial cycles, the probabilities grow correspondingly larger. There is thus a relatively low probability that the ice margin zone with high groundwater flux would come to a temporary halt above the repository, especially when considering the rarer stillstands of long duration. In this context, it should again be pointed out that the assumption of a completely stable ice margin over the repository for 1000 years is a highly pessimistic case compared with what is known from the last deglaciation.

4.5.2 Evolution of the Baltic Sea and the Forsmark relative sea-level

The evolution of the Baltic Sea

During the initial phase of the *reference glacial cycle climate case*, when climate is getting colder and ice-sheets expand globally, global sea-levels fall. At the same time, the rate of isostatic rebound from the last glacial cycle decreases. However, even if the rate is low, the amount of remaining uplift for parts of Fennoscandia is significant. For the central parts of the Fennoscandian ice-sheet it has been estimated to ~100 m, and in the distal parts to ~25 m. As long as the Baltic Sea is connected to the Atlantic, the relative sea-level along the Baltic Sea coast is determined by isostatic rebound and global sea-level change. If and when the relative sea-level at Darss sill, in the southern Baltic Sea south of Denmark, falls below the sill depth (at present 18 m below mean sea-level), the Baltic Sea is transformed into a lake. The surface level of this lake is determined by the altitude of the contemporary Darss sill.

In the *reference glacial cycle climate case*, results from the GIA simulations (Section 3.3.4) indicate that the Baltic Sea is isolated from the Atlantic around 9 ka AP. However, due to the uncertainties in the GIA modelling, discussed in Section 3.3.4, it is likely that the suggested timing for this isolation is too early. Given these uncertainties, the salinity of the Baltic Sea could thus remain high for a considerably longer period than until 9 ka AP. If extrapolation of present observed relative sea-level trends (Appendix D) is made, it seems unlikely that isolation of the Baltic Sea from the Atlantic would occur at all, even if excluding the possibility of a considerable future global sea-level rise due to global warming.

In addition, the northern part of the Baltic Sea, i.e. the Gulf of Bothnia at which the Forsmark site is located, will be isolated from the rest of the Baltic Sea due to the remaining isostatic uplift. This occurs around 25 ka AP (see the **Biosphere synthesis report**), i.e. well before the onset of the first phase of glacial conditions in the Forsmark region in the *reference glacial cycle climate case* (after 60 ka AP), see Figure 4-26. The salinity in the Gulf of Bothnia is reduced because of this isolation, since the Gulf at this stage constitutes a large lake fed by freshwater from surrounding terrestrial regions. This freshwater stage is formed regardless of the isostatic and eustatic conditions in the southern Baltic Sea (Darss sill). Note that at his stage, the Forsmark site is situated far from the shoreline of the Gulf of Bothnia due to land uplift, see the **Biosphere synthesis report**.

In the *reference glacial cycle climate case*, the isostatic load from the first major ice-sheet advance, at ~60 ka AP (Figure 4-26), most likely depresses the Gulf of Bothnia lake threshold so that the Gulf of Bothnia regains contact with the southern part of the Baltic Sea. However, it is uncertain if the Baltic Sea has contact with the Atlantic or not at this stage. The uncertainties in the GIA simulations for the southern Baltic Sea region are too large to give useful information for that region at that time. However, according to modelling studies by Lambeck et al. (2010), the Baltic may have constituted a freshwater lake during MIS 3 of the Weichselian, which corresponds to the period following the deglaciation of the first glacial period of the *reference glacial cycle climate case*.

Following the deglaciation of the second and larger ice-sheet coverage, at around 110 ka AP (Figure 4-26) the Baltic regains contact with the Atlantic. Given that the *reference glacial cycle climate case* is based on the repetition of conditions reconstructed for the last glacial cycle (including the Holocene), the development of the Baltic Sea for this future post-glacial period is envisaged to follow the Holocene development, which includes both saline and freshwater stages. After this deglaciation, large parts of southern Sweden are submerged by a predominantly saline Baltic Sea. At the end of the *reference glacial cycle climate case*, and as isostatic rebound proceeds, the Baltic Sea is transformed to an inland brackish sea, similar to today's situation.

Relative sea-level change at Forsmark

At the start of a GIA model run, the Earth is assumed to be in isostatic equilibrium. In reality, the Earth is unlikely to reach such a state if glaciations occur with similar periodicity as in the past. To correct for this, the GIA-modelling, Section 3.3.4, has been initiated by a glacial loading history yielding relative sea-levels comparable to those reported by Funder et al. (2002) at the peak of marine inundation in the Early Eemian about 130 ka BP.

In the *reference glacial cycle climate case* the projected relative sea-level from the GIA modelling of the Weichselian glacial cycle (Figure 4-20) is shifted 120 ka into the future. However, this approach overestimates the present-day relative sea-level at Forsmark by ~80 m (see value at 120 ka BP in Figure 4-20). To correct for this mismatch the GIA curve is combined with an empirical relative-sea-level curve for the Holocene (based on Påsse and Daniels 2015; see Appendix D), resulting in a combined curve ranging from −10.8 to 120 ka AP.

In general, it is assumed that the termination of each glacial cycle follows the reconstructed relative sea-level curve of the Holocene, and that the projected relative sea-level from the GIA modelling is primarily used elsewhere in time (Table 4-3). In the *reference glacial cycle climate case*, the Holocene curve is also extrapolated 8 ka into the future (from −10.8 to 8 ka AP) (Table 4-3), to ensure a smooth transition to the GIA curve. Extrapolating the empirical Holocene curve into the future, for which there is no observational data, needs to be made with great caution. However, as it is also expected to occur in the real world, the mathematical formulation of the Holocene curve (based on Påsse and Daniels 2015; see Appendix D) ensures that the isostatic depression will continue to gradually decrease over the next thousands of years. Because of this, a certain amount of extrapolation of the Holocene curve can be justified, at least for a couple of thousands of years. A similar technique was also used in the SR-Site safety assessment to ensure a smooth transition between the relative sea-level curves from the Holocene and GIA modelling (SKB 2010a).

It is possible to use the tide gauge data to roughly estimate the error associated with the extrapolation into the future (Appendix D, Section D2.3). For present conditions, the Holocene curve results in approximately 2 mm a^{-1} lower relative sea-level change than the tide gauge data (Appendix D, Figure D-4). Assuming that this difference is constant in time, and that the future relative sea-level development will otherwise be similar to that predicted by the Påsse and Daniels (2015) equations for the Holocene curve, the extrapolation would result in a 16 m lower relative sea-level value at 8 ka AP for Forsmark than obtained by using the observed present-day relative rate of sea-level change.

The difference in relative sea-level change for the present-day in the Holocene reconstruction with respect to tide gauge data is likely attributed to a considerably underestimated eustatic contribution in the Holocene reconstruction (0.4 mm a^{-1}; see Appendix D, Section D1.3). To this end, it is important to note that the eustatic signal recorded in the tide gauge data is primarily a result of the current anthropogenic global warming, a feature that has *not* been accounted for in the Holocene reconstruction. Hence, in the absence of global warming, the recorded relative sea-level changes from the tide gauges would be more closely comparable with the estimates in Holocene reconstruction. As a result of this, and because the *reference glacial cycle climate case* represents a case of natural climate variability without anthropogenic influence, the extrapolation of the relative sea-level curve can be justified for this climate case.

A summary of the construction of the Forsmark relative sea-level for the entire period between −10.8 and 120 ka AP in the *reference glacial cycle climate case* is compiled in Table 4-3, and the resulting relative sea-level curve is shown in Figure 4-27.

Table 4-3. Data used for the construction of the Forsmark relative sea-level curve from −10.8 to 120 ka AP for the *reference glacial cycle climate case*.

Time period (ka AP)	Data used
−10.8 to 8	From equation based on Påsse and Daniels (2015) (Appendix D)
8 to 12	Linear interpolation
12 to 112	Glacial Isostatic Adjustment (GIA) modelling
112 to 114	Linear interpolation
114 to 120	From equation based on Påsse and Daniels (2015) (Appendix D)

For the first 30–40 ka of the *reference glacial cycle climate case*, the Forsmark site continues to rise due to post-glacial isostatic uplift. When the isostatic uplift is completed, the site is, according to the GIA simulations (Section 3.3.4), elevated ~70 m above the contemporary sea-level (Figure 4-27).

During the first glaciated period of the *reference glacial cycle climate case*, at 60–70 ka AP, the Forsmark site is isostatically depressed by the weight of the ice-sheet (Figure 4-27). The glacial phase is followed by interstadial ice-free conditions around 65–90 ka AP. In connection with the deglaciation that follows the first glaciated period, the isostatic depression results in the Forsmark site being situated below the Baltic Sea water level, at around 70 ka AP (Figure 4-27). In line with the description of the development of the Baltic Sea above, it is uncertain if the site during this stage is submerged by a freshwater lake only, or if the water is more saline as a result of contact with the Atlantic.

Subsequently during this future interstadial, isostatic recovery results in the Forsmark site rising above the Baltic water level, after 75 ka AP. At this time in the *reference glacial cycle climate case*, the Forsmark site is situated above sea-level, and is free of ice, for approximately 15 ka.

During the second and main phase of glaciated conditions around 100–110 ka AP (Figure 4-26) the Forsmark site is again isostatically depressed (Figure 4-27). After the deglaciation that follows this glaciated period, at around 110 ka AP, the Baltic Sea is in contact with the Atlantic and the Forsmark site is submerged by a saline sea. In line with the development of the Baltic Sea presented above, the development of salinity over the Forsmark site during this submerged period follows that of the Holocene. The site finally rises above the Baltic Sea-level again during a brackish phase at around 120 ka AP (corresponding to present-day conditions).

During periods of maximum salinity in the Baltic Sea, generally following sometime after periods of maximum glaciation, the Forsmark site is submerged (Figure 4-27). A more detailed description of the development of salinity in the Baltic Sea for this submerged period of the *reference glacial cycle climate case* is found in the **Biosphere synthesis report**.

The most important factor affecting modelled relative sea-level change is the Earth structure and ice loading history, primarily the near-field history. The uncertainty in modelled relative sea-level mainly manifests itself in that reported relative sea-level values are too high, resulting from an overestimation of isostatic depression during glaciated periods, see Section 3.3.4. The size of the uncertainty varies over the modelled glacial cycle. Postulating that the ice-sheet evolution is correct, the mean overestimation of relative sea-level over the whole glacial cycle may be up to 45 m for Forsmark.

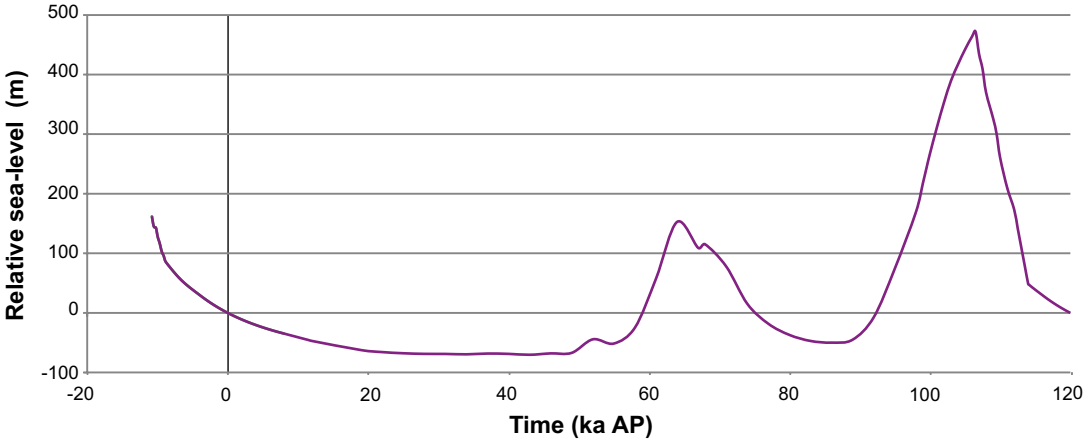

Figure 4-27. *Relative sea-level at Forsmark during the reference glacial cycle climate case. The first ~8000 years of the future period are based on observed relative sea-level data (Påsse and Daniels 2015) whereas the following part of the curve is constructed from Glacial Isostatic Adjustment modelling (Section 3.3.4). A detailed description of how the relative sea-level curve was constructed is provided in Appendix D. The relative sea-level is expressed relative to the contemporary Baltic sea-level. Positive numbers indicate that the site is submerged and vice versa. Note that for most of the time when the figure show submerged conditions, the site is covered by an ice-sheet (Figure 4-26). The figure also includes the relative sea-level from the time of deglaciation up to present, used in e.g. the PSAR biosphere programme.*

4.5.3 Permafrost evolution

The permafrost modelling is described in Section 3.4.4. The input data of geological, hydrogeological, geothermal, geochemical and geomechanical properties are based on site-specific descriptions and are summarised in SKB (2006a) and Hartikainen et al. (2010). In the reconstruction of last glacial cycle conditions, permafrost develops during the progressively colder phases of the glacial cycle. When the ice-sheet subsequently comes to cover an area of permafrost, the permafrost typically stops developing and starts to slowly diminish. When the ground is re-exposed to a cold climate, permafrost starts to grow again.

In the PSAR *reference glacial cycle climate case*, the development of permafrost at Forsmark starts about 7 ka AP (Figure 4-28 and Figure 4-29). The 1D modelling approach used for the results in Figure 4-28 could, in certain situations, result in somewhat higher temperatures than would be calculated using a multi-dimensional model. However, a comparison between the 1D modelling results (SKB 2006a) and the results from the 2D model (Hartikainen et al. 2010), using the same air temperature curve as input, shows that the results for this site and settings are in line with each other (Figure 4-29). Since lateral groundwater flow only has a minor role in permafrost development compared with heat conduction (e.g. Hartikainen 2010), it is likely that modelling including a 3D groundwater flow (instead of the used 2D groundwater flow, and the 1D approach without groundwater flow) would only contribute minor changes to the permafrost and perennially frozen depths.

When permafrost starts to grow over the site, it starts as sporadic permafrost (i.e. with a spatial coverage less than 50 %). As climate gets colder, discontinuous permafrost (with a spatial coverage between 50 and 90 %) and continuous permafrost (more than 90 % spatial coverage) form over the site (Figure 4-30). Examples of permafrost development along the investigated profile (for profile location, see Figure 3-48) for the dry climate variant of the *reference glacial cycle* are seen in Figure 4-31. The upper panel in Figure 4-31 shows the situation at 8.5 ka AP when a Subarctic climate prevails at the site. The profile is partially submerged by the Baltic and sporadic permafrost has started to grow at the site (too shallow to be seen in the figure). At that time, the temperature is at its maximum within the repository, which has a large influence on the temperature of surrounding bedrock. Figure 4-31 middle panel shows the situation at 25 ka AP in the *reference glacial cycle climate case*, with discontinuous permafrost coverage over the site. In Figure 4-31 lower panel, the situation 50 ka AP is shown. At that time, an Arctic climate prevails at the site which has resulted in a continuous permafrost cover. Also at that time, the permafrost reaches its maximum depth in the *reference glacial cycle climate case*. As seen from the temperature contours, the heat from the repository has decreased considerably at this time.

During periods of permafrost an unfrozen active layer develops above the permafrost during summer conditions. The thickness of the active layer could typically be c 40–70 cm deep, depending on the vegetation and soil. For a bare surface the active layer thickness is greater, up to ~1 m.

During the permafrost development prior to the first ice-sheet advance, unfrozen taliks are formed under the two future lakes that are located along the profile (Figure 3-48).This is exemplified by the dry climate variant of the *reference glacial cycle climate case* (Figure 4-32). The upper panel shows the situation at 25 ka AP when the taliks have formed 9 and 15 km from the south–western starting point of the profile. Groundwater recharge and/or discharge are likely to occur in such taliks. The lower panel of Figure 4-32 shows the situation at 46 ka AP. At that time, permafrost growth has developed further and none of the taliks reach through the permafrost anymore. In this situation, groundwater flow is heavily reduced or stopped.

The permafrost and frozen ground depth reach a maximum prior to the first major glacial advance, at about 50 ka AP. At that time, the maximum modelled permafrost depth reaches ~260 m at Forsmark (Figure 4-28 and Figure 4-29). The perennially frozen depth is, at the same time, a few tens of metres shallower. When the ice-sheet advances over the site, the permafrost stops developing and instead starts to diminish, for example around 60 ka AP. Subsequently, permafrost develops again at the site during the ice-free interglacial period between the two major ice advances, but to a somewhat shallower depth, about 180 m (Figure 4-28). During the major phase of ice coverage, including the ice-sheet maximum at more than 100 ka AP, the maximum permafrost depth (defined by the 0 °C isotherm) is around 100 m at Forsmark. Note that, at that time, the permafrost consists only of a completely unfrozen cryopeg due to the insulation effect of the ice-sheet and due to the high pressure induced by the ice load. Hence all bedrock is at the pressure melting point temperature (Figure 4-28).

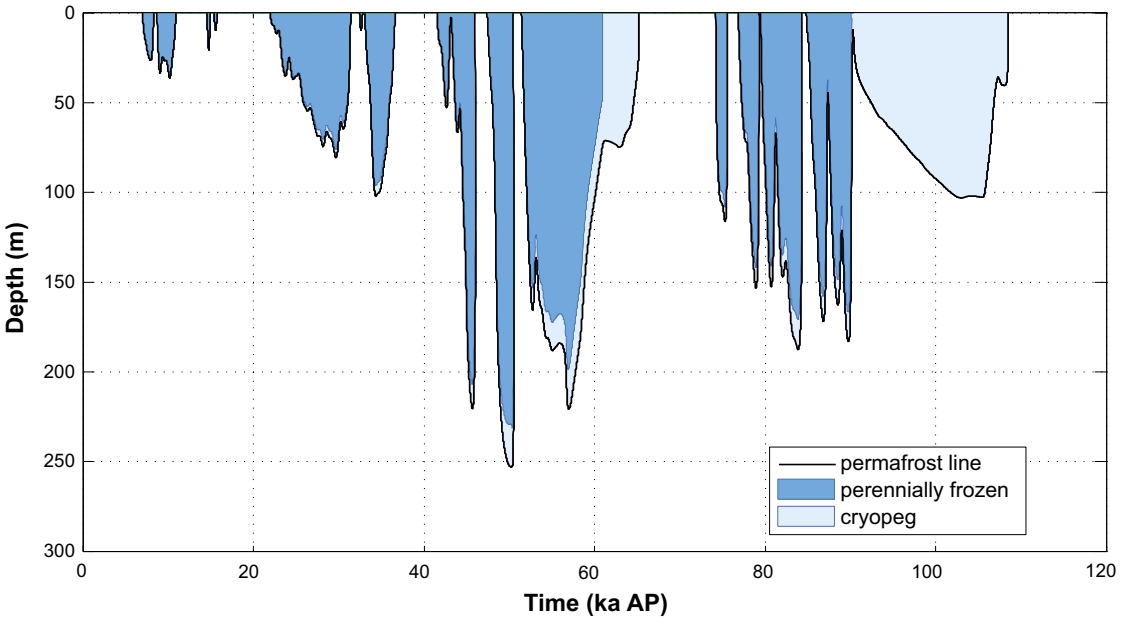

Figure 4-28. *Evolution of permafrost and perennially frozen ground depth for the reference glacial cycle climate case for the repository location in Forsmark. The results were obtained using a 1D permafrost model (Section 3.4.4). Due to the high pressure, a thick unfrozen cryopeg exists within the permafrost (defined by the 0 °C isotherm) after 60 and 90 ka AP.*

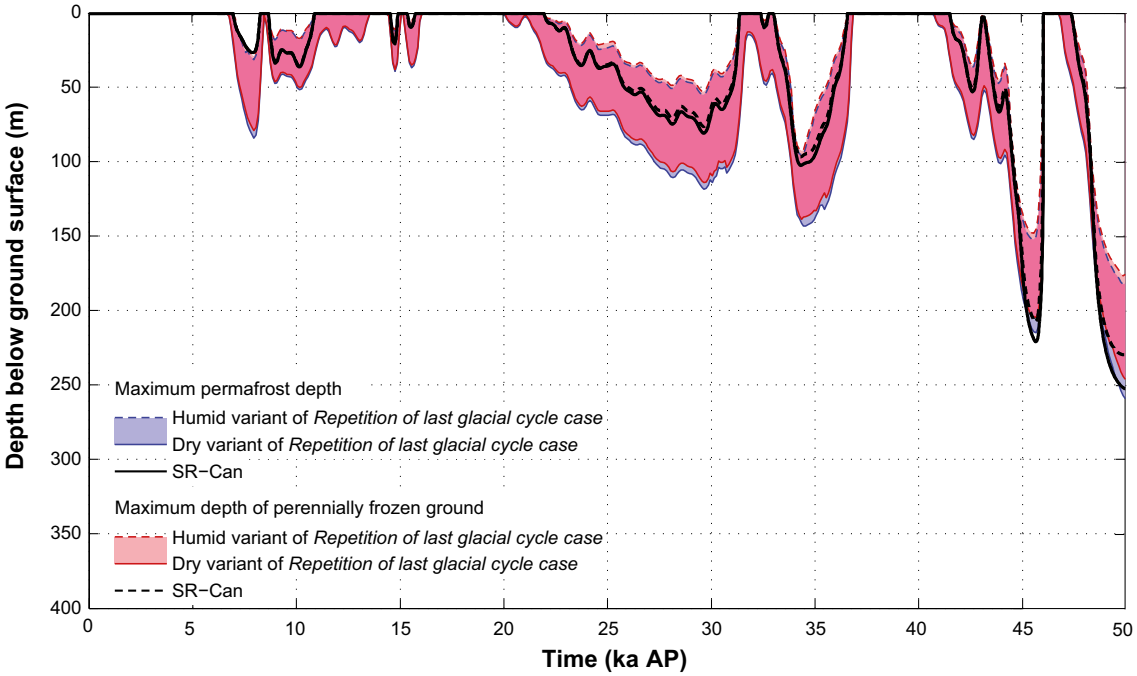

Figure 4-29. *Evolution of permafrost and perennially frozen ground depth at the repository location for the first 50 ka of the reference glacial cycle climate case as simulated by the 2D and 1D permafrost models (Section 3.4.4). The 2D simulations (coloured shaded areas) were made for SR-Site whereas the 1D simulations (black lines) were made for SR-Can. The shaded area in blue and red represents the range obtained from the 2D modelling when considering one wet and one humid climate variant. Further uncertainties in the permafrost modelling are discussed in Section 3.4.4. Both model simulations show that permafrost starts to grow around 7 ka AP and that the maximum permafrost depth is ~250 m around 50 ka AP.*

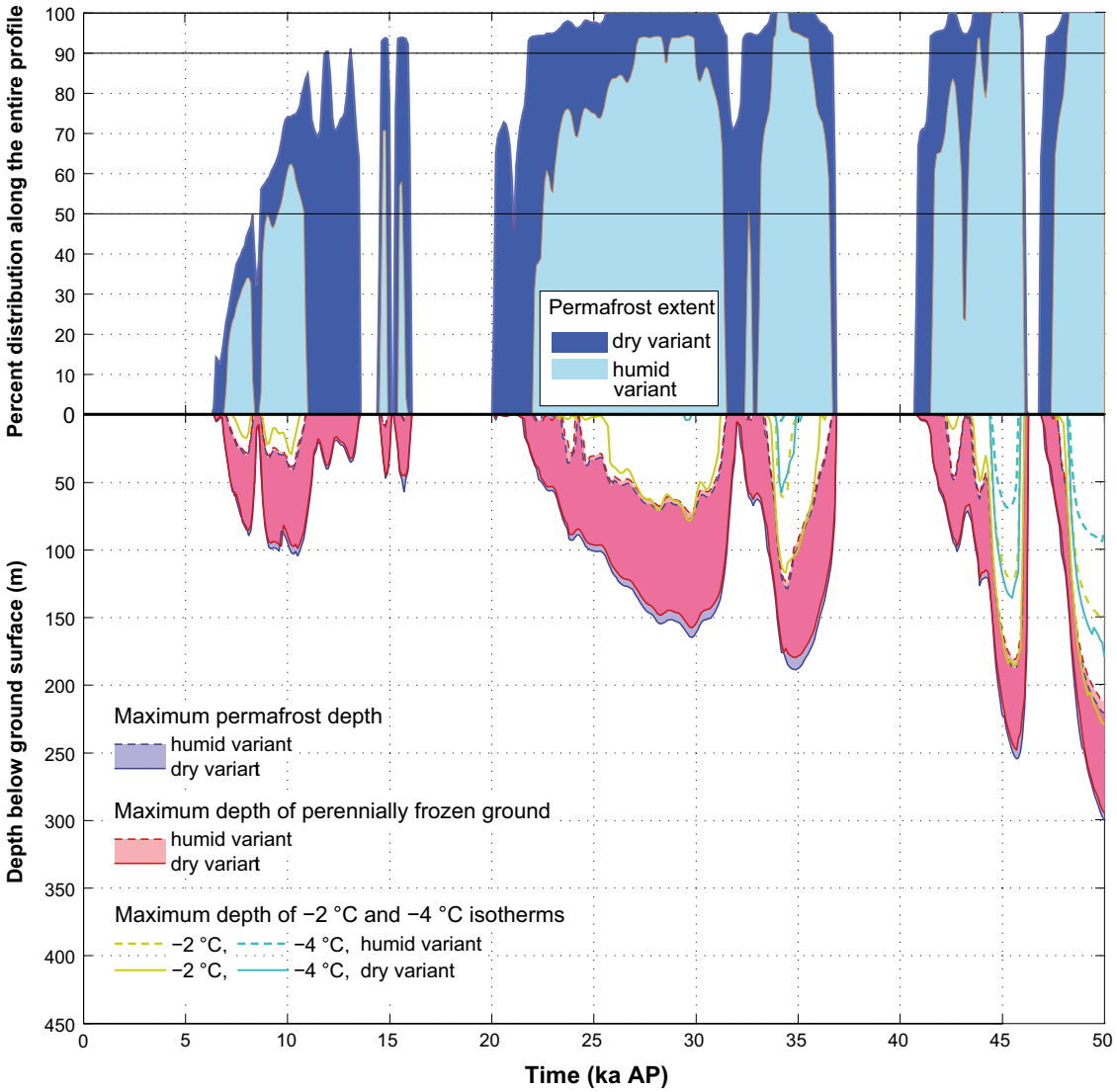

Figure 4-30. *Evolution of maximum permafrost depth, maximum freezing depth and percent permafrost distribution over the entire investigated profile (Figure 3-48) for the first 50 ka of the reference glacial cycle climate case. Upper panel: the transition from sporadic to discontinuous permafrost occurs at 50 % spatial coverage and from discontinuous to continuous permafrost at 90 % coverage. Lower panel: the shaded area in blue and red represents the range obtained when considering one dry and one humid climate variant of the reference glacial cycle climate case. The lilac colour indicates that the results for permafrost and perennially frozen ground overlap.*

Some of the input data for the permafrost simulations are associated with significant uncertainty. The largest uncertainly relates to the air temperature curve reconstructed for the Forsmark site for last glacial cycle, which is estimated up to ±6 °C (Appendix A). If this uncertainty in air temperature is combined with the uncertainty in climate humidity, the permafrost (e.g. 0 °C isotherm) uncertainty range in the *reference glacial cycle climate case* reach a maximum depth of ~410 m, while the uncertainty range for the perennially frozen ground reaches ~380 m (Figure 3-69).

Uncertainties related to other surface conditions (vegetation type, surface wetness, snow cover) and subsurface conditions (thermal conductivity and diffusivity, and geothermal heat flow) have a smaller impact on the simulated permafrost results. If they all are combined with the uncertainty in climate humidity, they result in a permafrost uncertainty interval down to between ~170 to ~290 m depth (Figure 3-75).

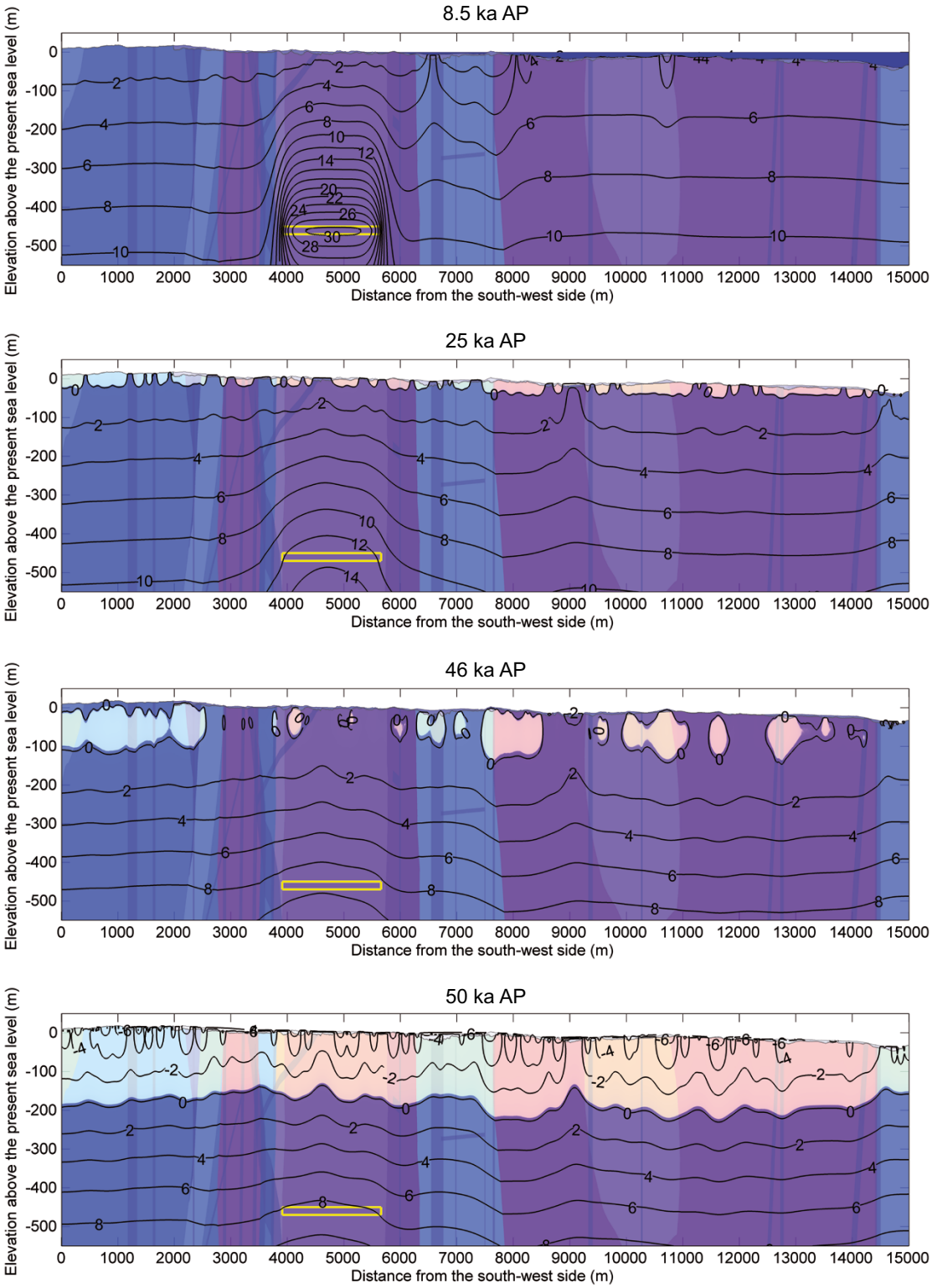

Figure 4-31. *Temperature contours in (°C) and the extent of perennially frozen ground (light colour) and permafrost (0 °C isotherm) at times 8.5, 25, 46 and 50 ka AP for the reconstruction of last glacial cycle conditions (humid climate variant, see Section 3.4.4). Blue colour on the top of the profile at 8.5 ka AP shows the Baltic Sea. The yellow rectangle indicates the location of the repository. Vertical areas with various light colours denote different rock domains. At 8.5 ka AP (upper panel) a subarctic climate prevails. At that time the profile is partially submerged and the exposed ground surface is partially underlain by permafrost (too thin to be seen in the figure). At that time the ground temperature is at its maximum within the repository. At 25 ka AP (middle panel) a subarctic climate prevails and discontinuous permafrost is developing. At 50 ka AP (lower panel) an arctic climate prevails and continuous permafrost reaches its maximum depth in this humid climate variant of the reference glacial cycle climate case. In the dry climate variant, the permafrost grows deeper (Figure 4-30 and Figure 4-32).*

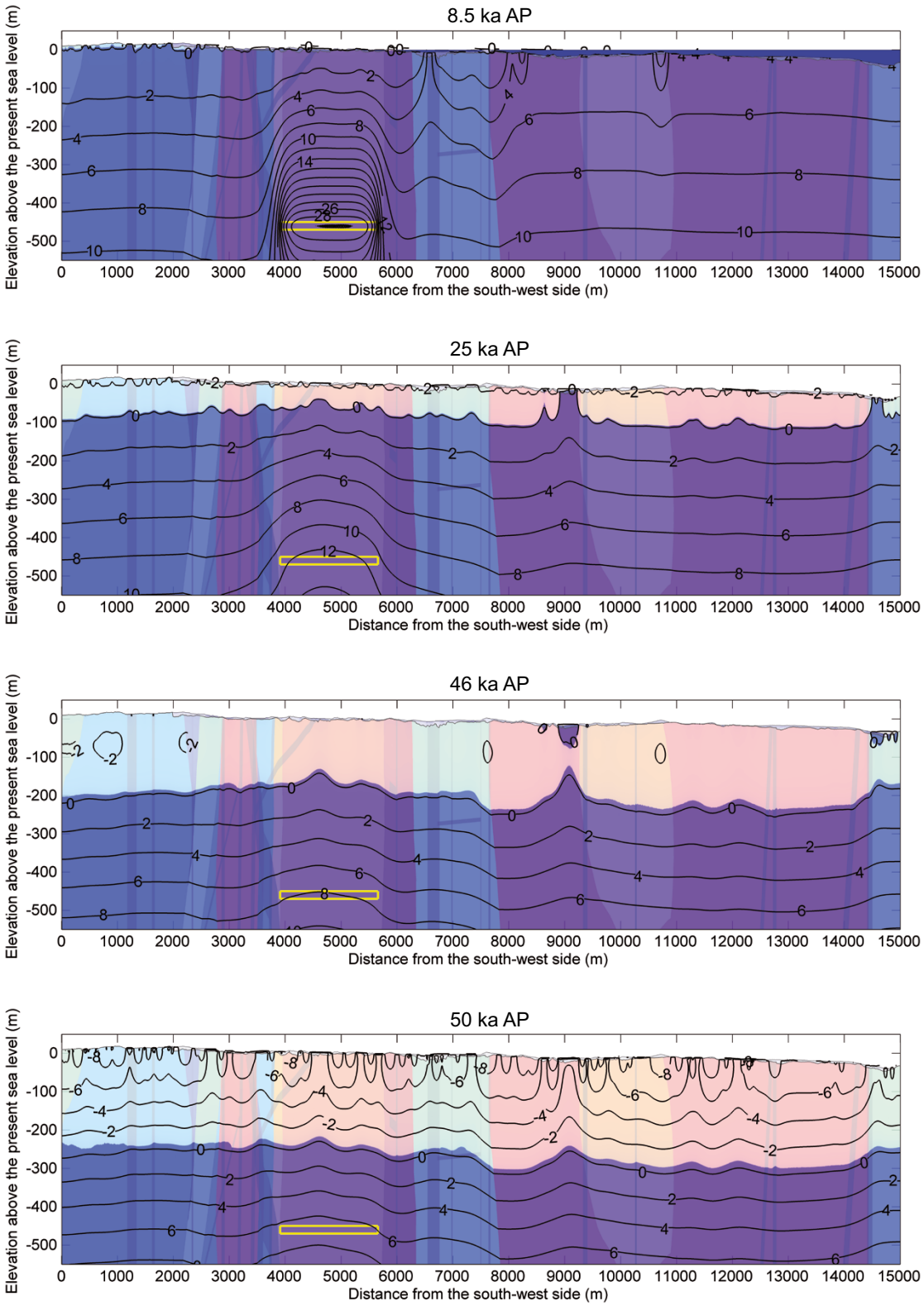

Figure 4-32. *Temperature contours in (°C) and the extent of perennially frozen ground (light colour) and permafrost (0 °C isotherm) at times 8.5, 25, 46 and 50 ka AP for the reference glacial cycle climate case (dry climate variant, see Section 3.4.4). The yellow rectangle indicates the location of the repository. Vertical areas with various light colours denote different rock domains. At 25 ka AP (Upper panel) a subarctic climate prevails and continuous permafrost has developed. Two major taliks have formed under the future lakes located at c 9000 and 14600 m along the profile. At 46 ka AP (middle panel), the taliks are shallow, and not in contact with the deep groundwater. At 50 ka AP (lower panel) an arctic climate prevails and continuous permafrost reaches its maximum depth in the reference glacial cycle climate case. The maximum permafrost depth is shallower in the humid climate variant (Figure 4-30 and Figure 4-31).*

Setting *all* known uncertainties (in air temperature curve, climate humidity, surface wetness, vegetation, snow cover, bedrock thermal conductivity and diffusivity, and geothermal heat flux) at their most extreme values favourable for permafrost growth, the permafrost uncertainty range reaches a maximum depth of ~460 m, whereas the uncertainty range for the perennially frozen ground reaches a maximum depth of ~420 m (Figure 3-76). It must be noted, however, that this most extreme combination of uncertainties is unrealistic. Given that the uncertainty in the maximum depth of perennially frozen ground does not reach 450 m depth even in the most extreme combination of all uncertainties, freezing of groundwater at repository depth is excluded in the *reference glacial cycle climate case*. For a more detailed description of e.g. individual contributions of uncertainty from various parameters affecting permafrost growth, see Section 3.4.4 and Hartikainen et al. (2010).

The presence of permafrost and perennially frozen ground may impact the buffer and backfill material, and in turn also the canister and surrounding bedrock, respectively. The temperature criterion used in SR-Site for buffer freezing was −4 °C, whereas the corresponding temperature for the backfill material in e.g. deposition tunnels was −2 °C (SKB 2011, Section 12.3). In the PSAR, the temperature for which a frozen buffer clay and backfill material may start having detrimental effects on the canister and surrounding host rock has been updated to −6 °C for both materials, see the **Post-closure safety report** Section 8.3.2 and 8.4.4. The reference glacial cycle evolution of the 0 °C (i.e. permafrost depth), −2 °C and the −4 °C isotherms for the repository location are shown in Figure 4-33. The figures show results from the dry climate variant, i.e. the climate variant with deeper permafrost. The 0 °C, −2 °C and −4 °C isotherms reach a maximum depth prior to the first major ice advance, around 50 ka AP. As previously mentioned the 0 °C isotherm (permafrost) reaches a maximum depth of ~250 m, whereas the −2 °C and −4 °C isotherms, respectively, reach a maximum depth of 200 m and ~150 m (Figure 4-33) in the *reference glacial cycle climate case*.

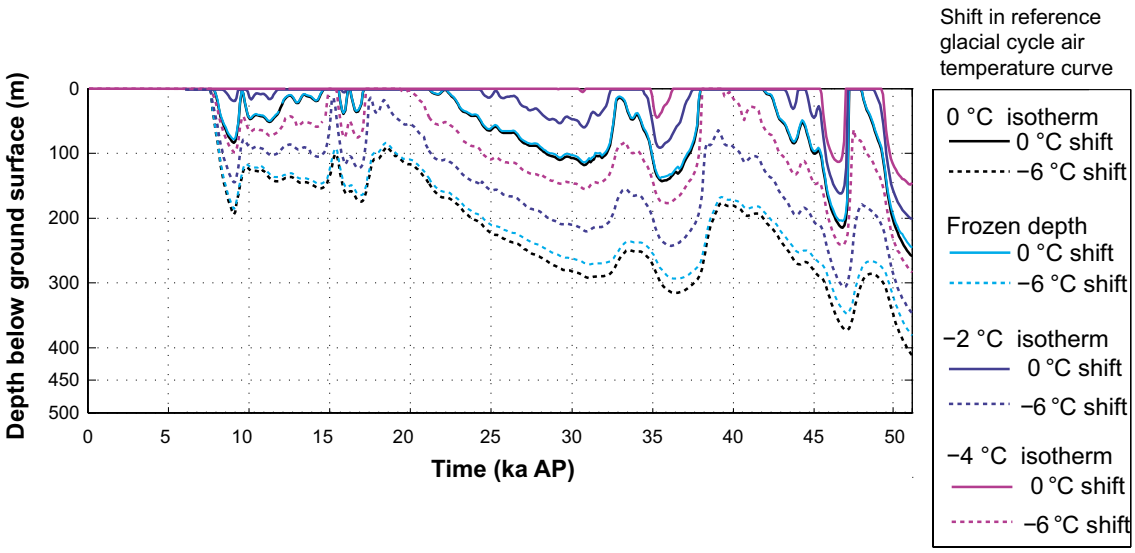

Figure 4-33. *Evolution of 0 °C isotherm (permafrost depth), perennially frozen ground and −2 and −4 °C isotherms at the Forsmark repository location for the first ~50 ka of the reference glacial cycle climate case (solid lines, i.e. 0 °C shift of reference glacial cycle air temperature curve). Dashed lines show the lower boundaries of the corresponding uncertainty intervals when considering the maximum uncertainty in air temperature (±6 °C) (Appendix A). The results are from the dry climate variant, i.e. the variant with deeper permafrost, see Section 3.4.4. For corresponding results for other shifts of the temperature curve, see Hartikainen et al. (2010).*

Table 4-4 summarizes the maximum permafrost depths, frozen depths, and depths of the −2 °C isotherm and −4 °C isotherm for the *reference glacial cycle climate case*, and also presents the maximum depth of the associated uncertainty intervals.

In this context it should be noted that the depths presented above and in Table 4-4, which were calculated including the (declining) contribution of heat from the repository, are relevant for the first future glacial cycle. In the PSAR, the full safety assessment period is 1 Ma. This means that for the second and following glacial cycles, the permafrost and frozen depths will be somewhat deeper (~37 m), see Figure 3-77, since the heat contribution from the repository will have become insignificant. This issue is included in the analysis in the PSAR buffer freezing scenario, see the **Post-closure safety report**, Section 12.3.

Table 4-4. Maximum depths of permafrost (0 °C isotherm), perennially frozen ground, −2 °C isotherm and −4 °C isotherm for the reference glacial cycle climate case calculated using the 2D permafrost model (Hartikainen et al. 2010). The uncertainty interval includes the unlikely combination of having all uncertainties, including air temperature, set at the most pessimistic values favouring permafrost growth. Note that in the PSAR, the temperature for which a frozen buffer clay and backfill material may start having detrimental effects on the canister and surrounding host rock has been updated to −6 °C for both materials, see the Post-closure safety report Section 8.3.2 and 8.4.4. The −6 °C isotherm is located at shallower depth than the −2 and −4 °C used as freezing criterion in SR-Site, which in turn results in a larger margin to freezing of the buffer and backfill in the PSAR.

	Maximum permafrost depth (0 °C isotherm) [max uncertainty interval]	Maximum depth perennially frozen ground [max uncertainty interval]	Maximum depth −2 °C isotherm [max uncertainty interval]	Maximum depth −4 °C isotherm [max uncertainty interval]
Reference glacial cycle climate case	259 m [down to 463 m]	246 m [down to 422 m]	200 m [down to 388 m]	148 m [down to 316 m]

The climate that may prevail in the Forsmark region during periods of periglacial climate domain was, as previously described, studied by climate modelling Kjellström et al. (2009, including erratum Feb 2010), see Section 4.3.2.

The results show that, given a prescribed restricted ice-sheet coverage during the interstadial between the two phases of ice-sheet coverage (Figure 4-26), the climate at Forsmark is subject to dry and cold periglacial conditions at the end of the interstadial. For the selected modelled period (44 ka BP), the climate in the Forsmark region is considerably colder and drier than at present. The modelled mean annual air temperature is 12 °C colder than at present whereas the precipitation is reduced by more than 30 % (Section 4.3.2). The results of the study thus show that climate conditions are clearly favourable for permafrost growth during this cold stadial of the *reference glacial cycle climate case*. This climatological description, and several other climatic parameters reported in Kjellström et al. (2009), together give one detailed example of the climatic characteristics that may prevail at the Forsmark site during periods of periglacial climate domain. In addition to the climate modelling performed by Kjellström et al. (2009), the same study also simulated vegetation types associated with the different climate cases studied. The results of the vegetation simulations for e.g. the periglacial climate case are reported in Kjellström et al. (2009) and in the **Biosphere synthesis report**.

Some general conclusions about the site-specific evolution of permafrost and perennially frozen ground for the *reference glacial cycle climate case* can be drawn.

- Permafrost (i.e. the 0 °C isotherm) reaches a depth of ~250 m in the *reference glacial cycle climate case*.
- If considering the combined uncertainties related to surface conditions (vegetation types, snow cover and climate humidity) and subsurface conditions (e.g. bedrock thermal conditions and geothermal heat flow), the uncertainty range for the perennially frozen ground reaches a maximum depth of ~290 m (Figure 3-75).
- If considering the uncertainties in climate (in air temperature curve and humidity), the uncertainty range for the perennially frozen ground reaches a maximum depth of 380 m (Figure 3-69).

- If considering the extreme and unrealistic combination of setting *all* known uncertainties (in air temperature curve, climate humidity, surface wetness, vegetation, snow cover, bedrock thermal conductivity and diffusivity, and geothermal heat flux) at their values most favourable for permafrost growth, the uncertainty range for the permafrost depth reaches a maximum depth of ~460 m and for the perennially frozen ground ~420 m (Figure 3-76).
- The maximum depth of the −2 °C and −4 °C isotherms, respectively, reach a depth of 200 m and ~150 m over the repository in the *reference glacial cycle climate case* (Figure 3-59).
- Including the extreme and unrealistic combination of setting *all* uncertainties (in air temperature curve, climate humidity, surface wetness, vegetation, snow cover, bedrock thermal conductivity and diffusivity, and geothermal heat flux) in their most favourable setting for permafrost growth, the uncertainty range for the −2 °C and −4 °C isotherms reach a maximum depth of ~390 m and ~320 m, respectively (see Figure 3-76).

Given these results, freezing of groundwater at repository depth is excluded in the *reference glacial cycle climate case*.

The maximum depths of permafrost, frozen ground, −2 °C isotherm, −4 °C isotherm, and uncertainties for the *reference glacial cycle climate case* are summarised in Table 4-4. For a detailed description of the uncertainties associated with the permafrost modelling, see Section 3.4.4.

4.5.4 Evolution of climate domains

Based on the above evolutions of ice-sheet, relative sea-level and permafrost, the climate development at the Forsmark site for the *reference glacial cycle climate case* can be described as successions of climate domains and submerged periods (Figure 4-34). The temporal evolution of all climate domains relevant for Forsmark in the PSAR *reference glacial cycle climate case* is presented in Figure 4-35. Considering that the development of permafrost in Figure 4-35 has been simulated specifically for the repository location (Section 3.4.4 and 4.5.3), the development of climate domains in Figure 4-34 and Figure 4-35 also refers specifically to the repository location and not to the entire Forsmark site (Figure 3-48). For a description of the spatial representativity and development of the climate domains, see the description on *Transitions between climate domains* below in this section.

At Forsmark, periods with a periglacial climate domain correspond to 38 % of the total time of the *reference glacial cycle climate case* (Figure 4-34), whereas periods with a temperate climate domain occupy 24 %, the glacial climate domain 23 % and periods with submerged conditions 15 % of the *reference glacial cycle climate case*, see also Table 4-5.

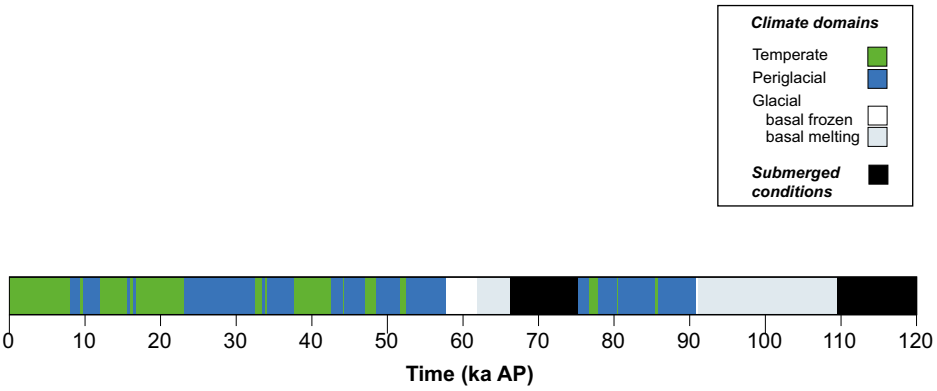

Figure 4-34. *Succession of climate domains and submerged conditions at Forsmark in the PSAR reference glacial cycle climate case. Other possible future climate developments are described in Chapter 5.*

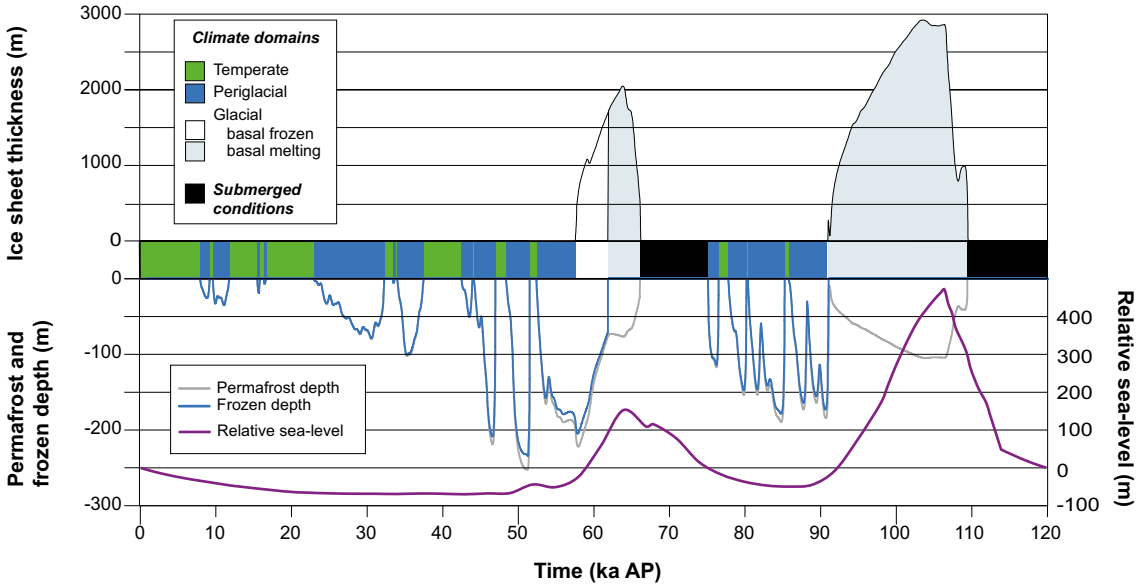

Figure 4-35. *Evolution of important climate-related variables at Forsmark for the coming 120 ka in the PSAR reference glacial cycle climate case. Other possible future climate developments are described in Chapter 5.*

Table 4-5. Duration of climate domains in the PSAR reference glacial cycle climate case.

Climate domain	Duration (% of reference glacial cycle climate case)	Duration (years)
Temperate climate domain	24 %	28200
Periglacial climate domain	38 %	46000
Glacial climate domain	23 %	27300
Submerged conditions (with simultaneous prevailing temperate- or periglacial climate domains)	15 %	18500

The climate succession bar in Figure 4-34 shows that the Forsmark site is dominated by temperate climate conditions for the first ~25 ka, although short periods of periglacial climate domain occur around 10 ka AP. Subsequently, up to the first period of glacial climate domain, temperate conditions are gradually replaced by periglacial conditions. The ice-free interstadial period around 80–90 ka AP in the *reference glacial cycle climate case* is dominated by permafrost conditions. The trend with gradually more dominating permafrost conditions is a natural result of the progressively colder climate during the glacial cycle. An exception to this trend is the short period after the submerged phase that follows the final deglaciation, at the very end of the scenario. At that time, ice-free conditions are again dominated by temperate conditions in a warm interglacial climate. Yet another effect of the progressively colder climate during the glacial cycle is the increasing length of the periods with glacial climate domain.

Periods of temperate climate domain occurs in Forsmark in the early phase of the glacial cycle, during short periods of the interstadial between the two major ice advances, and during the interglacial period following the glacial maximum. The periods of temperate climate domain in the early phases of the *reference glacial cycle climate case* are generally warmer and longer than those occurring during interstadials in the later part of the glacial.

During the first 50 ka of the *reference glacial cycle climate case*, and in the period between the two ice advances, the increasingly colder climate results in progressively longer periods of periglacial conditions. The total duration of the periglacial climate domain at Forsmark is about 41 ka (Table 4-5). During the most severe permafrost periods in the *reference glacial cycle climate case*, at around 70 ka BP (Figure 4-35), the permafrost at the repository location develops to between ~180 and ~250 m depth depending on assumed ground cover. The corresponding depths of perennially frozen conditions are between ~180 and ~250 m. The maximum permafrost depth along the entire profile investigated for permafrost development (Figure 4-22) is between 220 and 300 m for the same simulation. The maximum depth of perennially frozen ground along the profile is from 210 to 300 m. The uncertainties related to the simulated permafrost depths are described in Section 3.4.4 and 4.5.3.

Forsmark is exposed to two major ice advances and retreats during the *reference glacial cycle*, the first advance occurs around 60 ka AP and the second after about 90 ka AP (Figure 4-35). Prior to both these glaciated periods, the Forsmark site is situated above sea-level with prevailing permafrost conditions when the ice-sheet advances towards and over the site. A period of basal frozen conditions initiates the first major period of glacial climate domain. The period of basal frozen conditions is ~4 ka long.

After the first glacial period, the site is submerged under the Baltic Sea (Figure 4-35). Following from the warm climate conditions reconstructed for the first part of MIS 3 during the Weichselian (Section 4.3.2), with present-day air temperatures during summer in northern Fennoscandia, temperate climate conditions are envisaged to prevail at Forsmark during the first several thousands of years of the submerged period (not seen in Figure 4-35). That is, if the site were not submerged after the first glacial period, due to a thinner ice-sheet and less isostatic depression, subaerial temperate climate conditions would prevail at the site for considerable amount of time after ~66 ka AP.

The landscape is in a state of continuous permafrost coverage during the time of the first ice advance over the site, at around 60 ka AP (Figure 4-30 and Figure 4-35). At this time, all present and future lakes at the Forsmark site are infilled (see the **Biosphere synthesis report**), and hence there are no taliks present under lakes. Nevertheless, a hypothetical situation with an ice-sheet co-existing with taliks under lakes at the Forsmark site is investigated by groundwater modelling in Vidstrand et al. (2010).

When the ice-sheet expands over the site, it insulates the ice-sheet bed from the cold air temperatures and in time induces ice-sheet basal melting conditions. During periods of ice-sheet coverage, the development of subglacial permafrost is more restricted than permafrost development during ice-free conditions (Figure 4-35). The total length of periods of glacial climate domain in the *reference glacial cycle climate case* is 28 ka at Forsmark (Table 4-5). During this time, basal melting conditions dominate.

For detailed examples of how the climate may be characterized in Sweden and in the Forsmark region under periglacial and glacial conditions, see the exemplified climates of the Weichselian glacial cycle in Section 4.3.

The climate simulations (Kjellström et al. 2009), show that there is a large range in possible climates for the Fennoscandian region in a 100 ka time perspective. Excluding the situation when the region is covered by an ice-sheet, annual mean air temperatures for the Forsmark region differ from the simulated cold MIS 3 stadial climate (Section 4.3.2) to the future warm climate (Section 5.1.7) by 12–15 °C. Correspondingly, annual mean precipitation is almost a factor two higher in the future warm climate compared with MIS 3 at these sites.

Figure 4-36 shows both the first and second repetition of conditions reconstructed for the last glacial cycle (i.e. the *reference glacial cycle climate case*), illustrating how glacial cycles are envisaged to follow each other in the 1-million-year time perspective of the safety assessment reference evolution, see the **Post-closure safety report**.

The first full interglacial period, following the present one, is shown at around 110 to 130 ka AP (Figure 4-36). The onset and ending of this future interglacial period, as well as the corresponding onset and ending of the Holocene, is here defined from the development in the Forsmark region; the onset of an interglacial is defined by the timing of the deglaciation of the area, whereas the ending is defined by the first occurrence of permafrost in the *reference glacial cycle climate case* (Figure 4-36). The timing and duration of the Holocene and future interglacial periods in Figure 4-36 is thus determined from the development in the *reference glacial cycle climate case*, which for this part of the glacial cycle is based on site-specific observations and modelling. The resulting, *locally defined*, Holocene interglacial and future interglacial periods have a length of ~18 ka. This duration is in line with the longer of the two types of interglacials, with durations roughly of either ~20 or ~10 ka, that have occurred during the past eight glacial cycles (Tzedakis et al. 2009).

The uncertainties in the *actual* length of the present and future interglacial periods are naturally very large. Given these uncertainties, it is again emphasized that the evolution of climate domains as described in the *reference glacial cycle climate case* (Figure 4-34, Figure 4-35, Figure 4-36), and corresponding base case of the PSAR main scenario (Figure 1-3), is not an *expected* future climate evolution. It is one relevant example of an evolution covering the climate-related conditions that can be met in a 100 ka time perspective. Other possibilities for the length of the present interglacial period are handled in the additional climate cases, including the *global warming climate case* and *extended global warming climate case* (Chapter 5).

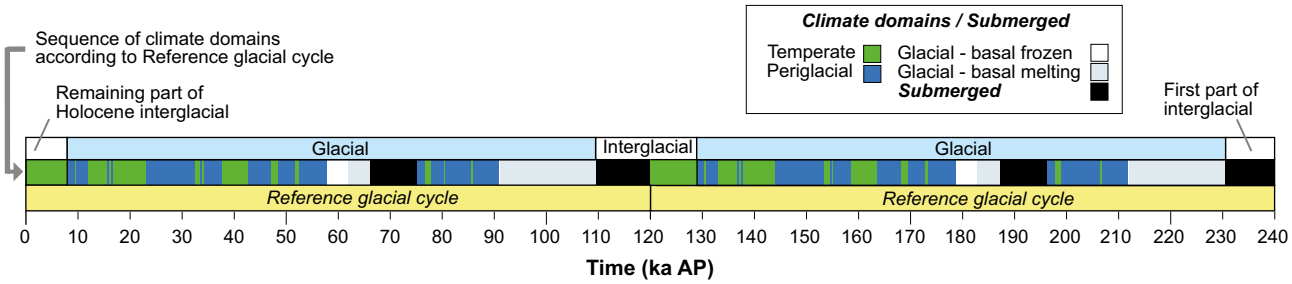

Figure 4-36. *Evolution of climate at Forsmark for the coming 240 ka using repetitions of the reference glacial cycle climate case. The figure illustrates how the reference glacial cycle is repeated to cover the 1-million-year time perspective of the PSAR reference evolution see the Post-closure safety report. The resulting duration of the locally defined interglacial periods, see the text, is in this case approximately 18 ka. For approximately half of that interglacial time, the Forsmark site is submerged under the Baltic water level. Other possible future climate developments are described in Chapter 5.*

The sequence of main climate-related events for the *reference glacial cycle climate case*, including times of transitions between events and corresponding climate domains, is summarized in Table 4-6.

For the set-up of the groundwater modelling, a simplified climate development for the reference glacial cycle has been produced (Figure 4-37, Table 4-7). In the simplified reference glacial cycle, climate periods of short duration have been removed and longer periods are used to describe the general climate development in Figure 4-34 and Figure 4-35.

Table 4-6. Sequence of climate-related events for the reference glacial cycle climate case, including the full Holocene. The same sequence of events is seen in Figure 4-34 and Figure 4-35.

Event	Time for transition between events	Climate domain
Deglaciation/Start Holocene interglacial (locally defined as time of deglaciation of Forsmark)	10800 BP (8800 BC)	-
Holocene interglacial	-	Temperate climate domain (incl. submerged conditions)
Present	0 BP	
End of Holocene interglacial (locally defined as first occurrence of permafrost in reference glacial cycle climate case)	7000 AP (9000 AD)	-
Periglacial and temperate conditions (progressively longer periods of permafrost conditions)	-	Periglacial- and temperate climate domains (progressively shorter phases of temperate climate conditions)
End of periglacial and temperate conditions. Start of glacial conditions	57600 AP (59600 AD)	-
First phase with glacial conditions	-	Glacial climate domain
Deglaciation at site. Start interstadial conditions	66200 AP (68200 AD)	-
Interstadial conditions	-	Mainly periglacial climate domain (incl. submerged conditions and short temperate periods)
End of interstadial conditions. Start of glacial conditions	90800 AP (92800 AD)	-
Second and main phase with glacial conditions	-	Glacial climate domain
Deglaciation/start of interglacial (locally defined as time of deglaciation of Forsmark)	109500 AP (111500 AD)	-

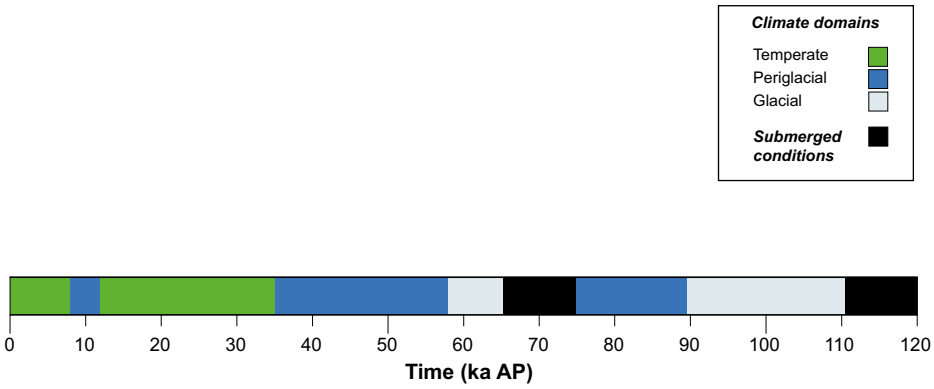

Figure 4-37. *Simplified reference glacial cycle. The total durations of the climate domains are the same as in the detailed reference glacial cycle climate case seen in Figure 4-34.*

Table 4-7. Simplified climate development for the reference glacial cycle.

Climate domain/ Submerged conditions	Time (ka AP)	Year AD	Duration (ka)
Temperate	0–8	2000–10000	8
Periglacial	8–12	10000–14000	4
Temperate	12–35	14000–37000	23
Periglacial	35–58	37000–60000	23
Glacial	58–65	60000–67000	7
Submerged	65–75	67000–77000	10
Periglacial	75–89	77000–91000	14
Glacial	89–111	91000–113000	22
Submerged	111–120	113000–122000	9

Transitions between climate domains

Depending on what spatial scale is considered, the transitions between climate domains need to be described differently. If considering the repository site only, or even the central part of the repository, the transitions between climate domains (temperate-, periglacial-, glacial domain and submerged conditions) may be described as more or less instantaneous in time, as perceived from the way the succession of climate domains is depicted in Figure 4-35. This is in line with the fact that the permafrost modelling used for Figure 4-35 was conducted specifically for the repository site, see Section 3.4.4 and 4.5.3. (The ice-sheet and GIA modelling used for Figure 4-35 were done on a much coarser spatial scale, but the results from the larger model grid cells are here taken to represent the ice-sheet- and relative sea-level development at the repository location).

However, if looking at Forsmark on a site-scale, i.e. several hundreds of square km (see Figure 4-38), the transition between climate domains is of a gradual nature, both spatially and temporally. The main transitions within the *reference glacial cycle* occur when the site goes from i) temperate climate domain to periglacial climate domain, ii) periglacial climate domain to glacial climate domain, iii) glacial domain to submerged conditions and finally iv) from submerged conditions back to temperate climate domain.

The transient nature of the change from temperate climate domain to periglacial climate domain is illustrated in Figure 4-30. Sporadic permafrost starts to grow more or less simultaneously over the site. Subsequently, if climate allows, the permafrost may develop to a discontinuous- and continuous spatial coverage. The duration of such a full transition in the *reference glacial cycle climate case*, i.e. the development from a landscape without permafrost to a landscape with a permafrost coverage of 90 % or more at the Forsmark site, is approximately between 2 and 5 ka (Figure 4-30).

The transition from periglacial- to glacial climate domain manifests itself as an ice-sheet margin that advances over the site. A spatially transient change takes place in one specific direction over the Forsmark site, by which the periglacial climate domain is replaced with glacial climate domain following

the advance of the ice-sheet front. In the *reference glacial cycle climate case,* the ice-sheet margin advances over the site at a speed of ~50 m a^{-1}. The duration of this transition in the *reference glacial cycle climate case*, i.e. the time it takes for the ice-sheet to advance over the Forsmark site, is around 250 years. Note that permafrost may still exist under the ice-sheet for some of the time that the site is assigned to the glacial climate domain (Figure 4-35).

The transition from glacial to submerged conditions constitutes the deglaciation phase of the site, when ice-sheet conditions are replaced by submerged conditions. The retreat rate of the ice-sheet margin during deglaciation of the Forsmark site is, in the *reference glacial cycle climate case,* ~300 m a^{-1}. The duration of this transition, i.e. the time during which one deglaciation occurs over the Forsmark site in the reference glacial cycle climate case, is around 50 years.

According to the model reconstruction of the last phase of ice-sheet coverage in the Forsmark area (Section 3.1.4), the ice-flow direction during the MIS 2 ice-sheet advance was approximately from the north, whereas the ice-flow direction during the deglaciation was from north–west. This is in line with the interpretation of glacial striae, with a northerly direction recorded both in the oldest glacial striae and the oldest documented directional transport of the till material as recorded in clast fabric analysis (Sundh et al. 2004), and with an overall dominating younger striae system showing transport and deposition from the north–west (Sohlenius et al. 2004). This demonstrates that the transition to and from the glacial climate domain may be spatially different during phases of ice-sheet growth and decay.

The transition from submerged conditions to temperate climate domain is manifested by the relative sea-level change caused by the isostatic rebound that follows deglaciation. The duration of this transition in the *reference glacial cycle climate case*, i.e. the time it takes from the very first appearance of land at the site (Figure 4-38) until the last remnants of sea have disappeared from the site is around 12 ka, see the **Biosphere synthesis report**. This is the transition that is occurring at the Forsmark site at present, manifested by the slow movement of the shore line across the site. The transient nature of relative sea-level change over the site is further described in the **Biosphere synthesis report**.

The durations of the four transitions above are summarised in Table 4-8.

Given the climate evolution of the *reference glacial cycle climate case*, the assumptions made in all modelling exercises (Chapter 3), and the physiographical characteristics of the site, the glacial processes result in the fastest transition between climate domains (Table 4-8). The transition from glacial climate domain to submerged conditions for the Forsmark site is around 50 years. The transition from periglacial to glacial climate domain is about five times slower. These two fastest transitions relate to the glacial climate domain, i.e. to the relatively fast processes of ice-sheet advance and decay. The transition from temperate- to periglacial climate domain with continuous permafrost is 40 to 100 times slower than the transition from glacial climate domain to submerged conditions (Table 4-8). The slowest transition is the one from submerged conditions back to temperate climate domain, which, in the *reference glacial cycle climate case,* is around 240 times slower than the transition from glacial climate domain to submerged conditions. This is due to very slow glacial isostatic adjustment of the Earth's crust to the unloading associated with the ice-sheet deglaciation (Section 3.3).

Table 4-8. Approximate durations of full transitions between climate domains over the Forsmark site (as shown in Figure 4-38) for the PSAR reference glacial cycle climate case. To compare the duration of the transitions from and to various climate domains, the relative duration time of the transitions are in the last column expressed as ratios to the duration of deglaciation of the site.

Transition	Approximate duration in reference glacial cycle climate case	Relative duration of transition
Temperate- to periglacial climate domain with continuous permafrost coverage	~2000 to ~5000 years	40 to 100×
Periglacial- to glacial climate domain	~250 years	5×
Glacial climate domain to submerged conditions (deglaciation)	~50 years	1×
Submerged conditions to temperate climate domain	~12000 years	240×

Note that for any given time during these transitions, the Forsmark site (Figure 4-38) contains more than one type of climate domain. For instance, parts of the site may be subject to the periglacial climate domain, having permafrost conditions without an ice-sheet, at the same time as another part of the site may be overridden by an ice-sheet and thus subject to the glacial climate domain. Also note that the transition from one climate domain to another over the site does not need to be a full transition (as in the above examples). For instance, discontinuous permafrost may start to form within the site due to lower air temperatures, transforming the affected areas to periglacial climate domain. Thereafter, climate may become warmer and permafrost (and the periglacial climate domain) diminishes and disappears.

The hydrogeological consequences of the ongoing transition from submerged conditions to temperate climate domain at Forsmark is analysed in Salas et al. (2010). The hydrogeological consequences of transitions between temperate-, periglacial- and glacial climate domains are analysed in Vidstrand et al. (2010).

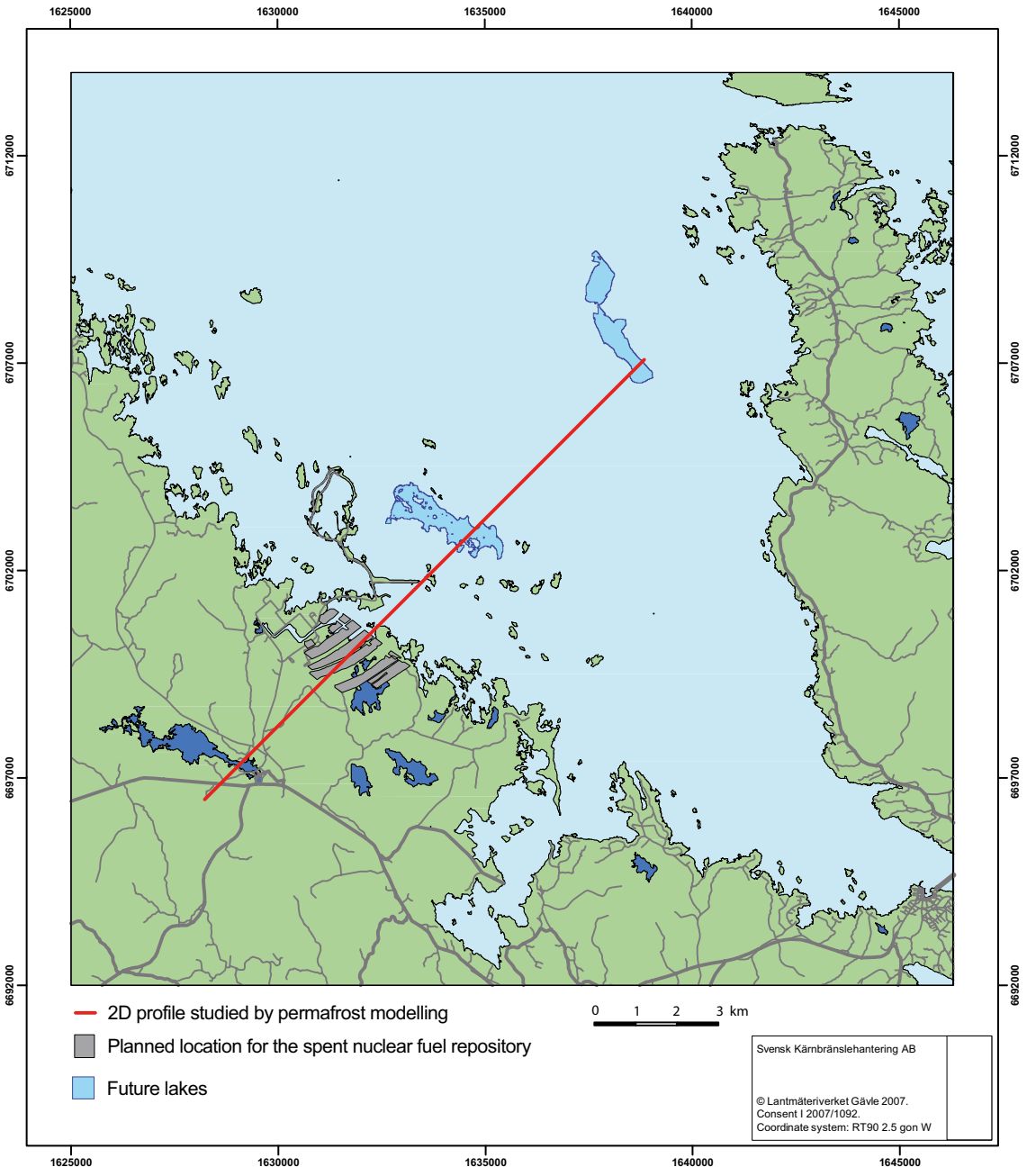

Figure 4-38. *The Forsmark site as defined and analysed in the PSAR biosphere programme (stippled) and the location of the profile studied by 2D permafrost modelling (red line) (Section 3.4.4). This figure is identical to Figure 3-48.*

4.5.5 Evolution of hydrological conditions and groundwater

In the PSAR, dedicated groundwater flow modelling was performed for all types of climate domains that occur in the *reference glacial cycle climate case*. Groundwater flow modelling of periods with temperate climate conditions is reported in Joyce et al. (2010), whereas groundwater modelling of periods with periglacial and glacial conditions is reported in Vidstrand et al. (2010). Geochemical developments during the different climate conditions are presented in Salas et al. (2010). An overview of the hydrological and groundwater conditions of the *reference glacial cycle climate case* is given below.

A schematic section through an arbitrary south–western sector of a Fennoscandian ice-sheet large enough to cover the Forsmark site is shown in Figure 4-39. A zone of basal melting reaches some hundreds of kilometres from the ice margin in the southeast. The production of basal melt water here varies between 1 and 10 mm a^{-1} and can be regarded as constant over the year. In the ablation area below the equilibrium line, melt water from the ice surface and rain is brought to the ice-sheet bed through crevasses and moulins. In the *reference glacial cycle* (Figure 4-24 and Figure 4-25) surface melt water production in the ablation area varies in both space and time. More ice melts in lower parts of the ice-sheet, and less ice closer to the equilibrium line. Typical melt rates in the ablation zone range from 4–8 m of water per year. During the final deglaciation of the ice-sheet in this *reference glacial cycle*, a maximum modelled surface melt rate of 14 m a^{-1} occurs. The modelled typical surface melt rate values of 4–8 m a^{-1} can be compared with observed present average surface ablation rates of the Greenland ice-sheet of a few metres per year (van de Wal et al. 2012) and up to ~10 m a^{-1} (Bøggild et al. 2004). During the deglaciation of the Weichselian ice-sheet, melt rates of more than 10 m a^{-1} may have occurred (Humlum and Houmark-Nielsen 1994).

During periods of temperate climate domain, the groundwater flow pattern is similar to the present ice-free situation, with a mixture of local areas of groundwater recharge, typically at topographically high positions, and discharge, typically in low positions. The groundwater flow is at this time to a large degree driven by topographic gradients in the landscape.

During the initial periods of periglacial climate domain, the permafrost distribution in the Forsmark region is first sporadic followed by discontinuous spatial permafrost coverage, see section on permafrost development above. This results in a modified pattern of groundwater flow, but still with significant groundwater recharge and discharge taking place. When climate gradually gets colder, permafrost grows progressively thicker and more widespread (see Section 4.5.3). When the climate is cold enough, continuous permafrost forms. When continuous permafrost occurs, the precipitation recharge of groundwater is strongly reduced or even stopped, since permafrost influences subsurface hydrology by drastically reducing the hydraulic conductivity of the frozen unit (Burt and Williams 1976, Vidstrand et al. 2010, Hartikainen et al. 2010). At locations of future deep lakes, unfrozen taliks may exist where groundwater recharge and discharge take place, see Section 4.5.3. Details on the permafrost and hydrological conditions during such situations are provided in Hartikainen et al. (2010) and Vidstrand et al. (2010).

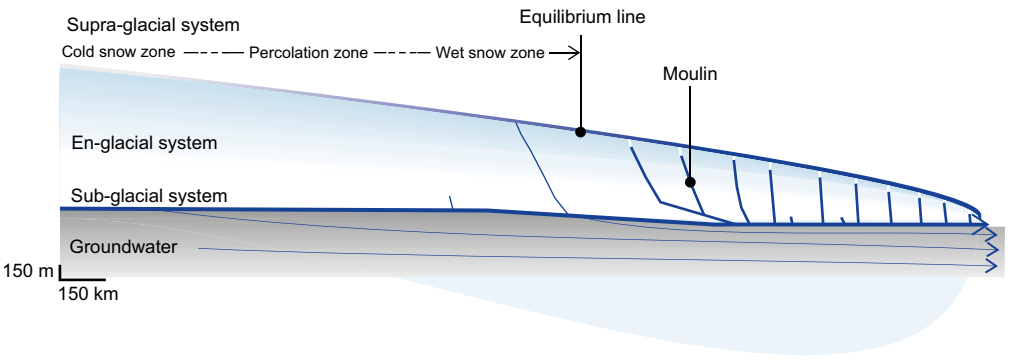

Figure 4-39. *Conceptual model of the ice-sheet hydrological system through an arbitrary south–western section through a Fennoscandian ice-sheet.*

In this context it is worth noting that even in cases when continuous permafrost is present in the landscape, it is unlikely that the permafrost layer has zero permeability for groundwater flow. Zero permeability would probably require a uniform and very deep permafrost distribution. In many cases, the permeability of the frozen ground could instead be large enough to allow for some groundwater flow through the permafrost. In addition, the increased groundwater flow associated with an advancing ice-sheet margin over permafrost terrain is likely to enhance the creation of taliks.

During the first period of glacial climate domain, the ice-sheet overrides ground with permafrost (Figure 4-34). In line with the situation with ordinary permafrost, subglacial permafrost under the ice-sheet margin acts as a hydrological barrier for groundwater flow (King-Clayton et al. 1997). Therefore, this phase is characterised by a period with no groundwater recharge under the frontal near part of the ice-sheet. Groundwater recharge may still take place further in under the ice-sheet, where permafrost may have melted. Even though the ice-sheet is cold-based in its frontal-near parts at this time, water from surface melting may still reach the glacier bed or forefield. However, since permafrost is present, this water does not contribute significantly to groundwater recharge.

Even if the 2D permafrost modelling (Section 3.4.4) did not indicate any taliks at the time of ice-sheet overriding (at 50 ka AP in the *reference glacial cycle climate case*) it is probably not correct to assume an effective large-scale permeability of zero for the pro-glacial landscape at this time. The permeability of the frozen ground can in places be large enough to allow some groundwater flow through the permafrost, and furthermore, the increased groundwater flow due to the large pressure gradient associated with an advancing ice-sheet (Vidstrand et al. 2010) could enhance a creation of taliks.

After the initial cold-based period, subglacial groundwater recharge again takes place at the Forsmark site, this time under the ice-sheet due to melting of basal ice (Figure 4-35). In local areas of former groundwater discharge, groundwater recharge typically occurs under glacial conditions (e.g. Breemer et al. 2002). This results in a dominant subglacial groundwater flow directed downwards under the major part of the warm-based ice-sheet, recharging the groundwater aquifer. Subglacial groundwater discharge may possibly occur close to the ice margin (Breemer et al. 2002, Vidstrand et al. 2010). Even if the permeability of the bedrock were to decrease under the load of an ice-sheet, the increased physical and hydraulic gradient, especially associated with passages of the ice-sheet margin, would likely increase groundwater flow in bedrock compared to temperate climate domain conditions (Hökmark et al. 2010, Vidstrand et al. 2010).

As known from present glaciers and ice-sheets (e.g. Jansson and Näslund 2009, Jansson et al. 2007), as well as from the esker and geomorphological record in e.g. Sweden, subglacial ice tunnels may be present at the ice-sheet bed. The reason why an ice tunnel may form, and is kept open, is the presence of a high enough basal water pressure and water flux. From observations from glaciers, it is known that atmospheric pressure may exist in parts of the tunnels during parts of the year, typically at the end of the melting season when the input of surface melt water is reduced or stopped, and the ice deformation has not yet reduced the size of the tunnel. However, the tunnel width and length are reduced during the winter season due to ice deformation and since no meltwater from the surface system is entering the glacial en- and subglacial hydrological system.

Fundamentally, the increasing ice thickness and horizontal extent of ice-sheets, compared with small mountain glaciers, should impact timescales and driving processes associated with drainage system processes. For instance, thick ice in the ice-sheet setting reduces the timescale for creep closure of a subglacial tunnel to ~ hours, essentially limiting conditions permitting atmospheric pressures beneath ice-sheets to areas close to the ice-sheet margin. However, observations from ice-sheets to support understanding of these processes are extremely rare. The Greenland Analogue Project (GAP), conducted in western Greenland and financed by SKB, Posiva and NWMO, and the follow-up project ICE funded by SKB, Posiva, NWMO and Nagra have provided valuable knowledge regarding glacial hydrology, hydrogeology, and hydrochemistry for an ice-sheet environment (Claesson Liljedahl et al. 2016, Harper et al. 2019). Specifically, measurements made in a network of 32 boreholes drilled to the ice-sheet bed as part of these projects have identified key characteristics of Greenland's subglacial drainage system. These measurements have revealed that basal water pressures vary over diurnal and seasonal scales as a basal drainage system response to varying surface melt. Despite this variability, the basal drainage system has been found to maintain high pressure during both winter and melt seasons; measured pressures in all but one borehole at sites ranging from < 1 km to 46 km from the ice margin ranged from 0.8 to 1.1 as a fraction of local overburden pressure from the ice-sheet (Figure 3-24).

The one exception was ~1 km from the margin. The measured pressure gradients support a view of a basal drainage system in which basal melt conduits grow in response to seasonal surface melt routed to the ice-sheet bed. The extent of conduit growth is limited to the ablation zone within 20–25 km of the margin (Figure 3-25) due to energy constraints and ice closure rates. Further inland, the basal and surface-derived melt is likely transported towards the margin by a conductive linked cavity system. The hydraulic measurements and analyses from the GAP study (Claesson Liljedahl et al. 2016) suggest that ice overburden hydraulic pressure (i.e. a hydraulic head corresponding to 92 % of ice thickness) provides an appropriate description of the basal hydraulic pressure as an average value over the year for an ice-sheet in a similar state as the present-day Greenland ice-sheet (Section 3.2.3).

For more results regarding the glacial hydrology from the GAP and ICE studies, see Section 3.2. The possibility of hydrostatic pressures exceeding the local ice overburden pressure, based on the results from GAP and ICE, is evaluated for the *maximum ice-sheet thickness climate case* in Section 5.4.7.

After the first period of glacial climate domain, the Forsmark site is submerged for up to 9 ka (Figure 4-35). When the site subsequently is situated above sea-level during this interstadial at around 80–90 ka AP (Figure 4-35), climate is generally cold, which induces new long periods of deep permafrost, and associated reduced conductivity in the upper part of the bedrock. During the short temperate conditions during this interstadial, groundwater flow may again be characterized by local areas of recharge and discharge.

During the second and most severe glacial phase, starting around 90 ka AP, the ice-sheet is cold-based for a considerably shorter initial time than during the first major glacial phase (Figure 4-35). This makes water from surface and basal melting available for groundwater recharge during most of this period of ice-sheet coverage. As in the case of the first ice-covered period, steeper physical and hydraulic gradients, especially associated with the passage of the ice-sheet front, may, for a limited period, induce more rapid and substantial groundwater flow than under present ice-free conditions, see Vidstrand et al. (2010).

Thereafter, at the very end of the *reference glacial cycle climate case*, an evolution corresponding to the Holocene occurs, with Forsmark first being submerged after deglaciation for around 10 ka. When the site emerges above sea-level, the climate is much warmer than during the non-submerged period between the two major glacial advances. The Forsmark site is again dominated by temperate climate conditions, with groundwater flow similar to that in present-day conditions. For a description of the geochemical evolution in this scenario, see the **Post-closure safety report**.

4.5.6 Evolution of mechanical conditions

During the *reference glacial cycle climate case* (Figure 4-24 and Figure 4-25) the temporal evolution of the ice-sheet will cause time-varying stresses and deformations in the Earth (Lund et al. 2009). Due to the long timespans both elastic and viscous deformation occurs. Properties of the ice-sheet controlling the deformation and stress change are duration, areal extent, thickness and slope of the ice margin. The evolution of stresses in the crust during a glacial cycle has been studied by Lund et al. (2009), who used numerical finite-element modelling of the glacially induced stresses based on the ice-sheet development in the *reference glacial cycle climate case*. As the ice-sheet advances and the load from the ice increases, the vertical and horizontal stresses will both increase in direct and immediate response to the increasing load. The elastic lithosphere will bend, and the viscoelastic mantle will flow laterally. This will, on a large scale, result in a depression beneath the load, where crustal flexure will give an additional slow increase in horizontal stresses in the upper crust. Outside the ice-sheet margin, crustal flexure will result in an up-warping peripheral bulge (see also Section 3.3.4), in which the horizontal stresses are reduced. The thicker the ice-sheet and the longer duration an area is covered by ice, the larger the induced bending stresses will become. When the growth rate of the ice-sheet decreases, the induced horizontal stresses under the load become larger than the vertical stress and remain so during times of steady-state ice conditions and all through the deglaciation phase. As the ice-sheet retreats during deglaciation, the depressed lithosphere will experience isostatic rebound, which is a much slower process than the ice-load removal process. Consequently, high horizontal stresses remain in the lithosphere for a significant amount of time after the ice-sheet-induced vertical stress has disappeared.

The pore pressures in the crust are increased during glaciation because of the consolidation of the bedrock, the recharge of meltwater available at the base of the ice-sheet and the additional hydrostatic pressure induced by the ice-sheet itself. Furthermore, increased pore pressure-levels may also potentially develop beneath an impermeable permafrost layer in front of an approaching ice-sheet (cf. Lönnqvist and Hökmark 2010). Estimates of the magnitude of the glacially induced pore pressure at different depths and during different phases of a glacial cycle have been made by Hökmark et al. (2010).

The discussion on glacially induced stresses and pore pressures implies that the effective rock stress (i.e. the normal stress reduced by the water pressure) varies both with changes in the mechanical load and changes in the pore pressure produced by the ice-sheet. The evolution and magnitude of the effective stress during the different parts of the glacial cycle will dictate the mechanical behaviour of rock fractures, and hence, also their water-conducting ability, see Hökmark et al. (2010). In general, the increase in total stress during ice-sheet advance will act to reduce the transmissivity of fractures and fracture zones. But since the vertical stress increases more rapidly than the horizontal stresses, upper crustal stress axes may rotate so that the vertical stress is the intermediate or largest principal stress. These stress changes, together with the increase in pore pressure as compared with non-glacial hydrostatic conditions, may result in changed transmissivity anisotropy.

Outside the edge of the ice-sheet, the reduction in horizontal stresses may give rise to a decreased normal stress acting across steeply dipping fractures, leading to an increase in transmissivity. In the absence of reduced temperatures or increased pore pressure levels due to proglacial permafrost, calculations by Hökmark et al. (2010) indicate that the increase will be modest. Hökmark et al. (2010) also considered two cases associated with the scenario of proglacial permafrost coinciding with the forebulge stress regime. Firstly, they consider the possibility of increased pore pressure-levels beneath the permafrost layer. Secondly, a further reduction of the horizontal stresses due to reduced temperatures (Hartikainen et al. 2010) was considered in combination with high pore pressures. (Hökmark et al. 2010) found that, for the former case, the transmissivity will increase by a factor 2–3 at most. For the latter case, significant transmissivity increases of some vertical fracture orientations (factor around 7) were found at shallow depths. For repository depth, more moderate increases by a factor 2–3 were found for identically oriented fractures.

Increased deviatoric stresses may also give rise to shearing of critically oriented fractures, which in turn can yield larger fracture apertures and increased transmissivities. The same effect may also result from elevated pore pressures that will act to reduce the shear strength. However, Hökmark et al. (2010) argued that transmissivity increases resulting from shear displacements taking place at high normal stress (> 6–7 MPa) are negligible. As described by Lönnqvist and Hökmark (2010), hydraulic jacking of fractures is also possible, but most likely not deeper than at most 200 metres.

In general, the emplacement of a large ice-sheet stabilises faults in the crust and suppresses earthquake activity. During deglaciation, however, the rapid decrease in vertical stress tends to destabilise the crust. Crustal pore pressures are of great significance in the faulting process, since an increased pore pressure decreases the effective normal stress on faults, and hence, reduces their shear strength. If the pore pressure is still enhanced at the end of glaciation, when the vertical load from the ice disappears, fault stability will be further reduced. Observations of large glacially induced faults in northern Fennoscandia show that such a process was indeed active at the end of the last glaciation.

4.5.7 Surface denudation

For the *reference glacial cycle climate case*, the average total amount of bedrock denudation for the Forsmark site, i.e. the combined bedrock lowering by surface erosion and weathering, is 1.7–3.6 m over the coming 120 ka. This range is based on the 1.6–3.5 metre most likely estimate (25 % and 75 % percentiles) of total denudation over the past 100 ka from the cosmogenic nuclide analysis in Hall et al. (2019a) (Section 3.5.4 Table 3-15). The *reference glacial cycle climate case* is 120 ka long, i.e. 20 ka longer than the 100 ka Weichselian period simulated by Hall et al. (2019a). Adding another 20 ka of non-glacial denudation (at a maximum rate of 5 mm ka^{-1}, see Section 3.5.4 and Hall et al. 2019a) in order to cover the full 120 ka of the *reference glacial cycle climate case*, yields a denudation of up to 0.1 metres for this 20 ka period, and hence a range of 1.7–3.6 metres (adding the 0.1 m to the 1.6–3.5 range) for the full 120 ka of this climate case.

The definition of the Weichselian glacial periods in Hall et al. (2019a) are similar to the ones derived in the reconstruction of the last glacial cycle in Section 4.4.1, and hence also similar to the glacial periods in the *Reference glacial cycle climate case* (Figure 4-35), but the glacial periods of Hall et al. (2019a) and the *Reference glacial cycle climate case* differ somewhat in their details. However, if using values on glacial erosion rates and non-glacial denudation rates from Hall et al. (2019a) (see a corresponding calculation and motivation of values in the *global warming climate case,* Section 5.1.6), and apply them to the durations of climate domains in Table 4-5 (taking into account the length of cold- and warm-based glacial conditions (cf. Figure 4-35) and assigning non-erosive conditions for submerged periods), the calculated denudation for the 120 ka period would be ~2.5 m. This is fully in line with the 1.7–3.6 metres of denudation derived from Hall et al. (2019a) based on the Weichselian glacial periods as defined therein. Therefore, the 1.7–3.6 metres range on denudation is judged appropriate to use for the *Reference glacial cycle climate case*.

The 1.7–3.6 m denudation range at Forsmark for the coming 120 ka in the *reference glacial cycle climate case* is in line with the independent results from the geomorphological analysis in Hall et al. (2019a), suggesting ~2 m of glacial erosion per future glacial cycle, with values exceeding 3 m in basins and trenches (Table 3-16). In this context, it is worth emphasising that the 1.7–3.6 m of bedrock lowering for the *reference glacial cycle climate case* is based on last glacial cycle conditions. The actual total denudation of bedrock at Forsmark over the first future 100 ka is expected to be even smaller, see Sections 5.1.6 and 5.2.6.

Over the coming 1 Ma, the estimated average total bedrock denudation at the Forsmark site is 5–28 m (25 % and 75 % percentiles), whereas the full range (5 % and 95 % percentiles) is 2–43 m, based on the cosmogenic nuclide analysis by Hall et al. (2019a) (Section 3.5.4, Table 3-15, and Appendix G).

The major part of the bedrock denudation in the *reference glacial cycle climate case* is a result of glacial erosion, occurring during phases of warm-based ice-sheet coverage. These warm-based periods of glacial erosion occur after ~60 ka, and between ~90 and ~110 ka into the *reference glacial cycle climate case* (Figure 4-35).

The relatively low amount of denudation, and hence also glacial erosion, at the Forsmark site in the *reference glacial cycle climate case* is mainly a result of the low relief of the bedrock surface in the area, and that the erosional capacity of the ice-sheet is relatively small compared with considerably more efficient erosion by more active parts of ice-sheets or smaller glaciers in other climatological and topographic settings, see Section 3.5.4.

The non-glacial component of surface denudation, resulting from all other active erosion and weathering processes, such as weathering and fluvial erosion during temperate- and periglacial climate conditions, is expected to be considerably smaller than the amount of glacial erosion. In the cosmogenic nuclide analysis of total denudation over last glacial cycle and for the future projections of denudation, the minimum and maximum non-glacial denudation rates were set to 0 and 5 mm ka^{-1} for the ice free periods (Hall et al. 2019a, see also Appendix G). The maximum value includes e.g. higher physical weathering rates for ice-free colder (periglacial) periods and higher chemical weathering rates for warm climate periods.

The dissected area with in places considerable relief in the coastal area ~25 km south–east of Forsmark may experience more efficient glacial erosion during future glaciations with similar erosional characteristics to those that occurred during the Weichselian (Section 3.5.4). In this area, glacial erosion of more than 10 m per glacial cycle may occur locally in low topographic positions. However, this is not the case for the Forsmark site and the repository location (see above and Section 3.5.4).

The removal of bedrock by surface denudation results in a reduction of the repository depth. A reduced repository depth could, in turn, lead to permafrost and frozen ground reaching closer to the repository. However, a total denudation of a few metres for the *reference glacial cycle climate case* has a negligible effect, in terms of repository safety, on the estimated permafrost- and freezing depths presented in Section 4.5.3 and 5.5.3. In this context, also the estimated total bedrock denudation of less than 50 m for the Forsmark site over the coming 1 Ma (see above and under the heading *Quantification of future erosion at Forsmark* in Section 3.5.4) is insignificant in terms of repository safety. In section 5.5.4, the consequences on freezing depths are investigated for a hypothetical case with a total denudation of 20 m per glacial cycle.

A climate case with an estimated larger amount of surface denudation than in the *reference glacial cycle climate case* is described in the *extended ice-sheet duration climate case* (Section 5.3).

5 Additional climate cases for the PSAR

In order to cover the uncertainty in future climate development, the *reference glacial cycle climate case* (Section 4.5) has been used to construct additional climate cases with a potentially larger impact on repository safety than the reference cycle, see Figure 1-3. Consequently, they form the basis for the global warming variant of the main PSAR safety assessment scenario, and also for other additional safety assessment scenarios, see Figure 1-3 and the **Post-closure safety report**. The climate-related issues having the greatest impact on repository safety functions are:

- Maximum permafrost and ground freezing depth;
- Maximum hydrostatic pressure;
- Penetration of oxygen to deep groundwater;
- Occurrence of dilute or extremely saline groundwater;
- Reduction of retardation in the geosphere due to high groundwater fluxes and/or mechanical influences on permeability.

These issues are mainly related to extremes within the temperate-, periglacial-, and glacial climate domains. For a description of the strategy for using and selecting the additional climate cases, see the section on *Strategy for managing long-term evolution of climate-related processes* (Section 1.2.3), and the section on *Rationale and general approach* (Section 4.1). In the PSAR, the climate cases presented in Table 4-1 are considered.

Chapter 5 describes climate cases 2–6 in Table 4-1 and Figure 1-3. In addition to the description of the parameters that the climate cases were designed to address, for instance the maximum thickness of ice-sheets, a description of expected surface denudation is also described for each case. The removal of bedrock by surface denudation affects the repository depth, which in turn may affect e.g. the possibility for permafrost- and frozen ground to reach the repository. Climate cases with an expected larger total denudation than in the *reference glacial cycle climate case* are therefore considered more important, and are thus described in more detail, compared with cases with an expected denudation smaller than in the *reference glacial cycle climate case*, which are described only briefly.

5.1 Global warming climate case

5.1.1 Background

In addition to naturally occurring processes, the climate is also influenced by human activities, most importantly by anthropogenic emissions of CO_2 and other greenhouse gases. As a result of these emissions, the global-mean surface air temperature has currently increased by approximately 1 °C since the pre-industrial era (e.g. IPCC 2018). This warming will continue also in the future until net emissions are cut to zero (e.g. IPCC 2013, 2018). The total warming will be roughly proportional to the cumulative emissions up until that time of net-zero emissions. Thus, regarding anthropogenic climate change, there is a large range of potential future warming to consider. One such case is described in the present *global warming climate case*. This case describes a future climate development influenced by both natural climate variability and climate change induced by anthropogenic emissions of greenhouse gases, with the latter resulting in weak to moderate global warming. In order to cover a broad array of future climate developments based on present knowledge, an *extended global warming climate case* is also included in the PSAR (Section 5.2), describing a situation with stronger and longer-lasting global warming.

The purpose of the *global warming climate case* and the *extended global warming climate case* is to give a picture of the possible impact of global warming on the repository and its environment, and to cover extremes of warm conditions with respect to repository safety. In general, temperate climate conditions are not negative for the repository safety, as the conceivable conditions occurring within the temperate domain have limited impact on repository safety functions. However, if for some reason, a release from the repository does occur, previous safety analyses have shown that peak doses occur

during periods when the area above the repository is situated above sea-level, and areas of discharge are located within that area. In addition, prolonged periods of temperate climate conditions above sea-level may result in lower groundwater salinity. The effect of this also needs to be assessed in terms of e.g. buffer stability (see the **Post-closure safety report**).

There is a large amount of published information on various aspects of global warming in recent literature. The intention with this section and the section on the *extended global warming climate case* is not to give a comprehensive description of the present status of knowledge on the global warming issue (causes, effects, uncertainties etc.). Instead, the aim is to include information and data that support the treatment of this complex topic at a level required for the safety assessment. To this end, both general scientific literature and SKB-funded studies are used. For additional information on the topic of global warming, the reader is referred to IPCC (2013a, 2018) and references therein.

Studies have shown that anthropogenic greenhouse-gas emissions, as well as future variations in insolation, have a large impact on the timing of the next glacial inception (see Lord et al. 2019 and Liakka et al. 2021). In the PSAR, there are two main reasons for analysing cases of climates warmer than in the *reference glacial cycle climate case*; i) modelling studies of the climate response to increased greenhouse gas emissions, mainly CO_2, indicate that global temperatures will increase in the future under such conditions (IPCC 2013a) and ii) natural long-term climate cycles are driven mainly by changes in solar insolation. The coming 100 ka period is initially characterised by exceptionally small amplitudes of insolation variations (Berger 1978, Laskar et al. 2004, 2011), suggesting that the present interglacial may be exceptionally long. Considering the known future changes in insolation, many studies suggest that the interglacial may end ~50 ka AP, particularly if future atmospheric CO_2 peaks at a relatively low levels (Figure 5-1). One study (Pimenoff et al. 2011) even suggest that the next glacial inception would occur at present under natural, pre-industrial, CO_2 concentrations (~280 ppmv). This hypothesis has been supported by some previous studies (e.g. Müller and Pross 2007, Ruddiman 2003), but also been rejected by others (e.g. Berger and Loutre 2002, Ganopolski et al. 2016, see Figure 5-1). For high future atmospheric CO_2 concentrations, most studies suggest that the next glacial inception will occur well beyond 100 ka AP (Figure 5-1). For further details on the timing of the next glacial inception, see Liakka et al. (2021).

In addition to handling future variations in insolation, the *global warming climate case* includes the effect of moderate global warming from an anthropogenic increase of atmospheric CO_2 levels, comparable to the Representative Concentration Pathway 4.5 (RCP4.5) scenario (for more information on the RCPs; see Appendix E, Meinshausen et al. 2011 and IPCC 2013a). This scenario assumes that the atmospheric CO_2 level stabilizes at c 540 ppmv around 2100 AD (Appendix E, Meinshausen 2011). The resulting global annual-mean surface air temperature is projected to increase by 1.1–2.6 °C (relative to present) by the end of 21st century (Appendix E) and to reach its maximum increase of 1.7–6.5 °C within the first hundred to thousands years after present (Figure 5-2).

At Forsmark, the surface air temperature increase is projected to be 1.2 to 1.5 times higher than the global average (Appendix F), culminating in a maximum average temperature increase of 5 °C above present within the next century to millennia (Figure 5-3 and Table 5-1; see also Appendix F). Subsequent to the peak increase, there is a slow decline of the surface air temperature anomaly (Figure 5-3) resulting from a slow exponential-like reduction of the atmospheric CO_2 concentration (e.g. Archer et al. 2009, Eby et al. 2009, Lord et al. 2016). In summary, the estimated surface air temperature by 12000 AD is comparable to the temperature by 2100 AD (Table 5-1), illuminating the slow decline of the surface air temperature over the coming millennia.

Precipitation at Forsmark is assumed to scale linearly with temperature changes (e.g. Appendix F, Pimenoff et al. 2012) resulting in peak average precipitation increase by nearly 20 % as a result of the 5 °C peak temperature increase (Figure 5-3). This corresponds to nearly 700 mm annual precipitation at Forsmark (Table 5-1).

The slow decline of the surface air temperature beyond its peak (Figure 5-3) suggests that the onset of colder climate conditions, after the initial temperate period, also would be a gradual and slow process. Therefore, it is appropriate to use the mild onset of colder climate conditions reconstructed for the last glacial cycle (Section 4.5.4) for the climate development following the initial temperate period. To describe the combined effect of known variations in insolation and global warming, the *global warming climate case* assumes that the present temperate climate domain, albeit with higher initial air

temperatures, will prevail for 50000 years longer than in the *reference glacial cycle climate case*. In the *global warming climate case*, it is hence assumed that the onset of the next glacial inception will occur earlier than suggested by most modelling studies under a moderate global warming (Figure 5-1). The choice of a shorter initial period of temperate conditions is however considered to be pessimistic, as it allows for an earlier occurrence of colder conditions and ice-sheet development at the Forsmark site compared to alternative developments with longer initial periods of temperate conditions, see the **Post-closure safety report**. Following the first 50 ka of additional temperate climate conditions in the *Global warming climate case*, the first 70 ka of the *reference glacial cycle climate case* is assumed to follow. This results in c 60 ka of temperate climate conditions at Forsmark before the ending of the present interglacial (the ending locally defined as the time of first occurrence of periglacial conditions with permafrost, see Section 4.5.4). This development is in broad agreement with results simulated for two global warming cases within the BIOCLIM project (BIOCLIM 2003).

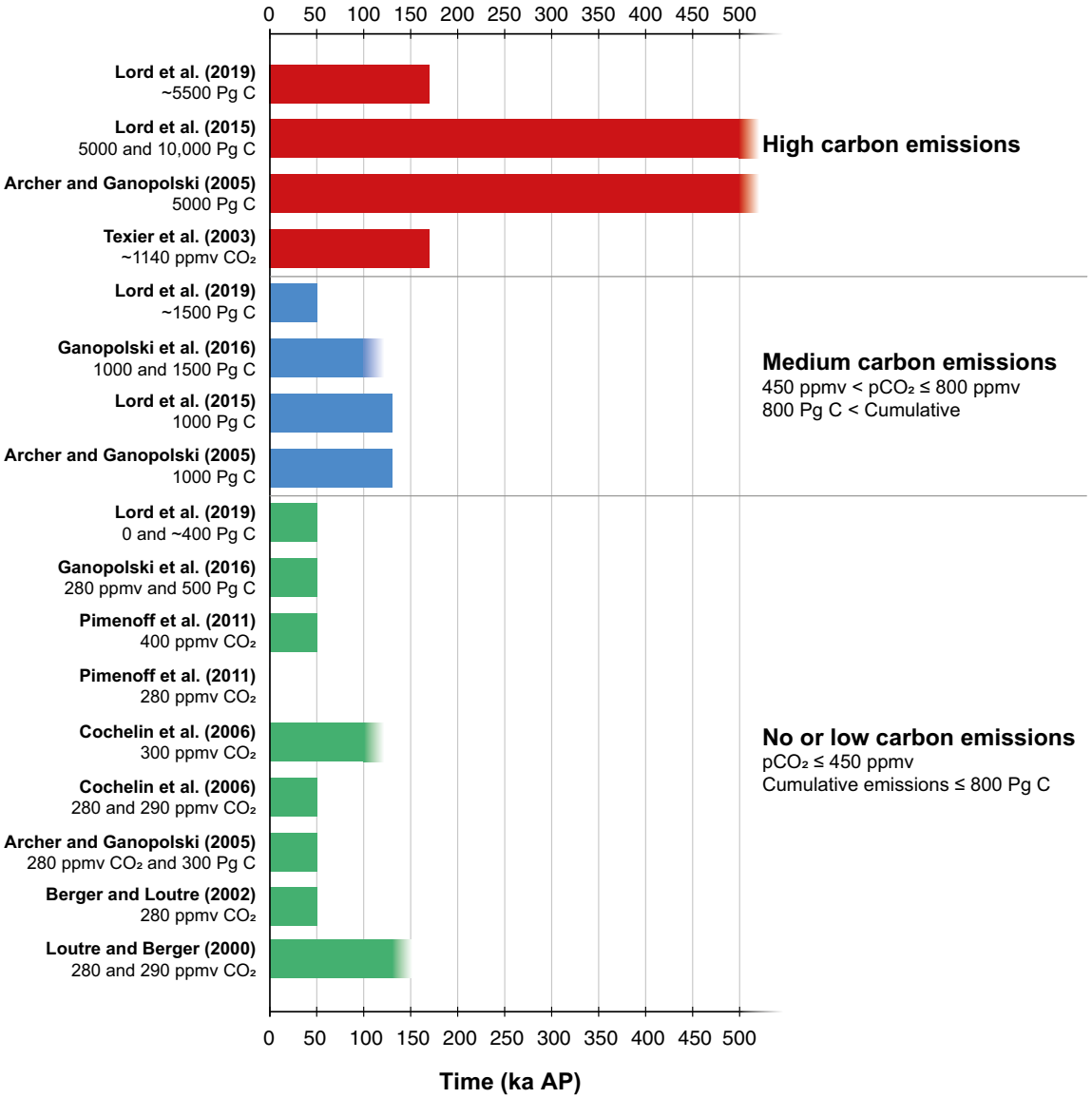

Figure 5-1. *Approximate timing of next glacial inception from different modelling studies. The bars ending with a colour-to-white gradient represent simulations that were not integrated sufficiently far into the future to project the next glacial inception. The study of Pimenoff et al. (2011) projects that glacial inception would be immediate for pre-industrial atmospheric CO_2 concentrations (280 ppmv). Minimum thresholds for medium and high carbon emissions are set to 800 and 2000 petagrams of carbon (Pg C; 1 Pg = 1015 g), respectively. These values correspond approximately to a maximum atmospheric CO_2 concentrations of 450 and 800 ppmv. Modified from Liakka et al. (2021).*

5.1.2 Ice-sheet evolution

In this case of moderate global warming, colder climates again arise in the latter half of the coming 120 ka. The climate cooling associated with a slow reduction in atmospheric greenhouse gas concentrations results in a Fennoscandian ice-sheet forming in the same way as in the *reference glacial cycle climate case*, but in this case 50000 years later. In the *reference glacial cycle climate case*, two main phases of ice-sheet coverage took place at Forsmark. In the *global warming climate case*, only the first of these two phases occurs, at around 110 ka AP. This timing of glacial inception at ~100 ka AP is in line with several recent modelling studies under medium greenhouse-gas emissions, see Figure 5-1, and is attributed to lowered atmospheric CO_2 concentrations together with a relatively low insolation at the Northern Hemisphere high latitudes. The characteristics of this glacial period are identical to the first major glacial period of the *reference glacial cycle climate case*. The maximum ice-sheet thickness during this event is just above 1600 m. The glacial climate domain persists for around 10 ka, of which the first half consists of cold-based ice-sheet conditions, without local formation of groundwater, whereas the second half consists of warm-based ice-sheet conditions with active sub-glacial groundwater formation at Forsmark. Prior to the ice-sheet overriding, periglacial conditions with permafrost exist at the site.

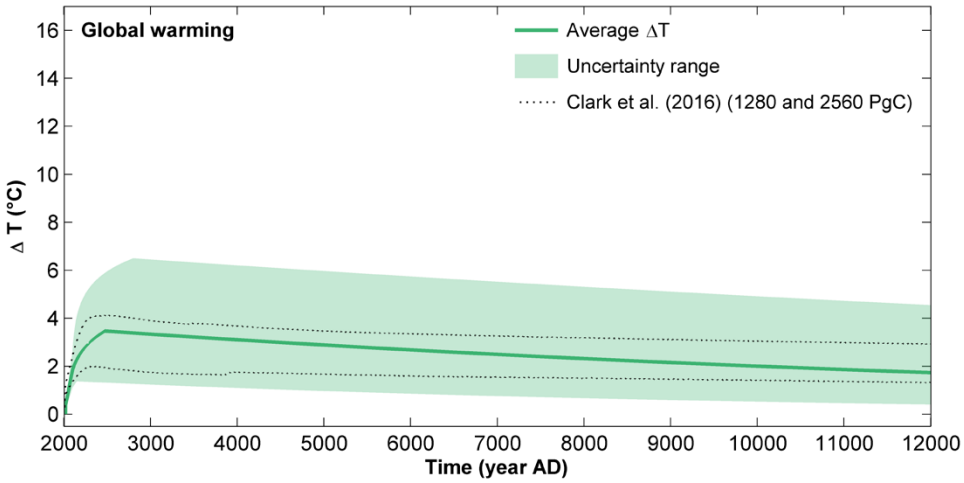

Figure 5-2. *Constructed global annual mean surface air temperature change until 12000 AD (relative to present) for the global warming climate case. The shading represents the uncertainty range, and the solid line is calculated from the average values of the parameters used to construct the uncertainty range. To that end, the solid line illustrates a typical mid-range global mean temperature change over the next 10 ka. The figure also shows the evolution of global annual mean surface air temperature change from the Clark et al. (2016) projections with 1280 and 2560 petagrams of carbon (Pg C) cumulative emissions (comparable to RCP4.5). Typical uncertainties in the Clark et al. (2016) projections are within the range of 1–2 °C (Table F-1 in Appendix F). Details on how the global mean temperature curve and its uncertainty range have been constructed are provided in Appendix F.*

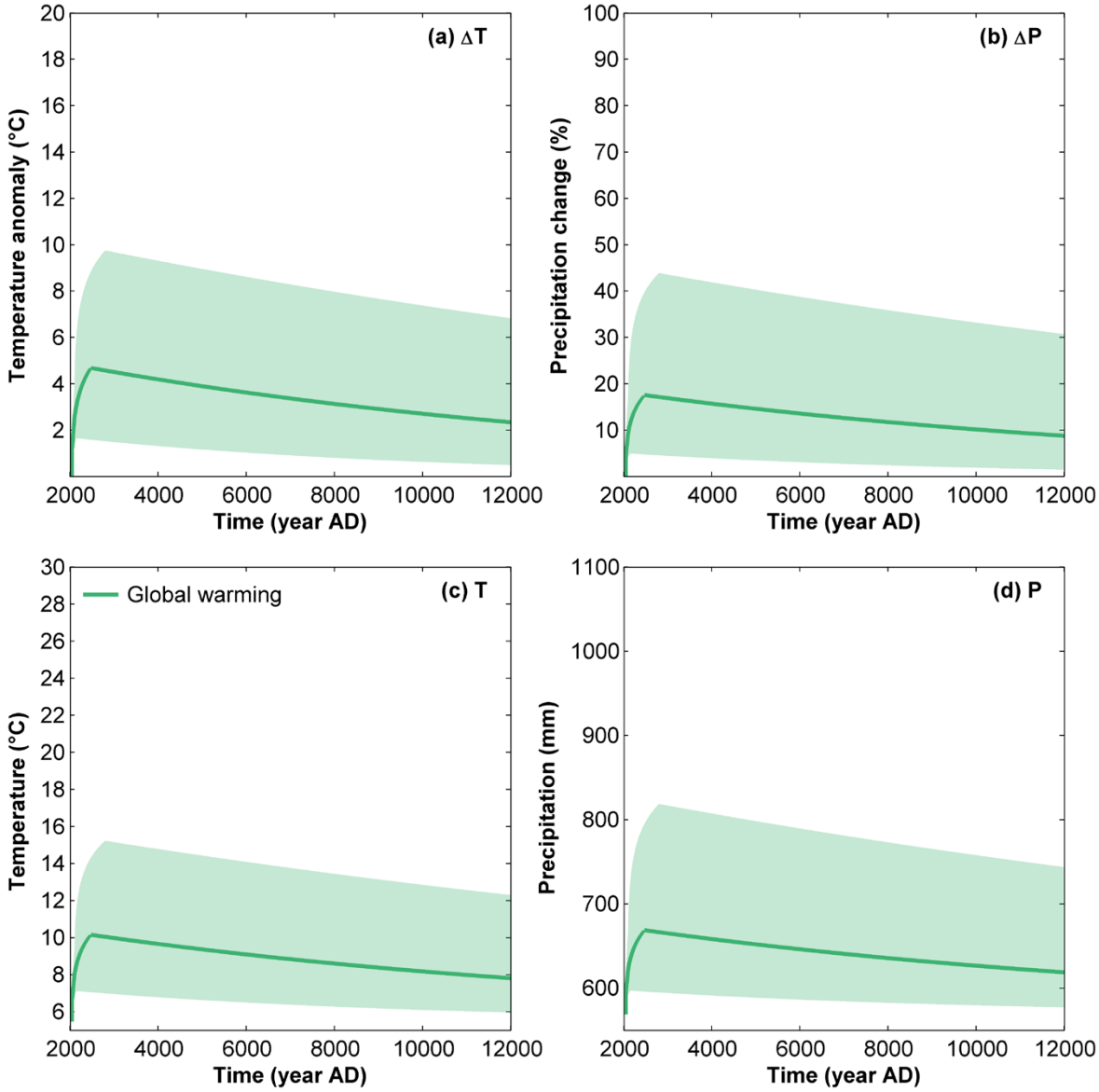

Figure 5-3. *Constructed changes in (a) annual mean surface air temperature and (b) annual precipitation at Forsmark until 12000 AD for the global warming climate case. Panels (c) and (d) show the resulting annual mean surface air temperature and annual precipitation at Forsmark calculated from the temperature and precipitation changes in panels (a) and (b) and the present-day climate in Table 2-1. The shaded areas represent uncertainty ranges, and the solid lines are calculated using average values of the parameters used to construct the uncertainty range. To that end, the solid lines illustrate typical mid-range temperature and precipitation changes at Forsmark over the next 10 ka. Details on how the temperature and precipitation curves have been constructed are provided in Appendix F. Note that the possible influence of a future AMOC collapse (e.g. Liu et al. 2017) on the surface air temperature at Forsmark has not been included in the uncertainty range in this figure due to the low confidence of this uncertainty assessment. This uncertainty is instead shown and discussed in detail in Appendix F.*

Table 5-1. Summary of Forsmark surface air temperature and precipitation until 12000 AD in the *global warming climate case*. The lower and upper bounds refer to the uncertainty range and the average estimate to the solid lines in Figure 5-3. Details on how the uncertainty range has been constructed are provided in Appendix F.

	Surface air temperature (°C)			Precipitation (mm)		
Time slice	Lower bound	Average estimate	Upper bound	Lower bound	Average estimate	Upper bound
2100 AD	6.8	8.0	9.4	590	630	680
Maximum value (2150–2800 AD)	7.5	10.5	15.2	600	680	850
12000 AD	6.1	8.0	12.3	580	620	760

5.1.3 Changes in sea-level and relative sea-level

At present, there are major uncertainties in the estimates of future sea-level rise due to global warming. The largest uncertainty relates to the response of the Greenland and Antarctic ice-sheets to increased temperatures (see below and Section 5.2.3). The West Antarctic and Greenland ice-sheets are expected to be particularly sensitive to a warming climate, whereas the East Antarctic ice-sheet is generally expected to be more stable (e.g. IPCC 2019, and references therein).

Due to the coastal location of the Forsmark site, one important question related to global warming is sea-level rise (eustasy) caused by melting ice-sheets and glaciers, and by thermal expansion of ocean water. Specifically, it is the change in *relative sea-level* at the Forsmark site that is of interest, i.e. the net result of sea-level changes and the ongoing post-glacial uplift of the Earth's crust (isostatic rebound).

In the following sections, the sea-level and relative sea-level at Forsmark is described for the *global warming climate case*, i.e. an intermediate carbon emission scenario (approximately RCP4.5). In Section 5.2.3, the same information is presented for the *extended global warming climate case*, corresponding to a high carbon emission scenario (approximately RCP8.5). Given that the climate in the latter scenario provides higher sea-levels and larger rises in relative sea-level, the description in that section is made at a greater level of detail than the corresponding descriptions for the global warming climate case.

Present-day relative sea-level change at Forsmark

The present-day relative sea-level change at Forsmark can be estimated from tide gauge data from the site, covering the period 1976–2017 AD (Holgate et al. 2013, PSMSL 2018). These data show an overall negative trend over the time period (Figure D-4 in Appendix D), resulting in an average rate of change in the relative sea-level by −4.1 mm a^{-1} (Table 5-2). This is a result of the active post-glacial isostatic uplift in the area that exceeds the ongoing anthropogenically induced sea-level rise. This is, however, a situation that may change in the near-future, see the next section.

It also is possible to estimate the present-day eustatic component (sea-level change) in Forsmark by taking the difference between the tide gauge data, which represents the total relative sea-level change, and the isostatic component which amounts to −6.7 mm a^{-1} (Vestøl et al. 2019, see Section 3.3.3). This calculation results in a present-day eustasy at Forsmark of 2.6 mm a^{-1} (Table 5-2), which is comparable to the estimated global-mean sea-level rise of 3.1 ±0.3 mm a^{-1} between 1993 and 2017 AD (Table 5-2). The slightly lower value at Forsmark with respect to the global average is possibly explained by the longer time-period in the tide gauge record, hence covering older data, with a lower eustatic component, than in the global-mean estimate. However, also rotational effects and changes in the gravity field associated with the melting of ice-sheets and water entering the ocean basins may contribute to explaining the difference in eustasy between Forsmark and the global average.

Table 5-2. Present-day rates of isostasy, eustasy and relative sea-level at Forsmark, and the estimated present-day global-mean sea-level rise from WCRP Global Sea Level Budget Group (2018). The relative sea-level is defined as the sum of the isostatic and eustatic contributions. For the Forsmark site, the relative sea-level change is obtained from tide gauge data (Holgate et al. 2013, PSMSL 2018) covering the period 1976–2017 AD (Appendix D), whereas the isostasy is estimated based on e.g. stationary GPS measurements (Vestøl et al. 2019). The eustatic contribution for Forsmark is indirectly estimated by calculating the difference between the relative sea-level measurements from tide gauges and the present-day isostatic uplift. Positive values are defined as a rise of sea relative to the land.

	Forsmark	Global average
Isostasy (vertical crustal movement)	−6.7 mm a^{-1}	-
Eustasy (sea-level change)	2.6 mm a^{-1}	3.1 ± 0.3 mm a^{-1}
Relative sea-level (or shore-line displacement)	−4.1 mm a^{-1}	-

Relative sea-level rise at Forsmark until 2100 AD

In the latest assessment report from IPCC (AR5), the maximum expected global mean sea-level (GMSL) rise at 2100 AD for a high-emission scenario was estimated to +0.98 m IPCC (2013a). The corresponding value in the previous IPCC assessment was +0.59 m (IPCC 2007). The maximum 2100 AD sea-level estimates for the different RCP emission scenarios in AR5 was, however, based on a narrow selection of models. The selection excluded all non-process-based models of which many, at the time, suggested a considerably larger GMSL rise than the processed-based models finally selected by IPCC. Hence, following IPCC (2013a), many studies have pointed to a larger sea-level rise than suggested in AR5.

Table 5-3 presents a selection of recent GMSL projections for 2100 AD under the IPCC RCP4.5 emission scenario (see Church et al. 2013 and Appendix E), published between 2012 and mid-2018, as well as one older study used in previous safety assessments (Pfeffer et al. 2008), the recent IPCC Special Report on the Ocean and Cryosphere in a Changing Climate (SROCC, IPCC 2019) and Forsmark mean relative sea-level projections from under the RCP4.5 emission scenario from Pellikka et al. (2020). As previously mentioned, the RCP4.5 scenario forms the basis for the *global warming climate case*.

Combined, the studies in Table 5-3 suggest that the *likely* range of GMSL rise (as defined by the 17–83 % confidence interval) under RCP4.5 is 0.35 to 1.25 m, whereas the *very likely* range (5–95 % confidence interval) is 0.22 to 1.58 m. Table 5-3 thus clearly demonstrates the large uncertainty associated with the projection of future GMSL rise for 2100 AD under a moderate global warming.

At Forsmark, the mean relative sea-level change by 2100 AD is projected to be significantly lower than the GMSL rise, primarily because the ongoing isostatic uplift in the Forsmark region (6.7 mm a^{-1}, Vestøl et al. 2019) compensates for a significant portion of the eustatic rise. This is also seen in the projections of the mean relative sea-level change at Forsmark in Table 5-3 (i.e. the eustatic rise compensated for the isostatic rebound), obtained from Pellikka et al. (2020). As a result of the isostatic rebound, Pellikka et al. (2020) projects that the relative sea-level at Forsmark under RCP4.5 will most likely decrease until 2100 AD, despite an increase of the GMSL (Table 5-3). However, similar to the GMSL projections, the uncertainty associated with the Forsmark relative sea-level change under RCP4.5 is large, demonstrated by a slight increase of the relative sea-level by 2100 AD for the upper 83 % and 95 % percentiles (Table 5-3).

In addition to the projections for 2100 AD, Pellikka et al. (2020) also reported relative sea-level changes by 2050 and 2080 AD. These results are summarized in Table 5-4. Compared to 2100 AD, the median percentile (50 % probability) of the relative sea-level is projected to be lower by 2050 and 2080 AD, suggesting that the most likely outcome under the RCP4.5 emission scenario is that the ongoing isostatic rebound will be greater than the eustatic rise for the entire period until 2100 AD. For the higher 83 and 95 % percentiles the situation is however reversed, with a higher Forsmark relative sea-level by 2100 AD compared to 2050 and 2080 AD. For these higher, less likely, percentiles, the eustatic rise at Forsmark is thus projected to be larger than the isostatic compensation.

A corresponding compilation of GMSL rise under moderate greenhouse-gas emissions, but for the period beyond 2100 AD and with projections of the resulting relative sea-level at Forsmark, is presented in the next section below. The consequences in terms of relative sea-level rise at Forsmark of the high emission RCP8.5 scenario until 2100 AD, including the short-term sea-level variability due to storm surges, is described in the *extended global warming climate case*, Section 5.2.3.

Table 5-3. Compilation of sea-level projections for 2100 AD under the IPCC RCP4.5 emission scenario and published since 2012. For a description of this emission scenario, see Church et al. (2013) and Appendix E. The table also includes Pfeffer et al. (2008) (not directly based on RCP4.5) since it was used in previous SKB safety assessments as a high end GMSL rise case. All values represent global mean sea-level (GMSL) rise, except for one value for Stockholm at the end of the table. Values are given as the median value and the 17 % and 83 % percentile values (typically called the *likely* range) and the 5 % and 95 % percentile values (typically called the *very likely* range). The uncertainty range for DeConto and Pollard (2016) and Clark et al. (2016) has been recalculated from 1σ standard error to the 5–95 % confidence interval. The unit Pg C refers to "petagrams of carbon".

Global mean sea-level 2100 AD (m) Median values (confidence interval within brackets)	Confidence interval used (comments within brackets)	Reference
(0.79–0.83)	-	Pfeffer et al. (2008)
0.52 (0.74–1.10)	5–95 %	Jevrejeva et al. (2012)
0.90 (0.64–1.21)	5–95 %	Schaeffer et al. (2012)
0.53 (0.36–0.71)	5–95 %	Church et al. (2013) (IPCC AR5)
0.86 (0.66–1.11)	17–83 %	Perrette et al. (2013)
0.59 (0.45–0.77) 0.59 (0.36–0.93)	17–83 % 5–95 %	Kopp et al. (2014)
0.54 (0.35–0.73)	17–83 %	Slangen et al. (2014)
0.54 (0.36–0.72) 0.54 (0.22–0.85)	17–83 % 5–95 %	Jackson and Jevrejeva (2016)
0.51 (0.39–0.69) 0.51 (0.33–0.85)	17–83 % 5–95 %	Kopp et al. (2016)
0.53 (0.37–0.77)	5–95 %	Mengel et al. (2016)
0.26 (−0.07–0.59) 0.55 (0.06–1.04)	5–95 % 1280 Pg C (from ±1σ, ±0.20 m) 5–95 % 2560 Pg C (from ±1σ, ±0.30 m)	Clark et al. (2016)
0.58 (0.12–1.05)	5–95 % (from ±1σ, ±0.28 m)	DeConto and Pollard (2016)
(0.54–0.97)	5–95 %	Bakker et al. (2017)
0.69 (0.55–0.84)	5–95 %	Goodwin et al. (2017)
0.91 (0.66–1.25) 0.91 (0.5–1.58)	17–83 % 5–95 %	Kopp et al. (2017)
0.55 (0.45–0.67)	17–83 %	Nauels et al. (2017)
0.77 (0.56–1.3)	5–95 %	Wong et al. (2017)
0.55 (0.39–0.72)	5–95 %	IPCC (2019) (Special Report on the Ocean and Cryosphere in a Changing Climate)
−0.21 (−0.37–0.05) −0.21 (−0.44–0.41)	17–83 % 5–95 %	Pellikka et al. (2020) **Forsmark**

Table 5-4. Projected Forsmark mean relative sea-level change (m, relative to 2000 AD) by 2050, 2080 and 2100 AD under the RCP4.5 emission scenario for the 50 % percentile (median), and the 17–83 % and 5–95 % confidence intervals. From Pellikka et al. (2020).

Percentile/confidence interval	2050 AD	2080 AD	2100 AD
50 %	−0.14	−0.19	−0.21
17–83 %	−0.19 to −0.07	−0.30 to −0.02	−0.37 to 0.05
5–95 %	−0.21 to 0.03	−0.35 to 0.21	−0.44 to 0.41

Relative sea-level change at Forsmark beyond 2100 AD and until 12000 AD

The long-term sea-level response to global warming, beyond 2100 AD, is naturally associated with major uncertainties, larger than the ones estimated for 2100 AD. It is clear that global sea-level will continue to rise far beyond 2100 AD as a response to continued global warming (IPCC 2013a and references therein). The effects on GMSL rise from the response of the Greenland and West Antarctic ice-sheets to global warming are discussed above, where complete collapses of the Greenland and West Antarctic ice-sheets are suggested to contribute sea-level rises around Fennoscandia of ~0 and ~3 m, respectively. There are major uncertainties related to the amount of global warming and the associated amount of ice-sheet disintegration, as well as on the timing of such events.

The usage of RCPs over timescales of 10 ka is not completely straightforward as these, even if including the extensions, are only defined until 2300 AD (Appendix E). Therefore, studies investigating the GMSL rise over longer timescales typically use other metrics to define future scenarios, such as a maximum increase of the global mean surface air temperature (Levermann et al. 2013) or simplified pathways based on total cumulative emissions (Clark et al. 2016). Here, the projected global mean surface air temperatures from those studies are compared with projected long-term temperature increase resulting from the RCP4.5 and RCP8.5 scenarios (Appendix E), in order to determine which of the GMSL rise experiments belong to the *global warming climate case* and *extended global warming climate case*, respectively.

Furthermore, the large uncertainty related to the long-term sea-level change implies that differences in the projected GMSL rise between studies may reach several tens of metres. Hence, in contrast to reported sea-level projections until 2100 AD, it is not relevant to report the published long-term projections in two separate height reference systems (as deviations from present-day and in RH2000), as the difference between those systems amounts to only 0.2 m. Therefore, the reported sea-levels in this section are only presented as differences to present-day, typically defined as year 2000 AD or the average between 1986 and 2005 AD.

Sea-level projections beyond 2100 AD for cases with full-scale ice-sheet collapses under strong global warming (comparable to RCP8.5), as well as the contribution from thermal expansion of ocean water, are summarized and discussed in the extended global warming climate case (Section 5.2.3). A compilation of selected global mean sea-level projections from 2200 AD up to 12000 AD, with focus on projections based on the IPCC RCP4.5 emission scenario, is presented in Table 5-5. Figure 5-4 displays the sea-level projections for the period 2200 to 12000 AD from the data in Table 5-5, as well as the estimated isostatic uplift for the Forsmark site, and the resulting local changes in relative sea-level.

Given that a major deglaciation of the Greenland and Antarctic ice-sheets under a warming climate would contribute with different sea-level rise fingerprints in Fennoscandia (e.g. Pellikka et al. 2020), it would have most useful if the projections in Table 5-5 had included the regional re-distribution of sea-level rise. This is however not the case for most of the studies, since they typically only describe GMSL rise. Nevertheless, for the long-term analysis beyond 2100 AD and up to 12000 AD it is assumed that the GMSL value is representative also for the eustatic sea-level in the Baltic Sea. If the GMSL projections would have been regionalised to Baltic sea conditions, the resulting 10 ka projections would have been a few metres lower than presented in Figure 5-4. The main reason for the lower sea-level rise in the Baltic sea compared to the global mean is attributed to a smaller contribution from the Greenland ice-sheet in this region, see e.g. Mitrovica et al. (2001) and Kopp et al. (2014).

Table 5-5. Compilation of global mean sea-level projections beyond 2100 AD up to 12000 AD with focus on projections based on the IPCC RCP4.5 emission scenario and published since 2012. All values represent global mean sea-level (GMSL), except where otherwise indicated. Values are given for the median value and a 17–83 % confidence interval (i.e. the likely range) and a 5–95 % confidence interval (i.e. the very likely range). It should be noted that the values are not directly comparable, since they may be based on different climate/emission scenarios and use different methodological assumptions. The surface air temperature response to the 2560 petagrams of carbon (Pg C) total emission scenario in Clark et al. (2016) approximately corresponds to the upper end of the constructed temperature range in the RCP4.5-based *global warming climate case*, whereas the 1280 Pg C scenario in Clark et al. (2016) and 2 °C warming scenario by Levermann et al. (2013) approximately correspond to the lower end (Figure 5-2). The highest long-term sea-level projection under the RCP4.5 moderate emission scenario result from the 2560 Pg C cumulative emissions in Clark et al. (2016), whereas the lowest projections are obtained in Levermann et al. (2013). The uncertainty range for DeConto and Pollard (2016) and Clark et al. (2016) has been recalculated from 1σ standard error to the 5–95 % confidence interval.

Year (AD)	Sea-level for RCP 4.5 (m) Median values (confidence interval within brackets)	Confidence interval used. (comments within brackets)	Reference
2200	1.30 (0.70–2.00)	17–83 %	Kopp et al. (2014)
	1.30 (0.40–2.70)	5–95 %	
2300	3.55 (2.12–5.27)	5–95 %	Schaeffer et al. (2012)
	1.92 (0.7–3.49)	17–83 %	Kopp et al. (2014) according to Horton et al. (2018)
	1.92 (0–5.31)	5–95 %	
	4.21 (2.75–5.95)	17–83 %	Kopp et al. (2017)
	4.21 (2.11–6.96)	5–95 %	
	1.76 (1.29–2.30)	17–83 %	Nauels et al. (2017)
2500	1.84 (0.72–4.30)	5–95 %	Jevrejeva et al. (2012)
	5.76 (4.12–7.40)	5–95 % (±1σ (±1.0 m)) Only Antarctic ice loss	DeConto and Pollard (2016)
4000	4.8 (2.6–7.5)	2 °C of warming	Levermann et al. (2013)
7000	4.72	Fast CO_2 drawdown	DeConto and Pollard (2016)
	4.48	Natural CO_2 drawdown No CO_2 drawdown	
	8.47	Only Antarctic ice loss.	
12000	25.2 (19.3–31.1)	5–95 % (±1σ (±3.6 m)) 1280 Pg C total emissions (~RCP4.5)	Clark et al. (2016)
	37.5 (33.7–41.2)	5–95 % (±1σ (±2.3 m)) 2560 Pg C total emissions (~RCP4.5)	Clark et al. (2016)
	10.9 (3.1–13.4)	2 °C of warming	Levermann et al. (2013)

In Figure 5-4, the upper solid green curve shows the isostatic uplift at Forsmark as projected by the GIA modelling for the *global warming climate case* (Section 3.3.4, see also Figure 5-6). The only feature included in the GIA modelling for the *global warming climate case* that could potentially influence the future eustatic development is a complete collapse of the Greenland Ice-sheet. However, the results from the GIA modelling (Section 3.3.4) and results by e.g. Milne et al. (2009) constitute robust evidence that such an event would have negligible impact (~0 m) on the relative sea-level in the Baltic Sea. Therefore, the future relative sea-level curve projected by the GIA modelling for the global warming climate case essentially only shows the isostatic signal for the Forsmark site. In Figure 5-4, the lower hatched green line (unrealistically) assumes that the present-day isostatic uplift rate (6.7 mm a^{-1}, see Table 5-2) will continue at the same rate in the future. The difference between the eustatic and isostatic curves constitutes the relative sea-level development at the Forsmark site, giving an estimate of potential periods of transgression and regression and hence also estimates on submerged and terrestrial periods at the site, as shown in the previous section, as described below.

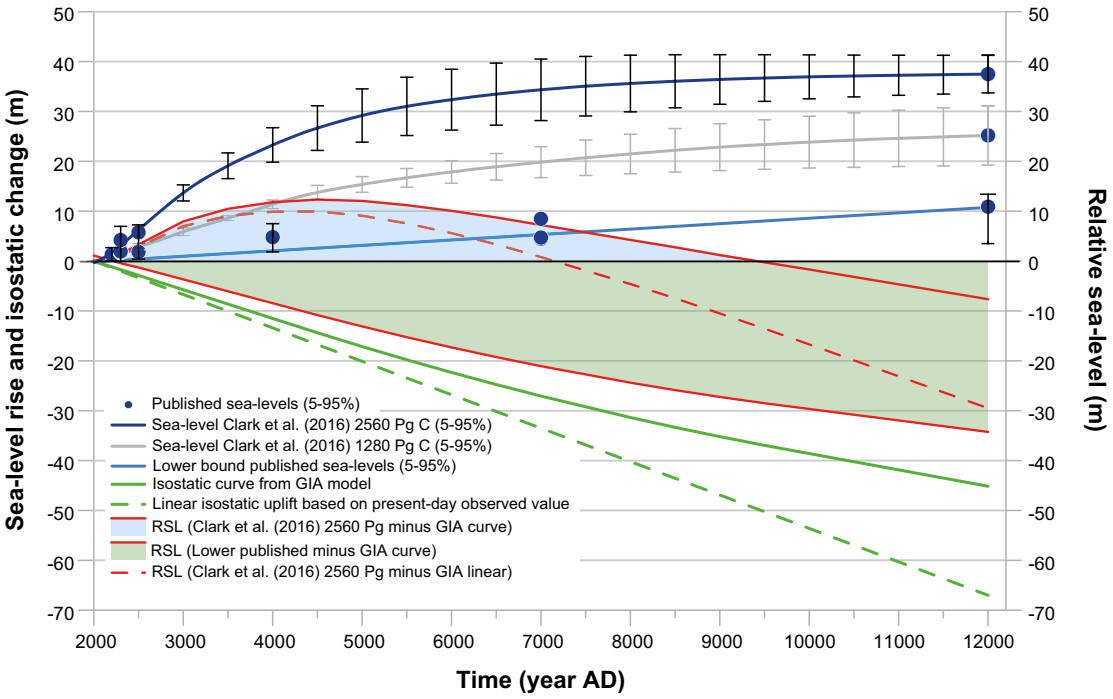

Figure 5-4. *Mean sea-level rise projections (blue dots) for the period 2200 to 12000 AD from the compilation in Table 5-5. The values constitute projections comparable with the IPCC RCP4.5 emission scenario, and as such they are compatible with the main notion of the global warming climate case. Median values are shown by blue dots. The 5–95 % confidence interval is shown by uncertainty bars. For the highest projected sea-level at 12000 AD (+37.5 ±3.8 m from Clark et al. (2016) for a 2560 Pg C total emission scenario), the projected sea-level development leading up to the maximum level has also been plotted together with the 5–95 % confidence interval (upper dark blue line with black bars), data from Clark et al. (2016, supplementary material). The 2560 Pg C emission scenario by Clark et al. (2016) represents the highest long-term sea-level projection, whereas Levermann et al. (2013) represents the lowest long-term sea-level projection under the RCP4.5 moderate emission scenario (Table 5-5). Also, the 1280 Pg C projection by Clark et al. (2016) (grey line) fits within the RCP4.5 scenario. Even though all sea-level projections are not directly comparable because of different methodologies etc, the substantial difference between the highest and lowest projections is striking, clearly demonstrating the large uncertainty within the field of future sea-level rise in a warming climate caused by moderate carbon emissions. The isostatic uplift rate for the Forsmark site as projected by GIA modelling (see the text and Section 3.3.4) is shown by the solid green line. The isostatic change at Forsmark, unrealistically assuming that the present-day uplift rate of 6.7 mm a^{-1} (Vestøl et al. 2019, see the text) would continue in the future, is shown by the hatched green line. The evolution of relative sea-level at Forsmark, constituting the net effect of the eustatic changes (blue lines) and isostatic changes (green lines) for the global warming climate case are shown in red. For an interpretation of the relative sea-level development at the Forsmark site (i.e. periods with transgression and regression, and associated periods of submerged conditions,) see the text. Also, for a description of the validity of using GMSL data for estimating the relative sea-level change at the Baltic coast (Forsmark site), see the text.*

The highest long-term sea-level projection until 12000 AD, comparable to RCP4.5 is obtained in Clark et al. (2016) by the 2560 petagrams of carbon (Pg C) scenario. The global mean surface air temperature increases for this scenario in Clark et al. (2016) is ~4 °C by 2300 AD and ~3 °C by 12000 AD (Figure 5-2), hence broadly representative of the upper bound of RCP4.5 (Appendix E). The rate of sea-level rise in this sea-level projection is fast over the initial thousands of years, whereas it has slowed down and is almost zero at the end of the 10000-year period. At 12000 AD the relative sea-level rise has reached a level of 37.5 ±3.8 m (Table 5-5 and Figure 5-4). The lowest sea-level projections for the same period are considerably lower, resulting in a rise of 10.9 m (3.1–13.4 m range) by 12000 AD (Levermann et al. 2013), assuming a 2 °C global warming relative to pre-industrial temperatures. This amounts to a little over 1 °C warming with respect to present-day, representative for the lower bound of RCP4.5 (Figure 5-2, Appendix F). The substantially lower GMSL projections in Levermann et al. (2013) compared to Clark et al. (2016) is explained by a much lower contribution from the Antarctic ice-sheets. Whilst Clark et al. (2016) projects a contribution from the Antarctic ice-sheets of ~30 m until 12000 AD, the total contribution to the sea-level rise from Antarctica only amounts to ~3 m in Levermann et al. (2013). The widely different Antarctic ice-sheet contributions between the studies are likely attributed to different amounts of global warming, but presumably also to a higher sensitivity of the ice-sheets to global warming in Clark et al. (2016) than in Levermann et al. (2013).

The sea-level rise according to the highest projection (upper dark blue line, from Clark et al. 2016) together with the isostatic curve for the Forsmark site from GIA modelling (solid green line) results in the relative sea-level curve shown by the upper solid red line. This line shows an initial transgression at the Forsmark site, peaking at around 4500 AD at a level of +12.3 m. This is followed by a regression back to the present-day situation at around 9500 AD (Figure 5-4). The transgression thus results in a ~7500 year long period with a higher relative sea-level than at present for the highest sea-level projection in the *global warming climate case*. To estimate the shortest time that a raised relative sea-level could prevail, with this eustatic projection, a comparison is given with the linear development of isostatic uplift (hatched green line). The resulting relative sea-level is shown by the hatched red line, showing that the period of raised relative sea-level caused by the transgression will not end before ~7500 AD (Figure 5-4), given the highest eustatic projection. The areas that would be permanently flooded with a relative sea-level rise of +12 m are shown in Figure 5-5.

In contrast to Clark et al. (2016), the lowest GMSL projections in Figure 5-4 do not provide much information on how the sea-level changes with time. Therefore, a general time evolution of a low-end GMSL evolution (E_{low}), ranging from 2000 to 12000 AD, is constructed for the *global warming climate case* using the following equation:

$$E_{low}(t) = a \arctan(bt), \qquad \text{Equation 5-1}$$

where t is the time (in ka) after 2000 AD, and $a = 1.70\ m$ and $b = 0.97\ ka^{-1}$. The parameters a and b have been determined under the constraints that (i) $E_{low} = +10.9\ m$ at 12000 AD, consistent with the lowest projection at this time under moderate global warming (Levermann et al. 2013, see Table 5-5), and (ii) the resulting relative sea-level change, obtained by combining E_{low} with the isostatic change, initially has the same rate as the observed present-day relative sea-level change at Forsmark (-4.1 mm a^{-1}, Table 5-2).

The constructed time series of the low-end GMSL evolution until 12000 AD is shown by the lower light blue curve in Figure 5-4. If this curve is used together with the isostatic curve based on GIA modelling (solid green line), the resulting relative sea-level change is shown by the lower solid red line. This relative sea-level development shows a continued regression at the site, from the present and up to 12000 AD and beyond.

All in all, the above analysis shows that the very large spread in long-term projections of future sea-level rise (Table 5-5 and Figure 5-4) for the RCP 4.5 emission scenario could result in either a transgression (more than + 12 m) at the Forsmark site, giving a higher-than-at-present relative sea-level over the next 5000–7500 years (up until 7000–9500 AD), or at the other end of the uncertainty spectrum, a situation with continued regression with no transgression at all at the site for the coming tens of thousands of years. Both evolutions fit within the uncertainty range of long-term future sea-level rise for the medium emission scenarios that form basis for the *global warming climate case*.

For an assessment of relative sea-level changes at Forsmark beyond 2100 AD and until 12000 AD for the *extended global warming climate case,* see Section 5.2.3.

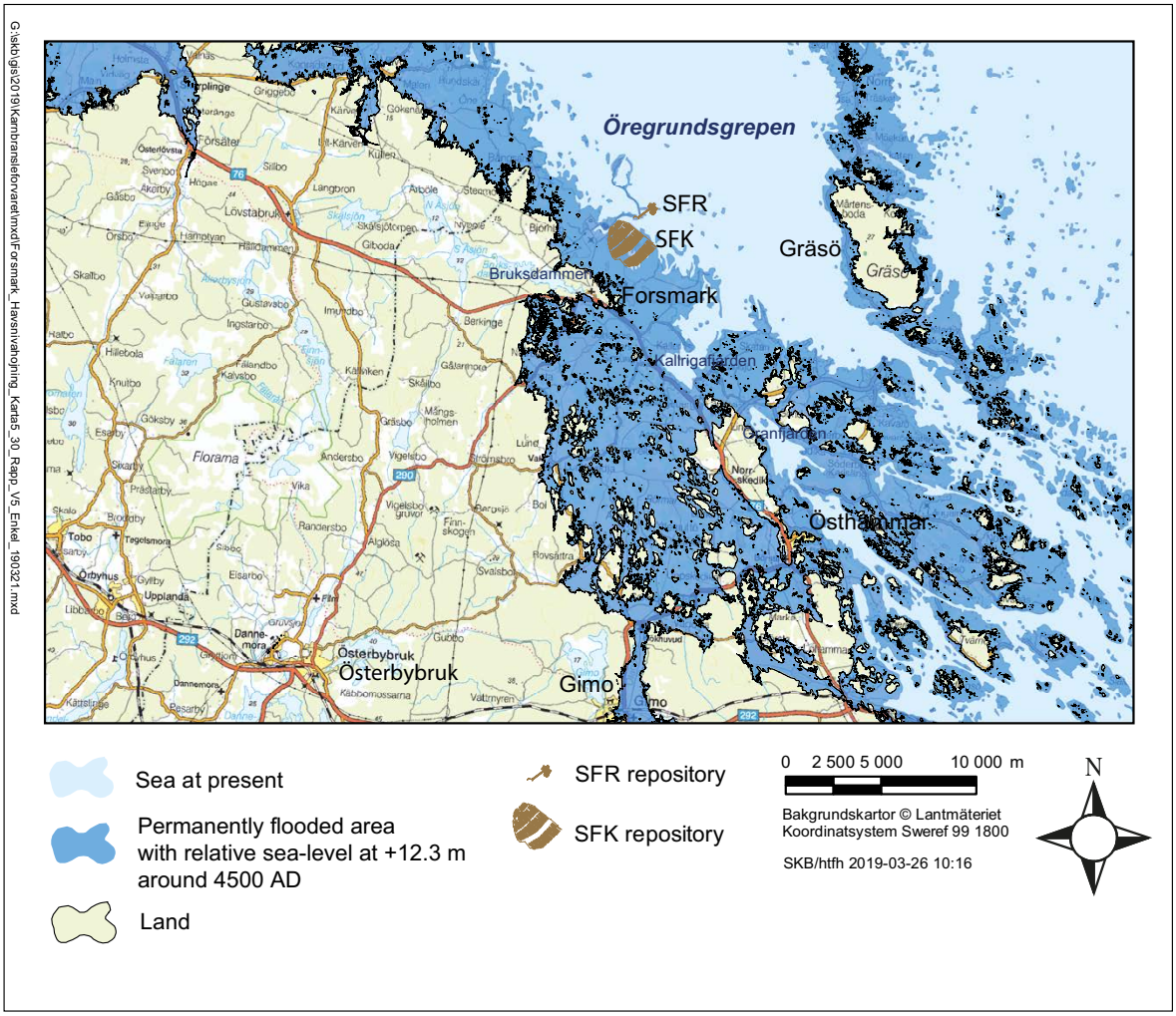

Figure 5-5. *Areas in the Forsmark region that will be permanently flooded with a relative sea-level at +12.3 m (RH2000) at around 4500 AD. This transgression results from the high long-term projection of GMSL rise of Clark et al. (2016) (Table 5-5 and Figure 5-4). In addition to this rise in mean sea-level, the sea-level may temporarily be higher than this by ~2 m during storm-surge events (cf. info on the 2100 AD surge level, Table 5-10 and Figure 5-17). A raised relative sea-level from this transgression would prevail until about 9500 AD, see the text. The present shore-line location is based on the Lantmäteriet Property map (www.lantmateriet.se). SFK: planned repository for spent nuclear fuel, SFR: existing repository for low- and intermediate-level waste.*

Relative sea-level change at Forsmark beyond 12000 AD until 120 ka AP

As mentioned above, the only feature included in the GIA modelling that could influence the eustatic development at Forsmark in the *global warming climate case* was a complete collapse of the Greenland ice-sheet. However, as was also noted above, such event would have a negligible impact on sea-level in the Baltic Sea and Forsmark area, implying that the GIA curve, in essence, describes the isostatic change in the Forsmark area rather than being a realistic representation of the relative sea-level. Because of this, the GIA curve can be used in combination with the estimated GMSL change from Clark et al. (2016) to broadly estimate the relative sea-level change in Forsmark for the next 10 ka (Figure 5-4), and also for the corresponding estimate for the *extended global warming climate case* (Section 5.2.3).

Just as for the reconstruction of last glacial cycle conditions (Section 3.1.4) and the resulting *reference glacial cycle climate case* (Section 4.5.2), the GIA modelling curve for the *global warming climate case* was also integrated for 120 ka into the future. In line with the approach used for the *reference glacial cycle*, the GIA model was initiated by running one full glacial cycle to obtain realistic initial uplift rates for the global warming scenario. This was followed by a 50 ka long period of no change

to the loading model, representative of a global warming climate without an ice-sheet forming in Fennoscandia. After that, the Weichselian reference glacial cycle with a 20 % reduction of the Fennoscandian ice-sheet thickness during the glaciated period was used for the remainder of the glacial cycle.

The relative sea-level curve from the GIA model was then combined with empirical relative sea-level data for the Holocene (based on the equations in Påsse and Daniels 2015; see Appendix D) in order to connect past relative sea-level changes, from the deglaciation of Forsmark (at 10.8 ka BP) to the present-day and the future. The construction of the relative sea-level curve for the next 120 ka is summarized in Table 5-6. In general, and in accordance with SR-Site methodology (SKB 2010a), it is assumed that the termination of each glacial cycle follows the reconstructed relative sea-level curve of the Holocene (Appendix D, Figure D-5), and that the simulated relative sea-level from the GIA modelling is primarily used otherwise (Table 5-6).

It is important to note that the Holocene curve based on Påsse and Daniels (2015), just as in the case of GIA modelling, does not include any global-warming-induced changes that could potentially influence the eustasy in the Baltic Sea (Appendix D). Therefore, the combination of these curves essentially describes the isostatic development at Forsmark until the onset of the next glaciation.

In order to also account for the effects of global warming on the relative sea-level at Forsmark for the next 120 ka, the GMSL curves derived from the 2560 Pg C cumulative emission scenario in Clark et al. (2016) and 2 °C of warming scenario in Levermann et al. (2013), both comparable to the RCP4.5 emission scenario (Figure 5-4), are added to the combined isostatic curve from GIA modelling and Påsse and Daniels (2015). The projections by Clark et al. (2016) and Levermann et al. (2013) bracket the uncertainty range associated with the GMSL rise until 12000 AD under a moderate global warming (Figure 5-4). It is assumed that the relative sea-level contributions from Clark et al. (2016) and Levermann et al. (2013) after 12000 AD remain constant at their maximum values (+37.5 m and +10.9 m, respectively; Table 5-5) until the next major glaciation, at which point the Greenland and Antarctic ice-sheets and the glaciers begin to re-grow significantly. Following the next glaciation, it is further assumed that the global warming signal has decayed sufficiently so that the Greenland and Antarctic ice-sheets attain their present-day configurations, and that the relative sea-level at Forsmark follows a trajectory dominated by natural climate variability as described by the *reference glacial cycle.*

The result is a coarse estimate of the relative sea-level change in Forsmark over the next 120 ka (Figure 5-6). Similar to the modelled relative sea-level change for the *reference glacial cycle* (grey curve in Figure 5-6), the low-end relative sea-level projection in the *global warming climate case*, based on Levermann et al. (2013), results in a continued initial regression at Forsmark until ~40 ka AP, by which the isostatic contribution has tapered off. In contrast, the high-end relative sea-level projection, based on Clark et al. (2016), results in an initial transgression, culminating in a sea-level rise of +12 m in about 2500 years (see also previous subsection). After this point, the relative sea-level slowly begins to decline due to the isostatic uplift (Figure 5-6). From 12000 AD until the first glaciation in the *global warming climate case* (~95 ka AP), the high-end relative sea-level projection is consistently about 35 m higher than the low-end projection. By the time of the first glaciation, both relative sea-level projections begin to increase as a result of the expanding Fennoscandian ice-sheet. Ultimately, the relative sea-level projections converge toward the maximum value of +85 m by 113 ka BP, after which they follow the relative sea-level development in the *reference glacial cycle* back to zero at 120 ka AP (Figure 5-6).

It is important to note that there are large uncertainties related to the relative sea-level projections for *global warming climate case* in Figure 5-6. Firstly, the assumption of a constant eustatic sea-level contribution from Clark et al. (2016) between 10 and 90 ka AP is probably not realistic. During this period there will be significant variations of the Earth's orbit (Berger and Loutre 2002, Laskar et al. 2004), yielding periods of both slightly colder and warmer temperatures than the ones simulated in Clark et al. (2016) for 12000 AD. Secondly, the climate during the next 100 ka will likely be influenced by a continued decline of the atmospheric CO_2 concentration, resulting in a long-term cooling trend (Lord et al. 2019). These two effects combined, along with accompanying climate feedbacks, will influence e.g. the amount of water that is locked up in the ice-sheets (and therefore the GMSL) both positively and negatively over this period. However, because the amplitude and timing of these changes are very uncertain, they have been omitted in the present analysis.

Table 5-6. Summary of the construction of the relative sea-level curve at from −10.8 to 120 ka AP for the global warming climate case, using empirical relative sea-level data for the Holocene (Appendix D) and future relative sea-level projections from GIA modelling (Section 3.3.4). Data from the two sources were combined into one curve by means of linear interpolation. Because the sea-level curves from both the Holocene model and GIA modelling essentially only represent isostatic changes (see main text), the effect of eustasy on the relative sea-level was parameterized using the global-mean sea-level (GMSL) projections from Clark et al. (2016) and Levermann et al. (2013). The projected GMSL rise values were added to the curve between 0 and 10 ka AP (2 and 12 ka AD) (see Figure 5-4), after which the GMSL was assumed to remain constant at its maximum value (+37.5 m) until the next glaciation in the global warming climate case (~95 ka AP; see also Figure 5-6).

Time period (ka AP)	Data used
−10.8 to 0	From equation based on Påsse and Daniels (2015) (Appendix D)
0 to 5	Linear interpolation
5 to 113	Glacial Isostatic Adjustment (GIA) modelling
113 to 114	Linear interpolation
114 to 120	From equation based on Påsse and Daniels (2015) (Appendix D)

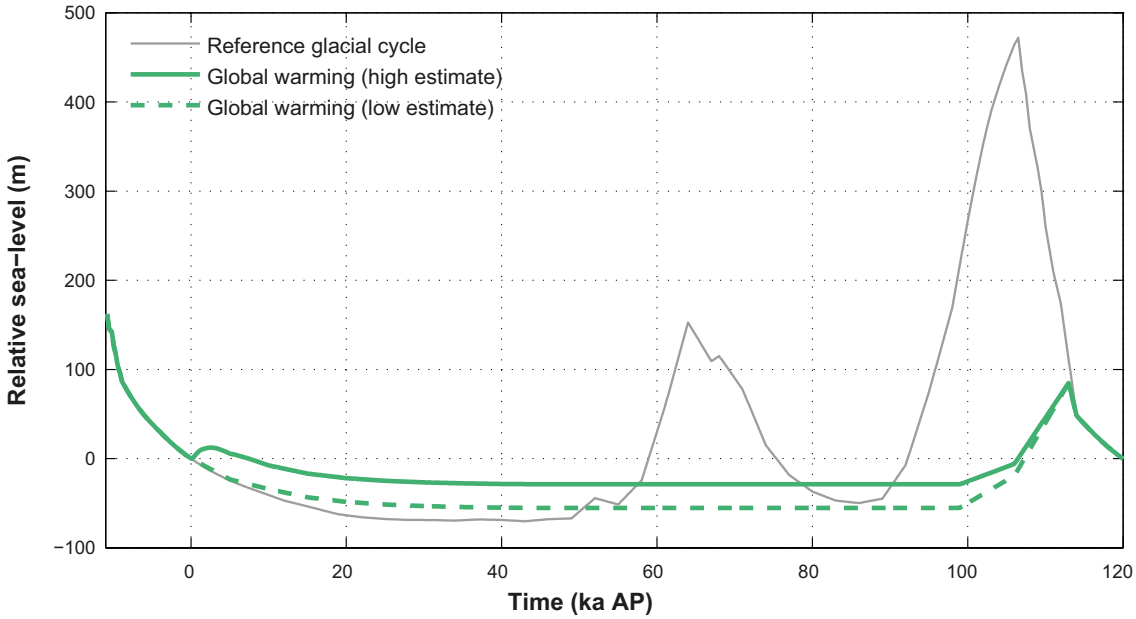

Figure 5-6. *Estimated relative sea-level change at Forsmark from −10.8 to 120 ka AP in the global warming climate case (green curves) and the reference glacial cycle climate case (grey curve). The solid green curve represents a high-end relative sea-level projection under a moderate global warming, based on the highest GMSL projection until 12000 AD (Clark et al. 2016), whereas the dashed green curve represents a low-end relative sea-level projection based on the lowest GMSL projection until 12000 AD (Levermann et al. 2013), also under moderate global warming. For more information on the projected relative sea-level change until 12000 AD, see previous subsection. For a comprehensive discussion on the relative sea-level changes between −10.8 and 120 ka AP for the reference glacial cycle climate case, see Section 4.5.2.*

5.1.4 Permafrost evolution

In the *global warming climate case,* the evolution of permafrost is postponed 50 ka compared with the development in the *reference glacial cycle climate case*. After the first 50 ka, the development of the temporal pattern and depths of permafrost is identical to the development in the *reference glacial cycle climate case*. The permafrost starts to develop at around 60 ka AP. After that, progressively longer periods of permafrost conditions and shorter periods of temperate climate conditions occur, up until the glacial period at around 110 ka AP. The maximum permafrost depth is, in this climate case, the same as in the *reference glacial cycle climate case*, ~260 m (with a maximum uncertainty interval down to ~460 m), but it occurs later, c 100 ka AP. At the same time, the depth of the frozen ground is somewhat shallower than the permafrost depth, due to the pressure and salinity; ~245 m (with a maximum uncertainty interval down to ~420 m).

5.1.5 Evolution of climate domains

The development of climate domains for the *global warming climate case* is shown in Figure 5-7. Given the assumption of a long initial period of temperate climate conditions, the temperate climate domain is dominating. Submerged conditions may last for 0 up to 7500 years (0 to ~6 % of the time) reflecting the large uncertainty associated with the projected future relative sea-level change (Figure 5-7, see also Section 5.2.3). This means that the temperate climate domain prevails between ~73500 and ~81000 years (61 or 68 % of the time, respectively), the periglacial domain for ~28000 years (23 % of the time) and the glacial domain for ~11000 years (9 % of the time).

In this climate case, the climate at Forsmark is dominated by the initial ~60 ka long period with temperate climate conditions. The variation in air temperature and precipitation is significant within this temperate period, with air temperatures and annual precipitation rates considerably higher than at present in the early phase of the 120 ka period (Figure 5-3).

A detailed example of the characteristics of a climate dominated by global warming in Forsmark is given below, derived from the climate modelling study by Kjellström et al. (2009). Over time, the high temperatures are slowly reduced, as a response to the slow decrease in atmospheric CO_2 concentrations. During the initial long temperate period, climate varies within a range that is larger than that of the preceding parts of the Holocene. The length of the initial period of temperate climate domain in the *Global warming climate case* does not constitute a prediction on how a future global warming climate will manifest itself. Given the present state of knowledge, this interglacial period is likely to be even longer than envisaged in the *Global warming climate case*, see Figure 5-1 and Section 5.2.

Between ~60 ka AP and more than 100 ka AP, periods of periglacial conditions with permafrost occur and get progressively more severe (Figure 5-7). The first major ice-sheet advance in the *global warming climate case* occurs at around 110 ka AP. The maximum ice-sheet thickness of about 1600 m, occurs at around 115 ka AP. Table 5-7 summarizes the sequence of events for the *global warming climate case*.

During the second half of the *global warming climate case* (Figure 5-7), climate varies within the same range as during the first part of the *reference glacial cycle climate case* (Section 4.5), and consequently the climate-related processes act in the same way as in the *reference glacial cycle climate case*. The global warming variant reduces the effects of climate-related processes of importance for repository safety that are related to cold climate conditions, i.e. in the periglacial- and glacial climate domains.

Another possible course of events within a generally warming global climate, is that the annual mean Atlantic Meridional Overturning Circulation (AMOC) in the North Atlantic is reduced (e.g. Wu et al. 2004, Zickfeld et al. 2007, Drijfhout et al. 2008, Gregory and Tailleux 2011, IPCC 2013a, Liu et al. 2017). This would result in less heat being transported towards Fennoscandia by the North Atlantic Drift sea current, which in theory could lead to a regional cooling over Fennoscandia. However, in the global warming climate simulations by Kjellström et al. (2009 including erratum Feb 2010), the AMOC is reduced by no more than 22 % compared with the control period (1961–2000). These changes are not large enough to cause regional cooling over Fennoscandia. This result is in general agreement with the Atmosphere Ocean General Circulation Model (AOGCM) simulations of the 21st

century as presented by Collins et al. (2013). They show that the AOGCMs suggest a decreased intensity of the AMOC in the 21st century in the range from 11 to 34 %. As in the simulations by Kjellström et al. (2009), none of these AOGCM simulations indicates a cooling over Fennoscandia. The possibility and potential impact of an AMOC collapse beyond 2100 AD is discussed in Appendix F.

Nevertheless, although it is believed that the general warming would be considerably larger than such a cooling effect, resulting in net warming in Fennoscandia (Kjellström et al. 2009, IPCC 2013a), a case with more severe permafrost development than in the *reference glacial cycle climate case* is investigated in the *severe permafrost climate case* (Section 5.5).

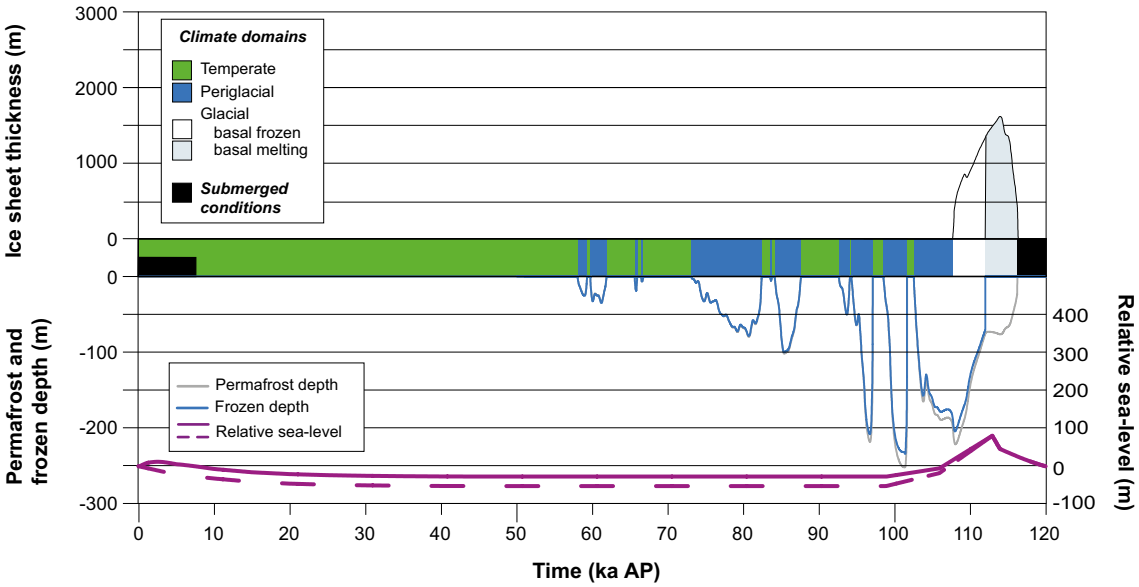

Figure 5-7. *Evolution of climate-related conditions at Forsmark as a time series of climate domains and submerged periods for the global warming climate case. Following from the assumption of this case, temperate climate conditions prevail at the site for more than 50 ka. Cold climate conditions are initiated at around the time of an insolation minimum occurring at ~54 ka AP. The initial period either experience terrestrial conditions with a warm temperate climate or submerged conditions up to 7500 AP (9500 AD), given the large uncertainty range in projected future sea-level rise indicated by the solid and dashed purple curves (see also Section 5.1.3 and Figure 5-4). The figure hence shows both end-members regarding the uncertain sea-level development associated with the RCP4.5 medium emission scenario (Section 5.1.3). Note that there is a very large range in e.g. temperature, precipitation and other climate parameters within the temperate conditions, ranging from very strong global warming conditions to conditions with temperatures significantly cooler than at present (prior to the development of periglacial conditions). For a detailed example of more extreme global warming conditions at Forsmark than envisaged for this case, see Section 5.2.5.*

Table 5-7. Sequence of climate-related events for the global warming climate case.

Event	Transition date (After present)	Transition date (BC/AD)	Climate domain
Deglaciation/ Start Holocene interglacial (locally defined)	–10800	8800 BC	-
Holocene interglacial	-	-	Temperate climate domain (incl. submerged conditions 0–7500 AP (2000–9500 AD))
End of Holocene interglacial (locally defined)	c 59400	c 61400 AD	-
Periglacial conditions (progressively longer periods of permafrost conditions)	-	-	Periglacial climate domain (incl. progressively shorter phases of temperate climate conditions)
End of periglacial conditions Start of glacial conditions	109600	111600 AD	-
First phase with glacial conditions	-	-	Glacial climate domain
Deglaciation at site, Start interstadial conditions	118200	120200 AD	-
Interstadial conditions (corresponding to MIS 3)	-	-	Periglacial climate domain (incl. submerged conditions and short temperate periods)

In the *global warming climate case*, the warmer annual mean air temperatures do not affect repository safety functions. Furthermore, the increase in annual precipitation would not affect groundwater formation significantly, since, on a regional scale, the major part of the groundwater aquifer is filled already by present-day precipitation rates. Instead surface-runoff is increased, discussed further under the section on surface denudation. However, low groundwater salinity due to persistent infiltration of meteoric water during the prolonged temperate periods in the greenhouse variant may have a potential effect on the function of the clay buffer (see the **Post-closure safety report**).

5.1.6 Surface denudation

The relative importance of different denudation processes, as well as the resulting amount of surface denudation, is expected to change in the *global warming climate case* as compared with the *reference glacial cycle climate case*. The major difference between the *global warming climate case* and the *reference glacial cycle climate case* is that glacial conditions with warm-based erosive ice only exist for 4.3 ka in the former case (cf. Figure 5-7) compared with 24 ka in the latter case (Section 4.5.1 and Figure 4-35). Glacial erosion is identified as the most important denudation process in the *reference glacial cycle climate case*, with the largest contribution to the total denudation rate (Section 4.5.7).

In the *global warming climate case*, the annual mean air temperature and annual precipitation are expected to increase in Forsmark during the initial part of the temperate climate domain, see above. For the first tens of thousands of years of this climate case, increased precipitation results in increased surface runoff, see above and Kjellström et al. (2009), which probably leads to increased fluvial erosion. In the *global warming climate case*, with 58000 initial years of temperate climate conditions, the effect of this increased fluvial erosion is however significantly smaller than the effect of the decrease in glacial erosion. The increased fluvial erosion most probably has a minor impact on total denudation rates for this climate case. Furthermore, even if the fluvial erosion process were to be large, the resulting amount of fluvial erosion is limited by the fact that it cannot erode deeper than the level of the Baltic Sea and that the site of the repository is located close to sea-level today (Section 3.5.2). The period of increased annual precipitation is accompanied by a slowly regressing, stationary or even transgressing sea-level (Section 5.1.3), which further precludes deep fluvial erosion during the period influenced by increased precipitation. In the *global warming climate case*, increased air temperatures could lead to higher chemical weathering rates.

Other, minor, differences compared with the *reference glacial cycle climate case* relate to periglacial conditions, which have a shorter duration in this climate case than in the *reference glacial cycle climate case*. Aeolian erosion is therefore expected to contribute even less to the total denudation in the *global warming climate case*.

Since the duration of periods with glacial erosion is significantly shorter in the *global warming climate case* than in the *reference glacial cycle climate case,* the expected amount of glacial erosion is also significantly smaller. This is shown by Hall et al. (2019a), whom, based on a first-order estimate of the timing and duration of future periods with glaciated conditions at Forsmark under different RCPs (Lord et al. 2019 Figure 4-10), estimated (based on all scenarios of Lord et al. 2019) that the total denudation of basement rock at Forsmark will be less than 1 metre over the coming 100 ka (Table 3-15). Specifically for the RCP4.5 emission scenario, used as basis for the *global warming climate case*, the calculated total denudation is up to 0.5 m at Forsmark over the coming 100 ka (Appendix G Table G-1). Since there is no ice-sheet coverage over Forsmark over the coming 100 ka in the RCP4.5 scenario of Lord et al. (2019), the estimated denudation over this time period is a result exclusively of non-glacial denudation processes (such as increased fluvial erosion and chemical weathering during warm climate periods and increased physical weathering and aeolian erosion during periglacial periods).

In order to also include the period from 100 to 120 ka AP (Figure 5-7) in the estimated denudation, i.e. to cover the full 120 ka period of the *global warming climate case*, another 20 ka of mixed non-glacial and glacial conditions needs to be added. Under this period, non-glacial conditions prevail for 11.4 ka, glacial warm-based conditions for 4.3 ka and glacial cold-based conditions also for 4.3 ka. Using i) a maximum non-glacial denudation rate of 5 mm ka^{-1} (see Section 3.5.4 and Hall et al. 2019a), ii) a glacial erosion rate of 89 mm ka^{-1} for warm-based glacial conditions (i.e. the 75 % percentile value of glacial erosion rate (constituting the upper end of the most likely range) from combined ^{10}Be and ^{26}Al simulations of past glacial erosion rates at Forsmark (Hall et al. 2019a), Appendix G), and iii) assigning no glacial erosion for cold-based glacial conditions (see Section 3.5.1 under the Glacial erosion heading) results in a total denudation of 0.44 m for the last 20 ka period of this climate case. The total denudation for the 120 ka of the *extended global warming climate case* is hence less than 1 metre (0.5+0.44 = 0.94 m). A total denudation of less than 1 metre for the *extended global warming climate case* is lower than the 1.7–3.6 metres of denudation in the *reference glacial cycle climate case*, see Section 4.5.7.

It is hence judged that the *global warming climate case* results in a smaller total bedrock denudation than the *reference glacial cycle climate case*, mainly because of the shorter duration of periods with the most efficient denudation process (glacial erosion), as identified in Section 3.5.4.

5.1.7 Exemplified climate conditions for the global warming climate case

In order to give a detailed example of how a climate influenced by global warming could appear in Forsmark, climate modelling was used to describe a situation with a temperate climate with increased greenhouse gas concentrations in the atmosphere (750 ppmv), a few thousands of years from now (Kjellström et al. 2009, including erratum Feb 2010). According to Lenton et al. (2006), a 750 ppmv CO_2 level still means that all "conventional" fossil fuel resources (including coal, oil, and gas) need not have been used.

In the climate modelling simulations, a complete loss of the Greenland ice-sheet was assumed. Since this deglaciation is a process that may take up to a couple of thousand years, it is very uncertain what other climate-related conditions may be prevailing at that time. According to climate-change scenarios from simulations with GCMs, irreversible melting of the Greenland ice-sheet may start at a time when the global mean temperature has increased by about 1.9–5.1 °C above today's conditions and the temperature over Greenland has increased by about 3–6.5 °C (Gregory et al. 2004, Gregory and Huybrechts 2006). Recent studies indicate that the ice-sheet might be more sensitive to increased concentrations of atmospheric greenhouse gases than previously thought (Stone et al. 2010).

Increases in temperature large enough to make the Greenland ice-sheet collapse are projected by GCMs within the 21st century for some emission scenarios, see Church et al. (2013). If such high temperatures persist for long enough (several hundreds to a couple of thousand years depending on the degree of warming) the Greenland ice-sheet will eventually collapse and disappear. In this time perspective, CO_2 levels will start to decrease again (when emissions cease). Nevertheless, at one thousand years from

now, the atmospheric CO_2 concentrations will remain considerably higher than today (Lenton et al. 2006). Here, the time period for the global warming simulation was chosen as a compromise between a high level of CO_2 (needed to simulate a warm climate that melts the Greenland ice-sheet), and a not too high a level (that remains in the atmosphere a long time after the emissions have ceased). Thus, the simulations can be considered as representative of the climate a few thousand years into the future after a complete melting of the Greenland ice-sheet and a partial recovery towards lower background CO_2 concentrations.

For these simulations, a global GCM model (Community Climate System Model version 3, CCSM3), a regional climate model (Rossby Centre Regional Climate Model RCA 3) and a vegetation model (LPJ-GUESS) were used. For the simulations performed and analysed within this study, atmospheric and land components of the CCSM3 used a grid spacing of approximately 2.8° in latitude and longitude. The vertical resolution is 26 levels in the atmosphere and 40 levels extending to 5.5-km depth in the ocean. The regional climate model used a horizontal resolution of 50 km and a time resolution of 30 minutes. For details on the models, how they were employed, and a discussion on model uncertainties, see Kjellström et al. (2009). The simulation of the global warming climate used a CO_2 concentration in the atmosphere of 750 ppmv. In order to include the effect of other greenhouse gases in the RCA 3 model, a CO_2 equivalent value of 841 ppmv was used (Kjellström et al. 2009). For a detailed description of the assumptions made in the modelling process, model forcing and initial conditions (such as astronomical and solar forcing, concentration of greenhouse gases and aerosols in the atmosphere, extents of ice-sheets, distribution of land and sea, topography and vegetation), also see Kjellström et al. (2009).

The simulated global warming climate should not be taken as a prediction or prognosis on how a future global warming climate will manifest itself. Instead, it is *a detailed example* of how such a climate may be manifested. Given another model forcing, for instance using a lower or higher CO_2 concentration, the resulting climate would have been different. However, the model results are useful for exemplifying a climate affected by global warming, in respect of local changes at Forsmark. In this context, it is worth noting that the results of Kjellström et al. (2009) resemble those for many of the scenarios for the 21st century from the climate model intercomparison project (CMIP5) (Collins et al. 2013). For a detailed discussion and comparison with other climate model results, see Kjellström et al. (2009, Section 3.1.4).

Global climate

Figure 5-8 shows the simulated global warming climate from the GCM simulations. Seasonal mean changes in temperature in the global warming simulation as compared with a simulation of the present (1961–2000) climate are also shown in Figure 5-8. The removal of the Greenland ice-sheet produces a strong heating of up to 17 °C over Greenland in both summer and winter. This heating is primarily due to a combination of i) the lowering of the surface by up to 3000 m and ii) the decrease in surface albedo and changes in heat fluxes between the atmosphere and the ground produced by the replacement of the glacier ice surface by tundra (Kjellström et al. 2009). Similarly to all greenhouse warming scenarios presented in the IPCC AR5 report (Collins et al. 2013), the Arctic region exhibits strong heating by up to 15 °C in winter (due to a substantial decrease in the Arctic sea-ice cover and a decrease in the snow cover). The seasonal mean temperature is up to 5 °C warmer in summer and up to 7.5 °C warmer in winter over Fennoscandia in the global warming simulation as compared with the simulation of the present climate. Seasonal mean summer temperatures in Sweden vary in the range 12–18 °C and winter temperatures vary in the range 0–6 °C. Sensitivity to changes in vegetation in these GCM simulations is discussed in Kjellström et al. (2009).

The change in precipitation in the global warming simulation as compared with the simulation of the present climate is also shown in Figure 5-8. The removal of the Greenland ice-sheet leads to a 25 % decrease in precipitation in particular over south–eastern Greenland in both summer and winter, indicating that much of the precipitation in that area in today's climate is triggered by the steep ice-sheet topography. Similarly to all greenhouse-warming scenarios presented in the IPCC AR5 report (Collins et al. 2013), precipitation is increased over mid-latitude Northern Hemisphere continents and the Arctic. For Fennoscandia there is an increase in precipitation, most notably in the north.

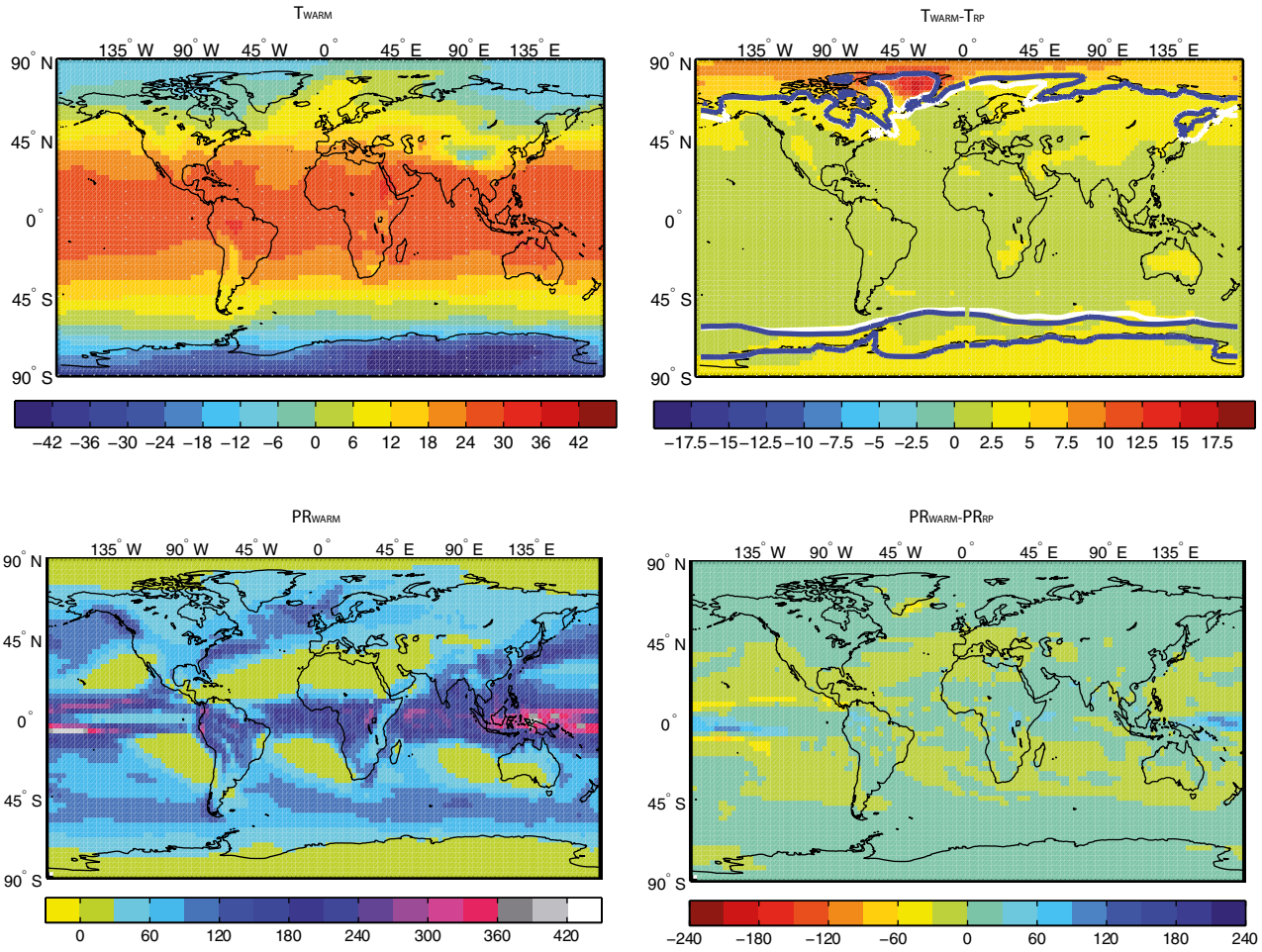

Figure 5-8. *Upper panels: Simulated near-surface air temperature in the global warming simulation (T_{WARM}) and the difference compared with the simulated present climate (T_{RP}) (1961–2000). Units are °C. Also shown by isolines in the rightmost panels is the extent of sea-ice in the simulation of the present climate (white) and in the global warming simulation (blue). Lower panels: Precipitation in the global warming simulation (PR_{WARM}) and the difference compared with the simulated present climate (PR_{RP}). Units are mm month^{-1}. From Kjellström et al. (2009).*

Climate in Europe and Sweden

The regional climate model was then used to downscale the model results of the global climate model in order to obtain higher resolution data over Europe and Sweden. The resulting climate over Europe was used to produce a new vegetation distribution with the vegetation model. This vegetation was in turn, used as input to the regional climate model, to produce a climate in line with the new vegetation. An evaluation of the results from this iterative process is given in Kjellström et al. (2009). Figure 5-9, Figure 5-10 and Figure 5-11 present selected results on temperature and precipitation from the regional modelling.

In the regional global warming simulation, the warming compared with the simulated present climate (1961–2000) is strongest over northern Europe in winter. The simulated temperature increase for the coldest month is more than 5 °C in northern Fennoscandia (Figure 5-9, second row, middle panel). In southern Europe the warming is stronger in summer, where the temperature of the warmest month increases by more than 4 °C in large areas (Figure 5-9, second row, left panel). The stronger warming in the areas of the Bothnian Bay, Bothnian Sea and in the Gulf of Finland in summer in this experiment is due to the land uplift converting sea to land in those areas. The same phenomenon is also responsible for the weaker warming in these areas in winter. Differences between the results of the global and regional model simulations are discussed in Kjellström et al. (2009).

As expected, the simulated climate of the *global warming climate case* clearly resembles many of the scenarios for the 21st century from the climate model intercomparison project (CMIP5) as presented by the IPCC (Collins et al. 2013). Seasonal mean changes in precipitation and temperature from a large number of the CMIP3 scenarios have been analysed for Sweden by Lind and Kjellström (2008). Lind and Kjellström (2008) report an increase in temperatures of 4–6 °C by the end of the 21st century in northern Sweden and about 3 °C in southern Sweden relative to the 1961–1990 period. The corresponding increases in precipitation are about 25 % in the north and only a small average increase in the south albeit with a large spread between the models. These changes are annual averages over a range of different emission scenarios. As noted in Kjellström et al. (2009), the uncertainties related to the future forcing in the global warming simulation are large and substantially lower or higher greenhouse-gas concentrations than the one used cannot be ruled out. Considering the large spread between the emission scenarios and the uncertainty related to the climate models one cannot rule out that a future warmer climate can be warmer than the one simulated in Kjellström et al. (2009). However, the high-end emission scenarios (A1FI and A2) (Nakićenović and Swart 2000) may have CO_2 concentrations that are too high to be sustained over the long period that it takes to melt the Greenland ice-sheet, which was part of the set-up here. But, even so, the CO_2 concentrations may very well reach levels high enough to sustain long-term (i.e. multi-century) temperature anomalies exceeding those simulated here.

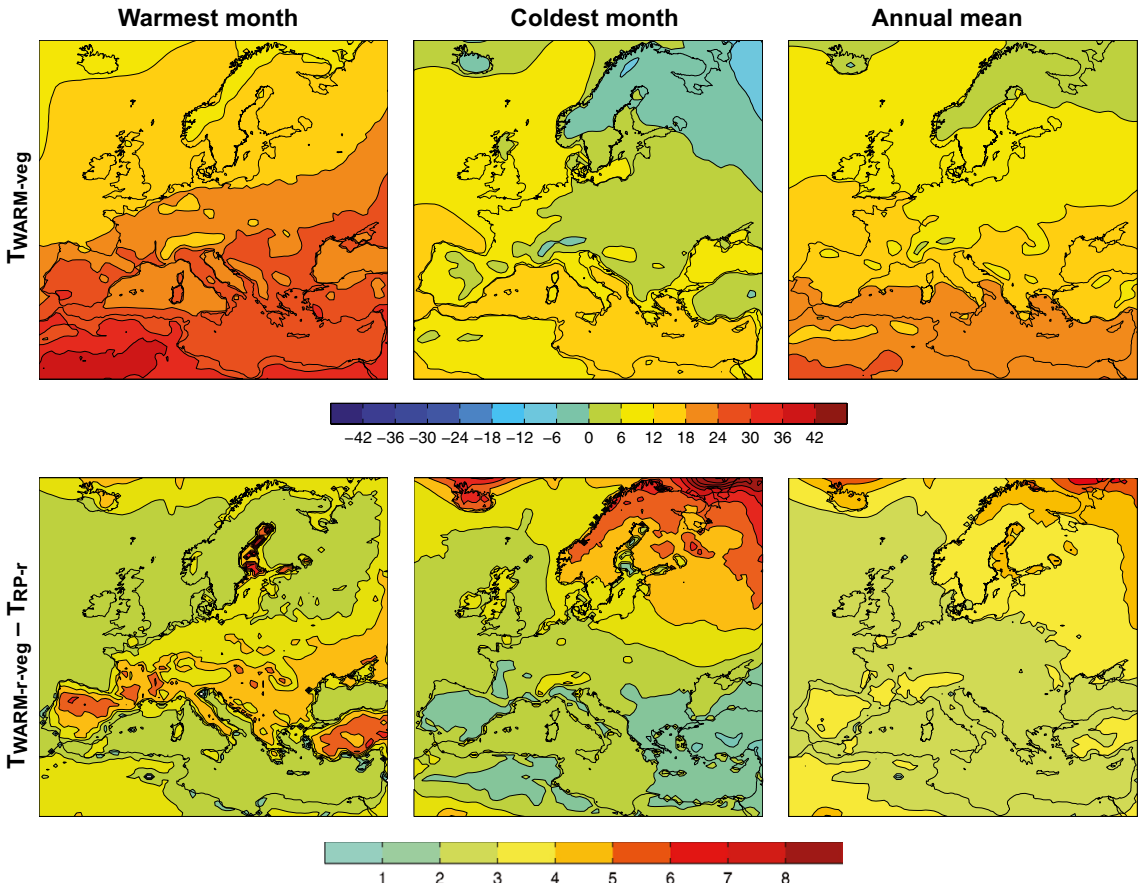

Figure 5-9. *Mean near-surface air temperatures of the warmest month, coldest month and annual mean in the global warming simulation with improved vegetation (upper row). Also shown are differences between the global warming simulation and the simulations of the present climate (RP-r) (1961–2000) (lower row). Units are °C. From Kjellström et al. (2009).*

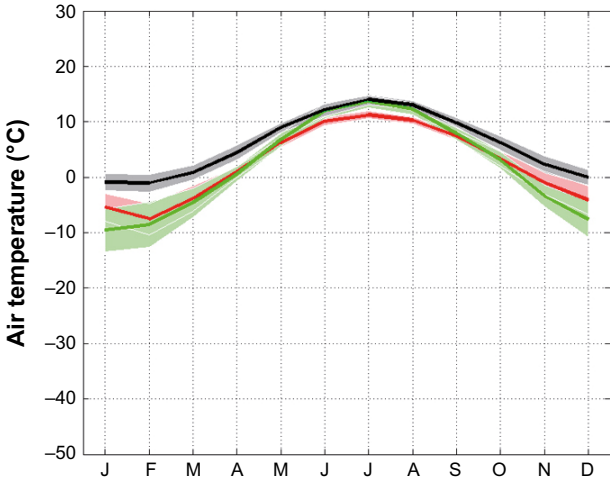

Figure 5-10. *Annual cycle of temperature for Sweden in the global warming (black line) and simulated present climate (1961–2000) (red line). Also shown is the CRU observational data from 1961–1990 (green line). Shaded areas in corresponding colours indicate the ±1 standard deviation calculated for the range of individual monthly averages in the three data sets. From Kjellström et al. (2009).*

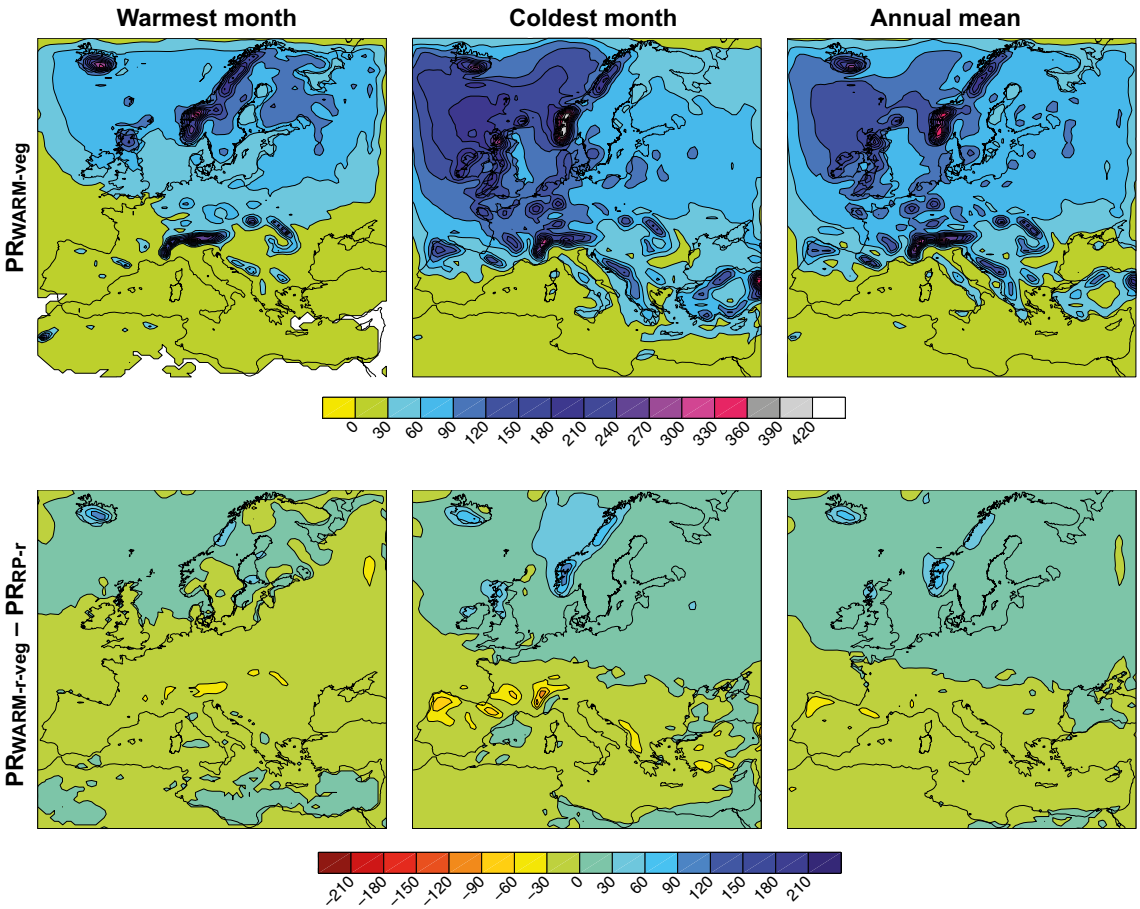

Figure 5-11. *Mean precipitation of the warmest month, coldest month and annual mean in the global warming simulation. Also shown are differences between the global warming simulation and the simulated present climate (RP-r) (1961–2000). Units are mm month^{-1}. From Kjellström et al. (2009).*

Clearly, the results from the regional model give a climate change signal that is within the range defined by the global model results for southern Sweden compiled in Lind and Kjellström (2008), see Figure 3-15 in Kjellström et al. (2009). The climate change signal for entire Sweden is +4 °C in winter and +3.5 °C in summer and the corresponding numbers for precipitation are +37 % in winter and no change (±0 %) in summer. Further model results and discussion for all of Sweden from the global- and regional climate modelling and from the vegetation modelling are presented in Kjellström et al. (2009).

The vegetation simulated by LPJ-GUESS for the global warming climate is reported in the context of the biosphere studies (see the **Biosphere synthesis report**).

Here it is also worth noting that the Greenland summer temperatures are well above 0 °C, clearly indicating that there is no chance of ice-sheet regeneration under these circumstances once the ice has been removed. A similar result was obtained previously for the pre-industrial climate when the Greenland ice-sheet was removed in the Hadley Centre HadCM3 coupled model (Toniazzo et al. 2004).

Climate in the Forsmark region

In the last step in the climate modelling study of the global warming climate, climatological data for the Forsmark region were extracted from the regional modelling. Figure 5-12 shows the grid boxes used for extraction of data. Information was extracted from the grid point located closest to the Forsmark site. As there is a high degree of spatial heterogeneity in land-sea distribution and topography, information from the surrounding eight grid boxes were also used to discuss uncertainties related to these inhomogeneities.

In addition to the results from the modelled case, data from the simulation of the present climate (1961–2000) (RP-r) and from the CRU observations representing conditions in the late 20th century are also shown for the Forsmark region (Figure 5-13). In addition to this, results from three other climate-change simulations with RCA3 for the 21st century as described in Persson et al.(2007) are also shown. These simulations follow the A2, A1B and B2 emission scenarios from IPCC AR4 (Nakićenović and Swart 2000). The A1B emission scenario leads to greenhouse-gas concentrations close to the one in the *global warming climate case* by the end of the 21st century. The two other scenarios have more (A2) or less (B2) emissions than the A1B scenario.

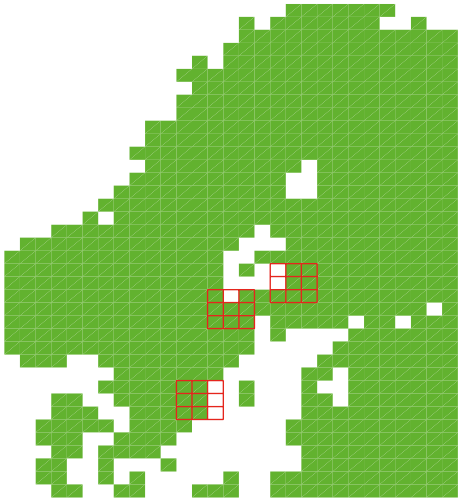

Figure 5-12. *Land (green) sea extent (white) in the regional climate model in the Fennoscandian region used for the global warming climate simulation. The 3 × 3-grids represent grid boxes covering the Forsmark, Oskarshamn and Olkiluoto sites (centre box) and the eight surrounding boxes. Grid boxes with a land fraction lower than 20 % are not filled. Results from Oskarshamn and Olkiluoto are presented in Kjellström et al. (2009).*

The fairly small annual temperature range in the present climate is even smaller in the future global warming climate for the Forsmark region (Figure 5-13, upper row, first column). This reduction in the seasonal cycle of temperature is a consequence of the future warming being stronger in winter than in summer. The snow season is much shorter, or even totally absent, in the warm climate. The seasonality of the runoff is closely connected to the presence or absence of snow. In the warmer future climate, the spring peak in runoff is absent and there is a more widespread wintertime maximum related to the large amounts of precipitation for that season.

In the global warming simulation, the spread in the presented variables due to differences in geographical location is reduced compared with that in the simulation of the present climate. This is partly a result of the land uplift turning two of the Baltic Sea grid boxes east of Forsmark into land in the *global warming climate case*. Thereby, the surrounding area becomes more homogeneous than in the present-day situation. When including also the uncertainty ranges based on results from the three other climate simulations for the 21st century, also simulated with RCA3 (Persson et al. 2007), it is seen that the weakening of the annual cycle is a robust trend when going to a warmer climate.

50-year averages values from the regional global warming climate simulation show that the annual mean air temperature in the Forsmark region is +8.3 °C. This is a temperature increase of 3.6 °C compared with the simulated present climate (1961–2000). The future warming is stronger in winter than in summer and there is an associated reduction in the seasonal cycle amplitude in temperature. The mean annual precipitation in the region is 804 mm, which is an increase of 138 mm (or 20 %) compared with the simulated present climate. Most of the precipitation increase occurs during the winter season (DJF). The snow season is much shorter than at present or even totally absent (Figure 5-13). Finally, the annual surface runoff is 337 mm in this exemplified global warming climate, which is an increase of 162 mm compared with the present climate. Given the uncertainties and assumptions used in the climate modelling, and the CO_2 level chosen, the model results thus show that the global warming climate in the Forsmark region, may be characterized by a clearly warmer and wetter climate than at present, and also that the surface runoff is significantly increased.

The major uncertainties in the climate simulation are related to uncertainties in forcing, model formulation and natural variability. These uncertainty aspects are discussed in detail in Kjellström et al. (2009).

Another recent study that focussed on regional climate modelling is Kjellström et al. (2010b) where changes in seasonal mean temperature, precipitation and wind over Europe were studied in an ensemble of 16 regional climate model simulations for 1961–2100. The study used the A1B emission scenario (Nakićenović and Swart 2000) in which the CO_2 equivalents in RCA 3 were set to 902 ppmv, somewhat higher than the 841 ppmv used in Kjellström et al. (2009). Six-member ensemble means of winter season (DJF) conditions suggest an increase in temperature by c 4 °C and precipitation by 20–30 % in south central Sweden, including the Forsmark region, by year 2100. Corresponding model ensemble means for the summer season (JJA) indicate an air temperature increase of 2–3 °C and a precipitation increase of c 10 %. The study also shows that the climate-change signal gets stronger the larger the forcing becomes, i.e. more greenhouse-gas emissions leads to a stronger warming and larger changes in precipitation. The results of the A1B-scenario-simulations are thus in line with the detailed results described above from Kjellström et al. (2009). Similar results were obtained also in the SWECLIM project (Rummukainen 2003, Tjernström et al. 2003). Other modelling results that give similar pictures of future global warming climates are reported in BIOCLIM (2003), Lind and Kjellström (2008) and Collins et al. (2013).

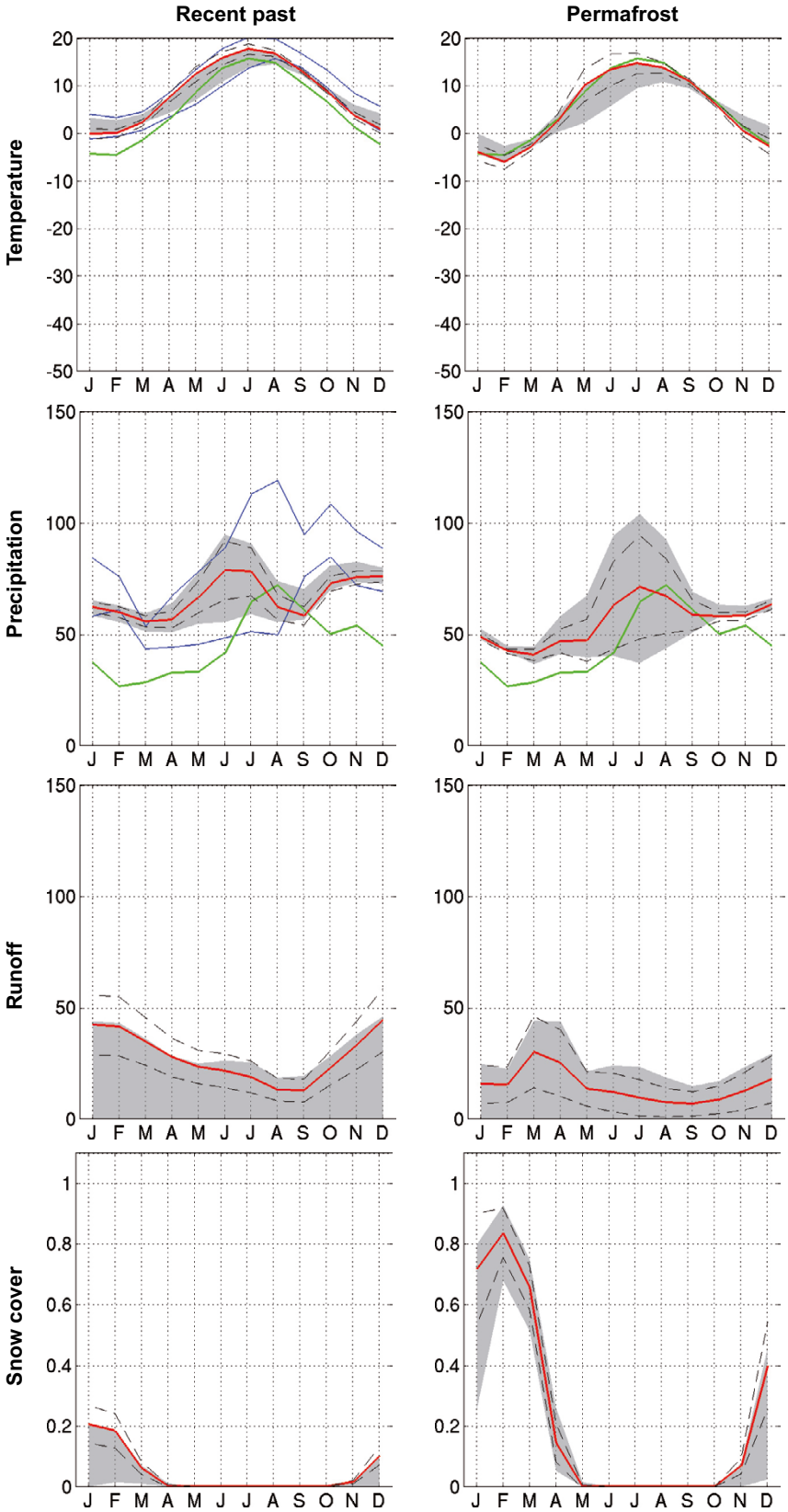

Figure 5-13. *Simulated seasonal cycles of temperature (°C), precipitation (mm month^{-1}), runoff (mm month^{-1}) and snow fraction (dimensionless ranging from 0 to 1) at the grid box closest to the Forsmark site (red line). The spatial variability in the 3 × 3-grid (Figure 5-12) is displayed with the dashed lines representing ± 1 standard deviation calculated from the 9 grid boxes, and the grey area representing the absolute maximum and minimum, of the 9 grid boxes. The green line for temperature and precipitation is the observed seasonal cycle from the CRU data set in the period 1961–1990. In the global warming climate case (left column), an additional uncertainty range defined by ± 1 standard deviation of the data calculated from the 9 surrounding grid boxes from three additional simulations for the 21st century with RCA3 is shown with blue full lines. From Kjellström et al. (2009).*

5.2 Extended global warming climate case

5.2.1 Background and definition of the climate case

There is a large range of potential future climate developments when considering the combined effect of natural climate variability and anthropogenic climate change (IPCC 2013a). One such case is the *global warming climate case* described in Section 5.1, approximately corresponding to the IPCC AR5 emission scenario RCP4.5. In order to cover a reasonably broad array of future climate developments based on present knowledge, an *extended global warming climate case* is also included in the PSAR. This case describes a future climate heavily influenced by anthropogenic emissions of greenhouse gases, resulting in a strong global warming comparable to the IPCC AR5 emission scenario RCP8.5. In this emission scenario, cumulative fossil-fuel emissions of ~5000 Pg C are envisaged by 2300 AD at the latest, and the global annual mean surface air temperature is projected to increase by 2.6–4.8 °C (relative to present) at the end of 21st century (Appendix E) and to reach its maximum increase of 4.9–12.5 °C within the first 500–1200 years after present (Figure 5-14). Hence, the global annual mean surface temperature in the *extended global warming climate case* is estimated to be about 2 °C higher by 2100 AD and on average 4 °C higher until 12000 AD than in the *global warming climate case* (Figure 5-14).

The surface air temperature increase at Forsmark is assumed to be 1.2 to 1.5 times higher than the global average (Appendix F), culminating in a maximum average temperature of nearly 17 °C (~11 °C higher than at present) within the next millennium (Figure 5-15 and Table 5-8). Put in perspective, the maximum average temperature at Forsmark under this scenario is comparable to present-day temperatures in southern Spain. Subsequent to the peak increase, there is a slow decline of the surface air temperature anomaly as a result of gradually lower atmospheric CO_2 concentrations (Figure 5-15). In summary, it is estimated that between 50 and 85 % of the maximum temperature anomaly will persist for longer than 10 ka (Appendix F).

As a result of the higher annual mean temperatures, also the annual precipitation at Forsmark is assumed to be higher in the *extended global warming climate case* than in the *global warming climate case*. The peak average precipitation increase is estimated to be ~45 % (Figure 5-15) which corresponds to more than 800 mm annual precipitation at Forsmark (Table 5-8).

It is worth noting that the assumed cumulative fossil-fuel emission for RCP8.5 is still lower than the known total carbon reserves available at present, estimated to be between ~9500 and 15700 Pg C (Rogner et al. 2012). One consequence of this emission scenario, together with the known future insolation changes from the orbital cycles, is the possibility of a very long duration of the present interglacial period, prior to the onset of the next cold glacial period. To this end, 100 ka of temperate climate conditions is added prior to the onset of the *reference glacial cycle* for the *extended global warming climate case*.

Table 5-8. Summary of the Forsmark surface air temperature and precipitation until 12000 AD in the *extended global warming climate case*. The lower and upper bounds refer to the uncertainty range and the average estimate to the solid lines in Figure 5-15. Details on how the uncertainty range has been constructed are provided in Appendix F.

	Surface air temperature (°C)			Precipitation (mm)		
Time slice	**Lower bound**	**Average estimate**	**Upper bound**	**Lower bound**	**Average estimate**	**Upper bound**
2100 AD	8.6	10.5	12.7	620	680	770
Maximum value (2550–3200 AD)	11.4	16.7	24.2	670	830	1100
12000 AD	8.5	13.1	21.4	620	740	1020

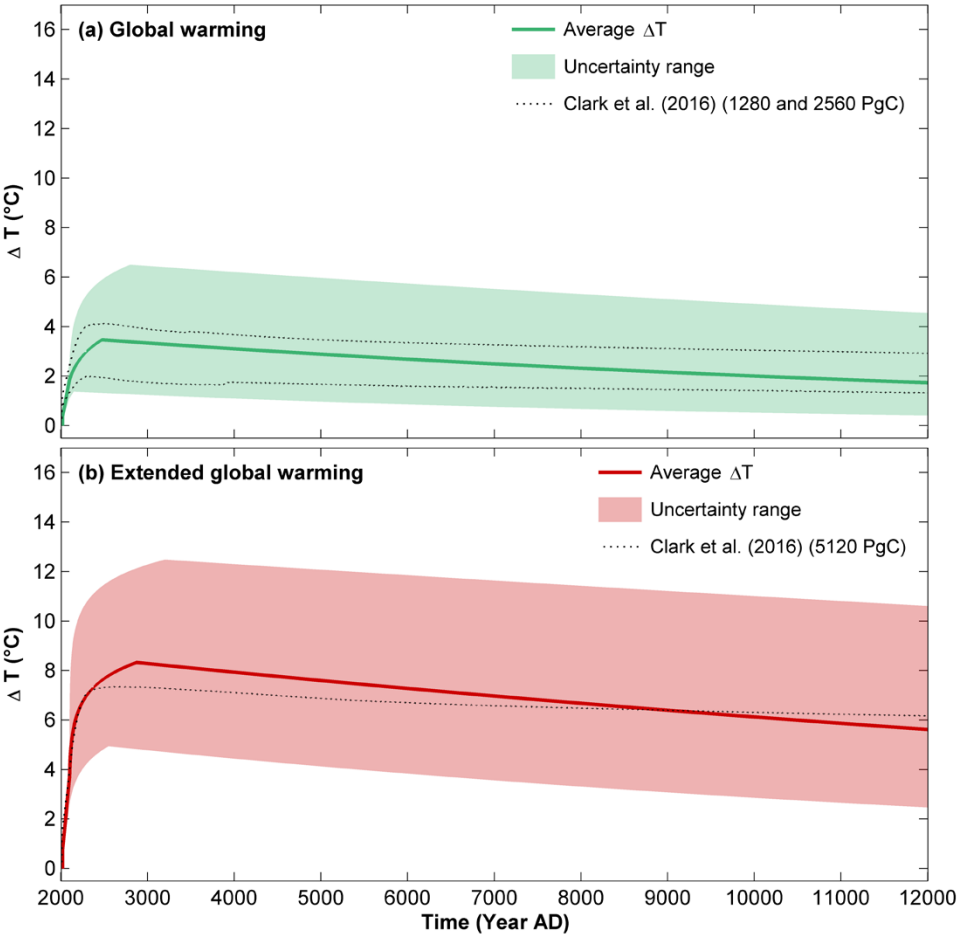

Figure 5-14. *Constructed global annual mean surface air temperature change until 12000 AD (relative to present) for (a) the global warming and (b) the expended global warming climate cases. The shaded areas represent uncertainty ranges. The solid lines have been calculated using average values of the parameters that were used construct the uncertainty range. To that end, the solid lines illustrate typical mid-range global-mean temperature changes over the next 10 ka. The figure also shows the evolution of global annual mean surface air temperature change from the Clark et al. (2016) projections with 1280 and 2560 Pg C cumulative emissions (comparable to RCP4.5; panel a), and 5120 Pg C cumulative emissions (comparable to RCP8.5; panel b). Typical uncertainties in the Clark et al. (2016) projections are within the range of 1–2 °C (Table F-1 in Appendix F). Details on how the global mean temperature curve and its uncertainty range have been constructed are provided in Appendix F.*

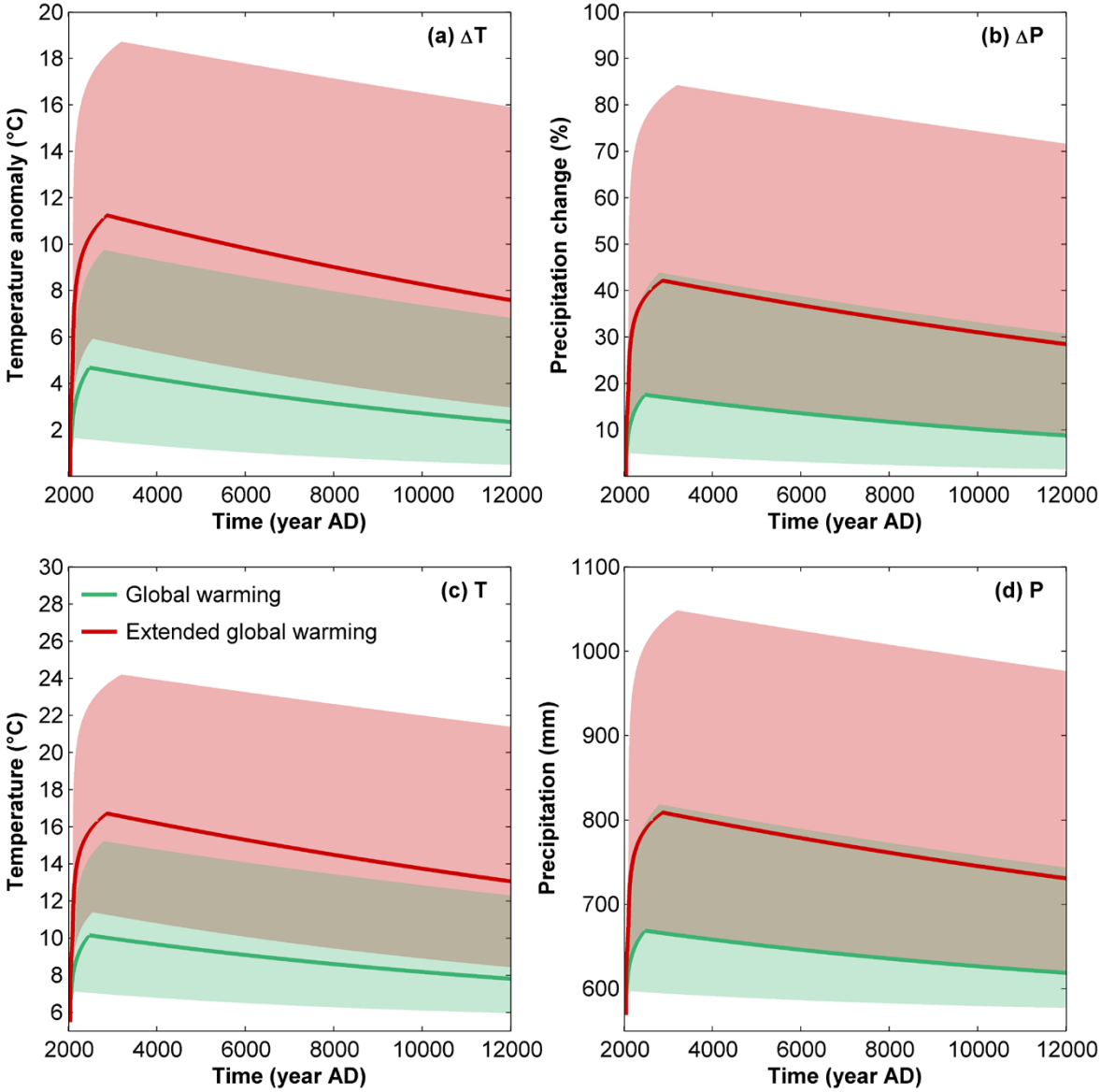

Figure 5-15. *Constructed changes in (a) annual mean surface air temperature and (b) annual precipitation at Forsmark until 12000 AD for the global warming (green) and extended global warming (red) climate cases. Panels (c) and (d) show the resulting annual mean surface air temperature and annual precipitation at Forsmark calculated from the temperature and precipitation changes in panels (a) and (b) and the present-day climate in Table 2-1. The shaded areas represent uncertainty ranges. The solid lines are calculated using average values of the parameters used to construct the uncertainty range. To that end, the solid lines illustrate typical mid-range temperature and precipitation changes at Forsmark over the next 10 ka. Details on how the temperature and precipitation curves have been constructed are provided in Appendix F. Note that the possible influence of a future AMOC collapse (e.g. Liu et al. 2017) on the surface air temperature at Forsmark has not been included in the uncertainty range in this figure due to the low confidence of this uncertainty assessment. This uncertainty is instead shown and discussed in detail in Appendix F.*

5.2.2 Ice-sheet evolution

The *extended global warming climate case* results in there being no ice-sheets present at the Forsmark site during the coming 120 ka. The first glacial conditions at Forsmark occur at ~160 ka (158 ka) after present.

5.2.3 Changes in sea-level and relative sea-level

Given the envisaged strong global warming in the *extended global warming climate case,* comparable to the RCP8.5 emission scenario (Appendix E), also the sea-level response to the warming is expected to be strong. During the last decade there has been a substantial increase in the number of research papers dealing with sea-level rise in a warming climate, with several key studies emerging over the last few years presenting sea-level projections based on the individual contributions from melting of the Greenland and Antarctic ice-sheets, melting of glaciers, and thermal expansion of ocean water as the main contributors. Several recent studies also focus on estimating the large uncertainties associated with the sea-level projections. The results of this rapidly developing field in terms of sea-level projections and uncertainty estimates are here compiled for the RCP8.5 emission scenario, and used as basis for assessing potential relative sea-level change at the Forsmark site under this scenario. The compilation is divided into relative sea-level change (i) until 2100 AD, (ii) between 2100 AD and 12000 AD, and iii) beyond 12000 AD for the next 120 ka.

Relative sea-level change at Forsmark until 2100 AD

Potential changes in relative sea-level until 2100 AD are of importance for the planning and construction of the spent nuclear fuel repository, since the planned operational phase covers the time span up to around 2080 AD. Relative sea-level changes over this time period are of importance also for motivating the initial state in the PSAR. Relative sea-level projections until 2100 AD at Forsmark are therefore assessed here, based on current scientific knowledge. Since the purpose is to provide input to e.g. construction planning of critical infrastructure, the present analysis does not focus on the most plausible projections of 2100 AD sea-level rise. Instead, the focus is on high-end low-probability projections, based on the RCP8.5 emission scenario (Meinshausen et al. 2011, Appendix E) which forms the basis for the *extended global warming climate case*.

Pessimistic scenarios of the total sea-level rise at Forsmark until 2100 AD need to consider contributions from both the rise of mean sea-level through slow long-term processes, such as ocean thermal expansion and ice-sheet melting, and the contributions from fast short-term processes, i.e. storm surges. When considering construction at coastal sites, it is therefore useful to distinguish between the slow rise of mean sea-level and temporary short storm surge contributions with a typical duration of days to weeks. A key point here is that it is possible to monitor the mean sea-level rise due to slow long-term processes over the coming decades. This gives the important opportunity to take further necessary action if and when mean sea-level rise proves to be higher than is foreseen and planned for at present.

The relative sea-level evolution at Forsmark and elsewhere is determined by the net effect of *eustatic* changes (i.e. the absolute changes in sea-level associated with e.g. changes in the volume and spatial distribution of ocean water) and *isostatic* changes (see also Section 3.3.1). At the Forsmark site, the latter is manifested through glacial isostatic rebound with an uplift rate of 6.7 mm a^{-1} (Vestøl et al. 2019). The present-day net effect of the two processes at the Forsmark site is a slow sea regression, i.e. a lowering and off-shore migration of the shoreline, at a rate of approximately 4.1 mm a^{-1} (Table 5-2).

An overview of the scientific knowledge on past, present and future sea-level evolution was given in IPCC AR5 (Church et al. 2013). The review presented by Church et al. included a wide range of processes contributing to eustatic changes, such as thermal expansion of ocean water, melting of glaciers and ice-sheets, rapid dynamics of ice-sheets, and land water storage. In the IPCC AR5, Church et al. (2013) stated that there is only low confidence in the projections made using semi-empirical models (e.g. Vermeer and Rahmstorf 2009), and also in kinematic constraints on ice-sheet melting (Pfeffer et al. 2008), and therefore excluded all available results from such models. Consequently, the final choice of AR5 sea-level projections for 2100 AD was based on a remarkably narrow selection of models/projections, which resulted in a narrow range of global-mean sea-level (GMSL) projections for 2100 AD presented by IPCC (0.52 to 0.98 m for RCP8.5).

Since the publication of AR5, many studies have reported the importance of including results not only from process-based models but also from semi-empirical and statistical models. Many of the more recent studies indicate that AR5 underestimated the GMSL rise to 2100 AD by the model selection made at the time. IPCC recently updated their sea-level projections in the Special Report on the Ocean and Cryosphere in a Changing Climate (SROCC, IPCC 2019). Compared to AR5, GMSL rise projections in SROCC are about 0.1 m higher under RCP8.5, and the 5–95 % confidence interval extends beyond a 1 m rise due to a larger projected ice loss from the Antarctic ice-sheet. For the *extended global warming climate case* in the PSAR, a review of published information on future sea-level projections since 2012 is made for the RCP8.5 emission scenario.

The different processes contributing to high relative sea-level stand at Forsmark 2100 AD are discussed in the following.

Mean relative sea-level change (slow long-term change)

The slow long-term processes that contribute to changes in mean sea-level include thermal expansion of warming ocean water, melting of the Greenland and Antarctic ice-sheets and of glaciers, rapid ice-sheet dynamics and changes in land water storage. Sea-level rise associated with these processes is distributed over the world oceans. However, the distribution is not uniform – some regions experience a smaller rise than the global-mean value whereas the situation is the opposite in other regions. These regional differences, which may be substantial, are caused by gravitational and rotational effects, ocean dynamics, regional differences in water temperature and salinity, winds and air pressure, and air-sea heat and freshwater fluxes, see Church et al. (2013), IPCC (2019) and references therein. The present GMSL rise amounts to 3.1 ± 0.3 mm a^{-1} with an acceleration of 0.1 mm a^{-2} over the period 1993–2017 (WCRP Global Sea Level Budget Group 2018). Between 1993 and 2015, the relative contributions to GMSL rise from thermal expansion, glaciers, Greenland and Antarctica have been 49 %, 20 %, 17 % and 11 % respectively (IPCC 2019). This is in line with Nerem et al. (2018) who describes an ongoing acceleration in ice loss from the Antarctic and Greenland ice-sheets. Studies showing that the GMSL rise is accelerating make the case for considering worst-case sea-level rise scenarios strong, an approach that is adopted in the present *extended global warming climate case*.

For the present analysis of potential sea-level rise at Forsmark until 2100 AD, a starting point is to assess the spread in projections of GMSL rise in the scientific literature. Therefore, a review of published sea-level projections made since 2012 for the RCP8.5 emission scenario has been compiled (Table 5-9). The table includes most of the recent estimates of GMSL rise as well as associated local projections of relative sea-level for Stockholm and Forsmark available in a few of the studies. Studies that only provide regional sea-level estimates from other regions have not been included. The compilation includes studies from 2012 to 2018, as well as one older study, previously used by SKB (Pfeffer et al. 2008), the recent IPCC SROCC (IPCC 2019) and relative sea-level projections under the RCP8.5 scenario from a recent dedicated study on sea-levels at Forsmark (Pellikka et al. 2020). In cases where values in review papers or reports differ from the corresponding values in the original papers, the values from the original publication have been used. Some compilations do not mention the reason for not using original paper values, whereas other do (Horton et al. 2018). The compilation of RCP8.5 GMSL for 2100 AD is illustrated in Figure 5-16.

As can be seen in Figure 5-16, most GMSL median values under the RCP8.5 emission scenario are lower than 1 m, whereas the upper end of the 17–83 % confidence interval (usually called the *likely* range[4]) is typically around 1 m. The upper end of the 5–95 % percentile range (i.e. the *very likely* range[4]) is typically around 1.5 m or between 1.5 and 2 m (light blue bars in Figure 5-16). High-end GMSL values are typically around 2 m and in some case above 2.5 m, depending on the selected confidence interval (red colours in Figure 5-16). Estimated local relative sea-level values for Stockholm and Forsmark are clearly below the corresponding GMSL values. This is because the ongoing isostatic uplift in the region compensates for a significant portion of the eustatic rise, see below.

[4] Because it is more likely that the sea level would end up in the broader 5–95 % interval than in the narrower 17–83 % interval, the former interval is often called the very likely range and the latter the likely range.

The compilation in Table 5-9 and Figure 5-16 clearly demonstrates the large spread in recent estimates of 21st century sea-level rise projections. The differences relate to e.g. different methodologies used in the studies (for instance the use of process-based models versus statistical models/semi-empirical models) and also to how different processes related to ice-sheet melting have been handled. Overall, the large spread in the projections reflect the large prevailing uncertainty within this scientific field. This uncertainty mainly relates to the uncertainties in the response of the Greenland and Antarctic ice-sheet to climate warming.

A pessimistic assessment of the maximum mean sea-level rise at Forsmark until 2100 AD for the *extended global warming climate case* can be based on the information compiled in Table 5-9. In terms of high-end projections, two studies stand out in the compilation – the *likely* and *very likely* ranges by Kopp et al. (2017) and Le Bars et al. (2017) (Figure 5-16 and Table 5-9). These two studies are the only ones that have accounted for potential sea-level rise as a result of the Antarctic marine ice cliff instability (MICI) hypothesis, first described by DeConto and Pollard (2016). While it has long been known that marine ice-sheets are vulnerable to an adverse feedback loop once their retreat is triggered (the marine ice-sheet instability or MISI hypothesis), the modelling study of DeConto and Pollard (2016) took into account new potential physical processes regarding the dynamics of vertical ice cliffs. The Antarctic coastline is fringed by large floating ice shelves that buttress the flow of ice and hence have a stabilizing effect on the grounded part of the ice-sheet. The MICI hypothesis suggests that the vertical ice cliffs created by the disintegration of ice shelves could collapse rapidly, causing a significant additional contribution to sea-level rise. At the time of writing, however, the hypothesis is controversial and under debate in the scientific community (e.g. Edwards et al. 2019). In addition, Edwards et al. (2019) argue that the interpretation made by Le Bars et al. (2017) about the shape of the probability distribution of the Antarctic contribution leads to an overestimation of the GMSL rise. Because of this, the assessment of the Forsmark sea-level rise until 2100 AD is not solely based on the maximum values of Kopp et al. (2017) and Le Bars et al. (2017).

Instead, the assessment of the Forsmark mean sea-level rise until 2100 AD is based on a dedicated study of Pellikka et al. (2020). In this study, the mean sea-level rise under RCP8.5 was analysed using a selected ensemble of GMSL projections from nine recent studies (highlighted by asterisks in Table 5-9). The ensemble intentionally includes both process-based and semi-empirical projections, including the high-end projections by Kopp et al. (2017) and Le Bars et al. (2017). It also includes low-end projections such as Church et al. (2013). To obtain a sea-level rise estimate for Forsmark, the nine global projections were first normalized to a common time interval (2000–2100 AD) by assuming a constant acceleration until 2100 AD and an initial eustatic sea-level rise of 3.2 mm a^{-1}. The assumption of a constant acceleration between 2000 and 2100 AD stems from the fact that many studies have shown that the GMSL rise until 2100 AD is typically about 3–5 times greater than until 2050 AD (e.g. Jevrejeva et al. 2012, Mengel et al. 2016, Kopp et al. 2017). Subsequently, the normalised GMSL projections were regionalised to the Forsmark area by accounting for the regional-to-global ratio of the ocean thermal expansion as well as the uneven regional distribution of sea-level rise due to melting of the Greenland and Antarctic ice-sheets and the world's glaciers. The resulting Forsmark sea-level rise from the regionalisation procedure in Pellikka et al. (2020) was found to be about 20 % lower than the GMSL rise. Finally, to combine all the included studies in the Pellikka et al. (2020) ensemble into a single estimate of the mean sea-level rise at Forsmark, the normalised and regionalised projections were summed into new probability distributions, assuming equal weight for all nine projections (i.e. all projections were assessed to be equally likely). The resulting probability distribution was then used to project the mean sea-level rise at Forsmark for the years 2050, 2080 and 2100 AD for different carbon emission scenarios. As previously mentioned, for the *extended global warming climate case*, the results from the RCP8.5 emission scenario are used.

Apart from the MICI-modulated high-end estimates by Kopp et al. (2017) and Le Bars et al. (2017), the upper 95 % uncertainty of the Forsmark sea-level rise (assuming no compensation by local isostasy) in Pellikka et al. (2020), +1.79 m by 2100 AD, is among the highest in the compilation (Table 5-9,) and is therefore suitable for the present analysis. Furthermore, the projections of the 2100 AD mean sea-level rise in Pellikka et al. (2020) results in very similar values for Forsmark as the regional probability distribution modelling of Grinsted et al. (2015), see Table 5-9 and Figure 5-16. This also points to the appropriateness of using Pellikka et al. (2020) for the present analysis. Adding the isostatic contribution, i.e. 6.7 mm a^{-1} (Vestøl et al. 2019, see Table 5-2), results in a median (50 % probability) Forsmark *relative* sea-level that is comparable to the present level. The high-end low-probability Forsmark relative

sea-level projections in Pellikka et al. (2020) amounts to +1.11 m, +1.66 m and +2.17 m for the upper 95 %, 99 % and 99.9 % uncertainty levels, respectively. These values describe a pessimistic high mean relative sea-level projection for Forsmark in 2100 AD for the *extended global warming climate case*.

Table 5-10 and Figure 5-17 present the Forsmark values on mean sea-level rise until 2050, 2080 and 2100 AD under the RCP 8.5 emission scenario from Pellikka et al. (2020).

Table 5-9. Compilation of sea-level projections for 2100 AD under the IPCC RCP8.5 emission scenario published between 2012 and 2018. The table also include the recent IPCC SROCC compilation (IPCC 2019) and relative sea-level projections for Forsmark from a recent study by Pellikka et al. (2020). For a description of the emission scenario, see Church et al. (2013) and Appendix E. All values represent global mean sea-level (GMSL) rise, except for some values for Stockholm and Forsmark at the end of the table. The local values represent relative sea-levels for the sites, i.e. they are compensated for isostatic uplift. Most values are characterised by the median value and a 17–83 % confidence interval (i.e. the *likely range*) and a 5–95 % confidence interval (i.e. the *very likely range*). Note that the studies use different reference periods. Whilst some of the studies (e.g. the IPCC) use the 1986–2005 AD period as a baseline, other studies (e.g. Pellikka et al. 2020) use the mean sea-level in 2000 AD. The uncertainty range for DeConto and Pollard (2016) has been recalculated from 1σ standard error (± 0.36 m) to the 5–95 % confidence interval. In addition to the median, 5–95 %, and 17–83 % percentiles, the table also includes high-end sea-level projections using the 99 % and 99.9 % percentiles. The study by Pfeffer (2008) is included since it constituted the worst-case 2100 AD GMSL value in the previous safety assessment performed by SKB (SKB 2015). Some studies present several GMSL projections under the RCP8.5 emission scenario. From these studies, only the projection with the highest GMSL rise is included in this compilation. Note that the high-end projections by Pfeffer (2008) and Miller et al. (2013) are not calculated based on RCP8.5. Studies included in the ensemble of GMSL projections used in Pellikka et al. (2020) are indicated with an asterisk.

Sea-level 2100 AD (m) for RCP 8.5 Median values (percentile range within brackets)	Percentiles used for ranges in column one (comments within brackets)	High-end projections Percentile within brackets	Reference
0.74(0.52–0.98)	5–95 %	-	Church et al. (2013) (IPCC AR5)*
-	(Not RCP8.5)	2.0	Pfeffer et al. (2008)
1.10 (0.81–1.65)	5–95 %	-	Jevrejeva et al. (2012)*
1.02 (0.60–1.20)	5–95 %	-	Schaeffer et al. (2012)
-	-	2.25	Sriver et al. (2012)
0.77 (0.43–1.41)	(Not RCP8.5)	2.70	Miller et al. (2013)
(0.70–1.20) (0.50–1.50)	17–83 % 5–95 %	-	Horton et al. (2014)
0.80 (0.58–1.20) 0.80 (0.45–1.83)	17–83 % 5–95 %	-	Jevrejeva et al. (2014)*
0.79 (0.52–1.21) 0.79 (0.62–1.00)	5–95 % 17–83 %	1.80 (99 %) 2.50 (99.9 %)	Kopp et al. (2014)*
1.80	95 %	-	Rohling et al. (2013)
0.74 (0.45–1.04)	17–83 %	1.30	Slangen et al. (2014)
0.80 (0.58–1.20) 0.80 (0.45–1.83)	17–83 % 5–95 %	1.80 (99 %)	Grinsted et al. (2015)
0.75 (0.54–0.98) 0.75 (0.37–1.18)	17–83 % 5–95 %	 0.84 (0.51–1.67) High end 2.22 (99 %)	Jackson and Jevrejva (2016)
0.76 (0.59–1.05) 0.76 (0.52–1.31)	17–83 % 5–95 %		Kopp et al. (2016)*
0.85 (0.57–1.31)	5–95 %	-	Mengel et al. (2016)*

Table 5-9 continued.

Sea-level 2100 AD (m) for RCP 8.5 Median values (percentile range within brackets)	Percentiles used for ranges in column one (comments within brackets)	High-end projections Percentile within brackets	Reference
1.14 (0.55–1.73)	5–95 % (only Antarctic contribution)		DeConto and Pollard (2016)
0.90 (0.76–1.05)	5–95 %		Goodwin et al. (2017)*
1.46 (1.09–2.09) 1.46 (0.93–2.43)	17–83 % 5–95 %	-	Kopp et al. (2017)*
1.84 (0.81–2.92)	5–95 %		Le Bars et al. (2017)*
0.79 (0.65–0.97) 0.79 (0.58–1.11)	17–83 % 5–95 %	-	Nauels et al. (2017)
1.50 (1.03–1.90)	5–95 %	-	Wong et al. (2017)
0.84 (0.61–1.10)	5–95 %	-	IPCC (2019) (Special Report on the Ocean and Cryosphere in a Changing Climate)
0.37 (0.16–0.61)	5–95 %	-	SMHI (Nerheim et al. 2017) **Stockholm**
0.25 (0.04–0.49)	5–95 %	2.30 (95 % and including c 1.8 m storm surge)	SMHI (Nerheim et al. 2017) **Forsmark**
0.17 (−0.17–0.52) 0.17 (−0.41–0.80)	17–83 % 5–95 %	-	Kopp et al. (2014) **Stockholm**
0.25 (0.02–0.6) 0.25 (−0.13–1.17)	17–83 % 5–95 %	-	Grinsted et al. (2015) **Stockholm**
0.1 (−0.13–0.45) (−0.28–1.01)	17–83 % 5–95 %	- -	Grinsted et al. (2015) **Forsmark**
0.02 (−0.19–0.49) 0.1 0.02 (−0.29–1.11)	17–83 % 5–95 %	1.66 (99 %) 2.17 (99.9 %)	Pellikka et al. (2020) **Forsmark**

Storm surges and wave height (fast temporary changes)

Sea-level at coastal sites, such as Forsmark, varies on short time-scales due to variations in atmospheric pressure and winds associated with temporary weather systems. The resulting maximum present-day storm surge level at Forsmark, with an exceedance frequency of 10^{-2} events per year (i.e. a 100-year return period), was previously estimated to be +1.46 m (in RH2000) based on observations for the period 1976–2000 AD (Engqvist 2013, personal communication). The storm contribution to Forsmark sea-level rise for 2000 AD was also estimated by Pellikka et al. (2020) using an 850 year long simulation with a multi-component sea-level model. In their simulation, the storm surge level was found to be +1.56 m (in RH2000) for an exceedance frequency of 10^{-2} events per year. Similar values of the present-day storm surge levels at Forsmark have also been derived from SMHI (Nerheim et al. 2017). It should be noted that an exceedance frequency of 10^{-2} events per year means that there is a 45 % probability that a sea-level rise of this magnitude or higher occurs once in a 60-year time period (i.e. approximately the length of the operational period of the spent nuclear fuel repository), see Table 5-11. The sea-level may thus occasionally rise above this value, as illustrated by the highest observed storm surge in Forsmark, +1.45 m above mean sea-level for the year (corresponding to +1.59 m in RH2000), which occurred in 2007.

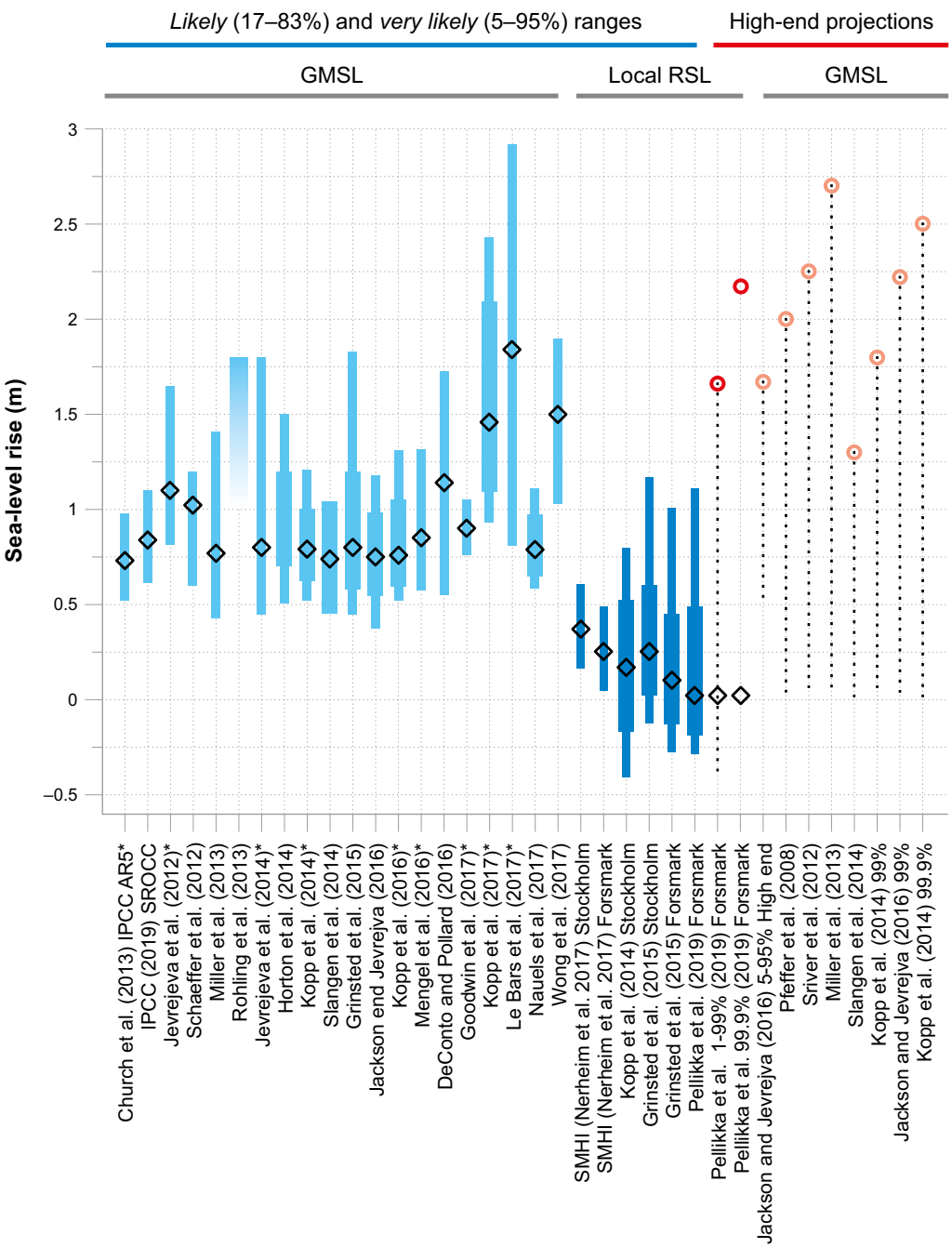

Figure 5-16. *Compilation of sea-level projections for 2100 AD under the IPCC RCP8.5 emission scenario and published between 2012 and 2018 (Table 5-9). The figure also include the recent IPCC SROCC compilation (IPCC 2019) and relative sea-level projections for Forsmark from a recent study by Pellikka et al. (2020). Rhomb symbols show median values (the 50 % percentile). Blue colours show the "likely" range (17–83 % confidence interval) and "very likely" range (5–95 % confidence interval), displayed as broad and narrow bars respectively. Red circles show high-end RCP8.5 projections (99 % and 99.9 % percentiles). Values representing global mean sea-level are shown in lighter blue and red colours, whereas local relative sea-level values (for Stockholm and Forsmark) are shown in darker blue and red colours. The local values are compensated for the isostatic uplift along the Baltic coast and therefore yield considerably lower maximum sea-level rise values (for corresponding percentiles) compared with GMSL values. The relatively small uncertainty interval given by SMHI (Nerheim et al. 2017), for example for Forsmark, compared with other recent estimates (e.g. Pellikka et al. 2020), is a result of SMHI using the IPCC AR5 (Church et al. 2013) estimates as a basis, which are known to include only a narrow selection of GMSL models/projections. Also note that the high-end projections by Pfeffer (2008) and Miller et al. (2013) are not calculated based on RCP8.5 (Table 5-9). Studies included in the ensemble of GMSL projections used in Pellikka et al. (2020) are indicated with an asterisk.*

A 10^{-2} exceedance frequency is arguably too high to be used in the planning and construction of coastal-near critical infrastructure such as the spent nuclear fuel repository. Therefore, in order to make a more useful assessment of the storm surge contribution to sea-level rise, it is necessary to account for lower probability events characterised by lower exceedance frequencies, such as 10^{-3}, 10^{-4} and even 10^{-5} events per year (Table 5-11). To estimate the 2000 AD sea-level rise for these low exceedance probabilities, Pellikka et al. (2020) extrapolated the probability distribution of daily sea-level maxima from the 850 year sea-level simulation towards lower frequencies. Their result suggests that the sea-level increases by ~0.2–0.3 m for every order of magnitude reduction of the exceedance frequency, resulting in a present-day temporary storm surge level of +1.81 m, +2.06 m and +2.32 m (in RH2000) for an exceedance frequency of 10^{-3}, 10^{-4} and 10^{-5} events per year, respectively.

The storm surge contributions from Pellikka et al. (2020), used in the assessment of maximum sea-level rise at Forsmark, are summarised in Table 5-10 and Figure 5-17.

Table 5-10. Contributions to extreme relative sea-level rise at Forsmark in 2050, 2080 and 2100 AD under the RCP8.5 emission scenario from Pellikka et al. (2020). The contributions are divided into mean relative sea-level rise (i.e. slow long-term eustatic change compensated for isostatic rebound) and storm surges (i.e. fast temporary processes). The sea-level rise is given both in relation to the present-day sea-level at Forsmark, defined as the mean sea-level in 2000 AD, and in the Swedish national reference height system RH2000. The difference in Forsmark in mean sea-level between RH2000 and 2000 AD is +0.17 m. (https://www.smhi.se/hfa_coord/BOOS/dbkust/mwreg_MWekvationer_2020.pdf). The mean relative sea-level change is presented for the 95 %, 99 % and 99.9 % percentiles (corresponding to a 5 %, 1 % and 0.1 % probability of exceedance, respectively). Contributions from storm surges and the total relative sea-level rise are presented for exceedance probabilities of 10^{-3}, 10^{-4} and 10^{-5} events per year. The probability distributions for the mean relative sea-level change and the daily sea-level maxima were summed into a new distribution under the assumption that they are independent (Pellikka et al. 2020).

Type of contribution	Contribution to relative sea-level rise at Forsmark 2050 AD (m)	Contribution to relative sea-level rise at Forsmark 2080 AD (m)	Contribution to relative sea-level rise at Forsmark 2100 AD (m)
Mean relative sea-level rise (m)	**Relative to mean sea-level in 2000 AD:**	**Relative to mean sea-level in 2000 AD:**	**Relative to mean sea-level in 2000 AD:**
	+0.20 (95 %)	+0.66 (95 %)	+1.11 (95 %)
	+0.34 (99 %)	+1.01 (99 %)	+1.66 (99 %)
	+0.48 (99.9 %)	+1.35 (99.9 %)	+2.17 (99.9 %)
	RH2000:	**RH2000:**	**RH2000:**
	+0.37 (95 %)	+0.83 (95 %)	+1.28 (95 %)
	+0.51 (99 %)	+1.18 (99 %)	+1.83 (99 %)
	+0.65 (99.9 %)	+1.52 (99.9 %)	+2.34 (99.9 %)
Storm surge level (m) with exceedance frequency (events per year)	**Relative to mean sea-level in 2000 AD:**	**Relative to mean sea-level in 2000 AD:**	**Relative to mean sea-level in 2000 AD:**
	+1.64 (10^{-3})	+1.64 (10^{-3})	+1.64 (10^{-3})
	+1.89 (10^{-4})	+1.89 (10^{-4})	+1.89 (10^{-4})
	+2.15 (10^{-5})	+2.15 (10^{-5})	+2.15 (10^{-5})
	RH2000:	**RH2000:**	**RH2000:**
	+1.81 (10^{-3})	+1.81 (10^{-3})	+1.81 (10^{-3})
	+2.06 (10^{-4})	+2.06 (10^{-4})	+2.06 (10^{-4})
	+2.32 (10^{-5})	+2.32 (10^{-5})	+2.32 (10^{-5})
Total combined relative sea-level rise during storm (m) with exceedance probability (events per year)	**Relative to mean sea-level in 2000 AD:**	**Relative to mean sea-level in 2000 AD:**	**Relative to mean sea-level in 2000 AD:**
	+1.70 (10^{-3})	+2.44 (10^{-3})	+3.35 (10^{-3})
	+1.96 (10^{-4})	+2.70 (10^{-4})	+3.62 (10^{-4})
	+2.21 (10^{-5})	+2.95 (10^{-5})	+3.88 (10^{-5})
	RH2000:	**RH2000:**	**RH2000:**
	+1.87 (10^{-3})	+2.61 (10^{-3})	+3.52 (10^{-3})
	+2.13 (10^{-4})	+2.87 (10^{-4})	+3.79 (10^{-4})
	+2.38 (10^{-5})	+3.12 (10^{-5})	+4.05 (10^{-5})

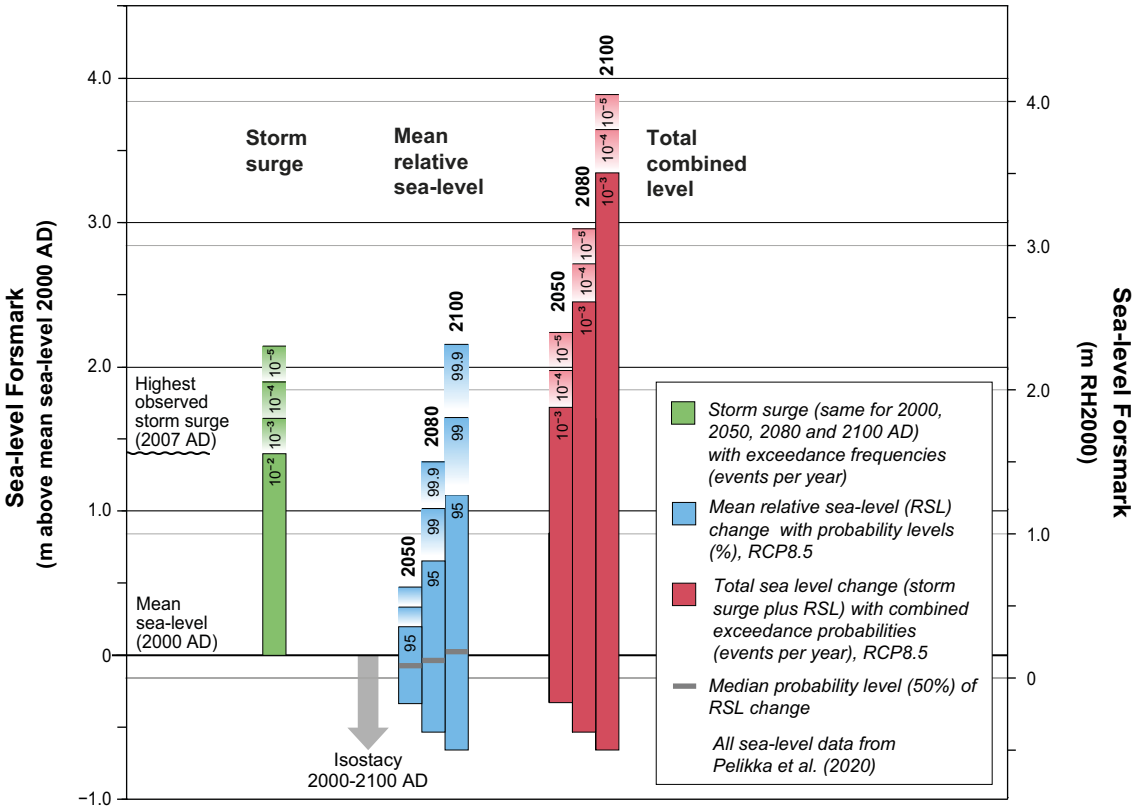

Figure 5-17. *Relative sea-level projections for 2050, 2080 and 2100 AD under the RCP8.5 emission scenario for Forsmark, based on data from Pellikka et al. (2020) presented in Table 5-10. The projected maximum total relative sea-level is obtained by combining the contribution from the long-term mean relative sea-level rise and the maximum contribution from fast but temporary storm surges. The rise in Forsmark mean relative sea-level is shown for the median probability level (grey horizontal lines within the blue bars) as well as for the 95 %, 99 % and 99.9 % percentiles, corresponding to 5 %, 1 % and 0.1 % probability, respectively. Because of the ongoing glacial isostatic rebound, a significant portion of the mean sea-level rise at Forsmark is compensated for by the isostatic uplift (amounting to 0.34 m, 0.54 m and 0.67 m until 2050, 2080 and 2100 AD, respectively). The storm surge levels are given for a range of exceedance frequencies between 10^{-2} and 10^{-5} events per year, and are assumed to be constant-in-time for the entire period between 2000 and 2100 AD, see the text. The total combined relative sea-level is shown for a range of combined exceedance probabilities between 10^{-3} and 10^{-5} events per year. The left axis shows the sea-level rise relative to the mean sea-level in 2000 AD, whereas the right axis shows corresponding elevations in the RH2000 system. In Forsmark, the difference between RH2000 and the mean sea-level in 2000 AD is +0.17 m (https://www.smhi.se/hfa_coord/BOOS/dbkust/mwreg_MWekvationer_2020.pdf).*

Table 5-11. Relationship between return time, exceedance frequency, and probability. The relationship is described by $P = 1-(1-1/T)^n$, where P is the probability, n is the length of the period over which the probability is computed (years), and T is the return time (years). The exemplified 60 year period in column three approximately corresponds to the planned length of the operational period for the spent nuclear fuel repository (2020–2080 AD).

Return time (T) [years]	Exceedance frequency [events per year]	Probability (P) n = 60 years	Probability (P) n = 100 years (e.g. 2000–2100 AD)
100	10^{-2}	45 %	63 %
1000	10^{-3}	6 %	10 %
10000	10^{-4}	0.6 %	1 %
100000	10^{-5}	0.06 %	0.1 %

The storm surge contribution to the sea-level rise at Forsmark until 2100 AD is potentially also influenced by changes in the near-surface wind field in a warmer RCP8.5 climate. For example, the modelling study of Meier (2006) suggests that the changes in the weather patterns in a warmer climate may serve to increase the temporary high sea-level in 2100 AD by approximately 0.3 m in the Forsmark region compared to present day. The notion of higher storm surges in warmer climate is however somewhat refuted in Pellikka et al. (2020). Based on their own investigations and other studies, e.g. Ruosteenoja et al. (2019), they argue that there is no significant systematic change of the near-surface wind field in climate modelling projections until 2100 AD. Therefore, the storm surge contributions in Pellikka et al. (2020), estimated for the year 2000 AD, are assumed to be identical for the entire period from 2000 to 2100 AD.

During storms, windy conditions typically contribute to an increase in the height of the waves entering the Forsmark shoreline. Wave height around the location of the spent nuclear fuel repository, induced by a northerly storm of 25 m s^{-1}, was modelled in Brydsten et al. (2009) using the STWAVE model, which simulates wave refraction and shoaling, wave breaking, diffraction, wind-induced wave growth, wave-wave interactions and white capping (McKee Smith et al. 2001). The resulting wave height (defined as the distance between the wave crust and through) is shown in Figure 5-18. The wave height in the northern part of Öregrundsgrepen amounts to more than 7 metres, but declines rapidly down towards Forsmark. The highest waves in the vicinity of the planned spent nuclear fuel repository are at most ~0.6–1 m. Since the wave height in STWAVE is defined as the distance between the wave crest and through, the contribution from those waves on the temporary sea-level rise would be approximately 50 %, i.e. ~0.3–0.5 m. However, this simulation was not made in enough detail in order to resolve the detailed effects of these waves on the Forsmark shoreline. Also, the modelled wind speed was not pessimistically chosen for storm conditions. Therefore, these results are used only as a first-order indication of wave heights during storm, but not in the assessment of the maximum temporary sea-level rise at Forsmark by 2100 AD.

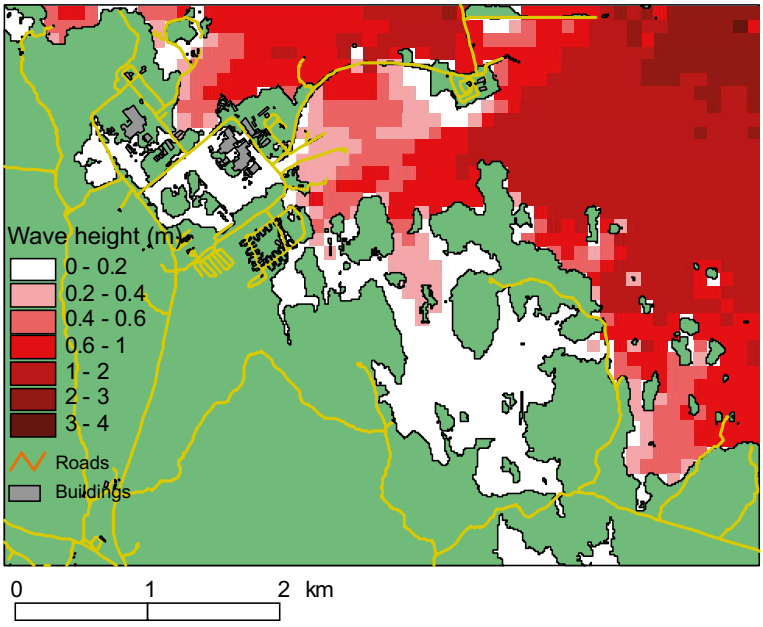

Figure 5-18. *Calculated storm-induced wave height by northerly winds of 25 m s^{-1} using the STWAVE model. Wave height is defined as the distance between the wave crest and trough. The contribution from wave height to the temporary sea-level rise would thus be approximately 50 % of the values shown in this figure. In the vicinity of the spent nuclear fuel repository this means that the maximum wave height contribution is ~0.3–0.5 m. From Brydsten et al. (2009).*

Resulting total relative sea-level rise at Forsmark until 2100 AD

As previously mentioned, for the planning and construction of the spent nuclear fuel repository, it is important to assess the risk that the total sea-level, during storm, will exceed a certain height for the entire operational period. To that end, it is necessary to assess the probability of the combined maximum sea-level rise resulting from the long-term relative sea-level change and short-term sea-level variability due to storm surges.

The combined probability of mean relative sea-level change and storm surges under RCP8.5 was analysed for Forsmark by Pellikka et al. (2020). The probability distributions for the mean relative sea-level change and the daily sea-level maxima were summed into a new distribution under the assumption that they are independent (convolution). The resulting combined probabilities were reported for the years 2050, 2080 and 2100 AD, and are summarized in and Table 5-10.

For the year 2100 AD, the maximum total sea-level during severe storms is projected to be +3.52 m, +3.79 m and +4.05 m (in RH2000) for an exceedance probability of 10^{-3}, 10^{-4} and 10^{-5} events per year, respectively. For the years 2050 and 2080 AD, the maximum total sea-level during severe storms for each exceedance probability is consistently lower than for 2100 AD. For example, in 2080 AD the maximum sea-level with an exceedance probability of 10^{-5} events per year is projected to be almost 1 metre lower than in 2100 AD, and in 2050 AD the corresponding sea-level is approximately 0.7 m lower than in 2080 AD.

The consistently higher maximum sea-levels in 2100 AD compared to 2050 and 2080 AD are attributed to an acceleration of the projected rise in mean sea-level. Similar to the presently accelerating sea-level rise (see above and e.g. Nerem et al. 2018), also future sea-level rise is expected to accelerate with time. In Pellikka et al. (2020), the sea-level acceleration was assumed to be constant in time. Relative to 2000 AD, this translates to a four times higher mean sea-level rise by 2100 AD compared to 2050 AD. The assumption of a constant acceleration is in line with most recent studies, which show that the GMSL rise by 2100 AD is about three to five times the GMSL rise by 2050 AD (see above and e.g. Jevrejeva et al. 2012, Mengel et al. 2016 and Kopp et al. 2017).

To visualise the acceleration in mean sea-level rise in the projections by Pellikka et al. (2020), the temporal evolution of the projected mean relative sea-level (i.e. excluding the storm surge contribution) at Forsmark is shown in Figure 5-19 for the different pessimistically chosen probability percentiles. As evident in Figure 5-19, the fastest mean relative sea-level rise is projected to occur between 2080 and 2100 AD, whereas the RSL rise is considerably slower in the near future. For the percentiles considered here, the rise in mean relative sea-level between 2080 and 2100 AD is projected to be greater than the equivalent rise between 2000 and 2050 AD. Importantly, the rise in mean relative sea-level between 2050 and 2080 AD, corresponding to the latter part of the planned operational period, is also projected to be considerably larger than the rise between 2020 and 2050 AD, in part corresponding to the planned early part of the operational period. The latter part of the operational period is also, as expected, associated with greater uncertainties in the relative sea-level projections. This highlights the necessity of monitoring the mean relative sea-level rise over the entire constructional and operational period, in order to assess the actual development of future sea-level rise.

Another important feature of Figure 5-19 is that the maximum rise of mean relative sea-level at Forsmark (excluding storm surge) is projected to increase by less 0.5 m until 2050 AD compared to present day, even for the most extreme sea-level scenarios. The relatively slow increase of sea-level rise during this period, i.e. during the construction and early operational phases of the spent nuclear fuel repository, enables a greater flexibility to adjust for changed circumstances in the future, e.g. if sea-level projections for the time of repository closure proves to be higher than foreseen at present.

Figure 5-20, Figure 5-21 and Figure 5-22 show areas at Forsmark that are permanently flooded and flooded during severe storms in 2080 AD, the planned closure time for the spent nuclear fuel repository, for different levels of statistical probability. The maps show sea-levels compensated for isostatic uplift, as described also in Table 5-10 and Figure 5-17.

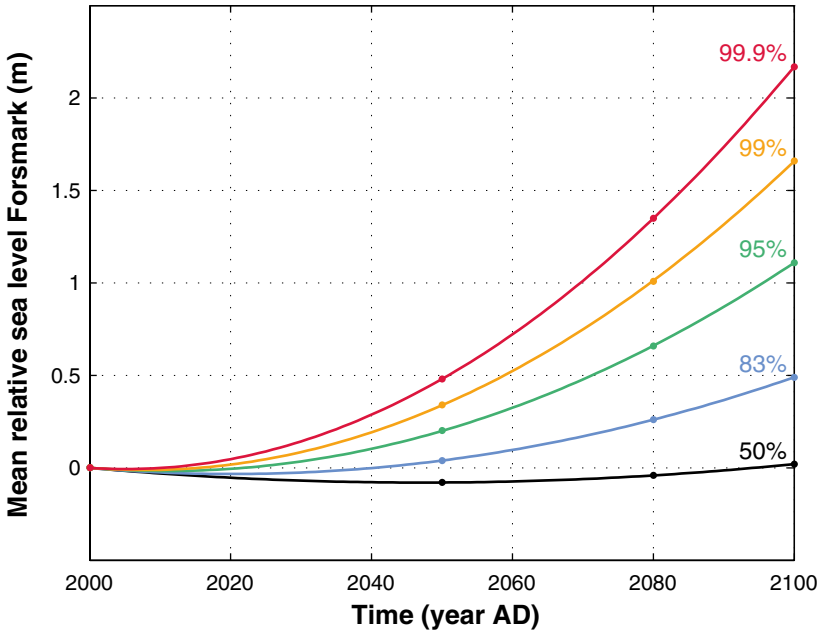

Figure 5-19. *Temporal evolution of mean relative sea-level rise (i.e. excluding the storm surge contribution) at Forsmark from 2000 to 2100 AD under the RCP8.5 emission scenario for different statistical percentiles (Pellikka et al. 2020). The dots show the mean relative sea-levels from Pellikka et al. (2020) in 2050, 2080 and 2100 AD (Table 5-9 and Table 5-10), whereas the coloured lines represent fitted second-order polynomials for each percentile, following the approach in Pellikka et al. (2020). The choice of a second-order polynomials ensures a constant acceleration, as applied in Pellikka et al. (2020) which is in approximate agreement with most studies on the future sea-level rise, see the text. Note that the probability of occurrence can be estimated by subtracting the percentile from 100 %, implying e.g. a 0.1 % and 1 % probability respectively for the 99.9 % and 99 % percentiles. The large uncertainties, combined with the accelerating rise, in the sea-level projections highlights the need for detailed monitoring of mean relative sea-level rise at the Forsmark site during the constructional and entire operational period of the spent nuclear fuel repository.*

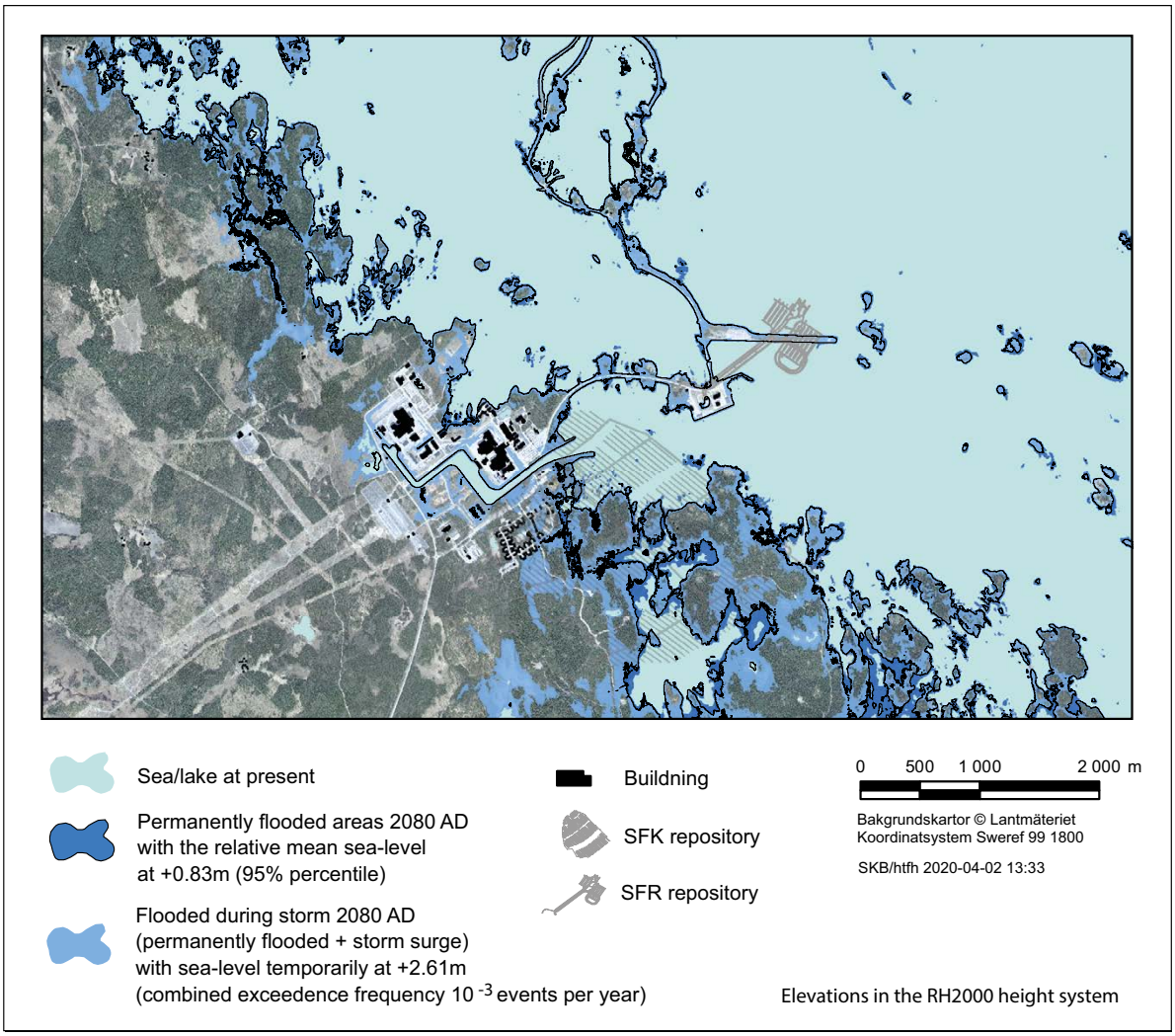

Figure 5-20. *Areas at Forsmark that are permanently flooded (dark blue colour) in 2080 AD (the planned closure time for the spent nuclear fuel repository) as described by the 95 % percentile probability distribution under the RCP8.5 emission scenario (Table 5-10 and Pellikka et al. 2020). The relative mean sea-level rise at this time, i.e. sea-level rise compensated for isostatic uplift, amounts to +0.83 m. For an exceedance probability of 10^{-3} events per year, a total temporary sea-level rise of +2.61 m may occur during severe storms at this time (light blue colour) (Table 5-10 and Pellikka et al. 2020). See also Figure 5-17. Figure 5-21 and Figure 5-22 show similar information, but for lower statistical probabilities. The present shore line is based on the Lantmäteriet Property map (www.lantmäteriet.se).*

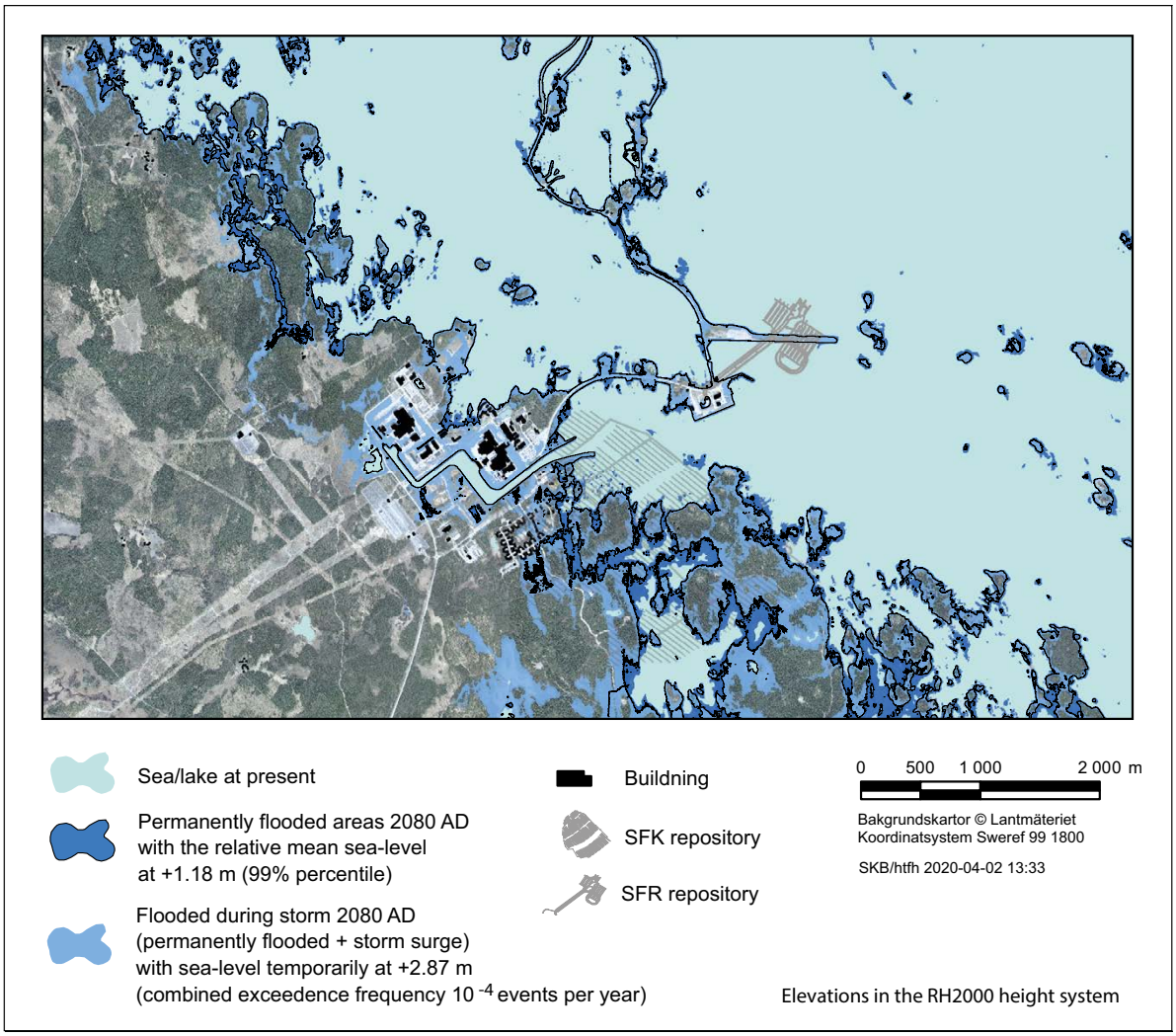

Figure 5-21. *Areas at Forsmark that are permanently flooded (dark blue colour) in 2080 AD (the planned closure time for the spent nuclear fuel repository) as described by the 99 % percentile probability distribution under the RCP8.5 emission scenario (Table 5-10 and Pellikka et al. 2020). The relative mean sea-level rise at this time, i.e. sea-level rise compensated for isostatic uplift, amounts to +1.18 m. For an exceedance probability of 10^{-4} events per year, a total temporary sea-level rise of +2.87 m may occur during severe storms at this time (light blue colour) (Table 5-10 and Pellikka et al. 2020). See also Figure 5-17. Figure 5-22 show similar information, but for lower statistical probabilities. The present shore line is based on the Lantmäteriet Property map (www.lantmäteriet.se).*

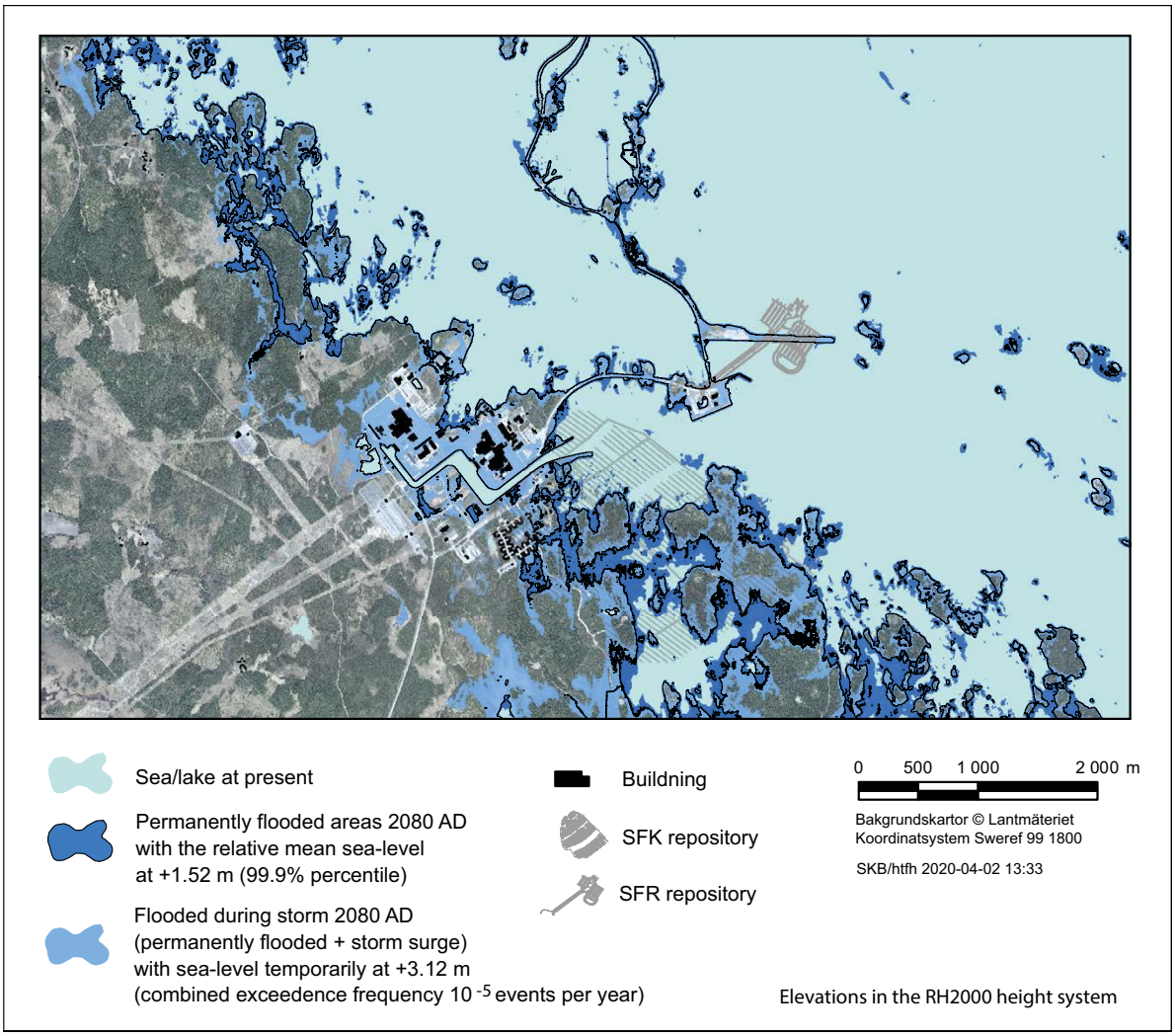

Figure 5-22. *Areas at Forsmark that are permanently flooded (dark blue colour) in 2080 AD (the planned closure time for the spent nuclear fuel repository) as described by the 99.9 % percentile probability distribution under the RCP8.5 emission scenario (Table 5-10 and Pellikka et al. 2020). The relative mean sea-level rise at this time, i.e. sea-level rise compensated for isostatic uplift, amounts to +1.52 m. For an exceedance probability of 10^{-5} events per year, a total temporary sea-level rise of +3.12 m may occur during severe storms at this time (light blue colour) (Table 5-10 and Pellikka et al. 2020). See also Figure 5-17. Figure 5-20 and Figure 5-21 show similar information, but for higher statistical probabilities. The present shore line is based on the Lantmäteriet Property map (www.lantmäteriet.se).*

Relative sea-level change at Forsmark beyond 2100 AD and until 12000 AD

As described in the section on relative sea-level rise until 2100 AD above, the uncertainty in future sea-level response to global warming is large within the coming century (see Figure 5-16). Sea-level change beyond 2100 AD is naturally associated with even larger uncertainties. As shown by the main conclusions related to sea-level change beyond 2100 AD presented in IPCC AR5 (Church et al. 2013), sea-level will continue to rise in a warming climate. Some of the main conclusions in Church et al. (2013) are the following.

- It is virtually certain that GMSL rise will continue beyond 2100 AD, with sea-level rise due to thermal expansion continuing for many centuries. Longer term sea-level rise depends on future emissions.
- The available evidence indicates that global warming greater than a certain threshold would lead to the near-complete loss of the Greenland ice-sheet over a millennium or more, causing a GMSL rise of about 7 m.
- Ocean heat uptake and thermal expansion take place not only while atmospheric greenhouse gas concentrations are rising but will continue for many centuries to millennia after stabilisation of radiative forcing, at a rate which declines on a centennial timescale.

To assess the effects of uncertainties associated with sea-level change beyond 2100 AD, a compilation of published estimates of GMSL rise beyond 2100 AD (Table 5-12) was made. The compilation was used for estimating the potential sea-level rise at Forsmark until 12000 AD with focus on its uncertainties. The published GMSL rise numbers typically include the contributions from i) ocean thermal expansion, ii) melting of the Greenland and Antarctic ice-sheets, iii) melting of all glaciers and ice caps, and some in cases iv) changes in land water storage. Some of the studies only deal with the contribution from specific sources, as indicated in Table 5-12. The published GMSL rise projections beyond 2100 AD (Table 5-12) are illustrated in Figure 5-23.

The large uncertainty related to the long-term sea-level change implies that differences in the projected GMSL rise between studies may reach several tens of metres. Hence, in contrast to reported sea-level projections until 2100 AD, it is not relevant to report the published long-term projections in two separate height reference systems (as deviations from present-day and in RH2000), as the difference between those systems amounts to only 0.2 m. Therefore, the reported sea-levels in this section are only presented as differences to present-day, typically defined as year 2000 AD or the average between 1986 and 2005 AD.

It is worth noting that Table 5-12 only includes the rise of GMSL. Short-term effects that do not add to the long-term rise of mean sea-level (i.e. storm-surge events) are not included. During such events, the sea-level would temporarily rise up to a few meters higher, which may be exemplified by reference to the situation at 2100 AD (Figure 5-17).

Table 5-12. Compilation of selected recent global mean sea-level projections beyond 2100 AD up to 12000 AD with a focus on projections based on the IPCC RCP8.5 emission scenario and published since 2012. All values represent global mean sea-level (GMSL), except when otherwise indicated. It should be noted that the values are not directly comparable, since they may be based on different climate/emission scenarios and use different methodological assumptions. The 5120 Pg C total emission scenario by Clark et al. (2016) corresponds to a temperature rise of up to ~7 °C (Figure 5-14), equivalent to the mid (for 2300 AD) to upper (2100 AD) bound of the RCP8.5 scenario, whereas Levermann et al. (2013) use a 4 °C warming scenario which approximately corresponds to the lower bound of RCP8.5 (Appendix E). Hence the range in sea-level projections approximately represents the range in temperature increase for the RCP8.5 emission scenario. The 5120 Pg C emission scenario by Clark et al. (2016) thus results in the highest long-term sea-level projection found in the literature, whereas Levermann et al. (2013) yields the lowest long-term projection under the RCP8.5 high emission scenario. The uncertainty range for DeConto and Pollard (2016) and Clark et al. (2016) has been recalculated from 1σ standard error to the 5–95 % confidence interval.

Year (AD)	Sea-level rise (m)	Notes	Reference
2200	2.7 5	83 % percentile 95 % percentile	Rohling et al. (2013)
	1.3–2.8 1.0–3.7	17–83 % percentile. RCP8.5 5–95 % percentile. RCP 8.5	Kopp et al. (2014)
	3 m per century	Worst case	Winkelmann et al. (2015)
	> 1 m		DeConto and Pollard (2016)
	1.0–3.7	RCP8.5	Sweet et al. (2017b)
	9.7	Extreme	
2300	0.92–3.59	RCP8.5	IPCC (2013a)
	2–3		Horton et al. (2014)
	0.6–3	Only Antarctic ice loss	Golledge et al. (2015)
	4.73 (3.41–6.82)	RCP8.5	Nauels et al. (2017)
	11.7 (9.1–15.6)	RCP8.5	Kopp et al. (2017)
2500	1.51–6.63		IPCC (2013a)
	15.65 (12.36–18.94)	5–95 % (±1σ (±2.0 m)) RCP8.5. Only Antarctic contribution	DeConto and Pollard (2016)
	5.48 (2.26–11.51)	5–95 %	Jevrejeva et al. (2012)
3000	1–2	Only Antarctic ice loss	Sutter et al. (2016)
3500	> 20	Only Antarctic ice loss	DeConto and Pollard (2016)
4000			Levermann et al. (2013)
	9.0 (5.7–12.1)	4 °C of warming (lower end of RCP8.5)	
5000	≤4	Only Antarctic ice loss	Sutter et al. (2016)
7000	9.55	Fast CO_2 drawdown	DeConto and Pollard (2016)
	15.41	Natural CO_2 drawdown	
	35.99	No CO_2 drawdown	
		RCP8.5. Only Antarctic ice loss	
12000	25.2 (19.3–31.1) 37.5 (33.7–41.3) 45.7 (42.2–49.2) 52 (47.9–56.1)	1280 Pg C total emissions (~RCP4.5) 2560 Pg C total emissions 3840 Pg C total emissions 5120 Pg C total emissions (medium to upper end of RCP8.5)	Clark et al. (2016), supplementary material
	25 ~38	For a 2.0 °C temp rise Specifically for RCP8.5	Clark et al. (2016) in Sweet et al. (2017a) Levermann et al. (2013)
	13.9(11.8–15.9)	4 °C of warming (lower end of RCP8.5)	

Given that a major deglaciation of the Greenland and Antarctic ice-sheets under a warming climate would contribute with different sea-level rise fingerprints in Fennoscandia, as described in Section 5.1.3, it would have most useful if the projections in Table 5-12 had included the regional re-distribution of sea-level rise. This is however not the case for most of the studies, since they typically only describe GMSL rise. Nevertheless, for the long-term analysis beyond 2100 AD and up to 12000 AD it is assumed that the GMSL value is representative also for the eustatic sea-level in the Baltic Sea. If the GMSL projections would have been adapted to Baltic sea conditions, the resulting 10 ka projections would have been a few metres lower than presented in Figure 5-23. The main reason for the lower sea-level rise in the Baltic sea compared to the global mean is attributed to a smaller contribution from the Greenland ice-sheet in this region, see e.g. Mitrovica et al. (2001) and Kopp et al. (2014).

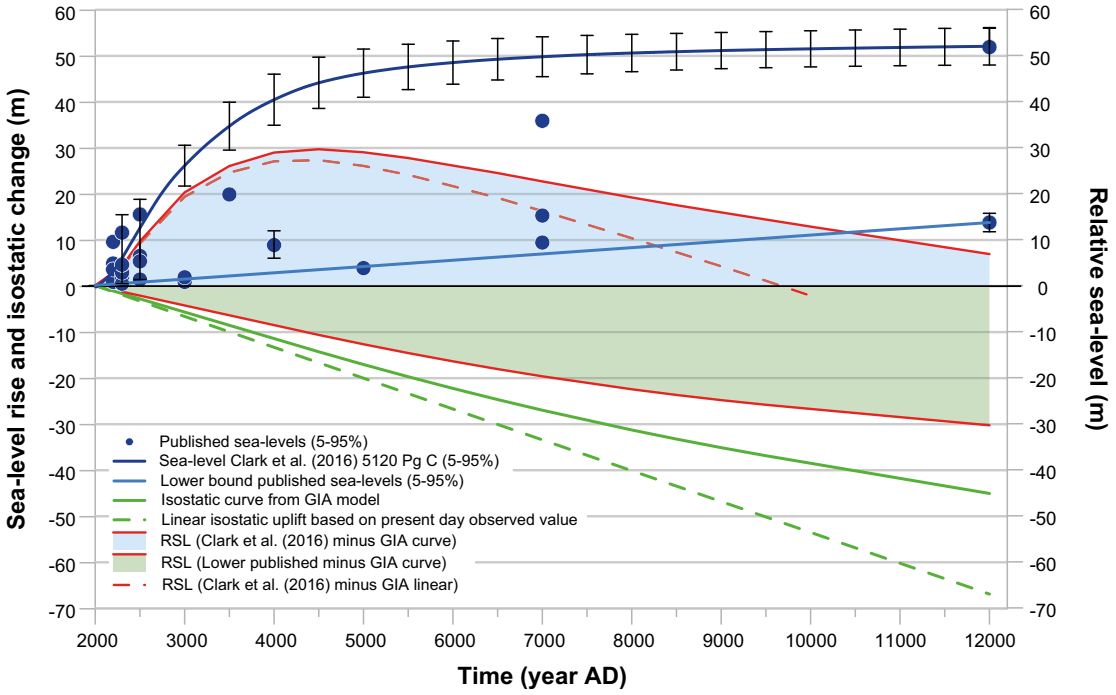

Figure 5-23. *Mean sea-level rise projections from 2200 to 12000 AD for the extended global warming climate case from the compilation in Table 5-12. The values constitute sea-level projections under the IPCC RCP8.5 emission scenario or other high emission scenarios (Table 5-12), and as such they are compatible with the main notion of the extended global warming climate case. Median values are shown by blue dots. The 5–95 % percentiles, when available, are shown by uncertainty bars. For the highest projected sea-level at 12000 AD (+52.5 ±4.1 m from Clark et al. 2016 for a 5120 Pg C total emission scenario), the projected sea-level development leading up to the maximum level has also been plotted together with the 5–95 % percentile error bars (upper dark blue line), data from Clark et al. (2016, supplementary material).The considerably slower sea-level rise according to the lowest projections in Table 5-12 is shown by the lower light blue line. In this way, the 5120 Pg C emission scenario by Clark et al. (2016) represents the highest long-term sea-level projection, whereas Levermann et al. (2013) (Table 5-12) represents the lowest long-term projection. Even though all sea-level projections are not directly comparable because of different methodologies etc, the substantial difference between the highest and lowest projections is striking, clearly demonstrating the large uncertainty within the field of future sea-level rise in a warming climate caused by high-end greenhouse-gas emissions. The isostatic uplift rate for the Forsmark site as projected by GIA modelling (see the text and Section 3.3.4) is shown by the solid green line. The isostatic change at Forsmark, assuming unrealistically that the present-day uplift rate of 6.7 mm a^{-1} (Vestøl et al. 2019, see the text) would continue in the future, is shown by the hatched green line up to 12000 AD. The evolution of relative sea-level at Forsmark, constituting the sum of the eustatic changes (blue lines) and isostatic changes (green lines) for the extended global warming climate case are shown in red. For an interpretation of the resulting relative sea-level at the Forsmark site (i.e. periods with transgression and regression) and the associated periods of submerged conditions, see the text. Also, for a description of the validity of using GMSL data for estimating the relative sea-level change at the Baltic coast (Forsmark site), see the text.*

The timing of the maximum contributions to sea-level rise differs for the different processes involved (ice-sheet melting, thermal expansion sea-level rise etc). The thermal expansion contribution to GMSL rise may for example reach a maximum value at ~2300 AD (Clark et al. 2016). The temporal aspects of the various processes contributing to a rise in GMSL are included in the respective studies compiled in Table 5-12. To estimate future sea-level changes and changes in relative sea-level at the Forsmark site for the *extended global warming climate case*, the maximum and minimum eustatic development over the next 10 millennia are of interest (i.e. the longest time span for which future sea-level projections exist). The highest 12000 AD sea-level projection is the one given by Clark et al. (2016) (Table 5-12). This projection is based on a high emission scenario with a total release of 5120 Pg C, corresponding to a temperature rise of more than ~7 °C by 2300 AD (Figure 5-14), which corresponds to medium- to upper-end RCP8.5 temperatures (Appendix E). The resulting GMSL rise is +52 ±4.1 m by 12000 AD (Figure 5-23, Table 5-12).

Figure 5-23 also includes the eustatic development leading up to this level, showing a rapid rise in GMSL over the coming 2–3 millennia, followed by a progressively slower increase up to 12000 AD. For the 5120 Gg C emission scenario, Clark et al. (2016) state that Greenland becomes ice free by ~4500 AD contributing with about 7 m of GMSL rise by that time, the Antarctic ice-sheets contribute with 45 m of GMSL rise by 12000 AD, thermal expansion contributes with 2.8 m by the same time, whereas melting glaciers contribute with another 0.35 m GMSL rise within the coming few centuries. The sum of the above contributions is somewhat larger than the model ensemble mean sea-level rise of 52 m by 12000 AD reported by Clark et al. (2016). The same study also suggests that the 470 Pg C already released by 2000 AD (IPCC 2013a) has committed Earth to a future GMSL rise of about 1.7 m (1.2 to 2.2 m). The minimum GMSL projections for the same 10 ka period include +1 m for 2200 AD (Kopp et al. 2014, Sweet et al. 2017b), 0.92 m for 2300 AD (for a RCP8.5 scenario in IPCC 2013a), 1–2 m at 3000 AD (for Antarctic ice-sheet loss only, in Sutter et al. 2016), 6 m at 4000 AD (for a 4 °C warming scenario in Levermann et al. 2013) and 12 m at 12000 AD (for a 4 °C warming scenario in Levermann et al. 2013) (Table 5-12 and Figure 5-23). The substantially lower GMSL projections in these studies compared to Clark et al. (2016) is primarily explained by a much lower contribution from the East Antarctic ice-sheet. For example, whilst Clark et al. (2016) projects that the East Antarctic ice-sheet contributes with several tens of metres to the GMSL rise until 12000 AD, the projection in Levermann et al. (2013) suggests that this contribution would be only be at most a couple of metres. The widely different responses of the East Antarctic ice-sheet between the studies are likely attributed to different amount of global warming (~7 °C in Clark et al. 2016 versus 4 °C in Levermann et al. 2013), but possibly also to a higher sensitivity of East Antarctic ice-sheet to global warming in Clark et al. (2016) than in Levermann et al. (2013).

In contrast to Clark et al. (2016), the lowest GMSL projections in Figure 5-23 do not provide much information on how the sea-level changes with time. Therefore, similar to the *global warming climate case*, a general time evolution of a low-end GMSL evolution (E_{low}), ranging from 2000 to 12000 AD, is constructed for the *extended global warming climate case* using Equation 5-1. In this climate case, $a = 20.62\ m$ and $b = 0.080\ ka^{-1}$. The parameters a and b have been determined under the constraints that (i) $E_{low} = +13.9\ m$ at 12000 AD, consistent with the lowest projection at this time under a strong global warming (Levermann et al. 2013, see Table 5-12), and (ii) the resulting relative sea-level change, obtained by combining E_{low} with the isostatic change, initially has the same rate as the observed present-day relative sea-level change at Forsmark (−4.1 mm a^{-1}, Table 5-2). The constructed time series of the low-end GMSL evolution until 12000 AD is shown by the lower light blue curve in Figure 5-23.

Figure 5-23 also shows two curves of the isostatic uplift at the Forsmark site. The upper solid green curve shows the isostatic uplift at Forsmark as projected by the GIA modelling for the *global warming climate case* (Section 3.3.4, see also Figure 5-25). The lower hatched green line, unrealistically, assumes that the present-day isostatic uplift rate (6.7 mm a^{-1}, see Table 5-2) would continue at the same rate over the coming 10 millennia. The difference between the eustatic and isostatic curves constitutes the relative sea-level development at the Forsmark site, giving an estimate of periods of transgression and regression and hence also estimates on submerged and terrestrial periods at the site.

The highest sea-level projection (upper blue curve in Figure 5-23), in combination with the isostatic curve from GIA modelling (solid green curve) shows that the Forsmark site will be subject to a substantial initial transgression, since the isostatic uplift is far from being able to compensate for the strong eustatic rise over the coming millennia. The transgression peaks at around 4500 AD, with a RSL rise of

~30 m. Areas that would be flooded by a 30 m rise in RSL are illustrated in Figure 5-24. If instead the linear isostatic curve is used (based on a constant present-day uplift rate, thus constituting the highest isostatic value that theoretically could prevail over this period of time), the resulting relative sea-level rise shows a similar peak at 4500 AD, and that this peak will be at least +27 m, given the high-end eustatic curve of Clark et al. (2016). Following the transgression, the results when using the isostatic curve from GIA simulations show a subsequent slow regression over many millennia, with the relative sea-level reaching zero at around 15700 AD (off the scale in Figure 5-23). This combination of highest projected eustatic rise and isostatic change according to the GIA simulations thus shows a higher-than-at-present relative sea-level at the Forsmark site up to 15700 AD.

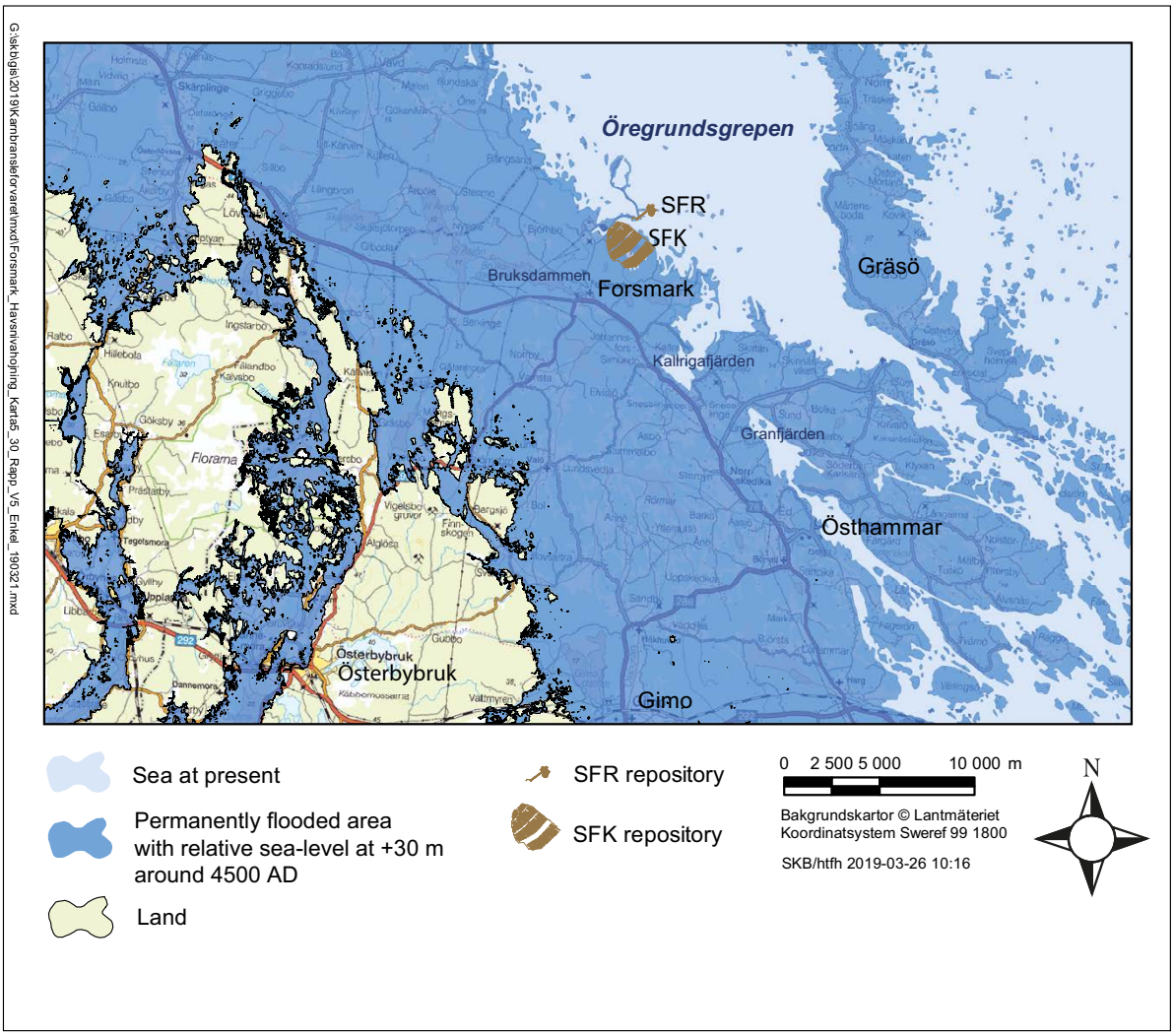

Figure 5-24. *Areas in the Forsmark region that will be permanently flooded with a relative sea-level at +30 m (RH2000) at around 4500 AD. This transgression results from the high emission long-term projection of GMSL rise of Clark et al. (2016) (Table 5-12 and Figure 5-23). In addition to this rise in mean sea-level, the sea-level may temporarily be higher than this by ~2 m during storm-surge events (cf. info on the 2100 AD surge level, Table 5-10 and Figure 5-17). A raised relative sea-level from this transgression would prevail until at least ~10000 AD but more likely up to 15700 AD, see the text. The present shore-line location is based on the Lantmäteriet Property map (www.lantmäteriet.se). SFK: planned repository for spent nuclear fuel, SFR: existing repository for low- and intermediate-level waste.*

This is in contrast to the result that follows from assumption of a constant isostatic rate for the next 12 ka (hatched green line in Figure 5-23), which most certainly overestimates the long-term isostatic development. However, the resulting relative sea-level curve (hatched red line) from using the linear isostacy and the highest sea-level projection, conclusively shows that the period with a raised relative sea-level would not end sooner than ~10000 AD. Hence, the two isostatic curves in Figure 5-23 can be regarded as representatives of two end members of possible isostatic developments at Forsmark. For the highest sea-level projections over the next 10 ka, this implies that Forsmark will be submerged at least up to ~10000 AD but more probably up to 15700 AD, when using the highest projection of sea-level rise (Clark et al. 2016, 5120 Pg C emission case) (Figure 5-23, Table 5-12).

The results depicting a transgression up to around 15700 AD (Figure 5-23) for the high emission eustatic projection by Clark et al. (2016), is in line with the results of potential future sea-level rise at Forsmark at 2100 AD under the IPCC RCP8.5 emission scenario (Figure 5-17). In that analysis, the highest sea-level projections from both process-based methods and non-process-based methods (see Pellikka et al. 2020) results in a clearly higher relative sea-level at 2100 AD compared with at present (2000 AD) (Table 5-10, Figure 5-17, Figure 5-20 to Figure 5-22).

For the lowest sea-level projections in Figure 5-23 (lower light blue line), the comparison with the isostatic curve from GIA (solid green line) show that the Forsmark site will not be subject to a transgression at any time during the coming 10 ka. Instead, the present-day trend of a lowering of the relative sea-level (a regression) would continue, even though this is a warm RCP8.5 development within the *extended global warming climate case*. The same result, with no transgression, would be obtained if combining the lowest sea-level projections with the isostatic development based in a linear present-day uplift rate (green hatched line).

All in all, the above analysis shows that the very large spread in long-term projections of future sea-level rise (Table 5-12 and Figure 5-23) could result in either a very substantial transgression at the Forsmark site (up to +30 m in relative sea-level rise) with resulting conditions with a raised relative sea-level prevailing for up to 12.5 millennia (up until 15700 AD), or at the other end of the spectrum, a continued regression with no transgression at all at the site for the coming tens of thousands of years. Both evolutions fit within the uncertainty range of long-term future sea-level rise for the high emission scenarios that form basis for the *extended global warming climate case*.

For an assessment of relative sea-level changes at Forsmark beyond 12000 AD for the *extended global warming climate case,* see next subsection.

Relative sea-level change at Forsmark beyond 12000 AD until 120 ka AP

In a similar way as done for the *global warming climate case* (Section 5.1.3) it is possible, with some basic assumptions, to construct a coarse relative sea-level curve at Forsmark over the next 120 ka also for the *extended global warming climate case*. The constructed relative sea-level change at Forsmark until 120 ka AP in the *extended global warming climate case* is identical to the *global warming climate case* except for the following two changes:

- The slow onset of the next glacial is shifted further into the future, from ~50 ka AP in the *global warming climate case* to ~100 ka AP in the *extended global warming climate case*. In the former case, the first ice-sheet reaches the Forsmark site at around 105 ka AP, whereas in the latter case Forsmark remains free of ice within the next 120 ka. This is in line with the enhanced warming (comparable to the RCP8.5 scenario) that occurs in the *extended global warming climate case* and the dominance of temperate conditions at Forsmark until 120 ka AP (Section 5.2.1, see also Figure 5-26).
- The eustatic contribution to the relative sea-level at Forsmark is projected to be significantly larger in the *extended global warming climate case*. This is consistent with the assumption of a stronger global warming, and therefore also a larger GMSL rise until 2100 AD and beyond in the *extended global warming climate case.*

Therefore, the sea-level projections based on the high-end 5120 Pg C emission scenario from Clark et al. (2016) and the low-end 4 °C scenario from Levermann et al. (2013) are used as the eustatic contribution to the relative sea-level in the Forsmark area (Figure 5-23). The projections by Clark et al. (2016) and Levermann et al. (2013) bracket the uncertainty range associated with the GMSL rise until 12000 AD under a strong global warming (Figure 5-23). It is assumed that the relative sea-level contributions from Clark et al. (2016) and Levermann et al. (2013) after 12000 AD remain constant at their maximum values (+52 m and +13.9 m, respectively; Table 5-12).

The constructed relative sea-level at Forsmark between −10.8 and 120 ka AP for the *extended global warming climate case* is shown in Figure 5-25, together with the construction for the *reference glacial cycle climate case*. Similar to the modelled relative sea-level change for the *reference glacial cycle* (grey curve in Figure 5-6), the low-end relative sea-level projection in the *extended global warming climate case*, based on Levermann et al. (2013), results in a continued initial regression at Forsmark until ~40 ka AP by which the isostatic contribution has tapered off. In contrast, the high-end relative sea-level projection, based on Clark et al. (2016), results in an initial transgression, culminating in a sea-level rise of +30 m in about 2500 years (see also previous subsection). After this point, the relative sea-level slowly begins to decline due to the isostatic uplift (Figure 5-25). From ~40 ka AP both relative sea-level projections remain virtually constant until 120 ka AP (Figure 5-25).

As was discussed in the corresponding section on the *global warming climate case* (Section 5.1.3), the assumption of a constant eustatic sea-level over a timescale of 100 ka is probably not realistic. During this period the climate will likely be influenced by variations of the Earth's orbit (Berger and Loutre 2002, Laskar et al. 2004) and by a continued decline of the atmospheric CO_2 concentration (Lord et al. 2019). Combined, these two effects and their associated impact on the climate will also influence the GMSL by changing the thermal expansion of ocean water and the global ice volume budget. However, as was also noted in the *global warming climate case*, the amplitude and timing of such changes are very uncertain and therefore they have been omitted in the present analysis.

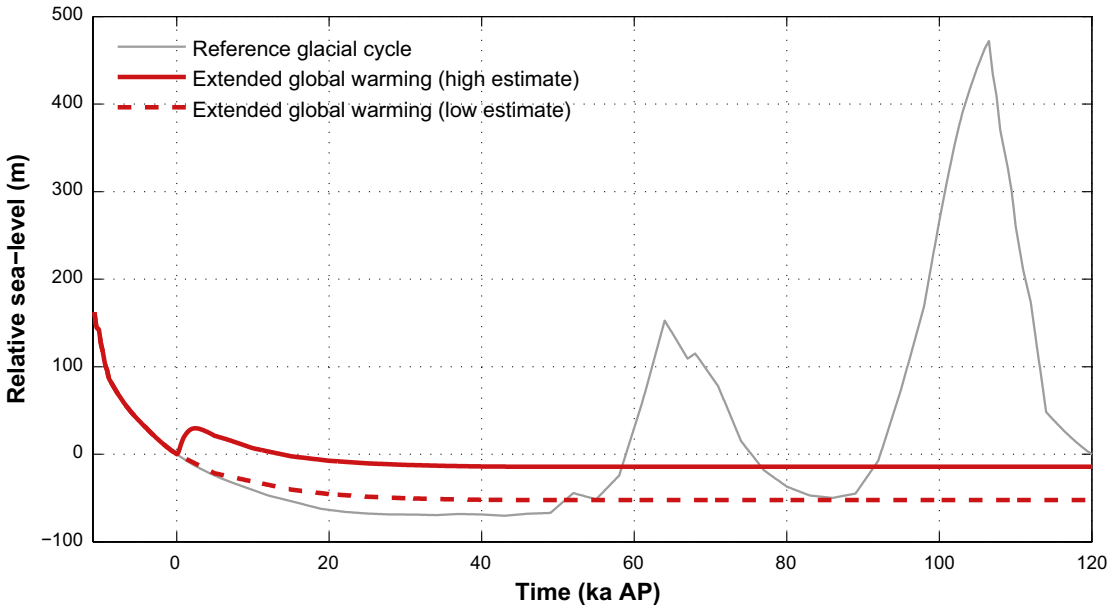

Figure 5-25. *Estimated relative sea-level change at Forsmark from −10.8 to 120 ka AP in the extended global warming climate case (red curves) and the reference glacial cycle climate case (grey curve). The solid red curve represents a high-end relative sea-level projection under a strong global warming, based on the highest GMSL projection until 12000 AD (Clark et al. 2016), whereas the dashed red curve represents a low-end relative sea-level projection based on the lowest GMSL projection until 12000 AD (Levermann et al. 2013), also under strong global warming. For more information on the projected relative sea-level change until 12000 AD, see previous subsection. For a comprehensive discussion on the relative sea-level changes between −10.8 and 120 ka AP for the reference glacial cycle climate case, see Section 4.5.2.*

5.2.4 Permafrost evolution

In the *extended global warming climate case*, the very long period of temperate climate conditions is followed by permafrost development at the Forsmark repository location at ~110 ka (107 ka) after present. Subsequently, temperate climate conditions develop again before the end of the first 120 ka. Given the local definition of the end of the present interglacial (by the development of permafrost at the repository location, see Section 4.5.4), the Holocene ends per definition at ~110 ka AP in this climate case. Periglacial conditions with permafrost prevail for c 4 ka (3 %) of the coming 120 ka.

5.2.5 Evolution of climate domains

As mentioned above, a 100 ka long period of temperate climate conditions is added before a slow onset of the first *reference glacial cycle* for the *extended global warming climate case*. After these additional 100 ka of temperate conditions, ~100 ka long Late Quaternary glacial cycles, represented by the *reference glacial cycle* described in Section 4.5, are envisaged to follow (Figure 5-26). This results in there being ~160 ka before the first glacial conditions occur at the Forsmark site, whereas the first permafrost occurs at ~110 ka AP. The climate development in the *extended global warming climate case* thus describes a situation without periglacial- or glacial climate conditions in central Sweden, including Forsmark, for a very long time.

Peak air temperatures are envisaged to be reached within the first few hundreds to thousands of years as a result of high emissions of anthropogenic greenhouse gases, at which point the annual mean surface air temperature at Forsmark is estimated to be substantially higher than at present (Figure 5-15 and Table 5-8). The changes in climate also result in a large increase in annual precipitation. In the *global warming climate case* the annual average precipitation was projected increase by ~20 % (Figure 5-3), comparable to projected change at Forsmark in Kjellström et al. (2009). In line with the higher temperatures in the *extended global warming climate case*, the annual precipitation change is estimated to be approximately doubled compared to the *global warming climate case* (Figure 5-15).

The higher temperatures are also envisaged to affect sea-level. For the *extended global warming climate case* (based on the IPCC emission scenario RCP8.5) there is a very large uncertainty in future sea-level rise. The uncertainty resulted in one variant with a continued sea regression and terrestrial conditions over the repository and another variant with a sea transgression and submerged conditions up until 15700 AP (Figure 5-26).

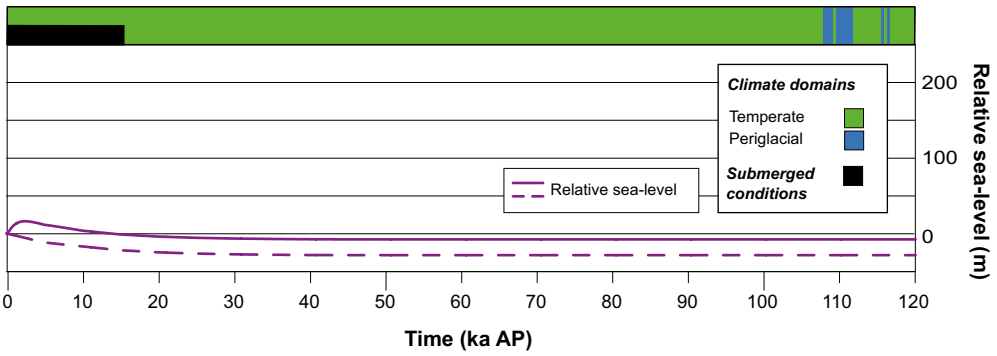

Figure 5-26. *Evolution of climate conditions at Forsmark for the extended global warming climate case. Following from the assumptions of this case, temperate climate conditions prevail at the site for more than 100 ka. A few thousands of years of periglacial conditions occur at the end of the period associated with a minimum in insolation at ~100 ka AP. In the initial period the site either experiences terrestrial conditions with a warm temperate climate or submerged conditions up to 15700 AP (17700 AD), given the large uncertainty range in projected future sea-level indicated by the solid and dashed purple curves (see also Section 5.2.3 and Figure 5-23). The figure hence shows both end-members regarding the very large uncertain sea-level rise associated with the RCP8.5 high emission scenario (Section 5.2.3). Note that there is a very large range in e.g. temperature, precipitation and other climate parameters within the temperate conditions, ranging from strong global warming conditions to conditions with temperatures significantly cooler than at present (prior to the development of periglacial conditions). For a detailed example of more moderate global warming conditions at Forsmark than envisaged for this case, see Section 5.1.5.*

Following the cessation of anthropogenic greenhouse-gas emissions, annual mean air temperatures and precipitation amounts are envisaged to slowly decline for the rest of the long interglacial period, in response to the slow decline in atmospheric CO_2 concentration (e.g. Archer et al. 2009, Eby et al. 2009, Lord et al. 2016).

The cryosphere response to the extreme global warming results in raised global sea-levels and potentially submerged conditions at the Forsmark site at the start of the period (Figure 5-26). The length of the initial submerged period could be shorter or longer than illustrated in Figure 5-26, or not exist at all (see Section 5.2.3).

5.2.6 Surface denudation

Since the *extended global warming climate case* envisages an even larger fossil fuel CO_2 climate perturbation (in line with the RCP8.5 emission scenario) than in the *global warming climate case*, fluvial erosion and chemical weathering in the wetter and warmer climate are anticipated to be more efficient than in the *global warming climate case* (Section 5.1). For a description of denudation processes that are anticipated to change compared with the *reference glacial cycle climate case*, see the description of denudation under the *global warming climate case*.

Even if fluvial erosion and chemical weathering are expected to increase in this climate case compared with the *reference glacial cycle climate case* and the *global warming climate case*, the *extended global warming climate case* mainly comprises temperate climate conditions for the entire 120 ka, and entirely excludes the most efficient denudation process (glacial erosion) as defined in Section 3.5.4. Also, just as in the *global warming climate case*, the one process that theoretically could give a larger contribution to increased denudation, fluvial erosion, is strongly limited by the near-sea-level location of the repository (see also Section 3.5.2), especially when also considering the potentially higher relative sea-levels envisaged for long periods of time for the *extended global warming climate case* (Section 5.2.3).

As mentioned in Section 5.1.6, Hall et al. (2019a) used an estimate of the timing and duration of future periods with glaciated conditions at Forsmark under different RCPs (Lord et al. 2019, Figure 4-10), to estimate the total denudation of basement rock at Forsmark over the coming 100 ka. Since there are no periods with ice-sheet coverage over the coming 100 ka in Lord et al. (2019), all denudation results from non-glacial processes (mainly fluvial erosion and chemical weathering under the warmer temperate climate conditions of the *extended global warming climate case*). The results for RCP8.5 by Hall et al. (2019a) indicate a total denudation of up to 0.5 metres over the coming 100 ka for Forsmark (Appendix G Table G-1). Adding another 20 ka of non-glacial denudation (at a maximum rate of 5 mm ka^{-1}, see Section 3.5.4 and Hall et al. 2019a) in order to cover the full 120 ka of the *extended global warming climate case*, yields a total denudation of up to 0.6 metres (0.5+0.1 = 0.6 m) for this climate case. Furthermore, if combining all scenarios of Lord et al. (2019), the total denudation over the coming 100 ka is still less than 1 metre (Table 3-15). A denudation of up to 0.6 metres for the *extended global warming climate case* is less than the 1.7–3.6 m of total bedrock denudation in the *Reference glacial cycle climate case* (Section 4.5.7). Surface denudation is therefore not described and treated further in the *extended global warming climate case*.

5.2.7 Results from a climate study of the coming 1 Ma: timing of the next glaciation under elevated atmospheric CO_2 conditions

In Lord et al. (2019), a combination of Earth system modelling techniques is used to simulate the possible evolution of future climate over the next 1 Ma for a range of anthropogenic CO_2 emission scenarios. The future evolution of the atmospheric CO_2 concentration in response to anthropogenic CO_2 emissions is calculated in a carbon cycle impulse function (Lord et al. 2016), and the future changes in relative sea-level, used as a proxy for the glacial–interglacial cycles, is estimated by the insolation and atmospheric CO_2 variations in an insolation threshold model (Paillard 1998). A statistical climate emulator (Lord et al. 2017) is then used to project the future evolution of a range of climate variables forced by atmospheric CO_2 concentration, orbital variations, and global ice-sheet volume changes.

The simulated future climates in Lord et al. (2019) vary substantially in response to the changes in atmospheric CO_2 concentration (of both anthropogenic and natural origin; Figure 5-27b) and orbital forcings (Figure 5-27a and Figure 5-28). The period of anthropogenic CO_2 emissions in each

emission scenario is accompanied by a period of warming which lasts for up to 50 ka in to the future. This is followed by an increased dominance of orbital forcing on climate, and fluctuations between interglacial and glacial states. The results suggest that the timing of the next glacial inception may be strongly affected by anthropogenic CO_2 emissions (Figure 5-27c). The scenarios with low and medium emissions (RCP2.6 and RCP4.5) are projected to undergo glacial inception in ~50 ka, whilst the high emission scenario (RCP8.5) is suggested to extend the current interglacial for approximately 170 ka (Figure 5-27c).

Put in perspective, the timing of the next glacial inception in Lord et al. (2019) is in good agreement with a number of previous modelling studies on the topic, summarised in Figure 5-1 and in the review by Liakka et al. (2021). For example, several studies have suggested that under pre-industrial atmospheric CO_2 concentrations or for low CO_2 emissions, the next glacial inception may occur either imminently (Pimenoff et al. 2011) or in ~50 ka (e.g. Berger and Loutre 2002, Cochelin et al. 2006, Ganopolski et al. 2016). For CO_2 scenarios with medium emissions, studies have suggested the end to the current interglacial period occurring in approximately 50 ka (Berger et al. 2003) or 130 ka (Archer and Ganopolski 2005, Lord et al. 2015). For high emissions of 5000 Pg C, Archer and Ganopolski (2005) concluded that the next glacial inception may be delayed for more than 500 ka, in agreement with Lord et al. (2015), but in contrast to Texier et al. (2003), who estimated that the current interglacial would end in ~167 ka under high emissions.

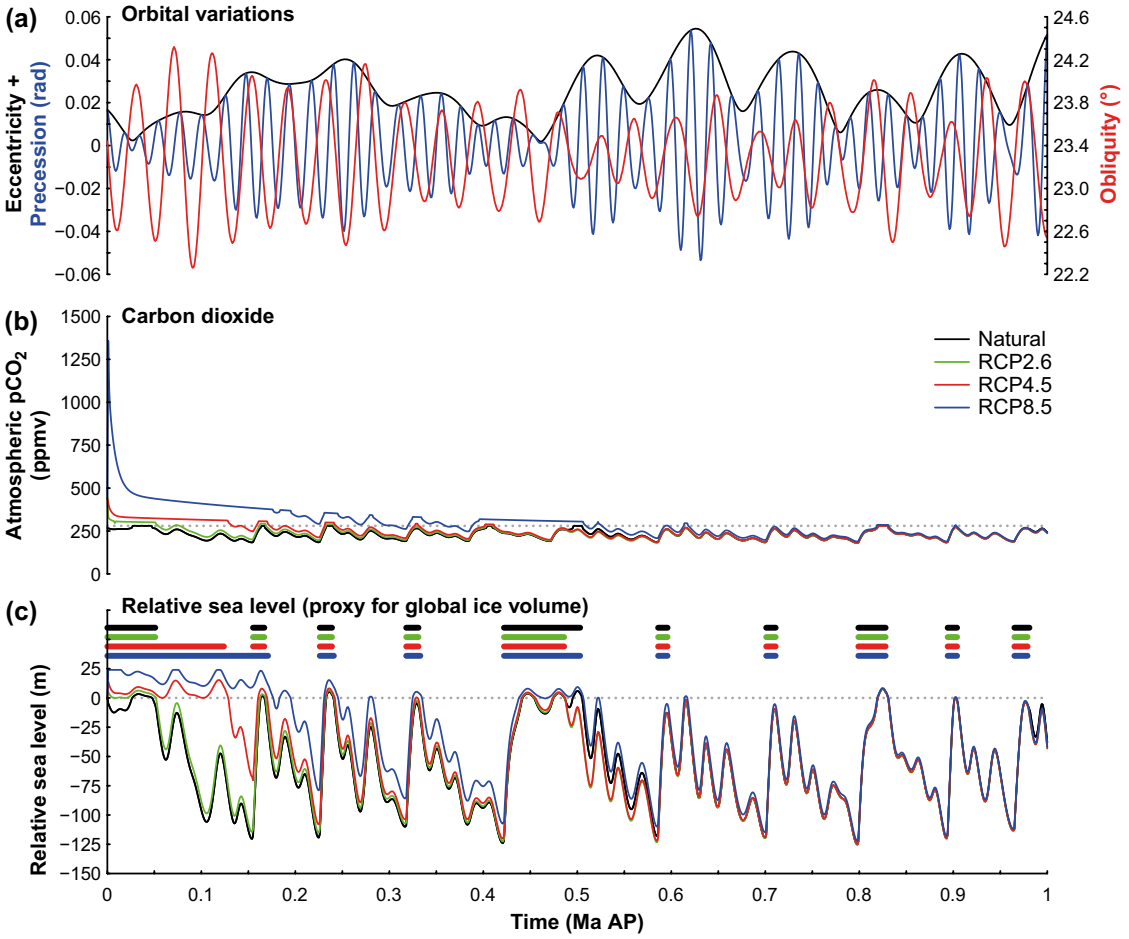

Figure 5-27. *Climate forcing data used as input to the climate emulator in Lord et al. (2019) for the next million years. (a) Time series of orbital variations (Laskar et al. 2004), showing eccentricity (black) and precession (radians; blue) on the left axis, and obliquity (degrees; red) on the right axis. (b) Time series of atmospheric CO_2 concentration (ppmv) for the natural (black line), RCP2.6 (green line), RCP4.5 (red line), and RCP8.5 (blue line) emission scenarios, predicted using the carbon cycle impulse response function of Lord et al. (2016), and updated to include the impact of global temperature/CO_2 feedbacks. The pre-industrial CO_2 concentration is also shown (grey dotted line). (c) Time series of global sea-level (m) for the four emission scenarios, shown as an anomaly compared with pre-industrial. Periods of interglacial conditions for each emission scenario are indicated by thick horizontal bands. From Lord et al. (2019).*

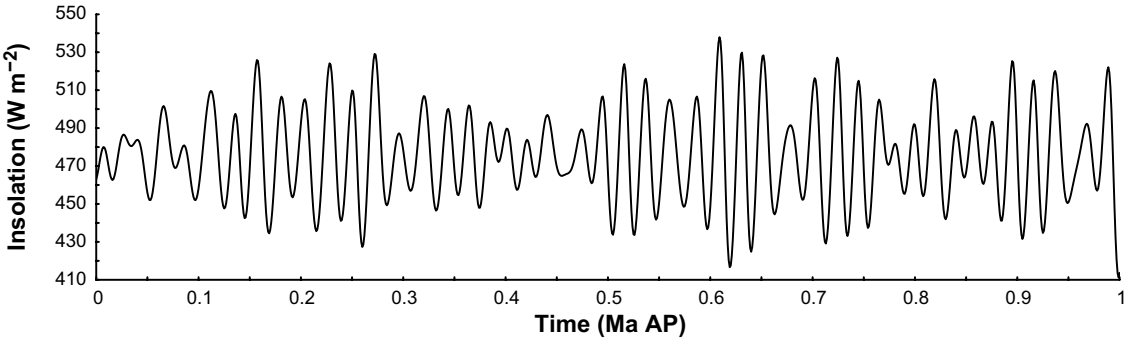

Figure 5-28. *Evolution of summer (June) insolation (W m^{-2}) at 65 °N for the next million years, calculated using the method of Laskar et al. (2004). From Lord et al. (2019).*

5.3 Extended ice-sheet duration climate case

5.3.1 Background

In order to cover the uncertainty in duration of ice-sheet coverage for the coming 120 ka, a climate case with extended ice-sheet duration is constructed, describing a situation with a longer time of ice-sheet coverage than in the *reference glacial cycle climate case*. To this end, a climate evolution similar to that of the *reference glacial cycle climate case* is used, with the important exception that the long interstadial with ice-free conditions between the two ice advances does not occur at Forsmark. In the *reference glacial cycle climate case*, interstadial conditions, dominated by periglacial climate conditions with permafrost, occur between 66 and 91 ka (Table 4-6, Figure 4-35). In the present case, no ice-free conditions occur during this period. Accordingly, the scenario with extended ice-sheet coverage describes one long single phase of ice-sheet coverage at Forsmark, with a timing of glaciation and deglaciation according to Table 5-13.

This ice-sheet evolution is similar to the Weichselian glacial history presented by Lundqvist (1992). In Lundqvist (1992), the main phase of the Weichselian glaciations starts ~50 ka BP with the ice-sheet envisaged to cover Sweden continuously up to the final Weichselian deglaciation, see the literature review on ice-marginal fluctuations during the Weichselian glaciation by Lokrantz and Sohlenius (2006). Several recent studies suggest that there was a long period of ice-free interstadial conditions over large parts of Fennoscandia during MIS 3 (59–24 ka BP), i.e. in the middle of the main phase of glaciation as traditionally suggested, see Section 4.2.

The duration of ice-sheet coverage over the Forsmark region in the *extended ice-sheet duration climate case* is comparable with the total time of ice-sheet coverage as coarsely deduced from the Weichselian reconstruction by Lundqvist (1992). In the Lundqvist reconstruction, most of Fennoscandia is covered by ice from the mid-Weichselian (around 50 ka BP) until the deglaciation (around 10 ka BP), and during a phase of the early Weichselian (90–80 ka BP), which gives a total time of ice-sheet coverage for the major part of Fennoscandia of roughly 50 ka. Acknowledging that the Lundqvist reconstruction was not intended to give a detailed picture of ice-sheet durations, the *approximate* duration in the Lundqvist reconstruction is similar to the duration of ice-sheet coverage at Forsmark (60 ka) in the present climate case. In line with the ice-sheet reconstruction by Lundqvist (1992), the Fennoscandian ice-sheet is assumed to have started to grow considerably earlier than the time of ice-sheet overriding at Forsmark. For a compilation of information on Weichselian glacial history, see Section 4.2 and references therein.

5.3.2 Ice-sheet evolution

As an illustration of a situation with a persistent ice-sheet coverage over the site for a long time (also during the ice-free phase corresponding to MIS 3 during the Weichselian glaciation, 70–90 ka BP), ice thickness data from an uncalibrated ice-sheet model reconstruction of the Fennoscandian ice-sheet are used (Figure 5-29). The data were produced by the same ice-sheet model that was used for the simulation of the calibrated ice-sheet development used for the *reference glacial cycle climate case* (Section 3.1.4). In this climate case, the precise evolution of the ice thickness is not important. Therefore, the uncalibrated ice-sheet simulation may be used to illustrate the ice-sheet development for the case when it covers the Forsmark site without interstadial conditions between the two glacial phases in the *reference glacial cycle climate case*.

As during the initial 4 ka of the first glacial phase of the *reference glacial cycle climate case* (Figure 4-35), cold-based conditions with subglacial permafrost are envisaged to exist under the first 4 ka of glacial conditions in this case. Subsequently, the subglacial permafrost melts, and the ice-sheet becomes warm-based at around 56 ka and remains so for the rest of the glacial period.

Table 5-13. Duration of climate domains at the Forsmark site in the extended ice-sheet duration climate case.

Temperate climate domain [ka] (percent of time of glacial cycle)	Periglacial climate domain [ka] (percent of time of glacial cycle)	Glacial climate domain [ka] (percent of time of glacial cycle)	Submerged conditions [ka] (percent of time of glacial cycle)
28 ka (23 %)	22 ka (18 %)	60 ka (50 %)	10 ka (8 %)

The ice-sheet evolution for this case starts with glacial conditions at c 50 ka AP (Figure 5-29), i.e. around 7 ka earlier than in the *reference glacial cycle climate case*. Glacial conditions persist until c 110 ka AP when the site is deglaciated (Figure 5-29 and Figure 5-30). The duration of all climate domains is summarized in Table 5-13. The ice thicknesses in this uncalibrated model run are somewhat smaller than in the *reference glacial cycle climate case*. In this context, it should be noted that the maximum possible ice thickness over Forsmark, used for the safety assessment scenario for canister failure due to isostatic load (see the **Post-closure safety report)**, is not derived from this climate case or the *reference glacial cycle climate case*, but from the case describing a maximum ice-sheet thickness (Section 5.4).

In light of recent results indicating that the Weichselian ice-sheet exhibited a more dynamic behaviour during the middle Weichselian than traditionally assumed (see above and Section 4.3), the ice-sheet development in Figure 5-29 is considered a pessimistic estimate of the duration of ice-sheet coverage for the coming 120 ka. The degree of pessimism in this case may also be seen in the light of the inferred present global warming, which may result in a longer than usual interglacial, and consequently a shorter time of glacial conditions than in the *reference glacial cycle climate case* (Section 4.5 and 5.2).

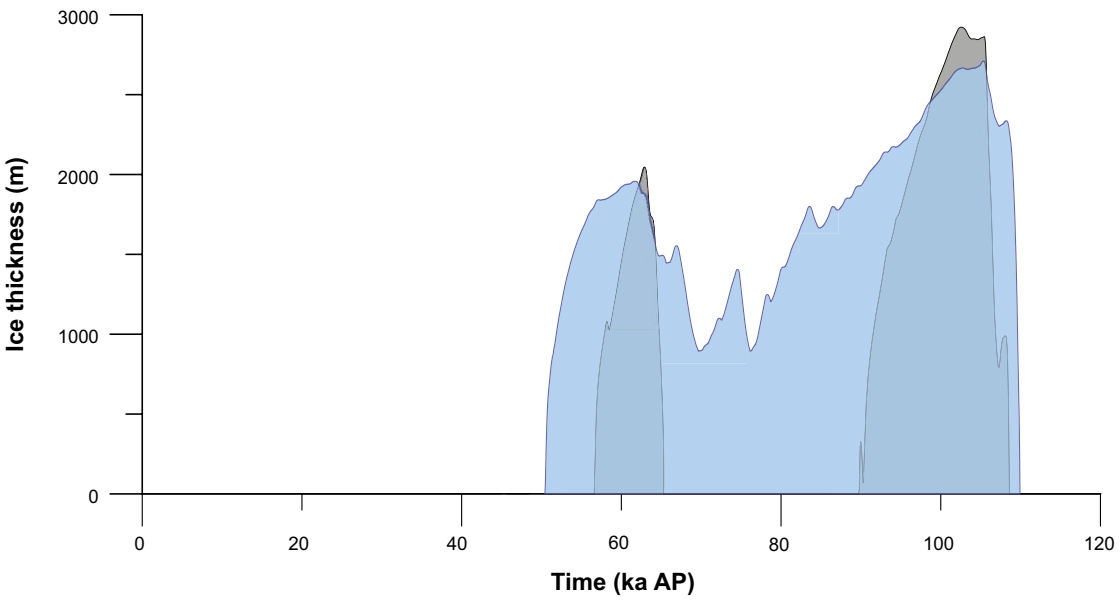

Figure 5-29. *Ice-sheet coverage over Forsmark in the extended ice-sheet duration climate case (blue). For comparison, the ice-sheet development of the reference glacial cycle climate case, based on the reconstruction of Weichselian conditions, is also shown (grey).*

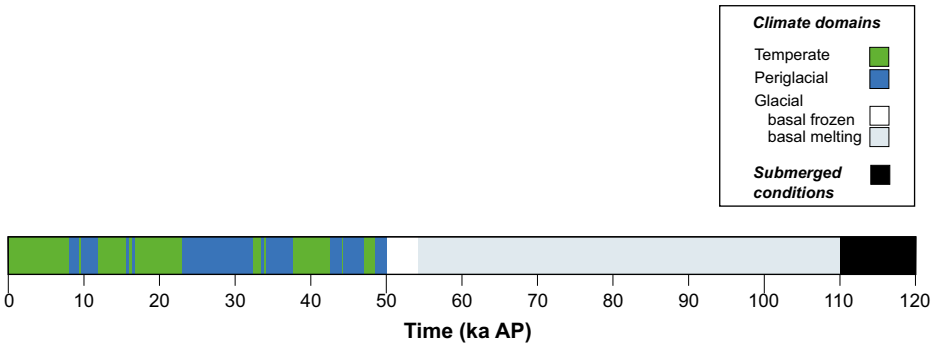

Figure 5-30. *Evolution of climate conditions at Forsmark as a time series of climate domains and submerged conditions for the extended ice-sheet duration climate case. Glacial conditions start earlier and lasts considerably longer than in the reference glacial cycle climate case (Section 4.5.4).*

5.3.3 Surface denudation

The *extended ice-sheet duration climate case* results in the period with warm-based ice-sheet conditions, and associated glacial erosion over the repository, being longer than in the *reference glacial cycle climate case* (Section 4.5.4 and 4.5.7). Given that the ice-sheet duration is about twice as long in this case (Figure 5-29) compared with the *reference glacial cycle climate case* (Section 4.5.4), the average amount of glacial erosion is estimated to be around twice as large as the average (25 % and 75 % percentiles) in the *reference glacial cycle climate case* over a 120 ka period (Section 4.5.7). The average amount of total bedrock denudation over the Forsmark site, including glacial erosion, is thus estimated to be around 3–7 m for the *extended ice-sheet duration climate case* over a 120 ka period, both at the Forsmark site and over the repository footprint (cf. Table 3-15). However, if periods of cold-based, non-erosive, conditions are longer in this climate case, which could well be the case if climate conditions were colder, the duration of periods with glacial erosion would be shorter and the amount of erosion smaller.

Surface denudation results in a reduction of repository depth. A reduced repository depth could in turn lead to that permafrost and frozen ground reach closer to the repository. However, a 3–7 m reduction in repository depth for a glacial cycle with prolonged ice-sheet duration has a negligible effect, in terms of repository safety, on the estimated permafrost- and freezing depths presented in Section 4.5.3 and 5.5.3. Also in the 1 Ma time perspective, Hall et al. (2019a) estimated, from the cosmogenic nuclide analysis, the full range (5 % and 95 % percentiles) of total denudation of basement rock over the coming 1 Ma to be 2–43 m (Section 3.5.4 and Table 3-15). This result, and other results from e.g. the geomorphological analysis in Hall et al. (2019a), lead to a conservative estimate of the maximum total denudation of bedrock (i.e. by glacial erosion, non-glacial erosion, and weathering) at the Forsmark site over the coming 1 Ma of 50 m, see Section 3.5.4.

If combining a likely denudation development over the coming 100 ka (with a total denudation of less than 1 m, see Section 3.5.4), with a pessimistic repetition of the upper (7 m) denudation value (from the average 3–7 m denudation range above) for all following seven glacial cycles to obtain a total period of 1 Ma, the total bedrock denudation would be 50 m.

The amount of non-glacial denudation is somewhat smaller than in the *reference glacial cycle climate case*, since the duration of temperate- and (mainly) periglacial climate conditions are shorter than in the *reference glacial cycle climate case*.

5.4 Maximum ice-sheet thickness climate case

5.4.1 Background

For glacial conditions, an additional hydrostatic pressure related to the ice-sheet thickness is added to the hydrostatic pressure resulting from ice-free conditions. The extremes regarding hydrostatic pressure in the glacial climate domain depend on the ice-sheet configuration and on its hydraulic systems. Numerous sub-glacial lakes have been observed (e.g. Smith et al. 2009, Wright and Siegert 2012) and modelled (e.g. Livingstone et al. 2013) under the Antarctic ice-sheet. A few subglacial lakes have been shown to exist also under the Greenland ice-sheet (Palmer et al. 2015, Willis et al. 2015). The hydrostatic pressure in these lakes correlates with the ice overburden pressure. A hydro-thermo-mechanical balance is assumed, where supply of basal melt water, re-freezing and ice deformation result in a hydrostatic equilibrium where the ice-sheet rests, or floats, on the water surface (e.g. Pattyn et al. 2004). As further justified below, it is reasonable to assume that also for the Fennoscandian ice-sheet, the maximum ice-sheet thickness sets a limit to the maximum hydrostatic pressure that may occur at the ice-sheet-substrate interface.

In contrast to their horizontal extents, there is virtually no direct observational evidence of the maximum vertical extents of past ice-sheets, although indirect evidence comes from post-glacial isostatic rebound. Therefore, thickness estimates of past ice-sheets are often based on experiments with numerical thermo-mechanical ice-sheet models. In the *reference glacial cycle climate case*, the maximum ice thickness during the LGM was simulated to be ~2900 m over Forsmark (see Section 4.4.1), which is comparable with other contemporary reconstructions of the LGM ice-sheet in Eurasia (e.g. Peltier 2004, Kleman et al. 2013).

Although the last glacial cycle is among the longest, coldest and driest glaciations of the Pleistocene, geological information reveals that the Fennoscandian ice-sheet was significantly larger during the penultimate Late Saalian glaciation (~192–135 ka BP; Svendsen et al. 2004, Lambeck et al. 2006, Colleoni et al. 2009). In fact, the Late Saalian is the most extensive glaciation in Eurasia of the last 2 Ma which is known from geological records.

During the peak of this glaciation (MIS 6), i.e. the Late Saalian glacial maximum at ~140 ka BP, the area of the Fennoscandian ice-sheet was at least twice as large as during the LGM (Svendsen et al. 2004), manifested by an ice-sheet margin reaching approximately 200 km further south and 1000 km further east than the LGM counterpart (Figure 5-31). Because of its massive size, the MIS 6 glacial maximum provides an excellent target period for evaluating the maximum possible ice-sheet thickness that could occur over Forsmark over the next 1 million years.

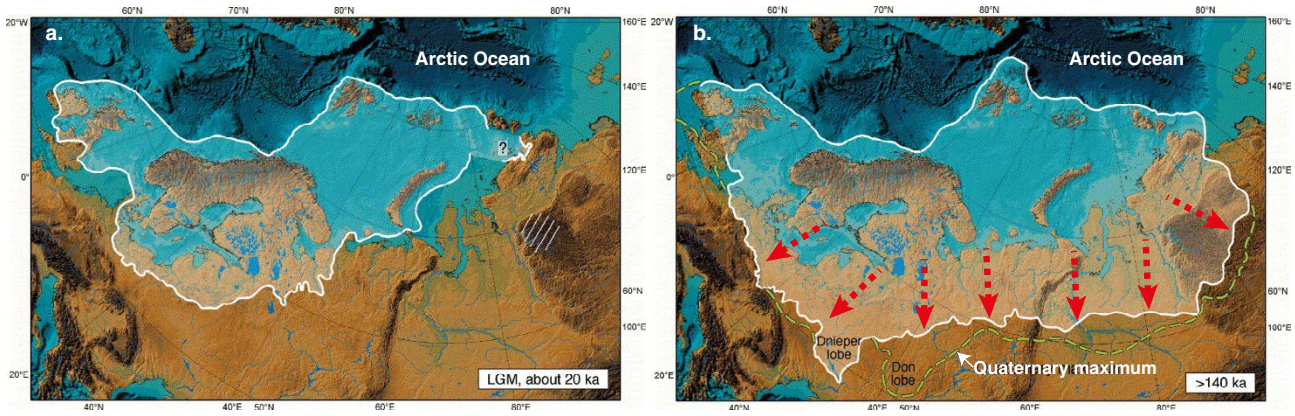

Figure 5-31. *Comparison of the Eurasian ice-sheet extent between (a) the Last Glacial Maximum (~21 ka BP) and (b) the Late Saalian (MIS 6) glacial maximum (~140 ka BP; after Svendsen et al. 2004). Compared with the LGM Eurasian ice-sheet extent, the Late Saalian ice-sheet expands further south and east (b), red arrows). The largest LGM Eurasian ice-sheet reconstruction (ICE-5G, Peltier 2004) corresponds to an ice volume of ~22 m SLE, which is about three times smaller than the Late Saalian Eurasian ice volume (~70 m SLE) simulated by Peyaud (2006). The LGM ice-sheet extent in (a) is identical to the lower panel of Figure 4-5. Figure from Colleoni et al. (2014).*

Most modelling efforts of the MIS 6 ice-sheet in Eurasia indicate that the Eurasian ice-sheet was slightly thicker than during the LGM. Lambeck et al. (2006) simulated an ice thickness of ~3400 m over the Forsmark region at 140 ka BP. Similar values can be inferred from Colleoni et al. (2009). The study of Lambeck et al. (2006) was used as basis for the maximum ice thickness assessment in SR-Site (SKB 2010a, SKB 2011 Section 12.7). In SR-Site, the maximum ice thickness was set to 3400 m over Forsmark.

Although Lambeck et al. (2006) provide useful information on the typical ice thickness associated with an extensive glaciation in Eurasia, they did not explore the sensitivity of the ice thickness to various uncertainties in any great detail. Therefore, their estimates on ice-sheet thickness are not necessarily pessimistic in terms of a maximum number to be used in the assessment of long-term repository safety. To describe the uncertainties associated with simulations of the peak Saalian ice-sheet configuration, a dedicated combined climate- and ice-sheet modelling study was performed.

5.4.2 Late Saalian sensitivity experiments

The importance of the uncertainties related to the initial condition, climate forcing and ice-sheet model parameters for the MIS 6 ice-sheet thickness over Forsmark was thoroughly evaluated by Colleoni et al. (2014) and Quiquet et al. (2016). Both studies simulated the MIS 6 Eurasian ice-sheet with the GRISLI ice-sheet model (GRenoble Ice Shelf and Land Ice model; Ritz et al. 2001) using climate forcing derived from two AOGCM experiments performed within the study with the NCAR CESM1.0.5 climate model (Gent et al. 2011). Both AOGCM experiments were identical except for different representations of the Laurentide ice-sheet in North America. The configuration of the MIS 6 Laurentide ice-sheet is not known, but its size (relative to the LGM) can be qualitatively inferred from marine proxy records of past sea-level changes in first approximation. Because the estimated sea-level change from the MIS 6 glacial maximum was similar to that of the LGM (Figure 1-2), while the Eurasian ice-sheet was larger, and assuming that the Greenland and the Antarctic ice-sheets had comparable dimensions to those during LGM, the MIS 6 Laurentide ice-sheet must have been smaller at the LGM.

To account for the large uncertainties in the Laurentide ice-sheet extent and elevation, the first AOGCM experiment in Colleoni et al. (2014) and Quiquet et al. (2016) used the (relatively large) LGM Laurentide configuration (from Peltier 2004; hereafter referred to as *topo1*, see Figure 5-32), and the second experiment used a smaller Laurentide configuration (from Colleoni 2009; hereafter referred to as *topo2*), in better agreement with the global sea-level records from MIS 6 (Figure 5-32). Both experiments used the same configuration of the MIS 6 Eurasian ice-sheet (Peyaud 2006, based on Svendsen et al. 2004; maximum elevation is ~3500 m). Orbital parameters and greenhouse-gas concentrations were set to appropriate values for 140 ka BP in both experiments.

The resulting near-surface air temperature and precipitation fields from the *topo1* and *topo2* AOGCM experiments were subsequently used as climate forcing in the GRISLI ice-sheet model experiments. In GRISLI, three different types of ice flow are represented: grounded ice, ice streams and ice shelves. Areas of grounded ice (inland ice) are subjected to the Shallow Ice Approximation (SIA, Hutter 1983), whereas ice streams and ice shelves are simulated using the Shallow Shelf Approximation (SSA, MacAyeal 1989). The horizontal resolution was set to 20 km in both studies, which is too coarse to resolve the dynamics of ice streams. Therefore, the effect of ice streams in GRISLI is parameterized by applying the SSA to areas that have the large-scale characteristics of ice streams, i.e. narrow valleys, thick basal sediment layers saturated by meltwater, and areas with low effective basal pressure. All ice-sheet experiments were carried out with constant-in-time forcing and boundary conditions and integrated until steady state (~200 ka). Hence, no transient simulations were performed.

Combined, Colleoni et al. (2014) and Quiquet et al. (2016) conducted several sensitivity experiments to evaluate the influence of various uncertainty sources on the MIS 6 (steady-state) ice-sheet thickness over Forsmark, including potential errors associated with the initialization of the ice-sheet model, climate forcing, and choice of models. In addition, both studies thoroughly analysed the sensitivity of the ice-sheet thickness to poorly constrained parameters in the ice-sheet model. In Colleoni et al. (2014), the ice thickness sensitivity to the parameter space was mostly evaluated by means of uni-variate sensitivity experiments. In Quiquet et al. (2016), the Latin Hypercube Sampling (LHS) sampling technique was employed to conduct a multi-variate analysis of the parameter space to investigate the effect on the ice-sheet thickness.

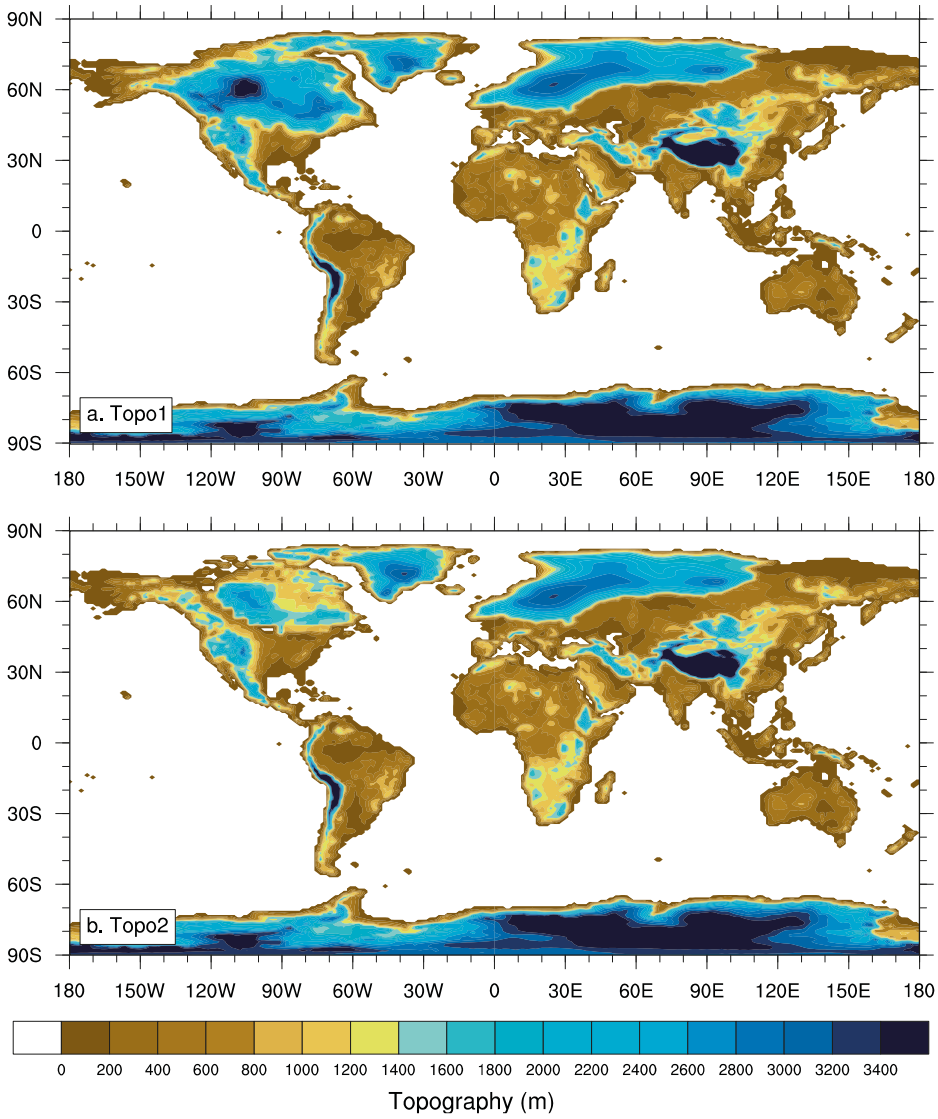

Figure 5-32. *Global maps of the surface topography used in the AOGCM experiment of the MIS 6 glacial maximum in Colleoni et al. (2014) and Quiquet et al. (2016). The maps are identical except for the representation of the Laurentide ice-sheet in North America. In* ***a.*** *the Laurentide ice-sheet corresponds to the ICE-5G (Peltier 2004) LGM reconstruction (topo1), and in* ***b.*** *to the MIS 6 topography as reconstructed in Colleoni (2009) (topo2). From Colleoni et al. (2014).*

The simulated MIS 6 ice-sheet thickness over Forsmark was generally more sensitive to variations of ice-sheet model parameter values than to other uncertainty sources. The ice-sheet model parameter sensitivity experiments also resulted in the thickest ice-sheets. Therefore, the most important results from those experiments will be discussed in the next subsections. The results and potential implications from the other sensitivity experiments are briefly discussed in Section 5.4.3. For a more comprehensive review of all the sensitivity experiments, the reader is referred to the original studies (Colleoni et al. 2014; Quiquet et al. 2016).

In addition to the steady-state MIS 6 ice-sheet simulations described above, a transient MIS 6 simulation has also been performed (Colleoni and Liakka 2020), mainly for the purpose of using as input to Earth stress modelling.

Main uncertainties and ice-sheet thicknesses from the uni-variate parameter sensitivity analysis

In Colleoni et al. (2014), the influence of different ice-sheet model parameters on the MIS 6 ice-sheet thickness over Forsmark was, as previously mentioned, investigated by means of a uni-variate sensitivity analysis. This type of analysis explores the influence of changing each parameter separately while keeping all other parameter values constant at their default values (defined by a reference state). In total, they carried out 70 sensitivity experiments (including the reference simulations) to analyse the isolated impact of 13 parameter related to GRISLI's treatment of climate forcing, surface mass balance (SMB), ice-stream areas, ice-shelf areas and the solid earth. The simulated (steady-state) ice thickness over Forsmark in those experiments varied between 2991 m and 3472 m using the climate forcing data from the *topo1* AOGCM simulation, and between 2650 m and 3195 m when using the *topo2* climate forcing data (see Table 5-14).

In Colleoni et al. (2014), the ice-sheet thickness was mostly sensitive to parameters related to ice-stream areas (Figure 5-33). Specifically, the thinnest ice-sheets were obtained when reducing the sediment thickness (or reducing the critical threshold for sediment saturation), and the thickest ice-sheets resulted from an increase of the basal drag coefficient for fast-flowing ice (see Colleoni et al. 2014 for details).

Table 5-14. Average, minimum and maximum ice-sheet thickness over Forsmark (in m) resulting from the uni-variate (Colleoni et al. 2014) and multi-variate (Quiquet et al. 2016) ice-sheet model parameter sensitivity analysis. Note that ~50 % of the experiments in Quiquet et al. (2016) failed to simulate an ice cover over Forsmark. The values in the table refer only to the experiments that resulted in an ice-covered Forsmark. The *topo1* case refers to a relatively large Laurentide ice-sheet and *topo2* to a case with a considerably smaller, and more realistic (see the text), Laurentide ice-sheet.

	topo1			*topo2*		
	mean	**min**	**max**	**mean**	**min**	**max**
Colleoni et al. (2014)	3168 m	2991 m	3472 m	2973 m	2650 m	3195 m
Quiquet et al. (2016)	3578 m	2707 m	4150 m	3153 m	581 m	3957 m

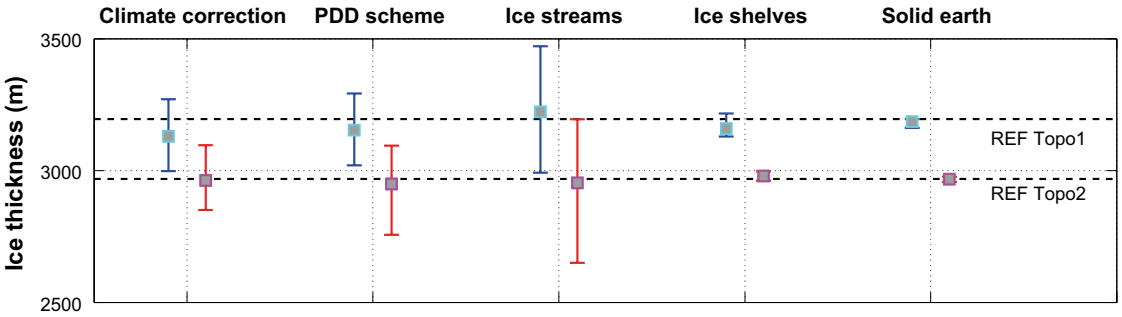

Figure 5-33. *Ensemble mean Eurasian ice thickness over Forsmark for each of the five groups of the uni-variate sensitivity experiments (Colleoni et al. 2014) using topo1 (cyan squares) and topo2 (pink squares) climate forcing. The maximum and minimum ice thickness of each group is shown by blue and red bars, respectively. Corresponding values for the reference experiments in Colleoni et al. (2014) are indicated by black dashed lines. Figure has been modified from Colleoni et al. (2014).PDD stands for Positive Degree Days which is a temperature-index based method to estimate ice-sheet ablation.*

Main uncertainties and ice-sheet thicknesses from the multi-variate parameter sensitivity analysis

The uni-variate parameter sensitivity analysis in Colleoni et al. (2014) helped to identify critical parameters that are important for determining the ice-sheet thickness. However, the drawback of that analysis is that it only considered the isolated impact of changing each parameter separately, but not the potential effects from systematically changing a combination of two or more parameters. To cover also these more complex cases, Quiquet et al. (2016) used the Latin Hypercube Sampling (LHS) method (Iman 2008) to allow for a more systematic exploration of the parameter space. They also explored a wider range of the potential parameter values compared with Colleoni et al. (2014), to account for the full range of the values found in the literature. In total, they carried out 100 experiments for each climate forcing field (*topo1* and *topo2*; same as in Colleoni et al. 2014) with different combinations of 10 parameters (Table 5-15).

Table 5-15. Evaluated parameters in multi-variate ice-sheet model sensitivity experiments (Quiquet et al. 2016).

Parameter		Units
Ice ablation coefficient	C_{ice}	mm °C^{-1} d^{-1}
Snow ablation coefficient	C_{snow}	mm °C^{-1} d^{-1}
Topographic lapse rate	λ	°C km^{-1}
Daily temperature variability	σ	°C
Solid precipitation threshold	p_{solid}	°C
Accumulation ratio	γ	°C^{-1}
Thermoactive layer thickness	d	m
SIA enhancement factor	E_{sia}	-
GHF modificator	γ_{GHF}	-
Basal drag coefficient	C_f	-

The simulated MIS 6 ice-sheet thickness over Forsmark from the multi-variate sensitivity experiments are shown in Figure 5-34 and Figure 5-35 for the *topo1* and *topo2* climate forcing fields, respectively. As a result of the wide range of evaluated parameter values in Quiquet et al. (2016), about 50 % of the sensitivity experiments failed to simulate an ice-sheet over Forsmark (red stars in Figure 5-34 and Figure 5-35). In the other experiments, the minimum ice-sheet thickness over Forsmark is 2707 m (581 m), and the maximum thickness 4150 m (3957 m) for the *topo1* (*topo2*) climate forcing (Table 5-14).

The sensitivity of the simulated ice thickness to each of the evaluated parameters can be identified by the slope of the black stars in Figure 5-34 and Figure 5-35. For most of the tested parameters, the black stars are distributed more or less horizontally along the x-axis, indicating that there is virtually no correlation between the simulated ice thickness and those parameters. However, there are two exceptions to this rule: for the flow enhancement factor (E_{sia}) there is a slight negative correlation (thicker ice for lower values of E_{sia}), and for the basal drag coefficient (C_f) there is an even stronger positive correlation (thicker ice for higher values of C_f). Hence, in agreement with Colleoni et al. (2014), the simulated steady-state ice-sheet thickness in the multi-variate experiments is also most sensitive to the basal drag coefficient.

The thicker simulated ice-sheets in the multi-variate compared to the uni-variate sensitivity experiments can be partly explained by the fact that the basal drag coefficient was allowed to vary by a factor 10 in Quiquet et al. (2016) as opposed to a factor 3 in Colleoni et al. (2014). Quiquet et al. (2016) motivated their choice of using such a wide range of basal drag coefficients by the absence of reliable direct observations of this parameter. Furthermore, indirect estimates below present-day ice-sheets and glaciers suggest that this parameter has a very large spatial variability (e.g. Schaeffer et al. 2012, Morlighem et al. 2013), implying that those studies cannot be used to constrain this parameter. Therefore, one cannot conclude that lower values of the basal drag coefficient are more likely than higher ones, or vice versa. Another reason why the ice-sheets became thicker in the multi-variate compared to the uni-variate sensitivity experiments is that combinations of different ice-sheet model parameters that yield thick ice are included in the multi-variate study.

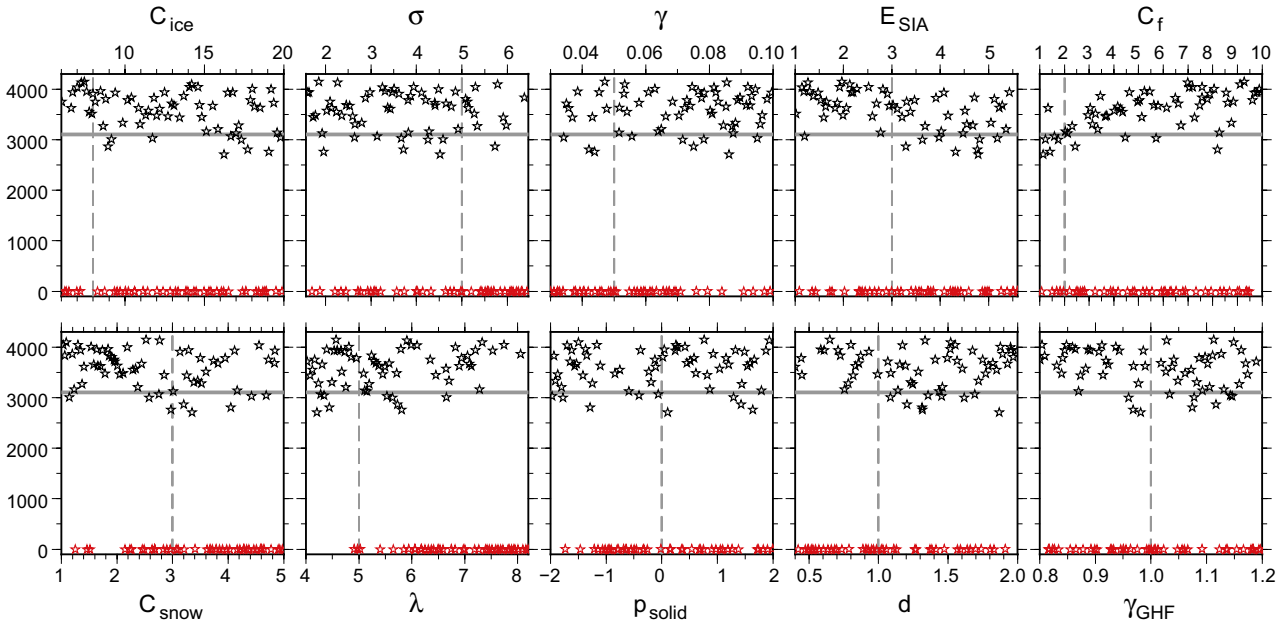

Figure 5-34. *Ice thickness over Forsmark using the topo1 climate forcing for each member of the multi-variate ensemble as a function of parameter values (Quiquet et al. 2016). Horizontal lines correspond to the ice thickness simulated in the reference simulation in Colleoni et al. (2014). The vertical dashed lines either correspond to the parameter value used in the reference simulation (if this parameter was used), or to a standard value from literature. The red stars are the simulations that are discarded since they do not preserve ice (thickness less than 500 m) at the Forsmark site (i.e. an unrealistically large ice-sheet retreat). A description of each parameter is provided in Table 5-15. From Quiquet et al. (2016).*

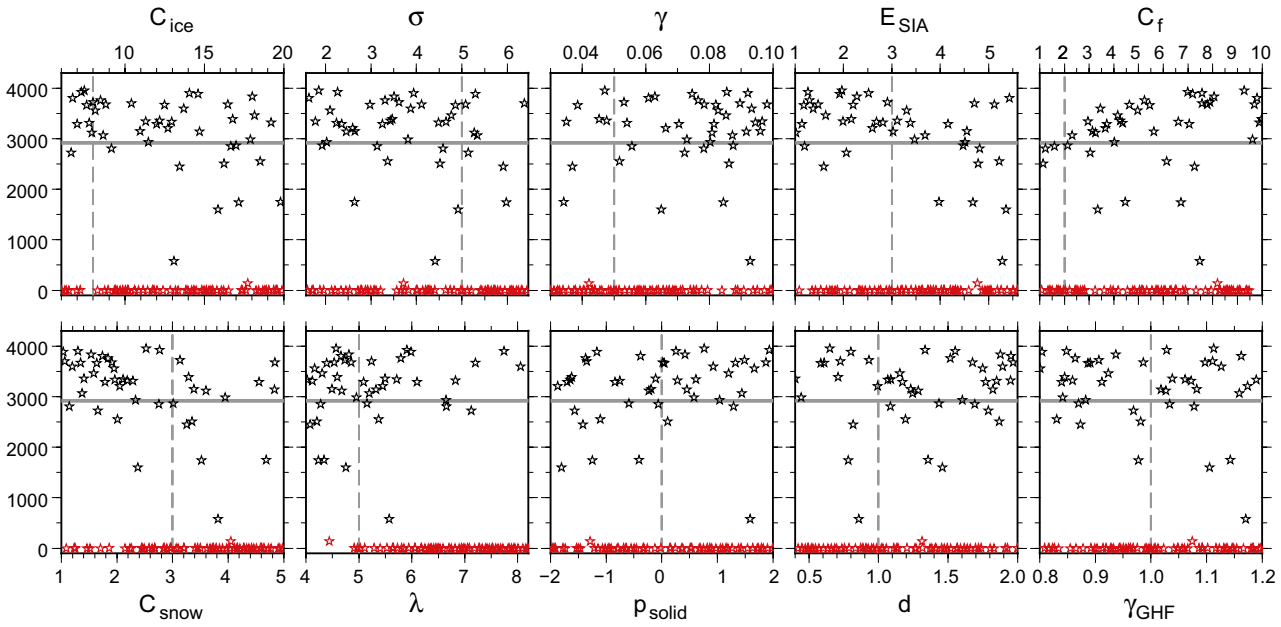

Figure 5-35. *Same as Figure 5-34, but for the topo2 climate forcing. A description of each parameter is provided in Table 5-15. From Quiquet et al. (2016).*

5.4.3 Discussion on additional uncertainty sources

In the previous subsections, ice-sheet model experiments by Colleoni et al. (2014) and Quiquet et al. (2016) have been described. The objective of those experiments was to estimate the maximum possible thickness of the Eurasian ice-sheet over Forsmark during the MIS 6 glacial maximum, which is the most extensive glaciation in Eurasia known from geological records. Combined, Colleoni et al. (2014) and Quiquet et al. (2016) carried out a total of 270 parameter sensitivity experiments with the GRISLI ice-sheet model, using the climate forcing fields from two AOGCM experiments with different representations of the MIS 6 Laurentide ice-sheet (*topo1* and *topo2*).

While Colleoni et al. (2014) mostly carried out uni-variate sensitivity experiments to evaluate the effect of isolated parameter changes on the ice thickness, Quiquet et al. (2016) conducted a multivariate sensitivity analysis to enable a larger part of the parameter space to be explored. As a result, the maximum ice thickness obtained in Quiquet et al. (2016) is about 680 m (760 m) larger than in Colleoni et al. (2014), resulting in a maximum thickness amounting to 4150 m (3957 m) when using the *topo1* (*topo2*) climate forcing. The average ice thickness over Forsmark among all the parameter sensitivity experiments amounts to 3168 m (2973 m) in Colleoni et al. (2014) and 3578 m (3157 m) in Quiquet et al. (2016) (not counting the experiments that failed to simulate ice over Forsmark) for the *topo1* (*topo2*) climatology (Table 5-14).

The mean ice-sheet thicknesses resulting from the simulations in Quiquet et al. (2016) (~3200–3600 m) is regarded as the most realistic range of the Saalian maximum ice thickness over Forsmark. It is comparable with the maximum ice thickness estimates in Colleoni et al. (2014) and in SR-Site based on Lambeck et al. (2006) (3400 m).

In the following subsections, the existence of additional uncertainty sources and their potential importance for the MIS 6 ice-sheet thickness are discussed. In summary, these uncertainties have an overall smaller influence on the ice-sheet thickness than the uncertainties related to the parameters in the ice-sheet model. Therefore, the results from those experiments are given less attention in the maximum ice-thickness assessment for Forsmark. Note that the following discussion only includes uncertainties that have been quantified in ice-sheet model experiments. For a comprehensive discussion on other, less important, uncertainties (e.g. the vegetation cover in the AOGCM or the representation of the bedrock depression) the reader is referred to Colleoni et al. (2014).

Initialization of the ice-sheet model

The ice-sheet model experiments in Colleoni et al. (2014) and Quiquet et al. (2016) were initialized from a pre-defined MIS 6 ice-sheet configuration in Eurasia based on Peyaud (2006). This choice may have a substantial impact on the resulting steady-state ice-sheets, particularly if the ice-sheet grows in a climate regime that enables multiple steady-state solutions. However, Colleoni et al. (2014) found that this is not the case for the MIS 6 ice-sheets. In a sensitivity experiment, they initialized the ice-sheet model with ice-free conditions which was compared to the experiment with a pre-defined initial ice-sheet (all other parameters and boundary conditions were identical between the experiments). The resulting steady-state ice-sheets from the two experiments are virtually identical (see Figure 5-2 in Colleoni et al. 2014), suggesting that this potential error source is not important for the maximum ice thickness over Forsmark when using long model integration times as was the case in these simulations (see also discussion in Quiquet et al. 2016).

Climate forcing

Some of the sensitivity to climate forcing was investigated in Colleoni et al. (2014) and Quiquet et al. (2016) by changing climate-forcing-related parameters in the ice-sheet model (Figure 5-33, Figure 5-34 and Figure 5-35). However, these experiments did not account for the seasonal and spatial variations in climate forcing data related to changes in climate dynamics.

The simplest way to assess the importance of such changes is to derive the climate forcing from several different AOGCMs. However, aside from CESM1.0.5 no other climate models have yet been used to simulate the MIS 6 climate. To get around this problem, Quiquet et al. (2016) let the difference in the pre-industrial climates between CESM1.0.5 and six other AOGCMs represent "typical" model biases in those models. The pre-industrial climate anomalies were then added to the MIS 6 *topo1* and *topo2* climate forcing fields. Subsequently, these fields were used as climate forcing in steady-state experiments with GRISLI.

The resulting ice thickness over Forsmark varied between ~2800 m (~2600 m) to ~3700 m (~3400 m) for *topo1* (*topo2*) depending on the applied AOGCM-derived climate forcing field. As reference, using "default" model CESM1.0.5 resulted in a thickness of ~3100 m (~2900 m) for *topo1* (*topo2*).

Next to the ice-sheet model parameters, the sensitivity of the ice-sheet thickness to AOGCM-derived climate forcing is the highest among the sensitivity experiments in Colleoni et al. (2014) and Quiquet et al. (2016). However, the range of Forsmark ice-sheet thickness estimates from these experiments is still considerably lower than the range resulting from varying the basal drag coefficient in the multi-variate parameter experiments (Figure 5-34 and Figure 5-35; Quiquet et al. 2016). In addition, the thick ice-sheets resulting from high values of the basal drag coefficient yields very cold conditions over most of the ice-sheet surface (due to the atmospheric lapse rate). Under these cold conditions, typical climate anomalies associated with model biases have a very limited influence on the surface mass balance. Hence, the sensitivity of the ice-sheet thickness to the basal drag coefficient is fairly insensitive to how the climate forcing related parameters in the ice-sheet model have been defined (Figure 5-34 and Figure 5-35), suggesting that the basal drag is the most critical parameter for the ice-sheet thickness.

Thermo-mechanical formulation in the ice-sheet model

As with climate models, also ice-sheet models have different representations of various physical processes. As a result, one cannot expect that the results from GRISLI would be perfectly reproducible in another ice-sheet model. To evaluate the potential influence of ice-sheet model on the ice thickness, Quiquet et al. (2016) repeated some of the steady-state GRISLI experiments with SICOPOLIS (Greve 1997), which is another typical state-of-the-art ice-sheet model. There are two main differences in the physical representations between these two models. In contrast to GRISLI, there is no representation of areas with fast-flowing ice (SSA) in SICOPOLIS. On the other hand, SICOPOLIS has a physical formulation for calculating the evolution of polythermal ice (a thermally complex structure including both warm and cold ice, see Section 3.1.1); this feature is not included in GRISLI.

In light of the high sensitivity of the ice thickness to the basal drag in ice stream areas (Figure 5-33, Figure 5-34 and Figure 5-35; Colleoni et al. 2014, Quiquet et al. 2016), the lack of SSA representation in SICOPOLIS is expected to result in larger the ice thicknesses over Forsmark compared to GRISLI. Because there is robust evidence of large ice streams related to the Eurasian ice-sheet during the past glaciations (Svendsen et al. 2004, Ottesen et al. 2005, Dowdeswell et al. 2006, Kleman and Glasser 2007), as well as in present-day ice-sheets (cf. Bamber et al. 2000, Joughin et al. 2004), the results from SICOPOLIS are used to evaluate the importance of fast flowing ice for the ice thickness rather than estimating the range of realistic ice thicknesses.

Surface mass balance formulation

Following Charbit et al. (2013), Quiquet et al. (2016) also implemented four alternative surface mass balance parameterizations in GRISLI. These modifications only had a modest and mostly decreasing effect on the ice thickness. The steady-state ice thickness over Forsmark in these experiments all ended up between ~2500 m and ~3200 m.

5.4.4 Evaluation of using MIS 6 as a target period for maximum glaciation for the next 1 million years

In this section, the choice of using the MIS 6 glaciation as an analogy for the largest possible glaciation over the next 1 million years is evaluated. The evaluation is done by comparing the results from Colleoni et al. (2014) and Quiquet et al. (2016) with results from the ice-sheet model experiments of Northern Hemisphere ice-sheet evolution for the next 1 million years in Huybrechts (2010).

The main result from Huybrechts (2010) is shown in Figure 5-36. The most striking result from this study is that none of the simulated glacial maxima over the next 1 million years has a significantly larger extent than the LGM ice extent. According to Huybrechts (2010), future glacial maxima occur in about 60, 102, 419, 433, 467, 694 and 890 ka, most of which show similar glacial extents as the LGM. The latest of these maxima (in 890 ka) has a slightly increased global ice extent, but the Eurasian ice-sheet extent in that experiment is not significantly larger than during the LGM (Figure 9 in Huybrechts

2010). The fact that future glaciations in Huybrechts (2010) remain relatively modest, or at least do not become significantly larger than the LGM ice configuration, is mostly attributed to the climate representation. The climate forcing used in Huybrechts (2010) is taken from BIOCLIM (2003), which is calculated from future variations of Earth's orbital parameters and projected CO_2 concentrations based on proxy data from the Vostok ice core record (Burgess 1998). As a result, the climate cooling related to future glaciations is slightly reduced or similar to that of the LGM. Some of the simulated future glaciations have a longer duration than the Weichselian glaciation, contributing to further ice growth. However, this contribution is counteracted by a reduced cooling for those glaciations.

The results in Figure 5-36 were obtained by assuming a relatively cold future climate scenario (scenario A3 in BIOCLIM 2003). The BIOCLIM scenarios based on natural climate variability (A4a and A4b) resulted in even less extensive glaciations in the Northern Hemisphere (Huybrechts 2010). This is most likely also the case for the remaining climate scenarios in Huybrechts (2010), which include the effect of higher concentrations of anthropogenic greenhouse gases (scenarios A1, A2, B and C).

Projecting the climate over the next 1 million years undoubtedly has a lot of uncertainties. The study of Huybrechts (2010) is based upon the assumption that the spatial variability of future glacial climates will be similar to that of the LGM. Hence, the climate forcing ensures that the simulated future ice-sheets are not radically different from the most recent glaciation. Moreover, in Huybrechts (2010) it is assumed that anthropogenic climate change is negligible for the later glaciations.

A comparison between the MIS 6 ice-sheet reconstructions (Colleoni et al. 2014, Quiquet et al. 2016) and projected future ice-sheets (Huybrechts 2010) reveals that the Eurasian ice-sheet during MIS 6 was significantly larger than any of the projected future Eurasian ice-sheet extents. The geographical maximum MIS 6 ice-sheet extent in Eurasia was at least twice as large as the LGM counterpart, which in turn had a similar size as most of the projected future glaciations in Huybrechts (2010). It should be noted though, that neither the MIS 6 nor the LGM ice-sheet reached their maximum extents simultaneously in all areas that were ice covered, but at different times in different regions. Nevertheless, the substantial general difference in size between the MIS 6 ice-sheet and the LGM/reconstructed future ice-sheets by Huybrechts suggests that using the MIS 6 glaciation as a benchmark for estimating the maximum thickness of future ice-sheets in the next 1 million years is a valid approach.

5.4.5 Maximum ice-sheet thickness assessment for Forsmark

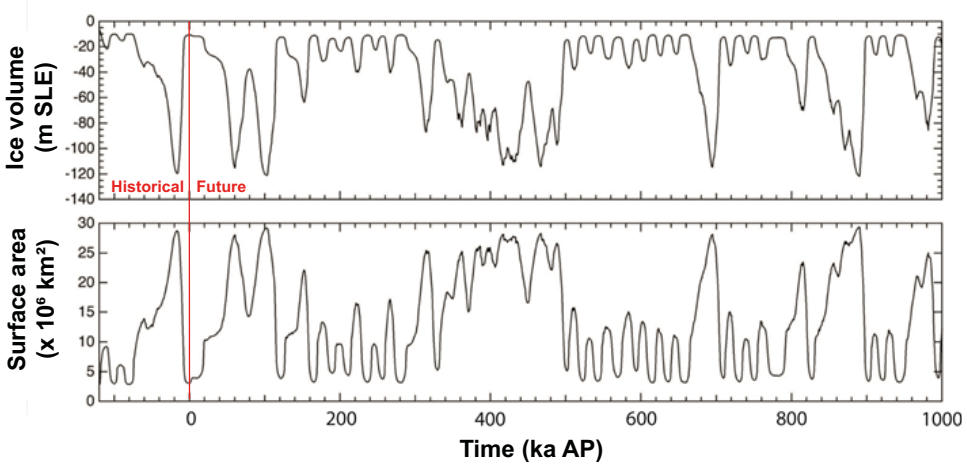

Figure 5-36. *Results from the transient ice-sheet model experiments of Northern Hemisphere glaciations during the Weichselian, and for the next 1 million years (Huybrechts 2010). The figure shows the experiments that resulted in the largest ice-sheets. The ice volume (upper panel) is displayed as changes in the eustatic sea-level relative to present-day. See Huybrechts (2010) for details. The results show repeated glaciations in the future, of which none is significantly greater than during the LGM. Modified from Huybrechts (2010).*

The following maximum ice-sheet thickness assessment for Forsmark is based on the multi-variate ice-sheet parameter sensitivity analysis (Quiquet et al. 2016), since these experiments resulted in the thickest ice cover over Forsmark. Based on the uncertainty assessment made in these experiments, and including considerations of their experimental design and assumptions made in relation to knowledge on the behaviour of the natural ice-sheet/climate system, the maximum ice-sheet thickness over Forsmark over the coming 1 million years is set to 4000 m (Table 5-16). This value is slightly lower than the maximum ice-sheet thickness from the multi-variate sensitivity experiments (4150 m; Table 5-14; Quiquet et al. 2016). The number is larger than the 3400 m used in SR-Site (SKB 2010a, SKB 2011, Section 12.7). The choice of 4000 m as a maximum ice-thickness value is motivated in the following subsections.

Table 5-16. Ice thickness and associated hydrostatic pressure contribution over Forsmark based on the reference glacial cycle climate case (Section 4.5), and the maximum ice-sheet thickness case in this report.

	Ice thickness	Hydrostatic pressure
Reference glacial cycle	2900 m	26 MPa
Maximum ice-sheet thickness	4000 m	36 MPa

Knowledge on North American ice-sheet volume

The thickest ice-sheets in Quiquet et al. (2016) were obtained when using the *topo1* climate forcing, which was derived from an AOGCM experiment using the large LGM configuration of the Laurentide ice-sheet in North America. Using the climate forcing based on the smaller Laurentide ice-sheet configuration (*topo2*; see Figure 5-32) resulted in overall thinner ice-sheets (Table 5-14). The maximum ice-sheet thickness over Forsmark in the *topo2* experiments never exceeded 4000 m (~3957 m; see Table 5-14).

As already discussed, using the large LGM configuration of the Laurentide ice-sheet in combination with an extensive and thick MIS 6 ice-sheet in Eurasia is unrealistic as it does not match the estimates on sea-level records from that time. In other words, it exceeds the global ice volume budget recorded from that time. The sea-level records suggest that the Laurentide ice-sheet during the MIS 6 glacial maximum was considerably smaller than during the LGM (e.g. Colleoni et al. 2016). In addition, records of ice-rafted debris from the Hudson Bay area reveal that the fluxes of icebergs from the Laurentide ice-sheet during the MIS 6 glacial maximum were considerably lower than during the LGM (de Abreu et al. 2003, Channell et al. 2012). This is a clear indication that ice dynamics and size of the Laurentide ice-sheet was reduced during MIS 6 compared with the LGM.

In summary, the smaller *topo2* version of the Laurentide ice-sheet is a more realistic estimate of the MIS 6 North American topography than the *topo1* version. Because of this, the ice-sheet model experiments based on the *topo2* climate forcing has been more strongly weighted in the maximum ice-sheet thickness assessment than those based on the *topo1* climate forcing.

Assumption of ice-sheet in steady state

All ice-sheet model experiments in Colleoni et al. (2014) and Quiquet et al. (2016) were integrated to steady state (integration time more than 100 ka) using a constant-in-time climate forcing. Using a constant climate for such long time is unrealistic as it is well known that the climate has a substantial variability over multiple timescales. For the timescale of glacial cycles, which is of main interest here, the climate variability is primarily determined by variations in Earth's orbital configuration and changes in atmospheric greenhouse gas concentrations. Omitting this variability, as in the methodology used in Colleoni et al. (2014) and Quiquet et al. (2016), results in either an over- or underestimation of the "true" ice-sheet thickness that would result from including all scales of variability in the climate forcing data.

To evaluate the first-order impact of the steady-state assumption on the resulting ice-sheet thickness, the MIS 6 glacial climate is compared with some average conditions during glacial cycles. Each glacial cycle can be divided into so-called stadials and interstadials, where stadials corresponds to cold periods with ice growth, and interstadials to comparatively warm periods when the global ice volume is reduced or remain relatively unchanged. If the evaluated steady-state climate is more like a stadial, the absence

of warm periods would likely allow further ice growth, resulting in thicker ice-sheets. On the other hand, if the steady-state climate were more like an interstadial, the absence of cold periods would likely hinder significant ice growth, resulting in thinner and smaller ice-sheets.

Colleoni et al. (2014) and Quiquet et al. (2016) used a climate forcing representative for MIS 6, which is known from the geological records to be a typical cold stadial. Hence, the steady-state assumption in Colleoni et al. (2014) and Quiquet et al. (2016) most likely resulted in an overestimation of the "true" MIS 6 peak ice-sheet thickness over Forsmark. Transient, more realistic, simulations would therefore probably have resulted in a thinner ice-sheet.

A steady-state ice-sheet is thus not considered realistic in nature. The simulations using a steady-state assumption gives an upper boundary of the thickness that an ice-sheet modelling can generate under these conditions. However, for the PSAR, a maximum ice-sheet thickness of 4000 m is pessimistically assumed based on the steady-state simulations.

Timing of the MIS 6 Eurasian ice-sheet

Geological evidence shows that a major retreat of the Late Saalian ice-sheet occurred at ~150 ka BP (Astakhov 2004, Svendsen et al. 2004). Considering that the Late Saalian extent used in Colleoni et al. (2014) and Quiquet et al. (2016) corresponds to the MIS 6 glacial maximum at ~140 ka BP, the Eurasian ice-sheet must have re-grown to this large extent in only 10 ka. This timing is not reasonable and suggests that the major extent could have been reached at different moments of the cycle rather than at 140 ka BP.

This would implicate that the Eurasian ice-sheet extent used in the AOGCM and as initialization of the ice-sheet model represents the combined maximum extents over a longer period, rather than the extent at a certain point in time. If that is the case, the ice-sheet extent at the MIS 6 glacial maximum must have been smaller than the reconstruction used in Colleoni et al. (2014) and Quiquet et al. (2016) (Figure 5-32). A smaller ice-sheet extent would require even more extreme and unlikely conditions to sustain a thickness of more than 4000 m.

5.4.6 Additional hydrostatic pressure from maximum ice thickness

The additional hydrostatic pressure from the maximum possible ice thickness over Forsmark (4000 m) is 36 MPa (Table 5-16). For the reference glacial cycle climate case, the additional hydrostatic pressure related to ice thickness over Forsmark is 26 MPa (Table 5-16), which is the same value used in SR-Site (SKB 2010a, 2011).

5.4.7 Hydrostatic pressure exceeding ice overburden pressure

The reported basal hydrostatic pressures from the ice thicknesses in Table 5-16 represent estimates of the ice overburden pressure, i.e. the pressure exerted on the basal hydrological system by the local ice thickness. However, there is also the possibility that the basal pressures could exceed ice overburden pressure in some situations. This has been observed on mountain glaciers with soft (till) beds (Roberts et al. 2000, Kavanaugh 2009, Kavanaugh et al. 2010).

In order to investigate if basal water pressures higher than overburden pressure are to be observed also in an ice-sheet setting, either as short-lived pressure pulses or more persistent high pressures, detailed measurements of basal water pressure were made within the GAP study (Claesson Liljedahl et al. 2016, Harper et al. 2016) and the ICE study (Harper et al. 2019) in a sector of the ablation zone of the Greenland ice-sheet. Over daily to seasonal timescales, they reported that the basal water pressure varied between 0.8 and 1.1 times the overburden pressure. In this context, it is important to note that the measurements were all made in the ablation zone where basal meltwater is abundant. No equivalent measurements have been made in the ice-sheet interior where the ice-sheet is 2 to 3 times thicker than in the ablation zone. However, because there is virtually no surface melt input within the ice-sheet interior, it is unlikely that the maximum basal pressures (i.e. pressure above overburden) found in the ablation zone should scale with ice overburden pressure in the ice-sheet interior.

Localized regions with water pressure persisting above ice overburden may still be plausible over longer timescales due to increased stress induced by ice flow against steep bedrock bumps. However, to first order, the magnitude of such stress perturbation does not scale with the overlying ice pressure, but rather with the basal shear stress at the bed that the feature must support (Weertman 1957). Hence, there is no physical justification as to why the reported pressures above overburden over daily to seasonal timescales in the ablation zone should also be present in the ice-sheet interior (Harper et al. 2019).

In addition, basal hydrostatic pressures can also occur in the form of pressure pulses over shorter timescales, with a typical a duration of seconds or minutes. The existence of such short duration pulses has been identified below smaller glaciers with till beds. For example, Kavanaugh (2009) and Kavanaugh et al. (2010) measured thousands of subglacial pressure pulses on Trapridge and West Washmawapta glaciers with magnitudes exceeding the local ice overburden pressure. The possibility of transient short pressure pulses beneath the Greenland ice-sheets was therefore also investigated during the ICE project (Harper et al. 2019). The measurements identified rapid pressure pulses to be exceedingly rare. A total of five pulses were identified in two data sets covering 143 and 52 days of measurements in two boreholes 180 m apart. The pulses were up to an order of magnitude larger than measured diurnal pressure variations at the same site. Importantly, the measured pulses all occurred as pressure drops and therefore did not contributed to basal pressures higher than overburden pressure. In addition, none of the pulses were transmitted between the two holes. This demonstrates that the measured pressure pulses are localized events that occur over length scales much less than an ice thickness (Harper et al. 2019). Even if extension of the measured high frequency pressure dataset to the broader basal system is hindered by an incomplete understanding of the potential cause(s) of the few measured pulses, the localized characteristics of the pressure pulses detected in the ICE study makes it implausible that a pressure pulse event, even if it were to be positive, could impact a location at 450 m repository depth in bedrock.

5.4.8 Timing of maximum ice thickness over Forsmark in the future

In the SR-PSU safety assessment it was postulated that an extensive glaciation, similar to MIS 6, is unlikely to occur within the next 100 ka (SKB 2014). This assessment is based on known future variations of the Earth's orbit, as well as the anthropogenic warming resulting from higher concentrations of atmospheric greenhouse gases.

Huybrechts (2010) argues that the coldest climate within the next 1 million years could occur in ~890 ka, associated with a period of low insolation values in the northern high latitudes. However, the ice-sheet model experiments in Huybrechts (2010) result in a significantly smaller ice-sheet in Eurasia for this period compared to the MIS 6. Together with previous assessments of the climate evolution for the next 100 ka (SKB 2014), the experiments in Huybrechts (2010) indicate that glaciations of similar extent as MIS 6 glacial maximum are rare and very unlikely to occur within the next 100 ka, and possibly also for the coming 1 Ma.

5.4.9 Surface denudation

The large size of this ice-sheet would take a longer time to build than the maximum ice-sheet of the *reference glacial cycle climate case* (Section 4.5.1), but not a longer time than the 60 ka of ice-sheet presence in the *extended ice-sheet duration climate case* (Section 5.3). Therefore, this climate case does not contribute to a longer time of glacial erosion, or resulting larger total amount of denudation, than the *extended ice-sheet duration climate case*. For that reason, surface denudation is not described and treated further in the *maximum ice-sheet thickness climate case*.

5.5 Severe permafrost climate case

5.5.1 Background

The main factors of importance for repository safety in the permafrost climate domain are the permafrost- and frozen depths, the depth of the isotherm at which the buffer and backfill freezes, and the possible freezing out of salt that may result in a zone with high salinity beneath the freeze front. The prevailing climate conditions are the main factor determining the evolution of permafrost, see Section 3.4.4 and Hartikainen et al. (2010). A mean annual air temperature well below 0 °C for long periods is a prerequisite for the development of permafrost to greater depth, Section 3.4.4.

In order to investigate remaining uncertainties within the periglacial climate domain that were not studied in the permafrost simulations reported in Section 3.4.4 and 4.5, a *severe permafrost climate case* was investigated (Hartikainen et al. 2010). These remaining uncertainties mainly consist of the possibility of having a cold dry climate at Forsmark, but without the presence of an ice-sheet. An assumption of a cold periglacial climate is here combined with an assumption of a very dry climate to favour permafrost growth. In this climate case, the dry climate also limits ice-sheet growth so that an ice-sheet does not reach the Forsmark site during the first glacial cycle. If an ice-sheet covers the site, any pre-existing permafrost decays due to the insulating effect of the ice-sheet, especially if the ice-sheet is warm-based (Section 4.5.4). In line with the dry and cold assumption, and that no ice-sheet forms over the site, it is further assumed that no post-glacial periods of submerged conditions occur, and that no insulating winter snow and vegetation cover exist.

In addition to the simulation using the above assumptions, several sensitivity studies have also been done in order to investigate the climate conditions required to develop permafrost and perennially frozen ground to repository depth.

5.5.2 Ice-sheet evolution

One of the main assumptions in the *severe permafrost climate case* is that there is no ice-sheet coverage over the Forsmark site for the coming 120 ka, and consequently there is no ice-sheet development in this climate case.

5.5.3 Permafrost evolution

The *severe permafrost climate case* is analysed with the same 2D permafrost model that was used for the *reference glacial cycle climate case* and for the sensitivity experiments on surface, subsurface and air temperature parameters (Section 3.4.4). The *severe permafrost climate case* was simulated for a full glacial cycle, from 115 ka BP to present. However, for the present section the results have been projected for a future glacial cycle, in the same way as the reconstruction of last glacial cycle conditions (Section 3.4.4) were used to construct a future *reference glacial cycle climate case* (Section 4.5).

In this context it should be noted that the exact way in which the start of the previous reconstructed glacial cycle is taken to form the start of the present climate case will affect the detailed timing of permafrost events, such as the detailed timing of the first permafrost development. However, for the safety assessment of a KBS-3 repository, the precise timing of permafrost and freezing events is not of importance. Instead it is the maximum simulated permafrost and freezing *depths* that are of importance. Therefore, the temporal uncertainties arising from the onset of the future glacial cycle in the *severe permafrost climate case* do not affect the analysis of e.g. the PSAR freezing scenario, see the **Post-closure safety report**.

The following assumptions were made for the *severe permafrost climate case*:

- The climate is so dry that no ice-sheet forms that is large enough to reach the Forsmark site at any time during the glacial cycle, i.e. ice-free conditions prevail during the entire glacial cycle.
- In line with the above assumption, it is assumed that the repository location is not isostatically depressed below sea-level.
- The climate is so dry that there is no insulating snow cover during winter.
- There is no vegetation to insulate the ground from low air temperatures.
- The temperature curve reconstructed for the last glacial cycle, but without a presence of ice-sheets and submerged conditions (Figure 3-43, red line) was employed for calculating ground surface temperatures.

Initial conditions are assumed to correspond to the present-day conditions (temperature, salinity and groundwater pressure). Heat generated by the radioactive decay of the spent fuel in the repository is included in the simulation. The modelled 2D profile is seen in Figure 3-48.

Regarding the choice of using the temperature curve reconstructed for the last glacial cycle also for the analysis of a *severe permafrost climate case*, the following needs to be considered. Northern Hemisphere mid-latitude ice-sheets form essentially as a response to low air temperatures, see Section 3.1. In line with this, there is a correlation between cold interstadial periods during glacial

cycles and large ice-sheet configurations. In the *severe permafrost climate case*, the main assumption is that the climate is cold but without an ice-sheet reaching the Forsmark site, see above. This means that the maximum ice-sheet configuration for this hypothetical case does not reach mid-central Sweden at any time during the glacial cycle. This ice-sheet thus is significantly smaller, at all times, than during the Weichselian glacial cycle. This, in turn, strongly implies that that air temperatures during the fictive glacial cycle of the *severe permafrost climate case* would be higher than in the reconstruction of the last glacial cycle that hosted the Weichselian ice-sheet (but still significantly colder than temperate climate conditions). If temperatures were to be the same during the *severe permafrost climate case* as during the Weichselian, a larger ice-sheet would likely form and cover the Forsmark site for parts of the glacial cycle. It is difficult to estimate what temperatures would correspond to a glacial cycle as envisaged for the *severe permafrost climate case*. However, it is likely that the temperature curve used for permafrost simulations for the *severe permafrost climate case* would, in line with the above reasoning, be slightly warmer than the one used for the reconstruction of the last glacial cycle.

On the other hand, the temperature curve reconstructed for the last glacial cycle also has a significant uncertainty interval, see Appendix A. The comparison of the reconstructed last glacial cycle temperature curve with (the few) existing quantitative proxy data on Weichselian temperatures from the Fennoscandian region seems, however, to indicate that the reconstructed temperature curve is in broad agreement with proxy data, see Appendix A. Furthermore, the comparison suggests that the temperature curve does not overestimate temperatures for the compared last glacial cycle stadials and interstadials. Instead, the general picture from the comparison with Fennoscandian proxy data is that the reconstructed temperature curve gives roughly correct or slightly too low temperatures by a few degrees.

In order to make a reasonable choice of temperature curve for the *severe permafrost climate case*, with the above issues in consideration, air temperatures were pessimistically assumed to fall according to the reconstructed temperature curve for the *reference glacial cycle climate case*, but without a presence of ice-sheets and submerged conditions (Figure 3-43).

Surface and subsurface properties and conditions

Just as for the 2D permafrost modelling for the *reference glacial cycle climate case* (Section 3.4.4), the significant uncertainties associated with descriptions of the surface conditions motivate the analysis of two climate variants of the *severe permafrost climate case*, one humid and one dry. This is to yield a lower and upper limit for the permafrost and perennially frozen ground development, see further below.

Based on the Köppen climate classification (Lohmann et al. 1993) and long-term observations (Eugster et al. 2000) the climate of the *severe permafrost climate case* may be divided into three climate zones: *Boreal*, *Subarctic* and *Arctic*, which may be characterized by the annual mean air temperature, the monthly mean maximum summer air temperature and the monthly mean minimum winter air temperature, together with the monthly mean maximum summer and winter precipitations (Table 5-17), see Hartikainen et al. (2010). The large ranges in the monthly mean air temperatures and precipitations are explained by the fact that the description and modelling of surface conditions involve significant data-, conceptual- and model uncertainties, see Hartikainen et al. (2010).

Table 5-17. Climate information for the severe permafrost climate case. Summer precipitation is close to 5 mm month^{-1} for dry case whereas it is close to 50 mm month^{-1} for the humid case. The winter precipitation is the same (< 1 mm month^{-1}) for both cases.

Climate zone	Annual mean air temperature (°C)	Monthly mean max. summer air temperature (°C)	Monthly mean min. winter air temperature (°C)	Monthly mean max. summer precipitation (mm month^{-1})	Monthly mean max. winter precipitation (mm month^{-1})
Boreal	> 0	+10 – +20	–15 – +5	5 – 50	< 1
Subarctic	0 – −6	+5 – +15	–25 – −10	5 – 50	< 1
Arctic	< –6	< +5 – +10	–35 – −20	5 – 50	< 1

Other surface properties and conditions are the same as in the 2D permafrost modelling of the *reference glacial cycle climate case* (Section 3.4.4). All subsurface properties for the *severe permafrost climate case* are the same as for the 2D permafrost modelling of the *reference glacial cycle climate case* (Section 3.4.4).

In order to construct an air temperature curve for a full glacial cycle without the presence of an ice-sheet at the Forsmark site, the site-specific air temperature curve reconstructed for the last glacial cycle (Figure 3-43, blue line) was used together with the ice-sheet surface elevations of the *reference glacial cycle* to making a correction for the difference in elevation between the height of the ice-sheet and that of the ice-free ground surface (see also Appendix A). Subsequently, by using the same n-factor approach as in the modelling of the *reference glacial cycle climate case*, calculations of ground-surface temperatures were made from air temperature (Section 3.4.4). The resulting air temperature curve for the *severe permafrost climate case* is seen in Hartikainen et al. (2010, Figure 2-15).

Figure 5-37 exemplifies modelled ground-surface temperatures along the profile at four different times for the *severe permafrost climate case* considering different climate conditions: 8.5 ka AP – Subarctic and partially submerged, 16.5 ka AP – Boreal, 25 ka AP – Subarctic, 50 ka AP – Arctic. The partially submerged conditions at 8.5 ka AP refer to locations away from the repository location, the repository location is never submerged in this climate case. For details on the setup of the *severe permafrost climate case*, see Hartikainen et al. (2010).

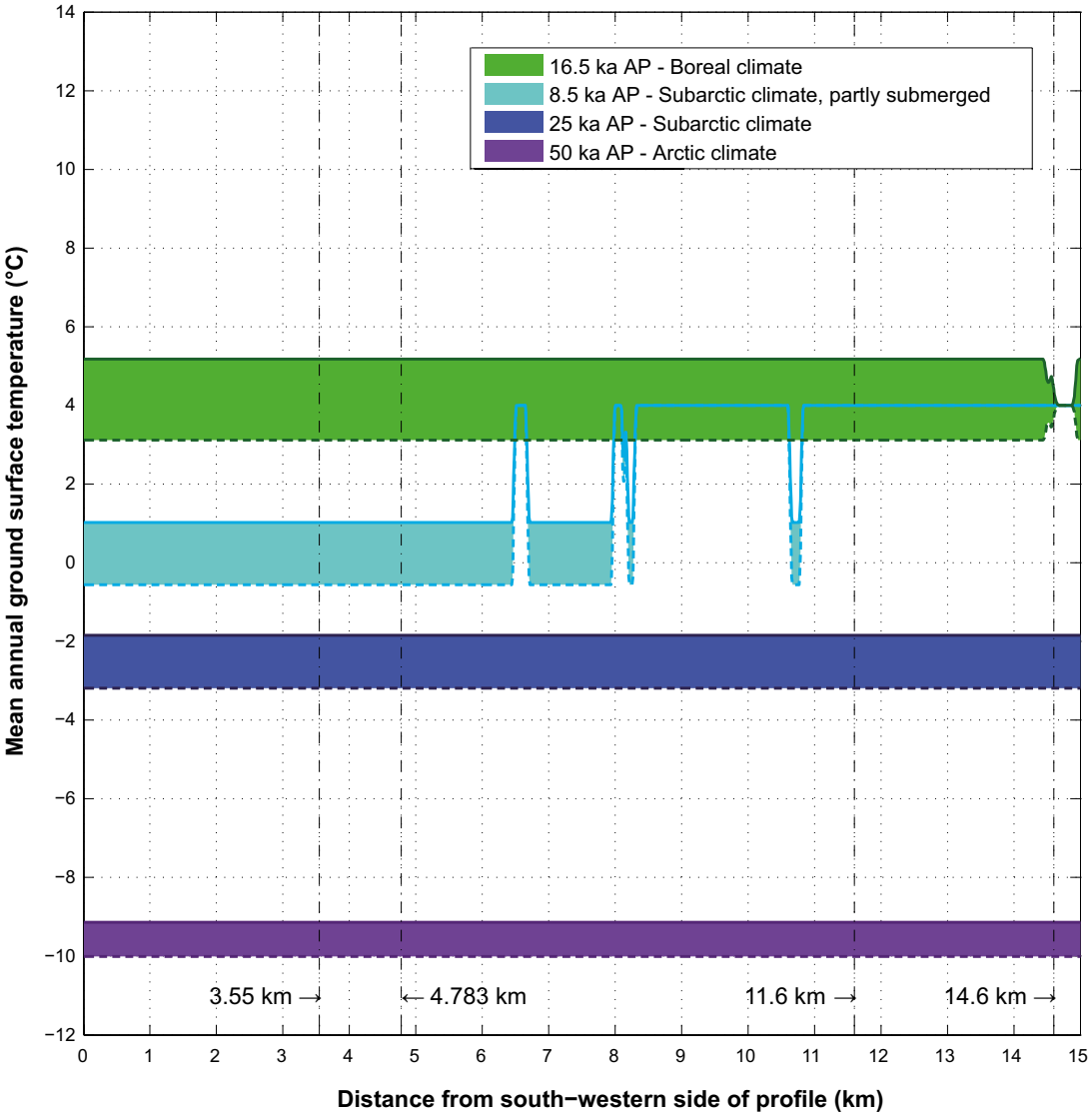

Figure 5-37. *Modelled ground surface temperatures along the profile at four different times for the severe permafrost climate case considering different climate conditions: 8.5 ka AP – Subarctic and partially submerged (assuming a +4 °C water temperature for submerged periods), 16.5 ka AP – Boreal, 25 ka AP – Subarctic, 50 ka AP – Arctic. The solid border lines of the coloured areas indicate the dry variant of the climate case and dashed ones the humid variant of the same case. For the 8.5 ka case, periods with a +4 °C temperature is a result of submerged conditions. For details on the calculations of ground surface temperatures, see Hartikainen et al.(2010).*

The extent of perennially frozen ground over the Forsmark site for the *severe permafrost climate case* is exemplified by time slices at 8.5, 25, 46, 50 ka AP in Figure 5-38 and Figure 5-39. The evolution of maximum permafrost depth and depth of perennially frozen ground at the repository location is shown in Figure 5-40. Figure 5-41 shows the same results over the whole profile, as well as the extent of permafrost summarised along the investigated profile.

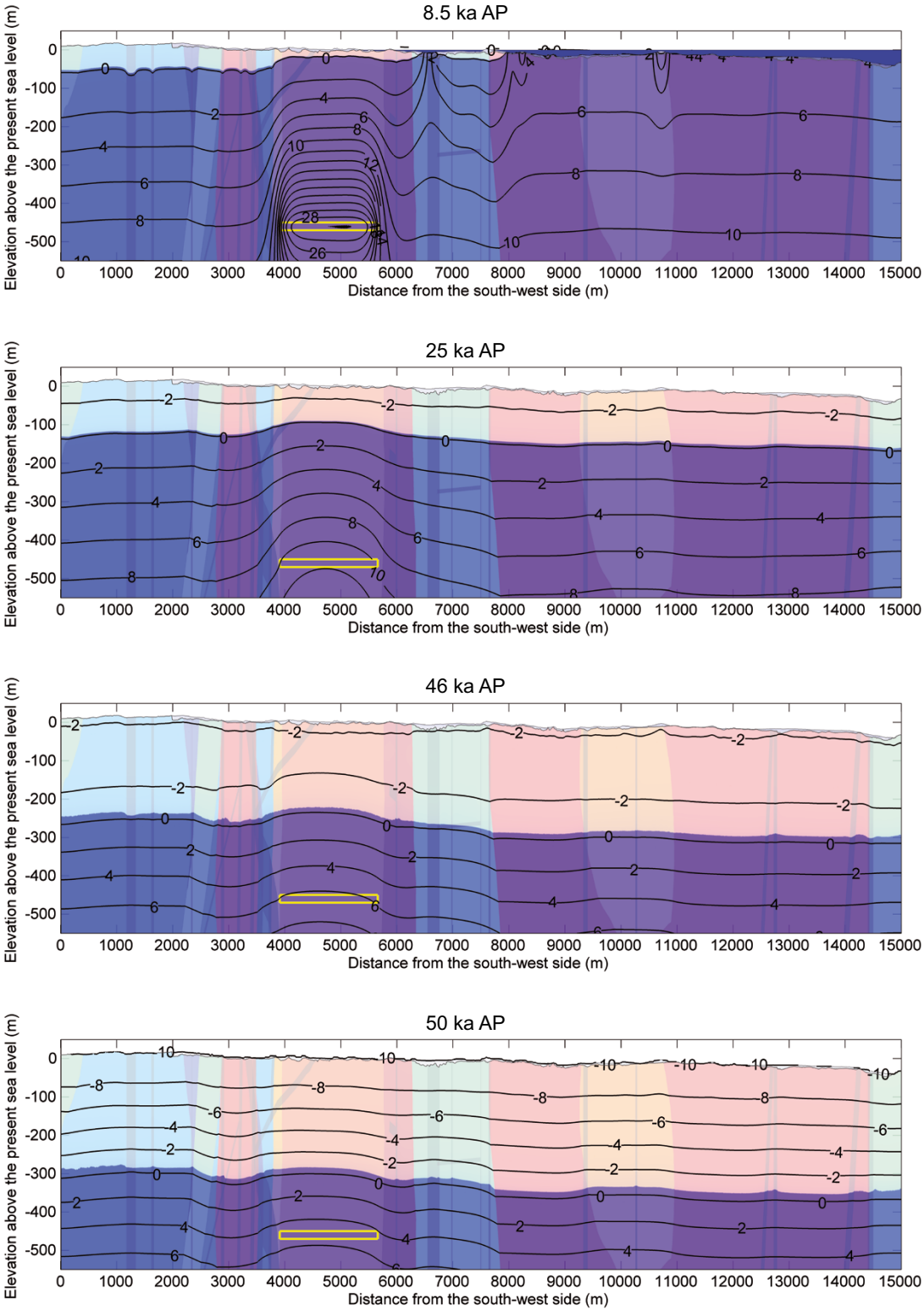

Figure 5-38. *Exemplified temperature contours in (°C) and the extent of perennially frozen ground (light colour) within permafrost (0 °C isotherm) at times 8.5, 25, 46, 50 ka AP for the humid variant of the severe permafrost climate case. Blue colour blue on the top of the profile at 8.5 ka AP shows the Baltic Sea. The yellow rectangle indicates the location of the repository.*

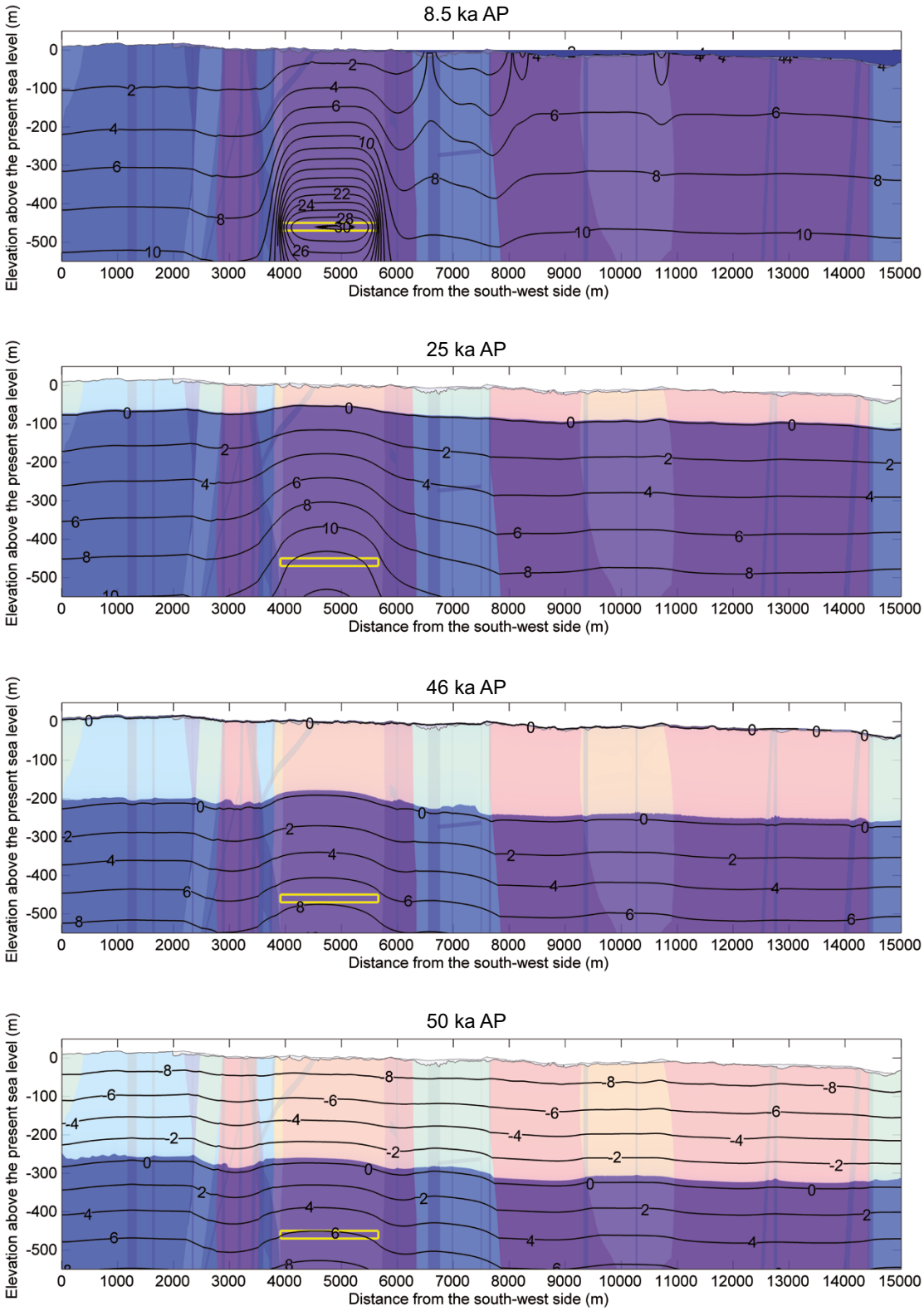

Figure 5-39. *Exemplified temperature contours in (°C) and the extent of perennially frozen ground (light colour) within permafrost (0 °C isotherm) at times 8.5, 25, 46, 50 ka AP for the dry variant of the severe permafrost climate case. Blue colour blue on the top of the profile at 8.5 ka AP shows the Baltic Sea. The yellow rectangle indicates the location of the repository.*

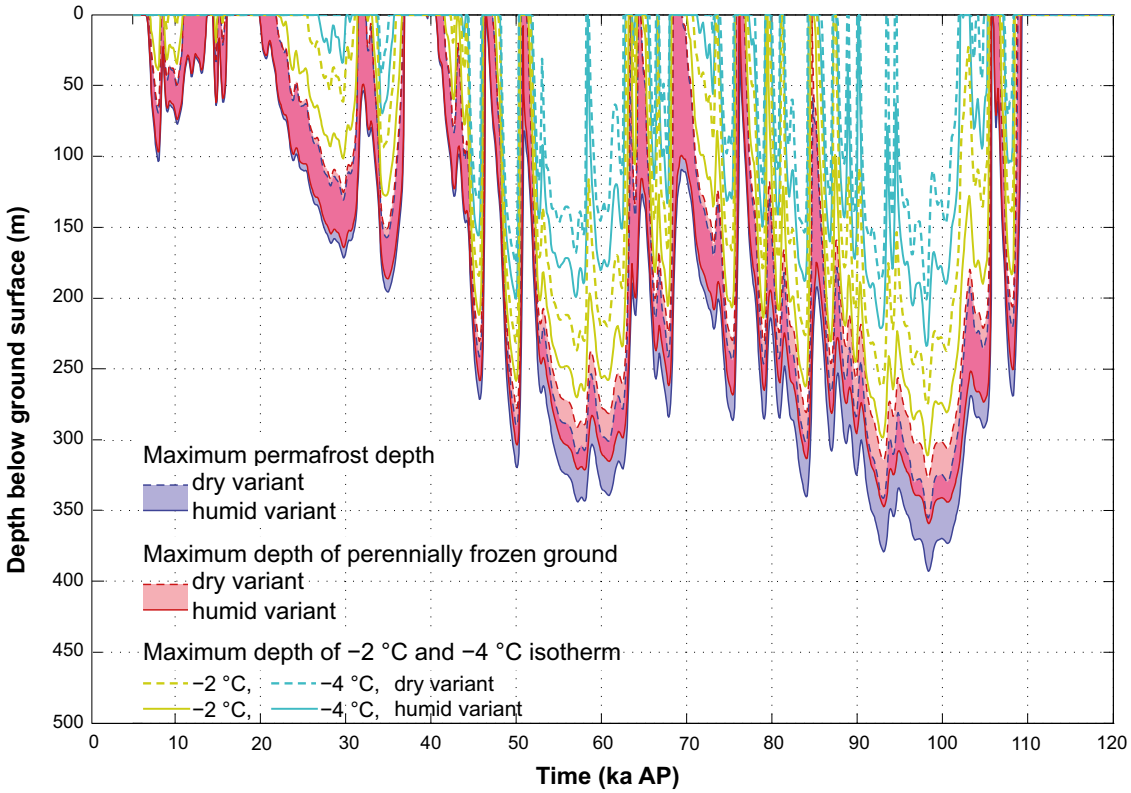

Figure 5-40. *Evolution of maximum permafrost depth, maximum depth of perennially frozen ground and maximum depth of −2 and −4 °C isotherms over the repository for the severe permafrost climate case. The upper permafrost surface, for periods of permafrost degradation from above, is not shown. The shaded area in blue and red represents the range when considering the dry and humid climate variants of the severe permafrost climate case. The darker lilac colour indicates that the results for permafrost and perennially frozen ground overlap.*

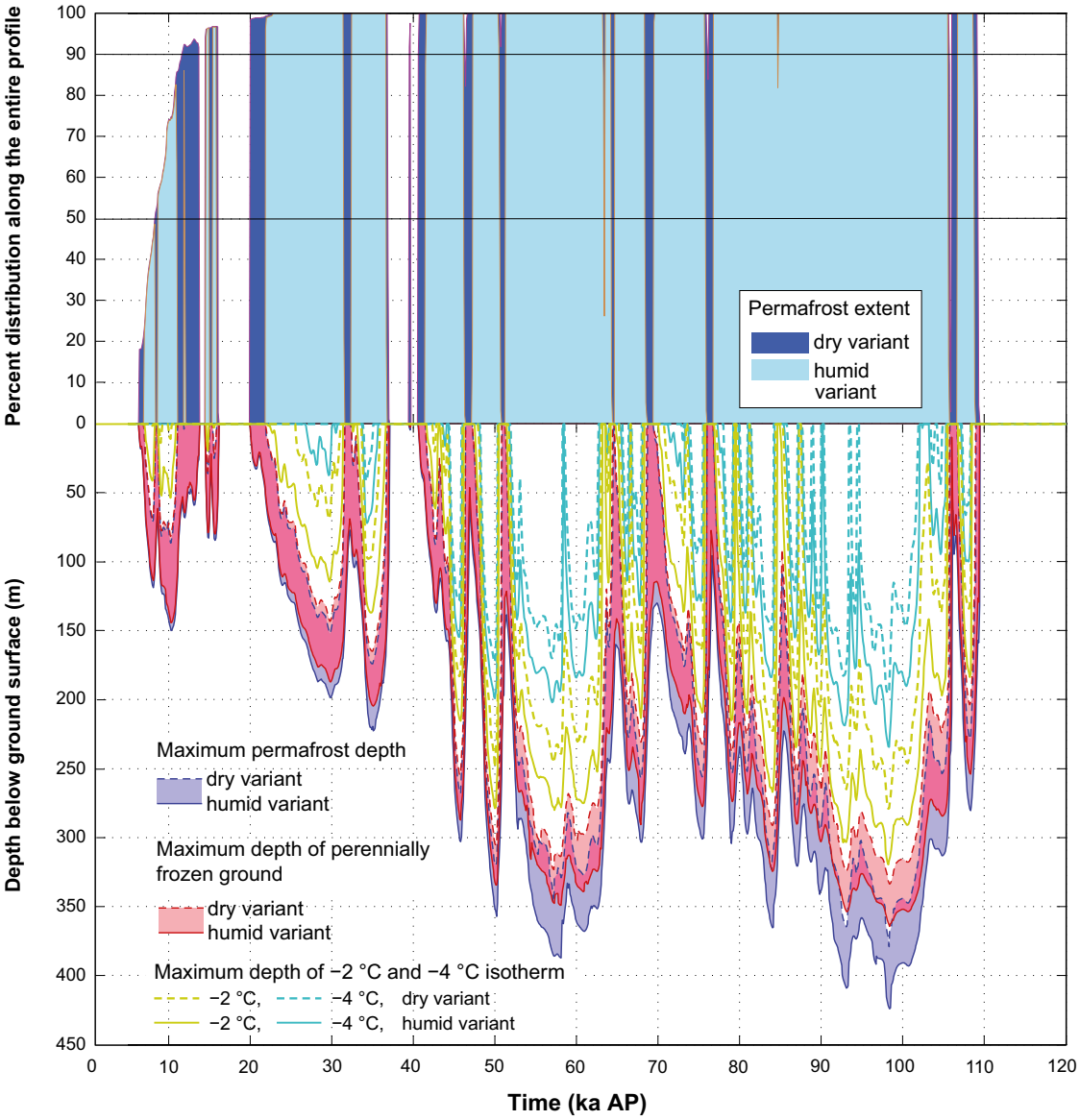

Figure 5-41. *Evolution of maximum permafrost depth, maximum depth of perennially frozen ground and maximum depth of −2 and −4 °C isotherms over the whole profile for the severe permafrost climate case. The figure also shows the percent permafrost distribution along the profile. The transition from sporadic to discontinuous permafrost occurs at 50-% coverage and from discontinuous to continuous permafrost at 90-% coverage, indicated by two horizontal lines. The upper permafrost surface, for periods of degradation from above, is not shown. The shaded area in blue and red represents the range when considering the dry and humid climate variants. The darker lilac colour indicates that the results for permafrost and perennially frozen ground overlap.*

The maximum permafrost depths, maximum depths of perennially frozen ground, and the extent of permafrost distribution are summarised in Table 5-18 and Table 5-19. In addition, Table 5-20 describes the evolution of permafrost depth and depth of perennially frozen ground at the repository site. For a corresponding table for the entire profile, see Hartikainen et al. (2010).

The results show that development of continuous permafrost is characteristic of both the dry and humid variants of the *severe permafrost climate case* (Figure 5-41). As expected this is a difference compared with the *reference glacial cycle climate case* where longer periods of discontinuous permafrost prevailed both in the dry and humid climate variants (Figure 4-30).

Table 5-18. Times of permafrost occurrence and associated maximum permafrost depth and maximum depth of perennially frozen ground over the whole profile and over the repository location for the future humid variant of the severe permafrost climate case. The table also gives the time and horizontal location of maximum permafrost depth and the percent extent of permafrost distribution.

Time periods of permafrost occurrence (ka AP)	Over the whole profile					Over the repository			
	Maximum permafrost depth (m)	Time of occurrence of maximum permafrost depth (ka AP)	Distance from the south–west side (m)	Maximum depth of perennially frozen ground (m)	Percent extent of permafrost distribution (%)	Maximum permafrost depth (m)	Time of occurrence of maximum permafrost depth (ka AP)	Distance from the south–west side (m)	Maximum depth of perennially frozen ground (m)
6.4 – 13.7	150	10.3	100	144	75	104	8	3950	97
14.5 – 16.1	85	15.7	12280	80	97	64	14.8	5650	62
19.9 – 37	223	35.1	14910	205	100	196	34.9	5650	186
39.5 – 39.6	5	39.6	14870	3	95	3	39.6	5610	1
40.6 – 109.4	424	98.4	12240	364	100	393	98.4	5650	359

Table 5-19. Times of permafrost occurrence and associated maximum permafrost depth and maximum depth of perennially frozen ground over the whole profile and over the repository location for the future dry variant of the severe permafrost climate case. The table also gives the time and horizontal location of maximum permafrost depth and the percent extent of permafrost distribution.

Time periods of permafrost occurrence (ka AP)	Over the whole profile					Over the repository			
	Maximum permafrost depth (m)	Time of occurrence of maximum permafrost depth (ka AP)	Distance from the south–west side (m)	Maximum depth of perennially frozen ground (m)	Percent extent of permafrost distribution (%)	Maximum permafrost depth (m)	Time of occurrence of maximum permafrost depth (ka AP)	Distance from the south–west side (m)	Maximum depth of perennially frozen ground (m)
7 – 8.3	72	8	3020	68	44	69	8	3950	64
8.7 – 11	87	10.3	7990	81	74	52	10.2	5650	50
11.8 – 12	4	11.9	12360	1	79	2	11.9	5620	0
14.6 – 15	36	14.8	14280	35	96	33	14.8	5650	32
15.4 – 15.8	25	15.6	14280	22	97	21	15.6	5650	20
21.9 – 31.5	152	29.8	14840	143	100	131	29.7	5650	125
32.4 – 36.7	174	34.9	14880	165	100	157	34.8	5650	151
41.5 – 46.3	268	45.7	13890	255	100	242	45.7	5650	231
47.2 – 50.8	320	50.1	13790	306	100	290	50	5650	277
51.3 – 64.4	326	58	14890	314	100	310	57.2	5650	291
64.7 – 68.6	257	67.9	14980	231	100	241	67.8	5650	224
69.5 – 75.9	256	75.4	14980	232	100	244	75.4	5650	230
76.8 – 105.7	379	98.3	13940	333	100	355	98.3	5650	327
106.7 – 108.9	229	108.2	14980	204	100	221	108.2	5650	206

Table 5-20. Evolution of maximum permafrost depth and maximum depth of perennially frozen ground at the repository site for the severe permafrost climate case. For comparison the table also include the results from the reference glacial cycle climate case. The table also shows the prevailing mean annual air temperatures. For a table describing model results for the full glacial cycle of the severe permafrost climate case, see Hartikainen et al. (2010 Appendix K).

Time (ka AP)	Mean annual air temperature (°C)	Maximum permafrost depth (m)				Maximum depth of perennially frozen ground (m)			
		Humid variant of the reference glacial cycle climate case	Dry variant of the reference glacial cycle climate case	Humid variant of the severe permafrost climate case	Dry variant of the severe permafrost climate case	Humid variant of the reference glacial cycle climate case	Dry variant of the reference glacial cycle climate case	Humid variant of the severe permafrost climate case	Dry variant of the severe permafrost climate case
8	−3.4	31	84	104	69	29	79	97	64
8.5	−0.6	0	3	30	0	0	1	27	0
10	−3.5	15	47	71	46	15	46	68	44
12	−1.5	0	22	44	0	0	21	42	0
14	2.5	0	0	0	0	0	0	0	0
16	−0.6	0	6	33	0	0	5	30	0
18	1.6	0	0	0	0	0	0	0	0
20	−0.3	0	0	7	0	0	0	5	0
22	−1.9	2	30	55	9	0	28	52	8
24	−2.9	18	62	102	56	16	60	97	53
25	−3.2	23	69	110	64	20	66	105	61
26	−3.9	35	84	127	86	33	81	122	82
28	−4.8	49	108	158	117	47	103	151	113
30	−4.1	45	112	168	123	43	107	161	118
32	−0.9	0	15	54	0	0	13	49	0
34	−6.4	73	116	155	120	71	113	149	115
36	−3.1	31	108	164	105	29	104	156	98
38	2.1	0	0	0	0	0	0	0	0
40	0.4	0	0	0	0	0	0	0	0
42	−2.5	12	52	88	37	10	50	84	35
44	−4.2	45	101	147	102	43	97	140	98
45	−10.4	135	186	232	204	131	179	219	194
46	−1.3	85	180	256	211	77	168	241	198
48	−3.6	33	86	130	78	31	82	124	74
50	−10	181	259	319	290	175	246	303	277

For the *severe permafrost climate case*, i.e. when considering no ice-sheet, sea, vegetation or snow cover over the Forsmark site throughout the glacial cycle, permafrost (0 ºC isotherm) can reach a depth between ~360 m and ~390 m over the repository and between ~380 m and ~420 m outside the repository, in a time frame of 100 ka. Meanwhile, the maximum depth of perennially frozen ground may vary between ~330 m and ~360 m over both the repository and the rest of the profile, see Figure 5-40 and Figure 5-41.

Examples of vertical profiles of bedrock temperature at one selected location (in the middle of the repository location, at 4783 m along the profile) corresponding the fresh-moist surface cover types are presented in Figure 5-42 (humid climate variant) and Figure 5-43 (dry climate variant). The white envelope represents the range of bedrock temperature fluctuation simulated over the glacial cycle. Other examples of vertical bedrock temperature profiles, with other surface cover types (wet, dry, peatland) are found in Hartikainen et al. (2010).

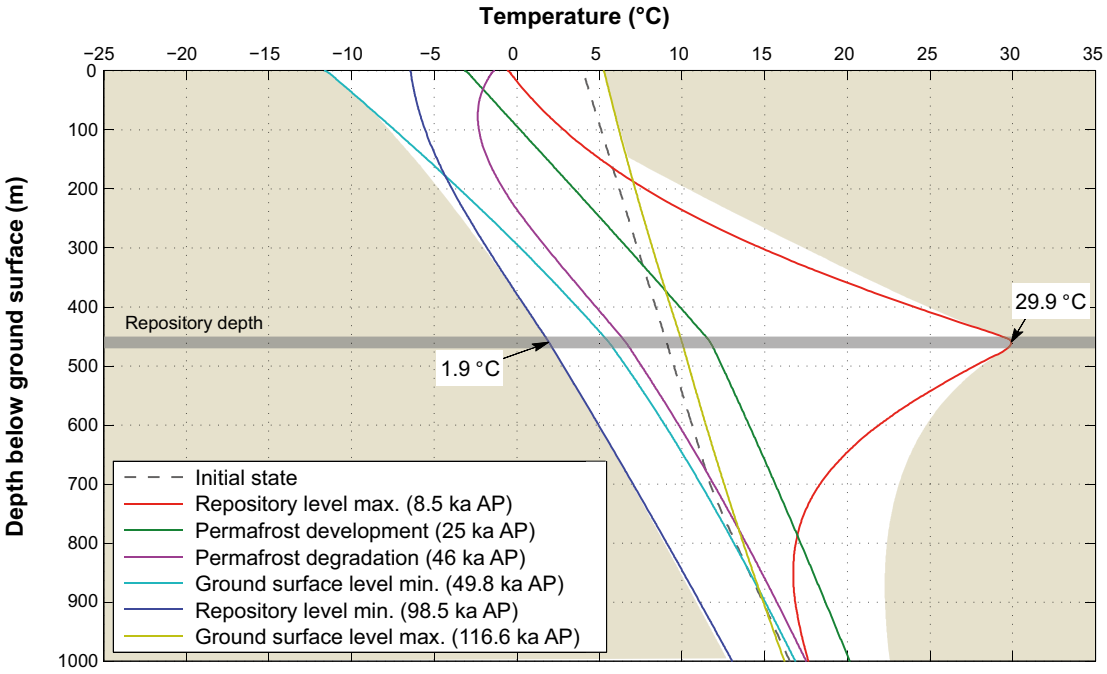

Figure 5-42. *Ground temperature along a vertical profile located in the middle of the repository for the humid variant of the severe permafrost climate case and dry surface condition type. The white envelope represents the range of bedrock temperature fluctuation simulated over the glacial cycle.*

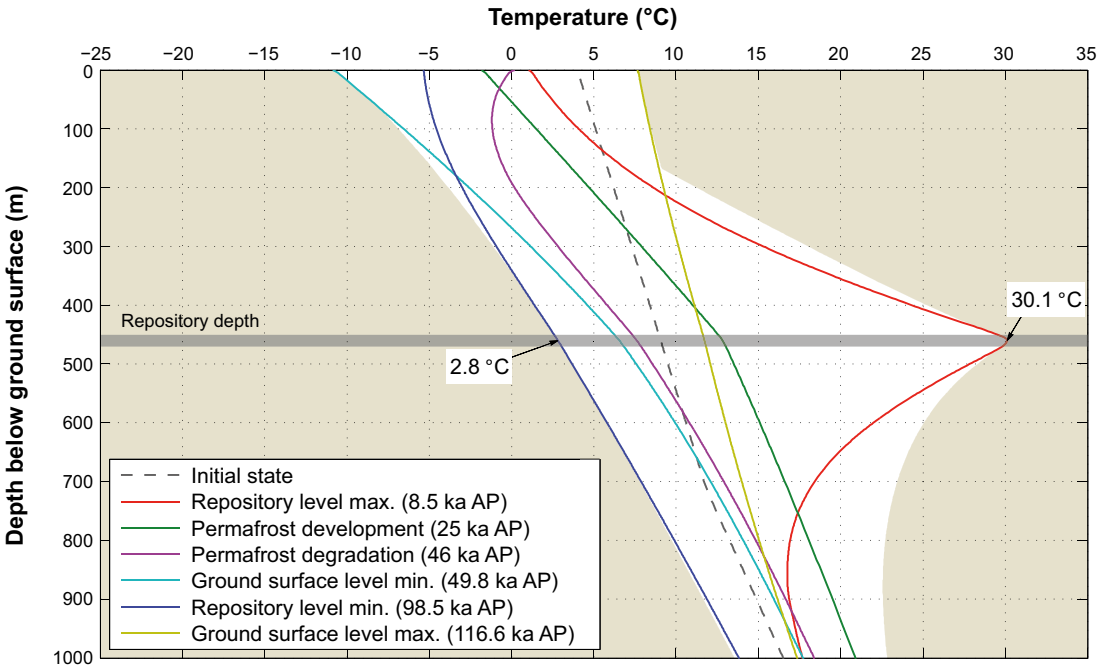

Figure 5-43. *Ground temperature along a vertical profile located in the middle of the repository for the dry variant of the severe permafrost climate case and dry surface condition type. The white colour envelope represents the range of bedrock temperature fluctuation simulated over the glacial cycle.*

Given the permafrost and freezing results presented above for the *severe permafrost climate case*, the associated results on salinity concentration are illustrated in Figure 5-44 and Figure 5-45. In this study, the effect of freezing-out of salt is small. Due to low salinity concentrations at shallow depths, the impacts of freezing on salinity exclusion and redistribution are difficult to see from the results. However, under more extreme conditions than simulated in the *severe permafrost climate case*, if the air temperature curve reconstructed for the last glacial cycle is lowered by 8 °C, the freezing occurs more intensively and an increase in salinity concentration due to salt exclusion can be seen (Figure 5-46).

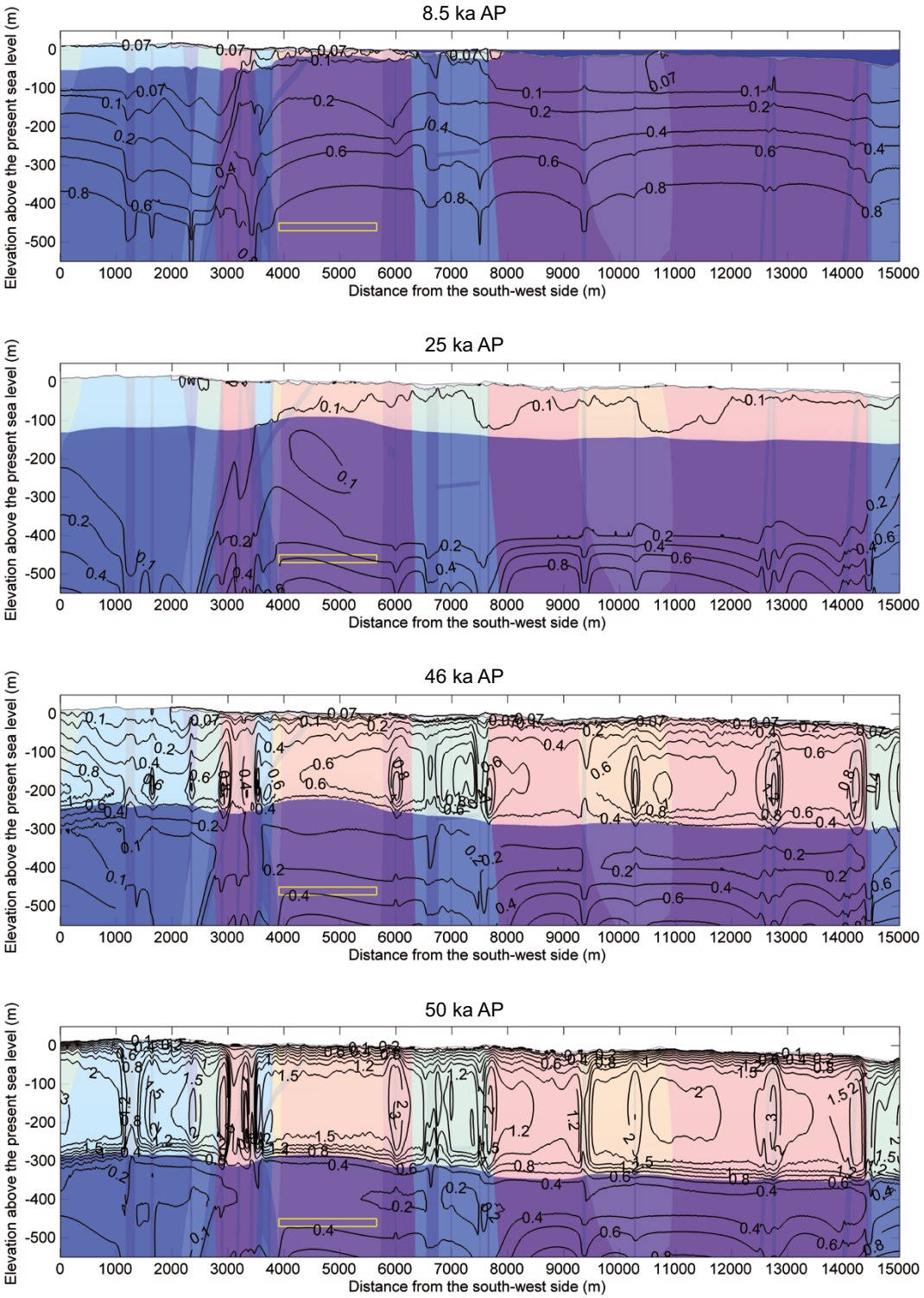

Figure 5-44. *Salinity concentration isolines at times 8.5, 25, 46, 50 ka AP for the humid variant of the severe permafrost climate case. The isolines show salinity concentrations of 0.07, 0.1, 0.2, 0.4, 0.6, 0.8, 1, 1.2, 1.5, 2, 3, 4, 5 mass-%. Blue colour on the top of the profile at 8.5 ka AP shows the Baltic Sea and the light colour the extent of perennially frozen ground.*

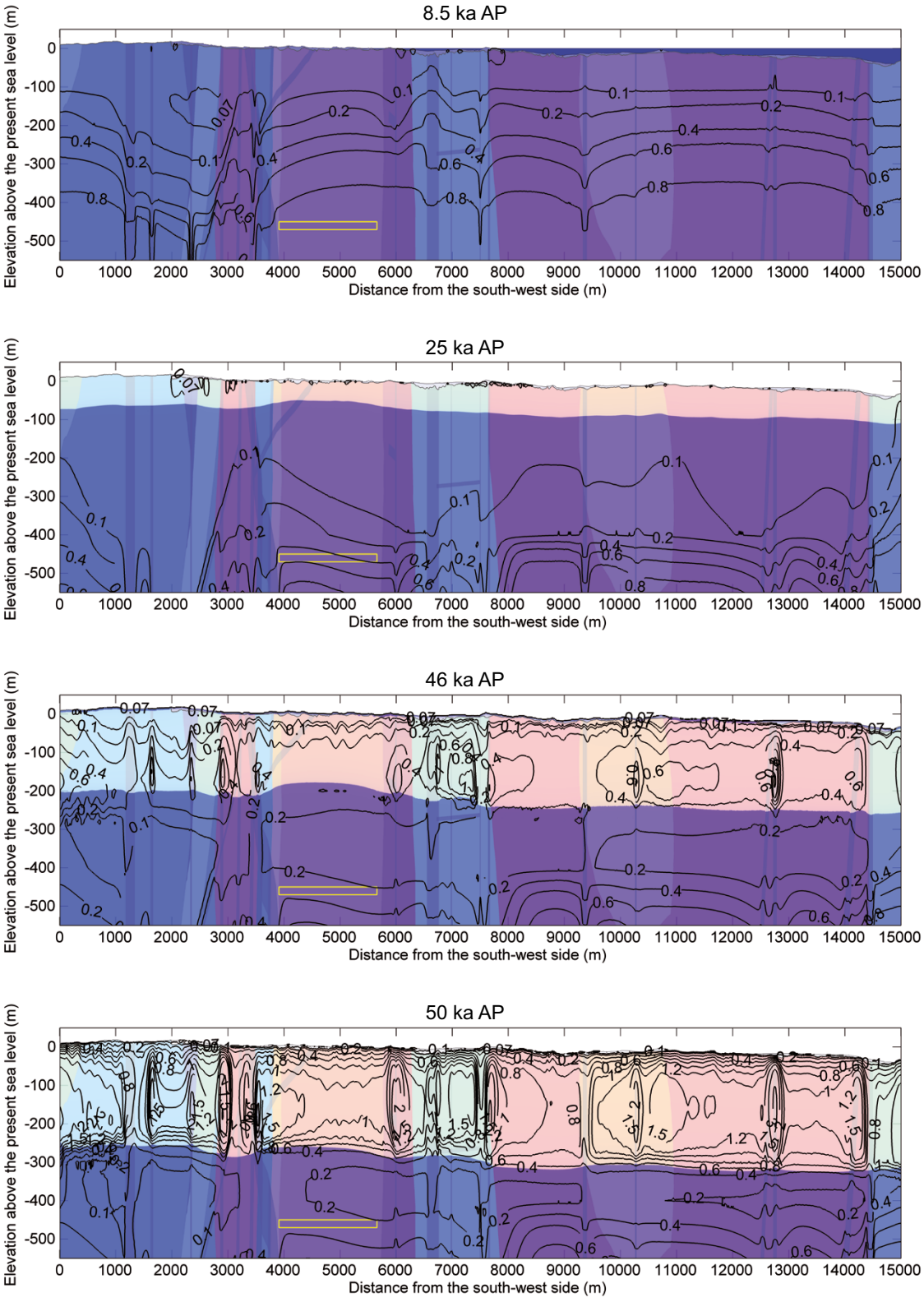

Figure 5-45. *Salinity concentration isolines for the dry variant of the severe permafrost climate case at times 8.5, 25, 46, 50 ka AP. The isolines show salinity concentrations of 0.07, 0.1, 0.2, 0.4, 0.6, 0.8, 1, 1.2, 1.5, 2, 3, 4, 5 mass-%. Blue colour on the top of the profile at 8.5 ka AP shows the Baltic Sea and the light colour the extent of perennially frozen ground.*

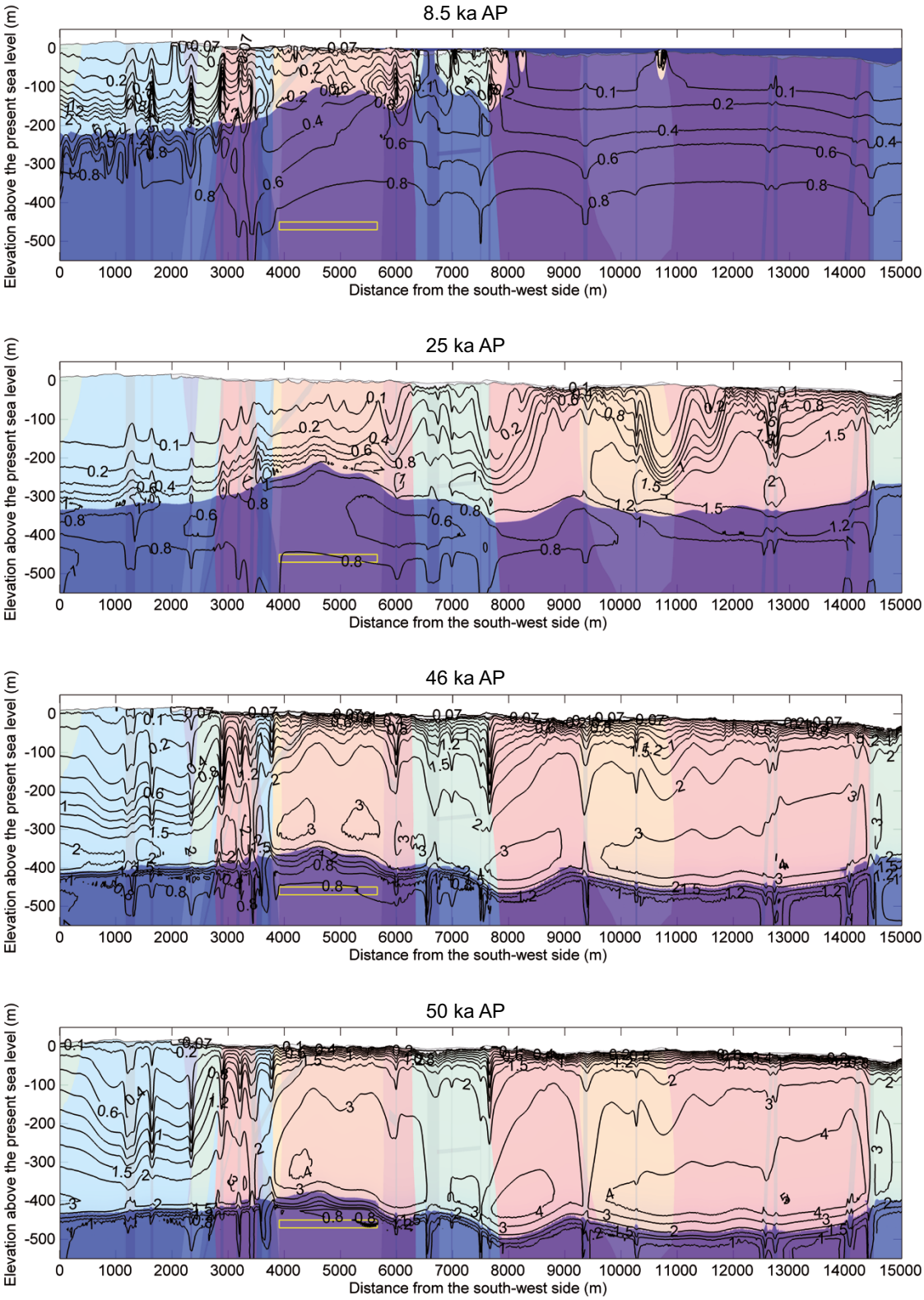

Figure 5-46. *Salinity concentration isolines at times 8.5, 25, 46, 50 ka AP for the humid variant of the severe permafrost climate case and air temperature decreased by 8 °C. The isolines show the salinity concentrations 0.07, 0.1, 0.2, 0.4, 0.6, 0.8, 1, 1.2, 1.5, 2, 3, 4, 5 mass-%. Blue colour on the top of the profile at 8.5 ka AP shows the Baltic Sea and the light colour the extent of perennially frozen ground.*

Sensitivity experiments

In addition to the *severe permafrost climate case* simulations described above, a sensitivity experiment was made to study the effects of uncertainties in bedrock thermal properties together with uncertainties in surface conditions (excluding air temperature) for this case, i.e. the same experiment as sensitivity experiment number 6 conducted for the *reference glacial cycle climate case*. To this end, the uncertainty interval is obtained by combining the dry climate variant with the thermal properties enhancing permafrost development, and the humid climate variant with thermal properties diminishing permafrost development, see Section 3.4.4. The resulting evolution of maximum permafrost depth and maximum depth of perennially frozen ground over the repository are shown in Figure 5-47.

Sensitivity studies have also been made to investigate the climate conditions required to develop permafrost and perennially frozen ground to repository depth (Hartikainen et al. 2010). Based on the results of a similar study performed in SR-Can (SKB 2006a), this was made by lowering the entire temperature curve reconstructed for the last glacial cycle by 4, 6, 8, 10, 12, 14 and 16 °C.

The results show that if the reconstructed temperature curve for the last glacial cycle is lowered by 8 °C, the 0 °C isotherm (permafrost) reaches repository depth (450 m) (Figure 5-48). The temperature curve needs to be lowered by more than 10 °C in order to make the −2 °C isotherm reach repository depth (Figure 3-36), and it needs to be lowered by as much as 14 °C in order make the −4 °C isotherm reach repository depth (Figure 5-50).

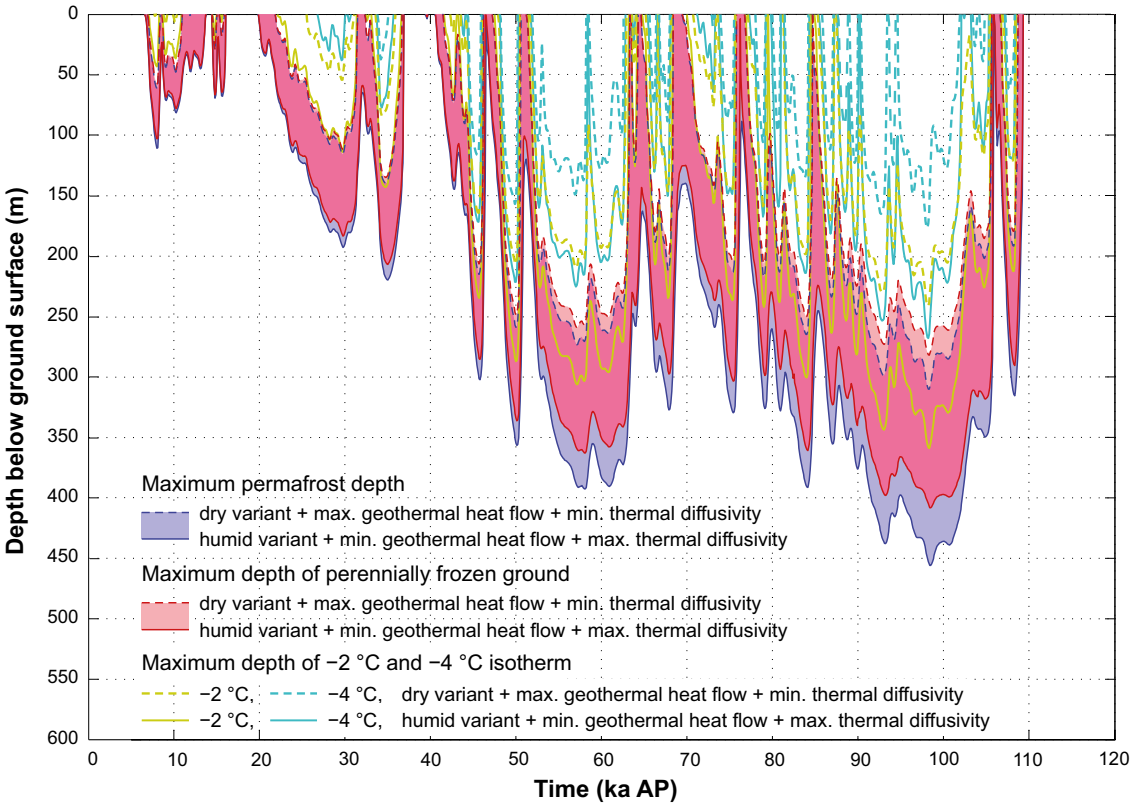

Figure 5-47. *Evolution of maximum permafrost depth, maximum depth of perennially frozen ground and maximum depth of −2 and −4 °C isotherms over the repository for the severe permafrost climate case when considering combined uncertainties in surface conditions and thermal properties favourable for permafrost growth. The shaded area in blue and red represents the range when considering the dry and humid climate variants. The darker lilac colour indicates that the results for permafrost and perennially frozen ground overlap.*

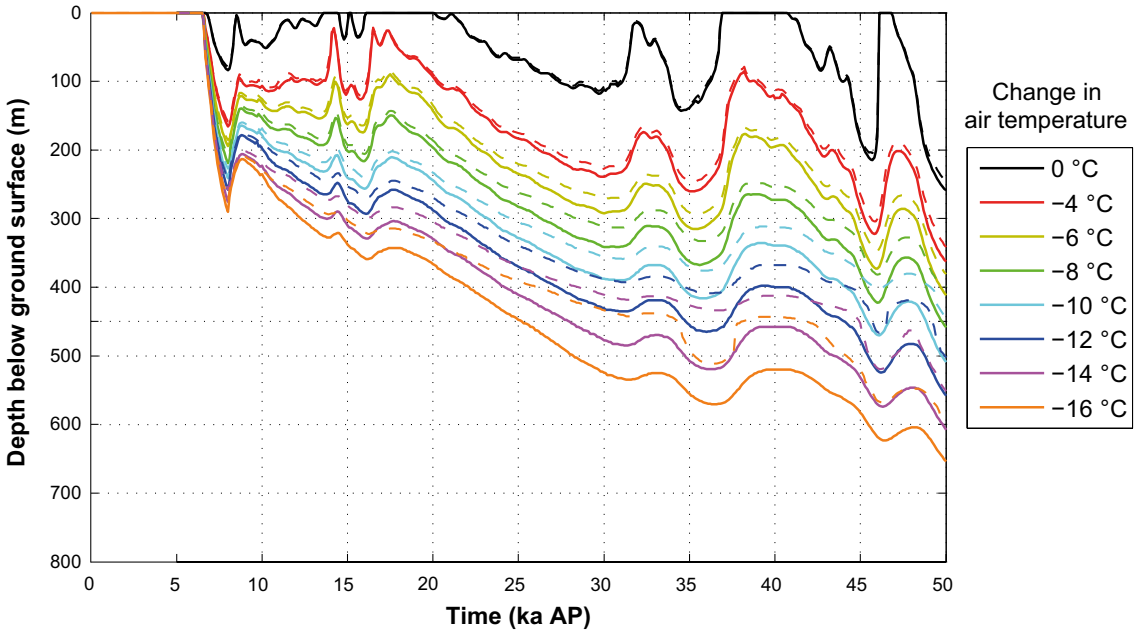

Figure 5-48. *Evolution of 0 °C isotherm (permafrost) depth (black solid line) and depth of perennially frozen ground (black dashed line) at the repository location for the reference glacial cycle (dry climate variant, see Section 3.4.4). The figure also shows corresponding results for simulations where the temperature curve reconstructed for the last glacial cycle has been lowered by −4, −6, −8, −10, −12, −14 and −16 °C compared with the reference glacial cycle climate case.*

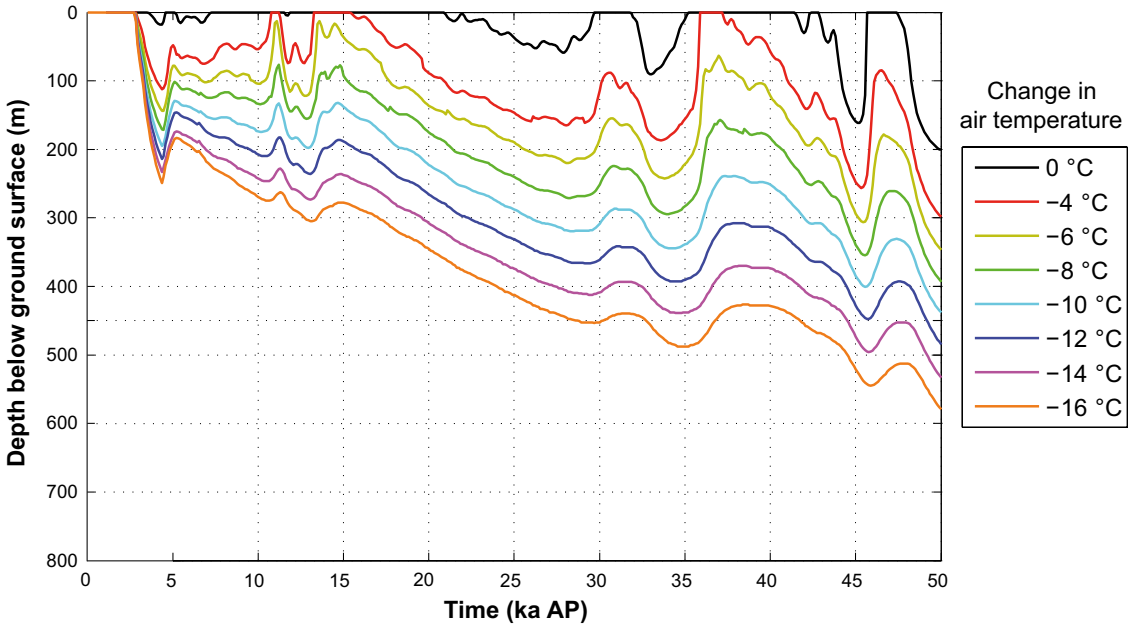

Figure 5-49. *Evolution of −2 °C-isotherm depth at the repository location for the reference glacial cycle (dry climate variant, see Section 3.4.4) (black line). The figure also shows corresponding results for simulations where the temperature curve reconstructed for the last glacial cycle has been lowered by −4, −6, –8, −10, −12, −14 and −16 °C compared with the reference glacial cycle climate case (coloured lines).*

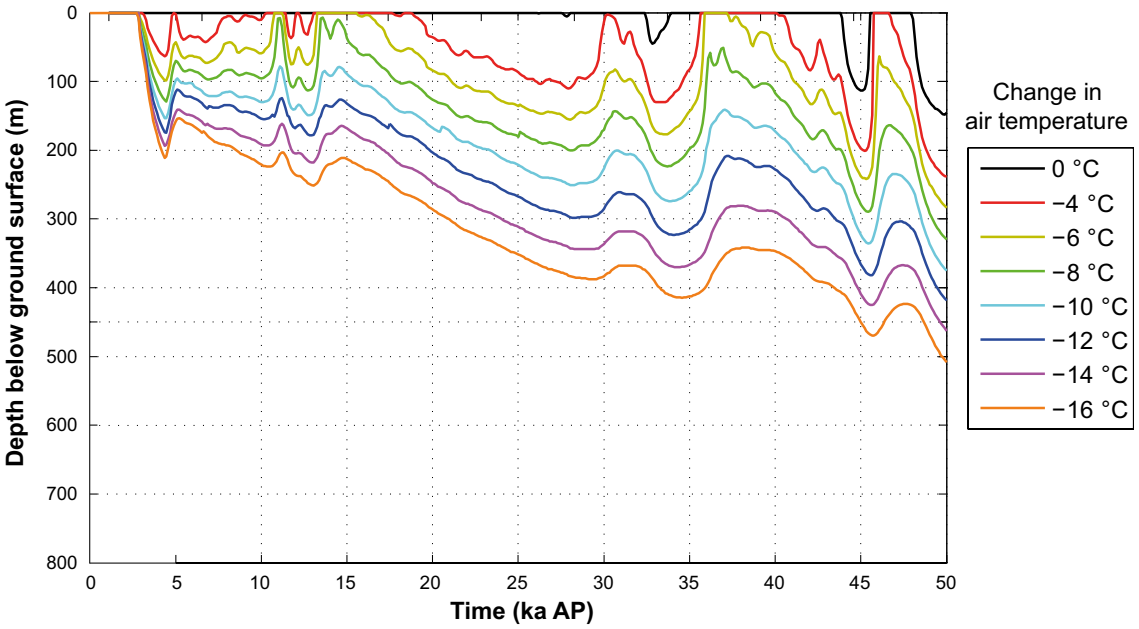

Figure 5-50. *Evolution of −4 °C-isotherm depth at the repository location for the reference glacial cycle ((dry climate variant, see Section 3.4.4) (black line). The figure also shows corresponding results for simulations where the temperature curve reconstructed for the last glacial cycle has been lowered by −4, −6, −8, −10, −12, −14 and −16 °C compared with the reference glacial cycle climate case (coloured lines).*

The evolution of subsurface temperatures and residual pore water pressures at a depth of 400 m at Forsmark for a case similar to the *severe permafrost climate case* described above is found in SKB (2006a, Figure 3-64).

Summary of the severe permafrost climate case and sensitivity studies

In the following, the main conclusions from the *severe permafrost climate case* and the sensitivity studies are summarized. When assuming a glacial cycle without any cover of ice-sheet, sea, vegetation or snow, the range for the maximum permafrost depth (the 0 °C isotherm) over the repository is 360–390 m depending on the surface conditions. The corresponding range for the entire investigated profile is 380–420 m. Likewise, for the same assumptions, the maximum depth of perennially frozen ground over the repository and the entire profile ranges between 330 and 360 m depending on the surface conditions. Very low surface temperatures are required to give an increase in salinity concentration due to salt exclusion. Making the unrealistic combination of the *severe permafrost climate case* (which assumes no ice-sheet, winter snow, vegetation or sea coverage during the entire glacial cycle), with maximum thermal conductivity and minimum heat capacity for the subsurface, as well as using the minimum geothermal heat flow value, the simulated maximum permafrost depth over the repository may extend to 450 m depth in 95 ka. However, it should be noted that this combination of assumptions is unrealistic. Assuming a similar climate variability as during the last glacial cycle, the temperature curve reconstructed for the last glacial cycle needs to be lowered by 8 °C order in order to make the 0 °C isotherm (permafrost) reach repository depth, while the temperature curve needs to be lowered by more than 10 °C in order make the −2.5 °C isotherm reach repository depth. Also, when considering the significant estimated maximum uncertainty in the reconstructed air temperature curve (±6 ºC, Appendix A), this corresponds to an unrealistically large change in glacial climate conditions.

It should here be remembered that the *severe permafrost climate case* was designed to take care of remaining uncertainties (mainly related to ice-sheet coverage) that were not covered in the extensive investigation of uncertainties reported in the *reference glacial cycle climate case* (Section 4.5 and 3.4.4). Therefore, the resulting maximum uncertainty interval for e.g. permafrost and frozen depths (Table 5-21) may reach deeper in the *reference glacial cycle climate case* than in the *severe permafrost climate case* (whereas calculated depths without the uncertainty interval are deeper for the *severe permafrost climate case*).

Table 5-21. Maximum depths of permafrost (0 °C isotherm), perennially frozen ground, −2 °C isotherm (buffer freezing criteria used in SR-Site) and −4 °C isotherm (backfill freezing criteria used in SR-Site) for the severe permafrost climate case and the reference glacial cycle climate case. The uncertainty interval for the severe permafrost climate case includes all uncertainties (set to their most pessimistic values) except air temperature, since lower air temperatures are not compatible with the main assumption of having no ice-sheet development over the site. The uncertainty interval for the reference glacial cycle climate case includes the unlikely combination of having all uncertainties, including air temperature, set to their most pessimistic values favouring permafrost growth. Note that in the PSAR, the temperature for which a frozen buffer clay and backfill material may start having detrimental effects on the canister and surrounding host rock has been updated to −6 °C for both materials, see the Post-closure safety report Section 8.3.2 and 8.4.4. The relevant isotherm in the PSAR (−6 °C) is therefore located at shallower depth than the corresponding isotherms (−2 and −4 °C) used in SR-Site and seen in the table.

	Maximum permafrost depth (0 °C isotherm) [max uncertainty interval]	Maximum depth perennially frozen ground [max uncertainty interval]	Maximum depth −2 °C isotherm [max uncertainty interval]	Maximum depth −4 °C isotherm [max uncertainty interval]
Severe permafrost climate case	393 [down to 456]	359 [down to 408]	311 [down to 359]	234 [down to 268]
Reference glacial cycle climate case	259 m [down to 463 m]	246 m [down to 422 m]	200 m [down to 388 m]	148 m [down to 316 m]

The information on freezing depths from the *severe permafrost climate case* and the *reference glacial cycle climate case* is used to assess the potential for freezing of groundwater, buffer clay and deposition tunnel backfill material in the safety assessment freezing scenario, see Section 12.3 in the **Post-closure safety report**. In the PSAR, the temperature for which a frozen buffer clay and backfill material may start having detrimental effects on the canister and surrounding host rock has been updated to −6 °C for both materials, see the **Post-closure safety report** Section 8.3.2 and 8.4.4. The effect of this is discussed in Section 12.3 in the **Post-closure safety report**.

The development of climate domains for the *severe permafrost climate case* is shown in Figure 5-51. For this construction, the dry climate variant, with most permafrost, was chosen. Temperate climate conditions prevail for 24 ka or 20 % of the time, whereas periglacial conditions prevail for 96 ka or 80 % of the time. There are no periods of glacial conditions.

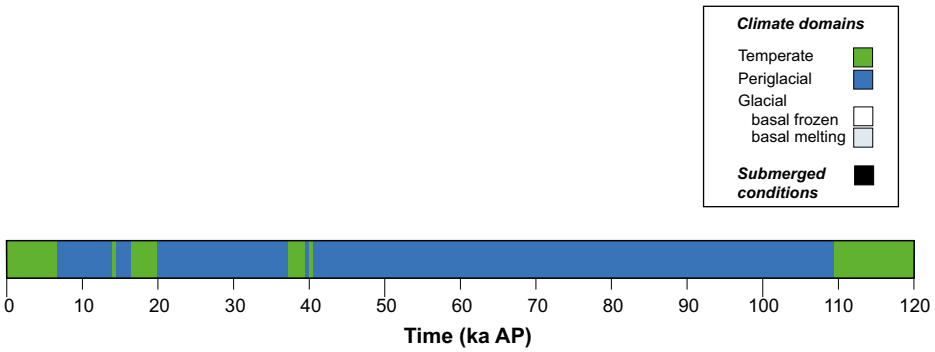

Figure 5-51. *Evolution of climate conditions at the Forsmark repository location as a time series of climate domains for the severe permafrost climate case. Following from the assumptions used for this climate development, there are no periods of glacial or submerged conditions. The glacial cycle is dominated by periglacial conditions, with longer-lasting temperate climate conditions during periods that correspond to interglacial conditions.*

5.5.4 Surface denudation

In the *severe permafrost climate case*, the main assumption is that there is no ice-sheet present at Forsmark during the glacial cycle, and consequently the denudation process that contributed to the largest amount of denudation in the *reference glacial cycle climate case* (i.e. glacial erosion) does not take place. In line with this, it is assumed that the amount of surface denudation in this climate case is smaller than in the *reference glacial cycle climate case*, and also smaller than in the *extended ice-sheet duration climate case*. Therefore, surface denudation is not described and treated further in the *severe permafrost climate case* in SR-Site. Nevertheless, in the following subsection, a theoretical case with glacial erosion amounting to 20 metres of bedrock per glacial cycle (i.e. ten times the maximum glacial erosion used in SR-Site) is presented, to show the effect on permafrost and freezing depths.

A hypothetical case with permafrost depths affected by ten times higher glacial erosion than used in SR-Site

As a complement to the permafrost and freezing depths reported in SR-Site, an exemplification of permafrost depths for the very pessimistic situation with ten times higher glacial erosion than used in SR-Site is given here, describing a situation with 20 metres of glacial erosion above the repository per glacial cycle instead of 2 metres. 20 metres of glacial erosion per glacial cycle is also considerably more than the updated total denudation depths used in the PSAR (see Sections 3.5.4, 4.5.7 and 5.3.3). This exemplified calculation case corresponds to a situation where the maximum permafrost depth reaches 20 metres deeper per glacial cycle. As noted in the previous section, it should be emphasised that the maximum permafrost depths used for this calculation required a permafrost simulation *without* ice-sheet coverage during the entire glacial cycle (Section 5.5.3). In this hypothetical case, these maximum permafrost depths are, unrealistically, combined with the presence of an ice-sheet. Furthermore, this ice-sheet is envisaged to result in an unrealistically large amount glacial erosion for each glacial cycle (20 metres) everywhere, cf. Section 3.5.4 for realistic estimates on glacial erosion. These two facts, combined with the fact that the permafrost simulations were also made with all uncertainties in the model set to the most pessimistic setting (promoting maximum permafrost growth), makes this exemplification case highly unlikely. Furthermore, when comparing with this case with the generally low denudation rates at Forsmark in the past and with the projected future amount of total denudation for the coming 100 ka and 1 Ma (up to a few metres and less than 50 m respectively), see Section 3.5.4, this case is considered hypothetic.

Table 5-22 presents the resulting maximum depths for the reference evolution case, inclusive of their maximum uncertainty when pessimistically assuming 20 metres of glacial erosion per glacial cycle, resulting in permafrost and freezing reaching 20 m deeper per glacial cycle. The first thing that can be noted is that this assumption does not affect the maximum permafrost and freezing depth during the *first* coming glacial cycle of the reference evolution (the first 120 ka). This is because the deepest permafrost during a glacial cycle is reached *before* the first period with ice-sheet coverage, and associated glacial erosion, above the repository, see Figure 4-35. The following periods with permafrost during this first glacial cycle has a c 60 m shallower permafrost- and freeze depth in the SKB reference evolution Figure 4-28), and would therefore, despite of a hypothetical glacial erosion up to 20 m, not result in deeper permafrost than the period with maximum permafrost before the period. However, for the following seven glacial cycles, the ground surface is lowered 20 m per glacial cycle at every occurrence of maximal permafrost depth (Table 5-22). Towards the end of the analysed period of 1 Ma, the permafrost would therefore penetrate c 140 m deeper than during the first glacial cycle (Table 5-22).

Table 5-22. Depth of permafrost, frozen ground, the −2 °C and −4 °C isotherms with a 10 times larger maximum glacial erosion than used in SR-Site. This theoretical case assumes that glacial erosion removes 20 metres of bedrock per glacial cycle above the repository, instead of 2 metres as used in SR-Site. The uncertainty intervals for the depths are based on a very pessimistic permafrost model simulation where all uncertainties are set to be most favourable for permafrost growth, see Section 4.5.3. Since no glacial erosion happens before the time for maximal permafrost depth during first glacial cycle, see text, the data in the first row is the same as reported in Table 5-21. Values in bold indicate repository depth or deeper. For an analysis of the realism of the assumption of 20 m of erosion per glacial cycle, based on new studies of denudation and erosion at the Forsmark site, see the text.

Glacial cycle number (ka AP)	Maximum permafrost depth (0 °C degrees isotherm) (m) [uncertainty interval]	Maximum freezing depth ground water (m) [uncertainty interval]	Maximum depth for −2 °C-isotherm (freezing criterion for bentonite used in SR-Site) (m) [uncertainty interval]	Maximum depth for −4 °C-isotherm (freezing criterion for bentonite used in SR-Site) (m) [uncertainty interval]
1 (0–120)	259 [**463**]	246 [422]	200 [388]	148 [316]
2 (120–240)	279 [**483**]	266 [442]	220 [408]	168 [336]
3 (240–360)	299 [**503**]	286 [**462**]	240 [428]	188 [356]
4 (360–480)	319 [**523**]	306 [**482**]	260 [448]	208 [376]
5 (480–600)	339 [**543**]	326 [**502**]	280 [**468**]	228 [396]
6 (600–720)	359 [**563**]	346 [**522**]	300 [**488**]	248 [416]
7 (720–840)	379 [**583**]	366 [**542**]	320 [**508**]	268 [436]
8 (840–960)	399 [**603**]	386 [**562**]	340 [**528**]	288 [**456**]

Based on Table 5-22, the following conclusions can be drawn from assuming a ten times higher glacial erosion:

i) There is no impact on maximum permafrost depth, freezing depth or depth for e.g. the −2 °C and −4 °C (or −6 °C) isotherms during the first future glacial cycle compared to Table 5-21 and what was been reported in SR-Site.

ii) For the following glacial cycles, permafrost and the temperature needed for freezing of groundwater and buffer clay reaches 20 m closer to the repository for each glacial cycle.

iii) Under the very pessimistic assumptions of this hypothetic case, this means that freezing of groundwater could occur at repository depth from glacial cycle number 3.

iv) Under the same pessimistic assumptions, the results show that the −2 °C isotherm could reach repository depth from glacial cycle number 5 and the −4 °C isotherm during the last glacial cycle (number 8).

However, since SR-Site a detailed glacial erosion study have been made for the Uppland province and the Forsmark site (Section 3.5.4 and Hall et al. 2019a). The cosmogenic nuclide analysis performed within this study showed that the last glacial cycle typically removed 1.6–3.5 m of basement rock in the vicinity of the planned repository at Forsmark (Section 3.5.4). The results of the cosmogenic nuclide analysis also showed that the typical total amount of bedrock denudation, including glacial erosion, over the coming 1 Ma could be between 5 and ~30 m, whereas the corresponding full range is 2–43 m (Table 3-15). Similarly, the geomorphological analysis performed by Hall et al. (2019a) indicate around 2 m of glacial erosion per glacial cycle, with values exceeding 3 m in basins and trenches (Section 3.5.4 and Table 3-16). These results readily show that the theoretical case with 20 m of glacial erosion per glacial cycle is a clear overestimation, and that this case therefore should not be considered realistic.

Here it is also worth noting that in the PSAR, the temperature for which a frozen buffer clay and backfill material may start having detrimental effects on the canister and surrounding host rock has been updated to −6 °C for both materials, see the **Post-closure safety report** Section 8.3.2 and 8.4.4. The −6 °C isotherm is located at a shallower depth than the −2 and −4 °C isotherms used as freezing criteria for the backfill material and buffer clay in SR-Site (and seen in Table 5-22). Even for this theoretical and unrealistic erosion case, the −6 °C isotherm would not reach repository depth, given that the −4 °C isotherm does not reach this depth until the very last glacial cycle.

Furthermore, if the groundwater in potential buffer erosion cavities were to freeze, a maximal pressure of 26–27 MPa is calculated to occur from the expansion of the freezing water (Appendix C). This is considerably lower than the critical pressure for capsule collapse that is described in the scenario for capsule collapse due to isostatic pressure (see the **Post-closure safety report**, Section 12.7.2). Furthermore, it is worth noting is that the buffer clay regains its properties after being exposed to freezing and thawing (Birgersson et al. 2010).

In addition to the verification of the permafrost model that has been reported in Hartikainen et al. (2010) and Hartikainen (2018), a further evaluation of the permafrost model is ongoing at the Greenland Analogue Project (GAP) investigation site at Greenland.

5.6 Summary of climate cases for the PSAR

As stated in Section 1.3, a single most likely future climate evolution cannot be predicted with enough confidence and detail for the analyses of post-closure safety of repositories for spent nuclear fuel. The longest safety assessment timescales range up to around 100 ka and 1 Ma, see the **Post-closure safety report**. The 100 ka timescale corresponds to the timescale of glacial cycles during the past 700 ka. The selected approach in the PSAR, as well as in previous SKB safety assessments such as SR-Site, is therefore to use a reasonable future climate evolution, consisting of a repetition of conditions reconstructed for the last glacial cycle, as well as complementary climate evolutions with potentially larger impacts on repository safety (Section 1.3 and Figure 1-3). Given that the safety assessment needs to analyse repository safety on these very long timescales, the existing uncertainties in future climate development result in a wide range of possible climate developments that need to be addressed. Figure 5-52 and Table 5-23 summarise the climate developments included in the PSAR. These cases are based on the processes that have been identified as important for long-term KBS-3 repository safety and on the present scientific knowledge and uncertainties of future climate development with focus on these processes. The climate cases are used as input to the description and analysis of various PSAR post-closure scenarios, see Figure 1-3 and the **Post-closure safety report**.

The *reference glacial cycle climate case* (Figure 5-52 and Section 4.5) contributes with a reasonable development of climate and climate-related conditions for the coming 120 ka, whereas the *global warming climate case* (Section 5.1) contributes with a variant of this development. The longest period of temperate climate conditions for the coming 120 ka, including an initial period with the warmest and wettest climate conditions, highest sea-level, as well as longest period of groundwater formation from precipitation, is found in the *extended global warming climate case* (Section 5.2). The most extended period of periglacial climate conditions, with longest periods of permafrost at Forsmark, is found in the *severe permafrost climate case* (Section 5.5). The deepest permafrost and frozen ground are also found in the *severe permafrost climate case.* The largest uncertainty for the development of permafrost and frozen ground, which is future air temperature, is however connected to the *reference glacial cycle*, resulting in the deepest uncertainty interval for freezing being documented in this climate case. The longest period of glacial conditions, and associated period of groundwater formation from glacial meltwater, is found in the *extended ice-sheet duration climate case* (Section 5.3). The maximum future ice-sheet thickness, and resulting largest increase in hydrostatic pressure at repository depth, is found in the *maximum ice-sheet thickness climate case* (Section 5.4) (a case not depicted in Figure 5-52). The six climate cases together cover the expected maximum range within which climate and climate-related conditions of importance for long-term repository safety may vary within the timescales analysed in the PSAR.

In the light of present-day knowledge on climate, some of the climate cases in Figure 5-52 might be regarded as more likely than others. However, the adopted approach in the PSAR is to handle *all* possible future climate developments relevant for repository safety. Therefore, there is in the safety assessment no need to quantify the probabilities of the identified individual climate developments. The *actual* development of climate and climate-related processes at the Forsmark site for the coming 120 ka is expected to lie within the range covered by the six climate cases presented in Figure 5-52.

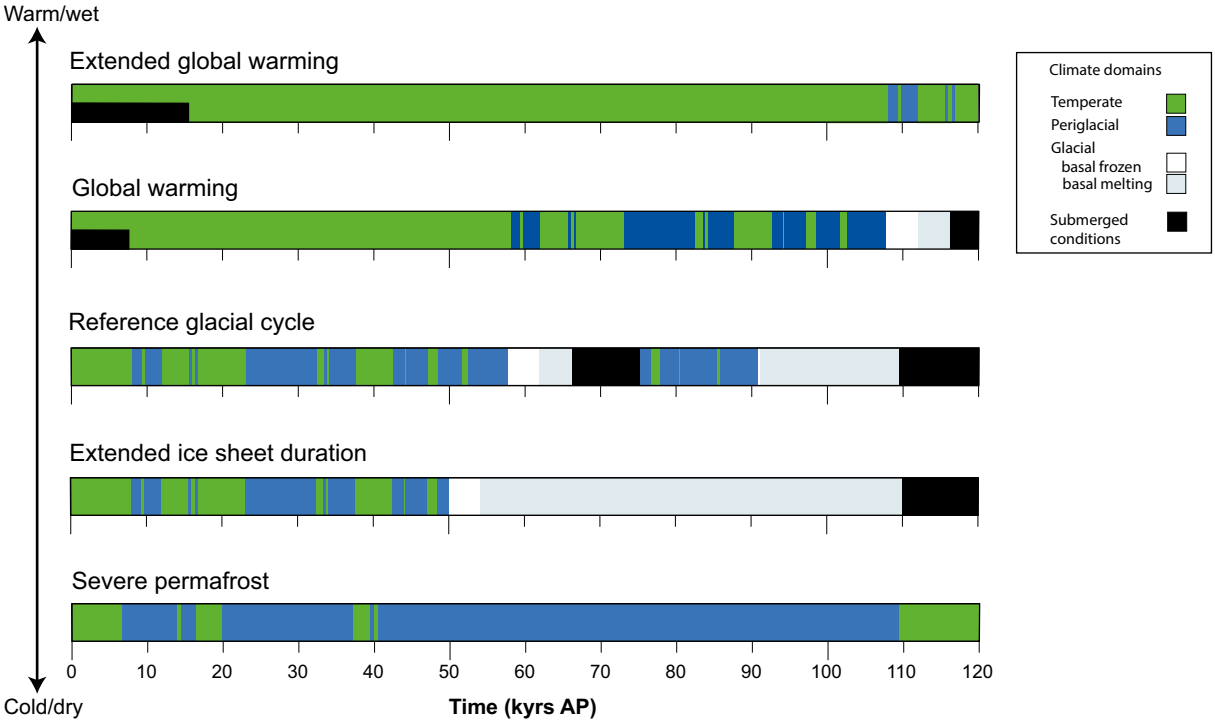

Figure 5-52. *Summary of future climate cases analysed in the PSAR. The cases go from warmer/wetter climates at the top to colder/dryer climates at the bottom. The maximum ice-sheet thickness climate case is not shown. However, it could be contained within the temporal development of the extended ice-sheet duration climate case. For the global warming and extended global warming climate cases, two variants with different initial conditions concerning submerged and terrestrial conditions are given, based on the large uncertainty in future sea-level projections, see Section 5.1.3 and 5.2.3.*

Table 5-23. Summary of duration of climate domains for the climate cases in Figure 5-52. The duration of the temperate climate domain and submerged conditions is shown as ranges for the global warming and extended global warming climate cases in order to reflect the large uncertainty in future sea-level projections (Section 5.1.3 and 5.2.3). For definitions of the climate domains, see Section 1.2.3.

Climate case	Temperate climate domain [ka] (percent of time of glacial cycle)	Periglacial climate domain [ka] (percent of time of glacial cycle)	Glacial climate domain [ka] (percent of time of glacial cycle)	Submerged conditions [ka] (percent of time of glacial cycle)
Extended global warming (Section 5.2)	103.5–116 ka (86 %–97 %)	4 years (3 %)	0 years (0 %)	0–12.5 ka (0–10 %)
Global warming (Section 5.1)	73.5–81 ka (61–68 %)	28 ka (23 %)	11 ka (9 %)	0–7.5 ka (0–6 %)
Reference glacial cycle (Section 4.5)	28 ka (24 %)	46 ka (38 %)	27 ka (23 %)	19 ka (15 %)
Extended ice-sheet duration (Section 5.3)	28 ka (23 %)	22 ka (18 %)	60 ka (50 %)	10 ka (8 %)
Severe permafrost (Section 5.5)	24 ka (20 %)	96 ka (80 %)	0 ka (0 %)	0 ka (0 %)

5.7 Summary of key parameters and values for the PSAR

Table 5-24 presents a summary of key parameters and values obtained from the various climate cases considered in the PSAR (e.g. Figure 5-52), including references to the sections where they are derived. For a summary of changes in relative sea-level at Forsmark up to 2050, 2080 and 2100 AD under different greenhouse-gas emission scenarios and for different statistical levels, see Table 5-10 in Section 5.2.3.

Table 5-24. Summary of key parameters and values for the Forsmark site from the climate cases considered in the PSAR.

Parameter	Period	Value	Climate case	Section in report
Maximum depth of perennial frozen ground	120 ka reference glacial cycles	246 m (with uncertainty span down to 422 m)	*Reference glacial cycle*	4.5.3
	Over the coming 1 Ma	359 m (with uncertainty span down to 408)	*Severe permafrost*	5.5.3
Maximum ice-sheet thickness [Maximum contribution to isostatic pressure]	120 ka reference glacial cycles	~2900 m [26 MPa]	*Reference glacial cycle*	4.5.1
	Over the coming 1 Ma	4000 m [36 MPa]	*Maximum ice-sheet thickness*	5.4.5 and 5.4.6
Future denudation of crystalline basement rock	120 ka reference glacial cycles	1.7–3.6 m	*Reference glacial cycle*	4.5.7
	Over the initial 120 ka	< 1 m (0.9 m)	*Global warming*	5.1.6
	Over the initial 120 ka	< 1 m (0.6 m)	*Extended global warming*	5.2.6
	Maximum denudation over coming 1 Ma	50 m	*Extended ice-sheet duration* Section on glacial erosion	5.3.3 3.5.4
Maximum duration of initial submerged conditions above repository	Until ~16000 AD	-	*Extended global warming*	5.2.3
Average basal hydraulic pressure (head) for an ice-sheet over the year*	-	92 % of the total ice thickness	All climate cases that include ice-sheet coverage	-

* Applies for an ice-sheet in a similar state as the present-day Greenland ice-sheet.

6 List of abbreviations

List of abbreviations, except expressions in equations, chemical expressions and common units.

1D	One dimensional
2D	Two dimensional
3D	Three dimensional
a	Annum (year)
A1B	IPCC AR4 emission scenario
A1FI	IPCC AR4 emission scenario
A2	IPCC AR4 emission scenario
ACIA	Arctic Climate Impact Assessment
AD	Anno Domini
AMS	Accelerator Mass Spectrometer
AMOC	Atlantic Meridional Overturning Circulation
AOGCM	Atmosphere-Ocean General Circulation Model
AP	After Present
AR4	Fourth Assessment Report of IPCC
AR5	Fifth Assessment Report of IPCC
B2	IPCC AR4 emission scenario
BC	Before Christ
BIFROST	Baseline Inferences for Fennoscandian Rebound, Sea-level, and Tectonics
BIOCLIM	Modelling sequential BIOsphere systems under CLIMate change for radioactive waste disposal
BP	Before Present
CCSM3	Community Climate System Model 3
CRU	Climate Research Unit (East Anglia)
CSM	Climate System Model
CMIP3	Climate Model Intercomparison Project, phase 3
CMIP5	Climate Model Intercomparison Project, phase 5
DEM	Digital Elevation Model
Dfb	Köppen climate classification class (temperate, humid cold climate with year-round precipitation)
dGPS	Differential Global Positioning System
DJF	December, January, February (winter season)
DO event	Dansgaard-Oeschger event
DVM	Dynamic Vegetation Model
EAIS	East Antarctic Ice-Sheet

EISMINT	European Ice-Sheet Modelling Initiative
ELA	Equilibrium Line Altitude
EMIC	Earth System Model of Intermediate Complexity
EPICA	European Project for Ice Coring in Antarctica
FEPs	Features, Events and Processes
GAP	Greenland Analogue Project
GCM	General Circulation Model, Global Circulation Model
GIA	Glacial Isostatic Adjustment
GIS	Geographical Information System
GISP2	Greenland Ice-Sheet project 2
GMSL	Global mean sea-level
GPS	Global Positioning System
GRACE	Gravity Recovery and Climate Experiment
GRIP	European Greenland Ice Core Project
GS 12	Greenland Stadial number 12
HadCM3	Hadley Centre Coupled Climate Model, version 3
HFD	Heat Flow Density, *or* geothermal heat flow
ICE-3G	Global ice-sheet reconstruction
ICE-5G	Global ice-sheet reconstruction
InSAR	Interferometric Synthetic Aperture Radar
IPCC	Intergovernmental Panel on Climate Change
JJA	June, July, August (summer season)
KTH	Royal Institute of Technology (Stockholm)
LGM	Last Glacial Maximum
ka	kilo annum (thousands of years)
KBS-3	Kärnbränslesäkerhet 3 (method for final storage of spent nuclear fuel)
LPJ-GUESS	A dynamic vegetation model
Ma	Mega annum (millions of years)
MIS	Marine Isotope Stage
MX-80	Bentonite clay
NCAR	National Centre for Atmospheric Research
NEA	Nuclear Energy Agency
NGRIP	North Greenland Ice core Project
NorthGRIP	North Greenland Ice core Project
NSF	National Science Foundation
NWMO	Nuclear Waste Management Organization
OSL	Optically Stimulated Luminescence

PMIP1	Paleoclimate Modelling Intercomparison Project, phase 1
PMIP2	Paleoclimate Modelling Intercomparison Project, phase 2
PREM	Preliminary Reference Earth Model
QA	Quality assurance
RCA 3	Rossby Centre Regional Climate Model
RCP	IPCC AR5 emission scenario
RCM	Regional Circulation Model
RH2000	Rikets höjdsystem 2000 (national elevation system in Sweden)
RH70	Rikets höjdsystem 1970 (national elevation system in Sweden)
RT-90	Rikets Triangelnät 1990 (national coordinate system in Sweden)
ScanSAR	Scanning Synthetic Aperture Radar
SCAR	Scientific Committee on Antarctic Research
SGU	Geological Survey of Sweden
SKB	Swedish Nuclear Fuel and Waste Management Organisation
SMHI	Swedish Meteorological and Hydrological Institute
SRES	Special Report on Emission Scenarios
SROCC	Special Report on the Ocean and Cryosphere in a Changing Climate
SSTs	Sea Surface temperatures
SWECLIM	Swedish Regional Climate Modelling Programme
THM	Thermo-Hydro-Mechanical
TWI	Topographic Wetness Index
UMISM	University of Maine Ice-Sheet Model
UNFCCC	United Nation’s Framework Convention on Climate Change
WAIS	West Antarctic Ice-Sheet

References

SKB's (Svensk Kärnbränslehantering AB) publications can be found at www.skb.com/publications.

References with abbreviated names

Biosphere synthesis report, 2010. Biosphere analyses for the safety assessment SR-Site – synthesis and summary of results. SKB TR-10-09, Svensk Kärnbränslehantering AB.

Data report, 2022. Post-closure safety for the final repository for spent nuclear fuel at Forsmark – Data report, PSAR version. SKB TR-21-06, Svensk Kärnbränslehantering AB.

FEP report, 2010. FEP report for the safety assessment SR-Site. SKB TR-10-45, Svensk Kärnbränslehantering AB.

Geosphere process report, 2022. Geosphere process report for the final repository for spent nuclear fuel at Forsmark – Geosphere process report, PSAR version. SKB TR-21-04, Svensk Kärnbränslehantering AB.

Model summary report, 2022. Post-closure safety for the final repository for spent nuclear fuel at Forsmark – Model summary report, PSAR version. SKB TR-21-05, Svensk Kärnbränslehantering AB.

Post-closure safety report, 2022. Post-closure safety for the final repository for spent nuclear fuel at Forsmark – PSAR version. SKB TR-21-01, Svensk Kärnbränslehantering AB.

Regular references

ACIA, 2005. Arctic Climate Impact Assessment. Cambridge: Cambridge University Press.

Ahonen L, 2001. Permafrost: occurrence and physicochemical processes. Helsinki: Posiva.

Allen D, Michel F, Judge A, 1988. Paleoclimate and permafrost in the Mackenzie Delta. In Proceedings of the fifth international conference on permafrost. Trondheim, 2–5 August 1988. Vol 1. Trondheim: Tapir.

Alley R B, 1992. Flow-law hypotheses for ice-sheet modeling. Journal of Glaciology 38, 245–256.

Alley R B, Dupont T K, Parizek B R, Anandakrishnan S, 2005. Access of surface meltwater to beds of sub-freezing glaciers: preliminary insights. Annals of Glaciology 40, 8–14.

Alley R B, Dupont T K, Parizek B R, Anandakrishnan S, Lawson D E, Larson G J, Evenson E B, 2006. Outburst flooding and the initiation of ice-stream surges in response to climatic cooling. Geomorphology 75, 76–89.

Andersen B G, Mangerud J, 1989. The last interglacial–glacial cycle in Fennoscandia. Quaternary International 3–4, 21–29.

Andrews J T, Barber D C, 2002. Dansgaard-Oeschger events: is there a signal off the Hudson Strait Ice Stream? Quaternary Science Reviews 21, 443–454.

Archer D, Ganopolski A, 2005. A movable trigger: Fossil fuel CO_2 and the onset of the next glaciation. Geochemistry, Geophysics, Geosystems 6, Q05003. doi:10.1029/2004GC000891

Archer D, Eby M, Brovkin V, Ridgwell A, Cao L, Mikolajewicz U, Caldeira K, Matsumoto K, Munhoven G, Montenegro A, Tokos K, 2009. Atmospheric lifetime of fossil fuel carbon dioxide. Annual Review of Earth and Planetary Sciences 37, 117–134.

Archibold O W, 1994. Ecology of world vegetation. New York: Springer.

Árnadóttir T, Lund B, Jiang W, Geirsson H, Björnsson H, Einarsson P, Sigurdsson T, 2009. Glacial rebound and plate spreading: results from the first countrywide GPS observations in Iceland. Geophysical Journal International 177, 691–716.

Arnold N, Sharp M, 2002. Flow variability in the Scandinavian ice-sheet: modelling the coupling between ice-sheet flow and hydrology. Quaternary Science Review 21, 485–502.

Arnold N, Richards K, Willis I, Sharp M, 1998. Initial results from a distributed, physically based model of glacier hydrology. Hydrological Processes 12, 191–219.

Artemieva I M, Mooney W D, 2001. Thermal thickness and evolution of Precambrian lithosphere: a global study. Journal of Geophysical Research 106, 16387–16414.

Astakhov V, 2004. Middle Pleistocene glaciations of the Russian North. Quaternary Science Reviews 23, 1229–1271.

Bakker A M R, Wong T E, Ruckert K L, Keller K, 2017. Sea-level projections representing the deeply uncertain contribution of the West Antarctic ice-sheet. Scientific Reports 7, 3880. doi:10.1038/s41598-017-04134-5

Balling N, 1984. Gravity and isostasy in the Baltic Shield. In Galson D A, Mueller S, Munch B (eds). Proceedings of the first workshop on the European Geotraverse Project (EGT): The northern segment. Strasbourg: European Science Foundation, 53–66.

Bamber J L, Vaughan D G, Joughin I, 2000. Widespread complex flow in the interior of the Antarctic Ice-Sheet. Science 287, 1248–1250.

Bamber J L, Alley R B, Joughin I, 2007. Rapid response of modern day ice-sheets to external forcing. Earth and Planetary Science Letters 257, 1–13.

Barber D C, Dyke A, Hillaire-Marcel C, Jennings A E, Andrews J T, Kerwin M W, Bilodeau G, McNeely R, Southon J, Morehead M D, Gagnon J-M, 1999. Forcing of the cold event of 8200 years ago by catastrophic drainage of Laurentide lakes. Nature 400, 344–348.

Bard E, Hamelin B, Fairbanks R G, 1990. U-Th ages obtained by mass spectrometry in corals from Barbados: sea-level during the past 130000 years. Nature 346, 456–458.

Bard E, Hamelin B, Arnold M, Montaggioni L, Cabioch G, Faure G, Rougerie F, 1996. Deglacial sea-level record from Tahiti corals and the timing of global meltwater discharge. Nature 382, 241–244.

Bartholomew I, Nienow P, Mair D, Hubbard A, King M A, Sole A, 2010. Seasonal evolution of subglacial drainage and acceleration in a Greenland outlet glacier. Nature Geoscience 3, 408–411.

Bartholomew I, Nienow P, Sole A, Mair D, Cowton T, King M A, 2012. Short-term variability in Greenland Ice-Sheet motion forced by time-varying meltwater drainage: implications for the relationship between subglacial drainage system behaviour and ice velocity. Journal of Geophysical Research: Earth Surface 117. doi:10.1029/2011JF002220

Bassett S E, Milne G A, Mitrovica J X, Clark P U, 2005. Ice-sheet and solid Earth influences on far-field sea-level histories. Science 309, 925–928.

Bauder A, Mickelson D M, Marshall S J, 2003. Modelling ice-sheet permafrost interaction around the southern Laurentide ice-sheet. EGS – AGU – EUG Joint Assembly. Abstracts from the meeting held in Nice, France, 6–11 April 2003, abstract 12348.

Beardsmore G R, Cull J P, 2001. Crustal heat flow: a guide to measurement and modelling. Cambridge: Cambridge University Press.

Bell R E, 2008. The role of subglacial water in ice-sheet mass balance. Nature Geoscience 1, 297–304.

Benn D I, Evans D J A, 1998. Glaciers & glaciation. London: Arnold.

Benson C S, 1961. Stratigraphic studies in the snow and firn of the Greenland ice-sheet. Folia Geographica Danica 9, 13–37.

Berger A, 1978. Long-term variations of daily insolation and Quaternary climatic changes. Journal of the Atmospheric Sciences 35, 2362–2367.

Berger A, Loutre M F, 1991. Insolation values for the climate of the last 10 million years. Quaternary Science Reviews 10, 297–317.

Berger A, Loutre M F, 2002. An exceptionally long interglacial ahead? Science 297, 1287–1288.

Berger A, Loutre M F, Crucifix M, 2003. The Earth's climate in the next hundred thousand years (100 kyr). Surveys in Geophysics 24, 117–138.

Bhattacharya I, Jezek K C, Wang L, Liu H, 2009. Surface melt area variability of the Greenland ice-sheet: 1979–2008. Geophysical Research Letters 36, L20502. doi:10.1029/2009GL039798

Bintanja R, van de Wal R S W, 2008. North American ice-sheet dynamics and the onset of 100000-year glacial cycles. Nature 454, 869–872.

BIOCLIM, 2003. Deliverable D7. Continuous climate evolution scenarios over western Europe (1000 km scale). Work package 2: Simulation of the future evolution of the biosphere system using the hierarchical strategy. Châtenay-Malabry: Andra.

Birch F, Roy R F, Decker E R, 1968. Heat flow and thermal history in New England and New York. In Zen E-an (ed). Studies of Appalachian geology: northern and maritime. New York: Interscience, 437–451.

Birgersson M, Karnland O, Nilsson U, 2008. Freezing in saturated bentonite – a thermodynamic approach. Physics and Chemistry of the Earth, Parts A/B/C 33, S527–S530.

Birgersson M, Karnland O, Nilsson U, 2010. Freezing of bentonite. Experimental studies and theoretical considerations. SKB TR-10-40, Svensk Kärnbränslehantering AB.

Björck S, 1995. A review of the history of the Baltic Sea, 13.0–8.0 ka BP. Quaternary International 27, 19–40.

Björck S, Noe-Nygaard N, Wolin J, Houmark-Nielsen M, Hansen H J, Snowball I, 2000. Eemian lake development, hydrology and climate: a multi-stratigraphic study of the Hollerup site in Denmark. Quaternary Science Reviews 19, 509–536.

Booth A D, Clark R A, Kulessa B, Murray T, Hubbard A, 2012. Thin-layer effects in glaciological seismic amplitude-versus-angle (AVA) analysis: implications for characterising a subglacial till unit, Russell Glacier, West Greenland. The Cryosphere 6, 909–922.

Bos J A A, Helmens K F, Bohncke S J P, Seppä H, Birks H J B, 2009. Flora, vegetation and climate at Sokli, northeastern Fennoscandia, during the Weichselian Middle Pleniglacial. Boreas 38, 335–348.

Bosson E, Sassner M, Sabel U, Gustafsson L-G, 2010. Modelling of present and future hydrology and transport – SR Site Biosphere. SKB R-10-02, Svensk Kärnbränslehantering AB.

Bougamont M, Bamber J L, Greuell W, 2005. A surface mass balance model for the Greenland Ice-Sheet. Journal of Geophysical Research 110, F04018. doi:10.1029/2005JF000348

Boulton G S, Clark C D, 1990. The Laurentide Ice-Sheet through the last glacial cycle: the topology of drift lineations as a key to the dynamic behaviour of former ice-sheets. Transactions of the Royal Society of Edinburgh: Earth Sciences 81, 327–347.

Boulton G S, Payne A, 1992. Simulation of the European ice-sheet through the last glacial cycle and prediction of future glaciation. SKB TR-93-14, Svensk Kärnbränslehantering AB.

Boulton G S, Kautsky U, Morén L, Wallroth T, 2001a. Impact of long-term climate change on a deep geological repository for spent nuclear fuel. SKB TR-99-05, Svensk Kärnbränslehantering AB.

Boulton G S, Zatsepin S, Maillot B, 2001b. Analysis of groundwater flow beneath ice-sheets. SKB TR-01-06, Svensk Kärnbränslehantering AB.

Brandefelt J, Otto-Bliesner B L, 2009. Equilibrium and variability in a Last Glacial Maximum climate simulation with CCSM3. Geophysical Research Letters 36, L19712. doi:10.1029/2009GL040364

Brandefelt J, Kjellström E, Näslund J-O, Smith B, Strandberg G, Voelker A H L, Wohlfarth B, 2011. A coupled climate model simulation of Marine Isotope Stage 3 stadial climate. Climate of the Past 7, 649–670.

Breckle S-W, 2002. Walter's vegetation of the earth: the ecological systems of the geo-biosphere. 4th ed. Berlin: Springer.

Breemer C W, Clark P U, Haggerty R, 2002. Modeling the subglacial hydrology of the late Pleistocene lake Michigan Lobe, Laurentide Ice-Sheet. Geological Society of America Bulletin 114, 665–674.

Brinkerhoff D J, Meierbachtol T W, Johnson J V, Harper J T, 2011. Sensitivity of the frozen/melted basal boundary to perturbations of basal traction and geothermal heat flux: Isunnguata Sermia, western Greenland. Annals of Glaciology 52, 43–50.

Brydsten L, 2009. Sediment dynamics in the coastal areas of Forsmark and Laxemar during an interglacial. SKB TR-09-07, Svensk Kärnbränslehantering AB.

Brydsten L, Engqvist A, Näslund J-O, Lindborg T, 2009. Expected extreme sea levels at Forsmark and Laxemar-Simpevarp up until year 2100. SKB TR-09-21, Svensk Kärnbränslehantering AB.

Burgess P, 1998. Future climatic and cryospheric change on millennial timescales: an assessment using two-dimensional climate modelling studies. PhD thesis. Climatic Research Unit, University of East Anglia, UK.

Burn C R, 2002. Tundra lakes and permafrost, Richards Island, western Arctic coast, Canada. Canadian Journal of Earth Sciences 39, 1281–1298.

Burt T P, Williams P J, 1976. Hydraulic conductivity in frozen soils. Earth Surface Processes 1, 349–360.

Bøggild C E, Mayer C, Podlech S, Taurisano A, Nielsen S, 2004. Towards an assessment of the balance state of the Greenland Ice-Sheet. Geological Survey of Denmark and Greenland Bulletin 4, 81–84.

Catania G A, Neumann T A, 2009. Persistent englacial drainage features in the Greenland Ice-Sheet. Geophysical Research Letters 37, L02501. doi:10.1029/2009GL041108

Catania G A, Neumann T A, Price S F, 2008. Characterizing englacial drainage in the ablation zone of the Greenland ice-sheet. Journal of Glaciology 54, 567–578.

Čermák V, Balling N, Kukkonen I, Zui V I, 1993. Heat flow in the Baltic Shield – results of the lithospheric geothermal modelling. Precambrian Research 64, 53–65.

Chandler D M, Wadham J L, Lis G P, Cowton T, Sole A, Bartholomew I, Telling J, Nienow P, Bagshaw E B, Mair D, Vinen S, Hubbard A, 2013. Evolution of the subglacial drainage system beneath the Greenland Ice-Sheet revealed by tracers. Nature Geoscience 6, 195–198.

Channell J E T, Hodell D A, Romero O, Hillaire-Marcel C, de Vernal A, Stoner J S, Mazaud A, Röhl U, 2012. A 750-kyr detrital-layer stratigraphy for the North Atlantic (IODP Sites U1302–U1303, Orphan Knoll, Labrador Sea). Earth and Planetary Science Letters 317, 218–230.

Chapman M R, Shackleton N J, 1999. Global ice-volume fluctuations, North Atlantic ice-rafting events, and deep-ocean circulation changes between 130 and 70 ka. Geology 27, 795–798.

Chappell J, Polach H, 1991. Post-glacial sea-level rise from a coral record at Huon Peninsula, Papua New Guinea. Nature 349, 147–149.

Chappell J, Omura A, Esat T, McCulloch M, Pandolfi J, Ota Y, Pillans B, 1996. Reconciliation of late Quaternary sea levels derived from coral terraces at Huon Peninsula with deep sea oxygen isotope records. Earth and Planetary Science Letters 141, 227–236.

Charbit S, Dumas C, Kageyama M, Roche D M, Ritz C, 2013. Influence of ablation-related processes in the build-up of simulated Northern Hemisphere ice-sheets during the last glacial cycle. The Cryosphere 7, 681–698.

Chen J L, Wilson C R, Tapley B D, 2006. Satellite gravity measurements confirm accelerated melting of Greenland ice-sheet. Science 313, 1958–1960.

Christoffersen P, Tulaczyk S, Wattrus N J, Peterson J, Quintana-Krupinski N, Clark C D, Sjunneskog C, 2008. Large subglacial lake beneath the Laurentide ice-sheet inferred from sedimentary sequences. Geology 36, 563–566.

Church J A, Gregory J M, Huybrechts P, Kuhn M, Lambeck K, Nhuan M T, Qin D, Woodworth P L, Anisimov O A, Bryan F O, Cazenave A, Dixon K W, Fitzharris B B, Flato G M, Ganopolski A, Gornitz V, Lowe J A, Noda A, Oberhuber J M, O'Farrell S P, Ohmura A, Oppenheimer M, Peltier W R, Raper S C B, Ritz C, Russell G L, Schlosser E, Shum C K, Stocker T F, Stouffer R J, van de Wal R S W, Voss R, Wiebe E C, Wild M, Wingham D J, Zwally H J, 2001. Greenland and Antarctic ice-sheets. In Houghton J T (ed). Climate Change 2001: the scientific basis. New York: Cambridge University Press, Chapter 11.2.3.

Church J A, Clark P U, Cazenave A, Gregory J M, Jevrejeva S, Levermann A, Merrifield M A, Milne G A, Nerem R S, Nunn P D, Payne A J, Pfeffer W T, Stammer D, Unnikrishnan A S, 2013. Sea Level Change. In Climate change 2013: the physical science basis. Contribution of Working Group I to the Fifth Assessment Report of the Intergovernmental Panel on Climate Change. Cambridge: Cambridge University Press.

Claesson Liljedahl L, Kontula A, Harper J, Näslund J-O, Selroos J-O, Pitkänen P, Puigdomenech I, Hobbs M, Follin S, Hirschorn S, Jansson P, Kennell L, Marcos N, Ruskeeniemi T, Tullborg E-L, Vidstrand P, 2016. The Greenland Analogue Project: Final report. SKB TR-14-13, Svensk Kärnbränslehantering AB.

Clason C C, Applegate P J, Holmlund P, 2014. Modelling Late Weichselian evolution of the Eurasian ice-sheets forced by surface meltwater-enhanced basal sliding. Journal of Glaciology 60, 29–40.

Clark J A, Farrell W E, Peltier W R, 1978. Global changes in postglacial sea level: a numerical calculation. Quaternary Research 9, 265–287.

Clark P U, Mix A C, 2002. Ice-sheets and sea level of the Last Glacial Maximum. Quaternary Science Reviews 21, 1–7.

Clark P U, Alley R B, Keigwin L D, Licciardi J M, Johnsen S J, Wang H X, 1996. Origin of the first global meltwater pulse following the Last Glacial Maximum. Paleoceanography 11, 563–577.

Clark P U, Shakun J D, Marcott S A, Mix A C, Eby M, Kulp S, Levermann A, Milne G A, Pfister P L, Santer B D, Schrag D P, Solomon S, Stocker T F, Strauss B H, Weaver A J, Winkelmann R, Archer D, Bard E, Goldner A, Lambeck K, Pierrehumbert R T, Plattner G-K, 2016. Consequences of twenty-first-century policy for multi-millennial climate and sea-level change. Nature Climate Change 6, 360–369.

Clarke G, Leverington D, Teller J, Dyke A, 2003. Superlakes, megafloods, and abrupt climate change. Science 301, 922–923.

Clauser C, Huenges E, 1995. Thermal conductivity of rocks and minerals. In Ahrens T J (ed). Rock physics and phase relations: handbook of physical constants. Washington, D.C.: American Geophysical Union 105–126.

Cochelin A-S B, Mysak L A, Wang Z, 2006. Simulation of long-term future climate changes with the green McGill paleoclimate model: the next glacial inception. Climate Change 79, 381–401.

Colleoni F, 2009. On the Late Saalian glaciation (160–140 ka): a climate modeling study. PhD thesis. Laboratoire de Glaciologie et de Géophysique de l'Environnement, Université Grenoble I.

Colleoni F, Liakka J, 2020. Transient simulations of the Eurasian ice-sheet during the Saalian glacial cycle. SKB TR-19-17, Svensk Kärnbränslehantering AB.

Colleoni F, Krinner G, Jakobsson M, Peyaud V, Ritz C, 2009. Influence of regional parameters on the surface mass balance of the Eurasian ice-sheet during the peak Saalian (140 kya). Global and Planetary Change 68, 132–148.

Colleoni F, Wekerle C, Masina S, 2014. Long-term safety of a planned geological repository for spent nuclear fuel in Forsmark – estimate of maximum ice-sheet thicknesses. SKB TR-14-21, Svensk Kärnbränslehantering AB.

Colleoni F, Wekerle C, Näslund J-O, Brandefelt J, Masina S, 2016. Constraint on the penultimate glacial maximum Northern Hemisphere ice topography (≈ 140 kyrs BP). Quaternary Science Reviews 137, 97–112.

Collins M, Knutti R, Arblaster J, Dufresne J-L, Fichefet T, Friedlingstein P, Gao X, Gutowski W J, Johns T, Krinner G, Shongwe M, Tebaldi C, Weaver A J, Wehner M, 2013. Long-term Climate Change: Projections, Commitments and Irreversibility. In Climate change 2013: the physical science basis. Contribution of Working Group I to the Fifth Assessment Report of the Intergovernmental Panel on Climate Change. Cambridge: Cambridge University Press.

Collinson J, 2005a. Erosional sedimentary structures. In Selley R C, Cocks L R M, Plimer I R (eds). Encyclopedia of geology. Amsterdam: Elsevier Academic Press.

Collinson J, 2005b. Depositional sedimentary structures. In Selley R C, Cocks L R M, Plimer I R (eds). Encyclopedia of geology. Amsterdam: Elsevier Academic Press.

Cuffey K M, Alley R B, Grootes P M, Bolzan J M, Anandakrishnan S, 1994. Calibration of the $\delta^{18}O$ isotopic paleothermometer for central Greenland, using borehole temperatures. Journal of Glaciology 40, 341–349.

Dahl-Jensen D, Gundestrup N, Gogineni S P, Miller H, 2003. Basal melt at NorthGRIP modelled from borehole, ice-core and radio-echo sounder observations. Annals of Glaciology 37, 207–212.

Danielson E W, Levin J, Abrams E, 2003. Meteorology. 2nd ed. New York: McGraw-Hill.

Dansgaard W, Johnsen S J, Clausen H B, Dahl-Jensen D, Gundestrup N S, Hammer C U, Hvidberg C S, Steffensen J P, Sveinbjörnsdottir A E, Jouzel J, Bond G, 1993. Evidence for general instability of past climate from a 250-kyr ice-core record. Nature 364, 218–220.

Das S B, Joughin I, Behn M D, Howat I M, King M A, Lizarralde D, Bhatia M P, 2008. Fracture propagation to the base of the Greenland ice-sheet during supraglacial lake drainage. Science 320, 778–781.

Davis J L, Mitrovica J X, 1996. Glacial isostatic adjustment and the anomalous tide gauge record of eastern North America. Nature 379, 331–333.

Davis J L, Mitrovica J X, Scherneck H G, Fan H, 1999. Investigations of Fennoscandian glacial isostatic adjustment using modern sea level records. Journal of Geophysical Research 104, 2733–2747.

de Abreu L, Shackleton N J, Schönfeld J, Hall M, Chapman M, 2003. Millennial-scale oceanic climate variability off the Western Iberian margin during the last two glacial periods. Marine Geology 196, 1–20.

DeConto R M, Pollard D, 2016. Contribution of Antarctica to past and future sea-level rise. Nature 531, 591–597.

de Fleurian B, Morlighem M, Seroussi H, Rignot E, van den Broeke M R, Munneke P K, Mouginot J, Smeets P C J P, Tedstone A J, 2016. A modeling study of the effect of runoff variability on the effective pressure beneath Russell Glacier, West Greenland. Journal of Geophysical Research: Earth Surface 121, 1834–1848.

Delisle G, 1998. Numerical simulation of permafrost growth and decay. Journal of Quaternary Science 13, 325–333.

Denton G H, Hughes T J (eds), 1981. The last great ice-sheets. New York: Wiley.

Denton G E, Sugden D E, 2005. Meltwater features that suggest Miocene ice-sheet overriding the Transantarctic Mountains in Victoria Land, Antarctica. Geografiska Annaler 87A, 67–85.

Dow C F, Hubbard A, Booth A D, Doyle S H, Gusmeroli A, Kulessa B, 2013. Seismic evidence of mechanically weak sediments underlying Russell Glacier, West Greenland. Annals of Glaciology 54, 135–141.

Dowdeswell J A, Ottesen D, Rise L, 2006. Flow switching and large-scale deposition by ice streams draining former ice-sheets. Geology 34, 313–316.

Drewry D, 1986. Glacial geologic processes. London: Arnold.

Drijfhout S, Hazeleger W, Selten F, Haarsma R, 2008. Future changes in internal variability of the Atlantic Meridional Overturning Circulation. Climate Dynamics 30, 407–419.

Duval P, Ashby M F, Anderman I, 1983. Rate-controlling processes in the creep of polycrystalline ice. Journal of Physical Chemistry 87, 4066–4074.

Dziewonski A M, Anderson D L, 1981. Preliminary reference earth model. Physics of the Earth and Planetary Interiors 25, 297–356.

Ebert K, 2009. Cenozoic landscape evolution in northern Sweden: geomorphological interpretation within a GIS-framework. PhD thesis. Department of Physical Geography and Quaternary Geology, Stockholm University. (Dissertations from the Department of Physical Geography and Quaternary Geology 19)

Eby M, Zickfeld K, Montenegro A, Archer D, Meissner K J, Weaver A J 2009. Lifetime of anthropogenic climate change: millennial time scales of potential CO_2 and surface temperature perturbations. Journal of Climate 22, 2501–2511.

Edwards T L, Brandon M A, Durand G, Edwards N R, Golledge N R, Holden P B, Nias I J, Payne A J, Ritz C, Wernecke A, 2019. Revisiting Antarctic ice loss due to marine ice-cliff instability. Nature 566, 58–64.

Ehlers J, Gibbard P L (eds), 2004. Quaternary glaciations: extent and chronology. Part I: Europe. Amsterdam: Elsevier. (Developments in quaternary science 2)

Ekman M, 1991. A concise history of postglacial land uplift research (from its beginning to 1950). Terra Nova 3, 358–365.

Enderlin E M, Howat I M, Jeong S, Noh M J, van Angelen J H, van den Broeke M R, 2014. An improved mass budget for the Greenland ice-sheet. Geophysical Research Letters 41, 866–872.

Engelhardt H, Kamb B, 1998. Basal sliding of Ice Stream B, West Antarctica. Journal of Glaciology 44, 223–230.

Engelhardt H, Humphrey N, Kamb B, Fahnestock M, 1990. Physical conditions at the base of a fast moving Antarctic ice stream. Science 248, 57–59.

Engels S, Bohncke S J P, Bos J A A, Brooks S J, Heiri O, Helmens K F, 2008. Chironomid-based palaeotemperature estimates for northeast Finland during Oxygen Isotope Stage 3. Journal of Palaeolimnology 40, 49–61.

Engels S, Helmens K F, Väliranta M, Brooks S J, Birks H J B, 2010. Early Weichselian (MIS 5d and 5c) temperatures and environmental changes in northern Fennoscandia as recorded by chironomids and macroremains at Sokli, northeast Finland. Boreas 39, 689–704.

EPICA community members, 2004. Eight glacial cycles from an Antarctic ice core. Nature 429, 623–628.

Eronen M, Gluckert G, Hatakka L, van de Plassche O, van der Plicht J, Rantala P, 2001. Rates of Holocene isostatic uplift and relative sea-level lowering of the Baltic in SW Finland based on studies of isolation contacts. Boreas 30, 17–30.

Ettema J, van den Broeke M R, van Meijgaard E, van de Berg W J, Bamber J L, Box J E, Bales R C, 2009. Higher surface mass balance of the Greenland ice-sheet revealed by high-resolution climate modeling. Geophysical Research Letters 36, L12501. doi:10.1029/2009GL038110

Eugster W, Rouse W R, Pielke R A Mcfadden J P, Baldocchi D D, Kittel T G F, Chapin F, Stuart F, Liston G E, Vidale P L, Vaganov E, Chambers S, 2000. Land-atmosphere energy exchange in Arctic tundra and boreal forest: available data and feedbacks to climate. Global Change Biology 6 (Suppl. 1), 84–115.

Evatt G W, Fowler A C, Clark C D, Hulton N R J, 2006. Subglacial floods beneath ice-sheets. Philosophical Transactions of the Royal Society A 364, 1769–1794.

Eyring V, Bony S, Meehl G A, Senior C A, Stevens B, Stouffer R J, Taylor K E, 2016. Overview of the Coupled Model Intercomparison Project Phase 6 (CMIP6) experimental design and organization. Geoscientific Model Development 9, 1937–1958.

Fahnestock M, Abdalati W, Joughin I, Brozena J, Gogineni P, 2001. High geothermal heat flow, basal melt, and the origin of rapid ice flow in central Greenland. Science 294, 2338–2342.

Fairbanks R G, 1989. A 17000-year glacio-eustatic sea level record: influence of glacial melting rates on the Younger Dryas event and deep-ocean circulation. Nature 342, 637–642.

Farrell W E, Clark J A, 1976. On postglacial sea level. Geophysical Journal of the Royal Astronomical Society 46, 647–667.

Fastook J L, 1990. A map-plane finite-element program for ice-sheet reconstruction: a steady-state calibration with Antarctica and a reconstruction of the Laurentide ice-sheet for 18000 BP. In Brown H U (ed). Computer assisted analysis and modelling on the IBM 3090. White Plains, NY: IBM Scientific and Technical Computing Department.

Fastook J L, 1994. Modeling the Ice Age: the finite-element method in glaciology. Computing Science and Engineering 1, 55–67.

Fastook J L, Chapman J E, 1989. A map plane finite-element model: three modeling experiments. Journal of Glaciology 35, 48–52.

Fastook J L, Holmlund P, 1994. A glaciological model of the Younger Dryas event in Scandinavia. Journal of Glaciology 40, 125–131.

Fastook J L, Prentice M, 1994. A finite-element model of Antarctica: sensitivity test for meteorological mass-balance relationship. Journal of Glaciology 40, 167–175.

Fettweis X, Box J E, Agosta C, Amory C, Kittel C, Lang C, van As D, Machguth H, Gallée H, 2017. Reconstructions of the 1900–2015 Greenland ice-sheet surface mass balance using the regional climate MAR model. The Cryosphere 11, 1015–1033.

Fisher U H, 2009. Glacial erosion: a review of its modelling. Nagra Arbeitsbericht NAB 09-23, Nagra, Switzerland.

Fitzpatrick A A W, Hubbard A L, Box J E, Quincey D J, van As D, Mikkelsen A P B, Doyle S H, Dow C F, Hasholt B, Jones G A, 2014. A decade (2002–2012) of supraglacial lake volume estimates across Russell Glacier, West Greenland. The Cryosphere 8, 107–121.

Fjeldskaar W, 1994. The amplitude and decay of the glacial forebulge in Fennoscandia. Norsk Geologisk Tidsskrift 74, 2–8.

Fleming K, Johnston P, Zwartz D, Yokoyama Y, Lambeck K, Chappell J, 1998. Refining the eustatic sea-level curve since the Last Glacial Maximum using far- and intermediate-field sites. Earth and Planetary Science Letters 163, 327–342.

Flowers G E, Clarke G K C, 2002a. A multicomponent coupled model of glacier hydrology. 1. Theory and synthetic examples. Journal of Geophysical Research 107, 2287. doi:10.1029/2001JB001122

Flowers G E, Clarke G K C, 2002b. A multicomponent coupled model of glacier hydrology. 2. Application to Trapridge Glacier, Yukon, Canada. Journal of Geophysical Research 107, 2288. doi:10.1029/2001JB001124

Forsström P-L, 2005. Through a glacial cycle: simulation of the Eurasian ice-sheet dynamics during the last glaciation. PhD thesis. University of Helsinki, Faculty of Science, Department of Geology, Geology and Palaeontology and Centre for Scientific Computing.

Forsström P-L, Sallasmaa O, Greve R, Zwinger T, 2003. Simulation of fast-flow features of the Fennoscandian ice-sheet during the Last Glacial Maximum. Annals of Glaciology 37, 383–389.

Forster R R, Box J E, van den Broeke M R, Miège C, Burgess E W, van Angelen J H, Lenaerts J T M, Koenig L S, Paden J, Lewis C, Gogineni S P, Leuschen C, Mcconnell J R, 2013. Extensive liquid meltwater storage in firn within the Greenland ice-sheet. Nature Geoscience 7, 95–98.

Fotiev S M, 1997. Permafrost groundwater Russian Literature Review. In Haldorsen S, Liebman M, Nelson G, van Everdingen R O, Boike J. State-of-the-art report on saturated water movement in permafrost areas. Report No 4/97 (lnr 54), Norges landbrukshøgskole, Norway.

Fountain A G, Walder J S, 1998. Water flow through temperate glaciers. Reviews of Geophysics 36, 299–328.

Fountain A G, Jacobel R W, Schlichting R, Jansson P, 2005a. Fractures as the main pathways of water flow in temperate glaciers. Nature 433, 618–621.

Fountain A G, Schlichting R, Jansson P, Jacobel R W, 2005b. Observations of englacial flow passages: a fracture dominated system. Annals of Glaciology 40, 25–30.

Fredén C (ed), 2002. Sveriges nationalatlas. Berg och Jord. Stockholm: SNA publishing. (In Swedish.)

French H M, 2007. The periglacial environment. 3rd ed. Chichester: Wiley.

Fronval T, Jansen E, 1996. Late Neogene paleoclimates and paleoceanography in the Iceland-Norwegian Sea: evidence from the Iceland and Vøring plateaus. In Thiede J, Myhre A M, Firth J V, Johnson G L, Ruddiman W F (eds). Proceedings of the Ocean Drilling Program, Scientific results, 151, 455–468.

Funder S, Demidov I, Yelovicheva Y, 2002. Hydrography and mollusc faunas of the Baltic and the White Sea-North Sea seaway in the Eemian. Palaeogeography, Palaeoclimatology, Palaeoecology 184, 275–304.

Furlong K P, Chapman D S, 1987. Crustal heterogeneities and the thermal structure of the continental crust. Geophysical Research Letters 14, 314–317.

Fyke J, Matthews H D 2015. A probabilistic analysis of cumulative carbon emissions and long-term planetary warming. Environmental Research Letters, 10, 115007. doi:10.1088/1748-9326/10/11/115007

Ganopolski A, Winkelmann R, Schellnhuber H J, 2016. Critical insolation–CO_2 relation for diagnosing past and future glacial inception. Nature 529, 200–203.

Garisto F, Avis J, Chshyolkova T, Gierszewski P, Gobien M, Kitson C, Melnyk T, Miller J, Walsh R, Wojciechowski L, 2010. Glaciation scenario: safety assessment for a deep geological repository for used fuel. NWMO TR-2010-10, Nuclear Waste Management Organization, Canada.

Gascoyne M, 2000. A review of published literature on the effects of permafrost on the hydrogeochemistry of bedrock. SKB R-01-56, Svensk Kärnbränslehantering AB.

Gent P R, Danabasoglu G, Donner L J, Holland M M, Hunke E C, Jayne S R, Lawrence D M, Neale R B, Rasch P J, Vertenstein M, Worley P H, Yang Z-L, Zhang M, 2011. The Community Climate System Model Version 4. Journal of Climate 24, 4973–4991.

Giovinetto M B, Zwally H J, 2000. Spatial distribution of net surface accumulation on the Antarctic ice-sheet. Annals of Glaciology 31, 171–178.

Glen J W, 1955. The creep of polycrystalline ice. Proceedings of the Royal Society of London, Series A 228, 519–538.

Golledge N R, Kowalewski D E, Naish T R, Levy R H, Fogwill C J, Gasson E G, 2015. The multi-millennial Antarctic commitment to future sea level rise. Nature 526, 421–425.

Goodfellow B W, Stroeven A P, Martel S J, Heyman J, Rossi M, Caffee M W, 2019. Exploring alternative models for the formation of conspicuously flat basement surfaces in southern Sweden. SKB TR-19-22, Svensk Kärnbränslehantering AB.

Goodwin P, Haigh I D, Rohling E J, Slangen A, 2017. A new approach to projecting 21st century sea-level changes and extremes. Earth's Future 5, 240–253.

Gregory J M, Huybrechts P, 2006. Ice-sheet contributions to future sea-level change. Philosophical Transactions of the Royal Society A 364, 1709–1731.

Gregory J M, Tailleux R, 2011. Kinetic energy analysis of the response of the Atlantic meridional overturning circulation to CO_2-forced climate change. Climate Dynamics 37, 893–914.

Gregory J M, Huybrechts P, Raper S C B, 2004. Threatened loss of the Greenland ice-sheet. Nature 428, 616.

Greve R, 1997. Application of a polythermal three-dimensional ice-sheet model to the Greenland ice-sheet: response to steady-state and transient climate scenarios. Journal of Climate 10, 901–918.

Greve R, Hutter K, 1995. Polythermal three-dimensional modelling of the Greenland ice-sheet with varied geothermal heat flux. Annals of Glaciology 21, 8–12.

Grigull S, Peterson G, Nyberg J, Öhrling C, 2019. Phanerozoic faulting of Precambrian basement in Uppland. SKB R-19-22, Svensk Kärnbränslehantering AB.

Grinsted A, Jevrejeva S, Riva R E, Dahl-Jensen D, 2015. Sea level rise projections for northern Europe under RCP8.5. Climate Research 64, 15–23.

Hagdorn M K M, 2003. Reconstruction of the past and forecast of the future European and British ice-sheets and associated sea-level change. PhD thesis. University of Edinburgh, School of GeoScience.

Hagdorn M, Hulton N, Payne A J, Rutt I, Boulton G, 2005. Introducing GLIMMER – a 3D thermo-mechanical ice-sheet model. Poster presented at European Geosciences Union General Assembly 2005, Vienna, Austria, April 24–29 2005.

Hall A, van Boeckel M, 2020. Origin of the Baltic Sea basin by Pleistocene glacial erosion. GFF 142, 237–252.

Hall A M, Ebert K, Goodfellow B W, Hättestrand C, Heyman J, Krabbendam M, Moon S, Stroeven A P, 2019a. Past and future impact of glacial erosion in Forsmark and Uppland. SKB TR-19-07, Svensk Kärnbränslehantering AB.

Hall A M, Krabbendam M, van Boeckel M, Ebert K, Hättestrand C, Heyman J, 2019b. The sub-Cambrian unconformity in Västergötland, Sweden: Reference surface for Pleistocene glacial erosion of basement. SKB TR-19-21, Svensk Kärnbränslehantering AB.

Hall A M, Krabbendam M, van Boeckel M, Goodfellow B W, Hättestrand C, Heyman J, Palamakumbara R N, Stroeven A P, Näslund J-O, 2020. Glacial ripping: geomorphological evidence from Sweden for a new process of glacial erosion. Geografiska Annaler, Series A. doi:10.1 080/04353676.2020.1774244

Hallet B, Hunter L, Bogen J, 1996. Rates of erosion and sediment evacuation by glaciers: a review of field data and their implications. Global and Planetary Change 12, 213–235.

Hambrey M J, Barrett P J, Ehrmann W U, Larsen B, 1992. Cainozoic sedimentary processes on the Antarctic continental margin and the record from deep drilling. Zeitschrift für Geomorphologie, Suppl. 86, 77–103.

Hanebuth T, Stattegger K, Grootes P M, 2000. Rapid flooding of the Sunda Shelf: a late-glacial sea-level record. Science 288, 1033–1035.

Hanna E, Huybrechts P, Steffen K, Cappelen J, Huff R, Shuman C, Irvine-Fynn T, Wise S, Griffiths M, 2008. Increased runoff from melt from the Greenland ice-sheet: a response to global warming. Journal of Climate 21, 331–341.

Haq B U, Hardenbol J, Vail P R, 1987. Chronology of fluctuating sea levels since the Triassic. Science 235, 1156–1165.

Harper J, Hubbard A, Ruskeeniemi T, Claesson Liljedahl L, Kontula A, Bougamont M, Brown J, Dirkson A, Dow C, Doyle S, Drake H, Engström J, Fitzpatrick A, Follin S, Frape S, Graly J, Hansson K, Harrington J, Henkemans E, Hirschorn S, Hobbs M, Humphrey N, Jansson P, Johnson J, Jones G, Kinnbom P, Kennell L, Klint K E S, Liimatainen J, Lindbäck K, Meierbachtol T, Pere T, Pettersson R, Tullborg E-L, van As D, 2016. The Greenland Analogue Project: Data and processes. SKB R-14-13, Svensk Kärnbränslehantering AB.

Harper J, Meierbachtol T, Humphrey N, 2019. Greenland ICE Project. Final report. SKB R-18-06, Svensk Kärnbränslehantering AB.

Harrington J A, Humphrey N F, Harper J T, 2015. Temperature distribution and thermal anomalies along a flowline of the Greenland ice-sheet. Annals Of Glaciology 56, 98–104.

Harrison S P, Braconnot P, Joussaume S, Hewitt C, Stouffer R J, 2002. Comparison of palaeo-climate simulations enhances confidence in models. EOS 83, 447.

Hartikainen J, 2004. Permafrost modeling in DECOVALEX III for BMT3. In Eloranta E (ed). DECOVALEX III, 1999–2003. An international project for the modelling of coupled ther-mo-hydro-mechanical processes for spent fuel disposal. Finnish national contributions. STUK-YTO-TR 209, Finnish Centre for Radiation and Nuclear Safety (STUK), Helsinki.

Hartikainen J, 2018. Continuum thermodynamic modelling of porous medium with application to ground freezing. PhD thesis. Aalto University.

Hartikainen J, Mikkola M, 2006. Thermomechanical modelling for freezing of solute saturated soil. In Gladwell G M L, Huyghe J M, Raats P A C, Cowin S C (eds). IUTAM Symposium on the mechanics of physicochemical and electromechanical interactions in porous media, 335–341.

Hartikainen J, Kouhia R, Wallroth T, 2010. Permafrost simulations at Forsmark using a numerical 2D thermo-hydro-chemical model. SKB TR-09-17, Svensk Kärnbränslehantering AB.

Hedenström A, Risberg J, 2003. Shore displacement in northern Uppland during the last 6500 calendar years. SKB TR-03-17, Svensk Kärnbränslehantering AB.

Heginbottom J A, Dubreuil M A, Harker P A, 1995. Canada – Permafrost. In National Atlas of Canada. 5th ed. Ottawa: National Atlas Information Service, Natural Resources Canada.

Heinrich H, 1988. Origin and consequences of cyclic ice rafting in the northeast Atlantic Ocean during the past 130000 years. Quaternary Research 29, 142–152.

Helmens K F, 2009. Climate, vegetation and lake development at Sokli (northern Finland) during early MIS 3 at ~50 kyr: Revising earlier concepts on climate, glacial and vegetation dynamics in Fennoscandia during the Weichselian. SKB TR-09-16, Svensk Kärnbränslehantering AB.

Helmens K, 2013. The last interglacial–glacial cycle (MIS 5–2) re-examined based on long proxy records from central and northern Europe. SKB TR-13-02, Svensk Kärnbränslehantering AB.

Helmens K F, 2019. The last 130000 years in Fennoscandia reconstructed based on a long and fossil-rich sediment sequence preserved at Sokli, northern Finland: new evidence for highly dynamic environmental and climate conditions. SKB TR-18-04, Svensk Kärnbränslehantering AB.

Helmens K F, Engels S, 2010. Ice-free conditions in eastern Fennoscandia during early Marine Isotope Stage 3: lacustrine records. Boreas 39, 399–409.

Helmens K F, Bos J A A, Engels S, Van Meerbeeck C J, Bohncke S J P, Renssen H, Heiri O, Brooks S J, Seppä H, Birks H J B, Wohlfarth B, 2007. Present-day temperatures in northern Scandinavia during the last glaciation. Geology 35, 987–990.

Helmens K F, Risberg J, Jansson K N, Weckström J, Berntsson A, Kaislahti Tillman P, Johansson P W, Wastegård S, 2009. Early MIS 3 glacial lake evolution, ice-marginal retreat pattern and climate at Sokli (northeastern Fennoscandia). Quaternary Science Reviews 28, 1880–1894.

Helmens K F, Väliranta M, Engels S, Shala S, 2012. Large shifts in vegetation and climate during the Early Weichselian (MIS 5d–c) inferred from multi-proxy evidence at Sokli (northern Finland). Quaternary Science Reviews 41, 22–38.

Helmens K F, Katrantsiotis C, Salonen J S, Shala S, Bos J A A, Engels S, Kuosmanen N, Luoto T P, Väliranta M, Luoto M, Ojala A, Risberg J, Weckström J, 2018. Warm summers and rich biotic communities during N-Hemisphere deglaciation. Global and Planetary Change 167, 61–73.

Helmens K F, Katrantsiotis C, Kuosmanen N, Luoto T P, Salonen J S, Väliranta M, 2021. Prolonged interglacial warmth during the Last Glacial in northern Europe. Boreas. doi:10.1111/bor.12495

Hemming S R, 2004. Heinrich events: massive late Pleistocene detritus layers of the North Atlantic and their global climate imprint. Reviews of Geophysics 42, RG1005. doi:10.1029/2003RG000128

Henton J A, Craymer M R, Ferland R, Dragert H, Mazotti S, Forbes D L, 2006. Crustal motion and deformation monitoring of the Canadian landmass. Geomatica 60, 173–191.

Hewitt I J, 2011. Modelling distributed and channelized subglacial drainage: the spacing of channels. Journal of Glaciology 57, 302–314.

Hewitt I J, 2013. Seasonal changes in ice-sheet motion due to melt water lubrication. Earth and Planetary Science Letters 371–372, 16–25.

Hills B H, Harper J T, Humphrey N F, Meierbachtol T W, 2017. Measured horizontal temperature gradients constrain heat transfer mechanisms in Greenland ice. Geophysical Research Letters 44, 9778–9785.

Hindmarsch C A, Boulton G S, Hutter K, 1989. Modes of operation of thermo-mechanically coupled ice-sheets. Annals of Glaciology 12, 57–69.

Hock R, 1998. Modelling of glacier melt and discharge. Zürich: Geographisches Institut ETH. (Zürcher Geographische Schriften 70)

Hock R, 2005. Glacier melt: a review of processes and their modelling. Progress in Physical Geography 29, 362–391.

Hock R, Jansson P, 2005. Modelling glacier hydrology. In Anderson M G, McDonnell J (eds). Encyclopedia of hydrological sciences. Chichester: Wiley, Vol 4, 2647–2655.

Hock R, Jansson P, Braun L, 2005. Modelling the response of mountain glacier discharge to climate warming. In Huber U M, Bugmann H K M, Reasoner M A (eds). Global change and mountain regions: an overview of current knowledge. Dordrecht: Springer, 243–252.

Hoffman M, Price S, 2014. Feedbacks between coupled subglacial hydrology and glacier dynamics. Journal of Geophysical Research: Earth Surface 119, 414–436.

Hoffman M J, Andrews L C, Price S A, Catania G A, Neumann T A, Lüthi M P, Gulley J, Ryser C, Hawley R L, Morriss B, 2016. Greenland subglacial drainage evolution regulated by weakly connected regions of the bed. Nature Communications 7, 13903. doi:10.1038/ncomms13903

Hohl V, 2005. Northern European long term climate archives. SKB TR-05-01, Svensk Kärnbränslehantering AB.

Hohmann M, 1997. Soil freezing – the concept of soil water potential. State of the art. Cold Regions Science and Technology 25, 101–110.

Holgate S J, Matthews A, Woodworth P L, Rickards L J, Tamisiea M E, Bradshaw E, Foden P R, Gordon K M, Jevrejeva S, Pugh J, 2013. New data systems and products at the Permanent Service for Mean Sea Level. Journal of Coastal Research 29, 493–504.

Holland D M, Thomas R H, de Young B, Ribergaard M H, Lyberth B, 2008. Acceleration of Jakobshavn Isbræ triggered by warm subsurface ocean waters. Nature Geoscience 1, 659–664.

Holmlund P, Fastook J, 1993. Numerical modelling provides evidence of a Baltic ice stream during the Younger Dryas. Boreas 22, 77–86.

Holmlund P, Fastook J, 1995. A time dependent glaciological model of the Weichselian ice-sheet. Quaternary International 27, 53–58.

Holmlund P, Jansson P, 2003. Glaciologi. Stockholm: Stockholm University and the Swedish Research Council. (In Swedish.)

Hooke R LeB, 1977. Basal temperatures in polar ice-sheets: a qualitative review: Quaternary Research 7, 1–13.

Hooke R LeB, 1984. On the role of mechanical energy in maintaining subglacial water conduits at atmospheric pressure. Journal of Glaciology 30, 180–187.

Hooke R LeB, 1989. Englacial and subglacial hydrology: a qualitative review. Arctic and Alpine Research 21, 221–233.

Hooke R LeB, 1991. Positive feedbacks associated with erosion of glacial cirques and overdeepenings. Geological Society of America Bulletin 103, 1104–1108.

Hooke R LeB, 2004. Principles of glacier mechanics. 2nd ed. Cambridge: Cambridge University Press.

Hooke R LeB, Lauman T, Kohler J, 1990. Subglacial water pressures and the shape of subglacial conduits. Journal of Glaciology 36, 67–71.

Horton B P, Rahmstorf S, Engelhart S E, Kemp A C, 2014. Expert assessment of sea level rise by AD 2100 and AD 2300. Quaternary Science Reviews 84, 1–6.

Horton B P, Kopp R E, Garner A J, Carling C H, Khan N S, Roy K, Shaw T A, 2018. Mapping sea level change in time, space, and probability. Annual Review of Environment and Resources 43, 481–521.

Houmark-Nielsen M, 2009. MIS 3 interstadial climate and rapid ice advances in the south–western Baltic. SKB P-09-10, Svensk Kärnbränslehantering AB.

Houmark-Nielsen M, Kjær K H, 2003. Southwest Scandinavia, 40–15 kyr BP: palaeogeography and environmental change. Journal of Quaternary Science 18, 769–786.

Howat I M, Joughin I, Tulaczyk S, Gogineni S, 2005. Rapid retreat and acceleration of Helheim Glacier, east Greenland. Geophysical Research Letters 32, L22502. doi:10.1029/2005GL024737

Howat I M, Joughin I, Scambos T A, 2007. Rapid changes in ice discharge from Greenland outlet glaciers. Science 315, 1559–1561.

Hubbard B, Nienow P, 1997. Alpine subglacial hydrology. Quaternary Science Reviews 16, 939–955.

Huber C, Leuenberger M, Spahni R, Flückiger J, Schwander J, Stocker T F, Johnsen S, Landais A, Jouzel J, 2006. Isotope calibrated Greenland temperature record over Marine Isotope Stage 3 and its relation to CH_4. Earth and Planetary Science Letters 243, 504–519.

Humlum O, Houmark-Nielsen M, 1994. High deglaciation rates in Denmark during the late Weichselian – implications for the palaeoenvironment. Geografisk Tidsskrift 94, 26–37.

Humphrey N F, Harper J T, Pfeffer W T, 2012. Thermal tracking of meltwater retention in Greenland's accumulation area. Journal of Geophysical Research 117, F01010. doi:10.1029/2011JF002083

Hutter K, 1983. Theoretical glaciology: material science of ice and the mechanics of glaciers and ice-sheets. Dordrecht: Reidel.

Huybrechts P, 1986. A three dimensional time-dependent numerical model for polar ice-sheets: some basic testing with a stable and efficient finite difference scheme. Report 86-1, Geografisch Instituut, Vrije Universiteit Brussel, Belgium.

Huybrechts P, 1990. A 3D model for the Antarctic ice-sheet: a sensitivity study on the glacial–interglacial contrast. Climate Dynamics 5, 79–92.

Huybrechts P, 2006. Numerical modeling of ice-sheets through time. In Knight P G (ed). Glacier science and environmental change. Malden: Blackwell Publishing, 406–412.

Huybrechts P, 2010. Vulnerability of an underground radioactive waste repository in northern Belgium to glaciotectonic and glaciofluvial activity during the next 1 million year. Report 10/01, Departement Geografie, Vrije Universiteit Brussel, Belgium.

Huybrechts H, T' Siobbel S, 1995. Thermomechanical modelling of northern hemisphere ice-sheets with a two-level mass-balance parameterization. Annals of Glaciology 21, 111–116.

Huybrechts P, Payne T, EISMINT Intercomparison Group, 1996. The EISMINT benchmarks for testing ice-sheet models. Annals of Glaciology 23, 1–12.

Hökmark H, Lönnqvist M, Fälth B, 2010. T-H-M issues in repository rock. Thermal, mechanical, thermo-mechanical and hydro-mechanical evolution of the rock at the Forsmark and Laxemar sites. SKB TR-10-23, Svensk Kärnbränslehantering AB.

Iman R L, 2008. Latin hypercube sampling. In Melnick E L and B. S. Everitt B S (eds). Encyclopedia of quantitative risk analysis and assessment. Wiley. doi:10.1002/9780470061596.risk0299

Imbrie J, Hays J D, Martinson D G, McIntyre A, Mix A C, Morley J J, Pisias N G, Prell W L , Shackleton N J, 1984. The orbital theory of Pleistocene climate: support from a revised chronology of the marine $\delta^{18}O$ record. In Berger A L, Imbrie J, Hays J D, Kukla G, Saltzman B (eds). Milankovitch and climate: understanding the response to astronomical forcing. Dordrecht: Reidel, 269–305.

IPCC, 2001. Climate change 2001: the scientific basis. Contribution of Working Group I to the third assessment report of the Intergovernmental Panel on Climate Change. New York: Cambridge University Press.

IPCC, 2007. Climate change 2007: the physical science basis. Contribution of Working Group I to the fourth assessment report of the Intergovernmental Panel on Climate Change. Cambridge: Cambridge University Press.

IPCC, 2013a. Climate change 2013: the physical science basis. Contribution of Working Group I to the fifth assessment report of the Intergovernmental Panel on Climate Change. Cambridge: Cambridge University Press.

IPCC, 2013b. Annex I: Atlas of Global and Regional Climate Projections. In Climate change 2013: the physical science basis. Contribution of Working Group I to the fifth assessment report of the Intergovernmental Panel on Climate Change. Cambridge: Cambridge University Press.

IPCC, 2018. Global warming of 1.5 °C. An IPCC Special Report on the impacts of global warming of 1.5 °C above pre-industrial levels and related global greenhouse gas emission pathways, in the context of strengthening the global response to the threat of climate change, sustainable development, and efforts to eradicate poverty. Masson-Delmotte V, Zhai P, Pörtner H O, Roberts D, Skea J, Shukla P R, Pirani, A, Moufouma-Okia W, Péan C, Pidcock R, Connors S, Matthews J B R, , Chen Y, Zhou X, Gomis M I, Lonnoy E, Maycock T, Tignor M, Waterfield T (eds). Geneva: World Meteorological Organization.

IPCC, 2019. IPCC special report on the ocean and cryosphere in a changing climate. Pörtner H O, Roberts D C, Masson-Delmotte V, Zhai P, Tignor M, Poloczanska E, Mintenbeck K, Alegría A, Nicolai M, Okem A, Petzold J, Rama B, Weyer N M (eds). Cambridge: Cambridge University Press.

Isaksen K, Holmlund P, Sollid J L, Harris C, 2001. Three deep alpine-permafrost boreholes in Svalbard and Scandinavia. Permafrost and Periglacial Processes 12, 13–26.

Iverson N R, 1991. Potential effects of subglacial water-pressure fluctuations on quarrying. Journal of Glaciology 37, 27–36.

Iverson N R, 1993. Regelation of ice through debris at glacier beds: implications for sediment transport. Geology 21, 559–562.

Iverson N R, 2000. Sediment entrainment by a soft-bedded glacier: a model based on regelation into the bed. Earth Surface Processes and Landforms 25, 881–893.

Iverson N R, Hanson B, Hooke R LeB, Jansson P, 1995. Flow mechanism of glaciers on soft beds. Science 267, 80–81.

Jackson L P, Jevrejeva S, 2016. A probabilistic approach to 21st century regional sea-level projections using RCP and high-end scenarios. Global and Planetary Change 146, 179–189.

Jansen E, Sjøholm J, 1991. Reconstruction of glaciation over the past 6 Myr from ice-borne deposits in the Norwegian Sea. Nature 349, 600–603.

Jansson P, Näslund J-O, 2009. Spatial and temporal variations in glacier hydrology on Storglaciären, Sweden. SKB TR-09-13, Svensk Kärnbränslehantering AB.

Jansson P, Hock R, Schneider T, 2003. The concept of glacier storage: a review. Journal of Hydrology 282, 116–129.

Jansson P, Näslund J-O, Rodhe L, 2007. Ice-sheet hydrology – a review. SKB TR-06-34, Svensk Kärnbränslehantering AB.

Jaquet O, Siegel P, 2006. Regional groundwater flow model for a glaciation scenario. Simpevarp subarea – version 1.2. SKB R-06-100, Svensk Kärnbränslehantering AB.

Jaquet O, Namar R, Jansson P, 2010. Groundwater flow modelling under ice-sheet conditions: scoping calculations. SKB R-10-46, Svensk Kärnbränslehantering AB.

Jevrejeva S, Moore J C, Grinsted A, 2012. Sea level projections to AD 2500 with a new generation of climate change scenarios. Global Planetary Change 80, 14–20.

Jevrejeva S, Grinsted A, Moore J C 2014. Upper limit for sea level projections by 2100. Environmental Research Letters 9, 104008. doi:10.1088/1748-9326/9/10/104008

Johansson E, 2016. The influence of climate and permafrost on catchment hydrology. PhD thesis. Stockholm University, Department of physical geography.

Johansson J M, Davis J L, Scherneck H-G, Milne G A, Vermeer M, Mitrovica J X, Bennett R A, Jonsson B, Elgered G, Elósegui P, Koivula H, Poutanen M, Rönnäng B O, Shapiro I I, 2002. Continuous GPS measurements of postglacial adjustment in Fennoscandia. 1. Geodetic results. Journal of Geophysical Research 107, 400–428.

Johansson P-O, 2008. Description of surface hydrology and near-surface hydrogeology at Forsmark. Site descriptive modelling, SDM-Site Forsmark. SKB R-08-08, Svensk Kärnbränslehantering AB.

Johnsen S J, Dahl-Jensen D, Dansgaard W, Gundestrup N, 1995. Greenland palaeotemperatures derived from GRIP bore hole temperature and ice core isotope profiles. Tellus 47B, 624–629.

Johnsen S J, Dahl-Jensen D, Gundestrup N, Steffensen J P, Clausen H B, Miller H, Masson-Delmotte V, Sveinbjörnsdottir A E, White J, 2001. Oxygen isotope and palaeotemperature records from six Greenland ice-core stations: Camp Century, Dye-3, GRIP, GISP2, Renland and NorthGRIP. Journal of Quaternary Science 16, 299–307.

Johnson J, 1994. A basal water model for ice-sheets. PhD thesis. University of Minnesota.

Johnson J, 2004. Estimating basal melt rate in Antarctica. International Symposium on Ice and Water Interactions: processes across the phase boundary. Portland, Oregon, 26–30 July 2004.

Joughin I, Tulaczyk S, 2002. Positive mass balance for the Ross Ice Streams, West Antarctica. Science 295, 476–480.

Joughin I, Tulaczyk S, Fahnestock M, Kwok R, 1996. A mini-surge on the Ryder Glacier, Greenland, observed by satellite radar interferometry. Science 274, 228–230.

Joughin I, Abdalati W, Fahnestock M, 2004. Large fluctuations in speed on Greenland's Jakobshavn Isbræ glacier. Nature 432, 608–610.

Joughin I, Das S B, King M A, Smith B E, Howat I M, Moon T, 2008. Seasonal speedup along the western flank of the Greenland Ice-Sheet. Science 320, 781–783.

Joussaume S, Taylor K E, 2000. The paleoclimate modeling intercomparison project. In Braconnot P (ed). Proceedings of the third Paleoclimate Modelling Intercomparison Project (PMIP) workshop. La Huardière, Canada, 4–8 October 1999. (WCRP-111, WMO/TD-1007)

Jouzel J, Stiévenard M, Johnsen S J, Landais A, Masson-Delmotte V, Sveinbjornsdottir A, Vimeux F, von Grafenstein U, White J W C, 2007. The GRIP deuterium-excess record. Quaternary Science Reviews 26, 1–17.

Joyce S, Simpson T, Hartley L, Applegate D, Hoek J, Swan D, Marsic N, Follin S, 2010. Groundwater flow modelling of periods with temperate climate conditions – SR-Site Forsmark. SKB R-09-20, Svensk Kärnbränslehantering AB.

Kageyama M, Laîné A, Abe-Ouchi A, Braconnot P, Cortijo E, Crucifix M, de Vernal A, Guiot J, Hewitt C D, Kitoh A, Kucera M, Marti O, Ohgaito R, Otto-Bliesner B, Peltier W R, Rosell-Melé A, Vettoretti G, Weber S L, Yu Y, MARGO project members, 2006. Last Glacial Maximum temperatures over the North Atlantic, Europe and western Siberia: a comparison between PMIP models, MARGO sea-surface temperatures and pollen-based reconstructions. Quaternary Science Reviews 25, 2082–2102.

Kahr G, Kraehenbuehl F, Stoeckli H F, Müller-Vonmoos M, 1990. Study of the water-bentonite system by vapour adsorption, immersion calorimetry and X-ray techniques: II. Heats of immersion, swelling pressures and thermodynamic properties. Clay Minerals 25, 499–506.

Kamb B, 1987. Glacier surge mechanism based on linked cavity configuration of the basal water conduit system. Journal of Geophysical Research 92, 9083–9100.

Kamb B, 2001. Basal zone of the West-Antarctic ice streams and its role in their rapid motion. In Alley R B, Bindschadler R A (eds). The West Antarctic ice-sheet: behaviour and environment. Washington D.C.: American Geophysical Union, 157–200.

Kapitsa A P, Ridley J K, Robin G de Q, Siegert M J, Zotikov I A, 1996. A large deep freshwater lake beneath the ice of central East Antarctica. Nature 381, 684–686.

Karnland O, Olsson S, Nilsson U, 2006. Mineralogy and sealing properties of various bentonites and smectite-rich clay materials. SKB TR-06-30, Svensk Kärnbränslehantering AB.

Karnland O, Olsson S, Dueck A, Birgersson M, Nilsson U, Hernan-Håkansson T, Pedersen K, Nilsson S, Eriksen T E, Rosborg B, 2009. Long term test of buffer material at the Äspö Hard Rock Laboratory, LOT Project. Final report on the A2 test parcel. SKB TR-09-29, Svensk Kärnbränslehantering AB.

Karunaratne K C, Burn C R, 2004. Relations between air and surface temperature in discontinuous permafrost terrain near Mayo, Yukon Territory. Canadian Journal of Earth Sciences 41, 1437–1451.

Kaufmann G, Lambeck K, 2002. Glacial isostatic adjustment and the radial viscosity profile from inverse modeling. Journal of Geophysical Research 107, 2280. doi:10.1029/2001JB000941

Kavanaugh J L, 2009. Exploring glacier dynamics with subglacial water pressure pulses: evidence for self-organized criticality? Journal of Geophysical Research 114, F01021. doi:10.1029/2008JF001036

Kavanaugh J L, Moore P L, Dow C F, Sanders J W, 2010. Using pressure pulse seismology to examine basal criticality and the influence of sticky spots on glacial flow. Journal of Geophysical Research 115, F04025. doi:10.1029/2010JF001666

Kim S-J, Crowley T J, Erickson D J, Govindasamy B, Duffy P B, Lee B Y, 2008. High-resolution climate simulation of the last glacial maximum. Climate Dynamics 31, 1–16.

King L, 1984. Permafrost in Skandinavien: Untersuchungsergebnisse aus Lappland, Jotunheimen und Dovre/Rondane. Heidelberg: Geographisches Institut der Univ. (Heidelberger geographische Arbeiten 76).

King-Clayton L (ed), Chapman N, Ericsson L O, Kautsky F, 1997. Glaciation and hydrogeology, Proceedings of the workshop on the impact of climatic change and glaciations on rock stresses, groundwater flow and hydrochemistry: past, present and future. Hässelby, Sweden, 17–19 April 1996. SKI Report 97:13, Swedish Nuclear Power Inspectorate.

Kjellström E, Strandberg G, Brandefelt J, Näslund J-O, Smith B, Wohlfarth B, 2009. Climate conditions in Sweden in a 100000-year time perspective. SKB TR-09-04, Svensk Kärnbränslehantering AB.

Kjellström E, Brandefelt J, Näslund J-O, Smith B, Strandberg G, Voelker A H L, Wohlfarth B, 2010a. Simulated climate conditions in Europe during a Marine Isotope Stage 3 stadial. Boreas 39, 436–456.

Kjellström E, Nikulin G, Hansson U, Strandberg G, Ullerstig A, 2010b. 21st century changes in the European climate: uncertainties derived from an ensemble of regional climate model simulations. Tellus A 63, 24–40.

Kleman J, 1994. Preservation of landforms under ice-sheets and ice caps. Geomorphology 9, 19–32.

Kleman J, Glasser N F, 2007. The subglacial thermal organisation (STO) of ice-sheets. Quaternary Science Reviews 26, 585–597.

Kleman J, Hättestrand C, 1999. Frozen-based Fennoscandian and Laurentide ice-sheets during the last glacial maximum. Nature 402, 63–66.

Kleman J, Stroeven A P, 1997. Preglacial surface remnants and Quaternary glacial regimes in northwestern Sweden. Geomorphology 19, 35–54.

Kleman J, Hättestrand C, Borgström I, Stroeven A, 1997. Fennoscandian palaeoglaciology reconstructed using a glacial geological inversion model. Journal of Glaciology 43, 283–299.

Kleman J, Stroeven A, Lundqvist J, 2008. Patterns of Quaternary ice-sheet erosion and deposition in Fennoscandia and a theoretical framework for explanation. Geomorphology 97, 73–90.

Kleman J, Fastook J, Ebert K, Nilsson J, Caballero R, 2013. Pre-LGM Northern Hemisphere ice-sheet topography. Climate of the Past 9, 2365–2378.

Klene A E, Nelson F E, Shiklomanov N I, Hinkel K M, 2001. The N-factor in natural landscapes: Variability of air and soil-surface temperatures, Kuparuk River Basin, Alaska. Arctic, Antarctic, and Alpine Research 33, 140–148.

Knutti R, Sedláček J, 2013. Robustness and uncertainties in the new CMIP5 climate model projections. Nature Climate Change 3, 369–373.

Kohler J, 1995. Determining the extent of pressurized flow beneath Storglaciären, Sweden, using results of tracer experiments and measurements of input and output discharge. Journal of Glaciology 41, 217–231.

Kopp R E, Horton R M, Little C M, Mitrovica J X, Oppenheimer M, Rasmussen D J, Strauss B H, Tebaldi C, 2014. Probabilistic 21st and 22nd century sea-level projections at a global network of tide-gauge sites. Earth's. Earth's Future 2, 383–406.

Kopp R E, Kemp A C, Bittermann K, Horton B P, Donelly J P, Gehreis W R, Hay C C, Mitrovica J X, Morrow E D, Rahmstorf S, 2016. Temperature-driven global sea level variability in the Common Era. Proceedings of the National Academy of Sciences 113, E1434–1441.

Kopp R E, DeConto R M, Bader D A, Horton R M, Hay C C, Kulp S, Oppenheimer M, Pollard D, Strauss B H, 2017. Implications of Antarctic ice-cliff collapse and ice-shelf hydrofracturing mechanisms for sea-level projections. Earth's Future 5, 1217–1233.

Koppes M N, Montgomery D R, 2009. The relative efficacy of fluvial and glacial erosion over modern to orogenic timescales. Nature Geoscience 2, 644–647.

Krabbendam M, Hall A M, 2019. Subglacial block removal – a preliminary analysis of driving and resisting forces under different glaciological scenarios. SKB TR-19-18, Svensk Kärnbränslehantering AB.

Krawczynski M J, Behn M D, Das S B, Joughin I, 2009. Constraints on the lake volume required for hydro-fracture through ice-sheets. Geophysical Research Letters 36, L10501. doi:10.1029/2008GL036765

Krinner G, Genthon C, Jouzel J, 1997. GCM analysis of local influence on ice core δ signals. Geophysical Research Letters 24, 2825–2828.

Krogh Andersen K, Svensson A, Rasmussen S O, Steffensen J P, Johnsen S, Bigler M, Röthlisberger R, Ruth U, Siggaard-Andersen M-L, Dahl-Jensen D, Vinther B M, Clausen H B, 2006. The Greenland ice core chronology 2005, 15–42 kyr. Part 1: constructing the time scale. Quaternary Science Reviews, 25, 3246–3257.

Kukkonen I, 1989. Terrestrial heat flow and radiogenic heat production in Finland, the central Baltic Shield. Tectonophysics 164, 219–230.

Kukkonen I T, Šafanda J, 2001. Numerical modelling of permafrost in bedrock in northern Fennoscandia during the Holocene. Global and Planetary Change, 29, 259–274.

Lachenbruch A H, 1968. Preliminary geothermal model of the Sierra Nevada. Journal of Geophysical Research 73, 6977–6989.

Lagerbäck R, 1988a. The Veiki moraines in northern Sweden – widespread evidence of an Early Weichselian deglaciation. Boreas 17, 469–486.

Lagerbäck R, 1988b. Periglacial phenomena in the wooded areas of northern Sweden – relicts from the Tärendö Interstadial. Boreas 17, 487–499.

Lagerbäck R, Robertsson A-M, 1988. Kettle holes – stratigraphical archives for Weichselian geology and palaeoenvironment in northernmost Sweden. Boreas 17, 439–468.

Lagerlund E, Persson K M, Krzyszkowski D, Johansson P, Dobracka E, Dobracki R, Panzig W-A, 1995. Unexpected ice flow directions during the Late Weichselian deglaciation of the South Baltic area indicated by a new lithostratigraphy in NW Poland and NE Germany. Quaternary International 28, 127–144.

Lambeck K, 1995. Late Devensian an Holocene shorelines of the British Isles and North Sea from models of glacio-hydroisostatic rebound. Journal of the Geological Society 152, 437–448.

Lambeck K, 1999. Shoreline displacements in southern-central Sweden and the evolution of the Baltic Sea since the last maximum glaciation. Journal of the Geological Society 156, 465–486.

Lambeck K, Chappell J, 2001. Sea level change through the last glacial cycle. Science 292, 679–686.

Lambeck K, Smither C, Johnston P, 1998. Sea-level change, glacial rebound and mantle viscosity for northern Europe. Geophysical Journal International 134, 102–144.

Lambeck K, Yokoyama Y, Purcell T, 2002. Into and out of the Last Glacial Maximum: sea-level change during Oxygen Isotope Stages 3 and 2. Quaternary Science Reviews 21, 343–360.

Lambeck K, Purcell A, Funder S, Kjær K H, Larsen E, Möller P, 2006. Constraints on the Late Saalian to early Middle Weichselian ice-sheet of Eurasia from field data and rebound modelling. Boreas 35, 539–575.

Lambeck K, Purcell A, Zhao J, Svensson N-O, 2010. The Scandinavian Ice-Sheet: from MIS 4 to the end of the Last Glacial Maximum. Boreas 39, 410–435.

Lambert A, Courtier N, Sasagawa G S, Klopping F, Winester D, James T S, Liard J O, 2001. New constraints on Laurentide postglacial rebound from absolute gravity measurements. Geophysical Research Letters 28, 2109–2112.

Landström O, Larsson S Å, Lind G, Malmqvist D, 1979. Geothermal investigations in the Bohus granite area in southwestern Sweden. Tectonophysics 64, 131–162.

Lang C, Leuenberger M, Schwander J, Johnsen S, 1999. 16 °C rapid temperature variation in central Greenland 70000 years ago. Science 286, 934–937.

Lang H, 1987. Forecasting meltwater runoff from snow-covered areas and from glacier basins. In Kraijenhoff D A, Moll J R (eds). River flow modelling and forecasting. Dordrecht: D. Reidel, 99–127.

Larson S A, Tullborg E-L, Cederbom C, Stiberg J P, 1999. Sveconorwegian and Caledonian foreland basins in the Baltic Shield revealed by fission-track thermochronology. Terra Nova-Oxford 11, 210–215.

Larsson-McCann S, Karlsson A, Nord M, Sjögren J, Johansson L, Ivarsson M, Kindell S, 2002. Meteorological, hydrological and oceanographical information and data for the site investigation program in the communities of Östhammar and Tierp in the northern part of Uppland. SKB TR-02-02, Svensk Kärnbränslehantering AB.

Laskar J, Robutel P, Joutel F, Gastineau M, Correia A C M, Levrard B, 2004. A long-term numerical solution for the insolation quantities of the Earth. Astronomy and Astrophysics 428, 261–285.

Laskar J, Fienga A, Gastinaeu M, Manche H, 2011. La2010: A new orbital solution for the long term motion of the Earth. Astronomy and Astrophysics 532. doi:10.1051/0004-6361/201116836

Latychev K, Mitrovica J X, Tamisiea M E, Tromp J, Moucha R, 2005. Influence of lithospheric thickness variations on 3-D crustal velocities due to glacial isostatic adjustment. Geophysical Research Letters 32, L01304. doi:10.1029/2004GL021454

Le Bars D, Drijfhout S, de Vries H, 2017. A high-end sea level rise probabilistic projection including rapid Antarctic ice-sheet mass loss. Environmental Research Letters 12. doi:10.1088/1748-9326/aa6512

Lemieux J-M, Sudicky E A, Peltier W R, Tarasov L, 2008a. Dynamics and groundwater recharge and seepage over the Canadian landscape during the Wisconsinian glaciation. Journal of Geophysical Research 113, F01011. doi:10.1029/2007JF000838

Lemieux J-M, Sudicky E A, Peltier W R, Tarasov L, 2008b. Simulating the impact of glaciations on continental groundwater flow systems: 1. Relevant processes and model formulation. Journal of Geophysical Research 113, F03017. doi:10.1029/2007JF000928

Lemieux J-M, Sudicky E A, Peltier W R, Tarasov L, 2008c. Simulating the impact of glaciations on continental groundwater flow systems: 2. Model application to the Wisconsinian glaciation over the Canadian landscape. Journal of Geophysical Research 113, F03018. doi:10.1029/2007JF000929

Lenton T M, Williamson M S, Edwards N R, Marsh R, Price A R, Ridgwell A J, Shepherd J G, Cox S J, The GENIE team, 2006. Millennial timescale carbon cycle and climate change in an efficient Earth system model. Climate Dynamics 26, 687–711.

Levermann A, Clark P U, Marzeion B, Milne G A, Pollard D, Radic V, Robinson A, 2013. The multimillennial sea-level commitment of global warming. Proceedings of the National Academy of Sciences 110, 13745–13750.

Lewis A R, Marchant D R, Kowalewski D E, Baldwin S L, Webb L E, 2006. The age and origin of the labyrinth, western Dry Valleys, Antarctica: evidence for extensive middle Miocene subglacial floods and freshwater discharge to the Southern Ocean. Geology 34, 513–516.

Liakka J, Näslund J-O, Brandefelt J, 2021. Timing of future glacial inception. In Haeberli W, Whiteman C (eds). Snow and ice-related hazards, risks and disasters. 2nd ed. Oxford Elsevier, Chapter 11.2.

Lidmar-Bergström K, 1995. Relief and saprolites through time on the Baltic shield. Geomorphology 12, 45–61.

Lidmar-Bergström K, 1997. A long-term perspective on glacial erosion. Earth Surface Processes and Landforms 22, 297–306.

Lidmar-Bergström K, Näslund J-O, 2002. Landforms and uplift in Scandinavia. In Doré A G, Cartwright J A, Stoker M S, Turner J P, White N (eds). Exhumation of the North Atlantic margin: timing, mechanisms, and implications for petroleum exploration. London: Geological Society. (Special publication 196), 103–116.

Lidmar-Bergström K, Näslund J-O, 2005. Major landforms and bedrock. In Seppälä M (ed). The physical geography of Fennoscandia, Oxford: Oxford University Press.

Lidmar-Bergström K, Olsson S, Olvmo M, 1997. Palaeosurfaces and associated saprolites in southern Sweden. In Widdowson M (ed). Palaeosurfaces: recognition, reconstruction and palaeoenvironmental interpretation. London: Geological Society. (Special publication 120), 95–124.

Lind P, Kjellström E, 2008. Temperature and precipitation changes in Sweden: a wide range of model-based projections for the 21st century. Norrköping: Sveriges meteorologiska och hydrologiska institut (Swedish Meteorological and Hydrological Institute). (SMHI reports. Meteorology and Climatology 113)

Lindborg T, 2017. Climate-driven landscape development: physical and biogeochemical long-term processes in temperate and periglacial environments. PhD thesis. Swedish University of Agricultural Sciences, Faculty of Forest Sciences, Department of Forest Ecology and Management, Umeå, Sweden.

Lindborg T, Thorne M, Andersson E, Becker J, Brandefelt J, Cabianca T, Gunia M, Ikonen A T K, Johansson E, Kangasniemi V, Kautsky U, Kirchner G, Klos R, Kowe R, Kontula A, Kupiainen P, Lahdenperä A-M, Lord N S, Lunt D S, Näslund J-O, Nordén M, Norris S, Pérez-Sánchez D, Proverbio A, Riekki K, Rübel A, Sweeck L, Walke R, Xu S, Smith G, Pröhl G, 2018. Climate change and landscape development in post-closure safety assessment of solid radioactive waste disposal: Results of an initiative of the IAEA. Journal of Environmental Radioactivity 183, 41–53.

Lisiecki L E, Raymo M E, 2005. A Pliocene-Pleistocene stack of 57 globally distributed benthic $d^{18}O$ records. Paleoceanography 20, 1–17.

Liu W, Xie S-P, Liu Z, Zhu J, 2017. Overlooked possibility of a collapsed Atlantic Meridional Overturning Circulation in warming climate. Science Advances 3, e1601666. doi:10.1126/sciadv.1601666

Livingstone S J, Clark C D, Woodward J, Kingslake J, 2013. Potential subglacial lake locations and meltwater drainage pathways beneath the Antarctic and Greenland ice-sheets. The Cryosphere 7, 1721–1740.

Lockwood J G, 1979. Causes of climate. London: Arnold.

Lohmann U, Sausen R, Bengtsson L, Cubasch U, Perlwitz J, Roeckner E, 1993. The Köppen climate classification as a diagnostic tool for general circulation models. Climate Research 3, 177–193.

Lokrantz H, Sohlenius G, 2006. Ice-marginal fluctuations during the Weichselian glaciation in Fennoscandia, a literature review. SKB TR-06-36, Svensk Kärnbränslehantering AB.

Lord N S, Ridgwell A, Thorne M C, Lunt D J, 2015. The 'long tail' of anthropogenic CO_2 decline in the atmosphere and its consequences for post-closure performance assessments for disposal of radioactive wastes. Mineralogical Magazine 79, 1613–1623.

Lord N S, Ridgwell A, Thorne M C, & Lunt D J, 2016. An impulse response function for the "long tail" of excess atmospheric CO_2 in an Earth system model. Global Biogeochemical Cycles 30, 2–17.

Lord N S, Crucifix M, Lunt D J, Thorne M C, Bouncer N, Dowsett H, O'Brien C L, Ridgwell A, 2017. Emulation of long-term changes in global climate: Application to the mid-Pliocene and future. Climate of the Past 13, 1539–1571.

Lord N S, Lunt D, Thorne M, 2019. Modelling changes in climate over the next 1 million years. SKB TR-19-09, Svensk Kärnbränslehantering AB.

Lucas-Picher P, Wulff-Nielsen M, Christensen J H, Aðalgeirsdóttir G, Mottram R, Simonsen S B, 2012. Very high resolution regional climate model simulations over Greenland: identifying added value. Journal of Geophysical Research 117, D02108. doi:10.1029/2011JD016267

Luckman A, Murray T, de Lange R, Hanna E, 2006. Rapid and synchronous ice-dynamic changes in East Greenland. Geophysical Research Letters 33, L03503. doi:10.1029/2005GL025428

Lunardini V J, 1978. Theory of n-factors and correlation of data. In Proceedings of the 3rd International Conference on Permafrost. Edmonton, Alta, 10–13 July 1978. Ottawa: National Research Council of Canada, Vol 1, 40–46.

Lunardini V J, 1981. Heat transfer in cold climates. New York: Van Nostrand Reinhold.

Lunardini V J, 1995. Permafrost formation time. CRREL Report 95-8, U.S. Army Cold Regions Research and Engineering Laboratory.

Lund B, Näslund J-O, 2009. Glacial isostatic adjustment: implications for glacially induced faulting and nuclear waste repositories. In Connor C B, Chapman N A, Connor L J (eds). Volcanic and tectonic hazard assessment for nuclear facilities. Cambridge: Cambridge University Press, 142–155.

Lund B, Schmidt P, Hieronymus C, 2009. Stress evolution and fault stability during the Weichselian glacial cycle. SKB TR-09-15, Svensk Kärnbränslehantering AB.

Lundqvist J, 1992. Glacial stratigraphy in Sweden. Geological Survey of Finland Special Paper 5, 43–59.

Lundqvist J, 2007. Surging ice and break-down of an ice dome – a deglaciation model for the Gulf of Bothnia. Geologiska Föreningens i Stockholm Förhandlingar 129, 329–336.

Lundqvist J, Wohlfarth B, 2000. Timing and east–west correlation of south Swedish ice-marginal lines during the Late Weichselian. Quaternary Science Reviews 20, 1127–1148.

Lundqvist J, Lundqvist T, Lindström M, Calner M, Sivhed U, 2011. Sveriges geologi från urtid till nutid. 3rd ed. Lund:Studentlitteratur. (In Swedish.)

Lunkka J P, Johansson P, Saarnisto M, Sallasmaa O, 2004. Glaciation of Finland. In Ehlers J, Gibbard P L (eds). Quaternary glaciations: extent and chronology. Part I: Europe. Amsterdam: Elsevier. (Developments in Quaternary Science 2), 93–100.

Luthcke S B, Zwally H J, Abdalati W, Rowlands D D, Ray R D, Nerem R S, Lemoine F G, Mccarthy J J, Chinn D S, 2006. Recent Greenland ice mass loss by drainage system from satellite gravity observations. Science 314, 1286–1289.

Lönnqvist M, Hökmark H, 2010. Assessment of potential for glacially induced hydraulic jacking at different depths. SKB R-09-35, Svensk Kärnbränslehantering AB.

MacAyeal D R, 1989. Large-scale ice flow over a viscous basal sediment: theory and application to ice stream B. Antarctica. Journal of Geophysical Research 94, 4071–4087.

MacGregor J A, Fahnestock M A, Catania G A, Aschwanden A, Clow G D, Colgan W T, Gogineni S P, Morlighem M, Nowicki S M J, Paden J D, Price S F, Seroussi H, 2016. A synthesis of the basal thermal state of the Greenland Ice-Sheet. Journal of Geophysical Research: Earth Surface 121, 1328–1350.

Mackay J R, 1997. A full-scale field experiment (1978–1995) on the growth of permafrost by means of lake drainage, western Arctic coast: a discussion of the method and some results. Canadian Journal of Earth Sciences 34, 17–33.

Mai H, Thomsen T, 1993. Permafrost studies in Greenland. In Proceedings of the sixth international conference on permafrost. Beijing, 5–9 July 1993. Guangzhou: South China University of Technology, Vol 2.

Malmqvist D, Larson S Å, Landström O, Lind G, 1983. Heat flow and heat production from the Malingsbo granite, central Sweden. Bulletin of the Geological Institutions of the University of Uppsala 9, 137–152.

Mangerud J, Gyllencreutz R, Øystein L, Svendsen J I, 2011. Glacial history of Norway. In Ehlers J, Gibbard P L (eds). Quaternary glaciations: extent and chronology. Part IV: a closer look. Amsterdam: Elsevier.

Marchant D R, Denton G H, Sugden D E, Swisher C C, 1993. Miocene glacial stratigraphy and landscape evolution of the western Asgard Range, Antarctica. Geografiska Annaler 75A, 303–330.

Marshall S J, Clarke G K C, 1997. A continuum mixture model of ice stream thermodynamics in the Laurentide Ice-Sheet. 1. Theory. Journal of Geophysical Research 102, 20599–20614.

Marks L, 2002. Last Glacial Maximum in Poland. Quaternary Science Reviews 21, 103–110.

Masson-Delmotte M, Jouzel J, Landais A, Stievenard M, Johnsen S J, White J W C, Werner M, Sveinbjörnsdottir A, Fuhrer K, 2005. GRIP deuterium excess reveals rapid and orbital-scale changes in Greenland moisture origin. Science 309, 118–121.

McConnell R K, 1968. Viscosity of the mantle from relaxation time spectra of isostatic adjustment. Journal of Geophysical Research 73, 7089–7105.

McIntyre K, Delaney M L, Ravelo A C, 2001. Millennial-scale climate change and oceanic processes in the late Pliocene and early Pleistocene. Paleoceanography 16, 535–543.

McKee Smith J, Sherlock A R, Resio D T, 2001. STWAVE: Steady-State Spectral Wave Model. User's manual for STWAVE, Version 3.0. Coastal and Hydraulics Laboratory U.S. Army Engineer Research and Development Center.

Meese D A, Gow A J, Alley R B, Zielinski G A, Grootes P M, Ram M, Taylor K C, Mayewski P A, Bolzan J F, 1997. The Greenland Ice-Sheet Project 2 depth-age scale: methods and results. Journal of Geophysical Research 102, 26411–26423.

Meier H E M, 2006. Baltic Sea climate in the late twenty-first century: a dynamical downscaling approach using two global models and two emission scenarios. Climate Dynamics 27, 39–68.

Meierbachtol T W, Harper J T, Johnson J V., Humphrey N F, Brinkerhoff D J, 2015. Thermal boundary conditions on western Greenland: observational constraints and impacts on the modeled thermomechanical state. Journal of Geophysical Research: Earth Surface 120, 623–636.

Meierbachtol T W, Harper J T, Humphrey N F, Wright P, 2016. Mechanical forcing on water pressure in a hydrologically isolated reach beneath Western Greenland's ablation zone. Annals of Glaciology 57, 62–70.

Meinshausen M, Smith S J, Calvin K, Daniel J S, Kainuma M L T, Lamarque J-F, Matsumoto K, Montzka S A, Raper S C B, Riahi K, Thomson A, Velders G J M, van Vuuren D P P, 2011. The RCP greenhouse gas concentrations and their extensions from 1765 to 2300. Climatic Change 109, 213–241.

Mengel M, Levermann A, Frieler K, Robinson A, Marzeion B, Winkelmann R, 2016. Future sea level rise constrained by observations and long-term commitment. Proceedings of the National Academy of Sciences 113, 2597–2602.

Mikolajewicz U, Gröger M, Maier-Reimer E, Schurgers G, Vizcaíno M, Winguth A M E, 2007. Long-term effects of anthropogenic CO_2 emissions simulated with a complex earth system model. Climate Dynamics 28, 599–633.

Miller K G, Kopp R E, Horton B P, Browning J V, Kemp A C, 2013. A geological perspective on sea-level rise and impacts along the U.S. mid-Atlantic coast. Earth's Future 1, 3–18.

Milne G A, 1998. Refining models of the glacial isostatic adjustment process. PhD thesis. University of Toronto.

Milne G A, Mitrovica J X, 1998. Postglacial sea-level change on a rotating Earth. Geophysical Journal International 133, 1–19.

Milne G A, Mitrovica J X, Davis J L, 1999. Near-field hydro-isostasy: the implementation of a revised sea-level equation. Geophysical Journal International 139, 464–482.

Milne G A, Davis J L, Mitrovica J X, Scherneck H-G, Johansson J M, Vermeer M, Koivula H, 2001. Space-geodetic constraints on glacial isostatic adjustment in Fennoscandia. Science 291, 2381–2385.

Milne G A, Mitrovica J X, Schrag D P, 2002. Estimating past continental ice volume from sea-level data. Quaternary Science Reviews 21, 361–376.

Milne G A, Mitrovica J X, Scherneck H G, Davis J L, Johansson J M, Koivula H, Vermeer M, 2004. Continuous GPS measurements of postglacial adjustment in Fennoscandia: 2. Modeling results. Journal of Geophysical Research 109, B02412. doi:10.1029/2003JB002619

Milne G A, Gehrels W R, Hughes C W, Tamisiea M E, 2009. Identifying the causes of sea-level change. Nature Geoscience 2, 471–478.

Ministry of the Environment, 2001. Sweden's third national communication on Climate Change: under the United Nations Framework Convention on Climate Change. Stockholm: Ministry of the Environment. (Ds 2001:71)

Mitrovica J X, 2003. Recent controversies in predicting post-glacial sea-level change. Quaternary Science Reviews 22, 127–133.

Mitrovica J X, Forte A M, 1997. Radial profile of mantle viscosity: results from the joint inversion of convection and postglacial rebound observables. Journal of Geophysical Research 102, 2751–2769.

Mitrovica J X, Forte A M, 2004. A new inference of mantle viscosity based upon joint inversion of convection and glacial isostatic adjustment data. Earth and Planetary Science Letters 225, 177–189.

Mitrovica J X, Milne G A, 2002. On the origin of late Holocene sea-level highstands within equatorial ocean basins. Quaternary Science Reviews 21, 2179–2190.

Mitrovica J X, Milne G A, 2003. On post-glacial sea level: I. General theory. Geophysical Journal International 154, 253–267.

Mitrovica J X, Peltier W R, 1991. On post-glacial geoid subsidence over the equatorial oceans. Journal of Geophysical Research 96, 20053–20071.

Mitrovica J X, Davis J L, Shapiro I I, 1994. A spectral formalism for computing three-dimensional deformations due to surface loads. 2. Present-day glacial isostatic-adjustment. Journal of Geophysical Research 99, 7075–7101.

Mitrovica J X, Tamisiea M E, Davis J L, Milne G A, 2001. Recent mass balance of polar ice-sheets inferred from patterns of global sea-level change. Nature 409, 1026–1029.

Moberg A, Sonechkin D M, Holmgren K, Datsenko N M, Karlén W, 2005. Highly variable Northern Hemisphere temperatures reconstructed from low- and high-resolution proxy data. Nature 433, 613–617.

Moberg A, Gouirand I, Wohlfarth B, Schoning K, Kjellström E, Rummukainen M, de Jong R, Linderholm H, Zorita E, 2006. Climate in Sweden during the past millennium – Evidence from proxy data, instrumental data and model simulations. SKB TR-06-35, Svensk Kärnbränslehantering AB.

Montagnat M, Duval P, 2000. Rate controlling processes in the creep of polar ice, influence of grain boundary migration associated with recrystallization. Earth and Planetary Science Letters 183, 179–186.

Moon T, Joughin I, 2007. Changes in ice front position on Greenland's outlet glaciers from 1992 to 2007. Journal of Geophysical Research 113, F02022. doi:10.1029/2007JF000927

Morlighem M, Seroussi H, Larour E, Rignot E, 2013. Inversion of basal friction in Antarctica using exact and incomplete adjoints of a higher-order model. Journal of Geophysical Research, Earth Surface 118, 1746–1753.

Munro-Stasiuk M J, 2003. Subglacial Lake McGregor, south–central Alberta, Canada. Sedimentary Geology 160, 325–350.

Müller F, 1962. Zonation in the accumulation area of the glaciers of Axel Heiberg Island, N.W.T, Canada. Journal of Glaciology 4, 302–313.

Müller U C, Kukla G J, 2004. North Atlantic Current and European environments during the declining stage of the last interglacial. Geology 32, 1009–1012.

Müller U C, Pross J, 2007. Lesson from the past: present insolation minimum holds potential for glacial inception. Quaternary Science Reviews 26, 3025–3029.

Myhre G, Highwood E J, Shine K P, Stordal F, 1998. New estimates of radiative forcing due to well mixed greenhouse gases. Geophysical Research Letters 25, 2715–2718.

Mäkinen J, Engfeldt A, Harsson B G, Routsalainen H, Strykowski G, Oja T, Wolf D, 2005. The Fennoscandian land uplift gravity lines 1966–2003. In Jekeli C, Bastos L, Fernades J (eds). Gravity, geoid and space missions. Berlin: Springer. (International Association of Geodesy symposia 129), 328–332.

Mörner N-A, 1977. Past and present uplift in Sweden: glacial isostasy, tectonism and bedrock influence. Geologiska föreningen i Stockholms förhandlingar 99, 48–54.

Mörner N-A, 1979. The Fennoscandian uplift and Late Cenozoic geodynamics: geological evidence. GeoJournal 3, 287–318.

Nakićenović N, Swart R (eds), 2000. Special report on emissions scenarios. A Special Report of Working Group III of the Intergovernmental Panel on Climate Change. Cambridge: Cambridge University Press.

Nauels A, Meinshausen M, Mengel M, Lorbacher K, Wigley T M, 2017. Synthesizing long-term sea level rise projections-the MAGICC sea level model v2.0. Geoscientific Model Development 10, 2495–2524.

Nerem R S, Beckley B D, Fasullo J T, Hamlington B D, Masters D, Mitchum G T, 2018. Climate-change-driven accelerated sea-level rise detected in the altimeter era. Proceedings of the National Academy of Sciences 115, 2022–2025.

Nerheim S, Schöld S, Persson G, Sjöström Å, 2017. Framtida havsnivåer i Sverige. Norrköping: SMHI. Klimatologi 48. (In Swedish.)

Nienow P, Sharp M, Willis I, 1998. Seasonal changes in the morphology of the subglacial drainage system, Haut Glacier d'Arolla, Switzerland. Earth Surface Processes and Landforms 23, 825–843.

Noël B, van de Berg W J, Machguth H, Lhermitte S, Howat I, Fettweis X, van den Broeke M R, 2016. A daily, 1 km resolution data set of downscaled Greenland ice-sheet surface mass balance (1958–2015). The Cryosphere 10, 2361–2377.

North G R, Stevens M J, 2006. Energy-balance climate models. In Kiehl J T and Ramanathan V (eds). Frontiers of Climate Modeling. Cambridge: Cambridge University Press, 52–72.

North G R, Cahalan R F, Coakley Jr J A, 1981. Energy balance climate models. Reviews of Geophysics 19, 91–121.

NorthGRIP community members, 2004. High-resolution record of the Northern Hemisphere climate extending into the last interglacial period. Nature 431, 147–151.

Nye J F, 1976. Water flow in glaciers: jökulhlaups, tunnels and veins. Journal of Glaciology 17, 181–207.

Näslund J-O, 1997. Subglacial preservation of valley morphology at Amundsenisen, western Dronning Maud Land, Antarctica. Earth Surface Processes and Landforms 22, 441–455.

Näslund J-O, 1998. Ice-sheet, climate, and landscape interactions in Dronning Maud Land, Antarctica. PhD thesis. Department of Physical Geography, Stockholm University. (Dissertation series 11)

Näslund J-O, 2001. Landscape development in western and central Dronning Maud Land, East Antarctica. Antarctic Science 13, 302–311.

Näslund J-O, Fastook J L, Holmlund P, 2000. Numerical modelling of the ice-sheet in western Dronning Maud Land, East Antarctica: impact of present, past, and future climates. Journal of Glaciology 46, 54–66.

Näslund J-O, Rodhe L, Fastook J L, Holmlund P, 2003. New ways of studying ice-sheet flow directions and glacial erosion by computer modelling – examples from Fennoscandia. Quaternary Science Reviews 22, 245–258.

Näslund J-O, Jansson P, Fastook J L, Johnson J, Andersson L, 2005. Detailed spatially distributed geothermal heat-flow data for modeling of basal temperatures and meltwater production beneath the Fennoscandian ice-sheet. Annals of Glaciology 40, 95–101.

Näslund J-O (ed), Wohlfarth B (ed), Alexanderson H, Helmens K, Hättestrand M, Jansson P, Kleman J, Lundqvist J, Brandefelt J, Houmark-Nielsen M, Kjellström E, Strandberg G, Knudsen K L, Krogh Larsen N, Ukkonen P, Mangerud J, 2008. Fennoscandian paleo-environment and ice-sheet dynamics during Marine Isotope Stage (MIS) 3. Report of a workshop held September 20–21, 2007 in Stockholm, Sweden. SKB R-08-79, Svensk Kärnbränslehantering AB.

Olvmo M, 2010. Review of denudation processes and quantification of weathering and erosion rates at a 0.1 to 1 Ma time scale. SKB TR-09-18, Svensk Kärnbränslehantering AB.

Olvmo M, Johansson M, 2002. The significance of rock structure, lithology, and pre-glacial deep weathering for the shape of intermediate-scale glacial erosional landforms. Earth Surface Processes and Landforms 27, 251–268.

Olvmo M, Lidmar-Bergström K, Ericson K, Bonow J M, 2005. Saprolite remnant as indicators of pre-glacial landform genesis in southeast Sweden. Geografiska Annaler 87A, 447–460.

O'Neill K, Miller R D, 1985. Exploration of rigid ice model of frost heave. Water Resources Research 21, 281–296.

Oswald G K A, Gogineni S P, 2008. Recovery of subglacial water extent from Greenland radar survey data. Journal of Glaciology 54, 94–106.

Ottesen D, Dowdeswell J A, Rise L, 2005. Submarine landforms and the reconstruction of fast flowing ice streams within a large Quaternary ice-sheet: The 2500-km-long Norwegian-Svalbard margin (57°–80 °N). Geological Society of America Bulletin 117, 1033–1050.

Otto-Bliesner B L, Brady E C, Clauzet G, Thomas R, Levis S, Kothavala Z, 2006. Last glacial maximum and Holocene climate in CCSM3. Journal of Climate 19, 2526–2544.

Otto-Bliesner B L, Hewitt C D, Marchitto T M, Brady E, Abe-Ouchi A, Crucifix M, Murakami S, Weber S L, 2007. Last Glacial Maximum ocean thermohaline circulation: PMIP2 model intercomparisons and data constraints. Geophysical Research Letters 34, L12706. doi:10.1029/2007GL029475

Paananen M, Ruskeeniemi T, 2003. Permafrost at Lupin: Interpretation of SAMPO electromagnetic soundings at Lupin. Report YST-117, Geological Survey of Finland.

Padilla F, Villeneuve J-P, 1992. Modelling and experimental studies of frost heave including solute effects. Cold Regions Science and Technology 20, 183–194.

Paillard D, 1998. The timing of Pleistocene glaciations from a simple multiple-state climate model. Nature 391, 378–381**.**

Palmer S, Mcmillan M, Morlighem M, 2015. Subglacial lake drainage detected beneath the Greenland ice-sheet. Nature Communications 6, 8408. doi:10.1038/ncomms9408

Paterson W S B, 1994. The physics of glaciers. 3rd ed. Oxford: Pergamon.

Patton H, Hubbard A, Andreassen K, Winsborrow M, Stroeven A P, 2016. The build-up, configuration, and dynamical sensitivity of the Eurasian ice-sheet complex to Late Weichselian climatic and oceanic forcing. Quaternary Science Reviews 153, 97–121.

Pattyn F, 2003. A new three-dimensional higher-order thermomechanical ice-sheet model: basic sensitivity, ice-stream development, and ice flow across subglacial lakes. Journal of Geophysical Research 108, 2382. doi:10.1029/2002JB002329

Pattyn F, Huybrechts P, Decleir H, 1989. Modelling glacier fluctuations in the Sør Rondane, Dronning Maud Land, Antarctica. Zeitschrift fur Gletscherkunde und Glazialgeologie 25, 33–47.

Pattyn F, de Smedt B, Souchez R, 2004. Influence of subglacial Vostok lake on the regional ice dynamics of the Antarctic ice-sheet: a model study. Journal of Glaciology 50, 583–589.

Pattyn F, Perichon L, Aschwanden A, Breuer B, Smedt B, Gagliardini O, Gudmundsson G H, Hindmarsh R C A, Hubbard A, Johnson J V, Kleiner T, Konovalov Y, Martin C, Payne A J, Pollard D, Price S, Rückamp M, Saito F, Souček O, Sugiyama S, Zwinger T, 2008. Benchmark experiments for higher-order and full-Stokes ice-sheet models (ISMIP–HOM). The Cryosphere 2, 95–108.

Payne A J, 1995. Limit cycles in the basal thermal regime of ice-sheets. Journal of Geophysical Research 100, 4249–4263.

Payne A J, Baldwin D J, 1999. Thermomechanical modelling of the Scandinavian ice-sheet: implications for ice-stream formation. Annals of Glaciology 28, 83–89.

Payne A J, Dongelmans P W, 1997. Self-organization in the thermomechanical flow of ice-sheets. Journal of Geophysical Research 102, 12219–12234.

Payne A J, Huybrechts P, Abe-Ouchi A, Calov R, Fastook J L, Greve R, Marshall S J, Marsiat I, Ritz C, Tarasov L, Thomassen M P A, 2000. Results from the EISMINT model intercomparison: the effects of thermomechanical coupling. Journal of Glaciology 46, 227–238.

Pellikka H, Särkkä J, Johansson M, Pettersson H, 2020. Probability distributions for mean sea level and storm contribution up to 2100 AD at Forsmark. SKB TR-19-23, Svensk Kärnbränslehantering AB.

Peltier W R, 1994. Ice age palaeotopography. Science 265, 195–201.

Peltier W R, 1998. Postglacial variations in the level of the sea: implications for climate dynamics and solid-earth geophysics. Reviews of Geophysics 36, 603–689.

Peltier W R, 2002. On eustatic sea level history: Last Glacial Maximum to Holocene. Quaternary Science Reviews 21, 377–396.

Peltier W R, 2004. Global glacial isostasy and the surface of the ice-age Earth: the ICE-5G (VM2) model and GRACE. Annual Review of Earth and Planetary Science 32, 111–149.

Peltier W R, 2005. On the hemispheric origins of meltwater pulse 1a. Quaternary Science Reviews 24, 1655–1671.

Peltier W R, Fairbanks R G, 2006. Global glacial ice volume and Last Glacial Maximum duration from an extended Barbados sea level record. Quaternary Science Reviews 25, 3322–3337.

Perrette M, Landerer F, Riva R, Frieler K, Meinshausen M, 2013. A scaling approach to project regional sea level rise and its uncertainties. Earth System Dynamics 4, 11–29.

Person M, McIntosh J, Bense V, Remenda V H, 2007. Pleistocene hydrology of North America: the role of ice-sheets in reorganizing groundwater flow systems. Reviews of Geophysics 45, RG3007. doi:10.1029/2006RG000206

Persson G, Bärring L, Kjellström E, Strandberg G, Rummukainen M, 2007. Climate indices for vulnerability assessments. Norrköping: Sveriges meteorologiska och hydrologiska institut (Swedish Meteorological and Hydrological Institute). (SMHI reports. Meteorology and Climatology 111.)

Peyaud V, 2006. Role of the ice-sheet dynamics in major climate changes. PhD thesis. Laboratoire de Glaciologie et de Géophysique de l'Environnement, Université Grenoble I.

Pfeffer W T, Harper J T, O'Neel S, 2008. Kinematic constraints on glacier contributions to 21st-century sea-level rise. Science 321, 1340–1343.

Pimenoff N, Venäläinen A, Järvinen H, 2011. Climate scenarios for Olkiluoto on a time-scale of 120000 years. Posiva 2011-04, Posiva Oy, Finland.

Pimenoff N, Venäläinen A, Järvinen H, 2012. Climate and sea level scenarios for Olkiluoto for the next 10000 years. Posiva 2012-26, Posiva Oy, Finland.

Placidi L, Greve R, Seddik H, Faria S H, 2010. Continuum-mechanical, Anisotropic Flow model for polar ice masses, based on an anisotropic Flow Enhancement factor. Continuum Mechanics and Thermodynamics 22, 221–237.

Poinar K, Joughin I, Das S B, Behn M D, Lenaerts J T M, van den Broeke M R, 2015. Limits to future expansion of surface-melt-enhanced ice flow into the interior of western Greenland. Geophysical Research Letters 42, 1800–1807.

Poinar K, Joughin I, Lilien D, Brucker L, Kehrl L, Nowicki S, 2017. Drainage of southeast Greenland firn aquifer water through crevasses to the bed. Frontiers in Earth Science 5. doi:10.3389/feart.2017.00005

Pollack H N, Hurter S J, Johnson J R, 1991. A new global heat flow compilation. [Online]. Available at: http://www.wdcb.ru/sep/data/hdata/hf_global.dat

Pollack H N, Hurter S J, Johnson J R, 1993. Heat flow from the Earth's interior: analysis of the global data set. Reviews of Geophysics 31, 267–280.

Porter S C, 1989. Some geological implications of average Quaternary glacial conditions. Quaternary Research 32, 245–261.

Posiva SKB, 2017. Safety functions, performance targets and technical design requirements for a KBS-3V repository. Conclusions and recommendations from a joint SKB and Posiva working group. Posiva SKB Report 01, Posiva Oy, Svensk Kärnbränslehantering AB.

Price S F, Payne A J, Catania G A, Neumann T A, 2008. Seasonal acceleration of inland ice via longitudinal coupling to marginal ice. Journal of Glaciology 54, 213–219.

PSMSL, 2018. Tide gauge data. Available at: http://www.psmsl.org/data/obtaining/

Påsse T, 2001. An empirical model of glacio-isostatic movements and shore-level displacement in Fennoscandia. SKB R-01-41, Svensk Kärnbränslehantering AB.

Påsse T, 2004. The amount of glacial erosion of the bedrock. SKB TR-04-25, Svensk Kärnbränslehantering AB.

Påsse T, Daniels J, 2015. Past shore-level and sea-level displacements. Uppsala: Geological Survey of Sweden. (Rapporter och meddelanden 137)

Quiquet A, Colleoni F, Masina S, 2016. Long-term safety of a planned geological repository for spent nuclear fuel in Forsmark, Sweden and Olkiluoto, Finland. Phase 2: impact of ice-sheet dynamics, climate forcing and multi-variate sensitivity analysis on maximum ice-sheet thickness. SKB TR-16-02, Svensk Kärnbränslehantering AB.

Radtke U, Grün R, Schwarcz H P, 1988. Electron spin resonance dating of the Pleistocene coral reef tracts of Barbados. Quaternary Research 29, 197–215.

Ramillien G, Lombard A, Cazenave A, Ivins E R, Llubes M, Remy F, Biancale R, 2006. Interannual variations of the mass balance of the Antarctica and Greenland ice-sheets from GRACE. Global and Planetary Change 33, 198–208.

Ramstein G, Kageyama M, Guiot J, Wu H, Hély C, Krinner G, Brewer S, 2007. How cold was Europe at the Last Glacial Maximum? A synthesis of the progress achieved since the first PMIP model-data comparison. Climate of the Past 3, 331–339.

Rasmussen S O, Andersen K K, Svensson A M, Steffensen J P, Vinther B, Clausen H B, Siggaard-Andersen M-L, Johnsen S J, Larsen L B, Dahl-Jensen D, Bigler M, Röthlisberger R, Fisher H, Goto-Azuma K, Hansson M E, Ruth U, 2006. A new Greenland ice core chronology for the last glacial termination. Journal of Geophysical Research 111, D06102. doi:10.1029/2005JD006079

Rasmussen S O, Seierstad I K, Andersen K K, Bigler M, Dahl-Jensen D, Johnsen S J, 2008. Synchronization of the NGRIP, GRIP, and GISP2 ice cores across MIS 2 and palaeoclimatic implications. Quaternary Science Reviews 27, 18–28.

Rath V, Sundberg S, Näslund J-O, Claesson Liljedahl L, 2019. Paleoclimatic inversion of temperature profiles from deep boreholes at Forsmark and Laxemar. SKB TR-18-06, Svensk Kärnbränslehantering AB.

Raymo M E, Ganley K, Carter S, Oppo D W, McManus J, 1998. Millennial-scale climate instability during the early Pleistocene epoch. Nature 392, 699–702.

Raymond C F, Harrison W D, 1975. Some observations on the behaviour of the liquid and gas phases in temperate glacier ice. Journal of Glaciology 14, 213–234.

Reiche P, 1950. Survey of weathering processes and products. (University of New Mexico publications in geology 3)

Remy F, Minster J F, 1993. Precise altimetric topography in ice-sheet flow studies. Annals of Glaciology 17, 195–200.

Richardson C, 2004. Spatial characteristics of snow accumulation in Dronning Maud Land, Antarctica. Global and Planetary Change 42, 31–43.

Riddihough R P, 1972. Regional magnetic anomalies and geology in Fennoscandia: a discussion. Canadian Journal of Earth Sciences 9, 219–232.

Ridley J K, Huybrechts P, Gregory J M, Lowe J A, 2005. Elimination of the Greenland ice-sheet in a high CO_2 climate. Journal of Climate, 18, 3409–3427.

Rignot E, Kanagaratnam P, 2006. Changes in the velocity structure of the Greenland ice-sheet. Science 311, 986–990.

Rignot E J, Gogineni S P, Krabill W B, Ekholm S, 1997. North and Northeast Greenland ice discharge from satellite radar interferometry. Science 276, 934–937.

Riis F, 1996. Quantification of Cenozoic vertical movements of Scandinavia by correlation of morphological surfaces with offshore data. Global and Planetary Change 12, 331–357.

Riseborough D W, Shiklomanov N, Etzelmüller B, Gruber S, Marchenko S, 2008. Recent advances in permafrost modelling. Permafrost and Periglacial Processes 19, 137–156.

Ritz C, Fabre A, Letreguilly A, 1996. Sensitivity of a Greenland ice-sheet model to ice flow and ablation parameters: Consequences for evolution through the last climatic cycle. Climate Dynamics 13, 11–24.

Ritz C, Rommelaere V, Dumas C, 2001. Modeling the evolution of Antarctic ice-sheet over the last 420000 years: Implications for altitude changes in the Vostok region. Journal of Geophysical Research 106, 31943–31964.

Roberts M J, Russell A J, Tweed F S, Knudsen Ó, 2000. Ice fracturing during jökulhlaups: implications for englacial floodwater routing and outlet development. Earth Surface Processes and Landforms 25, 1429–1446.

Rogner H-H, Aguilera R F, Archer C, Bertani R, Bhattacharya S C, Dusseault M B, Gagnon L, Haberl H, Hoogwijk M, Johnson A, Rogner M L, Wagner H, Yakushev V, 2012. Energy resources and potentials. In Global energy assessment: toward a sustainable future. Cambridge: Cambridge University Press, 423–512.

Rohling E J, Haigh I D, Foster G L, Roberts A P, Grant K M, 2013. A geological perspective on potential future sea-level rise. Nature Scientific Reports 3, 3461. doi:10.1038/srep03461

Rudberg S, 1954. Västerbottens berggrundsmorfologi: ett försök till rekonstruktion av preglaciala erosionsgenerationer i Sverige. PhD thesis. Uppsala University. Geographica 25.

Ruddiman W F, 2003. The anthropogenic greenhouse era began thousands of years ago. Climate Change 61, 261–293.

Rummukainen M, 2003. The Swedish regional climate modeling program, SWECLIM, 1996–2003. Final report. Norrköping: Sveriges meteorologiska och hydrologiska institut (Swedish Meteorological and Hydrological Institute). (SMHI Meteorologi 104.)

Ruskeeniemi T, Paananen M, Ahonen L, Kaija J, Kuivamäki A, Frape S, Moren L, Degnan P, 2002. Permafrost at Lupin: report of Phase I. Report YST-112, Geological Survey of Finland.

Ruskeeniemi T, Ahonen L, Paananen M, Frape S, Stotler R, Hobbs M, Kaija J, Degnan P, Blomqvist R, Jensen M, Lehto K, Moren L, Puigdomenech I, Snellman M, 2004. Permafrost at Lupin: report of Phase II. Report YST-119, Geological Survey of Finland.

Ruosteenoja K, Vihma T, Venäläinen A, 2019. Projected changes in European and North Atlantic seasonal wind climate derived from CMIP5 Simulations. Journal of Climate 32, 6467–6490.

Röthlisberger H, 1972. Water pressure in intra- and subglacial channels. Journal of Glaciology 11, 177–203.

Röthlisberger H, Lang H, 1987. Glacial hydrology. In Gurnell A M, Clark M J (eds). Glacio-fluvial sediment transfer: an alpine perspective. Chichester: Wiley.

Salas J, Gimeno M J, Molinero J, Auqué L F, Gómez J, Juárez I, 2010. SR-Site. Hydrogeochemical evolution of the Forsmark site. SKB TR-10-58, Svensk Kärnbränslehantering AB.

Sánchez Goñi M F, 2007. Introduction to climate and vegetation in Europe during MIS 5. In Sirocko F, Claussen M, Sánchez Goñi M F, Litt T (eds). The climate of past interglacials. Amsterdam: Elsevier. (Developments in Quaternary Sciences 7), 197–205.

Sawagaki T, Hirakawa K, 1997. Erosion of bedrock by subglacial meltwater, Soya Coast, East Antarctica. Geografiska Annaler 79A, 223–238.

SCAR, 2007. A need for more realistic ice-sheet models. SCAR report 30, Scientific Committee on Antarctic Research.

Schaeffer M, Hare W, Rahmstorf S, Vermeer M, 2012. Long-term sea-level rise implied by 1.5 °C and 2 °C warming levels. Nature Climate Change 2, 867–870.

Schenk F, Wohlfarth B, 2019. The imprint of hemispheric-scale climate transitions on the European climate during the last deglaciation (15.5 ka to 9 ka BP). SKB TR-18-05, Svensk Kärnbränslehantering AB.

Schenk F, Väliranta M, Muschitiello F, Tarasov L, Heikkilä M, Björck S, Brandefelt J, Johansson A V, Näslund J-O, Wohlfarth B, 2018. Warm summers during the Younger Dryas cold reversal. Nature Communications 9, 1634. doi:10.1038/s41467-018-04071-5

Scherneck H-G, Johansson J M, Vermeer M, Davis J L, Milne G A, Mitrovica J X, 2001. BIFROST project: 3D crustal deformation rates derived from GPS confirm postglacial rebound in Fennoscandia. Earth Planets Space 53, 703–708.

Schoof C, 2010. Ice-sheet acceleration driven by melt supply variability. Nature 468, 803–806.

Schneider T, 2000. Hydrological processes in the wet-snow zone of glaciers: a review. Zeitschrift fur Gletscherkunde und Glazialgeologie 36, 89–105.

Seipold U, 1995. The variation of thermal transport properties in Earth's crust. Journal of Geodynamics, 20, 145–154.

Selby M J, 1993. Hillslope materials and processes. 2nd ed. Oxford: Oxford University Press.

Shackleton N J, Kennett J P, 1975. Paleotemperature history of the Cenozoic and the initiation of Antarctic glaciation: oxygen and carbon isotopic analyses in DSDP sites 277, 279, and 281. In Kennett J P, Houtz R (eds). Initial reports of the Deep Sea Drilling Project 29, 743–755.

Sharp R P, 1960. Glaciers. Eugene: University of Oregon Press. (Condon lectures 1960).

Shepherd A, Hubbard A, Nienow P, King M, McMillan M, Joughin I, 2009. Greenland ice-sheet motion coupled with daily melting in late summer. Geophysical Research Letters 36, L01501. doi:10.1029/2008GL035758

Shin S-I, Liu Z, Otto-Bliesner B, Brady E C, Kutzbach J E, Harrison S P, 2003. A simulation of the Last Glacial Maximum climate using the NCAR-CSM. Climate Dynamics 20, 127–151.

Shreve R, 1972. Movement of water in glaciers. Journal of Glaciology 11, 205–214.

Shur Y L, Slavin-Borovskiy V B, 1993. N-factor maps of Russian permafrost region. Proceedings of the sixth international conference on permafrost. Beijing, 5–9 July 1993. Guangzhou: South China University of Technology, 564–568.

Siddall M, Rohling E J, Almogi-Labin A, Hemleben C, Meischner D, Schmelzer I, Smeed D A, 2003. Sea-level fluctuations during the last glacial cycle. Nature 423, 853–858.

Siegert M J, 2005. Lakes beneath the ice-sheet: the occurrence, analysis and future exploration of Lake Vostok and other Antarctic subglacial lakes. Annual Review of Earth and Planetary Sciences 33, 215–245.

Siegert M J, Dowdeswell J A, 1996. Spatial variations in heat at the base of the Antarctic ice-sheet from analysis of the thermal regime above subglacial lakes. Journal of Glaciology 42, 501–509.

Siegert M J, Dowdeswell J A, Gorman M R, McIntyre N F, 1996. An inventory of Antarctic sub-glacial lakes. Antarctic Science 8, 281–286.

Siegert M J, Carter S, Tabacco I, Popov S, Blankenship D D, 2005. A revised inventory of Antarctic subglacial lakes. Antarctic Science 17, 453–460.

Simons M, Hager B H, 1997. Localization of the gravity field and the signature of glacial rebound. Nature 390, 500–504.

Six D, Letréguilly A, Reynaud L, 2001. Greenland ice-sheet mass-balance distribution: a variance analysis of existing field data. Journal of Glaciology 47, 441–451.

Sjökvist E, Asp M, Axén Mårtensson J, Berggreen-Clausen S, Berglöv G, Björck E, Johnell A, Nylén L, Ohlsson A, Persson H, 2015. Framtidsklimat i Uppsala län – enligt RCP-scenarier. SMHI Klimatologi Nr 20. Available at: https://www.lansstyrelsen.se/download/18.76f16c3d1665eba4c3e9004/1539932731106/Framtidsklimat_i_Uppsala_L%C3 %A4n_Klimatologi_nr_20.pdf [11 November 2020]. (In Swedish.)

SKB, 2005. Preliminary site description. Forsmark area – version 1.2. SKB R-05-18, Svensk Kärnbränslehantering AB.

SKB, 2006a. Climate and climate-related issues for the safety assessment SR-Can. SKB TR-06-23, Svensk Kärnbränslehantering AB.

SKB, 2006b. Geosphere process report for the safety assessment SR-Can. SKB TR-06-19, Svensk Kärnbränslehantering AB.

SKB, 2010a. Climate and climate-related issues for the safety assessment SR-Site. SKB TR-10-49, Svensk Kärnbränslehantering AB.

SKB, 2010b. Comparative analysis of safety related site characteristics. SKB TR-10-54, Svensk Kärnbränslehantering AB.

SKB, 2011. Long-term safety for the final repository for spent nuclear fuel at Forsmark. Main report of the SR-Site project. SKB TR-11-01, Svensk Kärnbränslehantering AB.

SKB, 2014. Climate and climate-related issues for the safety assessment SR-PSU. SKB TR-13-05, Svensk Kärnbränslehantering AB.

SKB, 2015. Safety analysis for SFR Long-term safety. Main report for the safety assessment SR-PSU. Revised edition. SKB TR-14-01, Svensk Kärnbränslehantering AB.

Skinner L C, 2008. Revisiting the absolute calibration of the Greenland ice-core age-scales. Climate of the Past 4, 295–302.

Slangen A B A, Carson M, Katsman C A, van de Wal R S W, Köhl A, Vermeersen L L A, Stammer D, 2014. Projecting twenty-first century regional sea-level changes. Climatic Change 124, 317–332.

Smith M W, Riseborough D W, 1996. Permafrost monitoring and detection of climate change, Permafrost and Periglacial Processes 7, 301–309.

Smith B E, Fricker H A, Joughin I R, Tulaczyk S, 2009. An inventory of active subglacial lakes in Antarctica detected by ICES at (2003–2008). Journal of Glaciology 55, 573–595.

Smith L C, Chu V W, Yang K, Gleason C J, Pitcher L H, Rennermalm A K, Legleiter C J, Behar A E, Overstreet B T, Moustafa S E, Tedesco M, Forster R R, LeWinter A L, Finnegan D C, Sheng Y, Balog J, 2015. Efficient meltwater drainage through supraglacial streams and rivers on the southwest Greenland ice-sheet. Proceedings of the National Academy of Sciences 112, 1001–1006.

Sohlenius G, Hedenström A, Rudmark L, 2004. Forsmark site investigation. Mapping of unconsolidated Quaternary deposits 2002–2003. Map description. SKB R-04-39, Svensk Kärnbränslehantering AB.

Sole A, Nienow P, Bartholomew I, Mair D, Cowton T, Tedstone A, King M A, 2013. Winter motion mediates dynamic response of the Greenland Ice-Sheet to warmer summers. Geophysical Research Letters 40, 3940–3944.

Spring U, Hutter K, 1981. Numerical studies of jökulhlaups. Cold Regions Science and Technology 4, 227–244.

Sriver R L, Urban N M, Olson R, Keller K, 2012. Toward a physically plausible upper bound of sea-level rise projections. Climatic Change 115, 893–902.

Staiger J K W, Gosse J C, Johnson J V, Fastook J, Gray J T, Stockli D F, Stockli L, Finkel R, 2005. Quaternary relief generation by polythermal glacier ice. Earth Surface Processes and Landforms 30, 1145–1159.

Steffen K, Nghiem S V, Huff R, Neumann G, 2004. The melt anomaly of 2002 on the Greenland Ice-Sheet from active and passive microwave satellite observations. Geophysical Research Letters 31, L20402. doi:10.1029/2004GL020444

Stephens M B, 2010. Forsmark site investigation. Bedrock geology – overview and excursion guide. SKB R-10-04, Svensk Kärnbränslehantering AB.

Stone E J, Lunt D J, Rutt I C, Hanna E, 2010. Investigating the sensitivity of numerical model simulations of the modern state of the Greenland ice-sheet and its future response to climate change. The Cryosphere 4, 379–417.

Stroeven A P, Fabel D, Hättestrand C, Harbor J, 2002a. A relict landscape in the centre of Fennoscandian glaciation: cosmogenic radionuclide evidence of tors preserved through multiple glacial cycles. Geomorphology 44, 145–154.

Stroeven A P, Fabel D, Hättestrand C, Kleman J, 2002b. Quantifying the erosional impact of the Scandinavian ice-sheet in the Torneträsk-Narvik corridor, northern Sweden, based on cosmogenic radionuclide data. Geografiska Annaler 84A, 275–287.

Stroeven A P, Hättestrand C, Kleman J, Heyman J, Fabel D, Fredin O, Goodfellow B W, Harbor J M, Jansen J D, Olsen L, Caffee M W, Fink D, Lundqvist J, Rosqvist G C, Strömberg B, Jansson K N, 2016. Deglaciation of Fennoscandia. Quaternary Science Reviews 147, 91–121.

Sugden D E, 1977. Reconstruction of the morphology, dynamics and thermal characteristics of the Laurentide ice-sheet at its maximum. Arctic and Alpine Research 9, 27–47.

Sugden D E, 1978. Glacial erosion by the Laurentide ice-sheet. Journal of Glaciology 20, 367–391.

Sugden D E, John B S, 1976. Glaciers and landscape: a geomorphological approach. London: Arnold.

Sundal A V, Shepherd A, Nienow P, Hanna E, Palmer S, Huybrechts P, 2011. Melt-induced speed-up of Greenland ice-sheet offset by efficient subglacial drainage. Nature 469, 521–524.

Sundberg J, 1988. Thermal properties of soils and rocks. PhD thesis. Chalmers University of Technology, Sweden. (Geologiska institutionen publ. A 57)

Sundberg J, Back P-E, Ländell M, Sundberg A, 2009. Modelling of temperature in deep boreholes and evaluation of geothermal heat flow at Forsmark and Laxemar. SKB TR-09-14, Svensk Kärnbränslehantering AB.

Sundh M, Sohlenius G, Hedenström A, 2004. Forsmark site investigation. Stratigraphical investigation of till in machine cut trenches. SKB P-04-34, Svensk Kärnbränslehantering AB.

Sutter J, Gierz P, Grosfeld K, Thoma M, Lohmann G, 2016. Ocean temperature thresholds for Last Interglacial West Antarctic Ice-Sheet collapse. Geophysical Research Letters 43, 2675–2682.

Svendsen J I, Mangerud J, 1987. Late Weichselian and Holocene sea-level history for a cross-section of western Norway. Journal of Quaternary Science 2, 113–132.

Svendsen J I, Alexanderson H, Astakhov V I, Demidov I, Dowdeswell J A, Funder S, Gataullin V, Henriksen M, Hjort C, Houmark-Nielsen M, Hubberten H W, Ingólfsson O, Jakobsson M, Kjær K H, Larsen E, Lokrantz H, Lunkka J P, Lysså A, Mangerud J, Matiouchkov A, Murray A, Moller P, Niessen F, Nikolskaya O, Polyak L, Saarnisto M, Siegert C, Siegert M J, Spielhagen R F, Stein R, 2004. Late Quaternary ice-sheet history of northern Eurasia. Quaternary Science Reviews 23, 1229–1271.

Svensson A, Andersen K K, Bigler M, Clausen H B, Dahl-Jensen D, Davies S M, Johnsen S J, Muscheler R, Parrenin F, Rasmussen S O, Röthlisberger R, Seierstad I, Steffensen J P, Vinther B M, 2008. A 60000 year Greenland stratigraphic ice core chronology. Climate of the Past 4, 47–57.

Svensson P D, Hansen S, 2010. Freezing and thawing of montmorillonite – a time resolved X-ray diffraction study. Applied Clay Science 49, 127–134.

Swantesson J O H, 1992. Recent micro-weathering phenomena in southern and central Sweden. Permafrost and Periglacial Processes 3, 275–292.

Sweet W V, Horton R, Kopp R E, LeGrande A N, Romanou A, 2017a. Sea level rise. In Climate Science Special Report (CSSR): Fourth National Climate Assessment, Volume I. Washington, DC: U.S. Global Change Research Program, 333–363.

Sweet W V, Kopp R E, Weaver C P, Obeysekera J, Horton R M, Thieler E R, Zervas C, 2017b. Global and regional sea level rise scenarios for the United States. NOAA Technical Report NOS CO-OPS 083, National Oceanic and Atmospheric Administration.

Söderbäck B, 2008. Geological evolution, palaeoclimate and historical development of the Forsmark and Laxemar-Simpevarp areas. Site descriptive modelling. SDM-Site. SKB R-08-19, Svensk Kärnbränslehantering AB.

Tamisiea M E, Mitrovica J X, Milne G A, Davis J L, 2001. Global geoid and sea level changes due to present-day ice mass fluctuations. Journal of Geophysical Research 106, 30849–30863.

Tamisiea M E, Mitrovica J X, Davis J L, Milne G A, 2003. Long wavelength sea level and solid surface perturbations driven by polar ice mass variations: fingerprinting Greenland and Antarctic ice-sheet flux. Space Science Reviews 108, 81–93.

Taylor A E, 1995. Field measurements of n-factors for natural forest areas, Mackenzie Valley, Northwest Territories. Geological Survey of Canada, Current Research 1995-B, 89–98.

Taylor A E, 2001. Relationship of ground temperatures to air temperatures in forests. Geological Survey of Canada, Bulletin 547, 111–117.

Taylor K E, Stouffer R J, Meehl G A, 2012. An overview of CMIP5 and the experiment design. Bulletin of the American Meteorological Society 93, 485–498.

Tedstone A J, Nienow P W, Gourmelen N, Dehecq A, Goldberg D, Hanna E, 2015. Decadal slowdown of a land-terminating sector of the Greenland Ice-Sheet despite warming. Nature 526, 692–695.

Texier D, Degnan P, Loutre M, Paillard D, Thorne M, 2003. Modelling sequential BIOsphere systems under CLIMate change for radioactive waste disposal-Project BIOCLIM. In Proceedings of the International High-level Waste Management Conference, Las Vegas, 30 March – 2 April 2003.

Thomas M F, 1994. Geomorphology in the tropics: a study of weathering and denudation in low latitudes. Chichester: Wiley.

Thomsen H H, Thorning L, Olesen O B, 1989. Applied glacier research for planning hydro-electric power, Ilulissat/Jakobshavn, West Greenland. Annals of Glaciology 13, 257–261.

Tjernström M, Rummukainen M, Bergström S, Rodhe J, Persson G, 2003. Klimatmodellering och klimatscenarier ur SWECLIMS perspektiv (in Swedish). Norrköping: Swedish Meteorological and Hydrological Institute. (SMHI reports. Meteorology and Climatology 102).

Toniazzo T, Gregory J M, Huybrechts P, 2004. Climatic impact of a Greenland deglaciation and its possible irreversibility. Journal of Climate 17, 21–33.

Tushingham A M, Peltier W R, 1991. ICE-3G: a new global model of Late Pleistocene deglaciation based upon geophysical predictions of post-glacial relative sealevel change. Journal of Geophysical Research 96, 4497–4523.

Tzedakis P C, Raynaud D, McManus J F, Berger A, Brovkin V, Kiefer T, 2009. Interglacial diversity. Nature Geoscience 2, 751–755.

UNEP/GRID-Arendal, 2005. Permafrost distribution in the Arctic. UNEP/GRID-Arendal Maps and Graphics Library. Available at: https://www.grida.no/resources/7000 [11 November 2020].

van de Wal R S W, 1996. Mass-balance modelling of the Greenland ice-sheet: a comparison of an energy-balance model and a degree-day model. Annals of Glaciology 23, 36–45.

van de Wal R S W, Boot W, van den Broeke M R, Smeets C J P P, Reijmer C H, Donker J J A, Oerlemans J, 2008. Large and rapid meltinduced velocity changes in the ablation zone of the Greenland Ice-Sheet. Science 321, 111–113.

van de Wal R S W, Boot W, Smeets C J P P, Snellen H, van den Broeke M R, Oerlemans J, 2012. Twenty-one years of mass balance observations along the K-transect, West Greenland. Earth System Science Data 4, 31–35.

van den Broeke M, Bamber J, Ettema J, Rignot E, Schrama E, van de Berg W J, van Meijgaard E, Velicogna I, Wouters B, 2009. Partitioning recent Greenland mass loss. Science 326, 984–986.

van der Veen C J, 1998a. Fracture mechanics approach to penetration of surface crevasses on glaciers. Cold Regions Science and Technology 27, 31–47.

van der Veen C J, 1998b. Fracture mechanics approach to penetration of bottom crevasses on glaciers. Cold Regions Science and Technology 27, 213–223.

van der Veen C J, 2007. Fracture propagation as means of rapidly transferring surface meltwater to the base of glaciers. Geophysical Research Letters 34, L01501. doi:10.1029/2006GL028385

van Tatenhove F G M, Huybrechts P, 1996. Modelling of the thermal conditions at the Greenland ice-sheet margin during Holocene deglaciation: boundary conditions from moraine formation. Geografiska Annaler 78A, 83–99.

Velicogna I, Wahr J, 2006. Acceleration of Greenland ice mass loss in spring 2004. Nature 443, 329–331.

Vermeer M, Rahmstorf S, 2009. Global sea-level linked to global temperature. Proceedings of the National Academy of Sciences of the United States of America 106, 21527–21532.

Vestøl O, Ågren J, Steffen H, Kierulf H, Tarasov L, 2019. NKG2016LU: a new land uplift model for Fennoscandia and the Baltic Region. Journal of Geodesy 93, 1759–1779.

Vidstrand P, 2003. Surface and subsurface conditions in permafrost areas – a literature review. SKB TR-03-06, Svensk Kärnbränslehantering AB.

Vidstrand P, Follin S, Zugec N, 2010. Groundwater flow modelling of periods with periglacial and glacial conditions – SR-Site Forsmark. SKB R-09-21, Svensk Kärnbränslehantering AB.

Väliranta M, Birks H H, Helmens K F, Engels S, Piirainen M, 2009. Early-Weichselian interstadial (MIS 5c) summer temperatures were higher than today in northern Fennoscandia. Quaternary Science Reviews (rapid communications) 28, 777–782.

Waddington E D, 1987. Geothermal heat flux beneath ice-sheets. In Waddington E D, Walder J S (eds). The physical basis of ice-sheet modelling. Wallingford, Oxfordshire: International Association of Hydrological Sciences. (IAHS Publication 170), 217–226.

Waelbroeck C, Labeyrie L, Michel E, Duplessy J C, McManus J F, Lambeck K, Balbon E, Labracherie M, 2002. Sea-level and deep water temperature changes derived from benthic foraminifera isotopic records. Quaternary Science Reviews 21, 295–305.

Walder J S, Fowler A, 1994. Channelized subglacial drainage over a deformable bed. Journal of Glaciology 40, 3–15.

Walter F, Chaput J, Lüthi M P, 2014. Thick sediments beneath Greenland's ablation zone and their potential role in future ice-sheet dynamics. Geology 42, 487–490.

Washburn A L, 1979. Geocryology: a survey of periglacial processes and environments. 2nd ed. London: Arnold.

Watts A B, 2001. Isostasy and flexure of the lithosphere. Cambridge: Cambridge University Press.

WCRP Global Sea Level Budget Group, 2018. Global sea-level budget 1993 – present. Earth System Science Data 10, 1551–1590.

Weertman J, 1957. On the sliding of glaciers. Journal of Glaciology 3, 33–38.

Weertman J, 1972. General theory of water flow at the base of a glacier or ice-sheet. Reviews of. Geophysics and Space Physics 10, 287–303.

Weertman J, 1973. Can a water-filled crevasse reach the bottom surface of a glacier? In Symposium on the Hydrology of Glaciers, Cambridge, 7–13 September 1969. Wallingford, Oxfordshire: International Association of Hydrological Sciences. (IAHS Publication 95), 139–145.

Werder M A, Hewitt I J, Schoof C G, Flowers G E, 2013. Modeling channelized and distributed subglacial drainage in two dimensions. Journal of Geophysical Research: Earth Surface 118, 2140–2158.

Werner K, Sassner M, Johansson E, 2014. Hydrology and near-surface hydrogeology at Forsmark – synthesis for the SR-PSU project. SR-PSU Biosphere. SKB R-13-19, Svensk Kärnbränslehantering AB.

Werner M, Heimann M, Hoffman G, 2001. Isotopic composition and origin of polar precipitation in present and glacial climate simulations. Tellus 53B, 53–71.

Whitehouse P, 2009. Glacial isostatic adjustment and sea-level change. State of the art report. SKB TR-09-11. Svensk Kärnbränslehantering AB.

Whitehouse P L, 2018. Glacial isostatic adjustment modelling: historical perspectives, recent advances, and future directions. Earth Surface Dynamics 6, 401–429.

Williams P J, Smith M W, 1989. The frozen earth: fundamentals of geocryology. Cambridge: Cambridge University Press.

Willis M J, Herried B G, Bevis M G, Bell R E, 2015. Recharge of a subglacial lake by surface meltwater in northeast Greenland. Nature 518, 223–227.

Wingham D J, Wallis D W, Shepherd A, 2009. Spatial and temporal evolution of Pine Island Glacier thinning, 1995–2006. Geophysical Research Letters 36, L17501. doi:10.1029/2009GL039126.

Winkelmann R, Levermann A, Ridgwell A, Caldeira K, 2015. Combustion of available fossil-fuel resources sufficient to eliminate the Antarctic Ice-Sheet. Science Advances 1, e1500589. doi:10.1126/sciadv.1500589

Witt A, Schumann A Y, 2005. Holocene climate variability on millennial scales recorded in Greenland ice cores. Nonlinear Processes in Geophysics 12, 345–352.

Wohlfarth B, 2009. Ice-free conditions in Fennoscandia during Marine Oxygen Isotope Stage 3? SKB TR-09-12, Svensk Kärnbränslehantering AB.

Wohlfarth B, 2013. A review of Early Weichselian climate (MIS 5d–a) in Europe. SKB TR-13-03, Svensk Kärnbränslehantering AB.

Wohlfarth B, Näslund J-O (eds), 2010. Fennoscandian ice-sheet in MIS 3. Boreas 39, 325–456.

Wong T E, Bakker A M, Keller K, 2017. Impacts of Antarctic fast dynamics on sea level projections and coastal flood defence. Climatic Change 144, 347–364.

Wouters B, Chambers D, Schrama E J G, 2008. GRACE observe small-scale mass loss in Greenland. Geophysical Research Letters 35, L20501. doi:10.1029/2008GL034816

Wright A, Siegert M, 2012. A fourth inventory of Antarctic subglacial lakes. Antarctic Science 24, 659–664.

Wright P J, Harper J T, Humphrey N F, Meierbachtol T W, 2016. Measured basal water pressure variability of the western Greenland Ice-Sheet: Implications for hydraulic potential. Journal of Geophysical Research: Earth Surface 121, 1134–1147.

Wu P, Wood R, Stott P, 2004. Does the recent freshening trend in the North Atlantic indicate a weakening thermohaline circulation? Geophysical Research Letters, 31, L02301. doi:10.1029/2003GL018584

Wu H, Guiot J, Brewer S, Guo Z, 2007. Climatic changes in Eurasia and Africa at the last glacial maximum and mid-Holocene: reconstruction from pollen data using inverse vegetation modelling. Climate Dynamics 29, 211–229.

Wu P, Jackson L, Pardaens A, Schaller N, 2011. Extended warming of the northern high latitudes due to an overshoot of the Atlantic meridional overturning circulation. Geophysical Research Letters 38. doi:10.1029/2011GL049998

Yang K, Smith L C, 2016. Internally drained catchments dominate supraglacial hydrology of the southwest Greenland Ice-Sheet. Journal of Geophysical Research: Earth Surface 121, 1891–1910.

Yershov E D, 1998. General Geocryology. Cambridge: Cambridge University Press.

Yokoyama Y, Lambeck K, De Deckker P, Johnston P, Fifield L K, 2000. Timing of the last glacial maximum from observed sea level minima. Nature 406, 713–716.

Zickfeld K, Levermann A, Morgan M G, Kuhlbrodt T, Rahmstorf S, Keith D W, 2007. Expert judgement on the response of the Atlantic meridional overturning circulation to climate change. Climate Change 82, 235–265.

Zickfeld K, Eby M, Weaver A, Alexander K, Crespin E, Edwards N, Eliseev A, Feulner G, Fichefet T, Forest C, Friedlingstein P, Goosse H, Holden P, Joos F, Kawamiya M, Kicklighter D, Kienert H, Matsumoto K, Mokhov I, Monier E, Olsen S, Pedersen O, Perrette M, Berthier G, Ridgwell A, Schlosser A, Schneider Von Deimling T, Shaffer G, Sokolov A, Spahni R, Steinacher M, Tachiiri K, Tokos K, Yoshimori M, Zeng N, Zhao F, 2013. Long-term climate change commitment and reversibility: An EMIC intercomparison. Journal of Climate 26, 5782–5809.

Zwally H J, Abdalati W, Herring T, Larson K, Saba J, Steffen K, 2002. Surface melt-induced acceleration of Greenland ice-sheet flow. Science 297, 218–222.

Zweck C, Huybrechts P, 2003. Modeling the marine extent of northern hemisphere ice-sheets during the last glacial cycle. Annals of Glaciology 37, 173–180.

Appendix A

Air temperature data

A1 Introduction

With the approach used to handle climate issues in the safety assessment, as described in Section 1.3, estimates of past and possible future temperature variations are necessary for various studies within the safety assessment, such as simulations of ice-sheet and permafrost development. The approach taken in the PSAR is to reconstruct temperatures for the last glacial cycle and use them to construct a *reference glacial cycle climate case* for the coming 100 ka, see Section 1.3. This *reference glacial cycle climate case* is not a forecast of the future climate that will occur at Forsmark, but instead i) one relevant example of a possible future climate, and ii) a starting point for the construction of complementary, and more pessimistic, climate cases also to be analysed in the safety assessment.

In the following text the term *air temperature* is used as representing annual mean air temperatures, whereas *ground surface temperature* describes the annual mean temperature on the ground surface below vegetation including the humus layer. The ground can be mineral or organic soil or rock. *Subglacial temperature* describes the temperature at the interface between the basal part of an ice-sheet and its bed, while *submerged temperature* describes an assumed water temperature at the sea bed during periods when the site is submerges by the Baltic Sea.

A2 Greenland proxy data on last glacial cycle temperatures used for ice-sheet modelling

In the absence of a complete last glacial cycle palaeotemperature curve from Fennoscandia, proxy data on palaeotemperatures from the GRIP ice core (Dansgaard et al. 1993, Johnsen et al. 1995) are typically used in model simulations of the Weichselian ice-sheet (e.g. Fastook and Holmlund 1994, Holmlund and Fastook 1995, Hagdorn 2003, Hagdorn et al. 2005, Forsström 2005). The ice-sheet modelling used in the PSAR also uses palaeotemperature information from the GRIP core (Section 3.1.4). Figure A-1 (red line) shows the GRIP temperature curve (50-year average values plotted on the ss09 timescale, see below) used as input to the ice-sheet modelling performed with the University of Maine Ice-sheet Model (UMISM).

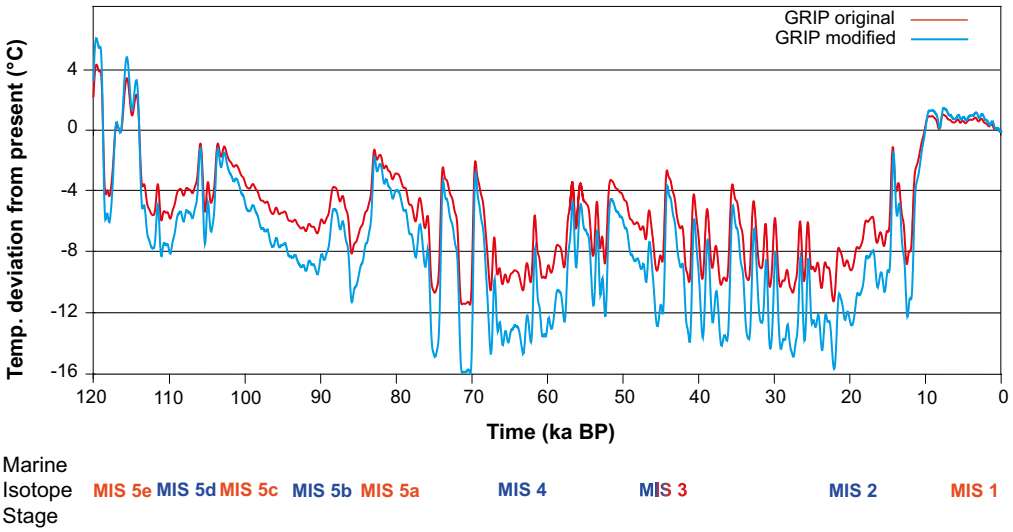

Figure A-1. *Palaeotemperature curve from the GRIP ice core (Johnsen et al. 1995) (red) and modified temperature curve resulting from the ice-sheet model calibration (blue). Cold stadials and warm interstadials are shown in blue and red text respectively, denoted by their Marine Isotope Stage (MIS) numbers. The uncertainty of the temperature curves is discussed in Section A5.*

Although $\delta^{18}O$ values from ice cores are useful temperature proxies, transferring $\delta^{18}O$ values to air temperatures and using them as proxy data for palaeotemperatures is not straightforward (e.g. Cuffey et al. 1994, Huber et al. 2006). In part, this is because of changes in the source of precipitation over time and changes in the distribution of snow on the ice-sheet. Also, seasonal variations in temperature and precipitation affect the isotopic composition of the ice core (Krinner et al. 1997). Studies of $\delta^{15}N$ isotopes from the NorthGRIP (NGRIP) ice core (NorthGRIP community members 2004) has shown that the $\delta^{18}O$-temperature relationship changes over time, for instance between glacial and interglacial periods and between stadials and interstadials (Huber et al. 2006). The results by Huber et al. (2006) may be used as input in an estimation of the errors present in the GRIP temperature curve. This is discussed in Section A5 together with the errors associated with using the GRIP temperature curve for reconstructing Fennoscandian temperatures. Despite the uncertainties, the temperature reconstructions from the Greenland ice cores are one of the best continuous archives of palaeoclimate information available in the vicinity of Fennoscandia.

In the simulation of the Weichselian ice-sheet, the modelled ice-sheet configurations were calibrated against known dated ice-marginal positions (Section 3.1.4). The calibration was done by making systematic changes of the entire input GRIP temperature curve. The resulting modified temperature curve after calibration is shown in Figure A-1. Keeping all other input data constant in the calibration process, the modified temperature curve after model calibration results in Late and Middle Weichselian ice-sheet configurations in good agreement with dated stadial ice-marginal positions from glacial geology and Early Weichselian configurations in reasonably good agreement with geological interpretations. The main difference between the original GRIP curve and the temperature curve after calibration is that the latter shows generally colder conditions during stadials (Figure A-1). The temperatures during interstadials are similar.

A3 Reconstructed last glacial cycle temperatures in the Forsmark region

A3.1 Air temperatures with and without a Weichselian ice-sheet

From the calibrated ice-sheet model, a regional temperature curve was extracted for the terrestrial grid cell closest to the Forsmark site (Figure A-2, blue line). This local temperature curve thus originates from the modified GRIP curve of Figure A-1. For periods without an ice-sheet cover over the Forsmark region, the extracted temperature curve shows air temperature in the Forsmark region as represented in the ice-sheet model simulation. For periods with ice-sheet cover over Forsmark, the curve shows the simulated basal ice temperatures from the ice-sheet model.

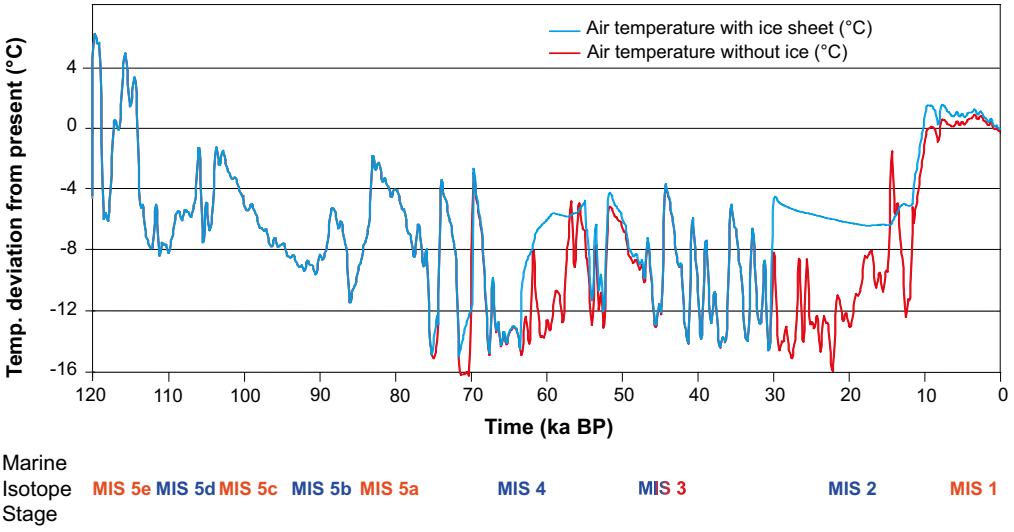

Figure A-2. *Extracted air temperature curve for the Forsmark region for the past 120 ka, obtained from the calibrated ice-sheet model (Section 3.1.4). The blue line shows the temperatures as obtained from the ice-sheet model, comprising ground-level temperatures for ice free periods and basal ice temperatures for glaciated periods. A temperature curve constructed to show conditions without the presence of the ice-sheet is shown by the red line. The uncertainty of the temperature curves is discussed in Section A1.7.*

In addition to the temperature curve containing ice-covered periods, a temperature curve was calculated to show glacial cycle temperatures *without* the presence of an ice-sheet. First, a calculation of the annual air temperature that would prevail at the ground-level if the ice-sheet was not present was made for the glaciated periods. This was done by applying an atmospheric lapse rate temperature dependence to the ice-sheet surface temperatures and ice-surface elevation variations. The resulting ground-level air temperatures were subsequently combined with the ground-level air temperatures for ice-free periods resulting in a temperature evolution without ice-sheet temperatures (Figure A-2).

A3.2 Adjustment of Forsmark air temperature curves to include estimated Eemian, Mid-Weichselian and Holocene conditions

Eemian conditions

In the temperature reconstruction for the past 120 ka (Figure A-2), the likely environmental conditions in the Forsmark region during interglacials and interstadials also need to be considered. Following the deglaciation of the large Saalian ice-sheet (with a maximum ice configuration at around 140 ka BP), it is very likely that the Forsmark site was submerged by the Baltic Sea during a large part of the Eemian interglacial, much in the same way as following the Weichselian glaciation. The reconstructed temperature curve (Figure A-2) was adjusted to reflect these submerged conditions. According to Björck et al. (2000), the Eemian interglacial period started at 127 ka BP and ended at 116 ka BP, resulting in an 11 ka long Eemian period. Other studies define the start of the Eemian at 133 and 130 ka BP. The length of the Eemian in the GRIP ice core is more than 15 ka, although with poor dating (Dansgaard et al. 1993). It can be concluded that the length and timing, especially the starting time, of the Eemian period from geological data is uncertain. However, to make a locally defined Eemian period for the Forsmark site, the ending of the Eemian is selected to occur at the time of the first permafrost development in the permafrost simulations made for the PSAR, at 114 ka BP.

Based on the Saalian glaciation having been more severe than the Weichselian, and with a thicker ice-sheet over Fennoscandia (Section 5.4), it was assumed that the Forsmark site was submerged for several thousands of years longer during the Eemian than in the Holocene. The uncertainty of how much longer the site may have been submerged is of course large. In accordance with this reasoning, the air temperature curve (Figure A-2) was adjusted to show a mean basal water temperature of +4 °C during the period −120 to −115 ka at Forsmark (Figure A-3). The Eemian temperatures for the period following submerged conditions were kept the same as in Figure A-2.

One result of including the very likely submerged conditions in the Forsmark region for the main part of the Eemian interglacial is that not much of the warm Eemian temperatures are seen in the resulting ground temperature curve (Figure A-3). After 115 ka BP, there is a 1000-year long period of warm Eemian terrestrial conditions before temperatures start to drop. It should be emphasized that this is a coarse reconstruction of Eemian conditions, both in terms of timing, length and prevailing conditions. Nevertheless, it is very likely that this reconstruction provides a better estimate of Eemian conditions for the Forsmark region than simply applying the air temperature curve without taking account of submerged conditions (Figure A-2). In addition, the assumption of a submerged temperature of +4 °C for the major part of the Eemian constitutes a pessimistic assumption of thermal conditions for the permafrost simulations, see Section 3.4.4 and Hartikainen et al. (2010). Keeping a long period of very warm terrestrial conditions would have heated the bedrock prior to cooling and resulted in less permafrost than with the approach taken here.

In the 1D permafrost reconstructions of Weichselian permafrost conditions, see Section 3.4.4 and SKB (2006a), the correction for submerged conditions at Forsmark during the Eemian was not made, whereas the temperature curve adjusted for submerged Eemian conditions was used for the 2D permafrost reconstructions (Hartikainen et al. 2010 and Section 3.4.4).

Mid-Weichselian conditions

In the reference glacial cycle climate case, ice-sheet modelling (Section 3.1.4) resulted in ice-free conditions at Forsmark during Marine Isotope Stage 3, between c 55 and 30 ka BP (Section 4.5). According to the results of the Glacial Isostatic Adjustment (GIA) model simulations (Section 3.3.4), the Forsmark region remained submerged beneath the Baltic Sea for the initial ~8 ka of this interstadial period (Section 4.5). Therefore, a submerged temperature of +4 °C was set for the first part of this ice-free period of MIS 3 (Figure A-3, blue curve).

Holocene conditions

The starting time for the Holocene period is here locally defined as the time of the Weichselian deglaciation of Forsmark, occurring at c 8800 BC (10800 years ago) (Söderbäck 2008). In line with the method above, the temperature curve has been adjusted to show a submerged temperature of +4 °C from that time up to near-present conditions (Figure A-3).

At present, the Forsmark site is located at the Baltic Sea shore. The past and future isostatic land uplift affects the site gradually, discussed in e.g. the section on transition between climate domains (Section 4.5.4). Detailed studies of how the land uplift is affecting the Forsmark site are presented in the **Biosphere synthesis report**. However, for the present temperature reconstruction, it is sufficient to use the estimate that the repository site in Forsmark emerged from the sea ~1000 years ago, and adjust the temperature curves accordingly (Figure A-3).

A3.3 Ground surface temperatures

As mentioned in e.g. Section 3.4 and in Figure 4-11, the annual mean ground surface temperature is typically a few degrees warmer that the annual mean air temperature. Therefore, the air temperature curve in Figure A-3 was used to calculate ground surface temperatures using the 1D permafrost model (SKB 2006a) (Figure A-4). This ground surface temperature has been used in the studies of Sundberg et al. (2009) and Vidstrand et al. (2010). For details on how the ground surface temperature was derived, see SKB (2006a).

In the 2D permafrost simulations (see Hartikainen et al. (2010) and Sections 3.4.4 and 5.5.3), ground surface temperatures were constructed from the same air temperature curve but in a more detailed way accounting for e.g. dry/wet climate conditions and various surface cover types, see Hartikainen et al. (2010). An example of the resulting ground surface temperatures is seen in Figure A-5. These ground surface temperatures were used to simulate the 2D permafrost development described in Section 3.4.4 and 5.5.

The more simplified ground surface temperature reconstruction (Figure A-4) typically lies within the range of ground surface temperatures reconstructed in a more detailed way (Figure A-5).

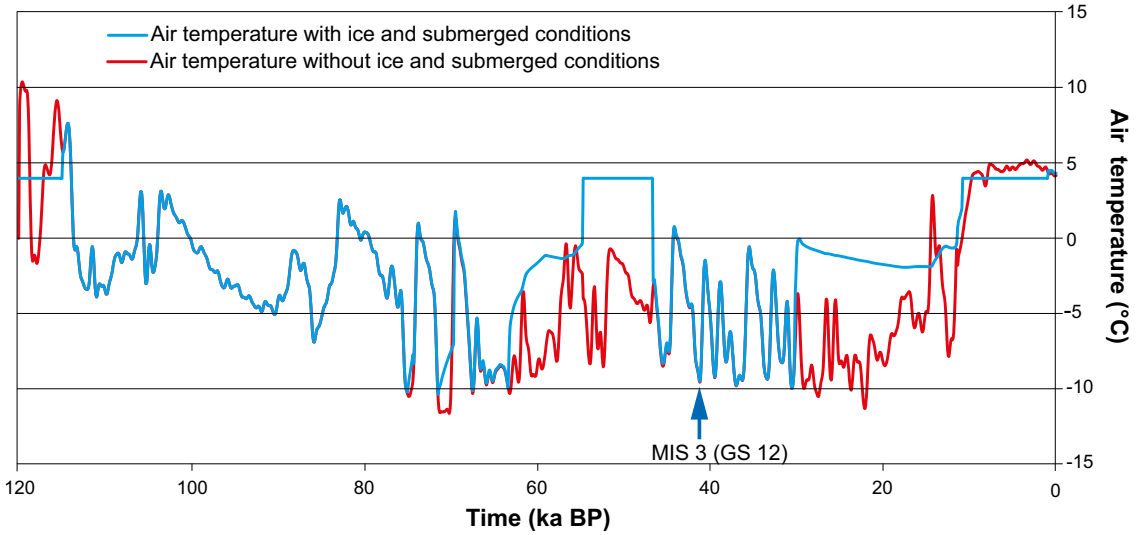

Figure A-3 . *Reconstructed air temperature curve for the Forsmark region for the past 120 ka, including estimated submerged periods of the Eemian, Mid-Weichselian and Holocene (blue line). The red line shows last glacial cycle air temperatures without the presence of an ice-sheet and submerged periods. The curves have been used as input to e.g. the 1D and 2D permafrost simulations (SKB 2006a, Hartikainen et al. 2010), see Section 3.4.4 and5.5. The uncertainties of the temperature curves are discussed in the present appendix, Section A5.2, and the implications for modelled permafrost depths in Section 3.4.4 (sensitivity studies made with the 2D model).*

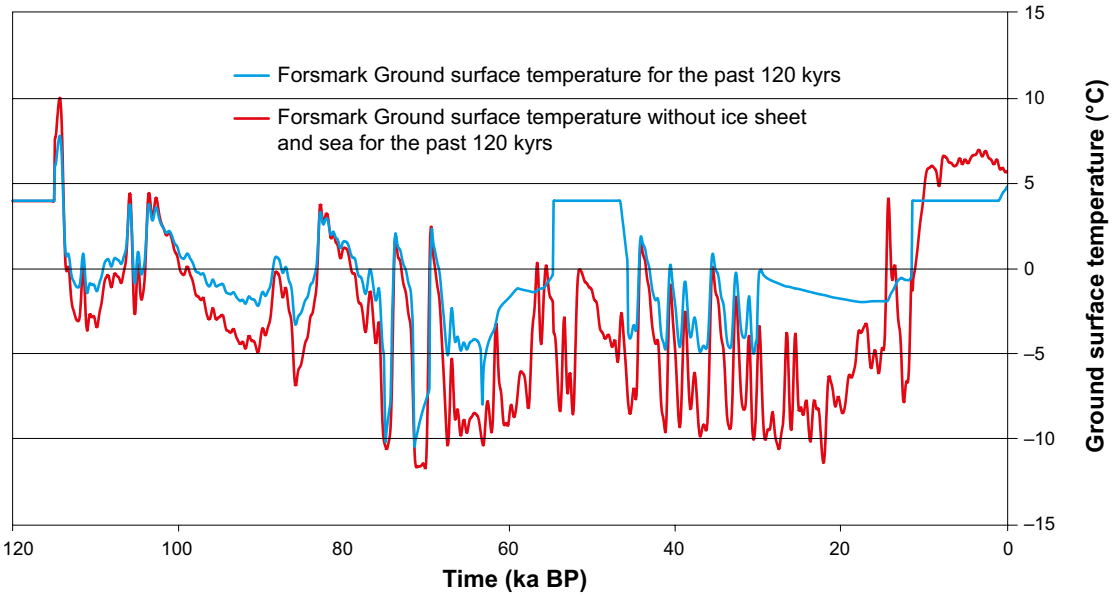

Figure A-4 . *Ground surface temperature for Forsmark for the past 120 ka with ice-sheet (blue) and without ice-sheet and sea (red) reconstructed with the 1D permafrost model (SKB 2006a). The ground surface temperature data has been used as input to Sundberg et al. (2009) and Vidstrand et al. (2010). The uncertainty of the temperature curves is discussed in Section A1.7.*

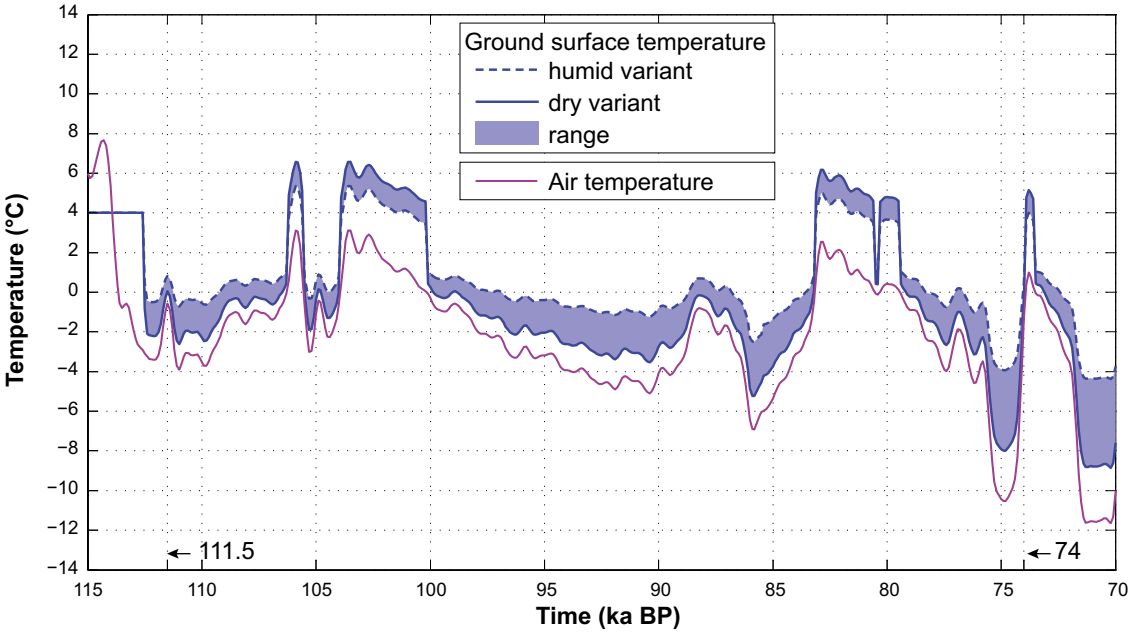

Figure A-5. *Examples of reconstructed ground surface temperatures for Forsmark for the first part of the last glacial cycle (see Section 3.4.4 and Hartikainen et al. (2010)). The ground surface temperatures cover a range of dry/humid climate conditions, see Hartikainen et al. (2010). The example is for one part of the 15 km long investigated profile, with fresh-moist surface conditions just above the repository location (~4800 m from the south–west side of the profile in Figure 3-48).*

A4 Temperature conditions during the Holocene and reference glacial cycle

A4.1 The ending and duration of the Holocene interglacial in the reference glacial cycle

In the *reference glacial cycle* (Section 4.5), reconstructed last glacial cycle conditions (Section 4.4) are assumed to be repeated during the coming 120 ka. To this end, the present day is selected to correspond to 120 ka BP in the reconstructed last glacial cycle. This, together with the local definition of the ending of the Holocene (defined as the time of the first occurrence of permafrost at the Forsmark repository location, see Section 4.5.4), results in a total duration of the Holocene period of ~18 ka (Table 4-6). This duration is in line with the longer of the two types of interglacials, with durations roughly of either ~20 or ~10 ka, that have occurred during the past eight glacial cycles (Tzedakis et al. 2009).

This way of defining the ending and duration of the Holocene interglacial is a simple way of treating a complicated subject. For instance, the *reference glacial cycle* described here should be seen as a climate development dominated by natural climate change, i.e. without anthropogenic warming. As mentioned in Section 4.5.4, the uncertainties in the *actual* length of the present interglacial period are naturally very large. Given this uncertainty, it is again emphasized that the evolution of climate domains as described in the *reference glacial cycle climate case* (Figure 4-34, Figure 4-35 and Figure 4-36)) is not an *expected* future climate evolution. It is one relevant example of an evolution covering the climate-related conditions that can be met in a 100 ka time perspective. Other possibilities for the length of the present interglacial period are handled in the additional climate cases, such as the *global warming climate case* (Section 5.1) and *extended global warming climate case* (Section 5.2).

Looking at Fennoscandia as a whole, glacial and permafrost conditions at other places would come and go at other times, which would result in shorter or longer locally defined interglacial periods if the same approach were to be applied. This way of using locally defined times for the start and end of the interglacial results in the Holocene in northern Sweden being many thousand years shorter in duration than in southern Sweden. From the safety assessment point of view, this is a proper approach to defining interglacial periods, since it is specifically the local conditions, such as the disappearance of an ice-sheet or development of permafrost, that are of importance for other relevant processes such as e.g. groundwater flow and chemistry, biosphere conditions, and thermo-mechanical conditions in the bedrock.

As mentioned above, the *reference glacial cycle climate case* assumes that the reconstructed development of ice-sheets, permafrost and relative sea-level are repeated during the coming 120 ka. Given this and the treatment of the onset of the last glacial cycle conditions described above, there is no need to explicitly repeat also the temperature curves reconstructed for the last glacial cycle into the future. This is also motivated by the fact that the temperatures at the ground surface, as such, are not of importance for repository safety. The temperature curves reconstructed for the last glacial cycle formed the basis for the reconstruction of last glacial cycle ice-sheet and permafrost development, and therefore also form the basis for the corresponding developments during the future *reference glacial cycle climate case*. Therefore, the temperature curves of Figure A-3 and Figure A-4 do not need to be repeated for the future *reference glacial cycle climate case*.

In this context it is important to note that the uncertainties estimated for the temperature curve reconstructed for the last glacial cycle (Figure A-3), discussed in Section A1.7, are dealt with: i) in dedicated sensitivity tests in the permafrost simulations (Section 3.4.4), and ii) in an indirect way by e.g. the complementary climate case dealing with larger future ice-sheets than those reconstructed for the last glacial cycle.

A4.2 Holocene temperatures

From extrapolations of measured temperature bore hole loggings in Forsmark, the present-day ground surface temperature is estimated as +6.5 °C (Sundberg et al. 2009). This value lies between the present-day ground surface temperatures suggested by the 2D permafrost modelling, which yields a value of +6.1 °C for the evolution with dry climate, and +7.4 °C for the evolution humid climate variant (Hartikainen et al. 2010). A future Holocene ground surface temperature of around +6.5 °C could therefore be envisaged for the remaining part of the Holocene. This estimate of *reference glacial cycle climate case* conditions (which is completely dominated by natural climate change, see Section 1.2.3

and 4.5) thus excludes the anthropogenic contribution to the ~0.8 degrees of climate warming that has taken place during the last 100 years (IPCC 2013a). For the climate cases with increased global warming, air- and ground-surface temperatures in at least the next few millennia are projected to be considerably higher than in the *reference glacial cycle climate case*, see Sections 5.1 and 5.2, and Appendix F.

As mentioned above, in the adopted approach to repeating last glacial cycle reconstructions of ice-sheet, permafrost and relative sea-level development for the coming 120 ka, there is no need to explicitly repeat also the air temperature curve used for these reconstructions. If such a projection were to be made, it would be very similar to the curve seen in Figure A-3 (blue line), with the exception that initial temperatures would not reflect submerged conditions (as the initial conditions in the last glacial cycle reconstruction). Submerged temperature conditions would however prevail later on in the development (as in Figure A-3 blue line).

A5 Estimates of uncertainties in the reconstructed temperature curve

There are a number of different uncertainties and assumptions that contribute to the overall uncertainty in the air temperature curve reconstructed for the Forsmark region for the last glacial cycle (Figure A-3): i) uncertainties in the calculations of air temperatures from $\delta^{18}O$ vales in the GRIP ice core, ii) temporal uncertainties in the timescales used for the ice-core data, iii) the representativity of GRIP ice-core data for Fennoscandian conditions.

A5.1 Uncertainties in the GRIP temperature curve

Uncertainties in calculated Greenland temperatures

The isotopic record used for the calculation of GRIP temperatures (Figure A-1, red line) is the one used in Johnsen et al. (1995). For the transformation of $\delta^{18}O$ values to air temperatures, Johnsen et al. (1995) used the relationship:

$$T = 1.5\ (\delta^{18}O + 35.27) \qquad \text{Equation A-1}$$

where T is the temperature deviation from year 1989, and $\delta^{18}O$ is the oxygen isotope value recorded in the ice core. Equation A-1 represents a *present day* $\delta^{18}O$-T relationship averaged for the last 50 years up to 1989, and assuming that the temperature over these 50 years is the same as in 1989 (Johnsen et al. 1995). As previously mentioned, it has been shown that the present day $\delta^{18}O$-T relationship is less suitable for glacial conditions, and that this relationship also changes between stadials and interstadials (Huber et al. 2006). Changes in the $\delta^{18}O$-T relationship over time are caused by several factors such as changes in the source of precipitation (Masson-Delmotte et al. 2005), changes in the distribution of precipitation on the ice-sheet (Werner et al. 2001), and by seasonal variations in temperature and precipitation (Krinner et al. 1997). This introduces errors in the temperature curve when produced according to Johnsen et al. (1995).

Results of Huber et al. (2006) show that the $\delta^{18}O$-T relationships during last glacial cycle interstadials are closer to the present-day relationship, used by Johnsen et al. (1995), than is the $\delta^{18}O$-T relationship during last glacial cycle stadials. It is therefore expected that stadial temperatures in the Johnsen et al. (1995) temperature curve (Figure A-1, red line) contain a larger error than the warmer interstadial temperatures. The uncertainty in the temperature estimates for Marine Isotope Stage 3 (MIS 3) by Huber et al. (2006) is a minimum of c 3 degrees and a maximum of c 6 degrees. From $\delta^{15}N$ measurements, a symmetric uncertainty of ± 3 °C would be applicable for these periods (Huber et al. 2006).

For a comparison with the temperatures reconstructed for the NGRIP ice core (Huber et al. 2006), $\delta^{18}O$ values from the NGRIP ice core (NorthGRIP community members 2004) were transformed to tentative temperatures using the same transfer function (Equation A-1) as used in the production of the GRIP temperature curve. The resulting curve is seen in Figure A-6 (green line), together with the original GRIP curve and the temperature curve modified in the ice-sheet model calibration process (Figure A-1). It is important to note that the temperatures calculated from the NorthGRIP data within the present study are not to be taken as solid scientific results. They are included only to make the first-order analysis of the errors introduced by using the present day $\delta^{18}O$-temperature relationship for the GRIP data.

Table A-1 summarizes the temperature amplitudes of individual Dansgaard-Oeschger (DO) events during MIS 3 from Huber et al. (2006) together with corresponding temperature amplitudes from using the present day δ^{18}O-T relationship of Johnsen et al. (1995) on the NGRIP δ^{18}O data (Figure A-6, green line). The results show that, during the MIS 3 DO events studied by Huber el al. (2006), the temperature lowering is underestimated by between c 20 and 40 % or c 2–4 °C (Table A-1) when using the present-day δ^{18}O-T relationship in the reconstruction of GRIP ice core Greenland temperatures (Figure A-1, red line).

This means that the temperature curve used for the ice-sheet model calibration (Figure A-1, red line) probably underestimates Greenland air temperatures during cold stadial periods by c 2–4 °C due to the use of the present day δ^{18}O-T relationship. This uncertainty needs to be considered in the overall estimate of uncertainty in the temperature curve reconstructed for Forsmark for the last glacial cycle (Figure A-3), see below. Given the result by Huber et al. (2006), using the present-day δ^{18}O-T relationship for warmer interstadial periods most probably introduces a considerably smaller error.

An additional error is introduced by the treatment of the air temperatures from the GRIP ice core as annual mean air temperatures when they are affected by a seasonality signal (Krinner et al. 1997).

Table A-1. Difference in temperature amplitude for Dansgaard-Oeschger (DO) events during MIS 3 between the NGRIP curve as described by Huber et al. (2006) and obtained by applying the simple present-day δ^{18}O-Temperature relationship used for the GRIP data. The results indicate that the GRIP data (Figure A-1 and Figure A-6) may underestimate the temperature amplitude associated with DO-events by up to 3–4 degrees. However, this also assumes that the climate signals in the NGRIP and GRIP temperature curves are the same.

Dansgaard-Oeschger event	Mean ΔT (°C) from NGRIP data (Huber et al. 2006)	ΔT obtained by applying the simple GRIP δ^{18}O-T relationship on NGRIP δ^{18}O data	Difference (°C and percent)
9	9	7	2 (−22 %)
10	11.5	8	3.5 (−30 %)
12	12.5	9.5	3 (−24 %)
14	12.5	8	4 (−32 %)
15	10	6	4 (−40 %)
16	9	5	4 (−44 %)
17	12	8	4 (−33 %)

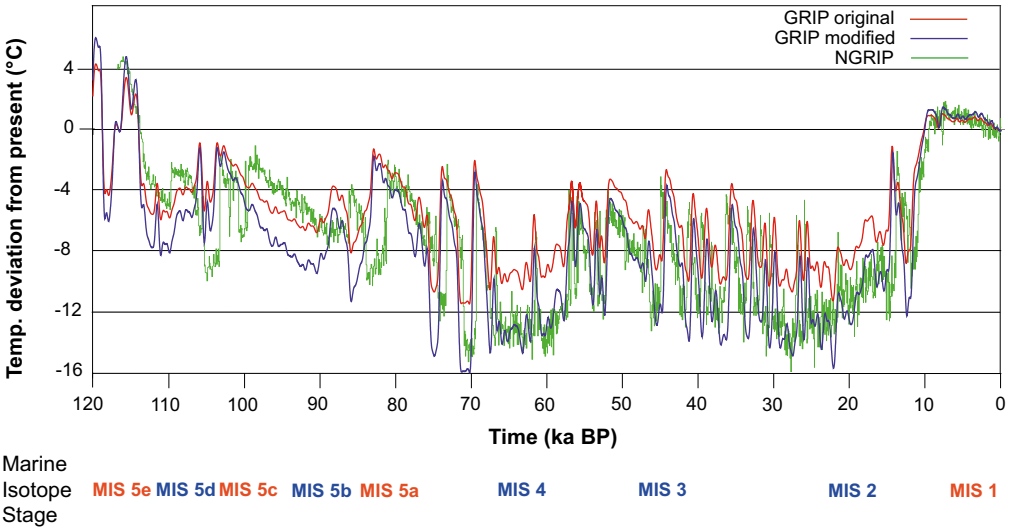

Figure A-6 . *Palaeotemperature curve from the GRIP ice core (Johnsen et al. 1995) (red) and modified GRIP temperature curve resulting from the ice-sheet model calibration (blue). For comparison, a tentative temperature record from the NGRIP ice core (NorthGRIP community members 2004) is shown in green, see the text. The NGRIP temperature curve was constructed within the present study. Note that the timescale only applies for the GRIP data. The NGRIP data is not plotted on the same timescale, which contributes to a temporal mismatch between GRIP and NGRIP results in the plot. However, the tentative NGRIP curve is here included only for general comparison of temperature amplitudes between the two ice cores.*

It is also worth noting that the modified GRIP temperature curve (from the ice-sheet model calibration process) (Figure A-6, blue line) specifically has resulted in that temperatures during stadial are colder than in the original GRIP curve, whereas warm interstadial temperatures are similar. This shows that the ice-sheet model calibration process has reduced the error introduced from using the present day δ^{18}O-T relationship for the original GRIP temperature curve.

Temporal uncertainties in the ice core data

In the Greenland ice cores, such as GRIP, NGRIP, GISP2 etc, temporal uncertainties exist in the timing of individual climatic events. From the beginning, different ice cores were dated by different methods, which yielded inherited differences in the resulting time-scales. The actual climate information also differs between the cores, which contributes to the difficulties in matching them against each other.

The most commonly used ice core timescales are the Meese-Sowers GISP2 stratigraphic timescale (Meese et al. 1997) and the modelled "ss09sea" timescale that was applied to the GRIP and NGRIP ice cores (Johnsen et al. 2001). The glacial section of the GRIP core (Figure A-1) was dated by employing an ice-flow model with an empirical δ^{18}O-accumulation relationship and two dated fix-points (Dansgaard et al. 1993, Johnsen et al. 1995). This resulted in the improved ss09sea timescale (Johnsen et al. 2001). According to Svensson et al. (2008), these timescales agree within 750 years back to 40 ka, but further back in time the disagreement becomes several thousands of years. Further adjustments of the timescales used for ice core data are also made (e.g. Skinner 2008, Svensson et al. 2008).

There are still significant temporal uncertainties related to the Greenland ice cores (e.g. Rasmussen et al. 2006, 2008, Skinner 2008, Svensson et al. 2008). For example, Skinner (2008) showed that the NGRIP age scale probably is missing up to 1200 years for the last glaciation period. Any reconstruction of last glacial cycle conditions based on these ice-core data also needs to includes these uncertainties. However, in the safety assessment work, the *exact* temporal development of temperature during the last glacial cycle, and more specifically the exact temporal development of other processes that are dependent on the temperature such as ice-sheets and permafrost, is of minor importance for repository safety (Section 1.2.3). Furthermore, the reconstructed last glacial cycle conditions (including their temporal uncertainties) are used to construct a future *reference glacial cycle climate case*, which in turn is complemented by other possible future climate developments in which e.g. permafrost and ice-sheets may develop at other times than in the *reference glacial cycle climate case*.

A5.2 Uncertainties in the reconstructed Forsmark region temperature curve – comparison with other data on Fennoscandian palaeotemperatures

As previously mentioned, the modified GRIP temperature curve (Figure A-1, blue line) was subsequently used to extract a temperature curve for the Forsmark region (Figure A1-2 and A1-3). Other independent proxy data and model data on Fennoscandian temperatures during the last glacial cycle may be used for a first-order check of the validity of this reconstructed Forsmark region temperature curve (Figure A-3). In such comparisons, it is important to remember that both climate proxy data and modelled climate data may contain significant uncertainties (e.g. Kjellström et al. 2010b). The temperature curve reconstructed for Forsmark is compared with other palaeoclimate data for the MIS 5d stadial, the MIS 5c interstadial, the early MIS 3 interstadial, and the middle MIS 3 stadial, see Sections 4.2 and 4.3.

The palaeoclimate data from the Sokli site in northern Fennoscandia (e.g. Helmens 2009, Väliranta et al. 2009, Engels et al. 2010), used in the comparisons, consists of reconstructed summer (July) air temperatures, whereas the temperature curve reconstructed for the Forsmark region (Figure A-3) reflects annual mean air temperatures. Therefore, the comparison between the two regions does not make use of absolute temperatures, but instead the *temperature difference* to present climate conditions in each region for each period. With this approach, potential differences between the sites in terms of the amount of change in the seasonal temperature cycle between present conditions and the past is neglected. However, it is considered that this is of minor importance and that the comparisons still contribute with important information.

Early Weichselian (MIS 5d stadial)

During ice-free stadial conditions of MIS 5d (the Herning stadial 117–105 ka BP), July summer temperatures of +12–14 °C were reconstructed for the Sokli site in northern Finland, see Section 4.3.1 and Helmens (2019). This is comparable with the present summer mean temperature of +13 °C. On the contrary, Engels et al. (2010) estimated the July summer temperature at Sokli to be about 6 °C lower during MIS 5d compared with present-day. The relatively large difference in the reconstructed summer temperature between Helmens (2019) and Engels et al. (2010) reflects the large uncertainty in estimating the temperature for the MIS 5d stadial period.

The reconstructed air temperature curve for the Forsmark region indicate MIS 5d annual mean air temperatures from c −1 °C down to c −4 °C (Figure A-3), i.e. around 6 down to 9 °C colder than at present.

Early Weichselian (MIS 5c interstadial)

During MIS 5c (the Brørup interstadial, 105–93 ka BP), summer temperatures inferred from plant macrofossil remnants indicate warm conditions in northern Fennoscandia. Reconstructed July temperatures for this period are as high as +16 °C, which is 3 °C warmer than at present (Väliranta et al. 2009, Engels et al. 2010, Helmens 2019). Other (lower-resolution) MIS 5c reconstructions from northern Fennoscandia indicate summer temperatures 6–7 °C lower than present, see Engels et al. (2010). However, several central European sites indicate that there was a phase during the MIS 5c interstadial that was characterized by high summer temperatures, see Engels et al. (2010).

The reconstructed annual air temperature for the Forsmark region during the MIS 5c interstadial (105–93 ka BP) is from c +2 °C down to c −4 °C (Figure A-3), i.e. between 3 and 9 °C lower than at present.

Middle Weichselian (early MIS 3 interstadial)

Mean July air temperatures for early MIS 3 (at ~50 ka BP) in northern Fennoscandia, inferred from fossil chironomids, are 12–13 ± 1.15 °C (Helmens 2009). This corresponds to the present-day summer temperature (13 °C) in the region. Mean July air temperatures inferred from terrestrial pollen data from the same site lie within the range of 11–12 ± 1.5 °C (Helmens 2009). The reconstructed high summer temperatures are in part ascribed to enhanced July insolation compared with present at the high latitude site of the site. Warm early MIS 3 temperatures are in line with the ice-free conditions in northern Fennoscandia and elsewhere (Section 4.2 and 4.3.2).

In the reconstructed annual air temperature curve (Figure A-3), the Forsmark region is submerged under the Baltic Sea during early MIS 3 (at ~50 ka BP). However, the values for non-submerged conditions are about −1 to −4 °C, which is between c 6 and 9 °C lower than at present.

Middle Weichselian (middle MIS 3 stadial)

Simulated temperatures for the MIS 3 (Greenland Stadial 12) period (44 ka BP), see 4.3.2 and Kjellström et al. (2009), suggest that the annual mean air temperature in the Forsmark region was −7.6 °C during this cold stadial. This is c 12.5 °C colder than the present annual mean air temperature.

The reconstructed last glacial cycle air temperature curve for Forsmark suggests that the annual air temperature during the same stadial was c −9 °C (Figure A-3, blue arrow), or c 14 °C colder than at present.

Discussion

In this comparison, it should be emphasized that all data on palaeotemperatures, from proxy data and from climate modelling, including the temperature curve reconstructed for the Forsmark region, contain uncertainties. Nevertheless, a comparison between the temperature reconstructions contributes with an overall picture of how the reconstructed curve for the Forsmark region (Figure A-3) relates to other independent estimates of palaeotemperatures.

Table A-2 summarizes the estimated approximate temperature difference between present day conditions and the conditions during the four last glacial cycle stadials and interstadials as described above.

Table A-2. Estimated approximate temperature difference between present day conditions and conditions during four last glacial cycle stadials and interstadials as reflected in the reconstructed temperature curve for the Forsmark region (Figure A-3) and in other palaeoclimate proxy- and model data (see the text). It should be noted that many of the reconstructed palaeotemperatures should be regarded with caution, such as the MIS 5d value for Northern Fennoscandia (Engels et al. 2010, Helmens 2019).

	Approximate ΔT MIS 5d stadial – present	Approximate ΔT MIS 5c interstadial – present	Approximate ΔT Early MIS 3 interstadial – present	Approximate ΔT Middle MIS 3 stadial – present
Northern Fennoscandia (Sokli region)	Comparable to present	3 °C warmer	0–2 °C colder	-
Other Fennoscandian MIS 5c sites	-	6–7 °C colder	-	-
South–central Sweden from modelling (Forsmark region)	-	-	-	12.5 °C colder
South–central Sweden from temperature curve (Forsmark region)	6–9 °C colder	3–9 °C colder	6–9 °C colder	c 14 °C colder

The only comparison above which uses the same geographical region, as well as estimates of absolute numbers on annual mean air temperature in both reconstructions, is the one for the middle MIS 3 stadial, where climate model results from the Forsmark region are compared with the reconstructed Forsmark region air temperature curve (Figure A-3). This comparison shows that, for this cold stadial period 44 ka BP, the reconstructed temperature curve gives a ~1.5 °C lower temperature than the climate model simulation (Table A-2), and thus that these two independent temperature estimates of temperature in the Forsmark region are in line with each other. This suggests that, although the temperature curve for Forsmark was constructed in a crude way, the resulting Middle Weichselian stadial temperatures in the Forsmark region curve may well be realistic.

For the Early Weichselian MIS 5d stadial and MIS 5c interstadial, values from the reconstructed Forsmark temperature curve indicates a similar, or some degrees larger, lowering of temperature than the other proxy data (Table A-2).

For the early MIS 3 interstadial (at ~50 ka BP), proxy data (e.g. Helmens 2009) suggests present-day summer temperature conditions in northern Fennoscandia. When such warm interstadial conditions prevail in northern Fennoscandia, similar near-present temperature conditions would be expected also in south–central Sweden, given that the region is free of ice such as in the *reference glacial cycle climate case*. However, for early MIS 3, the temperature in the reconstructed curve (Figure A-3) is c 6–9 °C colder than at present, i.e. far from present-day temperatures. This might be due to several reasons, i) similar near-present temperatures did occur also in south–central Sweden (including the Forsmark region), but the warm conditions over Fennoscandia did not have a corresponding rise in temperature over Greenland, and are thus not found in the ice-core record, ii) the climate in south–central Sweden was significantly colder than in northern Fennoscandia during this period, iii) one (or both) of the reconstructions may have a large error in reconstructed temperatures for this period (the temperature estimate by Helmens (2009) has an uncertainty of only ±1.5 °C, which in this case would indicate that the temperature reconstruction for the Forsmark region has temperatures that are much too low for this period), or iv) a combination of the above reasons.

The resulting overall picture from the comparisons is that the reconstructed temperature curve (Figure A-3) agrees with or gives somewhat lower temperatures (by some degrees) than the other reconstructions. The comparison thus suggests that the reconstructed temperature curve for Forsmark probably does not overestimate the temperatures during the investigated last glacial cycle stadials and interstadials. From the purpose of this safety assessment, this is cautious, since it emphasises the potential for cold region processes such as permafrost and freezing.

A5.3 Estimated temperature uncertainty and treatment of this uncertainty in the PSAR

The modified GRIP temperature curve (after ice-sheet model calibration) (Figure A-1) has reduced uncertainties present in the original GRIP curve, but there still remains a significant uncertainty of several degrees in this curve (Table A-1). When this curve was used to construct the temperature curve for the Forsmark region (Figure A-3 the reconstructed Forsmark temperature curve also has significant uncertainties. The comparison with proxy data seems, however, to indicate that the reconstructed Forsmark temperature curve is in broad agreement with the (few available) proxy data and furthermore that it does not overestimate temperatures for the compared last glacial cycle stadials and interstadials. The general picture from the comparison with Fennoscandian proxy data is that the reconstructed temperature curve gives roughly correct or slightly too low temperatures by a few degrees.

Based on how the air temperature curve has been constructed, on the comparison against Fennoscandian last glacial cycle stadial and interstadial proxy data, and on remaining uncertainties associated with the temperature curve that have not been quantified above, it is here pessimistically estimated that the uncertainty in the reconstructed Forsmark region temperature curve (Figure A-3) is not larger than 6 °C for the periods with largest uncertainties. Furthermore, an uncertainty of up to c 4–5 °C is estimated for the major part of the curve, and for some parts of the curve, such as for the Holocene and the Eemian, smaller than 4 °C.

In the PSAR, the uncertainties in the reconstructed temperature curve for the Forsmark region mainly affect the permafrost modelling, see Hartikainen et al. (2010) and Section 3.4.4 and 5.5.3 and Vidstrand et al. (2010). In the permafrost simulations performed for Forsmark, see Hartikainen et al. (2010), Section 3.4.4 and 5.5.3, the uncertainties in the air temperature curve are covered by a range of sensitivity tests specifically on the air temperature curve and on surface conditions (for the calculation of ground surface temperatures). In some of the sensitivity tests, the entire air temperature curve reconstructed for the last glacial cycle (Figure A-3) was lowered (and raised) by 6 °C, in accordance with the estimated maximum uncertainty. This was also done in combination with uncertainties in other parameters of importance for the development of permafrost, see Hartikainen et al. (2010) and Section 3.4.4. Other sensitivity tests on the air temperature curve for permafrost simulations covered a temperature range significantly wider than the estimated uncertainty described in this section, up to a 16 °C lowering of the air temperature curve in Figure A-3, see Hartikainen et al. (2010) and Section 3.4.4.

Uncertainties in the original GRIP temperature curve have a direct effect only on the ice-sheet modelling (Section 3.1.4), but the uncertainty is here to a large extent taken care of by the ice-sheet modelling process (in which the ice-sheet configurations during stadial periods, when the error is largest, were calibrated against known ice-marginal positions).

The *temporal* uncertainty in the reconstructed temperature curve, discussed above, is covered by the additional climate cases (Chapter 5), where e.g. permafrost might develop earlier than in the *reference glacial cycle climate case* (based on the Weichselian reconstruction that includes the reconstructed temperature curve).

Appendix B

Ice-sheet profiles

B1 Background

In various studies performed for the PSAR, e.g. on groundwater flow and THM processes, ice-sheet profiles are useful as input for investigating how these processes are affected by glacial conditions. This section gives background and data for selection of two ice-surface profiles used in the safety assessment. Two different types of ice-sheet profiles are discussed; ice profiles derived mainly from theoretical considerations, and ice profiles derived from more complex numerical ice-sheet modelling.

The steepness of an ice-sheet surface is determined by the combination and interplay of several factors such as basal shear stresses, englacial ice temperatures, temperatures at the ice-sheet bed, the basal hydrological conditions and the presence or absence of deformable sediments at the bed. As a rule, a retreating ice-sheet has a less steep profile than an advancing ice-sheet, and so does an ice-sheet ending in the sea compared with a terrestrial ice-sheet. Warm basal conditions, with presence of basal water, and presence of deformable bed sediments also results in less steep ice than cold-based conditions. The steepness of the ice-sheet surface is important for the ice flow and for the water routing and water flow at the base of the ice. In addition, it is also of high importance for e.g. the flow of groundwater in the bedrock and for the stress situation in the Earth's crust.

B2 Theoretical ice-sheet profiles

The easiest way of describing an ice-sheet profile is by assuming that ice is a perfectly-plastic material. One can further assume that this ice-sheet is circular and situated on a flat and horizontal bed, and that the ice-sheet is in steady-state, i.e. that no change in ice configuration occurs over time. In this case the ice-sheet surface profile constitutes a simple parabola (e.g. Paterson 1994), and is calculated by:

$$h^2 = \frac{2\tau_0}{\rho g}(L - x) \qquad \text{Equation B-1}$$

where h is the ice thickness at distance x from the centre, L is the radius of the ice-sheet, τ_0 is the basal shear stress, ρ is the ice density and g is the acceleration due to gravity. With L = 400 km, ρ = 0.9 kg dm^{-3}, g = 9.81 m s^{-2} and τ_0 set to 50 and 100 kPa, the resulting parabolas are as shown in Figure B-1. A basal shear stress of 100 kPa is more appropriate for small valley glaciers whereas 50 kPa (with large variation) is more representative for ice-sheet conditions.

To have a more realistic description, Equation B-2 introduces a flow of the ice (Paterson 1994). The same assumptions are made as above, except for a removal of the perfect-plasticity assumption, and the introduction of an assumption of basal frozen conditions.

$$(h/H)^{2+2/n} + (x/L)^{1+1/n} = 1 \qquad \text{Equation B-2}$$

Here H is the ice thickness at the centre of the ice-sheet and n is a flow parameter (the strain-rate exponent) in Glen's flow law of ice, often set to 3 (e.g. Paterson 1994). The resulting profile when L is set to 400 km and 900 km, H = 3000 m and n = *3* is shown also in Figure B-1.

Equation B-2 results in a steeper profile (for the corresponding profile length) than the parabolas described by Figure B-2, and presumably it is more in line with real ice-sheet profiles (Paterson 1994). For the further use of theoretical ice profiles, the steeper theoretical profiles of Equation B-2 are chosen. Furthermore, steeper profiles also give larger impacts in studies of groundwater flow and crustal stresses under glacial conditions, and thus represent a more pessimistic choice from the safety assessment point of view.

The theoretical profiles (Equations B-1 and B-2) are compared with an ice-sheet profile from the western part of the Greenland ice-sheet in Figure B-2, see also Jaquet et al. (2010). Note that in this figure the ice-sheet surface topography for the theoretical profiles is reflecting the full relief of the bed topography, which is not the case in the real world. The less steep theoretical profile is similar to the Greenland profile, whereas the steeper theoretical profile is steeper than the Greenland ice-sheet profile.

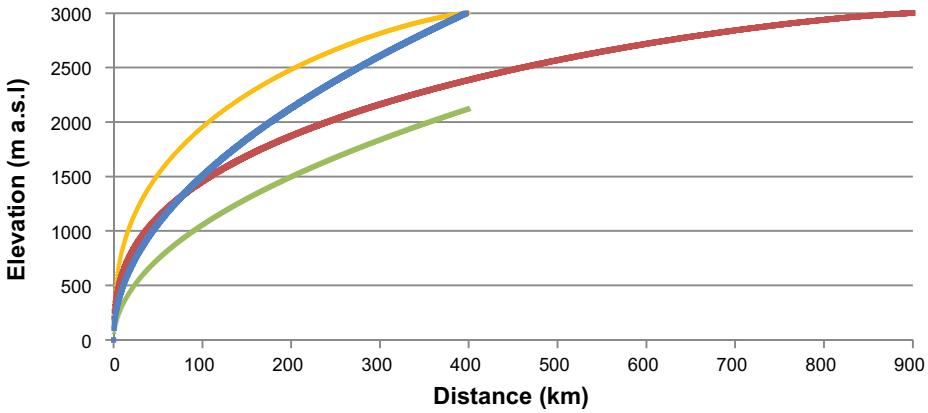

Figure B-1. *Theoretical steady-state ice-sheet profiles according to Paterson (1994). Parabolas produced by Equation B-1 are shown in green (400 km long profile with a basal shear stress of 50 kPa) and blue (400 km long profile with a basal shear stress of 100 kPa). The steeper profiles produced by Equation B-2 are shown in yellow (400 km long profile) and red (900 km long profile). The latter two profiles are considered to be more realistic representations of steady-state ice-sheet profiles (Paterson 1994).*

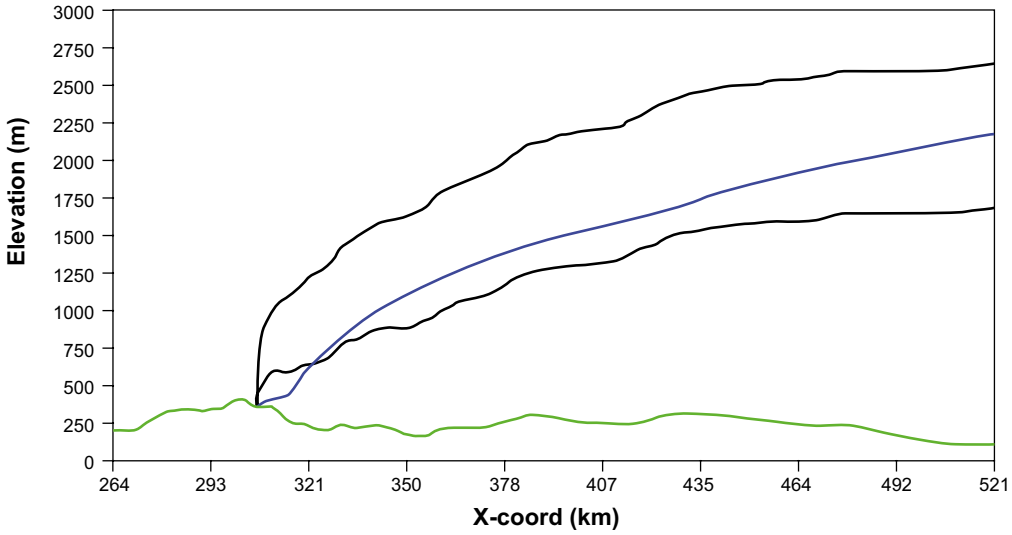

Figure B-2. *Comparison between the theoretical ice profiles (Equation B-1 with τ_0 set to 50 kPa upper black line and Equation B-2 lower black line) with an ice-sheet profile from the Greenland ice-sheet (blue). The bed is shown in green. The theoretical profiles are, unrealistically, displayed as reflecting the full relief of the bed topography, which has resulted in too much relief in the ice surface. From Jaquet et al. (2010).*

B3 Ice profiles from numerical ice-sheet simulations

Ice profiles were extracted from the time-transient reconstruction of the Weichselian ice-sheet simulated by the University of Maine Ice-sheet Model (UMISM), see Section 3.1.4. In the following text, this model simulation is denoted the *reference glacial cycle ice-sheet simulation*. The location of the transect from which the profiles were extracted is shown in Figure B-3. Several ice-sheet profiles from the last stadial of the reconstructed Weichselian ice-sheet (e.g. from MIS 2 that included the Last Glacial Maximum, see Section 4.2), are shown in Figure B-4. Figure B-4a shows profiles from the advancing phase and Figure B-4b from the retreating phase of the simulated MIS 2 ice-sheet.

In the Weichselian ice-sheet simulation, the ice-sheet advances over the Forsmark region from NW–NNW whereas during the deglaciation it generally retreats in a more northerly direction. All profiles in Figure B-4 were extracted along transect 1 (Figure B-3). The orientation of transect 1 was selected to capture the steepest surface gradients during ice advance (i.e. generally oriented along the flow lines of the advancing ice, perpendicular to the advancing ice margin). Consequently, profiles extracted along the same transect but for the retreat phase, which occurred in a somewhat other direction, are somewhat underestimating the steepness of the ice-sheet surface.

In addition to the profiles selected along transect 1 (Figure B-3), a c 900 km long retreat profile was selected along transect 2. This profile was extracted for the time 14300 ka BP. All profiles selected from the ice-sheet advance phase are discussed in Section B1.2, whereas all profiles from the retreat phase are discussed in Section B1.4.

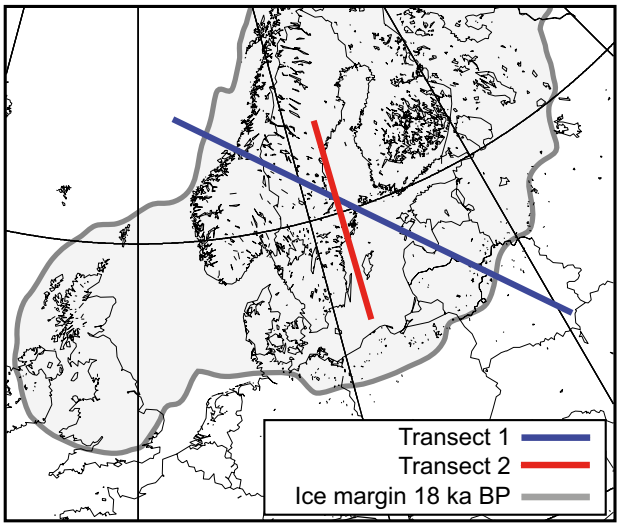

Figure B-3. *Locations of ice-sheet profiles. Transect 1: transect for all profiles shown in Figure B-4 a and b. Transect 2: location of retreat profile extracted for 14.3 ka BP shown in Figure B-7.*

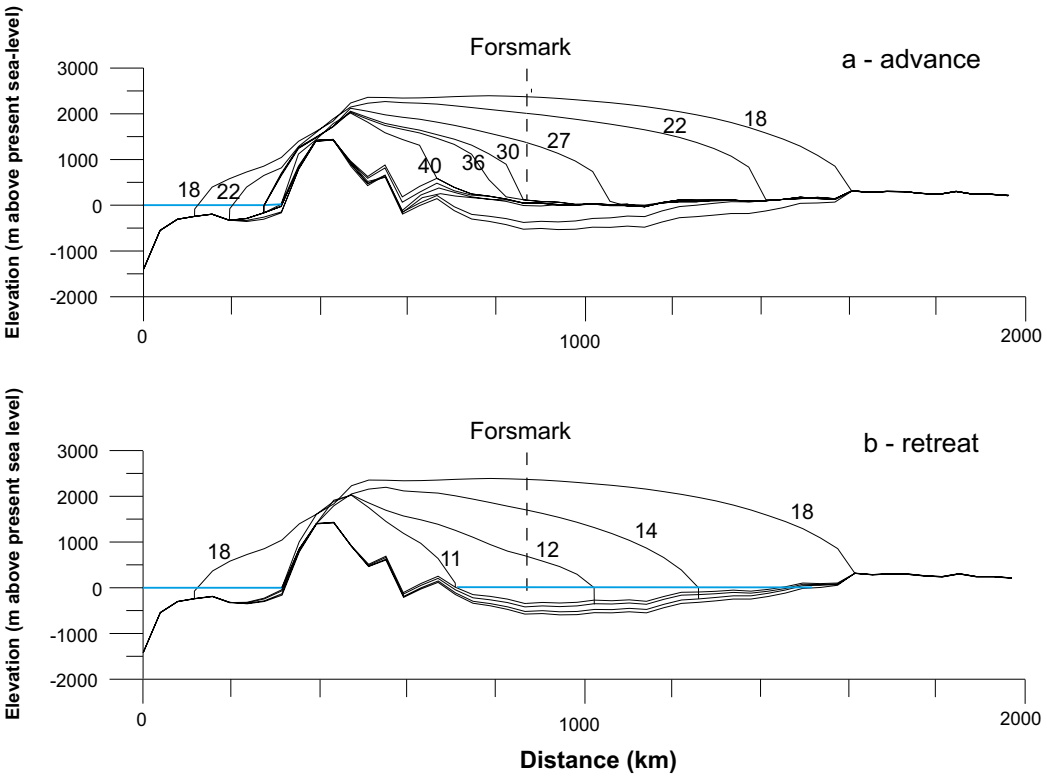

Figure B-4. *Examples of ice-sheet profiles from the Weichselian ice-sheet simulation during the MIS 2 advance and retreat. Profiles are extracted from transect 1 (Figure B-3). Numbers indicate time (ka BP). It should be noted that the y-scale has a vertical exaggeration of 100x and that sea-level change associated with ice-sheet growth is not shown. In the frontal-most part of the profile, the 10 km spatial resolution of the ice-sheet model can be seen as a sharp knick in the ice surface. Present-day sea-level is shown in blue. The LGM ice-sheet configuration, along this specific profile, occurs at around 18 ka BP.*

Ice surface gradients

Figure B-5 shows the ice surface gradients that occur above the Forsmark site in the *reference glacial cycle* ice-sheet model run. There are two phases of ice-sheet coverage in this model simulation, during MIS 4 and MIS 2, and hence two periods with gradients in Figure B-5. Steep gradients occur during the short periods when the ice front passes that area, whereas low gradients prevail during the long periods of time when the ice front is located far from the repository. For the second and main ice-covered period, the mean value of low gradients is around 0.06 degrees (or 0.98 m km^{-1}), corresponding to about one third of the present-day regional topographic gradient at Forsmark (3 m km^{-1}) (Vidstrand et al. 2010). The resulting steepest hydraulic gradient in the *reference glacial cycle* is about 0.8 degrees (0.014 m m^{-1}) over the first 10 km of the modelled ice-sheet profile.

B4 Comparison of ice profiles from numerical simulations with the theoretical profile

In all comparisons below, it should be remembered that at a given time, the ice configuration of a realistically modelled ice-sheet, such as the one used here, is quite complex; the ice surface is irregular on both small and large spatial scales, and thus far from being a circular and regularly shaped dome as in the theoretical examples. This is due to variations in the dynamics and flux of the ice as a response to e.g. varying mass balance at the surface and variations in bed topography. Such complex ice configurations are seen also on the present-day Greenland and Antarctic ice-sheets. Consequently, at a given time, ice-surface profiles derived from one part of the simulated ice-sheet may differ from profiles extracted from another part. When selecting profiles from the Weichselian ice-sheet simulation, the aim has been to select profiles both relevant for a broad understanding of how the ice-sheet looks and behaves and profiles specifically relevant for the Forsmark site.

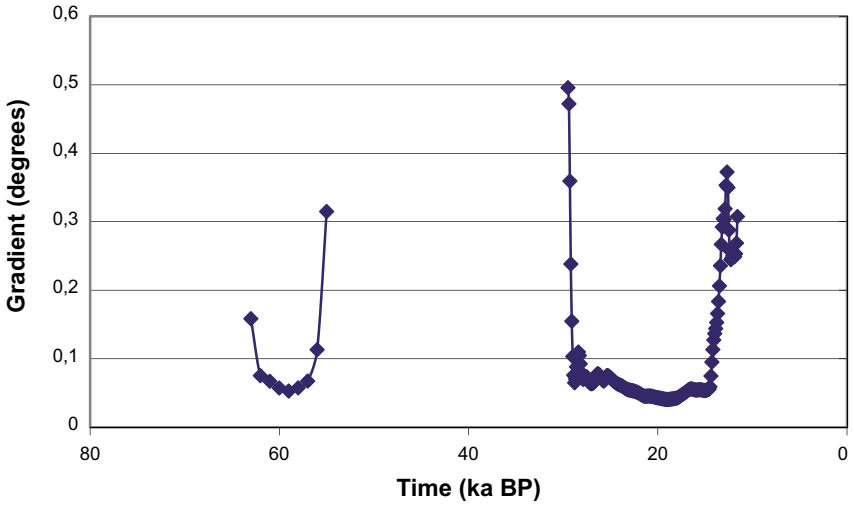

Figure B-5. *Modelled ice-surface gradients above the Forsmark site for the reference glacial cycle. Note that the steepest part of the ice-sheet is not included in the figure and is estimated to have an inclination of 0.8° (0.014 m m^{-1}). Steep gradients occur when the ice front passes the site, whereas low gradients prevail when the ice margin is situated far from the site.*

B4.1 Simulated advancing profiles compared with the theoretical steady-state profile

In the Weichselian ice-sheet simulation, the main phase of ice-sheet coverage at Forsmark takes place during the MIS 2 stadial (Section 4.4), with the ice-sheet margin reaching Forsmark at around 30 ka BP (Section 4.4.1 and Figure B-4a).

In Figure B-6, all extracted profiles from the ice-sheet *advance* phase (Figure B-4a) are stacked and compared with the theoretical profiles of Equation B-2 (Figure B-1). It is seen that none of the simulated advancing profiles is steeper than the two theoretical steady-state profiles.

It is also seen that the steepest advancing profile, at 30 ka BP, is close to being as steep as one of the theoretical profiles described by Equation B-2. The simulated 30 ka BP profile is the ice-sheet profile when the ice margin is located in the Forsmark area (Figure B-6).

Having the seeming contradiction that the steady-state profiles are not steeper than the advancing profiles, is in this case not surprising. Such differences are expected since the profiles are produced in completely different ways. All profiles derived from the numerical ice-sheet model incorporate a number of parameters with considerably more realistic representations than how they are treated in the theoretical profile calculation. The ice-sheet model includes for instance realistic bed topography instead of a flat horizontal bed, a description of ice-sheet thermodynamics, where ice flow and ice temperatures are allowed to interact, and also a better representation of basal conditions (Section 3.1.4). Even though the ice-sheet model is far from being a full and complete representation of the natural system, it is significantly better than the theoretical equations. Consequently, the simulated less-steep profiles are here considered more realistic for the advancing phases than the steeper theoretical profiles.

There are no large variations in the steepness of the advancing profiles extracted from the ice-sheet simulation (Figure B-6). The steepest simulated advancing profile (from 30 ka BP) is close to being as steep as the least steep theoretical profile. Although the simulated profiles are here considered more realistic than the theoretical profiles, the above results show that if one uses the theoretical profiles of Equation B-2, the ice-sheet steepness is not underestimated if compared with the simulated advancing profiles. Therefore, the theoretical profiles of Equation B-2 may be used as a good and pessimistic (from a safety assessment point of view) mathematical representation of an *advancing* ice-sheet over Forsmark (Figure B-6).

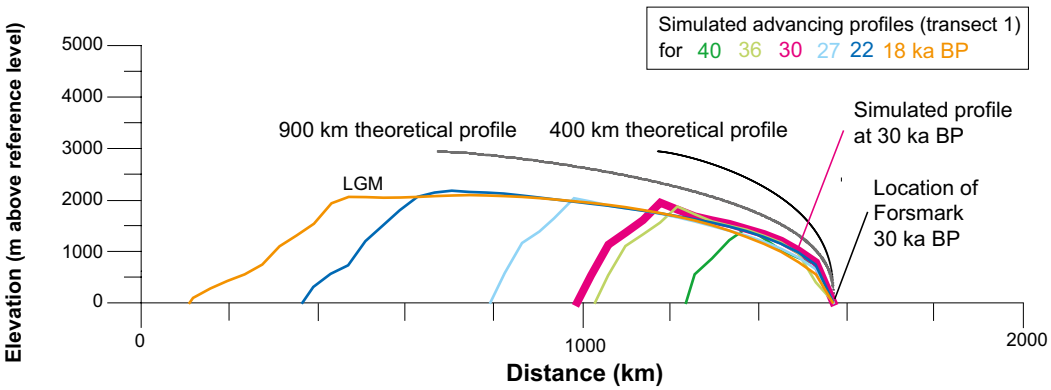

Figure B-6. *Comparison of ice surface topography from simulated advancing Weichselian ice profiles (from Figure B-4a) and two theoretical steady-state profiles of Equation B-2 (from Figure B-1) (Paterson 1994). In order to make the comparison meaningful, the fronts of all simulated profiles have been normalized to start at the same position and elevation (0 m) as the theoretical profile. Note that the simulated profiles would be somewhat "steeper" if they were to show ice thickness instead of surface elevation (since the bedrock in the ice-sheet simulation gets depressed, Figure B-4), i.e. if they were normalized also to have a flat bed, such as that of the theoretical profiles. However, for e.g. groundwater flow simulations, it is the gradient of the upper ice surface that is of interest for the water flux, and accordingly that is what is shown also for the simulated profiles. However, this results in differences between the theoretical and simulated profiles appearing larger. The frontal parts of all simulated advancing profiles are less steep than the theoretical steady-state profiles.*

In line with this, the theoretical profiles of Equation B-2 are used in several other, but not all, safety assessment studies where the effect of a simple mathematical ice profile advancing over Forsmark is studied, for instance in groundwater flow studies (Vidstrand et al. 2010) and THM studies of hydraulic jacking (Lönnqvist and Hökmark 2010).

B4.2 Simulated LGM profile compared with the steady-state profile

The LGM profile at 18 ka BP represents the profile closest to steady-state in the Weichselian ice-sheet simulation. In Figure B-6 it is seen that both theoretical steady-state profiles are steeper than the simulated LGM profile. Given the expected differences due to the different approaches taken to produce the profiles, see above, there is also one additional reason why the simulated LGM profile is less steep than the theoretical steady-state profile. It is likely that the modelled Weichselian ice-sheet never reached steady-state conditions during the LGM. This was most probably the case also for the real Weichselian ice-sheet. In nature, ice-sheets are constantly trying to adapt to the ever-changing climate conditions, and the ice-sheet probably did not have time to build a maximum-thick, steep ice at LGM.

B4.3 Simulated retreating profiles compared with theoretical steady-state profile

In Figure B-7, the extracted profiles from the *retreat* phase of ice-sheet model simulation (from Figure B-4b), together with the retreat profile extracted from year 14.3 ka BP (Figure B-3), are stacked and compared with the theoretical profiles of Equation B-2.

The profile extracted along transect 2 for 14.3 ka BP has an ice margin that ends in the Baltic Sea, and so do the 14 and 12 ka BP profiles along transect 1. When comparing the profiles in Figure B-7, only the grounded parts of all profiles are seen and compared, i.e. the parts of the profiles that are located upstream the grounding-line.

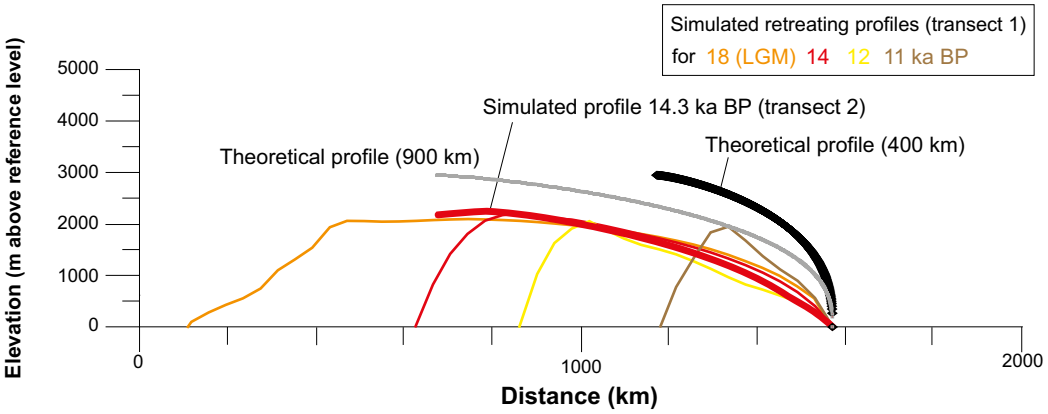

Figure B-7. *Comparison of ice-surface topography between simulated retreating reference glacial cycle ice profiles (from Figure B-4b and the profile extracted from transect 2 for 14.3 ka BP) and the theoretical steady-state profiles of Equation B-2 (from Figure B-1). To make the comparison meaningful, the fronts of all simulated profiles have been normalized to start at the same position and elevation (0 m) as the theoretical profiles. Note that the simulated profiles would be somewhat "steeper" if they were to show ice thickness instead of surface topography (since the bedrock in the ice-sheet simulation gets depressed, Figure B-4), i.e. if they were normalized also to have a flat bed, as with the theoretical profiles. However, for e.g. groundwater flow simulations, it is the gradient of the upper ice surface that is of interest for the water flux, and accordingly that is what is shown also for the simulated profiles. However, this results in the differences between the theoretical and simulated profiles appearing larger. The frontal parts of all retreating profiles are considerably less steep than the theoretical steady-state profiles. Profiles selected for other safety assessment studies are shown as bold lines.*

In line with theory, it can be seen when comparing Figure B-6 and Figure B-7 that the simulated profiles generally are steeper during the ice-sheet advance than for the retreat. In Figure B-7 it is also seen that the retreating profiles are, as expected, considerably less steep than the theoretical steady-state profiles. The steepest of the retreat profiles is from 11 ka BP. At this time the ice has a relatively steep profile caused by the steep bed topography in the mountainous region from where the profile is located (see Figure B-4b). These topographic conditions of the ice-sheet bed are not at all representative for the Forsmark area, and this profile is therefore not discussed further.

Comparing the steepness of the frontal parts of the profiles along transect 1, it can be seen that the steepest profile is the 18 ka BP (LGM) profile, followed by the 14, and 12 ka BP profiles (Figure B-7), i.e. the ice-sheet is getting less and less steep during the deglaciation over the lowland. It can also be noted that the 14.3 ka BP profile from transect 2 has a steepness that is very similar to the profile for 14 ka of transect 1 (Figure B-7), even though the profiles have different orientations. It is clearly seen that, for the Weichselian ice-sheet simulation, profiles describing the retreat phase should be considerably less steep than the theoretical profiles.

Average hydraulic gradients from the selected theoretical ice-sheet profile for various distances from the ice-sheet margin are given in Table B-1. The maximum hydraulic gradient associated with the steep frontal part of the theoretical profile is up to c 1.5 m m^{-1}.

B4.4 Selection of ice-sheet profiles for the PSAR

Since the theoretical profiles of Equation B-2 are considered to be more realistic than profiles from Equation B-1, and because it is steeper than the steepest of the simulated advancing ice profiles (Figure B-6), the steepest theoretical profile is selected to represent an advancing ice-sheet over Forsmark for the PSAR *reference glacial cycle climate case*.

The frontal near parts of the profile extracted for 14.3 ka BP (transect 2) is the least steep retreat profile from the Weichselian ice-sheet simulation (Figure B-7). This profile is selected to represent a retreating ice-sheet over Forsmark for the PSAR *reference glacial cycle climate case*.

The two selected profiles are shown by the bold lines in Figure B-7. These two profiles constitute, in their frontal parts, the steepest and the least steep profiles of all profiles analysed, and they are considered to cover a broad enough span of possible profiles to be employed in other studies, such as modelling of groundwater flow under glacial conditions (Vidstrand et al. 2010) and THM studies (Lönnqvist and Hökmark 2010).

B5 Conclusions

1. The steepest theoretical profile (Equation B-2, Figure B-7) (Paterson 1994) is selected to represent an advancing ice-sheet over Forsmark in the PSAR *reference glacial cycle climate case*. This profile is denoted "*the theoretical reference glacial cycle profile"*.
2. The least steep simulated profile from 14.3 ka BP (Figure B-7) is selected to represent a retreating ice-sheet over Forsmark in the PSAR *reference glacial cycle climate case*. This profile is denoted "*the simulated reference glacial cycle profile*".

Table B-1. Hydraulic gradients (m m^{-1}) from the selected theoretical ice-sheet profile (Equation B-2) averaged over various distances from the ice-sheet margin.

Distance from ice margin (m)	Hydraulic gradient (m m^{-1})	Hydraulic gradient (degrees)
100	1.49	56
200	0.96	44
400	0.62	32
1000	0.35	19
2000	0.23	13
4000	0.15	8.5

Appendix C

The combination of buffer erosion and freezing

C1 Background

Based on the results on freezing depths analysed in the *reference glacial cycle climate case* (Section 4.5.3) and the *severe permafrost climate case* (Section 5.5.3), freezing of water at repository depth was excluded from consideration for the first future glacial cycle in the buffer freezing scenario (see the **Post-closure safety report**). For subsequent glacial cycles in the 1 Ma-long safety assessment period, repository heat output steadily decreases. Adopting the most pessimistic combination of uncertainties in the input data to the permafrost simulations, there is a small risk of freezing of water at repository depth for these glacial cycles, while there is still ample margin to freezing of the bentonite buffer and deposition tunnel backfill material, see the scenario on buffer freezing in Section 12.3 in the **Post-closure safety report**. Because of this risk of freezing of water at repository depth, even if the risk is extraordinarily small, and for illustrative purposes, a combined case of buffer erosion and freezing at repository depth is presented here. If groundwater were to freeze in cavities formed by buffer erosion, the associated volume expansion would induce an additional pressure that possibly could affect the copper canister.

Two studies were made to illustrate the pressure effects of this hypothetical combined buffer erosion and freezing case. The first study (study A) investigated resulting freezing-point temperatures and freezing-induced pressures in buffer erosion cavities by considering various assumptions on compressibilities of remaining buffer, erosion cavity geometry, and surrounding ambient pressure (in this case surrounding groundwater pressure plus buffer clay swelling pressure). It was also assumed that the cavity was filled with ordinary compressible water, free from solutes and impurities. The second study (study B) considered the chemical potential of water in bentonite to investigate equilibrium pressures in systems with various proportions of ice and bentonite and the resulting freezing temperatures and pressures. Effects of erosion cavity geometries were not included.

C2 Study A

A simple model was used to estimate the freezing point and pressure increase in a ring-shaped erosion cavity surrounding the canister (Figure C-1). The full study was reported in SKB (2006a, Section 4.4.1). The compressibility of remaining clay was estimated from the swelling pressure of bentonite. It was also assumed that the erosion cavity was completely filled with ordinary compressible water, free from solutes and impurities. The effect of including these compressibilities is that they allow the freezing-induced expansion to occur at considerably higher temperatures than if the surroundings were incompressible. The compressibility of ice was also included, whereas the canister and the rock were assumed to be incompressible. Moreover, mean freezing temperatures for the erosion cavity as well as mean pressures for the erosion cavity and bentonite were assumed. For further details, see SKB (2006a, Section 4.4.1).

The surrounding groundwater pressure may vary between the ambient hydrostatic pressure, for completely unfrozen conditions, to a value up to the maximum freezing pressure for partially or fully frozen groundwater conditions. However, for a certain freezing temperature and for ambient pressures lower than the maximum freezing pressure, the pressure increase from freezing is affected by the ambient pressure, including the swelling pressure, in such a way that the resulting total pressure is constant, see below.

Calculations of freezing temperatures and associated pressure increases were made for ambient pressures between 4 and 100 MPa (SKB 2006a, Section 4.4.1). As an example, the results of the calculations for an ambient pressure of 10 MPa are shown in Figure C-2. Examples of pressure increase and total pressure after freezing for various ambient pressures are presented in Table C-1. For further results see SKB (2006a, Section 4.4.1).

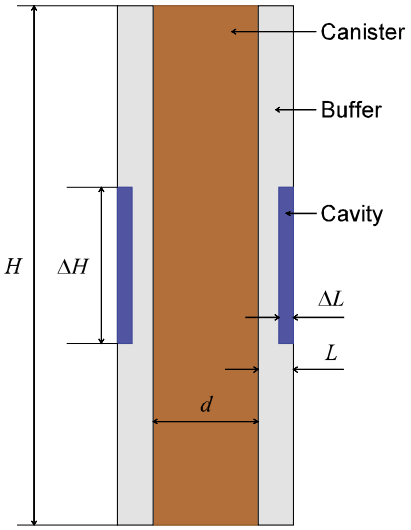

Figure C-1. *Geometry for calculations of freezing temperatures and freezing-induced pressures in buffer erosion cavities.*

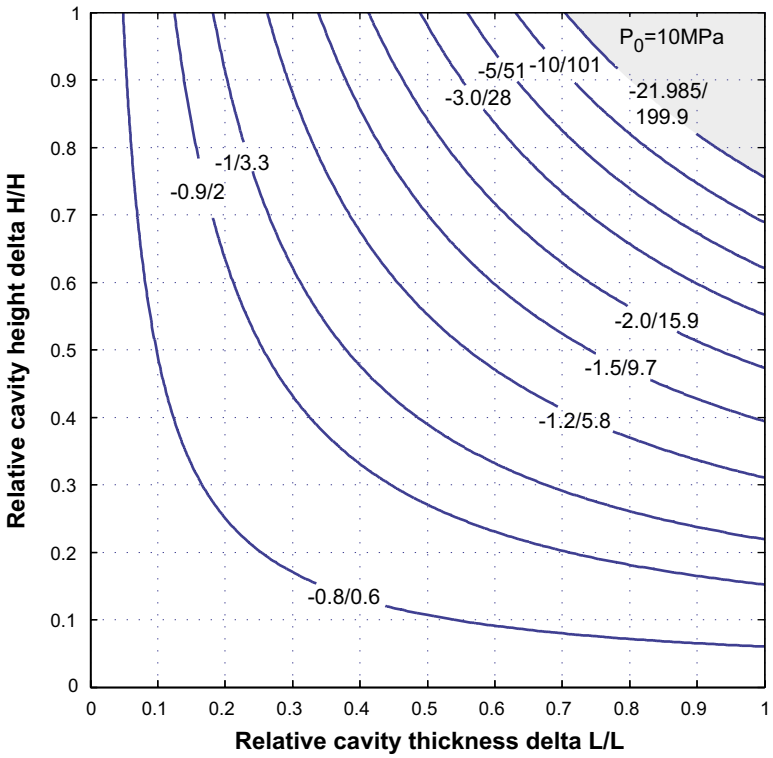

Figure C-2. *Freezing point temperature (°C) and associated maximum pressure increase (MPa) in the erosion cavity, as a function of relative cavity thickness and height, at an ambient pressure of 10 MPa. In the figure, the first number is the freezing temperature and the second number is resulting pressure (i.e. temp/pressure). The shaded area represents a region with very low temperatures, below approximately −22 °C.*

Table C-1 . Examples of pressure increase and total pressure after freezing in an erosion cavity for various ambient pressures at a freezing temperature of −2 °C. Note that the total pressure after freezing is independent of erosion cavity geometry and size.

Ambient pressure (sum of groundwater pressure and clay swelling pressure) (MPa)	Pressure increase from freezing in erosion cavity (MPa)	Total pressure (maximum freezing pressure) (MPa)
4	22	26
5	21	26
10	16	26
20	6	26
26	0	26
50	0 (no freezing occurs)	50

The results can be summarised as follows:

1. Freezing of water in an erosion cavity at a given freezing temperature can increase the pressure from the ambient pressure to the maximum freezing pressure, i.e. the maximum pressure at which freezing can occur at that temperature. For a freezing temperature of −2 °C for instance, the *maximum* freezing pressure is ~26 MPa. For a freezing temperature of −2 °C, the total pressure after freezing in the erosion cavity thus is between the ambient pressure and 26 MPa, depending on the size of the erosion cavity.
2. The *maximum* freezing pressure for a certain freezing temperature is independent of the geometry and size of the erosion cavity.
3. The pressure increase from freezing depends on the freezing temperature, the ambient pressure and the size or geometry of the erosion cavity. For certain combinations of freezing temperature and ambient pressure, complete freezing takes place and the resulting pressure increase grows with the size of the cavity. This occurs up to a certain point, at which the sum of the ambient pressure and the pressure increase equals the maximum freezing pressure. After that point, the freezing pressure is at its maximum and complete freezing can no longer take place.

If the ambient pressure exceeds the maximum freezing pressure of 26 MPa, no freezing can occur at a temperature of −2 °C, see also Table C-1.

C3 Study B

To assess the possible maximum pressure if an eroded KBS-3 buffer were to freeze, the equilibrium pressure between ice and bentonite was first considered. By considering this equilibrium pressure, and the expected deformation when ice is formed in a restricted volume, the maximum freezing pressure was estimated.

C3.1 Pressure of ice and bentonite in equilibrium

The chemical potential of water in bentonite is generally lower than in liquid bulk water at the same pressure and temperature. To reach equilibrium in a system with a confined clay sample contacted with an external reservoir of liquid water, a pressure difference between the clay and the external reservoir is therefore sustained. This pressure difference is usually referred to as the swelling pressure.

It is important to note that the occurrence of swelling pressure requires the external water reservoir to be mechanically separated from the clay, as is the case in a KBS-3 deposition hole where water is supplied by fractures in the surrounding rock or through the rock matrix itself. Liquid bulk water and bentonite at the same pressure cannot exist simultaneously in equilibrium (unless the clay density is very low).

The chemical potential of ice, on the other hand, can be lower, higher, or equal to that of bentonite water at the same pressure and temperature depending on the specific values of these variables as well as on the amount of water in the clay. In particular, this means that ice and bentonite can co-exist in equilibrium at the same pressure. The equilibrium pressure in a system containing both bentonite and ice can be derived by considering the following expression for the chemical potential of water in the bentonite (Birgersson et al. 2008).

$$\mu_{clay} = \mu_0 - s_{liq} \cdot T + v_{liq} \cdot P - v_{liq} \cdot P_s{}^0(w_u) \qquad \text{Equation C-1}$$

where μ_0 is the potential of a non-pressurized bulk water reference state at 0 °C, T denotes temperature in °C, P denotes pressure, $P_s{}^0(w_u)$ is the measured swelling pressure at water to solid mass ratio w_u at 0 °C, and s_{liq} and v_{liq} are the partial molar entropy and volume of liquid bulk water, respectively. Note that all chemical potentials used here refer to water in different phases. The partial molar quantities of the water in the clay is here approximated by the corresponding liquid bulk water properties and are further assumed independent of temperature and pressure. Note that $P_s{}^0(w_u)$ is not a physical pressure in the current state of the clay (the physical pressure is P), but rather a quantity describing the water retention properties of the specific clay under consideration. This function resembles an exponential expression at low enough water to solid mass ratios for typical bentonite materials, see e.g. Kahr et al. (1990).

$$P_s{}^0(w_u) \approx A e^{-B \cdot w_u} \qquad \text{Equation C-2}$$

Using the data in Karnland et al. (2006, 2009), the least square fitted parameters for MX-80 bentonite in the range 0.5–12 MPa are A ≈ 382 MPa and B ≈ 13.9. The chemical potential in the ice can be expressed in a similar way as for the bentonite water

$$\mu_{ice} = \mu_0 - s_{ice} \cdot T + v_{ice} \cdot P \qquad \text{Equation C-3}$$

Note that this expression lacks the water retention term and that the partial molar properties are associated with ice (naturally). The equilibrium pressure is deduced by putting the two above expressions for the chemical potential of water equal,

$$P = \frac{\Delta s \cdot T + v_{liq} \cdot P_s^0(w_u)}{\Delta v} \qquad \text{Equation C-4}$$

where Ds = $s_{liq} - s_{ice}$ and Dv = $v_{liq} - v_{ice}$.

Notice that Dv is a negative quantity since ice has a lower density than liquid bulk water. Note further that the equilibrium pressure becomes negative for a given value of w_u if the temperature is high enough (although negative), indicating that ice and bentonite do not co-exist in equilibrium under such conditions. Consequently, the temperature where the equilibrium pressure is zero also defines the freezing point of the bentonite under consideration

$$T_c(w_u) = -\frac{v_{liq} \cdot P_s^0(w_u)}{\Delta s} \qquad \text{Equation C-5}$$

This expression for the freezing point agrees with earlier derivations (Birgersson et al. 2010). Equation C-4 can be re-expressed using $T_c(w_u)$ as

$$P = \frac{\Delta s \cdot (T - T_c(w_u))}{\Delta v} \qquad \text{Equation C-6}$$

which can be viewed as a generalized Clausius–Clapeyron relation where the presence of clay influences the phase boundary between ice and liquid water by a shift of the temperature scale.

C3.2 Pressure increase due to ice formation in a restricted volume

When a confined and water-saturated bentonite sample freezes (e.g. a KBS-3 buffer), some of the water will leave the bentonite (the montmorillonite interlayers) to form a separate ice phase (small ice crystals) (Svensson and Hansen 2010). Because ice has a lower density than liquid (clay) water, a pressure increase is expected under such a transformation. The pressure increase can be quantified by first considering the volume change when a certain amount of water, Dm, is transferred from clay to ice under non-pressurized conditions in an initially ice-free bentonite sample of water to solid mass ratio w_{tot}

$$\Delta V = \left(\frac{1}{\rho_{ice}} - \frac{1}{\rho_w} \right) \cdot \Delta m = \left(\frac{\rho_w}{\rho_{ice}} - 1 \right) \cdot \frac{\Delta m}{\rho_w} = \xi \cdot \frac{m_s}{\rho_w} \left(w_{tot} - w_u \right) \qquad \text{Equation C-7}$$

Here r_{ice} and r_w denotes the density of ice and liquid bulk water, respectively, x º $r_w / r_{ice} - 1$, m_s is the mass of dry clay and w_u denotes the amount of water in the bentonite after the transition (i.e. the amount of unfrozen water). If the total system (bentonite + ice) is to be kept a constant volume, a pressure causing the deformation −DV must be applied. Assuming isotropic stress state (hydrostatic pressure), bulk modulus β, and using Equation C-7, the pressure after the transition is given by

$$P = -\beta \frac{-\Delta V}{V_w} = \beta \xi \frac{m_s}{V_w \cdot \rho_w} \left(w_{tot} - w_u \right) = \beta \xi \left(1 - \frac{w_u}{w_{tot}} \right) \qquad \text{Equation C-8}$$

where the first equality utilizes the definition of bulk modulus and V_w denotes the total water volume (liquid + ice). The presence of the total water volume rather than total volume in Equation C-8 is equivalent to assuming that the dry clay particles are uncompressible.

C3.3 Estimated pressure of confined bentonite below 0 °C

It can be shown (Birgersson et al. 2010) that the swelling pressure decreases approximately linearly with temperature in the range between the freezing point of the external water reservoir (here assumed to be 0 °C) and the freezing point of the bentonite. Furthermore, at the freezing point of the bentonite, the swelling pressure is zero. If the temperature of a confined bentonite sample is lowered below the freezing point, the pressure will start to increase due to the volume expansion of the water transformed from liquid state to ice. The equilibrium pressure at a given temperature below T_c can be deduced by first calculating the amount of unfrozen water by combining Equations C-2, C-4 and C-8 (assuming that the system has the total water to solid mass ratio w_{tot})

$$\frac{\Delta s \cdot T - v_{liq} \cdot A \cdot e^{-B \cdot w_u}}{\Delta v} = \beta \xi \left(1 - \frac{w_u}{w_{tot}} \right) \qquad \text{Equation C-9}$$

Once the unfrozen amount of water is calculated, the equilibrium pressure is given by either of Equations C-4 or C-8. All parameters in Equation C-9 except for the bulk modulus β are firmly determined by either fundamental properties of bulk water or by accurate swelling pressure measurements. The parameter set when applied to MX-80 bentonite is listed in Table C-2.

The specific value to be used of the bulk modulus, on the other hand, is not as clear. The compressibility of the full system will depend on the separate bulk moduli of clay, water and ice as well as the relative fraction of these phases. Hence, it is to be expected that β is a function of both w_u and w_{tot}. A way to treat this complication is to solve Equation C-9 for two limiting values of β to achieve a pressure interval for the actual equilibrium pressure. Here the limiting values of β is chosen as that of pure ice (8800 MPa) and that of liquid bulk water (2200 MPa), and these are assumed independent of temperature and pressure.

A solution to Equation C-9 for MX-80 bentonite (Table C-3) is illustrated in Figure C-3. This example assumes w_{tot} = 0.366, which corresponds to a swelling pressure at 0 °C of c 2.5 MPa, and a freezing point of −2 °C. In the diagram, the ice/clay equilibrium line at −3 °C (Equation C-4) is displayed. When lowering the temperature from −2 to −3 °C, water is expelled from the clay and pressure increases according to the compression curves (Equation C-8, with two different values of the bulk modulus). The actual pressure of the system is given by the intersection between the compression and the ice/clay

equilibrium curve. Hence, in the case of a bulk modulus of ice, the unfrozen water content is c 0.360 and pressure is c 13 MPa. If the bulk modulus instead is that of liquid bulk water, the unfrozen water content is c 0.351 and the pressure is c 8 MPa. Hence when lowering the temperature from −2 °C to −3 °C, this particular sample increases its pressure from 0 to 8–13 MPa.

Table C-2. Values of parameters used in Equation C-9. The partial molar entropies and volumes are approximated by bulk values (ice and liquid water) at 0 °C. The swelling pressure parameters (Equation C-2) are fitted to data for MX-80 bentonite (Karnland et al. 2006, 2009).

Δs	v_{ice}	v_{liq}	A	B	$\Delta v = v_{liq} - v_{ice}$	$\xi = v_{ice} / v_{liq} - 1$
[J/ (mol °C)$^{-1}$	[cm^3 mol^{-1}]	[cm^3 mol^{-1}]	[MPa]	[-]	[cm^3 mol^{-1}]	[-]
22.0	19.65	18.03	382.1	13.86	1.62	0.09

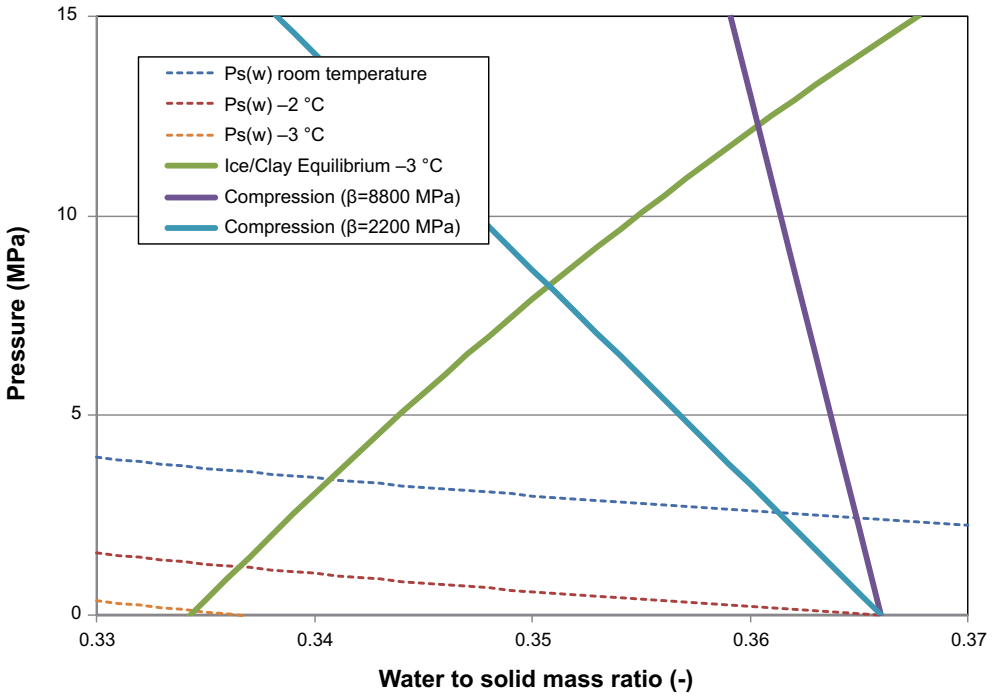

Figure C-3. *Illustration of the obtained equilibrium pressure when ice forms in a confined MX-80 sample. Equilibrium pressure is reached where the compression line intersects the Ice/clay equilibrium line. Included in the figure is also the swelling pressure curve for different temperatures (Birgersson et al. 2010).*

C3.4 The combination of erosion and freezing in a KBS-3 buffer

The nominal buffer density is 2.0 g cm^{-3}, corresponding to a water to solid mass ratio of ~0.27. The freezing point of the undisturbed buffer thus equals −7 °C according to Equation C-5. It is however evident from Equation C-2 that swelling pressure, and thereby the freezing point, is a strong function of water content in this density region. This means that the buffer freezing point is expected to increase substantially if bentonite is lost from the deposition hole due to erosion. A freezing point of −2 °C, for example, corresponds to a water to solid mass ratio of 0.366, or a density of 1.87 g cm^{-3}. This, in turn, corresponds to a mass loss of c 13 % or c 2.7×10^3 kg if the buffer density can be assumed homogeneous (initial mass: 2.0×10^4 kg).

Table C-3 shows the expected pressure intervals and unfrozen water contents at different temperatures for different values of buffer freezing points (i.e. different densities). Included in Table C-3 is also the case where all clay has eroded. The equilibrium pressures for this case are given by the ordinary Clausius-Clapeyron equation for phase equilibrium between liquid water and ice (Equation C-6 with $T_c = 0$) and are independent of the value of the bulk modulus.

Table C-3 lists the expected pressures in a frozen deposition hole whose buffer is eroded in such a way that the remaining clay is homogeneously distributed, which is the equilibrium state. However, since erosion occurs at the rock-buffer interface, substantial internal redistribution of the buffer mass is required to reach this state. Therefore, it cannot be excluded that the buffer density, to a certain degree, is inhomogeneous when it freezes, e.g. because of long equilibration times, or because of internal "friction". This means that freezing could occur above the freezing points listed in Table C-3, as these correspond to buffer mean density. Consider for instance a homogeneous buffer of (mean) density 1.87 g cm^{-3}. This system would not experience any pressure increase at −2 °C (which is the freezing point for this particular density). If instead the mass was distributed so that a certain fraction of the buffer had a density of 1.82 g cm^{-3} (and a density higher than 1.87 g cm^{-3} in the rest), a pressure increase would be experienced at −2° because the freezing point of the low-density part is −1 °C. The pressure increase, however, is smaller than for the case of a homogeneous buffer at density 1.82 g cm^{-3} because the entire buffer is involved in the deformation. Hence, the values in Table C-3 also put an upper limit for the pressure increase in inhomogeneous buffers if the density instead refers to minimum density.

It should be noted that the more heterogeneous the density distribution is the more unlikely the state, because larger and larger forces will act to redistribute the mass (Equation C-2). But even for the highly unrealistic density distribution of a bulk water cavity (ρ_b = 1.0 g cm^{-3}) in conjunction with unaffected clay (ρ_b = 2.0 g cm^{-3}), the pressure increase will never exceed that for the case of a completely eroded deposition hole. Note further that the pressure increases experienced in heterogeneously distributed buffers are transient states; when freezing occur (in the part of the buffer with lowest density), the stress state changes radically and mass redistribution is expected, leading to a more homogeneous state of the clay and lower pressures.

The above considerations have not taken into account the additional hydrostatic pressure present under unfrozen conditions in a KBS-3 repository. However, the effect of any additional load (affecting both clay and reservoir) would, on one hand, lower the freezing point according to the conventional Clausius-Clapeyron relation (ca 0.074 °C MPa^{-1}), but on the other hand the pressure would be non-zero at the freezing point (equal to the additional load). Similarly, if the groundwater (and thus the clay) contains a certain amount of salt, the freezing point of the external reservoir would be lower accordingly and also the ice/clay equilibrium would adjust in such a way that the clay would contain more water for a given temperature and pressure. Consequently, neither the effect of a hydraulic head, nor the effect of salt in the water, will contribute to increase the values listed in Table C-3.

Table C-3. The limiting pressures and unfrozen water contents at different temperatures for MX-80 bentonite of different freezing points (i.e. different densities). The listed eroded mass assumes a homogeneously distributed buffer with initial mass 2.0×10^4 kg.

T_c	w_{tot}	ρ_b	Eroded mass	At −1 °C		At −2 °C		At −3 °C		At −4 °C		At −5 °C	
				P	w_u	P	w_u	P	w_u	P	w_u	P	w_u
°C	-	g cm^{-3}	kg	MPa	-	MPa	-	MPa		MPa		MPa	
0	-	1.00	2.0×10^4	14	-	27	-	41	-	54	-	68	-
−1	0.416	1.82	3.8×10^3	0	0.416	10–13	0.396–0.409	18–25	0.377–0.403	26–38	0.361–0.396	33–49	0.346–0.390
−2	0.366	1.87	2.7×10^3	Unfrozen	0.366	0	0.366	8–13	0.351–0.360	15–24	0.338–0.355	22–35	0.326–0.350
−3	0.337	1.91	1.9×10^3	Unfrozen	0.337	Unfrozen	0.337	0	0.337	7–12	0.324–0.332	14–23	0.314–0.327
−4	0.316	1.94	1.4×10^3	Unfrozen	0.316	Unfrozen	0.316	Unfrozen	0.316	0	0.316	7–12	0.305–0.311

C4 Discussion and conclusions

The lowest temperature at repository depth when considering the results of maximum freezing depths in the *reference glacial cycle climate case* and the *severe permafrost climate case* (Table 5-21), and including the most pessimistic combination of all uncertainties relevant for the respective case, is approximately −0.5 °C. In line with this the −2 °C isotherm does not reach repository depth in the reference evolution, nor in the *severe permafrost climate case*. Nevertheless, as a pessimistic basis for a discussion on the theoretical consequences of the combined buffer erosion and freezing case, a lowest temperature of −2 °C is assumed at repository depth. This corresponds to a lowering of the entire temperature curve reconstructed for the last glacial cycle of more than 10 °C (Figure 5-49) which is considered unrealistic also when including the significant uncertainties associated with the temperature curve (Appendix A).

The results from study A show that for a temperature of −2 °C, the pressure increase from freezing of pure groundwater in buffer erosion cavities results in a maximum cavity pressure of 26 MPa (Table C-1). Freezing at higher temperatures would yield lower freezing-induced pressures (Figure C-2), while other ambient pressures would not result in a total pressure higher than 26 MPa. This pressure is in line with the maximum pressure obtained from study B for an ambient temperature of −2 °C. Here the pressure in the cavity is 27 MPa for a case with a completely eroded buffer (Table C-3), corresponding to a buffer loss of 20000 kg. Cases with a less eroded buffer (i.e. a partially eroded buffer with a higher buffer density and lower freezing point, Table C-3), yields lower erosion cavity pressures. For example, a buffer loss of 1400 kg, which is close to the value of 1200 kg of buffer loss that is used for the assumption of getting advective conditions in the buffer (see the **Post-closure safety report**), results in unfrozen conditions if the temperature is −2 °C (Table C-3). For this case, the temperature needs to be as low as −5 °C to freeze the buffer cavity, with a resulting maximum cavity pressure of 12 MPa.

A maximum pressure of 26–27 MPa in the erosion cavity is considerably lower than the maximum total pressure deduced for the PSAR post-closure scenario on maximum isostatic load where the maximum ice-sheet thickness from Section 5.4 (36 MPa) is combined with clay swelling pressure and hydrostatic pressure due to the repository depth, resulting in a total pressure of around 50 MPa (see the **Post-closure safety report**). Since this isostatic load scenario does not result in canister failure, see the **Post-closure safety report**, the same is here concluded for the hypothetical case combining buffer erosion and freezing.

If the pressure from a maximum large ice-sheet (36 MPa) (Section 5.4) were to be directly and unrealistically combined with the maximum pressure resulting from freezing in buffer erosion cavities (27 MPa), the resulting pressure would be 63 MPa. However, this case is not relevant since for ambient pressures greater than 26 MPa, a repository depth bedrock temperature of −2 °C would not be low enough to freeze water in erosion cavities. In addition, during phases of ice-sheet overriding, pre-existing permafrost degrades due to the insulation effect of the ice-sheet, e.g. (Section 4.5.3), which means that deep permafrost is not compatible with large ice-sheet thicknesses.

All in all, the following conclusions can be made:

- Based on the results on maximum permafrost and freezing depths in the *reference glacial cycle climate case* (Section 4.5.3) and in the *severe permafrost climate case* (Section 5.5.3), freezing of water at repository depth was excluded for the first future glacial cycle in the buffer freezing scenario (see the **Post-closure safety report**).
- Calculations made show that the maximum freezing-induced pressure in buffer erosion cavities would be 26–27 MPa for a pessimistically chosen ambient temperature of −2 °C. This case corresponds to a total loss of buffer in the deposition hole. This pressure is considerably lower than the critical pressure for canister collapse as discussed in the scenario treating canister collapse due to isostatic load (see the **Post-closure safety report**).
- The amount of buffer loss affects the freezing point of the remaining buffer and the resulting cavity pressures. A case with buffer loss approximately corresponding to the buffer loss assumed for getting advective conditions in the buffer does not result in frozen conditions in the erosion cavity if the ambient temperature is −2 °C. In this case, the temperature needs to be −5 °C to get freezing, with a resulting cavity pressure of up to 12 MPa as a result.

Also, freezing-induced pressure in buffer erosion cavities and large pressures from ice-sheet load do not occur simultaneously.

Appendix D

Holocene relative sea-level at Forsmark

To describe the long-term development of the landscape in general and biosphere objects in particular, the landscape development needs to be modelled continuously based on the change in relative sea-level covering the appropriate time period. SKB has done an extensive amount of work on relative sea-level and shoreline displacement at the Forsmark site and has also made many additional studies based on other types of analyses of these data, such as landscape development and groundwater flow modelling. To this end, the reconstructed relative sea-level of the Holocene, together with results from the GIA modelling (Section 3.3.4), constitutes the basis for the future assessments of the long-term relative sea-level changes at Forsmark.

D1 Background and previous work

In previous safety assessment reports, e.g. SR-Site (SKB 2010a), the shoreline displacement at Forsmark was described using a combination of empirically-based modelling of the Holocene relative sea-level (Påsse 2001) and GIA modelling (Section 3.3.4, Whitehouse 2009).

In the empirical model by Påsse (2001), the Holocene relative sea-level is calculated by the sum of two equations, representing the temporal evolution of global sea-level changes (eustasy) and the glacio-isostatic uplift after unloading of ice (isostasy). The eustasy is assumed to be spatially independent, and the equation for isostasy contains five site-specific parameters that are constrained by observational data, e.g. geological relative sea-level reconstructions and lake-tilting information.

Påsse (2001) calculated the empirical parameters for numerous sites across Fennoscandia, but unfortunately not for Forsmark. Instead, the Forsmark-specific parameter values were estimated in Brydsten (2009) by interpolating the parameter values from nearby sites in east–central Sweden and the Baltic Sea. In addition, Brydsten (2009) constrained these parameters by using the historic relative sea-level data from Hedenström and Risberg (2003) (hereafter referred to as HR2003; red dots in Figure D-1), who evaluated the shoreline displacement of the last 3.2 ka based on radiocarbon dating of terrestrial macrofossils from four lakes in the Forsmark area. They also included isolation ages from six additional lake basins located further away from Forsmark to extend their shoreline curve back to 6.3 ka BP.

The Holocene relative sea-level curve used in SR-Site (from Brydsten 2009) is displayed in Figure D-1 (blue line) together with observational data from HR2003 (red dots). The error bars in the HR2003 data represent the 95 % confidence interval (1.96 times the standard error) based on radiocarbon dating uncertainties. The standard error typically ranges from ~100–150 years for the youngest data points to ~200–300 years for older ones (see HR2003 for more details). As expected, because Brydsten (2009) used the HR2003 data to determine the Forsmark-specific parameters, the resulting relative sea-level curve agrees well with HR2003 (Figure D-1). For the early Holocene (prior to ~6 ka BP), the Forsmark relative sea-level from Brydsten (2009) is not constrained by any observational data but represents the "best guess" estimate based on the historic relative sea-level data from nearby sites, such as Stockholm and Gästrikland (Påsse 2001, Brydsten 2009).

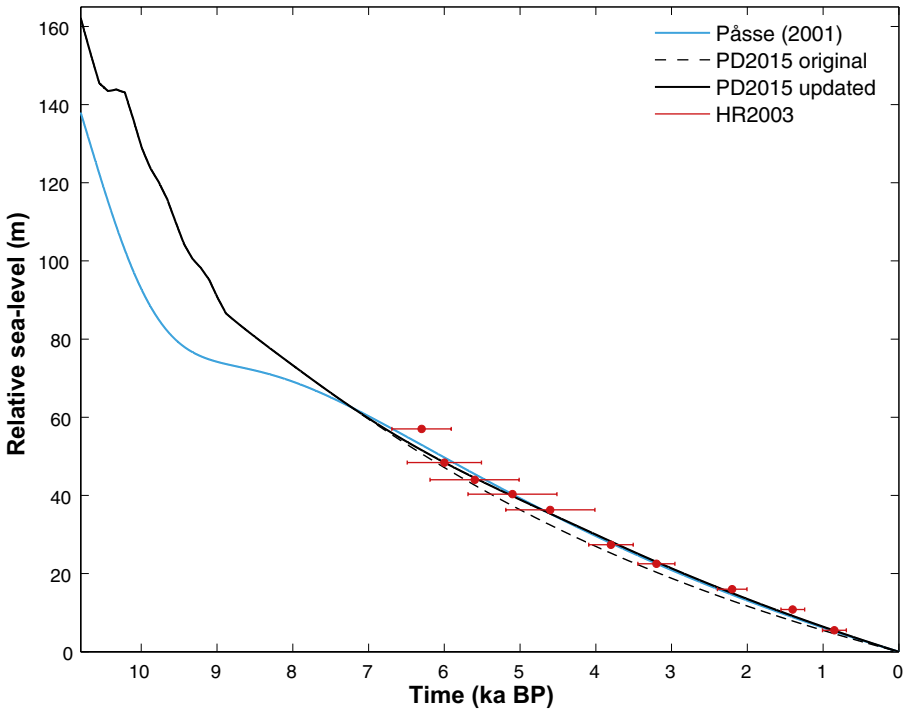

Figure D-1. *Holocene shoreline displacement for Forsmark based on Påsse (2001) (parameters were derived in Brydsten 2009; blue line), PD2015 with original parameter values (black dashed line), and PD2015 with updated parameter values (black solid line). The red points and associated horizontal lines, respectively, represent the relative sea-level data and the 95 % confidence intervals from HR2003. The Holocene shoreline displacement for Forsmark is updated from the blue curve ("Påsse 2001") in SR-Site to the black solid curve ("PD2015 updated") in the PSAR.*

Since Påsse (2001), a more recent empirical model of the Holocene shoreline displacement in Fennoscandia has been developed by Påsse and Daniels (2015) (hereafter referred to as PD2015). Although the general methodology in PD2015 is similar to that of Påsse (2001), there are also some notable differences:

- The governing equations in PD2015 have been simplified and contain three unknown site-specific parameters instead of the five used in Påsse (2001).
- PD2015 also used data from tide gauges and geological records of highest coastline levels to constrain the site-specific parameters. These datasets were not included in Påsse (2001).
- In contrast to Påsse (2001), the shoreline parameters were specifically estimated and presented for the Forsmark site in PD2015.
- The relative sea-level curve was updated to the new national height reference system RH2000 in PD2015 as opposed to the outdated RH70 height reference system used in Påsse (2001). This means that the year of zero relative sea-level has been shifted from 1970 AD to 2000 AD.

PD2015 is also the accepted official model for the Holocene shoreline displacement used by the Geological Survey of Sweden (SGU). Because of the improvements presented above, the Holocene relative sea-level for Forsmark is updated for the PSAR using the methodology outlined in PD2015. The results from the GIA modelling presented in this report are identical to SR-Site (SKB 2010a). In the following subsections, the construction of the updated Holocene relative sea-level curve based on PD2015 is outlined in detail.

D2 Updated Holocene relative sea-level

D2.1 The PD2015 model

Following Påsse (2001), the model presented in PD2015 is fully empirical. This means that the Holocene shoreline evolution in Fennoscandia is modelled using relatively straight-forward mathematical equations, for which the unknown parameters are constrained by observational data. The main advantage of the empirical modelling approach over physically-based modelling is that it is primed to give a good fit with observational data. One of the main disadvantages with empirical modelling is that the temporal coverage of the model is more or less limited by that of the observational data, implying that it cannot be used to predict the shoreline migration into the future with high accuracy. Therefore, it is crucial to resort to physically-based modelling, such as GIA modelling (Whitehouse 2009) for that purpose. As already discussed, PD2015 used data from geological relative sea-level curves, lake-tilting investigations and tide gauges as well as recorded levels of highest coastline to constrain the site-specific parameters.

The equation for the isostatic uplift (U) in PD2015 takes the following form

$$U = \frac{2}{\pi} A \left[\arctan\left(\frac{T}{B_e}\right) - \arctan\left(\frac{T-t}{B_e}\right) + \arctan\left(\frac{T}{B_v}\right) - \arctan\left(\frac{T-t}{B_v}\right)\right], \qquad \text{Equation D-1}$$

where t is time (in calendar years BP; 0 BP corresponds to 2000 AD according to the RH2000 height reference system), and

$B_v = 19A + 5000$.

Hence, the time-dependent isostatic uplift at a certain site is completely determined by three parameters (A, B_e and T), representing the download factor from the retreating ice-sheet (A), relaxation factor for the elastic uplift (B_e) and the time for the maximum uplift rate (T). The temporal eustatic evolution is defined as

$$E = -\frac{2}{\pi}\left[29\left(\arctan\left(\frac{9200}{1300}\right) - \arctan\left(\frac{9200-t}{1300}\right)\right) + 36\left(\arctan\left(\frac{13700}{1350}\right) - \arctan\left(\frac{13700-t}{1350}\right)\right)\right] \qquad \text{Equation D-2}$$

The reconstructed eustasy in PD2015 generally results in higher values compared to Påsse (2001), particularly in the early Holocene (see Figure D-2). In fact, the relatively large difference in the early Holocene relative sea-level between PD2015 and Påsse (2001) can be almost entirely explained by the difference in eustasy (Figure D-1 and Figure D-2). However, the higher eustatic values in PD2015 are in better agreement with other independent data from the early Holocene, e.g. eustatic migration data derived from corals (Peltier and Fairbanks 2006; see Figure 17 in PD2015) and is, therefore, considered to be an improvement with respect to Påsse (2001). Note that the present-day eustatic contribution in PD2015 does not account for any changes related to anthropogenic global warming, such as thermal expansion of the oceans and melting of the Greenland and Antarctic ice-sheets. The eustasy is therefore significantly underestimated for this period (see also Section D1.3).

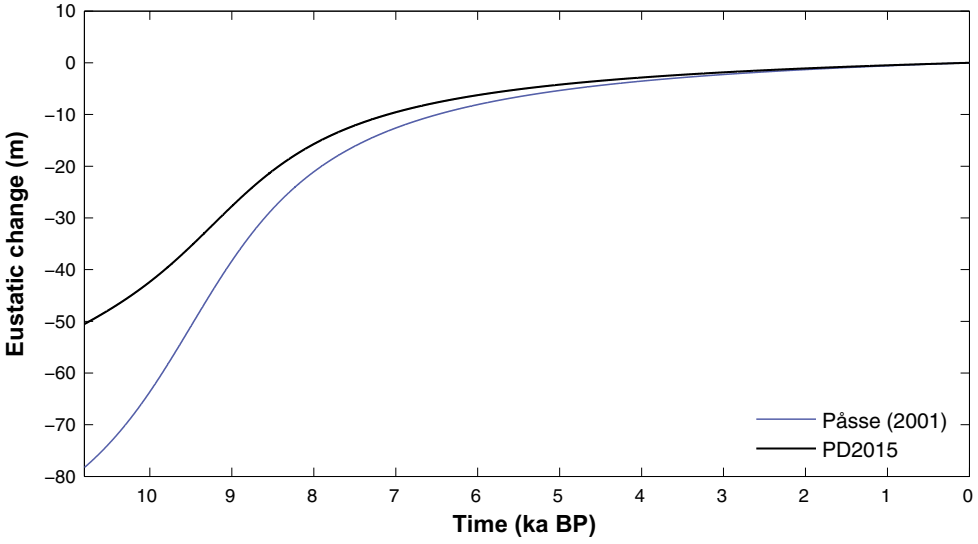

Figure D-2. *Holocene eustatic development based on equations from Påsse (2001) (blue line) and PD2015 (black line).*

The Baltic was also subject to two lake phases during the Holocene: the Baltic Ice Lake (~15–11.5 ka BP) and the Ancylus Lake (~10.5–9 ka BP). During those lake stages, the Baltic Sea was isolated from the Atlantic and hence not influenced by global eustatic changes. The influence of those lakes on the local relative sea-level is not taken into account in the equations above, so they need to be modelled separately for the times when Forsmark was free of ice. Because Forsmark became deglaciated ~10.8 ka BP (Table 4-6), it was still covered by the ice-sheet during the phase of the Baltic Ice Lake, whereas it was mostly ice-free during the Ancylus Lake stage. Hence, the shoreline displacement of the Baltic Ice Lake is omitted here, whereas the effect of the Ancylus Lake is parameterized.

The parameterized shoreline displacement resulting from the Ancylus Lake is shown in Figure D-3. (see also Figure 3 in PD2015). Its effect is also clearly visible by the bumpy part of the black lines at around 10 ka BP in Figure D-1. During the phase of rising water levels, i.e. the transgression phase, the outlet of the Ancylus Lake was located near Degerfors in west–central Sweden. This phase is characterized by rising water levels, culminating at ~17 m above the prevailing sea-level at ~10.2 ka BP. The outlet in Degerfors was eventually disconnected as a result of the rapid isostatic uplift in central Fennoscandia during this time, which created a new outlet at the Darss Sill south of Denmark. Meanwhile, the Ancylus Lake entered into its regression phase as a result of increasing eustatic levels. The shoreline displacement resulting from the Ancylus Lake (L) can thus be roughly estimated by the recorded relative sea-levels at Degerfors and Darss Sill from this time period (Table D-1); see also Påsse 2001 and PD2015), and takes the following form

$$L = \begin{cases} 0, & t \le 8990\ yrs\ BP, \\ \min(L_D, L_S), & 8990\ yrs\ BP < t \le 10\,440\ yrs\ BP, \\ 0, & t > 10\,440\ yrs\ BP, \end{cases} \qquad \text{Equation D-3}$$

where L_D and L_S are the Ancylus Lake level displacement recorded at Degerfors and the Darss Sill (Table D-1), respectively. It is important to note that the parameterization of the Ancylus Lake is highly uncertain as it is based on only a few data points outside the Forsmark area.

In summary, the Holocene shoreline displacement (S) is given by the sum of Equations D-1, D-2 and D-3:

$$S = U + E + L. \qquad \text{Equation D-4}$$

In the following subsection, the choice of parameters values for computing the isostatic uplift (U) in Forsmark is discussed.

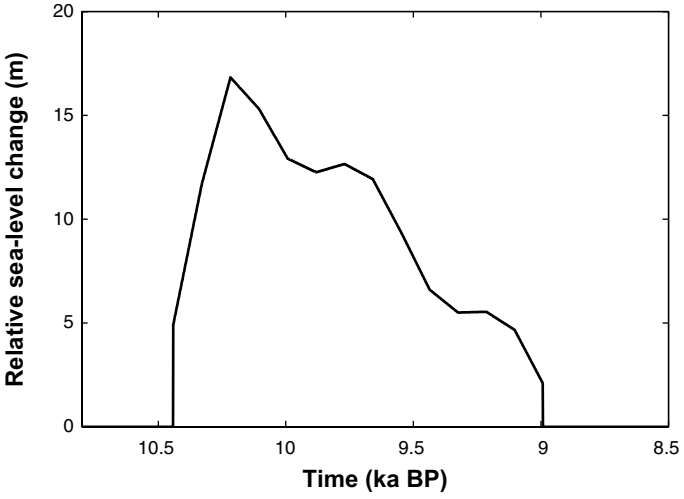

Figure D-3. *Estimated Forsmark shoreline displacement resulting from the transgression and regression of the Ancylus Lake, based on data from the outlets in Degerfors and Darss Sill (Table D-1).*

Table D-1. The level of damming (in m) in the Baltic during the Ancylus Lake stage as recorded in outlet the areas of Degerfors and the Darss Sill. Data is from the Swedish Geological Survey (based on Påsse 2001, PD2015).

Time (ka BP)	Degerfors (m)	Darss Sill (m)
10.4	4.9	17.1
10.3	11.7	17.9
10.2	16.8	17.6
10.1	20.5	15.3
10.0	28.4	12.9
9.9	31.1	12.3
9.8	33.4	12.7
9.7	35.3	11.9
9.6	36.8	9.3
9.4	37.9	6.6
9.3	38.8	5.5
9.2	39.5	5.5
9.1		4.7
9.0		2.1

D2.2 Parameter values and the resulting Holocene relative sea-level curve for Forsmark

As discussed in the previous subsection, three parameters (*A, B_e* and *T*) need to be determined to construct a Holocene relative sea-level curve for a specific location using the PD2015 equations. The original parameter values for Forsmark, presented in PD2015, were set to *A = 165, B_e = 1200* and *T = 11250*. These parameters were determined by combining historic relative sea-level data from nearby sites with tide gauge data from PSMSL (Permanent Service for Mean Sea Level; PD2015). However, although HR2003 contains the most recent and comprehensive analysis of the historic shoreline displacement in the Forsmark area, their data was *not* included to further constrain the parameters in PD2015. As a result, there is a clear mismatch between the original Forsmark curve from PD2015 and the HR2003 data (dashed black line and red dots in Figure D-1). For comparison, the Holocene relative sea-level curve from Brydsten (2009), which was used in SR-Site (SKB 2010a), shows a significantly better agreement with the HR2003 data than the original curve described in PD2015 (blue and dashed lines in Figure D-1).

To correct for this mismatch, an updated PD2015 curve was constructed using the data from HR2003. To determine the parameter values for this curve, a wide range of parameter combinations were explored and evaluated using the least squares method. The best fit with the HR2003 data, using this methodology, was obtained with the following parameter values: *A = 253*, *B_e = 1400* and *T = 14000*. Since those values are only constrained by the HR2003 data, the resulting relative sea-level curve is only applicable for the period covered by that data, i.e. from 0 to 6.3 ka BP. For the early Holocene, there are unfortunately no equivalent data that could be used to constrain the relative sea-level parameters in the Forsmark area; thus the original relative sea-level curve from PD2015 is primarily used for this period.

The details on how the original and updated PD2015 curves are combined to construct an updated relative sea-level curve through the Holocene are summarized in Table D-2. In general, a time-dependent cubic weight function, based on the Hermite basis functions, was applied to determine the relative importance of each curve. This technique is bound to give a smooth transition between the relative sea-level curves as the Hermite functions ensure that the values as well as their derivatives are continuous through the entire interpolation domain. Hence, the weight function (f_w) is defined as:

$$f_w = \begin{cases} 0, & r \le 0, \\ -2r^3 + 3r^2, & 0 < r \le 1, \\ 1, & r > 1, \end{cases}$$ Equation D-5

where

$$r = \frac{\mathrm{t} - t_1}{t_2 - t_1},$$ Equation D-6

and t_1 and t_2 represent the start and end times (in calendar years BP) of the interpolation, respectively. The resulting relative sea-level was subsequently calculated as:

$$S = f_w S_m + (1 - f_w) S_o, \qquad \text{Equation D-7}$$

where S_m and S_o are the calculated relative sea-level using the original parameter values (from PD2015) and the updated parameter values based on the HR2003 data, respectively. Here we used $t_1 = 3.8$ ka BP and $t_2 = 8.0$ ka BP as interpolation limits. Hence, for the early Holocene (t > 8.0 ka BP), the Forsmark relative sea-level is represented by the PD2015 curve with original parameter values, and for the late Holocene (t < 3.8 ka BP) by the curve with modified parameters based on the HR2003 data. Between those time limits, the two curves were interpolated according to the cubic weight function (Table D-2).

Table D-2. Data used for the construction of the Holocene relative sea-level curve for Forsmark. The site-specific parameters A, B_e and T are used in the PD2015 equations.

Time period (ka AP)	Data used	Comments
−10.8 to −8	PD2015 with A = 165, Be = 1400 and T = 11250	Forsmark parameter values from Table 1 in PD2015.
−8 to −3.8	Interpolation	Using cubic Hermite interpolation
−3.8 to 0	PD2015 with A = 253, Be = 1400 and T = 14000	Parameters derived from the relative sea-level data in HR2003.

The chosen interpolation domain ensures that the five youngest data points in HR2003 are fully weighted ($t < 3.8$ ka BP $\Rightarrow f_w = 1$) whereas the five oldest data points receive less weight. It is thus assumed that the older data from HR2003 is less important for describing the Holocene relative sea-level development in Forsmark than the younger data. The rationale for this choice is that the older sites are located further away from Forsmark (see Figure 1-1 in HR2003), and collectively have significantly larger uncertainties due to the radiocarbon dating than the younger sites (Figure D-1). The larger uncertainty interval of these older radiocarbon dates mainly relates to them constituting bulk samples instead of dating of individual macrofossils which was the case for the younger sites.

The updated Holocene relative sea-level curve for Forsmark, used in the PSAR, is depicted by the black solid line in Figure D-1. This curve agrees significantly better with the HR2003 data than the original PD2015 curve. For the late Holocene, the updated relative sea-level curve is similar to that of Brydsten (2009) who used data from HR2003 to constrain the parameters in Påsse (2001) (Figure D-1). During the middle Holocene, the updated relative sea-level curve slowly starts evolving towards the original PD2015 curve, eventually resulting in a complete merge of the two curves at 8 ka BP.

D2.3 Comparison with tide gauges and GPS data

In contrast to PD2015, relative sea-level data from tide gauges were not used to constrain the parameters in the updated relative sea-level curve constructed here. This choice is motivated by the relatively short temporal coverage of tide gauge data (1976–2017 AD), which provides very limited information on how the shoreline displacement changed through the Holocene. It should be noted that the model from PD2015 was primarily developed to cover the Holocene, i.e. a significantly longer timescale than those covered by the tide gauge and GPS data. Therefore, the primary aim of the Holocene relative sea-level presented here is to capture the overall relative sea-level migration through the Holocene. However, because the relative sea-level evolution within the next 10 ka is highly relevant for certain aspects related to the safety assessment, e.g. emergence of new biosphere objects (see the **Biosphere synthesis report**), it is also important to ensure that the modelled Holocene relative sea-level also captures the first-order behaviour of the observed present-day relative sea-level changes.

The annual relative sea-level in Forsmark based on the tide gauge data from PSMSL (Holgate et al. 2013, PSMSL 2018) is shown in Figure D-4 (red curve). These data reveal a significant annual variability, but also a clear overall negative trend over the period covered by the data. This indicates that the post-glacial isostatic uplift is still highly active in the area and exceeds the anthropogenic sea-level rise. The negative trend is also found in the Holocene relative sea-level curve used in SR-Site (Påsse 2001, Brydsten 2009) and in the updated relative sea-level curve for the PSAR.

A linear regression of the tide gauge data reveals that the current rate of shoreline displacement in Forsmark is −4.1[5] mm a^{-1}. The relative sea-level rise in the updated curve presented here is −6.1 mm a^{-1}, which is comparable to the relative sea-level curve from SR-Site (−5.8 mm a^{-1}). Thus, both curves overestimate the negative relative sea-level rate in Forsmark by ~50 % with respect the tide gauge data.

Using Equations D-1 and D-2, it is possible to decompose the present-day relative sea-level change, predicted by the updated relative sea-level curve, into its eustatic and isostatic components. The eustatic contribution to the present-day relative sea-level change in the updated curve is only 0.4 mm a^{-1}, and the isostatic contribution amounts to −6.5 mm a^{-1}. The modelled isostatic contribution is thus comparable to the observed isostasy for Forsmark from GPS data which amounts to −6.7 mm a^{-1} (Vestøl et al. 2019).

It is possible to estimate the present-day eustatic contribution (sea-level rise) in Forsmark by taking the difference between the tide gauge data, which represents the total relative sea-level change, and the measurement of the isostatic component by the GPS. This calculation results in a present-day eustatic sea-level rise of 2.6 mm a^{-1}, thus about 2 mm a^{-1} greater than in the PD2015 model. However, it is important to note that the eustatic signal recorded in the tide gauge data is primarily a result of the current global warming, which has *not* been accounted for in the PD2015 model. All in all, it is reasonable to believe that the large difference in the eustasy between tide gauges and the PD2015 model is explained by the anthropogenic global warming.

The estimated value of the eustasy from tide gauge and GPS provided here is comparable to other studies. For instance, Johansson et al. (2002) evaluated the eustatic contribution to be 1.9 mm a^{-1} in Fennoscandia. The global-mean sea-level rise was estimated by IPCC (2013a) to be about 2 mm a^{-1} towards the end of the last century mainly due to the thermal expansion of the oceans and the melting of glaciers (except Greenland and Antarctica). In a more recent study, Nerem et al. (2018) used a 25-year time series (1993–2017) of precision satellite altimeter data and estimated the global mean sea-level rise to be 3 ±0.4 mm a^{-1} for this period. It is hence likely that the difference between the present-day relative sea-level changes resulting from the PD2015 curve and the tide gauge data (2 mm a^{-1}; see Figure D-4) can be primarily explained by the underestimated present-day eustasy in the PD2015 model.

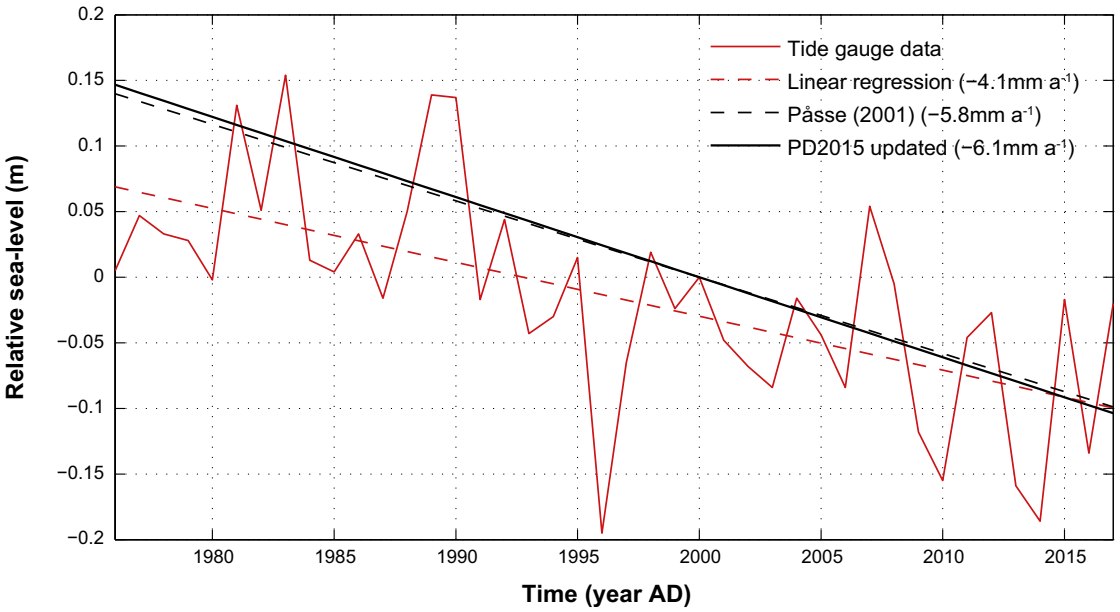

Figure D-4. *Annual relative sea-level in Forsmark (relative to year 2000) from tide gauge data (Holgate et al. 2013, PSMSL 2018) (red solid curve), its linear regression (red dashed line), and modelled relative sea-level using the model from Påsse (2001) (parameter values from Brydsten 2009) and the PD2015 equations with updated parameters (used in the PSAR; black solid line). The legend also shows the average present-day Forsmark relative sea-level change, given by the slope of each curve. The zero level is highlighted by the grey thin line.*

[5] The linear regression, which is used to calculate this value, is statistically significant at the 0.01 level ($p < 0.01$).

D2.4 Confidence intervals

The empirical modelling approach of the Holocene relative sea-level entails that the uncertainties in the observational data can be used to estimate confidence intervals. The study of HR2003 presents two major sources of quantifiable errors associated with (i) the estimated threshold height for the investigated lake, and (ii) the radiocarbon dating. The errors associated with the radiocarbon dating represent uncertainties in the age of the measured material and are depicted as horizontal bars in Figure D-1. In general, the radiocarbon-based errors are significantly larger (several orders of magnitude) than that of the threshold height measurements (HR2003). Therefore, in the following analysis, we only use the reported errors from radiocarbon dating in HR2003 to construct confidence intervals to the main relative sea-level curve.

As already discussed, the reported radiocarbon-induced error in HR2003 is significantly larger for the older data points than for the younger ones (Figure D-1). Because of this difference, the uncertainty ranges for the five youngest data points were computed separately from the older data. This implies that the data is effectively separated into two bins with different error characteristics. To construct the uncertainty ranges for each bin, the part of the relative sea-level curve covered by that bin was shifted along the x-axis until a best-fit agreement (using the least square method) with the radiocarbon-based confidence intervals from HR2003 was obtained. This approach hence resulted in four confidence interval curves, separated into the two bins on both sides of the main relative sea-level curve. The confidence intervals on each side of the main relative sea-level curve were ultimately connected using linear interpolation.

The resulting confidence intervals for the Forsmark relative sea-level are shown in Figure D-5. There is a clear transition of the uncertainty range between 3.8 and 4.6 ka BP as a result of the larger errors associated with the older data. This means that the 95 % confidence range of the Forsmark relative sea-level, based on uncertainties in the radiocarbon dating in HR2003, increases from ~3 m to ~10 m from the late to the middle Holocene.

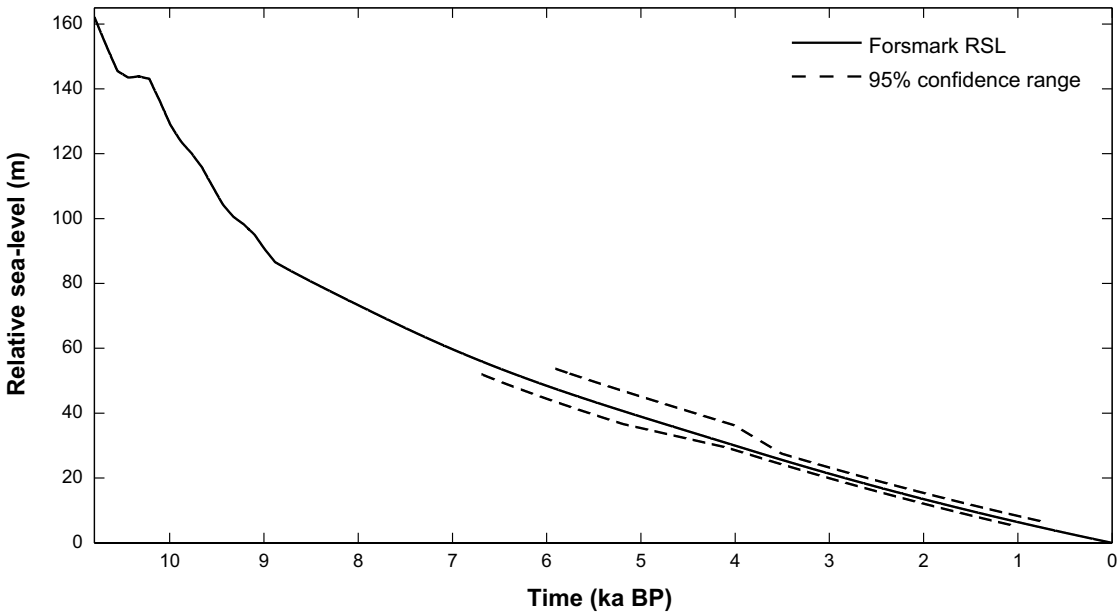

Figure D-5. *The Holocene relative sea-level curve for Forsmark used in the PSAR, constructed using the methodology summarized in Table D-2 (black solid line). The black dotted lines represent the lower and upper confidence intervals (at 95 % level) based on uncertainties in the radiocarbon dating (HR2003). The details on how the confidence intervals have been computed are provided in Section D1.4.*

D3 Conclusions

In this appendix an updated Holocene relative sea-level curve for Forsmark, ranging from 10.8 to 0 ka BP, has been described, based on a relatively recent and comprehensive empirical model (the PD2015 model). This model is considered to be an improved version of the model presented in Påsse (2001), which was used in previous safety assessments, e.g. SR-Site (SKB 2010a).

The difference in the Holocene relative sea-level representation between the PSAR and SR-Site is shown in Figure D-6. The updated relative sea-level curve results in only minor changes for the late and middle Holocene with respect to SR-Site. However, in the early Holocene, the difference becomes progressively larger, culminating at ~40 m around 10 ka BP. The small difference between the relative sea-level curves in the late and middle Holocene stems from using the same observational dataset (HR2003) to constrain the curves for those periods, whereas the relatively large difference in the early Holocene primarily results from an improved representation of the eustatic development in PD2015 compared to Påsse (2001).

The updated Holocene curve is used in combination with GIA modelling in the long-term future projections of the relative sea-level development at Forsmark for the *reference glacial cycle climate case* (Section 4.5.2), *global warming climate case* (Section 5.1.3) and *extended global warming climate case* (Section 5.2.3). It should be noted, however, that the analysis in this Appendix also supports the continued use of the historical relative sea-level curve developed for the previous safety assessments SR-Site and SR-PSU.

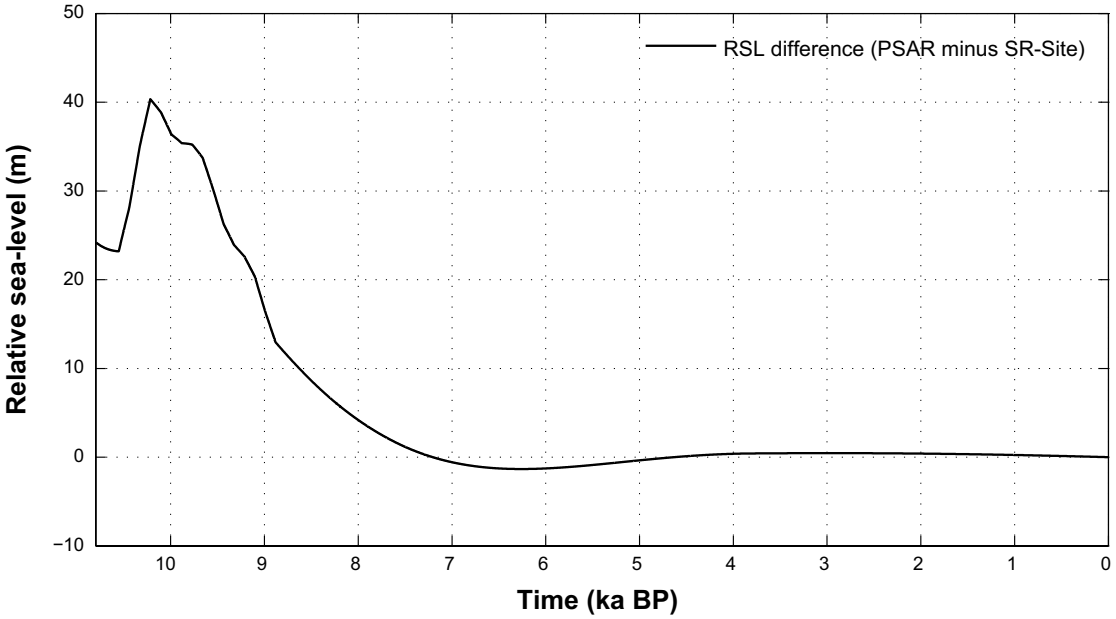

Figure D-6. *Difference in the Holocene relative sea-level development for Forsmark used in this report and in SR-Site. Note that the difference is small for the late and middle Holocene but becomes progressively larger for the early Holocene. The zero level is highlighted by the grey thin dashed line.*

Appendix E

IPCC Representative Concentration Pathways (RCP)

The assumed levels of warming in the *global warming climate case* (Section 5.1) and *extended global warming climate case* (Section 5.2) are comparable to the expected warming resulting from the different Representative Concentration Pathways (RCPs; Meinshausen et al. 2011). The RCPs are IPCC mitigation scenarios that assume policy actions will be taken to achieve certain emission targets. In IPCC (2013a), four RCPs have been formulated that are based on a range of projections of future population growth, technological development, and societal responses: RCP2.6, RCP4.5, RCP6.0 and RCP8.5.

The number associated with the RCP represents a rough estimate of the anthropogenic radiative forcing in year 2100 AD (relative to preindustrial conditions) under that scenario. For example, the radiative forcing in RCP8.5 increases throughout the twenty-first century before reaching a level of about 8.5 Wm^{-2} at the end of the century. In addition to this "high emission" scenario, there are two intermediate scenarios, RCP4.5 and RCP6, and a low so-called peak-and-decay scenario, RCP2.6, in which radiative forcing reaches a maximum near the middle of the twenty-first century before decreasing to an eventual nominal level of 2.6 Wm^{-2}. In addition, Extensions to the RCP scenarios, so-called ECPs, also exist that project emissions to 2300 AD (Meinshausen et al. 2011).

Table E-1 shows the atmospheric CO_2 concentration, cumulative fossil-fuel emissions and projected range of global warming by 2100 AD and 2300 AD for each RCP/ECP. In this report, the *global warming climate case* represents a situation with moderate global warming, approximately corresponding to the RCP4.5 scenario, whereas the *extended global warming climate case* assumes strong global warming comparable to RCP8.5.

Note that all RCP scenarios assume very low emissions beyond 2300 AD (Fyke and Matthews 2015) implying that the cumulative emissions will remain relatively constant for the subsequent centuries to millennia. However, even if all emissions of CO_2 and other greenhouse gases were to end at 2300 AD, the atmospheric CO_2 and the global temperature would remain high for a long period of time (Appendix F). It has been shown that even 10 ka after the CO_2 emission have ceased, between approximately 10 and 30 % of emissions may remain in the atmosphere (Archer et al. 2009). The temperature is expected to decline even more slowly: it is estimated that between 30 and 85 % of the maximum temperature anomaly persists for longer than 10 ka (Appendix F).

Table E-1. Atmospheric CO_2 concentration, cumulative fossil-fuel emissions and projected range of global annual mean surface air temperature increase by 2100 AD and 2300 AD for RCP2.6, RCP4.5, RCP6.0 and RCP8.5. The projected surface air temperature is shown as 5 to 95 % percentiles. The atmospheric CO_2 concentration for each scenario is taken from Meinshausen et al. (2011), and the projected surface air temperature increase is from Collins et al. (2013). The cumulative emissions are approximate estimates with respect to the pre-industrial era from Fyke and Matthews (2015). The corresponding expected temperature increase at Forsmark until 2100 AD is discussed in Section 2.2.2.

		RCP2.6	RCP4.5	RCP6.0	RCP8.5
Atmospheric CO_2 concentration (ppmv)	2100 AD	420	540	670	940
	2300 AD	361	543	752	1962
Cumulative fossil-fuel emissions (Pg C)	2100 AD	600	1100	1500	2200
	2300 AD	400	1300	2200	5200
Projected surface air temperature increase (°C)	2100 AD	0.3–1.7	1.1–2.6	1.4–3.1	2.6–4.8
	2300 AD	0.0–1.2	1.5–3.5	4.2*	3.0–12.6

* No temperature range is given for RCP6.0 until 2300 AD as data only exists from two climate models (Collins et al. 2013). The value 4.2 °C represents the average global-mean surface air temperature increase between those two models.

Appendix F

The construction of the surface air temperature and precipitation at Forsmark until 12000 AD

F1 Surface air temperature change until 12000 AD

F1.1 Background and theory

The construction of the annual mean surface air temperature until 12000 AD at Forsmark, illustrated in Figure 5-2 and Figure 5-14, was predominately based on the present knowledge from contemporary studies of long-term climate change (Table F-1). However, because the number of studies covering the topic of anthropogenic climate change over these long time-scales is very limited, it is also helpful to use conceptual modelling to gain a better understanding on the important mechanisms behind the long-term temperature change. Here a zero-order energy balance model (EBM) is used for that purpose (e.g. North et al. 1981, North and Stevens 2006):

$$C\frac{\partial T_s}{\partial t} = \frac{S}{4}(1-\alpha) - (A + BT_s), \qquad \text{Equation F-1}$$

where t is time, T_s the global annual mean surface air temperature, and C a numerical constant describing the heat capacity. Equation F-1 describes the evolution of the global mean surface air temperature as a result of the global mean net radiation at the top of the atmosphere, decomposed into the net incoming short-wave radiation ($S(1-\alpha(/4)$ and the outgoing long-wave radiation ($A + BT_s$). The net short-wave radiation is estimated from the solar constant S and the planetary albedo α, and the long-wave radiation is here assumed to increase linearly with the surface air temperature. The numerical constant A describes a background state about which the long-wave radiation is linearised, and the numerical constant B is the inverse of the climate sensitivity, i.e. it represents how the outgoing long-wave radiation responds to changes in temperature. Note that the relationship between temperature and outgoing long-wave radiation is approximately linear only for a realistic range of "Earth-like" temperatures (e.g. North and Stevens 2006). In reality, the long-wave radiation depends on the fourth-power of the absolute temperature according to Stefan-Boltzmann law.

To introduce the effect of anthropogenic greenhouse gases, the background long-wave radiation is first decomposed into a part describing the natural greenhouse gas effect (A_0) and another part describing the anthropogenic contribution (ΔA), such that $A = A_0 + \Delta A$. Similarly, the surface air temperature is decomposed as $T_s = T_{s0} + \Delta T_s$, where T_{s0} describes the global mean surface air temperature in the absence of anthropogenic greenhouse forcing and ΔT_s is the global mean temperature response to anthropogenic greenhouse gas forcing. Using the decompositions of A and T_s, it is possible to separate Equation F-1 into two new equations:

$$C\frac{\partial T_{s0}}{\partial t} + BT_{s0} = \frac{S}{4}(1-\alpha) - A_0, \qquad \text{Equation F-2}$$

and

$$C\frac{\partial \Delta T_s}{\partial t} + B\Delta T_s = -\Delta A. \qquad \text{Equation F-3}$$

Equation F-2 describes the evolution of the unperturbed global mean surface air temperature, and Equation F-3 yields the global mean temperature response to anthropogenic greenhouse gas forcing. To simplify the usage of the conceptual EBM, it is assumed that the combined effect of all anthropogenic greenhouse gases is represented only by the CO_2. The radiative forcing from CO_2 has been estimated to high accuracy from detailed radiative-transfer calculations (e.g. Myhre et al. 1998):

$$\Delta A = -5.35\ln(p/p_0), \quad , \qquad \text{Equation F-4}$$

where p_0 is the atmospheric CO_2 concentration in the absence of anthropogenic influence (~280 ppmv for pre-industrial conditions) and p describes the total CO_2 concentration including the anthropogenic contribution. Substituting Equation F-4 into Equation F-3 yields:

$$C\frac{\partial \Delta T_s}{\partial t} + B\Delta T_s = 5.35\ln(p/p_0). \qquad \text{Equation F-5}$$

Equation F-5 describes the temporal evolution of the global mean surface air temperature response to changes in the atmospheric CO_2 concentration. The magnitude and timing of the temperature response to a specific CO_2 pathway is largely controlled by the parameters B and C. The magnitude of the response can be estimated by assuming that the climate is in equilibrium ($\partial \Delta T_s / \partial t = 0$), resulting in $\Delta T_s = 5.35 \ln (p/p_0)/\mathrm{B}$, whereas the typical timescale (relative to the CO_2 forcing) is determined by $\tau = C/B$. Here $B = 1.9$ W m^{-2} K^{-1} is used, which is within the typical range of values found by satellite measurement and in the literature (North and Stevens 2006). Over the long time-scales considered here, the Earth's heat capacity is almost entirely controlled by the world's oceans. This means that the total heat capacity can be estimated as $C = c_{pw} \rho_w h_{ocean}$, where c_{pw} and ρ_w are the specific heat capacity and density of sea water, respectively, and h_{ocean} is taken to be the average depth of the oceans (3700 m). In reality only the thermal capacity of the upper layers of the oceans (first couple of hundred meters) is available on seasonal to centennial timescales, after which the heat in the upper ocean would be gradually transferred to the deep ocean by mixing processes. Hence, in a situation with a persistent atmospheric forcing over millennial timescales h_{ocean} (and therefore C) would effectively increase with time. However, because the time dependency of the EBM is only used for illustration in this chapter, a constant effective heat capacity reasonable for the long time-scales considered here (10 ka) is chosen for simplicity. In summary the total heat capacity assumed here is $C = (4 \times 10^3)(1 \times 10^3)(3.7 \times 10^3) \approx 1.5 \times 10^{10}$ J m^{-2} K^{-1}, resulting in an adjustment timescale of $\tau \approx 250$ years. Although this value of τ should be interpreted carefully due to the simplistic treatment of C, it demonstrates that global warming may continue for several centuries after the emissions have ceased.

In order to illustrate the behaviour of the EBM (Equation F-5), the resulting atmospheric CO_2 concentrations from the high emission scenario (5120 Pg C cumulative emissions) in Clark et al. (2016) are used (Figure F-1a). The amplitude of the associated global mean temperature response in the EBM is typically only 60–70 % of that in Clark et al. (2016) (Figure F-1b). This result is not surprising as many important climate feedbacks accounted for in Clark et al. (2016) are omitted in the EBM, e.g. increased melting of sea ice and land-based glaciers and ice-sheets, which would result in a reduced planetary albedo. As discussed in 5.2.3, the strong melting of the ice-sheets under the high emission scenario in Clark et al. (2016) is largely responsible for the relatively large projections of sea-level rise until 12000 AD found in their study.

However, aside from the amplitude, typical features of the CO_2-induced global mean temperature response in more sophisticated models are also captured by the conceptual EBM. For example, in both the models used by Clark et al. (2016) and the EBM, the initial temperature increase culminates sometime after the maximum CO_2 concentrations have been reached, after which the temperature slowly returns towards pre-industrial values. Furthermore, in both models the fractional reduction of the global mean temperature from its maximum to 12000 AD is significantly smaller than the equivalent reduction of CO_2 (see also Eby et al. 2009). This shows that the effects of global warming are present for a relatively long time even after the atmospheric CO_2 has returned to pre-industrial levels.

Figure F-1 also shows the global mean temperature from the conceptual EBM assuming that the climate responds instantaneously to the CO_2 forcing (i.e. the equilibrium response; $\partial \Delta T_s / \partial t = 0$ in Equation F-5). This curve is included to identify times during which the adjustment timescale plays an important role for the ΔT_s response, and when it can be neglected. In general, the equilibrium temperature response in the EBM is similar to the "full" response from the time of the maximum temperature change at ~3000 AD until 12000 AD (Figure F-1b). Hence, for this time period the surface air temperature is expected to be in quasi-equilibrium with the CO_2-forcing, implying that the amplitude of the temperature response within this time interval should be approximately proportional the amount of anthropogenic emissions remaining in the atmosphere.

In contrast to the latter part of the 10000 year period, for which the surface air temperature and CO_2 forcing are approximately in phase, the maximum temperature response reveals a significant time lag relative to the maximum CO_2 forcing. This is illustrated by the difference in timing of the maximum temperature responses between the thin and thick black curves in Figure F-1. As discussed above, this difference is ultimately controlled by the adjustment timescale of the EBM, given by C/B. However, the time lag is also dependent on the amplitude of the forcing, hence the peak CO_2 concentration. This is illustrated in Figure F-2, which shows the time lag of the maximum surface air temperature in the EBM following an instantaneous CO_2 pulse of different amplitudes. The timing of the peak temperature response is more sensitive at lower CO_2 concentrations than at higher ones. For example, increasing the CO_2 concentration relative to pre-industrial from 2 to 3 (560 to 840 ppmv, respectively, assuming $p_0 = 280$ ppmv as the baseline concentration) results in a similar delay of the peak temperature response (~100 years) as in the case in which the fractional CO_2 increases from 4 to 9 (1120 to 2520 ppmv for $p_0 = 280$ ppmv, respectively).

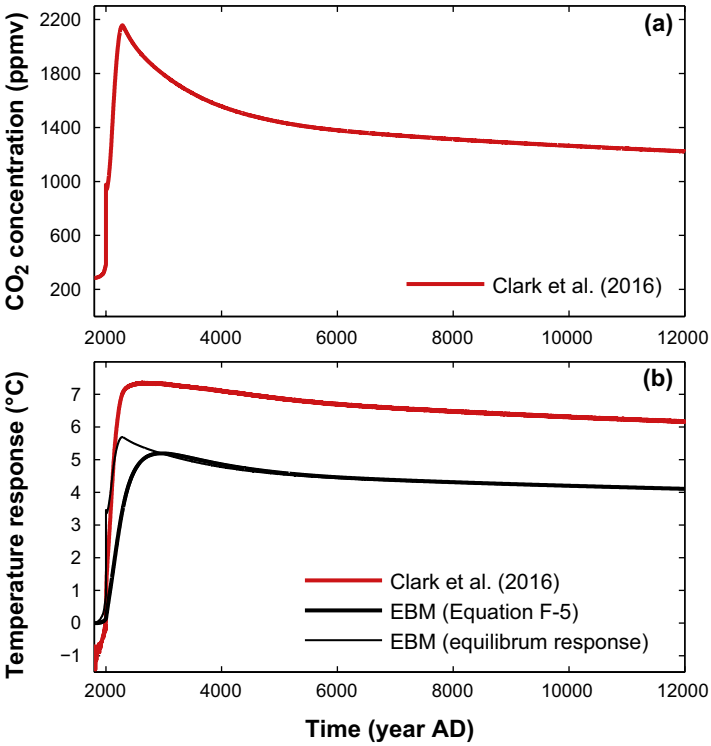

Figure F-1. *(a) Atmospheric CO2 concentration resulting from the high emission scenario of 5120 Pg C cumulative emissions in Clark et al. (2016), and (b) associated global mean surface air temperature responses as computed by Clark et al. (2016) (red curve), the conceptual EBM (Equation F-5; thick black curve) and the EBM, but assuming that the temperature is always in equilibrium with the CO2 forcing ($\partial \Delta Ts/\partial t = 0$) in Equation F-5; thin black line). The atmospheric CO2 concentration and temperature response from Clark et al. (2016) represent the ensemble mean across five versions of two different intermediate complexity Earth system models. In all the simulations in Clark et al. (2016), anthropogenic CO2 emissions were assumed to increase linearly between 2000 and 2100 AD, after which they drop linearly back to zero by 2300 AD.*

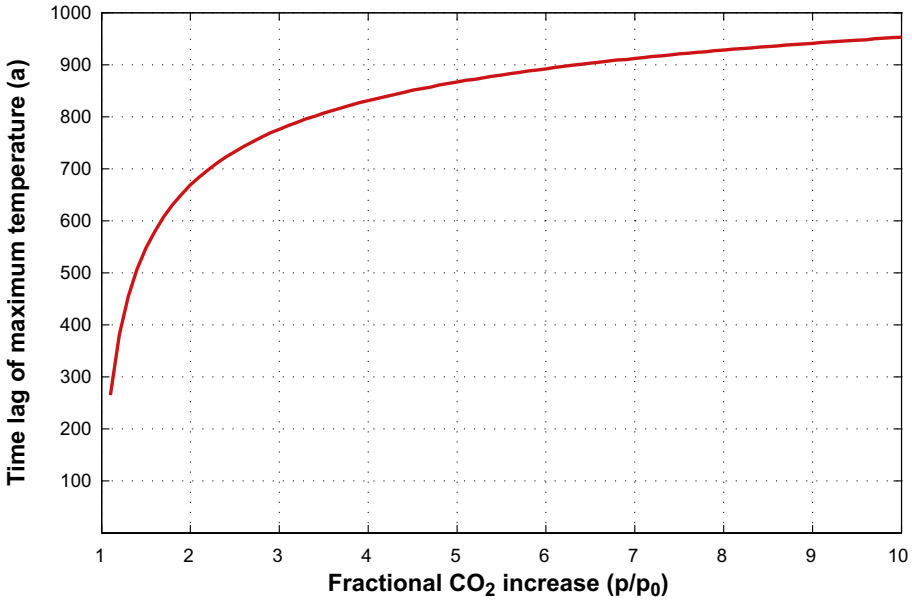

Figure F-2. *Time lag of the maximum global mean surface air temperature response following an instantaneous CO_2 pulse of different amplitudes (given by the x-axis).*

F1.2 Global mean surface air temperature change

In this section, results from modelling studies on long-term climate change are combined with the theoretical understanding from the conceptual EBM (Equation F-5) to estimate the lower and upper bounds of the global annual mean surface air temperature evolution until 12000 AD. The evaluation is performed for both a moderate global warming case, comparable to RCP4.5 and the *global warming climate case*, and a strong global warming case which approximately corresponds to RCP8.5 and the *extended global warming climate case*.

The studies used to estimate the global mean surface air temperature until 12000 AD are listed in Table F-1. The number of studies covering the temperature response over these timescales is very limited. Therefore, also shorter-range climate projections from the IPCC (Collins et al. 2013) are used in the evaluation, in particular for estimating the range of the projected temperature increase in the near future. The values used to construct the range of the global annual mean surface air temperature for the *global warming* and *extended global warming climate cases* are summarised in Table F-2, and the resulting temperature curves are shown in Figure F-3. The motivations and assumptions behind the values in Table F-2, and hence the temperature curves in Figure F-3, are discussed for different time periods in the following subsections.

Table F-1. Summary of the projected global annual mean surface air temperature change (relative to present) until 12000 AD as reported in the literature. The ranges in square brackets represent uncertainties associated with inter-model differences and/or internal variability. Only studies in which the models are integrated using historical emissions and realistic emission scenarios, comparable to RCP4.5 and RCP8.5 (Appendix E), are listed. In the following, scenario B1 and cumulative emissions < 3000 Pg C are comparable with RCP4.5 (*global warming climate case*), and scenario A2 and cumulative emissions > 5000 Pg C are comparable with RCP8.5 (*extended global warming climate case*).

Reference	Emission scenario/ Total carbon emissions	Max. ΔT (°C)	Timing of max. T increase (AD)	ΔT 2100 AD (°C)	ΔT 12000 AD (°C)
Mikolajewicz et al. (2007)[1]	B1[2]	2	2500	1	
	A2[2]	5	3000	2	
Eby et al. (2009)	1280 PgC[3]	2.5	3800	0.8	1.5
	2560 PgC[3]	4.7	3000	1.7	3.1
	5120 PgC[3]	7.8	3200	3.0	5.9
Collins et al. (2013)	RCP4.5			1.8[4] [1.1–2.6]	
	RCP8.5			3.7[4] [2.6–4.8]	
Clark et al. (2016)[5]	1280 PgC[6]	2.0 [0.8–3.2]	2300	1.3 [0.4–2.2]	1.3 [0.5–2.2]
	2560 PgC[6]	4.1 [3.0–5.2]	2500	2.4 [1.2–3.6]	2.9 [2.4–3.5]
	5120 PgC[6]	7.4 [7.0–7.7]	2600	3.9 [2.2–5.6]	6.2 [5.5–6.8]

[1] Earth system model simulations are run until 5000 AD.
[2] Emissions follow the SRES emission scenarios (used in the fourth assessment IPCC report, IPCC 2007) until 2100 AD, after which they are instantaneously reduced to zero.
[3] Emissions follow the A2 SRES emission scenario until 2100 AD, after which they decline linearly to zero by 2300 AD. The scenarios were then created by scaling the A2 emissions such that the cumulative emissions reached the values reported in this table by 2300 AD.
[4] Same as in Table E-1.
[5] Ensemble-mean surface air temperature response across eight versions of two different intermediate complexity Earth system models.
[6] Emissions increased linearly between 2000 and 2100 AD, after which they decline linearly back to zero by 2300 AD.

Table F-2. Construction of the lower and upper bounds, and the average change of the global annual mean surface air temperature change until 12000 AD (relative to present) for the *global warming* and the *extended global warming climate cases* (see also Figure F-3). The average temperature change has been calculated using average values of the parameters that were used construct the lower and upper bounds. For a description on how these parameters and the resulting temperature bounds have been derived, see the text.

Part of ΔT curve	Global warming			Extended global warming			Based on
	Lower bound	Average change	Upper bound	Lower bound	Average change	Upper bound	
ΔT at 2100 AD	1.1 °C	1.9 °C	2.6 °C	2.6 °C	3.7 °C	4.8 °C	Collins et al. (2013)
Maximum ΔT	1.7 °C	3.7 °C	6.5 °C	4.9 °C	8.3 °C	12.5 °C	Eby et al. (2009), Clark et al. (2016)
Timing of maximum ΔT	2150 AD	2475 AD	2800 AD	2550 AD	2875 AD	3200 AD	Eby et al. (2009), Meinshausen et al. (2011), Clark et al. (2016), Lord et al. (2016)
ΔT at 12000 AD	0.5 °C	1.9 °C	4.6 °C	2.5 °C	5.6 °C	10.6 °C	Archer et al. (2009), Eby et al. (2009), Clark et al. (2016), EBM (Equation F-5)

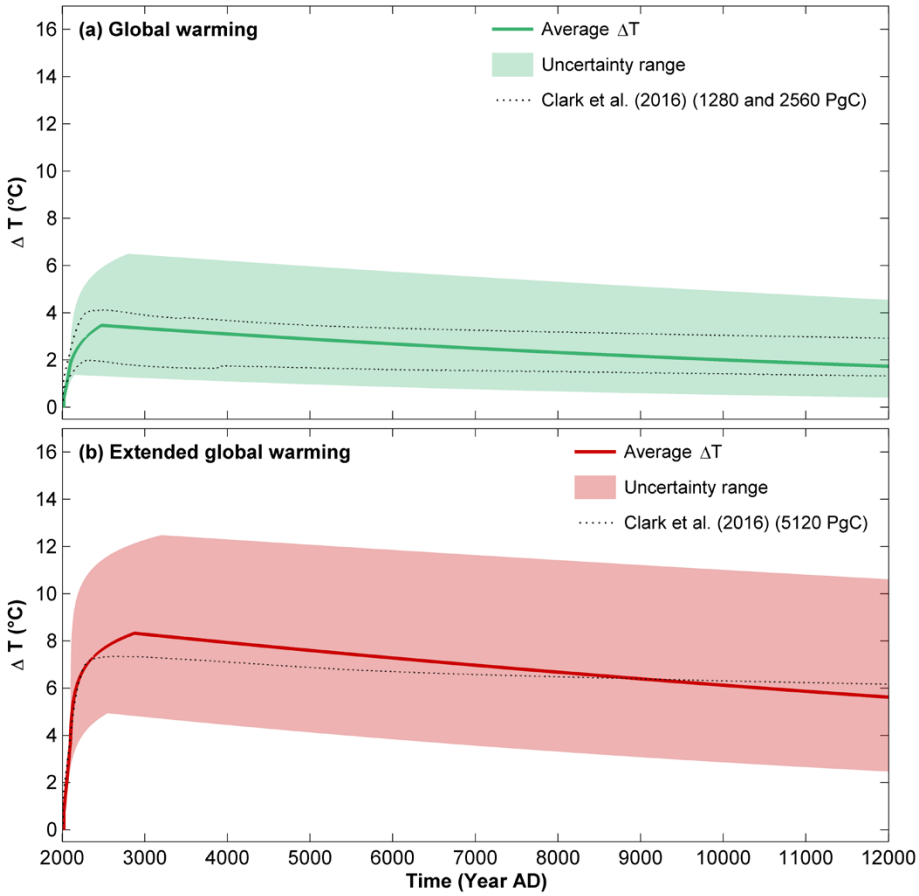

Figure F-3. *Constructed global annual mean surface air temperature change until 12000 AD (relative to present) for (a) the global warming and (b) the extended global warming climate cases. The uncertainty range has been constructed using the values in Table F-2. The average temperature change ("Average ΔT") has been calculated using average values of the parameters that were used construct the lower and upper bounds. To that end, average ΔT illustrates a typical mid-range temperature evolution over the next 12000 AD. The dotted lines show the evolution of ensemble-mean temperature change from the Clark et al. (2016) multi-model projections with 1280 and 2560 Pg C cumulative emissions (comparable with the global warming climate case; panel a), and 5120 Pg C cumulative emissions (comparable with the extended global warming climate case; panel b). Typical inter-model differences in the Clark et al. (2016) projections are shown in Table F-1.*

F1.2.1 Temperature change until 2100 AD

The global annual mean surface air temperature change until 2100 AD is completely based RCP4.5 and RCP8.5 scenarios from IPCC AR5 (Collins et al. 2013). The lower and upper bounds represent the 5 % and 95 % percentile of the distribution across all participating climate models (see also Table E-1).

F1.2.2 Maximum surface air temperature change

The maximum global annual mean surface air temperature change is first evaluated using the ratio of the peak temperature change to the temperature change at 2100 AD in Mikolajewicz et al. (2007), Eby et al. (2009) and Clark et al. (2016). These ratios are then multiplied by the 2100 AD temperature changes from Collins et al. (2013) (Table F-2) to obtain the range of peak temperatures for each climate case.

The lowest ratios (1.5 and 1.9), obtained from Clark et al. (2016), are multiplied by the lowest IPCC warming estimates for 2100 AD to yield the lower limit of the maximum temperature response. Similarly, the highest ratios (1.9 and 2.6; from Eby et al. 2009) are used in combination with the highest IPCC warming estimates to obtain the upper limit of the maximum temperature response.

F1.2.3 Timing of maximum surface air temperature change

The idealised experiments with the EBM (Equation F-5) suggest that the time of the peak temperature, following a specific CO_2 pathway, should increase as a result of higher emissions (Figure F-2). This is generally also the case in the studies of Eby et al. (2009) and Clark et al. (2016) (Table F-1). The only exception is found for low emissions in Eby et al. (2009), which results in a delayed temperature increase at around 3500–4000 AD due to "flushing events in the Southern Ocean" (Eby et al. 2009). However, since the existence of these events appears to be highly model-dependent, and non-existent in most Earth system models (Archer et al. 2009), they have been neglected in the present analysis.

An interesting feature in Table F-1 is the overall difference in timing of the peak temperature between Eby et al. (2009) and Clark et al. (2016). Except for the low-emission scenario in Eby et al. (2009), discussed above, the temperatures in Eby et al. (2009) typically reach their maximum values ~500 years later than in Clark et al. (2016), despite using comparable emission pathways. In other words, this means that the maximum temperature response lags the maximum CO_2 forcing by ~700–900 years in Eby et al. (2009) and ~50–300 years in Clark et al. (2016). For comparison, Lord et al. (2016) reported temperature lag times of ~60–700 years for a broad range of emission pulses between 1000 and 20000 Pg C. Hence, the results in Lord et al. (2016) broadly fall within the range of the lag times found in Eby et al. (2009) and Clark et al. (2016).

In addition to the time delay following the peak CO_2 forcing, the timing of the peak temperature response is naturally also dependent on the CO_2 pathway itself, in particular the time at which the CO_2 maximum is reached. The CO_2 pathways in both Eby et al. (2009) and Clark et al. (2016) assume peak emissions by year 2100 AD, resulting in a peak atmospheric CO_2 concentration by 2200–2250 AD for the lower emissions and 2250–2300 AD for the higher emissions. The timing of peak emissions in the IPCC RCP8.5 scenario is comparable to Eby et al. (2009) and Clark et al. (2016), whereas the RCP4.5 scenario assumes that emissions peak already by ~2050 AD, resulting in maximum concentrations by ~2100 AD (Meinshausen et al. 2011).

In summary, the timing of the peak temperature in the constructed global mean temperature anomaly (Table F-2 and Figure F-3) is primarily based on Clark et al. (2016) for the lower bound and Eby et al. (2009) for the upper bound. In addition to using Clark et al. (2016), the peak temperature of the lower bound in the *global warming climate case* has been shifted further toward the present-day by 100 years to account for the relatively early peak emissions from the RCP4.5 scenario (Meinshausen et al. 2011).

F1.2.4 Temperature change beyond the maximum until 12000 AD

The temperature change at 12000 AD is first evaluated by how much of the maximum temperature anomaly in Eby et al. (2009) and Clark et al. (2016) remains at 12000 AD. In Eby et al. (2009), the temperature by 12000 AD has declined to about 60 % of its maximum value for the lower emission scenarios and to about 75 % for the higher emissions. In Clark et al. (2016) the corresponding numbers are slightly higher, being approximately 65 and 85 %, respectively.

As illustrated by the zero-order EBM in Section F1.1, the temperature anomaly beyond the peak response should be roughly proportional to the remaining CO_2 concentration in the atmosphere (Figure F-1). This suggests that the slower temperature decline in Clark et al. (2016) relative to Eby et al. (2009) can be explained by a slower decline in the atmospheric CO_2 forcing. The emissions remaining by 12000 AD in Clark et al. (2016) are indeed consistently 5–10 % higher than in Eby et al. (2009), suggesting that the prediction from the EBM is (at the very least) qualitatively accurate.

It is important to note that although the Earth system model in Eby et al. (2009) predicts a faster decline of the CO_2 (and hence the temperature anomaly) compared to the multi-model ensembles in Clark et al. (2016), it still predicts a significantly slower decline than most other comparable models (Archer et al. 2009). This means that the studies of Eby et al. (2009) and Clark et al. (2016) do not cover the full range of literature values regarding the rate of temperature decline until 12000 AD. However, there is unfortunately not much information on the long-term global mean temperature change until 12000 AD from other Earth system models. Therefore, the proportional relationship between CO_2 forcing and temperature response found in the EBM is employed to extrapolate the temperature anomalies from Eby et al. (2009) into a regime of lower CO_2 concentrations. The result from this exercise is summarized in Table F-3.

As a first step, the global mean temperature anomaly at 12000 AD from Eby et al. (2009) is reproduced with the EBM. The reported climate sensitivity (global mean surface air temperature increase resulting from doubling of the atmospheric CO_2 concentration) in the model of Eby et al. (2009) is 3.5 °C. Assuming that the temperature is in equilibrium ($\partial \Delta T_s / \partial t = 0$ in Equation F-5), the global mean temperature change can be predicted by:

$$\Delta T_{s,ebm} = \frac{3.5}{\ln(2)} \ln(p/p_0). \qquad \text{Equation F-6}$$

Applying Equation F-6 to the three emission scenarios from Eby et al. (2009) results in very similar temperature responses at 12000 AD as obtained in Eby et al. (2009) (Table F-3). This result enables the use of Equation F-6 for predicting the temperature response to other CO_2 concentrations.

According to Archer et al. (2009) the models with the fastest CO_2 decline over the next 10000 years have about ~50 % less emissions remaining at 12000 AD than in the model of Eby et al. (2009). Assuming 50 % less CO_2 concentrations than in Eby et al. (2009), Equation F-6 yields a reduction of the temperature anomaly by ~45 % for lower emissions and ~35 % for the highest emission scenario. In other words, the reduced CO_2 forcing at 12000 AD means that only ~30–50 % of the maximum temperature anomaly persists at 12000 AD as opposed to ~60–75 % in Eby et al. (2009).

The fractional temperature decline at 12000 AD relative to the peak temperature, as predicted by the EBM with 50 % less remaining emissions, is used to construct the lower bound of the global mean surface air temperature curve (Table F-2 and Figure F-3). The upper bound of the 12000 AD temperature response is constructed using the fractional temperature decline from Clark et al. (2016), amounting to 70 % and 85 % of the peak temperature for *global warming* and *extended global warming climate cases*, respectively.

Table F-3. Atmospheric CO_2 concentration (p) and associated global annual mean surface air temperature anomalies at 12000 AD as predicted by the Earth System Model in Eby et al. (2009) ($\Delta T_{s,eby}$) and by Equation F-6 ($\Delta T_{s,ebm}$). The baseline CO_2 concentration is p_0 = 320 ppmv (from Eby et al. 2009). The right-most column shows the projected temperature anomaly (using Equation F-6) with the assumption that 50 % less of the emissions are remaining in the atmosphere by 12000 AD compared with Eby et al. (2009), thus roughly corresponding to lower-end estimates in Earth system models (Archer et al. 2009), see also the text. The %-values within square-brackets show how much of the maximum temperature increase remains by 12000 AD.

Scenario	p (ppmv)	$\Delta T_{s,eby}$ (°C)	$\Delta T_{s,ebm}$ (°C)	$\Delta T_{s,ebm}$ with 50 % less emissions remaining (°C)
1280 PgC	430	1.5 [60 %]	1.5	0.8 [32 %]
2560 PgC	600	3.1 [66 %]	3.2	1.8 [38 %]
5120 PgC	1050	5.9 [76 %]	6.0	3.8 [49 %]

F1.3 Surface air temperature change at Forsmark

To construct the annual mean surface air temperature change at Forsmark until 12000 AD two major modifications are made to the global annual mean curve (Table F-4). First, it is assumed that the temperature increase at Forsmark will be higher than the global average due to the Arctic temperature amplification (Section F1.3.1). Second, the potential impact of a collapse (defined here as a slowdown to an "off" state) of the Atlantic Meridional Overturning Circulation (AMOC) on the Forsmark temperature is considered (Section F1.3.2). The resulting estimated changes of the annual mean surface air temperature until 12000 AD at Forsmark are shown in Figure F-4. The specific modifications of these curves in relation to the global mean curves in Figure F-3 are summarized in Table F-4 and justified in the next two subsections.

Table F-4. Modifications of the constructed global annual mean surface air temperature change (Table F-2, Figure F-3), utilised to construct the annual mean surface air temperature change at Forsmark until 12000 AD (Figure F-4). The specific values in the table are discussed and justified in the text.

Modification	Global warming			Extended global warming			Based on
	Lower bound	Average change	Upper bound	Lower bound	Average change	Upper bound	
Arctic temperature amplification factor (1 = global average)	1.2	1.35	1.5	1.2	1.35	1.5	Eby et al. (2009), Collins et al. (2013)
ΔT due to AMOC collapse	−2.5 °C	-	-	−2.5 °C	-	-	Mikolajewicz et al. (2007), Pimenoff et al. (2012), Liu et al. (2017)
Duration of AMOC collapse	300 years	-	-	300 years	-	-	Liu et al. (2017)
Start year of AMOC collapse	2150 AD	-	-	2150 AD	-	-	Mikolajewicz et al. (2007), Pimenoff et al. (2012)

F1.3.1 Arctic temperature amplification

A well-known feature of anthropogenic global warming is that the northern high latitudes typically warm at a faster rate than the global average. State-of-the-art climate models demonstrate that the mean Arctic (67.5 °N to 90 °N) warming is between 2.2 and 2.4 times the global average warming by 2100 AD depending on the emission scenario (Collins et al. 2013). The same set of models project that the warming in the Forsmark region is between 1.25 and 1.5 times the global average by the end of the 21st century regardless of emission scenario (Figure 12.10 in Collins et al. 2013). The reduced temperature amplification at Forsmark compared with the Arctic average is partly explained by the relatively southern location of Forsmark (at 60 °N), but also by a weakened AMOC in the future climate projections (Section F1.3.2).

The Forsmark temperature amplification on longer timescales can be estimated from the study of Pimenoff et al. (2012), which shows the projected annual mean surface air temperature evolution until 12000 AD at the grid point closest to Olkiluoto in Finland from the model simulation in Eby et al. (2009). Since the distance between Forsmark and Olkiluoto is only ~200 km, the projected polar temperature amplification for Olkiluoto is likely also a good estimate for Forsmark. In summary, the model in Eby et al. (2009) predicts that the warming in Olkiluoto over the next 10000 years is approximately between 1.2 and 1.35 times the global average, thus slightly lower than the estimated temperature amplification in Collins et al. (2013).

In the following, the Forsmark temperature amplification based on low-end estimate from Pimenoff et al. (2012) is used to construct the lower bound of Figure F-4, and the high-end estimate from Collins et al. (2013) is used for the upper bound (Table F-4).

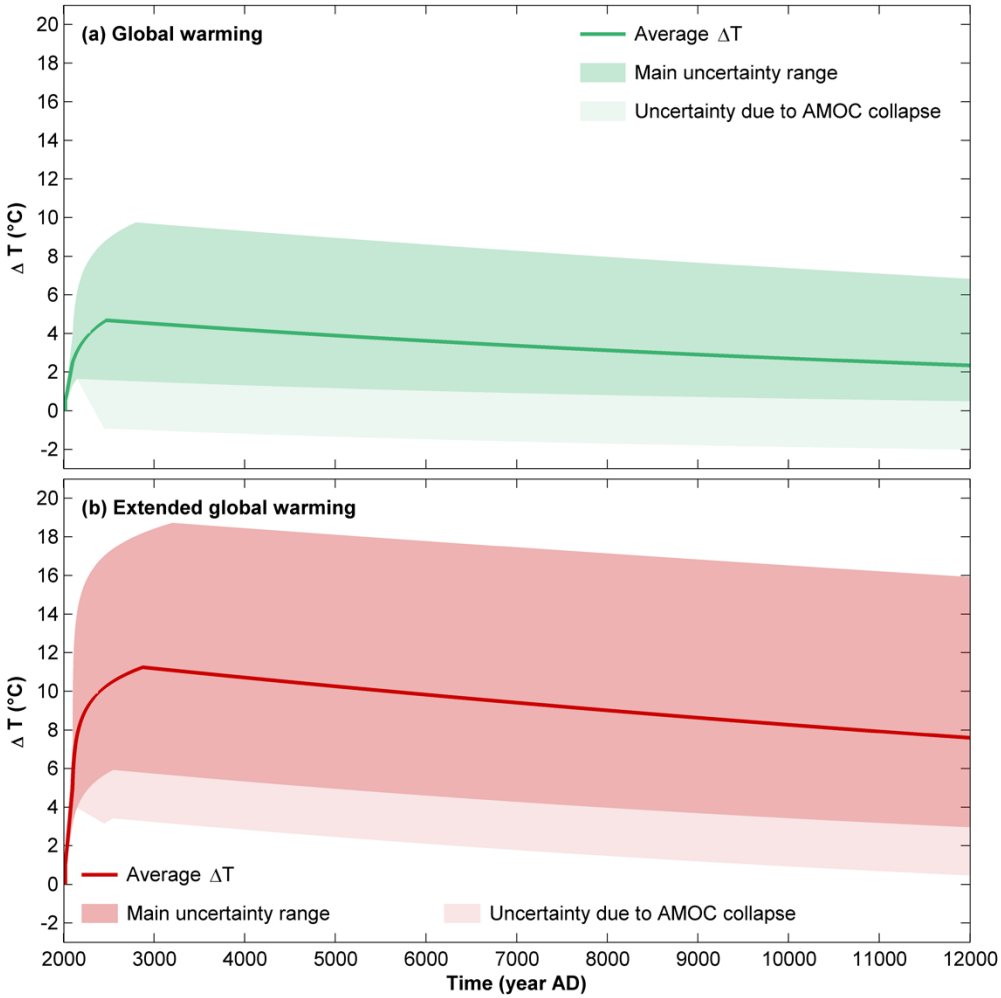

Figure F-4. *Constructed annual mean surface air temperature change until 12000 AD at Forsmark (relative to present) for (a) the global warming and (b) the extended global warming climate cases. The uncertainty ranges are constructed using the global annual mean surface air temperature change (Figure F-3) and the values in Table F-4. The average temperature change ("Average ΔT") has been calculated using average values of the parameters used to construct the lower and upper bounds. To that end, average ΔT illustrates a typical mid-range temperature evolution over the next 12000 AD. The uncertainty range associated with a collapse of the AMOC is illustrated with another colour to highlight the low confidence in the assessment of this uncertainty range.*

F1.3.2 Ocean circulation and AMOC instability

Until 2100 AD

Virtually all climate model projections show that the enhanced 21st century surface air temperature increase at high latitudes is also associated with increased precipitation (Collins et al. 2013). Both of these effects tend to make the high-latitude surface waters less dense and hence increase their stability. All the models included in IPCC AR5 show a weakening of the AMOC over the course of the 21st century (IPCC 2013a), but none of the models show a collapse over this time period. Most models even show a recovery of the AMOC once the greenhouse-gas forcing has stabilised. The recovery may include a significant overshoot if the anthropogenic radiative forcing is eliminated (Wu et al. 2011). The AMOC overshoot could give an extended period of anomalously strong northward heat transport, maintaining warmer northern high latitudes for decades after the atmospheric CO_2 concentration returns to preindustrial values.

Based on the assessment of climate model projections and of understanding from observations and physical mechanisms, IPCC conclude that it is very likely that the AMOC will weaken over the 21st century (Collins et al. 2013). It is however very unlikely that the AMOC will undergo an abrupt transition or collapse in the 21st century (Collins et al. 2013). This was concluded taking both the high latitude temperature and precipitation increase and a possible rapid melting of the Greenland ice-sheet into account.

The weakening of the AMOC in the 21st century contributes to reducing the warming in northern Europe, resulting in a slightly weakened temperature amplification in the area (Section F1.3.1, Collins et al. 2013). To roughly estimate the effect of the weakened AMOC by 2100 AD on the annual mean surface air temperature in the Forsmark region, the projected temperature increase in that region is compared with the projected warming further east at comparable latitudes, i.e. in central Russia. The rationale for this comparison is that central Russia is significantly less influenced by the North Atlantic sector, and hence also the dynamics of AMOC, than the Fennoscandia region. In general, the projected annual mean warming in the Forsmark area is ~1 °C smaller under RCP4.5 and ~1–2 °C under RCP8.5 than the projected warming in central Russia (Figure 12.11 in Collins et al. 2013). It should be emphasised that this methodology to evaluate the AMOC influence on the temperature is highly uncertain and should therefore only be regarded as a broad first-order estimate. In reality, there are also other features that likely contribute to the different warming rates between Fennoscandia and central Russia, e.g. differences due to changes in the atmospheric circulation and/or snow cover.

Beyond 2100 AD

For the centuries and millennia beyond 2100 AD the fate of the AMOC is more uncertain. In an EMIC intercomparison study, all models predicted an almost complete recovery of AMOC by 3000 AD under the low and intermediate RCPs (Zickfeld et al. 2013). However, under RCP8.5 the AMOC response was highly variable among the models; while some models simulate an almost complete recovery, others suggest a more persistent weakening. One of the 12 models even projected a collapse of AMOC under this scenario. A collapsed AMOC beyond 2100 AD was also projected under the high emission scenario (SRES A2, approximately equivalent to RCP8.5) in Mikolajewicz et al. (2007). Pimenoff et al. (2012) reported that the annual mean surface air temperature at the Olkiluoto region in Finland decreases by a total of ~3 °C between ~2150 and 2300 AD as a result of this AMOC collapse.

More recently, Liu et al. (2017) argued that the relatively moderate changes of AMOC in current state-of-the-art climate model projections may be attributed to a common model bias that favours a stable AMOC. In an attempt to adjust for this bias, Liu et al. (2017) reported that the AMOC may collapse also for moderate emission levels (doubling of the atmospheric CO_2 concentration relative to preindustrial). The duration of the AMOC collapse in Liu et al. (2017) is ~300 years and the resulting AMOC-induced temperature reduction is ~3.5 °C in the Forsmark region.

Here the results from Mikolajewicz et al. (2007), Pimenoff et al. (2012) and Liu et al. (2017) are used to construct a second uncertainty range that brackets the lower end of the surface air temperature evolution under the scenario of an AMOC collapse (Figure F-4). Because of the great uncertainties involved regarding the potential existence of an AMOC collapse beyond 2100 AD, and its effect on the Forsmark temperature, the uncertainty range is highlighted with a different colour in Figure F-4. The total annual mean surface air temperature reduction in the Forsmark region as a result of the AMOC collapse is assumed to be 3.5 °C for both the *global warming* and *extended global warming climate cases*. However, because the warming signal at Forsmark is expected to be attenuated by a weakened AMOC by 2100 AD, the effects of a modest AMOC weakening is already included in the main uncertainty range in Figure F-4. As discussed above, it is broadly estimated that the weakening until 2100 AD contributes to reduce the Forsmark temperature by ~1 °C, implying that the "remaining" temperature reduction resulting from a collapse is estimated to be 2.5 °C (Table F-4). The duration of the AMOC collapse is assumed to be 300 years and the collapse is assumed to begin at 2150 AD for both climate cases.

F1.3.3 Seasonal distribution of temperature

A set of future climate projections for Sweden until 2100 AD, performed with a regional climate model, is utilised to estimate the seasonal distribution of the surface air temperature increase at Forsmark. The results are available as seasonal averages for different regions in Sweden. The future projected changes presented for Uppsala County (Sjökvist et al. 2015) are here chosen to represent the projected seasonal change at Forsmark. The results presented by Sjökvist et al. (2015) were obtained using boundary conditions from nine different global climate models under the RCP4.5 and RCP8.5 scenarios. The projected seasonal temperature change is calculated for the period 2070–2099 AD from the ensemble mean across all nine global climate models.

The seasonal distribution of the warming at Forsmark is similar under both the RCP4.5 and RCP8.5 scenarios, i.e. the *global warming* and *extended global warming climate cases* considered here (Table F-5 and Table F-6, respectively): the largest warming occurs during the boreal winter season (December–February), estimated to be 1.2–1.25 times the annual average, and smallest warming occurs during summer (June–August) amounting to 0.8–0.85 times the annual average. During the spring (March–May) and autumn (September–November) the projected warming is more similar to the annual average. The constructed seasonal surface air temperature evolution until 12000 AD is shown in Figure F-5.

Table F-5. Summary of annual and seasonal averages of the constructed surface air temperature change at Forsmark in the *global warming climate case*. The values within square-brackets represent lower and upper bounds of the temperature change whereas the other values represent the average temperature change. The lower bound associated with the potential AMOC collapse (Figure F-4) has been omitted. The seasonal ratios to the annual mean temperature change are derived from Sjökvist et al. (2015); see the text.

Season	Global warming			
	Ratio to annual mean ΔT	ΔT 2100 AD (°C)	Max. ΔT (°C)	ΔT 12000 AD (°C)
Annual mean	1	2.5 [1.3–3.9]	5.0 [2.0–9.8]	2.5 [0.6–6.8]
December – February	1.25	3.1 [1.7–4.9]	6.2 [2.5–12.2]	3.1 [0.7–8.5]
March – May	1.05	2.6 [1.4–4.1]	5.2 [2.1–10.2]	2.6 [0.6–7.2]
June – August	0.8	2.0 [1.1–3.1]	4.0 [1.6–7.8]	2.0 [0.5–5.5]
September – November	0.9	2.2 [1.2–3.5]	4.5 [1.8–8.8]	2.2 [0.5– 6.1]

Table F-6. Summary of annual and seasonal averages of the constructed surface air temperature change at Forsmark in the *extended global warming climate case*. The values within square-brackets represent lower and upper bounds of the temperature change whereas the other values represent the average temperature change. The lower bound associated with the potential AMOC collapse (Figure F-4) has been omitted. The seasonal ratios to the annual mean temperature change are derived from Sjökvist et al. (2015); see the text.

Season	Extended global warming			
	Ratio to annual mean ΔT	ΔT 2100 AD (°C)	Max. ΔT (°C)	ΔT 12000 AD (°C)
Annual mean	1	5.0 [3.1–7.2]	11.2 [5.9–18.7]	7.6 [3.0–15.9]
December – February	1.2	6.0 [3.7–8.6]	13.5 [7.1–22.5]	9.1 [3.6–19.1]
March – May	1	5.0 [3.1–7.2]	11.2 [5.9–18.7]	7.6 [3.0–15.9]
June – August	0.85	4.2 [2.7–6.1]	9.6 [5.0–15.9]	6.4 [2.5–13.5]
September – November	0.95	4.7 [3.0–6.8]	10.7 [5.6–17.8]	7.2 [2.8–15.1]

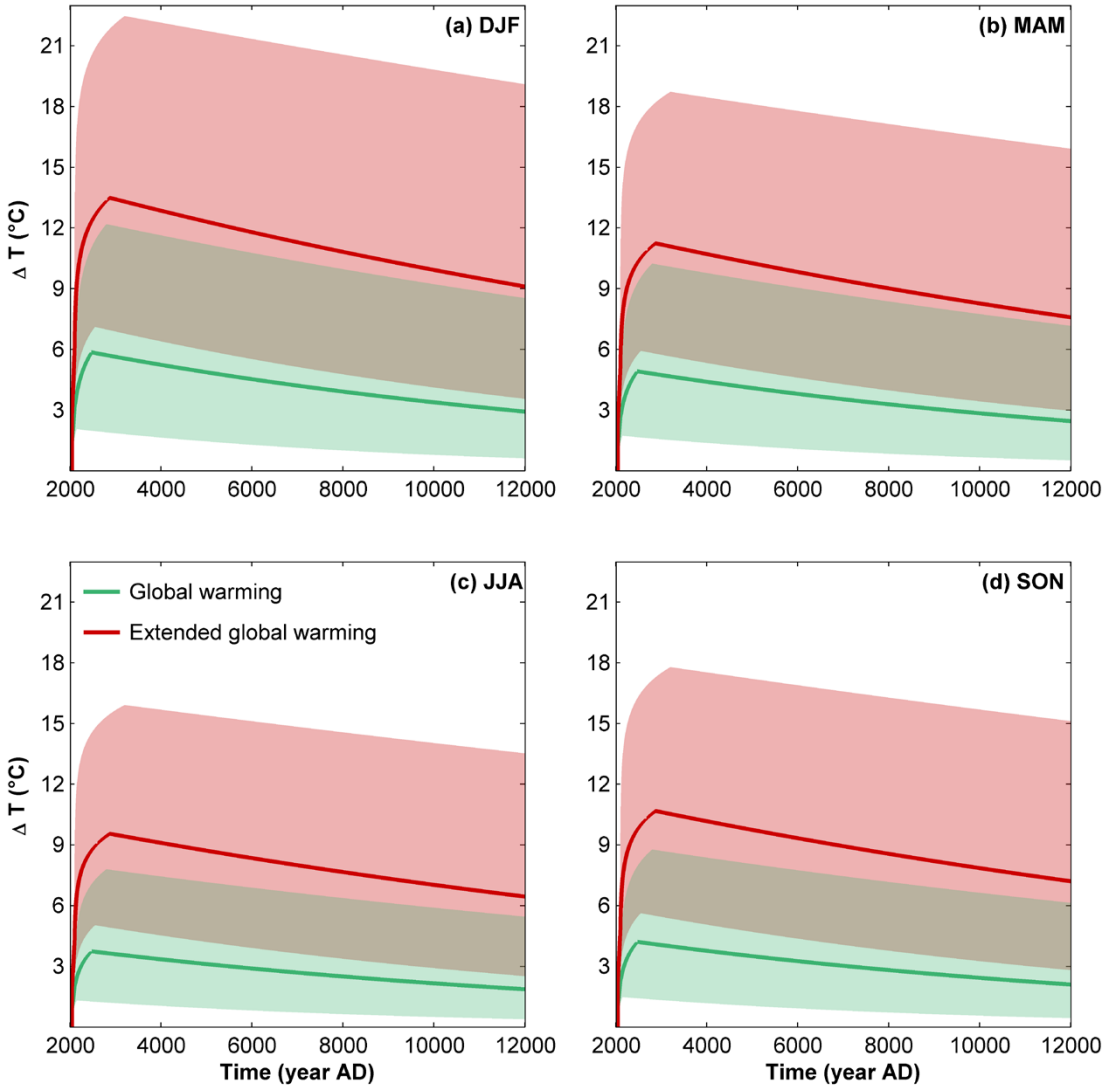

Figure F-5. *Constructed seasonal averages of the surface air temperature change until 12000 AD at Forsmark (relative to present) for (a) the global warming and (b) the extended global warming climate cases. The uncertainty ranges are constructed using the annual mean surface air temperature change (Figure F-4) multiplied by the ratios provided in the second column of Table F-5 and Table F-6. The solid lines have been calculated using average values of the parameter used to construct the lower and upper bounds. To that end, the solid lines illustrate typical mid-range temperature evolutions over the next 12000 AD. Abbreviations in the panel titles are DJF = December–January–February, MAM = March–April–May, JJA = June–July–August and SON = September–October–November.*

F2 Precipitation change at Forsmark until 12000 AD

Most global climate projections show a positive correlation between changes in annual precipitation and surface air temperature for the Forsmark region (e.g. Collins et al. 2013). Hence, any increase of the annual-mean temperature is expected to be accompanied by a higher precipitation. Using the global Earth system model simulations from Mikolajewicz et al. (2007), Pimenoff et al. (2012) found the annual precipitation in the Olkiluoto region increases approximately linearly with the annual mean surface air temperature change at a rate of ~3 % K^{-1}. An approximately linear relationship between changes in precipitation and temperature was also found in the multi-model climate projections of Uppsala County by Sjökvist et al. (2015), but with a slightly higher rate of change (~4.7 % K^{-1}) (Figure F-6).

Here the estimated relationship of changes in precipitation and temperature from Pimenoff et al. (2012) and Sjökvist et al. (2015) are used to construct the lower and upper bounds of the annual precipitation changes at Forsmark until 12000 AD (Table F-7). It should be noted that the precipitation and temperature changes are significantly better correlated in the winter season than in the summer season. The correlation coefficient (r^2) using decadal averages of the Sjökvist et al. (2015) data is ~0.92 in winter but only ~0.65 in summer. This difference is explained by the fact that the winter precipitation mostly comes from large-scale synoptic weather systems that are comparatively well resolved in climate models, whereas the summer precipitation to a larger degree stems from less predictable local convective systems. The constructed annual precipitation changes at Forsmark until 12000 AD are shown in Figure F-7.

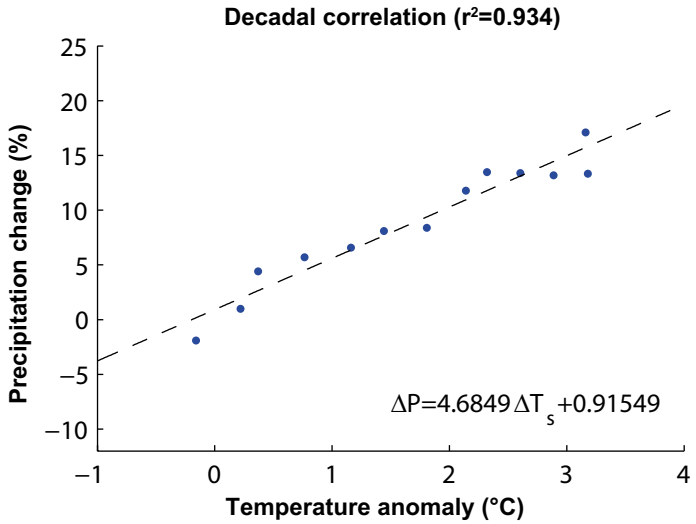

Figure F-6. *Correlation between fractional annual precipitation change (in %) and annual-mean temperature change (in °C) derived from the regional climate modelling data between 1970 and 2099 AD for Uppsala County (Sjökvist et al. 2015). All dots represent the average precipitation and temperature change. Each dot represents a different decadal average of the precipitation and temperature change, calculated from the average change across all 21 ensemble simulations (comprised of nine different global climate models for RCP4.5 and RCP8.5, and three models for RCP2.6). The dashed line represents the linear regression of the data, described by the equation in the bottom-right corner. The correlation coefficient (r^2) is displayed in the figure title.*

Table F-7. Coefficients for constructing the lower and upper bounds, and the average change of the annual precipitation change at Forsmark (relative to present). To obtain the total precipitation change the coefficients are multiplied by the lower and upper bounds and the average change of the Forsmark surface air temperature curves in Figure F-4. The potential effect of an AMOC collapse on the precipitation is omitted in the present analysis.

Global warming			Extended global warming			Based on
Lower bound	Average change	Upper bound	Lower bound	Average change	Upper bound	
3 % K^{-1}	4 % K^{-1}	5 % K^{-1}	3 % K^{-1}	4 % K^{-1}	5 % K^{-1}	Pimenoff et al. (2012), Sjökvist et al. (2015)

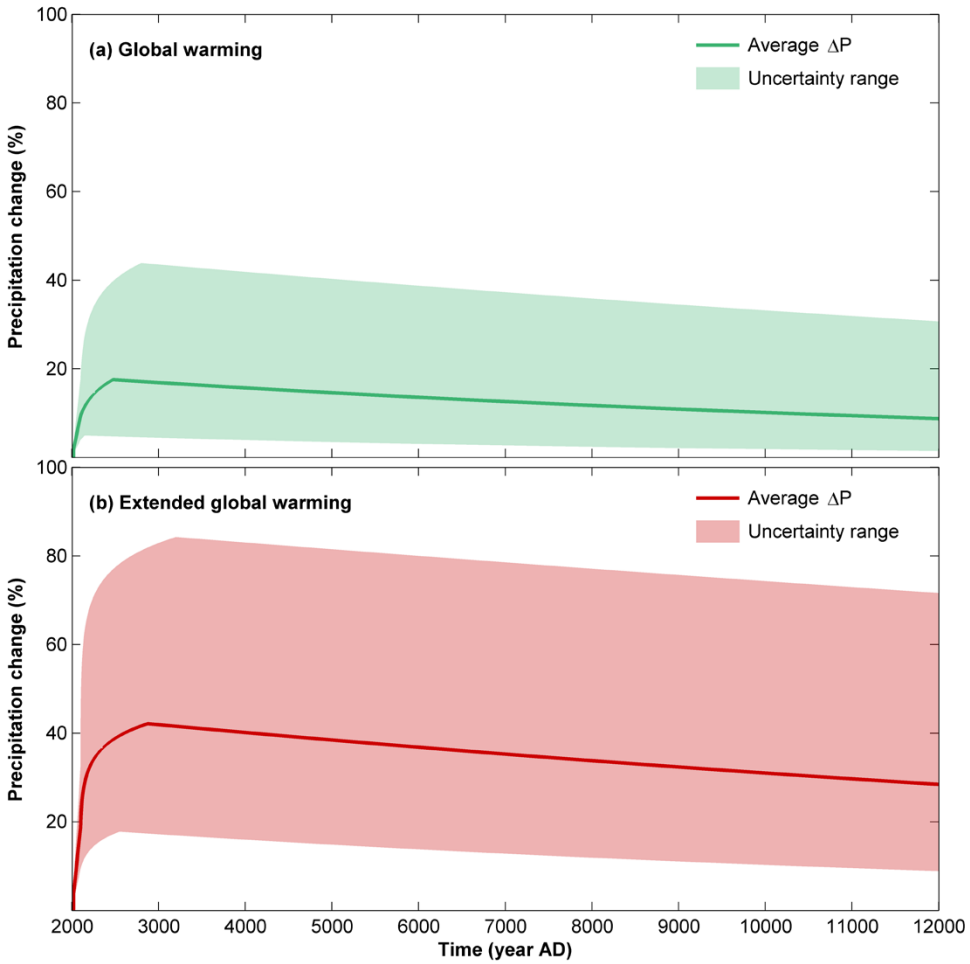

Figure F-7. *Constructed annual precipitation change until 12000 AD at Forsmark (relative to present) for (a) the global warming and (b) the extended global warming climate cases. The uncertainty ranges are constructed using the annual mean surface air temperature change (Figure F-4) and the coefficients in Table F-7. The average precipitation change ("Average ΔP") has been calculated using average values of the parameters used to construct the lower and upper bounds. To that end, average ΔP illustrates a typical mid-range precipitation evolution over the next 12000 AD.*

Appendix G

Total bedrock denudation at Forsmark over the coming 100 ka and 1 Ma

The results on total bedrock surface denudation over the coming 100 ka and 1 Ma as calculated by Hall et al. (2019a), for the higher-confidence future glacial periods of Lord et al. (2019), are presented in Tables G-1 and G-2 respectively. The tables present individual results for the RCP 2.6, 4.5, 8.5 IPCC emission scenarios and for a 'Natural' scenario without carbon emissions, i.e. the tables include the same results as in Figure 5-15 in Hall et al. (2019a). Table G-2 is similar to Table 5-2 in Hall et al. (2019a). The results in Tables G-1 and G-2 are valid under the assumption that typical erosion depths for Forsmark over the past 1 Ma are representative for future erosion depths during the high-confidence ice covered periods modelled by Lord et al. (2019).

Tables G-1 and G-2 also include denudation calculations using two different modes of glacial erosion, 'constant erosion rate' and 'erosion step', as performed within the cosmogenic nuclide analysis. The 'constant erosion rate' simulations assume, as the name implies, a constant glacial erosion rate during the time of ice-sheet coverage (in line with having warm-based erosive conditions at all times of ice coverage), whereas the 'erosion step' simulations assume no erosion up until the deglaciation, and at the time of deglaciation, a constant erosion depth is assumed. This is in line with a development of first having cold-based, non-erosive, conditions, followed by warm-based erosive conditions at the deglaciation. In effect, the two modes describe maximum (constant erosion rate) and a minimum (erosion step) models for glacial erosion. The combined ^{10}Be and ^{26}Al simulations, and the constant erosion rate mode, gives a 25–75 % percentile range of glacial erosion rate of 40–89 mm ka^{-1}, whereas the 5–95 % percentile range is 16–144 mm ka^{-1} (Table G-1 and G-2). Correspondingly, the erosion step mode gives a 25–75 % percentile range of glacial erosion of 0.39–1.09 m per glacial overriding phase, whereas the 5–95 % percentile range is 0.14–1.66 m per glacial overriding phase (Table G-1 and G-2). For further information on the erosion rate and erosion step calculations, see Hall et al. (2019a).

In Table G-1, note that none of the emission scenarios analysed in Lord et al. (2019) result in ice-sheet coverage at Forsmark over the coming 100 ka, and hence all denudation is a results of non-glacial processes (mainly fluvial erosion and chemical- and physical weathering). The one exception from this is the 'Natural' scenario which assumes no carbon emissions. In this scenario, a very short ice covered period of a few thousands of years is present at the very end of the 100 ka period (Lord et al. 2019). The 0.48 m value for the 'Natural' scenario with glacial erosion step mode in Table G-1 is slightly lower than the 0.5 m value for non-glacial conditions over the coming 100 ka. This is caused by the short ice-covered period at the end of the 100 ka period, for which cold-based non-erosive conditions are assumed. The deglaciation, with wet-based erosive conditions, of this glacial phase occurs after the 100 ka period.

Over the coming 1 Ma period, many periods of ice-sheet coverage over Forsmark are suggested by Lord et al. (2019, Figure 4-10). The results also show that glacial inception is delayed for the scenarios with higher carbon emissions. For example, the RCP8.5 high emission scenario results in that ice-free conditions prevail at the Forsmark site until ~400 ka AP (Lord et al. 2019, Figure 4-10), with glacial inception occurring elsewhere in Fennoscandia at ~200 ka AP. This, in turn, results in a significantly shorter total period of ice-sheet coverage at Forsmark over the coming 1 Ma compared to scenarios with lower emissions, and therefore also a shallower denudation depth (since glacial erosion is the most important denudation process). In Table G-2, it is readily seen that the higher-emission scenarios have resulted in lower denudation over the coming 1 Ma.

Table G-1. Projected future total denudation of the Forsmark region over the coming 100 ka based on cosmogenic nuclide-derived simulations of glacial erosion (Hall et al. 2019a) and tentative 'high-confidence' periods of future ice coverage at Forsmark (Lord et al. 2019). The percentiles of denudation are based on combined cosmogenic ^{10}Be and ^{26}Al glacial erosion simulations. For ice-free periods, a non-glacial denudation rate of either 0 mm a^{-1} (for the 25 % and 25 % percentiles) or 5 mm a^{-1} (for the 75 % and 95 % percentiles) have been assumed, resulting in either 0 or 0.5 m of denudation over the coming 100 ka for all scenarios except the 'Natural' scenario, see the text. The results are visualised in Figure 5-15 in Hall et al. (2019a).

	Most likely 100 ka denudation range (m) (25 % and 75 % percentiles)		Wider range 100 ka denudation (m) (5 % and 95 % percentiles)	
Glaciation/ emission scenario (Lord et al. 2019)	**Mode of glacial erosion: glacial erosion rate (40–89 mm ka^{-1})**	**Mode of glacial erosion: glacial erosion step (0.39–1.09 m/glaciation)**	**Mode of glacial erosion: glacial erosion rate (16–144 mm ka^{-1})**	**Mode of glacial erosion: glacial erosion step (0.14–1.66 m/glaciation)**
Natural (no emissions)	0.14–0.79	0–0.48	0.06–0.99	0–0.48
RCP 2.6 (low emissions)	0–0.5	0–0.5	0–0.5	0–0.5
RCP 4.5 (medium emissions)	0–0.5	0–0.5	0–0.5	0–0.5
RCP 8.5 (high emissions)	0–0.5	0–0.5	0–0.5	0–0.5

Table G-2. Projected future total denudation of the Forsmark region over the coming 1 Ma based on cosmogenic nuclide-derived simulations of glacial erosion (Hall et al. 2019a) and tentative 'high-confidence' periods of future ice coverage at Forsmark (Lord et al. 2019). The percentiles of denudation are based on combined cosmogenic ^{10}Be and ^{26}Al glacial erosion simulations. For ice-free periods, a non-glacial denudation rate of either 0 mm a^{-1} (for the 25 % and 25 % percentiles) or 5 mm a^{-1} (for the 75 % and 95 % percentiles) have been assumed. The results are visualised in Figure 5-15 in Hall et al. (2019a). From Hall et al. (2019a) Table 5-2.

	Most likely 1 Ma denudation range (m) (25 % and 75 % percentiles)		Wider range 1 Ma denudation depth (m) (5 % and 95 % percentiles)	
Glaciation/ emission scenario (Lord et al. 2019)	**Mode of glacial erosion: glacial erosion rate (40–89 mm ka^{-1})**	**Mode of glacial erosion: glacial erosion step (0.39–1.09 m/glaciation)**	**Mode of glacial erosion: glacial erosion rate (16–144 mm ka^{-1})**	**Mode of glacial erosion: glacial erosion step (0.14–1.66 m/glaciation)**
Natural (no emissions)	11–28	7–24	4–43	3–35
RCP 2.6 (low emissions)	11–27	8–25	4–42	3–37
RCP 4.5 (medium emissions)	9–24	7–22	4–36	2–32
RCP 8.5 (high emissions)	5–15	5–18	2–21	2–24

Arkitektkopia AB, Bromma, 2020

SKB is responsible for managing spent nuclear fuel and radioactive waste produced by the Swedish nuclear power plants such that man and the environment are protected in the near and distant future.

skb.se